Trigonal Based Copper Sites - A Natural Situation?

Thesis

Trigonal Based Copper Sites - A Natural Situation?

A thesis presented to the Faculty of Science at the
Open University, Milton Keynes

by

Joanne Lyssa Coyle, BSc.

A candidate for the degree of
DOCTOR OF PHILOSOPHY
May 1999

Declaration:

The work described in this thesis was carried out in the Department of Chemistry, The Queen's University, Belfast, between October 1994 and May 1998. The work has not been submitted for any other degree and is the original work of the author, except where acknowledged by reference.

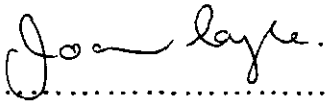

.....

Acknowledgements

First and foremost I would like to thank my supervisor, Professor Jane Nelson for all her excellent guidance, encouragement and especially her patience over the last four years. I am very grateful for her continuing support and friendship and for the many opportunities provided by her, both inside the field of chemistry and outside.

Thanks to the EPSRC and The Open University for providing financial support for this research. A special mention goes to Dr Charlie Harding, who made my visits to Milton Keynes both rewarding and enjoyable.

I was also fortunate to collaborate with some excellent research teams – At QUB I would like to express my thanks to, Professor Vickie McKee for her expertise in crystallography, Professor McGarvey and Dr Colin Coates for their help with Resonance Raman studies and Dr Raewyn Town for assistance with electrochemistry. Thanks to 'Charley' Farley and Chris Rowlands at the National EPR and ENDOR centre, for their hospitality and brave attempts to decipher the ENDOR. Thanks to Professor Hill, Drs. K. Lo and D. Keeley at the New Chemistry Laboratory, Oxford University for collaborating with electrochemistry studies.

I am also grateful to the academic and technical staff at Q.U.B Chemistry Department for helping life to run that little bit smoother. Special mention goes to poor Richard whom I tortured until my NMRs were perfect.

To all my fellow 'Nelson group' students in 1073, Grace, Noreen, Beatrice ("Sorry I'm French") and Yahn, best of luck for the future, I enjoyed working with you all. Good luck to the new members - Big David and wee David, it's easy-NOT!

To the 'old' 1073 gang - so many people coming and going but it was great while it lasted.....

The Friday night 'Bot' crowd comes and goes but the craic is always great! Thanks, Ian, Simon, Alan, Mandy, Stephanie, Yasmin (Yeahhhhhh!), Jennifer, Anthea, Paul, Woody(hands off my man), Jasper, Conor, Farmer, Ted and Hamish.

A special mention goes to the girls- to my close friend, proof reader, shoulder to cry on, Samana. I sincerely thank you and wish you all the best in your new job in Pharmacy. Nicola, the best drinking buddy, ever! Don't stay in Athlone too long. Tona, ever grateful for being the same size, don't stop shopping! Deirdre and Suzi, forever on the pull. To my great

friends, Siobhan, 'down under', Lynsey in Aberdeen, Gemma in Liverpool and soon to be Dr Povy you were my sanity away from the chemistry lab.

To my wonderful parents, grandparents, sister and brother -thank you for your never ending love and support, especially the handouts and taxi service!

Finally to Jim, who had to endure much moaning and groaning preparing this thesis, your poor head was turned! Seriously, you've always been there when I needed you, thanks for everything, love you loads.

Abstract

This thesis is concerned with the synthesis and characterisation of copper model compounds which are of interest in a biological context. These model compounds fall into two main classes; iminopodands and azacryptands.

The iminopodands are derived from the condensation of tris(2-aminoethyl)amine (tren) or tris(3-aminoisopropyl)amine (trpn) and a range of aromatic aldehydes. The compounds invariably co-ordinated Cu(I) and the structural consequences of the flexibility are examined and systematised. Their redox properties have also been studied and correlated with their structure.

The main topic of this thesis concerns average valence dicopper cryptates. The synthesis has been studied in full including a description of likely decomposition and/or by-products. Considerable attention has been given to the spectroscopy of the average valence dicopper cryptates; Resonance Raman, ESR/ENDOR and solution and solid state NMR have been described. Two additional properties which have been given serious attention are the redox chemistry and electron self exchange kinetics because of the relevance of these properties to the natural sites we are attempting to model i.e. the Cu_A site of cytochrome c oxidase.

In the final chapter preliminary experiments to synthesise a thiolate cryptand are reported in an attempt to model a S(cysteine) bridging function now known to exist in Cu_A.

CONTENTS

3A Average Valence Dicopper Complexes, Precursors and Related Compounds

3B: Resonance Raman Study of Average Valence Dicopper Cryptates

3C ENDOR Study of Copper Azacryptates

3D Electrochemistry of Copper Cryptates

CHAPTER 1

INTRODUCTION

1 Introduction

1.1 Copper Proteins and Copper Enzymes

Copper containing proteins and enzymes are known to carry out a wide variety of important biological functions, including: electron transfer, dioxygen binding, transport and activation, copper transport and storage, hydroxylation, dismutation and oxidation.[1]

In an aqueous medium, copper is remarkable among biologically relevant cations for the fact that redox potentials for the transitions Cu(II)/Cu(I) and Cu(I)/Cu(0) are close together.[2] Comparing the Cu(II)/Cu(I) redox potentials of copper proteins with those of other biologically relevant couples, in particular the Fe(III)/Fe(II) redox pairs in functionally analogous iron proteins, reveals mostly higher, more positive, potentials for the copper systems.[3]

Biologically active copper centres from proteins were, for many years, classified as type 1, type 2 and type 3.[4] This classification was originally sufficient to correlate function with spectroscopic properties. However, these correlation's can now be refined and extended due to increasing available structural information. In recent years several additional biological copper centres have been found that do not fit the conventional type 1-3 classification. These are the trinuclear centres[5] and the Cu_A site.[6] **Tables 1.1** and **1.2** summarise the properties of the biological copper centres.

Type 1 copper sites function as electron transfer centres in blue copper proteins.[7] They are characterised by a strong absorption band ($\varepsilon \approx 2000\text{-}5000\ M^{-1}cm^{-1}$) around 600 nm, a very positive redox potential and an unusually small ($< 65 \times 10^{-4} cm^{-1}$) value for the hyperfine coupling constant, $A_{//}$, in the EPR spectra.[8]

Type 2 copper sites have less intense electronic spectral absorptions ($\varepsilon \approx 500\ M^{-1}cm^{-1}$) than type 1 copper proteins. Copper proteins of this type exhibit normal Cu(II) ESR spectra ($g_{//} > g_{\perp} > 2.00$, $A_{//} > 140 \times 10^{-4} cm^{-1}$).[9] Type 2 copper is usually involved in oxidative catalysis during which the substrate reaction intermediate and/or products are co-ordinated to the copper centre.

Type 3 copper centres are characterised by the occurrence of pairs of copper(II) ions which are strongly antiferromagnetically coupled, leading to the absence of any EPR signal.

Proteins containing type 3 copper are involved in the binding and activation of dioxygen, e.g. haemocyanin and tyrosinase.[10]

A trinuclear cluster, formed from a type 3 and a type 2 copper site is present in the active sites of groups of related blue copper oxidases e.g. ascorbate oxidase, laccase and ceruloplasmin.

Cu_A is a recently discovered dinuclear copper site which is involved in electron transfer. It has been found in Nitrous oxide reductase (N_2OR) and Cytochrome c oxidase (COX).[11] The structure and physical properties of mixed-valence dicopper complexes which can function as models of the Cu_A site is the main subject of this present work.

Table 1.1 Properties of Unoxidised Copper Centres in Various Biomolecules

	Type 1	Type 2	Type (2+3) trimer	Type 3	Cu_A
Aggregation state	Mononuclear	Mononuclear	Trinuclear	Dinuclear	Dinuclear
Biological function	Electron transfer	Catalysis and redox reactivity	O_2 activation: oxidase function	O_2 activation: transport and oxygenation	Electron transfer
Occurrence	"blue" copper proteins, eg plastocyanin	amine oxidases, SOD,	ascorbate oxidase, laccase	hemocyanin, tyrosinase	N_2O reductase, COX

Table 1.2 Structural Characteristics and Spectroscopic Characteristics of the Oxidised or Oxygenated form

Typical co-ordination number	3 trigonal planar +1	4 or 5 (square-planar or pyramidal)	Cu^I: 3 (trigonal) Cu^{II} : 4	Cu^I: 3 (trigonal planar)	4
Co-ordinated atoms	S- (Cys-), 2N (His), S(Met)	3 N(His)	N(His) some (O) OH-	2 x 3 N (His) Cu^{II}::u-η^2 η^2- O_2^{2-}	2S- μ (Cys-), 2N (His), S(Met) or O peptide
EPR	Small ^{63}Cu/ ^{65}Cu hyperfine splitting (low g factor)	"Normal" Cu^{II} EPR parameters	"Normal" Cu^{II} EPR parameters	No signal (strong anti-parallel spin-spin coupling)	Very small Cu hyperfine splitting Low g factor
Light *absorption*	Intense *absorption* in the visible LMCT ($Cys^- \rightarrow Cu^{2+}$)	No intense *absorption*, "forbidden" ligand field transition	Intense *absorptions*: LMCT (O_2^{2-} - Cu^{2+})	Intense *absorptions*: LMCT (O_2^{2-} - Cu^{2+})	Absorption in the near IR region (MMCT)

1.2 Cu(II)

The copper(II) ion has a d^9 configuration, and consequently contains one unpaired electron. It is capable of forming complexes with co-ordination numbers of 2 - 8 with 4, 5 and 6 being the most common. In octahedral d^9 complexes the odd electron can occupy either the d_{x2-y2} orbital or the d_{z2} orbital which normally generate Jahn Teller distortions with strongly tetragonal distortion. Five co-ordinate complexes may be either trigonal bipyramidal, square pyramidal or quite often something in between.[12]

Using the Hard-Soft Acid-Base concept, Cu(II) is classified as a reasonably "hard" metal i.e. small and not easily polarisable which preferentially co-ordinates to hard bases e.g. nitrogen and oxygen containing ligands.[13] Complexes with soft donors, such as ; phosphorus-, sulfur- and bromine- containing ligands, can be prepared but are more difficult to handle due to the possibility of redox reactions. These ligands stabilise the softer Cu(I) cation. [14]

The interaction of copper with sulfur-containing ligands such as thiols and disulphides is of biological interest with respect to the blue copper proteins. If no steric factors prevent disulphide formation, the general reaction of Cu(II) with R-SH proceeds according to:[15,16]

$$2Cu(II) + 2RSH \leftrightarrow 2\,[Cu^{II}RS]^{+} + 2H^{+} \leftrightarrow 2Cu^{+} + RSSR + 2H^{+}$$

1.3 Electronic Spectra of Cu (II)

In the absence of X-ray crystallography, information on the geometries of a transition metal cation in its complexes, can be revealed by electronic spectroscopy. This arises due to the nature of the splitting of the d orbital with respect to the ligand field.

Copper(II) complexes give rise to two main types of electronic transitions i.e. pure d-d transitions and charge transfer transitions. The differences in the intensities of the bands observed for the transition metal complexes reflect the nature of the electronic transitions and its compliance with the selection rules which govern these transitions i.e. *Spin and the Laporte selection rule:* Spin selection rules states that $\Delta S = 0$ for allowed transitions and the Laporte selection rules states that *" In a centrosymmetric molecule or ion the only allowed transitions are those accompanied by a change in parity"*. Thus, d-d transitions are very weak if at all present for the free ion.

The situation changes upon complexation:-

Case 1. The ligand field may enforce a metal environment which lacks a centre of symmetry (e.g. tetrahedral) and in this case, the mixing of the d and p orbitals may result in partially allowed weakly intense transitions.

Case 2. If the transition metal ion lies in a centre of symmetry, the d and p orbitals cannot mix and these transitions may only become partially allowed by a much less efficient mechanism involving molecular vibrations called "vibronic".

As a result of these rules the intensity of the d-d transitions in tetrahedral complexes should be substantially larger than those observed for a metal ion in an octahedral geometry since the metal is not at a centre of symmetry.

While a d-d transition involves redistribution of electrons which are mainly localised on the metal atom, there are transitions in which an electron moves from an essentially ligand based orbital to a metal based orbital or *vice versa*. This results in charge being transferred from one part of the co-ordination sphere to another generating so called *charge transfer bands* in the electronic spectra.

For the Cu(II) complexes, if the electron passes from the negatively charged ligand based orbital to a metal based orbital it is referred to as a *Ligand-to-metal charge transfer, LMCT*. As the electron is not localised on the d orbital these transitions are "allowed" electronic transitions in every respect. No selection rule is violated and therefore the absorption intensity is about one thousand times greater than the typical d-d transitions.[17]

This results in typical extinction coefficients for the band type as follows:

Band Type	**ε max/ $M^{-1}cm^{-1}$**
Spin forbidden	< 1
Laporte forbidden d-d	20 - 100
Laporte allowed d-d	~ 250
Symmetry allowed	~ 1000 - 50000

Unlike typical transition metal ions, the Cu(II) ion is reluctant to take up a regular octahedral or tetrahedral stereochemistry. This is because the $3d^9$ outer electronic configuration lacks cubic symmetry and hence yields distorted forms of the stereochemistry. The reason behind this lies in the fact that the Cu^{2+} (d^9); $(t_2g)^6$ $(eg)^3$ configuration is doubly degenerate. If **Case 1** were to exist then the single electron in the dx^2-y^2 orbital would provide less efficient shielding and results in the ligands in the xy plane being more strongly attracted towards the nucleus than the ligands in the z axis and therefore the more screened the electrostatic interaction of the Cu(II) ion. In consequence the complex undergoes axial elongation. In some examples the ligand field is so strong that the axial ligands in the z axis move out to infinity and the four co-ordinate square planar geometry is observed.

Conversely axial contraction holds for **Case 2** when the unpaired electron is placed in the d_{z2} orbital, (**Figure 1.1**).

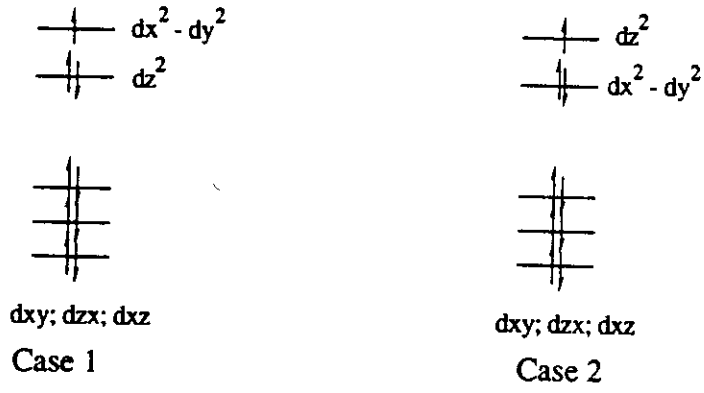

Figure 1.1

Consequently d_{z2} and d_{x2-y2} become differentiated in energy. This is an example of the operation of the *Jahn Teller effect* which states *" that for a non linear molecule that is in an electronic degenerate state, distortions must occur so as to lower symmetry, remove degeneracy and lower the energy"*.

Which case arises in practice is a matter of energetics rather than symmetry, however because the axial elongation affects only two bonds and the planar elongation would weaken

four bonds, axial elongation is more common than axial compression. This is also more favoured sterically.[18,19]

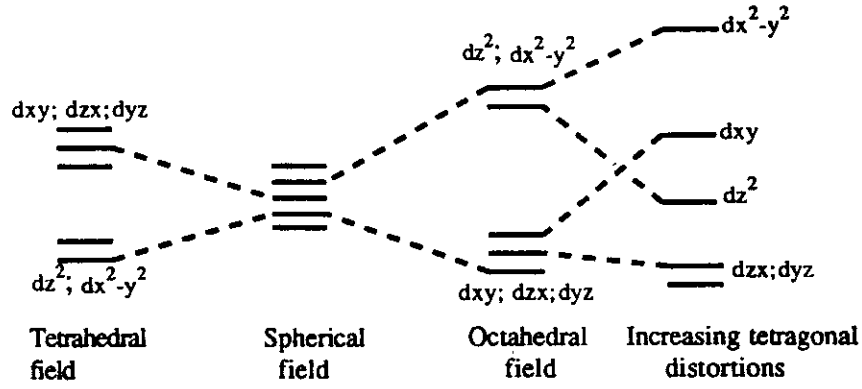

Figure 1.2 An energy level diagram showing the splittings of the d orbitals according to the ligand field applied

Some Cu(II) complexes may seem to be undistorted from the octahedral geometry, however, low temperature ESR studies indicate that in fact both aforementioned distortions are occurring simultaneously. This hopping from one conformation to another is called the *dynamic Jahn Teller effect.*[20]

1.3.1 Trigonal Bipyramid

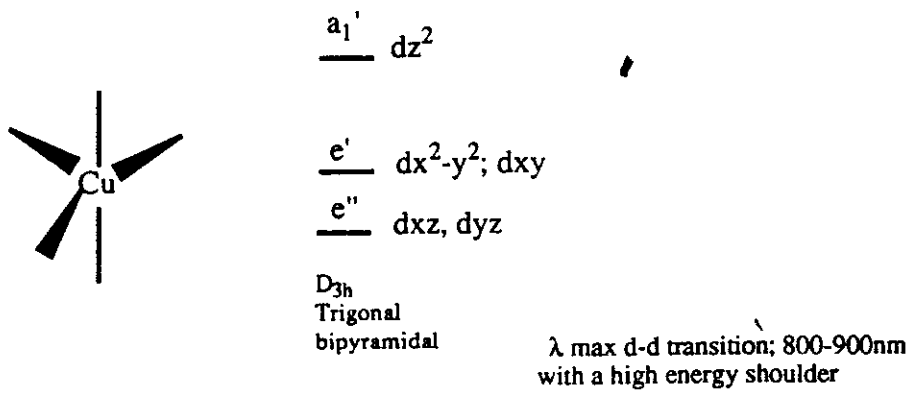

Figure 1.3

In trigonal bipyramid geometry, the d orbital splitting is calculated for D_{3h} symmetry giving rise to three states: $A_1 = z^2$; E" = xz, yz, and E' = xy, x^2-y^2. Therefore only two transitions are predicted i.e. dx^2-y^2, xy → dz^2 and dxz, dyz → dz^2. However, due to Franck Condon vibrational effects these transitions are 'enveloped' into one broad band with a poorly resolved high frequency shoulder.

1.3.2 Square Pyramidal

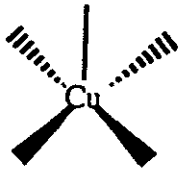

b_1 dx^2-y^2

b_2 dxy

a_1 dz^2

e dxz, dyz

C4v
Square
pyramidal

λ max d-d transition; 650-700nm with a low energy shoulder

Figure 1.4

The square pyramidal geometry has a C_{4v} point group with a d_{x2-y2} ground state. Therefore, three transitions may occur but again the spectra observed are broad typically with a low frequency shoulder.[21]

1.4 ESR of Cu(II)

In the absence of magnetic fields, the unpaired electron of the Cu(II) has two usually degenerate spin states M_I = ½ and - ½. On application of the magnetic field the degeneracy is removed because the magnetic dipoles of the unpaired electrons are aligned with the field. The energy difference is field dependent and when the energy gap gβH equals the frequency of the microwave radiation applied, a net absorption occurs. This results in a absorption peak being

recorded which is usually presented in the first derivative mode to assist resolution as ESR lines are broad. However, a number of factors, namely anisotropy, nuclear Zeemann and zero field effects tend to lead to much more complicated spectra.

1.4.1 Anisotropy

The $g_{//}$ signal is obtained when the magnetic field is oriented along the molecules axial direction (z axis) and $g_{\perp}$ signal is obtained when the field is in the equatorial plane (xy) plane.

The $g_{\perp}$ axes are doubly degenerate and consequently the probability of those transitions are twice as likely as for the $g_{//}$ and therefore $g_{\perp}$ typically exhibits twice the intensity observed in the $g_{//}$ spectrum.

1.4.2 Nuclear Zeemann Effect:

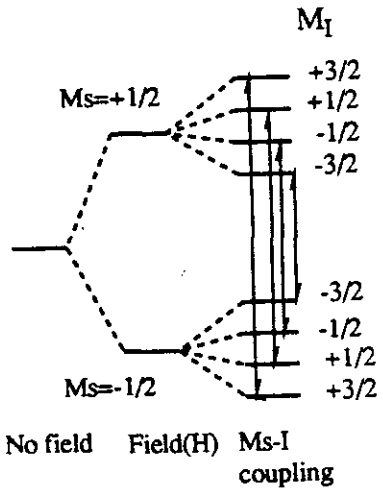

Figure 1.5

If the unpaired electron is associated with a nucleus possessing spin then the energy of the electron will depend on which of the possible nuclear spin states it is coupled to. This gives rise to hyperfine structure consisting of 2I+1 lines of equal intensity, I = nuclear spin state. The copper nucleus has a spin state I = 3/2 and thus a hyperfine pattern of four equally intense lines are produced with hyperfine splitting constant, A, ranging between 120-200 G. The hyperfine

structure is often observed in the $g_{//}$ and rarely in the $g_{\perp}$, but this depends on the geometry. With irregular geometry hyperfine coupling can be seen in both the $g_{//}$ and $g_{\perp}$.

1.4.3 Zero Field Splitting :

For dinuclear complexes in which the magnetic interactions may be mediated via a bridging unit, there may also be further splitting observed resulting from zero field splitting of the triplet state, (**Figure 1.6**). As a result of the triplet state splitting, in addition to the $\Delta m = 1$ transitions, the selection rule forbidden transition $\Delta m = 2$ may also arise as a weakly intense half band. The half band, being isotropic, usually exhibits a simple seven line pattern ($2nI+1 = 7$), n = number of nuclei interacting, arising from the transitions shown below, with a simple 1:2:3:4:3:2:1 ratio of intensities. The hyperfine splitting constant, A, is typically half that observed for the mononuclear Cu(II) spectra, because the unpaired spin is distributed over both nuclei.[22,23]

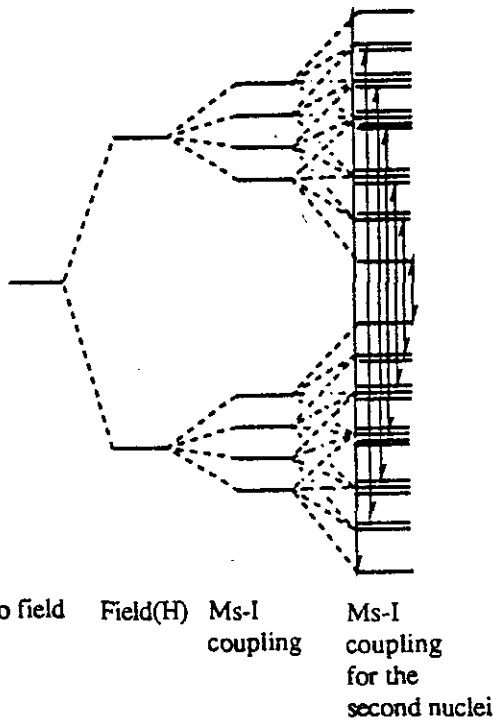

Figure 1.6 Zero field splitting

1.5 Cu(I)

Cu(I) has a filled $3d^{10}$ shell and therefore lacks ligand field stabilisation. The large number of Cu(I) complexes exist in a variety of stereochemistries with co-ordination numbers ranging from 2-5 with 4 predominating. The most common stereochemistries are linear two co-ordinate,[24] trigonal planar three co-ordinate,[25] and tetrahedral four-co-ordinate[26] with possible distortions of these geometries arising in the presence of chelating type ligands.

Cu(I) is regarded as being "softer" than Cu(II) and therefore binds to ligands which contain soft basic donors, *i.e. phosphorus, sulfur and unsaturated nitrogen containing ligands*, increasing the redox potential of Cu(II)/Cu(I) and so favouring Cu(I).[27,28] Aqueous solutions of Cu(I) are unstable due to disproportionation of Cu(I) to Cu(II) and metallic Cu(0), however the nature of the solvent can strongly influence the stability of Cu(I) relative to Cu(II). In acetonitrile it is apparent that the Cu(I) state is relatively stable.[29] Reduction potentials for the Cu(II)/Cu(I) couple tend to be more positive in acetonitrile than in e.g. water or dimethyl sulphoxide.

Reactions of Cu(I) with thiolates often leads to colourless, insoluble, polymeric products, such as Cu_4SR_6, Cu_8SR_{12} and $Cu_{10}SR_{16}$ which are of value in modelling copper metallothioneins.[30]

1.6 Structural Preference and Reactivity of Copper Oxidation States.

Copper is distinguished by redox potentials for the transitions Cu(II)/Cu(I) and Cu(I)/Cu(0) being so close together. Comparing the Cu(II)/Cu(I) redox potentials of copper proteins with those of other biologically relevant couples e.g. Fe(II)/Fe(III), reveals that the copper systems exhibit relatively higher potentials.

As a result of high redox potentials and a tendency for one electron transfer reactions, organocopper compounds are quite reactive.

$$Cu^{+} + e^{-} \rightarrow Cu \qquad E^{0} = +0.52V \qquad (1)$$

$$Cu^{2+} + e^{-} \rightarrow Cu^{+} \qquad E^{0} = +0.15V \qquad (2)$$

Giving

$$2Cu^{+} \rightarrow Cu^{0} + Cu^{2+} \qquad E^{0} = +0.37V \qquad (3)$$

As with other cations with variable valence the formal potential of the Cu(II)/Cu(I) redox couple is dependent on the co-ordination geometry of the metal ion, the nature of the bulk environment, the types of donor atoms and the proximity of electrostatic influences.

1.7 Type 1 Copper Centres (Blue Copper Proteins)

Type 1 copper proteins are ubiquitous electron carriers found in relatively small proteins that contain single copper ions such as plastocyanin and azurin,[31] **(Figure 1.7)**, as well as in complex multicopper oxidases e.g. laccase. The electron is the only known substrate of the blue copper sites, and the small blue copper proteins are generally thought to function as electron transferases. This role is well established for plastocyanin which forms part of the photosynthetic electron transport chain. Azurins, e.g. *A. dentrificans,* functions in the electron transport system of certain bacteria which are cultured anaerobically.[32]

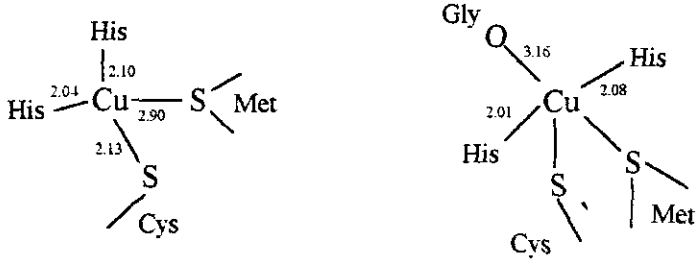

plastocyanin **azurin**

Figure 1.7 Active Sites of Type 1 Copper Proteins

Type 1 copper centres have attracted much interest due to their unique spectroscopic properties, (**Table 1.3**). Unlike ordinary monomeric, tetragonal Cu(II) centres, the blue copper proteins show a strong absorption band around 600 nm with extinction coefficients in excess of

5000 $M^{-1}cm^{-1}$. Interest in the origin of this remarkably intense colour sparked much research into the nature of metal-binding sites in these proteins and has now been assigned to sulfur-to-copper charge transfer. The EPR spectrum of the blue copper proteins exhibit a narrow hyperfine splitting $A_{//}$ of (50-90)x10^{-4} cm^{-1} suggesting that the unpaired electron is more delocalised than in other Cu (II) complexes, (**Figure 1.8**).

Table 1.3 Data for Type 1 Copper Proteins

Protein	E^0 (mV) (pH)	Blue band λ (nm) ε ($M^{-1}cm^{-1}$)	$A_{//}$ (x 10^4 cm^{-1})	Reference
Plastocyanin	+ 370 (7.0)	597 (4500)	63	7
Azurins				
P. Aeroginosa	+ 308	631 (3800)	60	31
A. denitrificans	+ 276 (7.0)	619 (5100)	60	1
Stellacyanin	+ 184 (7.1)	609 (3400)	37	1
Cucumber basic	+ 317 (7.0)	597 (4500)	55	8

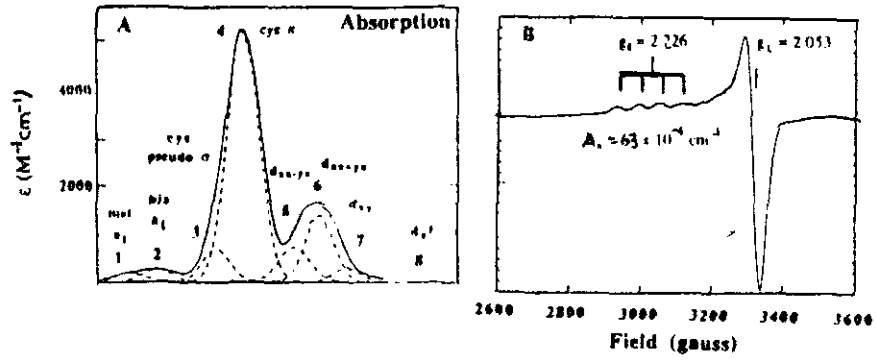

Figure 1.8 (A) shows the low temperature absorption spectrum of plastocyanin. The dashed lines indicate Gaussian band deconvolution of the spectrum. (B) shows the EPR spectrum of spinach plastocyanin.

In 1978, Freeman *et al* published the first crystal structures of plastocyanin.[33] This revealed that in the active sites of the type 1 copper proteins the copper ion is co-ordinated in a distorted tetrahedron or trigonal bipyramid with two histidine nitrogen atoms, a methionine thioether and a cysteine thiolate co-ordinating to the copper ion. The structure of *Pseudomonas aeruginosa azurin* reveals a quite similar overall protein fold. The copper site is similar to that in plastocyanin, although the metal is now five co-ordinate, with the cysteinate and two histidines forming a trigonal plane, and a methionine sulfur and a backbone amide oxygen forming long (≈ 3 Å) axial bonds,[34] **(Figure 1.9)**.

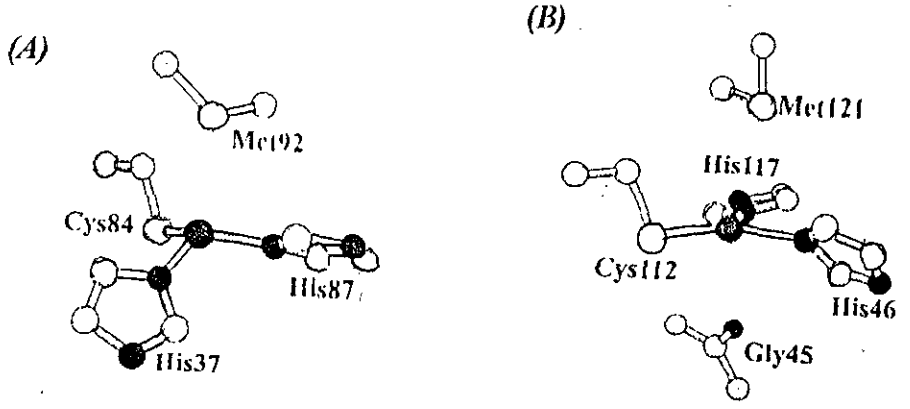

Figure 1.9 Crystal structures of the blue copper site in (A) plastocyanin from Enteromorpha prolifera and (B) Azurin from Pseudomonas aeruginosa at pH 5.5

The fast transfer rates (e.g. $[Cu^{I,II}(Az)]$ k_{ex}, = 2.4 (1.0) x 10^6 $M^{-1}s^{-1}$)[35] and very positive redox potential (**Table 1.3**) of type 1 copper sites have been explained by their distorted co-ordination geometries.[36] It is clear that this geometry is intermediate between the preferences for Cu(II) and Cu(I). This would account for the absence of large rearrangements during electron transfer which keeps the nuclear reorganisation energy at a minimum allowing fast electron transfer kinetics at low driving forces.[37]

1.8 Type 2 Copper Centres

Type 2 copper sites have less intense electronic spectral absorptions ($\varepsilon \approx 500\ M^{-1}cm^{-1}$) than type 1 copper proteins. Copper proteins of this type exhibit normal Cu(II) ESR spectra with large $A_{//}$ ($\sim 200 \times 10^{-4}cm^{-1}$). Type 2 copper is usually involved in oxidative catalysis during which the substrate reaction intermediate, and/or products are co-ordinated to the copper centre.

1.8.1 Galactose oxidase

Galactose oxidase, a mononuclear Cu(II) protein of the type 2 classification, catalyses the oxidation of virtually any primary alcohol to the corresponding aldehyde. This reaction is coupled to the reduction of O_2 to hydrogen peroxide.[38]

$$RCH_2OH + O_2 \rightarrow RCHO + H_2O_2$$

It was originally proposed that the catalytically active, oxidised form of galactose oxidase contains copper in the trivalent oxidation state. The oxidation of the alcohol to the aldehyde was thought to proceed via a two-electron transfer to the Cu(III) form of the enzyme which is thus reduced to the Cu(I) form. It has now been established (by EPR, Xanes and magnetism) that the active site contains a free radical coupled copper complex. This radical complex has been shown by stoichiometric substrate reactions to serve as a two-electron redox unit in galactose oxidase.[39]

The active structure, revealed from the X-ray crystallographic studies, (**Figure 1.10**), shows an unusual protein modification, a cysteine-tyrosine covalently linked at an aromatic ring carbon ortho to the phenolic hydroxyl group. This unusual amino acid side chain forms one of the ligands to the metal centre and further evidence supports the identification of this as a likely candidate for the radical forming site in the enzyme.

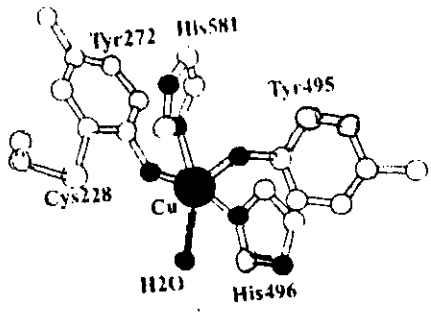

Figure 1.10 ***Crystallographic Structure of the Active Site Metal Complex of Galactose Oxidase.***

Thus, the complimentary information on the existence and characteristics of a free radical in the active site of galactose oxidase from spectroscopic and chemical data, and the recognition of a covalent crosslink in the active site from crystallography, combine to provide insight into the structure of the redox unit.

1.8.2 Dopamine-Beta-Hydroxylase

Dopamine-Beta-Hydroxylase (DBH) is a type 2 copper-ascorbate-dependent monooxygenase which catalyses the benzylic hydroxylation of dopamine to noradrenaline.[40]

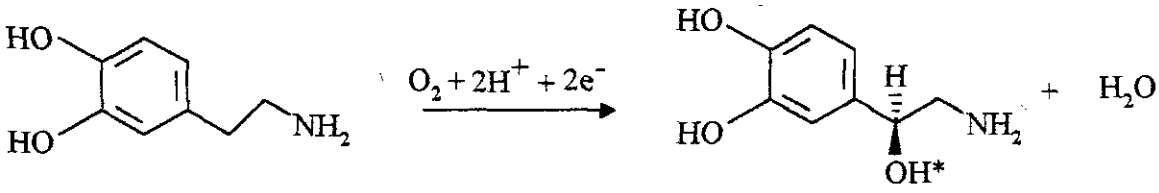

Figure 1.11 ***Benzylic Hydroxylation of Dopamine to Noradrenaline***

The enzyme contains two non-blue type 2 copper atoms per active site with a total of 8 atoms per tetramer. Despite the requirement for two copper centres per catalytic unit there is no evidence for short range magnetic interaction therefore it is believed that each Cu(II) centre is mononuclear. The co-ordination chemistry of the resting Cu(II), probed by ESR and

ESEEM, suggests a site composed of histidine residues with solvent accessible co-ordination positions on one or both of the Cu(II) centres providing binding sites for exogeneous ligands.[41]

The mechanism is known to proceed via a redox process in which 2 Cu(II) centres in the catalytic unit of the resting enzyme are first reduced by ascorbate to a Cu(I) intermediate within which dioxygen binding and substrate hydroxylation takes place.

1.8.3 Superoxide Dismutase (SOD)

The active site of the mixed zinc-copper enzyme, superoxide dismutase, also contains a type 2 copper centre. SOD is a highly efficient enzyme which catalyses the dismutation of potentially toxic superoxide anions to dioxygen and hydrogen peroxide. This is essential for the oxygen tolerance in many organisms.

$$2O_2^{\cdot} + 2H^{+} \rightarrow O_2 + H_2O_2$$

X-ray crystallography has shown, (**Figure 1.12**), that the active site of superoxide dismutase contains a 5 co-ordinate Cu(II) atom, bonded to four imidazole (histidine) nitrogens and an axial water molecule, in a distorted square pyramidal geometry. One imidazole is deprotonated and acts as a bridge between the copper and zinc, which is four co-ordinate in an approximately tetrahedral environment. The imidazolate bridge is not essential for biological activity.[42]

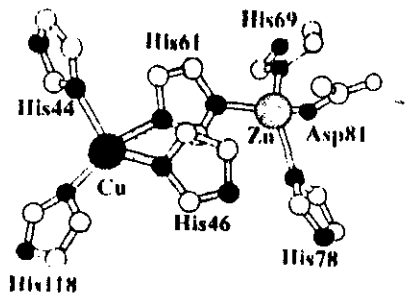

Figure 1.12 Structure of Copper-Zinc Superoxide Dismutase and its Dimetallic Core. For clarity the axial H_2O is omitted.

Metal ion replacement experiments show that the zinc atom may be replaced by copper (or other metals) without the loss of function, and the copper-substituted form (Cu_2Cu_2SOD) has been extensively studied as it provides some information not available from the native enzyme.[8]

1.8.4 Amine Oxidases

Copper-containing amine oxidases, one of the most widely distributed classes of type 2 copper-enzymes, catalyses the oxidative deamination of primary amines.

$$RCH_2NH_2 + O_2 + H_2O \rightarrow RCHO + H_2O_2 + NH_3$$

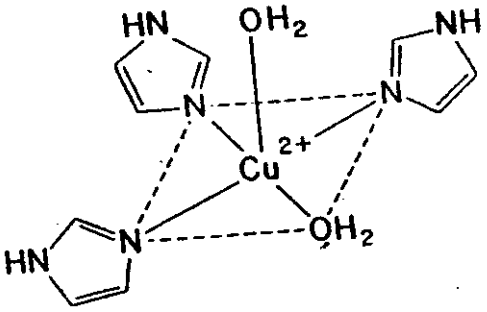

Figure 1.13 A Current Structural Model for the Copper Site in Amine Oxidases.[43]

1.9 Type 3 (ESR non-detectable) Copper

Type 3 copper proteins are characterised by the occurrence of pairs of Cu(II) atoms which are strongly antiferomagnetically coupled. The dicopper(II) site is ESR silent due to the diamagnetism resulting from the strong coupling. Type 3 proteins can act as two-electron donor/acceptors.

1.9.1 Haemocyanin (Hc)

Haemocyanins are high molecular weight O_2-carrying type 3 copper proteins which are found in molluscs and arthropods.[44] Two structures for *deoxyHc* have been reported.[45] The better resolved structure is that of the *L. polyhemus* (horseshoe crab) hexameric protein.[46] The dioxygen-binding site, (**Figure 1.14**), consists of two distorted trigonal, almost coplanar $[Cu^{I}(N.His)_3]$ units whose imidazole rings are staggered across a Cu.....Cu separation of 4.6 Å. The same basic arrangement emerges from the less accurate structure of *P.interruptus* (spiny lobster) hemocyanin.[47] At the lower resolution, the individual $[Cu^{I}(N.His)_3]$ units were reported to be more distorted from trigonal-planar stereochemistry and the Cu...Cu distance is much shorter (3.5 ± 0.3 Å).

The Cu(I) centres have vacant co-ordination sites enabling deoxy Hc to be kinetically efficient in binding O_2. Resonance Raman studies have shown that deoxy Hc reversibly binds one molecule of dioxygen per di-copper site to give a purple complex $[Cu(II)(\mu\text{-}O_2^{2-})Cu(II)]$. Instead of the weak d-d transitions at 600-700 nm normally observed for Cu(II) complexes, the absorption spectrum of oxyhemocyanin exhibits two characteristic bands one at ≈ 580nm with $\varepsilon \approx 1000\ M^{-1}cm^{-1}$ and an intense transition at 350 nm, $\varepsilon \approx 20{,}000\ M^{-1}cm^{-1}$ both attributable to $O_2^{2-} \rightarrow$ Cu(II) LMCT transitions.[48] The O-O stretching vibration determined by resonance Raman spectroscopy and mixed labelling experiments is unusually low (≈ 750 cm^{-1}) while the ν (O-O) value indicated that the dioxygen is bound to the dicopper site as a peroxide ion in a symmetric co-ordination mode.[49]

The two d^9 Cu(II) ions are so very strongly antiferromagnetically coupled that, at room temperature, the dinuclear centre is essentially diamagnetic and undetectable by EPR. Magnetic susceptibility studies showed that this derived from a strong antiferromagnetic coupling between the two Cu(II). This large antiferromagnetic coupling requires orbital overlap between the two Cu(II) and since EXAFS indicated that the coppers are ≈ 3.6 Å apart this must involve a superexchange pathway through a bridging ligand. Crystallography showed that each copper has three histidine ligands but no bridging ligand. Thus it was concluded that the superexchange pathway must be formed on binding dioxygen and oxidising the site.[1]

Kitajima and coworkers synthesised a model complex in which 2 Cu(II) ions were linked by an $\eta^2\eta^2\mu$ -peroxide as discussed in **Chapter 1.15.**[50,51] The spectroscopic properties of this complex, including its Raman spectrum, were found to be strikingly similar to those of oxyhemocyanin. When the crystal structure of *L. polyhemus* in the oxy form was determined, it revealed the presence of just this type of $\eta^2\eta^2$ peroxide moiety.[52]

This is an important example of when a correct structural model compound preceded the determination of the protein structure.

Dinuclear copper sites occur in several other metalloproteins besides hemocyanin, some of which fall into the spectroscopically defined type 3 copper category and all of which are involved in some aspect of O_2 metabolism.

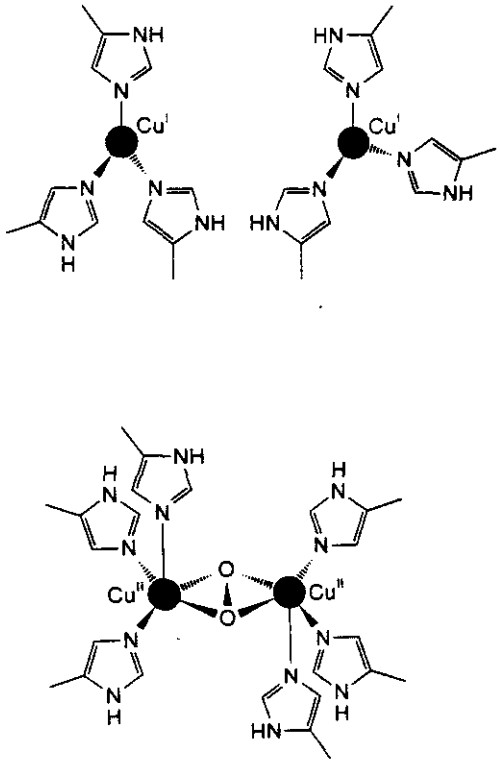

Figure 1.14 Schematic views of the structures of deoxyhemocyanin (top) and oxyhemocyanin (bottom) showing the binding of dioxygen as an $\eta^2\eta^2\mu$-peroxide.

1.9.2 Tyrosinase

Tyrosinase, a mammalian protein, is a mixed function oxidase enzyme which catalyses the two-electron oxidation of o-diphenols to o-quinones (catecholase activity) and the monoxygenation of phenols to o-diphenols.[53] The enzyme contains a binuclear type 3 copper active site, the reduced form of which reversibly binds one mole of dioxygen to produce oxytyrosinase which has spectral features similar to oxyhaemocyanin.

Tyrosinase has the additional feature that the site is highly accessible to substrate analogues which bind directly to a copper centre. This binding involves a structural rearrangement of the copper (from tetragonal to trigonal bipyramidal) which is stabilised by a strong interaction of the substrate with the protein pocket.

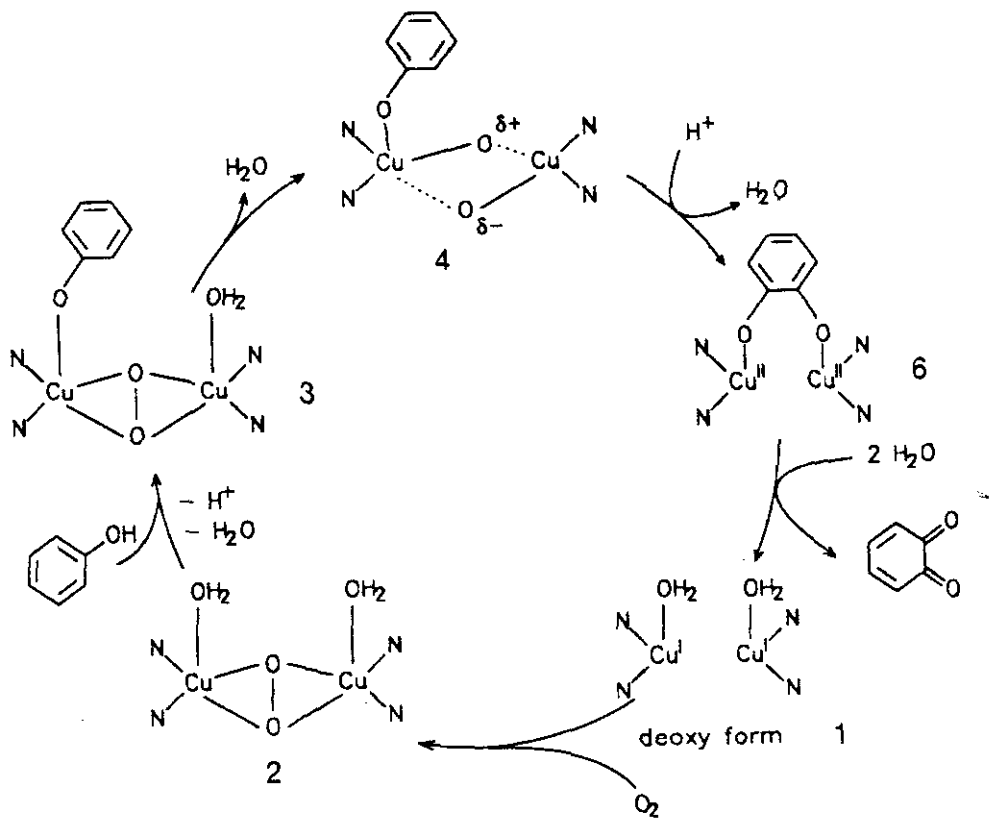

Figure 1.15 Monooxygenation and Oxidation by Tyrosinase.

1.10 Blue Copper Oxidases

The multicopper oxidases, e.g. ascorbate oxidase and laccase, couple the four-electron oxidation of organic susbstrates to the four-electron reduction of O_2 to water.[54] To meet the stringent requirements for multielectron catalysis, these, often dimeric, enzymes contain four copper atoms per subunit, one centre being a separate type 1 copper ion for electron transfer purposes. This type 1 centre is also responsible for the typical blue colour of these enzymes. The remaining three metal ions have a trinuclear arrangement with partially hydroxo-bridged metal centres and metal-metal distances between 3.4 and 5.1 Å, depending upon the co-ordination and on the oxidation state.[55]

Spectroscopic investigations have concentrated on laccase[56] because it is one of the simpler enzymes, containing one of each type of copper site per molecule. Good quality X-ray crystallographic data (1.9 Å resolution) have been obtained for the fully oxidized form of ascorbate oxidase from zucchini.[57] Spectroscopic and crystallographic data showed that the type 2 and type 3 sites are not independent and are better considered together as a single trinuclear site.

Dioxygen binding takes place at the tricopper cluster and reduction of three copper atoms is required in order for it to function. The structure of the ascorbate oxidase tricopper site is illustrated in **Figure 1.16**. The three copper atoms form an almost equilateral triangle of sides ca. 3.7 Å. The Cul and Cu2 atoms are bridged by OH or O^{2-} and make up the EPR-silent type 3 pair. Each copper atom is co-ordinated to three histidine residues and the Cu-N(His) distances are all comparable. In contrast to the heamocyanin active site, the copper ions have approximately tetrahedral co-ordination geometry and are not in identical environments. The third copper ion is co-ordinated to two histidine residues and to either hydroxide or water.

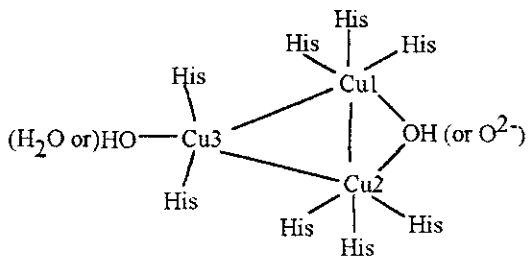

Figure 1.16

Structural determination of the oxidised form, the reduced state, the hydroperoxide-containing oxygenated form, and of bis(azido) derivative have provided the crystallographic basis for a detailed reaction mechanism.[58]

Starting from the completely oxidised, but not oxygenated form, electrons flow from the substrate to the catalytic trimer through the type 1 copper centre. After complete reduction the enzyme reacts with dioxygen to form a hydroperoxo adduct with oxidation of both "type 3" metal centres, one of which serves as a co-ordination site for HOO^-. Close to the transition state of the reaction, an additional intramolecular electron transfer from the remaining two Cu^I centres leads to O-O bond cleavage and to the release of two water molecules.[50]

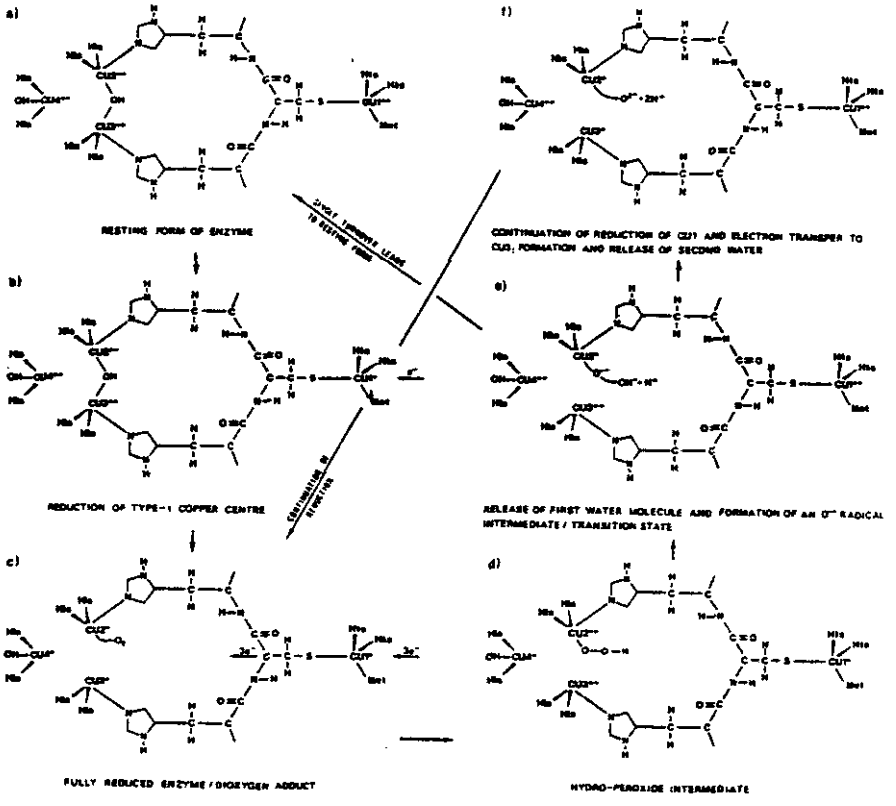

Figure 1.17 Proposal for the Catalytic Mechanism of Ascorbate Oxidase.

1.11 The Cu_A centre

The most recent of the biological copper redox centres to be characterised is the so-called Cu_A site found in cytochrome c oxidase (COX) and nitrous oxide reductase (N_2OR). The Cu_A site has long been recognised as being unusual. This is largely because of its unique EPR spectrum with small and unresolved Cu hyperfine splitting in the $g_{//}$ region and an absorption band at 830 nm associated with a characteristic MCD signal. However, the presence of intense overlapping bands from heme centres always complicates the interpretation of spectral data.[59] While formulated for some time as a mononuclear site, it was first recognised as a binuclear copper centre from ^{63}Cu EPR hyperfine splittings substantiated by Cu EXAFS and fully demonstrated by protein crystallography.[60]

1.11.1 *Cytochrome c oxidase (COX)*

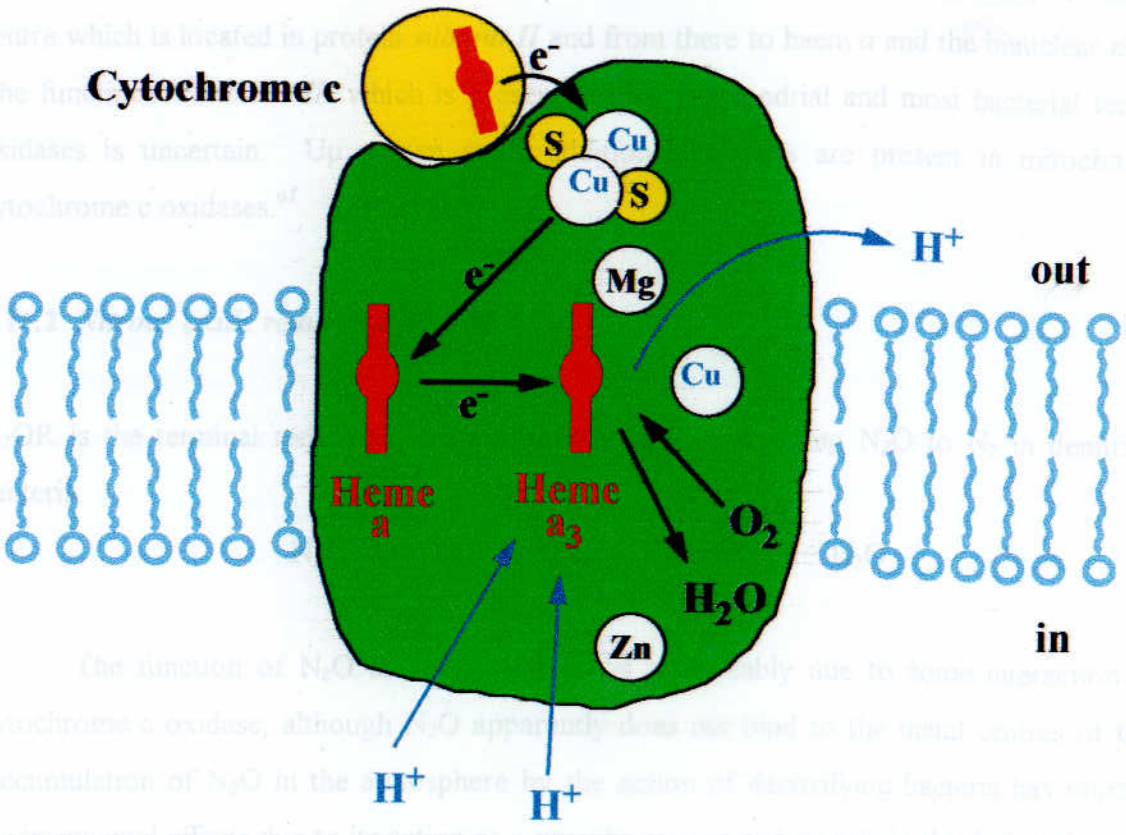

Figure 1.18 Cyctochrome C Oxidase

Cytochrome c oxidase resides in the inner mitochondrial membrane and is responsible (as the terminal enzyme of the respiratory chain) for catalysing the reduction of molecular oxygen to water according to:

$$O_2 + 4Cyt\ c^{2+}_{red} + 8H^+ \rightarrow 2H_2O + 4Cyt\ c^{3+}_{oxd} + 4H^+$$

The cytochrome c oxidases represent a large family of related enzymes which are membrane bound and of various compositions. All species have been found to contain three essential subunits.

Protein *subunit I* of most cytochrome c oxidases contains two haem A molecules, haem a and haem a_3, and copper B (Cu_B). Haem a_3 and Cu_B form a binuclear centre where molecular oxygen is reduced to water. Electrons from cytochrome c are first transferred to the Cu_A centre which is located in protein *subunit II* and from there to haem *a* and the binuclear centre. The function of *subunit III* which is present in all mitochondrial and most bacterial terminal oxidases is uncertain. Up to ten small additional subunits are present in mitochondrial cytochrome c oxidases.[61]

1.11.2 *Nitrous oxide reductase (N_2OR)*

N_2OR is the terminal reductase in a respiratory chain converting N_2O to N_2 in denitrifying bacteria.

$$N_2O + 2e^- + 2H^+ \rightarrow N_2 + H_2O$$

The function of N_2O as an anaesthetic is presumably due to some interaction with cytochrome c oxidase, although N_2O apparently does not bind to the metal centres of COX. Accumulation of N_2O in the atmosphere by the action of denitrifying bacteria has important environmental effects due to its action as a greenhouse gas and its role in the destruction of the ozone layer. The chemistry involved in the binding and activation of N_2O is therefore of considerable interest.[15]

1.11.3 Proposed Models of the Cu_A Center - Pre 1995.

The nature of the Cu_A site has long been a mystery.[62] As early as 1962, Beinert *et al.*[63] discussed the possibility of different copper valencies in COX, making it very different from any copper centre studied at the time. There had been two hypothesis about the detailed structure of Cu_A before the structures of the COX forms were reported in August 1995. One hypothesis relied mainly on information from EXAFS[59,64] while the other was based mostly on other spectroscopic data.

Detailed low frequency EPR studies established that the EPR detectable sites of N_2OR bear close spectroscopic similarities to the Cu_A centre of COX. This has also been proposed from MCD[65], EXAFS and ESEEM evidence. Kroneck first suggested the dimeric [Cu(1.5)...Cu(1.5)], s=½, mixed valence nature of Cu_A on the basis of the 7-line hyperfine splitting in the X-band EPR spectra of N_2OR and the absence of a 'g = 4' signal.[66] The 7-line hyperfine pattern is indicative of an unpaired electron which is able to interact equally between the 2 copper nuclei (I_{Cu} =3/2).

Blackburn *et al*[59] suggested a structure based on results of EXAFS of the soluble Cu_A domain prepared from *Bacillus subtilis* and on comparison to a model compound - a dicopper complex of the macrobicyclic octa-azacryptand ligand of known crystal structure. Like our previously reported analogue[67], this compound showed a short Cu-Cu distance (2.415 Å) and also a characteristic seven-line hyperfine splitting pattern. The model however lacked any sulfur ligands. On the basis of these comparisons the authors proposed a model featuring a short direct Cu-Cu bond, and two terminal His as well as Cys ligands with a 220 pm Cu-Cys distance symmetrically disposed on the Cu atoms, (**Figure 1.19**). It was considered possible that an additional Met and other unidentified residue were more weakly bound to complete a pseudo-4-coordination as expected in analogy to the type 1 Cu centre. This model was supported by a comparison of the resonance Raman spectra with excitation at 480 nm recorded on the soluble Cu_A domain of *B. subtilis*.[68,69]

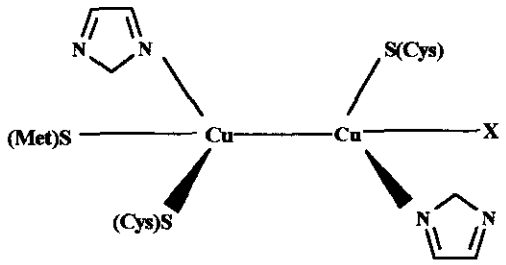

Figure 1.19 Possible Structure for the Dinuclear mixed-valence Cu_A site of COX and N_2OR proposed by Blackburn et al

Henkel *et al* reported findings from EXAFS experiments on intact beef heart COX. With intact oxidase there was an additional complication of a third Cu atom from Cu_B. and particular attention had to be paid to back scattering corrections. They proposed a model compound which contained two Cys as bridging ligands with two His as terminal ligands. A Cys - bridged model was proposed as it was concluded that there was more than two Cu - Cys interactions and this could only be achieved by a bridging model.[59]

Larsson *et al* proposed a model which was very similar to that of Nelson/Blackburn *et al.* They also postulated a Cu - Cu bond but now with asymmetrically disposed pairs of His and Cys ligands.[70]

Thomson *et al* suggested the same model as Larsson but preferred a model that contained bridging Cys ligands and terminal His ligands. This latter model was found to be a correct representation for the Cu_A site based on the X-ray structure obtained from a reconstituted purple fragment from a quinol oxidase. Thomson arrived at these model complexes from calculations based on the MCD features observed with the soluble Cu_A domain of *Paracoccus denitrificans* COX. Their preferred choice of the bridged model was mainly based on observations with the alkaline form of the soluble *Paracoccus* Cu_A domain, in which one His ligand is dissociated, and with a mutant, in which one of the His ligands is replaced with Asn. Both of these forms showed a mixed valence dimer but with localised valence due to the inequivalence of the two copper atoms. It was argued that in a non-bridged structure with one His missing one of the copper atoms would be lost. The only difference of the proposed model to the native structure was the absence of Met and Glu as more distance ligands.[68,71]

In the model the Cu-Cu distance is sufficiently short so that direct Cu-Cu interaction is possible. The model was also supported by extensive resonance Raman studies at 488 nm[72] excitation and by normal co-ordinate analysis[73] of the RR spectra which predicted that in the model with terminal Cys ligation, both of the v(Cu-S) modes lie between 340-350 cm^{-1}, whereas for the Cys-bridged structure intense vibrations at 260 and 339 cm^{-1} are expected as is observed experimentally. Woodruff *et al* studied the soluble Cu_A domains from *Paracoccus* and *B. Subtilis* by far-red RR spectroscopy (850 nm excitation) and concluded that the results strongly suggest the presence of a direct Cu-Cu bond.[74]

1.11.4 Crystallographically Determined Cu_A Structures

Two crystal structures of cytochrome c oxidases, one from *Paraccocus denitrificans* (4 subunits) and another from beef heart (13 subunits)[75] , both at 280-pm resolution, were published with a one-week interval in summer 1995. A few months later M. Wilmanns and coworkers obtained[76], what was described by Holm *et al* as "the most accurate structure of Cu_A"[60] from a soluble fragment of a quinol oxidase into which the binuclear site had been engineered. The structure of this site consists of two distorted tetrahedral co-ordination units bridged by two Cys-S ligands. Terminal co-ordination is completed by one His-N ligand at each copper atom trans to each other, a Met-S ligand at one copper atom and a backbone Glu-Co ligand at the other. The Cu - Cu distance was found to be 2.5 Å which is suggestive of a metal-metal bond. The oxidised site is a purple Cu^{II} Cu^{I} chromophore, described as class III mixed valent, (**Figure 1.20**).

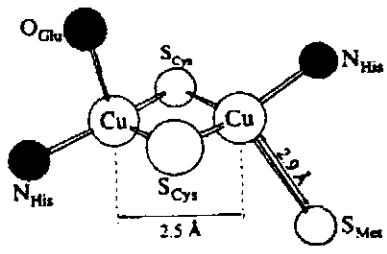

Figure 1.20 Cu_A site

1.12 Model Approach to Biological Copper Complexes.

Limited types of modification can be effected on proteins without disruption of protein structure and/or function. This coupled with their large size and complex structures often make detailed studies of proteins difficult (e.g. X-ray crystallography). It is therefore apparent that model complexes must be used to obtain information on structures and reaction mechanisms which is unavailable directly from studies on the proteins themselves.[77]

The aim of synthetic model studies is to duplicate the spectroscopic features and ultimately the function of the active site in a low molecular weight complex of known structure. This is generally a cyclic process as illustrated in **Figure 1.21**[8]

As understanding of a particular metalloprotein develops, it is often the case that "last years model" quickly becomes redundant. As Hill[78] and later Fenton[79] remarked, the normal progression is from speculative models, through corroborative ones to fully functional synthetic analogues. In modelling metalloproteins, the aim is to mimic the ligation, geometry and possible environment of the active site in question. If this is achieved it should be possible to reproduce the spectroscopic and other properties of the metalloprotein. The relative importance of each of the above factors varies from case to case, as does the relative importance of matching particular properties.

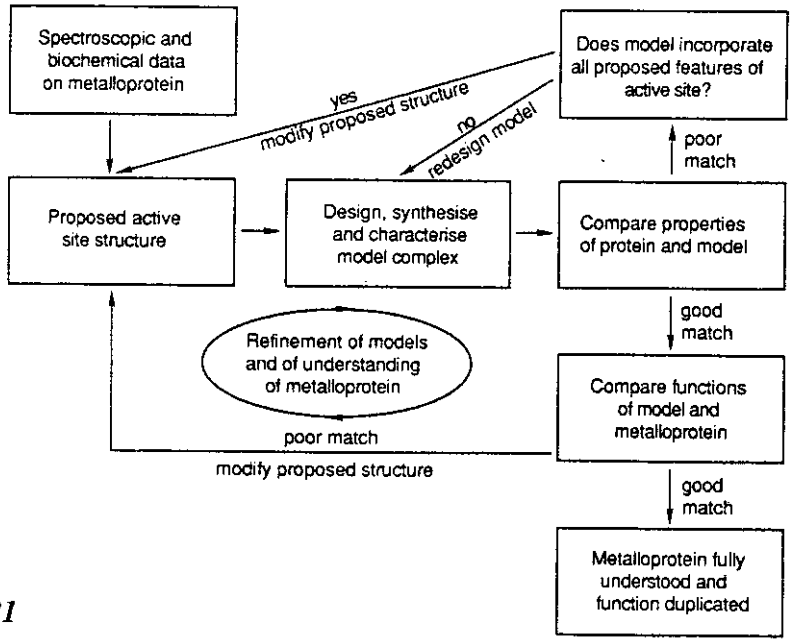

Figure 1.21

1.13 Co-ordination Compounds Related to Type 1 Copper

The typical spectroscopic properties of Type 1 or 'blue' copper proteins have been discussed. Both the intensely blue coloured Cu(II) and the colourless Cu(I) forms of these proteins are remarkably stable.

The structure of the copper binding sites in blue copper proteins was the subject of much research and debate until the structure of plastocyanin was solved. As crystallograpy has revealed much about the copper stereochemistry in the type 1 copper proteins, systematic investigations of the synthesis of low molecular weight copper complexes have gained importance.[80]

A long standing research objective has been to correlate the unusual physicochemical properties of the type 1 copper centres with their structural features. Although significant insight into the electronic structures of these electron carriers has been obtained through combined theoretical and spectroscopic studies, definitive integration of structural and spectral features has been hindered by a lack of suitable model complexes.[81]

The synthetic difficulties involved in the preparation of a Cu(II) complex that simultaneously exhibits : trigonal planar or distorted tetrahedral geometry, thiolate ligation with a short Cu-S bond length, and the appropriate electronic absorption and EPR spectroscopic features are substantial. Often the enforcement of alternative geometry overstabilises Cu(I) - only a narrow range of conditions permit the intermediate CuI/II stability which is so well exploited in biology.

The primary obstacle to modelling type 1 copper proteins with low molecular weight complexes is that the thiolate anion is rapidly oxidised to disulfide in the presence of Cu^{2+}.

$$2Cu^{2+} + 2RS^{-} \rightarrow 2Cu^{+} + RSSR$$

Another obstacle is the preference of Cu(II) to maintain a square planar geometry. If the ligands are not held in a rigid arrangement, Cu(II) will dictate the geometry surrounding it, preferring to adopt a tetragonal geometry.

For the design of model compounds for blue-copper proteins one should ideally incorporate two imidazole nitrogen atoms, a thioether sulphur and a thiolate sulphur. The binding of thiolate groups to Cu(II) is hard to accomplish in low molecular weight compounds due to disulphide formation as mentioned previously. The rigid conformation of the protein with only a single cysteine residue near the copper binding site obviously prevents the formation of the disulphide. Where this steric restriction is absent the cysteine thiolate function is often mimicked by a thioether function.

In 1979, Schugar *et al* succeeded in preparing the first stable CuN_4S(mercaptide) complex, $[Cu(tetb)(o\text{-}SC_6H_4CO_2)].H_2O$. Although it was a significant result at the time, inclusion of a thiolate sulfur was not sufficient to produce the blue copper properties. The copper (tet b) complex was spectroscopically a "normal copper", with no intense 600 nm absorption band and a normal ESR spectrum, and X-ray crystallography revealed a long 2.36 Å Cu-S bond.[82]

Casella *et al* reported the synthesis of a model system that "more faithfully" mimics cysteine thiolate co-ordination.[83] A series of ligands with N_2S_2-donor sets, derived from the condensation of (1R)-3-hydroxymethyleneborane-2-thione and 2-aminothia-alky-1-methyl benzimidazoles, give rise to tetrahedral Cu(II) complexes on the basis of visible and ESR spectral evidence. These Cu(II) systems were the first biomimetic models with N_2SS* donor ligands carrying an overall monopositive charge.

The spectral properties of the systems showed that a significant degree of tetrahedral distortion at Cu(II) can be imposed by lengthening of the carbon chains. Although the spectroscopic properties of the protein blue sites were far from being matched, it was noted that a shift of the LMCT bands towards the red and a decrease in the $A_{//}$ value change more than linearly with the degree of tetrahedral twist away from the square-planar configuration of the Cu(II) centre. Interestingly, the redox potential of the CuII/I couples for the model systems reported lie in the range displayed by the blue sites, showing that the extent of tetrahedral distortion at the metal is not so critical in determining the accessibility to the range of protein redox couples.

Bouwman *et al* have synthesised many copper co-ordination compounds with thioether -imidazole-containing ligands.[80] They found that bidentate NS ligands yielded a variety of

copper co-ordination compounds with mainly distorted octahedral geometry. In most cases the sulphur atom is co-ordinated to the copper ion at various distances although the sulphur atom in these ligands is not forced towards co-ordination of the copper ion through the chelate effect. With the tridentate N_2S ligands, 5 co-ordinate copper compounds were encountered, with geometries varying from trigonal bipyramidal to square pyramidal. The desired N_2SS^* chromophore could be obtained with the N_2S ligands and an extra sulphur donor atom.

As stated earlier, an ideal model compound for blue-copper proteins should contain two imidazole nitrogen atoms, a thioether sulphur and a thiolate sulphur. Bouwman proposed that for the modelling strategy, the N_2S ligands in combination with a thiol group as anion could be the best combination. To prevent oxidation of the thiol group to disulfide either the ligand should contain some bulky groups protecting the thiol function or the thiol function must be electronically constrained. 4-Imidazolyl is an example of an asymmetric tetradentate ligand which incorporates a thiolate function, **Figure 1.22.**

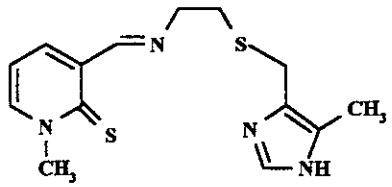

Figure 1.22 4-Imidazolyl (4Im16)

The spectroscopic properties of $[Cu(4Im16)](ClO_4)$ indicate an approximate tetragonal stereochemistry. The stability of this Cu(II) thiolate system is very high, but no crystal structures have been reported.

In the study of tetrahedral Cu(II) complexes of hindered tris(pyrazolyl)-borate ligands, a thiolate derivative of the form [Cu(Sbut)L] has been isolated at low temperature by Kitajima and coworkers.[84] The reaction of $Cu[HB(3,5\text{-}iPr_2pz)_3]_2(OH)_2$ with 2 equivalents of tBuSH was found to proceed smoothly at -20° C. The visible (strong absorption band at 680 nm,ε > 3500 at -16° C) and ESR spectra ($g_{//}$ = 2.21, $g_{\perp}$ = 2.07 and $A_{//}$ = 70 G) of the product

compound are promising for a model for a type 1 copper site, while the X-ray structure of the more stable analogue [$Tp^{t\text{-}Bu}$CuCl] establishes the co-ordination environment as tetrahedral.

Although the redox potential was found to be considerably lower than those of the blue copper proteins, the complexes showed that the striking spectrosocpic characteristics of the blue copper proteins can be mimicked by a simple synthetic model. However, the complexes are very unstable and can be studied only at low temperature (-20° C) and in non-aqueous solvents. This makes characterisation and functional studies such as electron transfer either extremely difficult or impossible.

A complete model system for a blue copper protein has not yet been prepared. However, through model studies, it has been demonstrated that the high redox potential can easily be obtained when sulfur donor atoms are inserted into the ligand. The real problem is in obtaining the small hyperfine splitting constant and the intense absorption in the visible region in low molecular weight model compounds. Some papers report such spectroscopic features on model systems in solution but those observations were described only at extremely low temperatures. At higher temperatures reduction of the Cu(II) ions occur.

1.14 Co-ordination Compounds Related to Type 2 Copper

As discussed in Chapter 1.8, copper proteins with spectroscopic properties characteristic of normal Cu(II) co-ordination compounds are considered to belong to type 2.

Several imidazolate-bridged dicopper(II) complexes have been described in the literature, but only with open chain or monocyclic ligands. The synthesis of a bis(diene) ligand by Lippard[85] and coworkers resulted in the best model of the [Cu_2(II)SOD] active site at that time.

Dicopper(I) complexes of cryptands have also been synthesised as possible models.[86,87] This is an important aspect in modelling this active site since during the catalytic cycle of the superoxide dismutation, the metal in its reduced state remains firmly bound to the ligand.

Few imidazolate-bridged heterobinuclear Cu-Zn complexes have been described.[88,89]. They consist of two independent mononuclear complexes, a Cu(II) and a Zn(II) complex, respectively, connected by an imidazolate bridge between the copper and zinc atoms. Not

only are these non-macrocyclic complexes less stable, the break of the imidazolate bridge would lead to three different molecules.

Pierre and co-workers[90] synthesised imidazolate-bridged dinuclear Cu(II) and imidazolate-bridged heterodinuclear Cu(II)-Zn(II) macrobicyclic complexes as models for superoxide dismutase, **(Figure 1.23)**. The X-ray crystal structures revealed that the Cu-Cu and Cu-Zn distances are 5.95 and 5.93 Å respectively, slightly shorter than the value in the (Cu-Cu)SOD or in the (Cu-Zn)SOD. Magnetic measurements and ESR spectroscopy of the dicopper complex have shown an antiferromagnetic exchange interaction with a coupling constant of -2J = 88 cm^{-1}. Both complexes are stable over large pH ranges but more importantly are capable of catalysing the dismutation of superoxide at biological pH. All the results indicate that these complexes act as good models for superoxide dismutase.

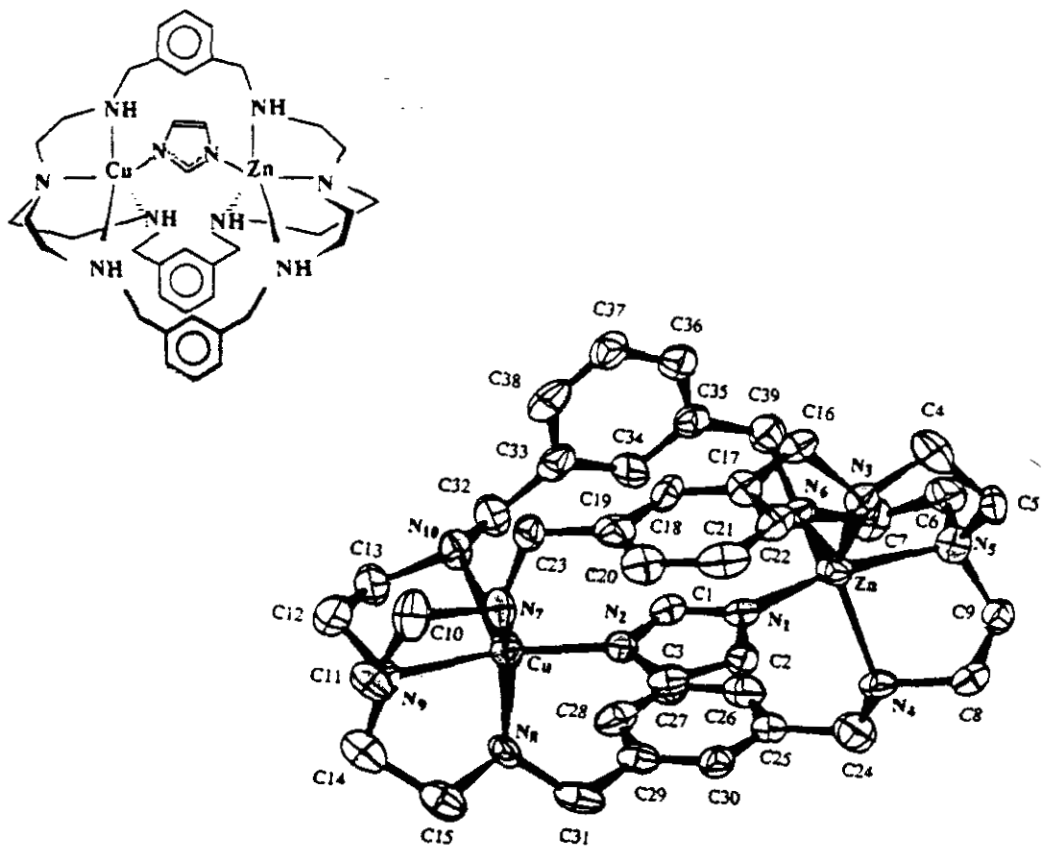

Figure 1.23

1.15 Co-ordination Compounds Related to Type 3 Copper

It is generally accepted that type 3 copper consists of pairs of Cu(II) ions coupled antiferromagnetically. Oxygen binds to the binuclear active site when both the copper atoms are in the Cu(I) state resulting in a Cu^{II}-O_2^{2-}-Cu^{II} adduct. The adduct can further react with the substrate, such as in tyrosinase, or release oxygen reversibly such as in hemocyanin.[3]

Interests in studies of the reactivity of dioxygen with copper ion complexes arises from the fact that copper-containing enzymes in biological systems[91] and copper compounds in synthetic systems have been established to be essential catalysts in oxidation and O_2-mediated reactions.[12] The structural model approach to a binuclear type 3 active site should provide binuclear copper complexes which present a large antiferromagnetic coupling in the Cu(II) state and are able to perform a reversible two-electron transfer. Likewise, binuclear Cu(I) complexes would be of particular interest for reversible oxygenation or catalytic activity in reactions involving molecular oxygen.[92]

1.15.1 Prerequisites for Reversible Binding of Dioxygen by Copper:

Some of the key features required for reversible binding of O_2 by Cu(I) have been reviewed and discussed elsewhere.[93,94] A summary of these is outlined :-

Electronic and co-ordination requirements :

1. The metal should have filled π bonding d-orbitals of intermediate energy to allow partial but not complete electron transfer from Cu(I) to O_2.
2. The co-ordination number and/or stereochemistry around the metal should be variable and compatible with Cu(I) for the deoxy-complex (2 or 3 co-ordinate) and compatible with Cu(II) for the oxy-complex (4 or 5 co-ordinate).

It is also important to suppress the formation of HO_2^- or H_2O_2 by excluding protons, as well as preventing reaction with other reductants to eliminate irreversible O-O bond cleavage.

Systematic variations on ligand systems and reaction conditions can help in the discovery of those factors which are important for reversible O_2 binding and/or activation. It is appropriate/interesting to compare the results of closely related systems.

Karlin and coworkers were successful in identifying and characterising discreet dioxygen-copper adducts. This was achieved by employing ligands and resulting complexes which allow for facile co-ordination and redox changes for both Cu(I) and Cu(II) structures as well as using low temperature syntheses and manipulations.

$[\{(TMPA)Cu\}_2(O_2)]^{2+}$, **(Figure 2.1)**, was the first structurally characterised Cu_2O_2 species.[95,96] It derives from the reaction of $[(TMPA)Cu(RCN)]^+$ with dioxygen at -80 ° C in EtCN or CH_2Cl_2. The binding of dioxygen is reversible with addition of either CO or PPh_3 giving the corresponding adduct. The centrosymmetric complex is best described as a peroxo dicopper(II) species. It contains a trans-μ-1,2-O_2^{2-} group bridging the two Cu(II) ions. The copper atom is pentacoordinate with a distorted trigonal bipyramidal geometry with the peroxo-oxygen atom occupying an axial site.

Karlin was able to synthesise a model complex based exclusively on imidazole nitrogen donors by employing low temperature techniques.[97] The three co-ordinate complex $[L_3Cu]^+$ reacts with dioxygen to give a brown solution of the peroxo-dicopper(II) complex $[\{L_3Cu\}_2(O_2)]^{2+}$, **(Figure 1.24)**.

Sorrell and coworkers developed analogous binuclear Cu(I) and Cu(II) complexes of a ligand, L2, that is nearly identical to a ligand developed by Karlin, L1. 1-pyrazolyl was used in the place of 2-pyridyl, **(Figure 1.24)**. In contrast to the reversible O_2 binding by L1, a binuclear Cu(I) complex of L2 reacts at low temperature irreversibly in a $Cu:O_2$ = 4:1 stoichiometry. Two binuclear units react per dioxygen molecule to give complete reduction of O_2 with O-O bond cleavage.[98] The Cu(I) complex of the pyrazolyl m-xylyl ligand L3, **(Figure 1.24)**, also shows different behaviour with dioxygen. In methanol an irreversible oxidation takes place ($Cu:O_2$ = 4.1) to give a dihydroxy-$Cu(II)_2$ binuclear complex.

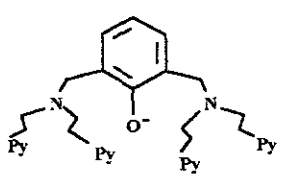

L1

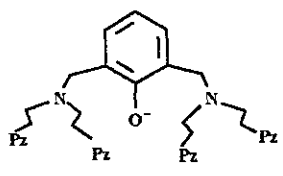

L2

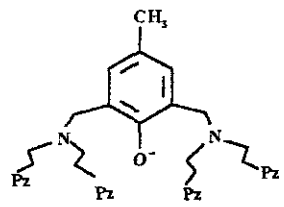

L3

Figure 1.23

Casella and coworkers[99] reported a series dinuclear Cu(I) complexes with the bis(imines) (derivatives of the condensation of benzene-1,3-dicarboxaldehyde and two molecules of histidine), which provide two nitrogen donors to each Cu(I) centre. The corresponding binuclear 4 co-ordinate μ-phenoxo and μ-hydroxo Cu(II) complexes are formed upon oxidation. This reaction mimics the reactivity of the copper monooxygenase tyrosinase.

Reglier and coworkers[100] reported a binuclear Cu(I) complex which features a flexible biphenyl nucleus as a spacer. The latter allows the copper-copper distance to be held at about 3.6 Å so that a dicopper μ-peroxo bridge can be accommodated as in tyrosinase. In the presence of dioxygen the complex exhibits phenolase and catecholase activity, **(Figure 1.25)**.

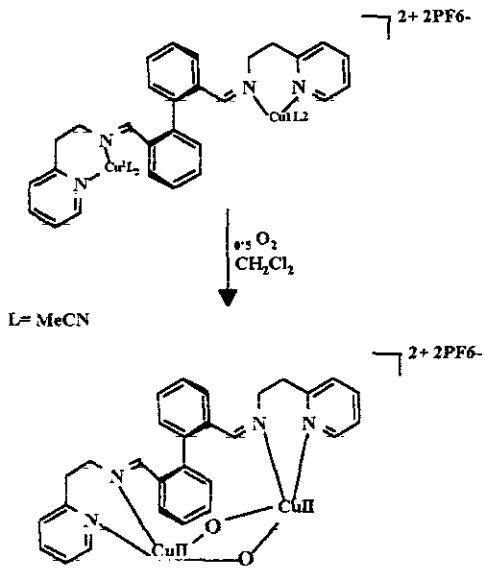

Figure 1.25 Tyrosinase Models featuring a Biphenyl Spacer

Kitajima was successful in elucidating the mode of binding of dioxygen to *deoxyHc*. The model compounds, sterically hinderedtris(pyrazolylborates),[101] were prepared from the reaction of O_2 with the appropriate $Tp^{RR'}Cu^{I}$ precursor or *via* treatment of a dicopper(II)-bis(μ-hydroxo) species with H_2O_2. Initial synthetic efforts focused on using Tp^{Me2} as a supporting ligand in the attempted preparation of a dicopper(II)-peroxo model complex. However the copper complex $[(Tp^{Me2}Cu)_2(O_2)]$, formed was found to readily decompose to the Cu(II)

monomer $Tp_2^{Me2}Cu$.[102] It was concluded that the 3,5-dimethyl substitution pattern on the Tp ligand was insufficient for inhibiting L_2M formation, so more hindered Tp^{Ph2} and $Tp^{i\text{-}Pr2}$ ligands were examined.

The model compounds $[(Tp^{R2}Cu)_2(O_2)]$ (R = Ph or iso-Pr) were found to be significantly more stable than the Tp^{Me2} analogues.[103] The complex persisted in solution below -10° C and was sufficiently stable, as a solid, to allow characterisation by X-ray crystallography at low temperature. The X-ray structure exhibited a novel, planar, side-on-bridged peroxide (μ-η^2:η^2) bound between two square pyramidal Cu(II) ions and encapsulated by a shroud of isopropyl groups from the ligands, **(Figure 1.26)**.

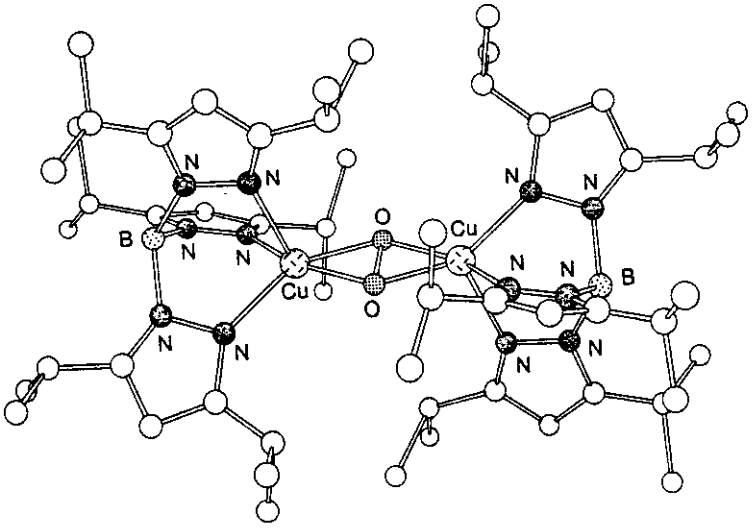

Figure 1.26 X-ray Crystal Structure of $[(Tp^{i\text{-}Pr2}Cu)_2(O_2)]$

The μ-η^2:η^2-peroxo co-ordination mode is rare in transition metal chemistry. Prevention of a square planar metal geometry in the Tp ligand, combined with the ligand field driven preference for tetragonal over tetrahedral co-ordination for the d^9 Cu(II) ion favours the μ-η^2:η^2 mode over another reasonable possibility for a symmetric peroxo ligand, trans-μ-1,2.

The successful isolation of the μ-η^2:η^2 complexes was possible partly due to the intermediate steric properties of the $Tp^{i\text{-}Pr2}$ and Tp^{Ph2} ligands. Both have the necessary high

degree of steric hindrance with which to encapsulate the peroxo moiety and inhibit any destructive side reactions, but they are able to support 5 co-ordinate metal geometries.

1.16 Co-ordination Compounds Related to Trinuclear Copper Centres

In principle, the parameters involved in designing model complexes for polynuclear sites are the same as those for dinuclear systems. Metal-metal interactions in polynuclear active sites can be very complicated and therefore good model systems are necessary for reliable interpretation of spectroscopic and magnetic data.[8]

A number of nonmacrocyclic, triangular tricopper complexes have been synthesised and characterised,[104] frequently showing interesting magnetochemistry. These complexes usually involve a bridging group, usually μ_3-hydroxo, which is largely responsible for maintaining the structure. Discovery of the trinuclear site in the multicopper oxidases has extended interest in modifying these systems so that they model the structure, and ultimately the chemistry, of the metalloenzyme active sites.

Fenton and co-workers have designed ligands in which two pendant arms are added to a dinucleating macrocycle.[105,106] These ligands, e.g. **Figure 1.27A**, were expected to co-ordinate one copper ion in each pyridine-diimine unit, whereas the pendant arms could co-ordinate a third metal atom in a different co-ordination site. The crystal structure of $[Cu_3(OH)(L47)(H_2O)]^{3+}$ is shown in **Figure 1.27B**. The geometry of the cation is unsymmetrical with each copper having a unique donor set and approximately square pyramidal geometry. The major feature of the structure in relation to the copper oxidases is that there is a μ_2-hydroxo bridge linking Cu1 and Cu2 but no direct bridge involving Cu3. The Cu1 - Cu2 distance is 3.62 Å, with the distances to Cu3 longer (4.9 and 5.9 Å for Cu1 and Cu2, respectively). The magnetic moment was reported as 1.66 B.M. per copper, suggesting some antiferromagnetic coupling between Cu1 and Cu2. This complex mimics the broad features of the protein site, a bridged and antiferromagnetically coupled pair of copper ions with a third copper making up a triangular array.

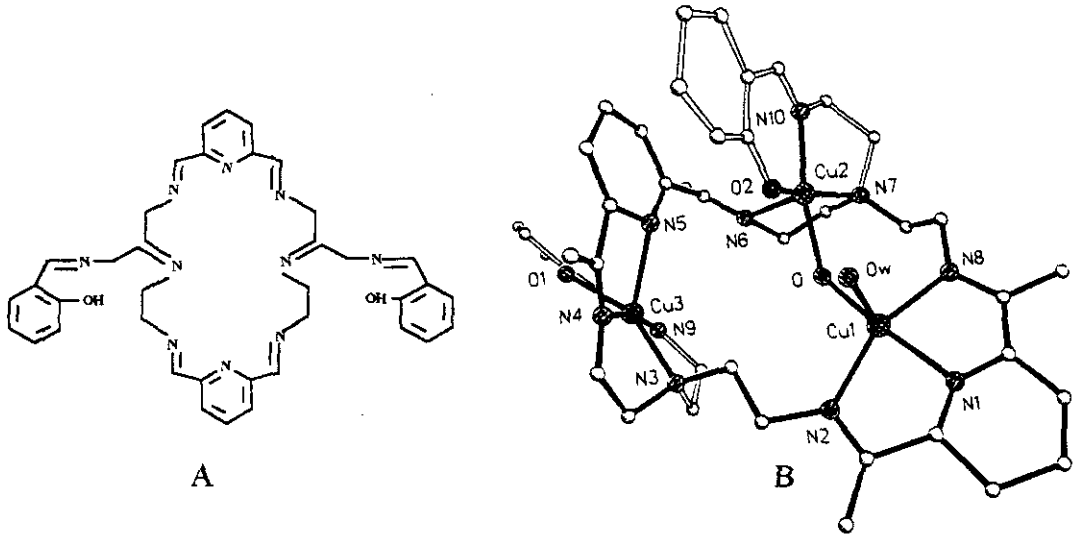

Figure 1.27 ***A. The Bibrachial Ligand H_2L47. B. $[Cu_3(OH)(L47)(H_2O)]^{3+}$***

Karlin *et al* reported a hexanuclear Cu(II) complex derived from a polypodal ligand.[107] There are two approximately isosceles triangular arrays of Cu(II) atoms present and each has a type 3-like pair of copper atoms having a 3.11 Å separation supported by an endogenous phenoxo-bridge derived from the ligand: the third copper is distant from the pair by 7.78 and 7.46 Å, respectively. **Figure 1.28** shows how the trinuclear Cu(I) complex reacts with oxygen to give the hexanuclear cluster (2a) in which L has been hydroxylated to L-O and whose structure has been confirmed by an X-ray crystallographic study of the azide analogue.

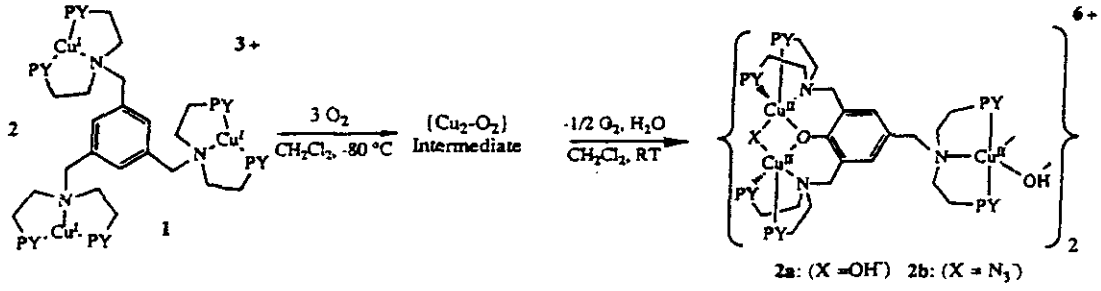

Figure 1.28

Hubberstey *et al*[108] recently reported a trinuclear Cu(I) cation which has several structural features more reminiscent of the trinuclear site of ascorbate oxidase. The trinuclear cation which has approximate two-fold symmetry, is based on a near isosceles triangle of copper atoms, held together by two approximately perpendicular planar tetradentate ligands. The structure is compared to that of the active site of ascorbate oxidase in **Figure 1.29**. They both contain two different types of copper atom and have approximate twofold symmetry. N - ligation predominates in both structures, and the distances between the copper atoms are similar. As a functional model however, this complex may prove to be limited owing to the spatial arrangement of the labile monodentate ligands on Cu(1) and Cu(3). However, the fact that the arrangement of the two cyanoguanidine molecules is distorted to allow hydrogen bond formation suggests sufficient flexibility to permit incorporation of bridging ligands between Cu(1) and Cu(3).

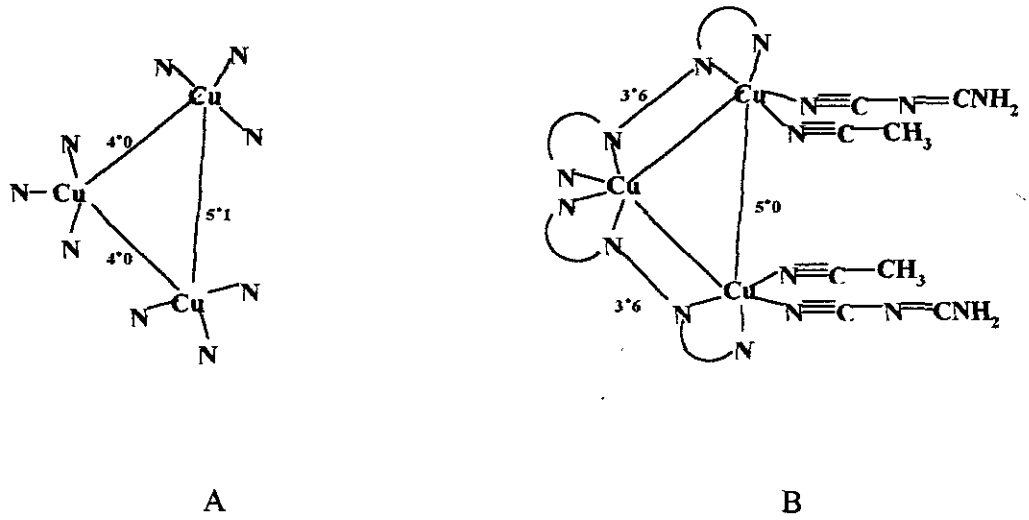

A B

Figure 1.28 A - Trinuclear Site of Ascorbate Oxidase, B - Hubberstey Model

1.17 Mixed Valence Copper

Mixed valence complexes are abundant in chemistry[109,110] and biochemistry.[111] Such systems are of interest because their properties are rarely just the sum of the properties of the two metal ions taken separately. As with resonating organic molecules, there frequently is an "interaction" between the metal ions which results in dramatic changes in the physical properties of the system. Thus, the study of electron transfer in mixed valence transition metal complexes can provide insight into electron transfer in oxidation-reduction, electrochemical and biological processes.

Mixed valence complexes were classified into 3 categories by Robin and Day:[110]

1. **Class I** : The ions of differing valences are in sites of very different symmetry and ligand field strength. i.e. the properties of the individual ions are clearly recognisable.
2. **Class II** : There is a sizeable interaction between the individual ions but the individual ions are still clearly recognisable. Delocalisation takes place but the two types of site are still distinguishable and so the optical electron does not spend equal time on them.
3. **Class III** : MV complexes in which the valences are completely shared and the individual ions are indistinguishable.

Mixed valence copper compounds have been known for a long time but only a few detailed studies have been reported. Many of the complexes belong to Class 1 or 2 including those prepared both chemically and electrochemically by Hendrickson *et al*[112], Gatteschi *et al*[113] and Gagne *et al*[114] as well as the half met forms of type 3 centres in hemocyanins reported by Wetmoreland *et al.*[115] Dunaj-Jurco and coworkers provided a comprehensive survey and classification of the structures for mixed-valence copper complexes in 1988.[116]

The discovery of mixed valence complexes of copper among other redox-active cations, has lead to a large amount of theoretical work.[117,109] As well as the ability to act as semi and sometimes even superconductors, class 1 and 2 mixed valence systems are ideally suited to the

study of innersphere electron transfer.[118] Hush was able to show the close connection to electron transfer reactions and the relation between optical and thermal electron transfer.

1.17.1 Spectroscopic Properties of Mixed Valence Copper Centres

The most obvious and striking feature of any mixed valence compounds is the presence of intense absorption in the visible region of the spectrum, not present in compounds containing either valence state alone.

1.17.2 EPR spectra

$Cu^{I}Cu^{II}$ mixed valence copper dimers have an odd number of electrons and exist in the S = ½ state. They are readily classified by the hyperfine structure displayed in their EPR spectra.

In **Class I** complexes the probability of finding the unpaired electron at the Cu(I) site is effectively zero and the EPR spectrum resembles that of a mononuclear Cu(II) complex i.e. four lines.

In **Class II** there is a non-zero but unequal probability of finding the odd electron on either site. This leads to two different sets of hyperfine couplings and many lines can be observed depending on a given molecular orientation.

In **Class III** complexes the probability of finding the odd electron on either site is identical. Thus the electron interacts equally strong with both copper nuclei resulting in a seven-line hyperfine pattern.

The localisation/delocalisation pattern depends on the measurement temperature and the 'time scale' of the method used to probe it. In intermediate Class II/III situations complicated patterns can arise.[112]

1.17.3 *Characteristics of the Four Classes of Mixed Valence Compounds.*

CLASS I	CLASS II	CLASS IIIA (discrete structure)	CLASS IIIB (extended structures)
Metal ions in ligand fields of different symmetry and/or strength	Metal ions in ligand fields of almost identical symmetry.	Metal ions indistinguishable but grouped into polynuclear clusters	All metal ions indistinguishable
$\alpha = 0$; valences very firmly trapped	$\alpha > 0$; valences distinguishable, some delocalisation	α maximally local	α maximal; complete delocalisation over the cation sublattice.
No mixed valence transitions in the visible region	One or more mixed valence transitions in the visible region	One or more mixed valence transitions in the visible or NIR region : intense	Absorption edge in the infrared, opaque with metallic reflectivity in the visible region
Clearly shows spectra of constituent ions.	Shows spectra of constituent ions at very nearly their normal frequencies	Spectra of constituent ions not discernible	Spectra of constituent ions not discernible
Magnetically dilute, paramagnetic or diamagnetic to very low temperature	Magnetically dilute, with both ferromagnetic and antiferromagnetic interactions at low temperatures	Magnetically dilute	Either ferromagnetic with a high Curie temperature or diamagnetic, depending upon the presence or absence of local moments

1.18 Mixed Valence Properties of the Cu_A Site

The recent X-ray crystallographic results along with spectroscopic and biochemical studies helped to resolve the controversy surrounding the structure of Cu_A. As discussed in Chapter 1.11.3 the combined data support a novel dithiolate-bridged delocalised mixed valence ($Cu^{1.5}$-$Cu^{1.5}$) resting-state formulation with 4 co-ordinate distorted tetrahedral copper ions in close proximity (2.6 Å apart).[119] The electronic structure of this novel mixed valence copper-thiolate centre is of considerable interest.

The elucidation of the structure of the Cu_A centre was achieved more readily from experiments on N_2OR. Initial experiments on COX had shown that at least two different species of Cu were constituents of COX and that adventitious contaminating Cu had caused much of the early confusion.

However, the similarity between the Cu_A centres in COX and N_2OR became apparent by comparison of the room temperature MCD spectrum of N_2OR and low temperature MCD spectrum of Cu_A.[120] Thomson *et al* later confirmed this by comparison of the MCD of N_2OR at low temperature. [121]

Spectroscopic Characteristics:

1.18.1 EPR

The unusual EPR characteristics of the oxidised Cu_A centres had previously been attributed to the co-ordination of 2 cysteinate ligands at one Cu(II) centre.[122] The possibility that Cu_A is a dinuclear copper centre was raised when Kroneck and coworkers demonstrated that N_2OR contains, in the resting state, a Cu_A-like centre having an EPR spectrum similar to that of COX but with some resolved copper hyperfine coupling at $g_{//}$, **(Figure 1.30)**.

The seven-line hyperfine pattern has been analysed in detail at several microwave frequencies and has been shown to be characteristic of a single unpaired electron interacting with 2 equivalent copper nuclei. [123] This indicated that Cu_A is a mixed valence class IIIA dimer in which both copper ions must be equivalent. Thus the Cu_A centre is best described by the term average valence.

Results from EXAFS[59] and from X-ray crystallography[61] verify the two-copper nature of Cu_A.

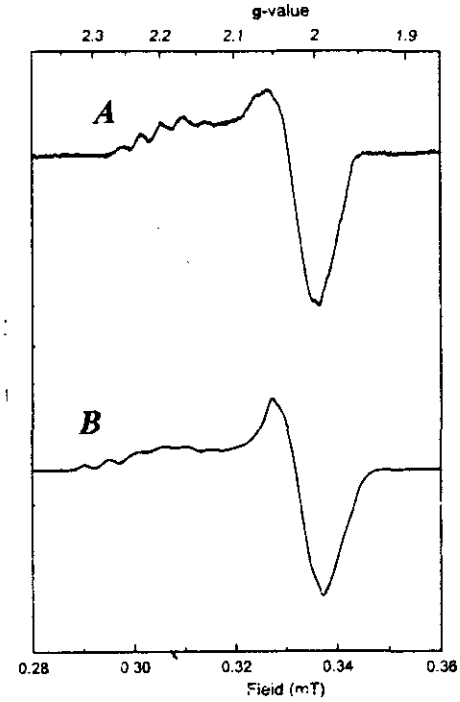

Figure 1.30 EPR spectrum of N_2OR (A) and Cu_A* of purple CyoA (B)

1.18.2 Optical Properties

In COX the optical properties of Cu_A are obscured in part by intense and overlapping transitions from the two cytochromes, a and a_3. The only absorption band which could be assigned to Cu_A was a peak at ~830 nm. Thomson used low temperature MCD characterisation to deconvolute the contribution of low spin heme from that of Cu_A. The application of a novel optical microwave double resonance method confirmed the presence of optical transitions of Cu_A at 480 nm and 520 nm, lying below the heme absorption MCD.

Thomson *et al* gathered a wide range of absorptions, MCD and CD spectra as well as EPR spectra for both Cu_A and Cu_A* (a Cu_A binding site engineered into the soluble domain of subunit II from the quinol oxidase of *Escherichia coli*) They showed that the electronic structures of the Cu_A and Cu_A* sites are different and identified the likely structural variation that cause these differences[124], (**Figure 1.31**).

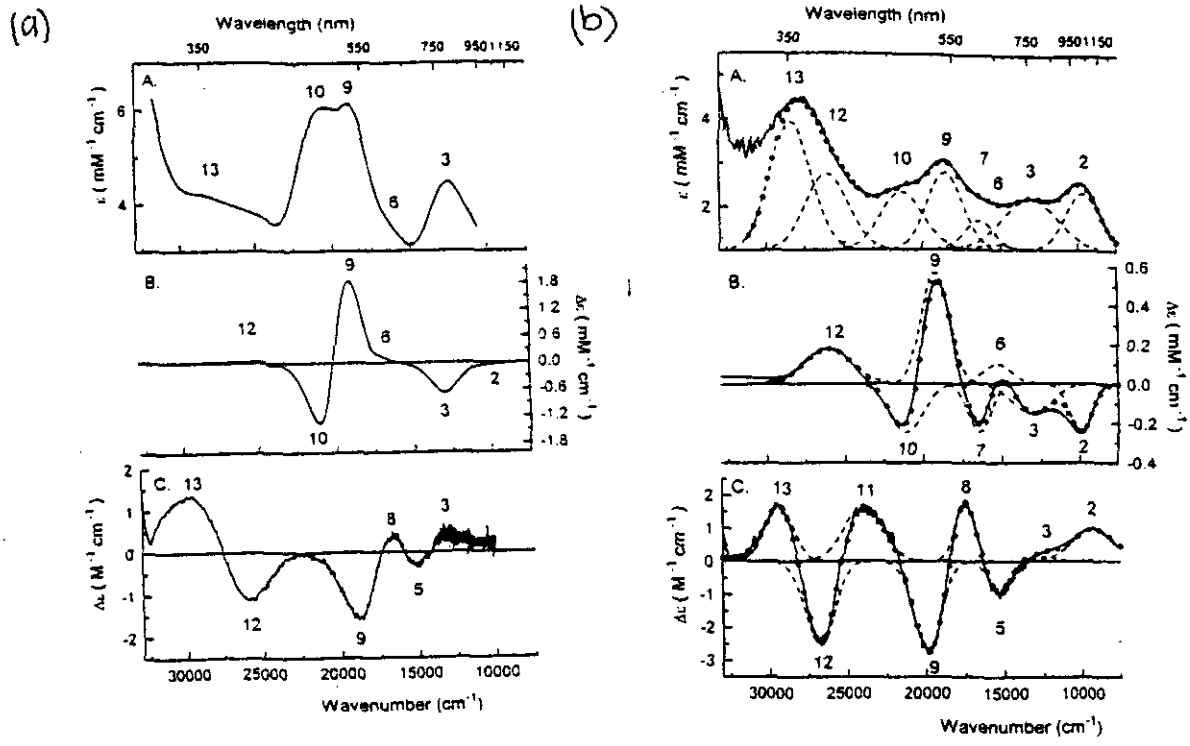

Figure 1.31 (a) Optical data of N_2OR V and (b) purple CyoA from 33 000 cm^{-1} to 7500 cm^{-1} (A) RT absorbance spectrum, (B) 4.2 K MCD spectrum. (C) RT CD spectrum

1.18.3 Resonance Raman (RR) Study of Cu_A

As discussed, structural studies show a short Cu-Cu distance ~2.6 Å which is unprecedented in biological copper systems. Woodruff *et al* addressed the question whether there is an actual Cu-Cu bond in addition to the 2 thiolate bridges between the copper atoms.[125]

The electronic transition of Cu_A near 830 nm provided the opportunity for excitation of specific RR observations of the vibrations of this chromophore. RR experiments were performed on Cu isotopically substituted, genetically modified forms of Cu_A from *Bacillus subtilis* and *Paracoccus denitrificans*. The Cu_A site of native beef heart was probed for comparison, **(Table 1.4).**

The blue RR study of Cu_A by Sanders-Loehr and coworkers,[126] showed that peaks below 200 cm^{-1} were not significantly enhanced and no attempt was made to assign them to specific modes. However, excitation into the band at ~830 nm enhances the peak below 200 cm^{-1} indicating that vibrations below 200 cm^{-1} may be associated with vibrations of a Cu-Cu bond.

Table 1.4 Cu_A resonance Raman isotope shift data (reproduced from 126)

Observed frequency[a]	Observed $^{63/65}$Cu isotope shift[a/b]	Predicted[c] $^{63/65}$Cu isotope shift[a]
	P. denitrificans	
139	1.9	2.0 (Cu-Cu) 0.7 (Cu-S) 1.1 (Cu-N)
261	1.1	4.2 (Cu-Cu) 1.4 (Cu-S) 2.1 (Cu-N)
339	1.3	5.4 (Cu-Cu) 1.8 (Cu-S) 2.8 (Cu-N)
125	2.3	2.0 (Cu-Cu)
258	0.8	0.7 (Cu-S)
340	0.8	1.1 (Cu-N)

[a]All values reported in units of cm^{-1}. [b]Estimated error ±0.3. [c]Predicted isotope shifts calculated using the harmonic oscillator approximation for a diatomic molecule.

$^{63/65}$Cu isotope labelling experiments indicated that the peaks at 125 and 139 cm^{-1} contained most Cu-Cu stretching vibrational character. The RR excitation profiles are consistent with this assignment. While this evidence is indicative of a Cu-Cu bonded structure neither of these observations constitute conclusive evidence as to whether Cu atoms are bonded or non-bonded. This is because Cu-S-Cu modes could be expected in similar regions with similar isotopic shifts to Cu-Cu modes. However, the frequency location of this peak compared to Cu-Cu stretching frequency assigned in the model complexes, is not incompatible with a direct Cu-Cu bond in addition to the thiolate bridges.

Synthetic Mixed Valence Dicopper Complexes

1.19 Delocalised Mixed-Valence Dicopper Complexes - Potential Cu_A Site Models

The identification of a Class III mixed valence copper dimer at the Cu_A site in N_2OR has stimulated the synthesis of four mixed valence dicopper compounds which show delocalised behaviour.

1.20 Tolman's model

Although several complexes with bis(μ-thiolato)dicopper (I,I) cores are known,[127] fully delocalised 'Class III' mixed-valence dicopper (I, II) complexes are extremely rare, and no example of such a species bridged by thiolates has appeared in the literature. Tolman *et al*[119] reported the successful synthesis and characterisation of a unique molecule with a $[Cu_2(\mu\text{-}RS)_2]^+$ core that closely mimics the resting-state Cu_A geometry, oxidation state and high degree of electron delocalisation as reflected by EPR studies, (**Figure 1.32**).

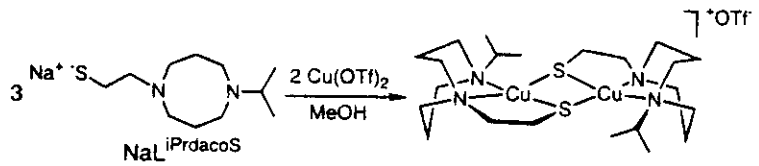

Figure 1.31 Synthesis of $[CuL^{iPrdacoS}]_2^+$

The complex, $[CuL^{iPrdacoS}]_2^+$, is the first example of a structurally characterised dithiolate bridged mixed valence copper dimer.

1.20.1 X-ray Structure

The Cu_2S_2 unit is planar with a Cu-Cu distance of 2.92 Å - this is significantly longer than that reported for Cu_A. The geometry of each metal ion is described as distorted trigonal

pyramidal with N1 and the bridging thiolate sulfur atoms defining the trigonal plane. The co-ordination geometry for each Cu is analogous to those of the trigonal type 1 copper protein sites and model complexes except that a NS_2 rather than an N_2S donor is incorporated. Also similar to type 1 centres, the ligand arrangement in this thiolate model can be construed to be intermediate between geometries favourable for Cu(I) or Cu(II) oxidation levels, presumably in order to accommodate redox reactions and to stabilize a [Cu (1.5)-Cu(1.5)] form.

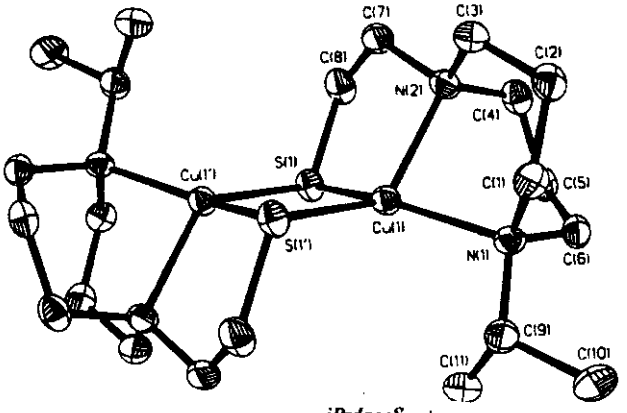

Figure 1.33 X-ray crystal structure of $[CuL^{iPrdacoS}]_2^+$

1.20.2 Optical Spectrum

The electronic spectrum in MeOH is shown in **Figure 1.34**. There are 3 visible absorption bands at λ (nm) max = 358 (ε = 2700 $M^{-1}cm^{-1}$), 602 (ε = 800 $M^{-1}cm^{-1}$), 786 (sh) and 1466 (1200 $M^{-1}cm^{-1}$). The visible absorption bands are red shifted and 2-3 times less intense relative to Cu_A* (See 1.18.2). They proposed that this was due to differences in the donor atom set (metal-metal distances (shorter in Cu_A) or copper geometries (the metal ions in Cu_A are similar to tetrahedrally distorted class of type 1 sites).

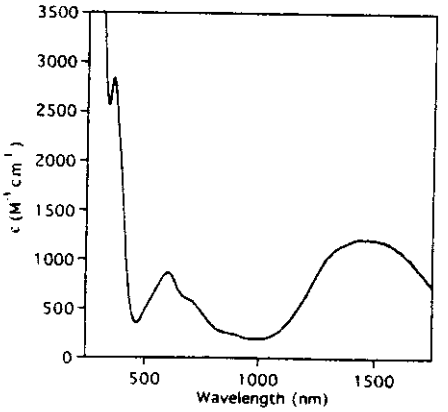

Figure 1.34

A recent investigation of the absorbtion, MCD and S K-edge of $[CuL^{iPrdacoS}]_2^+$ enabled the construction of an MO splitting diagram. This is compared to that for Cu_A in **Figure 1.35.**

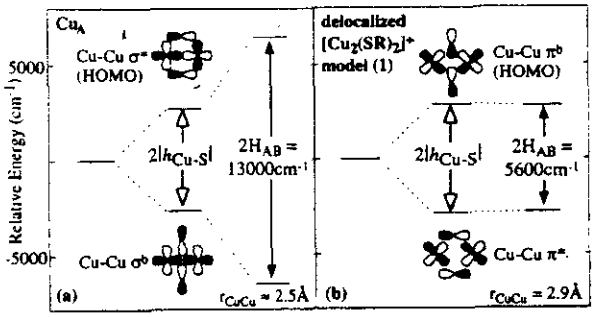

Figure 1.35 ***D_{2h}-idealised MO splittings in (a) Cu_A and (b) $[CuL^{iPrdacoS}]_2^+$***

Xα-SW calculations on $[CuL^{iPrdacoS}]_2^+$ predicted a HOMO (highest occupied molecular orbital) involving an in-plane π-bonding combination of Cu monomeric orbitals (π^b with respect to the metals), the π-antibonding combination (π*) being filled and at lower energy. Significantly, the greater energy of the π^b combination than its π* counterpart indicates that the splitting in $[CuL^{iPrdacoS}]_2^+$ is dominated by Cu-S interactions and demonstrates that valence delocalisation in $[CuL^{iPrdacoS}]_2^+$ is mediated by the bridging ligation rather than by direct Cu-Cu overlap. On the basis of the large Cu-Cu separation (2.9 Å) it has been assumed that only ligand contributions are significant. Similar Cu-S HOMO covalencies were measured for $[CuL^{iPrdacoS}]_2^+$ and Cu_A and this increase of $2H_{AB}$ in Cu_A to 13,000 cm^{-1} is interpreted as due to a direct Cu-Cu bonding interaction resulting from the significantly shorter Cu-Cu separation in Cu_A (~ 2.5 Å).

In contrast to the delocalisation in $[CuL^{iPrdacoS}]_2^+$, which is mediated exclusively by the sulphur bridges, the pathway for delocalisation in Cu_A is seen to contain comparable contributions from both Cu-Cu and Cu-S interactions. These results provided the basis for understanding the origin of valence delocalisation in Cu_A and $[CuL^{iPrdacoS}]_2^+$. The delocalisation observed in $[CuL^{iPrdacoS}]_2^+$ indicates that the value of $2H_{AB}$ = 5600 cm^{-1} is large relative to the vibronic trapping energetics of this dimer. Electronic coupling in $[CuL^{iPrdacoS}]_2^+$ was found to be large indicating that bridging superexchange contribution can be an efficient mediator of valence delocalisation. Direct 2.5 Å Cu-Cu bonding interaction in Cu_A is more than double the

magnitude of $2H_{AB}$ relative to the already large value found in $[CuL^{iPrdacoS}]_2^+$, thus stabilising the delocalisation in Cu_A despite its lower-symmetry protein environment.

1.20.3 Electrochemical Behaviour.

The electrochemical behaviour of $[CuL^{iPrdacoS}]_2^+$ revealed that the reduction, $[Cu_2]^{3+} \rightarrow [Cu_2]^{2+}$, is completely irreversible and the oxidation is chemically reversible only at high scan rates (> 1.0 Vs^{-1}). The authors have interpreted this as indicating significant stabilisation of the mixed valence state. However, it may indicate that there is a change of shape on redox, suggesting that $[CuL^{iPrdacoS}]_2^+$ is not such a good electron transfer agent.

1.21 Nelson Models

Nelson's initial studies indicated that the average-valence copper site is achievable within a host which constrains the copper-bonding distance (~2.4 Å) in a symmetric co-ordinate environment which is acceptable to both the +1 and +2 oxidation state. Trigonal bipyramidal co-ordinate geometry arises in the azacryptate host due to redox preferences and the effective overlap of the dz^2 orbitals. The three azacrptand ligands are shown in **Figure 1.36**.

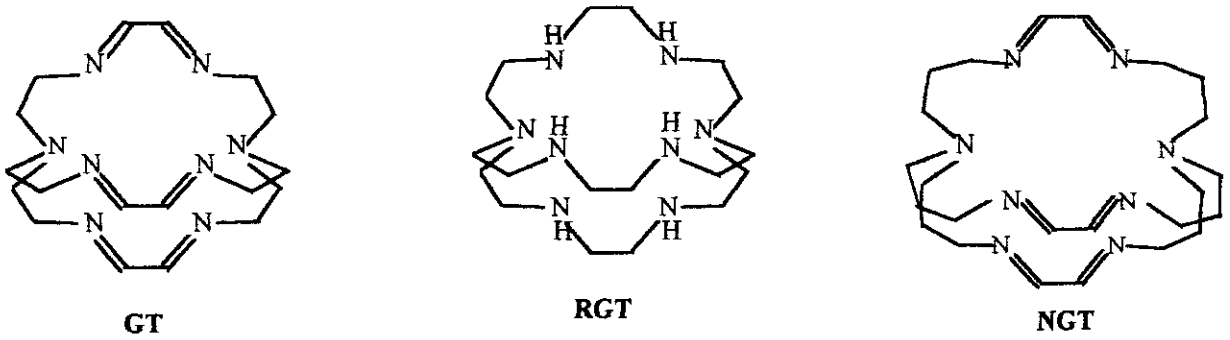

GT **RGT** **NGT**

Figure 1.36

1.21.1 Optical Properties

The similarity of the structures allowed the comparative interpretation of the observed electronic spectra. Each average valence dicopper cryptate shows an intense UV absorption around 300 nm which probably consists of a charge transfer transition. There is also longer wavelength absorptions at 600-650 nm (ε = 1500-3500 $M^{-1}cm^{-1}$) and a more intense band in the region 750-850 nm (ε = ~5000 $M^{-1}cm^{-1}$).

All MCD bands exhibited temperature dependence indicating that they arise from a paramagnetic ground state. In the 600-1100 nm region differently signed MCD bands are observed for each of the complexes. Those between 600 and 950 nm correspond to the variously allowed electronic absorption bands. The similarity of the MCD and optical spectra, irrespective of ligand unsaturation, suggests that neither metal-to-ligand charge transfer nor the opposite is involved in this region. The spectrum can be assigned to transitions within the d-orbitals delocalised over the Cu_2^{3+} assembly . It was proposed that the unpaired electron of the mixed-valence complex is in the antibonding dz^2 based molecular orbitals.[128]

The similarity of the EPR parameters for three systems which contain different co-ordination sites (amine versus imine) supports the hypothesis that these signals arise from delocalisation between the two copper nuclei.[129] The SOMO (singly occupied molecular orbital) is largely composed of the two equivalent dz^2 orbitals on copper. The temperature independence of the ESR parameters show that this is a relatively strong bond. As the unpaired electron is in an anti-bonding orbital, the σ-bond must be even stronger.

On the basis of μ^2-S involvement, Tolman's model is the closet available model for Cu_A. The complex mimics the electron-delocalisation mixed valence redox state and provides the bis-thiolate bridging geometry characteristic of the Cu_A core. However, the Cu-Cu distance in the model (2.93 Å) is far from that in the protein (~2.6 Å) with significantly less acute Cu-S-Cu bridging angles. However, Nelson's azacryptate series all exhibit shorter Cu-Cu interactions. The lack of any co-ordinate bridging ligands implicates Cu-Cu bonding as the origin of the strong Cu-Cu interaction.

Both complexes thus model different elements of the Cu_A site.

1.21.2 The Electronic Structure of the $[Cu_2GT]^{3+}$ Cryptate.

There is interest in understanding the newly discovered electronic structures of average-valence dicopper systems, in order to elucidate the pathways of electron delocalisation within the dicopper unit and to understand the role that such centres play in long distance electron transfer between redox centres in proteins.

Thomson and coworkers have presented an interpretation of the electronic transitions observed in the low-temperature magnetic circular dichroism and absorption spectra of $[Cu_2(1.5)GT]^{3+}$.[130] Their approach involves comparison of the electronic absorption and MCD spectra of a group of fully delocalised mixed valence copper compounds with copper-copper distances varying between 2.9 and 2.38 Å, with and without bridging thiolate ligands. Interest has been focused on the relative contribution to the delocalisation energy of direct metal-metal interaction versus that of the bridging ligands. A description of the electronic structure of the Cu_A centre led to the identification of the MV transition between the highly covalent bonding and antibonding copper-thiolate molecular orbitals, Ψ and Ψ^*, responsible for the electron exchange. In the case of a mixed valence copper (I, II) dimer the energy separation of the two Cu-Cu bonding and antibonding states is a direct measure of the delocalisation energy.

As this study is directly relevant to the mixed valence models investigated in this thesis the relevant points of the paper will be discussed.

The magnetic properties and optical spectra of the dicopper cryptates can be interpreted by considering a $[Cu_2]^{3+}$ unit which is perturbed by a trigonal ligand field around each copper ion. When only the first co-ordination sphere is considered the unit can be considered to have D_{3d} symmetry. **Figure 1.37** shows the axis system used, in which the Cu-Cu direction lies along the unique (Z) axis.

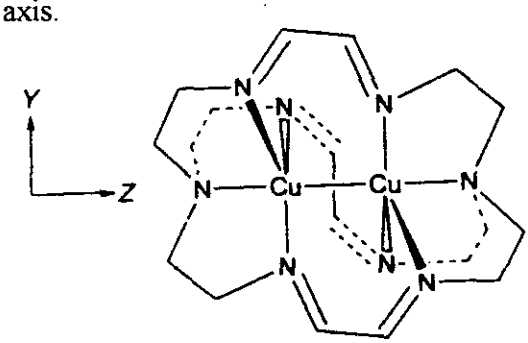

Figure 1.37

As the molecule is axially symmetric, orbital angular momentum of the copper 3d orbitals is maintained about the unique axis with $M_L = 0, \pm1, \pm2$ to give the molecular orbital shown in **Figure 1.38.** The dimer possesses one unpaired electron and therefore all the electronic states will be doubly degenerate with $S = ½$.

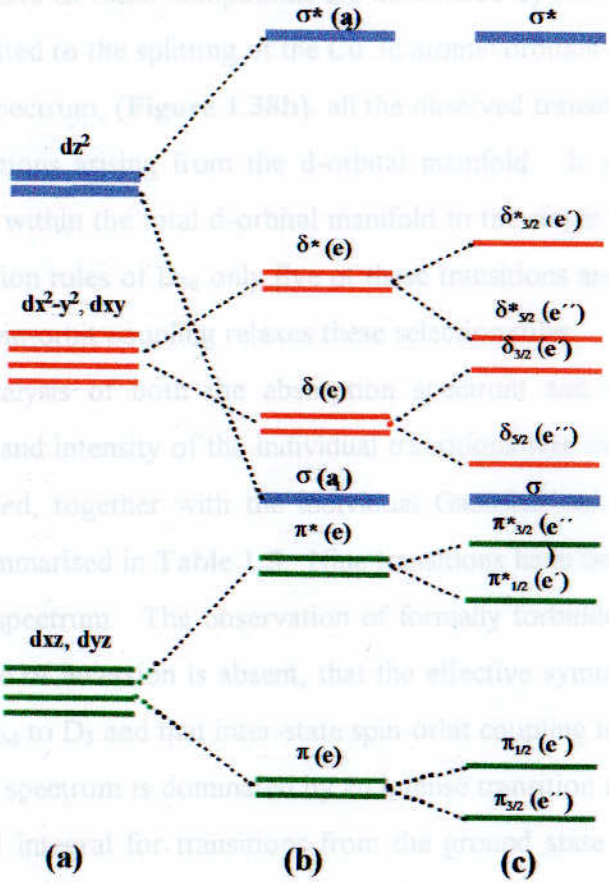

Figure 1.38 Proposed energy level diagram of $[Cu_2GT]^{3+}$, (a) under C_{3v} , (b) under D_3 and (c) after taking into account effect of first order spin orbit coupling.

Assignment of the ground state

The low temperature EPR spectrum of $[Cu_2GT]^{3+}$, described by Harding *et al*, exhibits an axial set of g values of $g_\perp = 2.148$ and $g_{//} = 2.004$.[130] The ground state has been assigned to $^2A_{2u}$ ($^2\Sigma^*$), on the basis of the g value ordering $g_\perp > g_{//}$. Spin-orbit coupling would be expected to mix a $^2A_{2u}$ ground state with $2E_u$ (Π^*) excited states giving rise to an orbital contribution to the magnetic moment along the X and Y axes.

Optical and MCD Spectra.

The 4.2 K absorption and MCD spectra between 25 000 and 7500 cm^{-1} of $[Cu_2GT]^{3+}$ are presented in **Figure 1.38** Interpretation of the electronic data is based on the view that the visible and near IR spectra of these compounds are dominated by the Cu-Cu entity, the effect of the ligands being limited to the splitting of the Cu 3d atomic orbitals.

For the MCD spectrum, **(Figure 1.38b),** all the observed transitions below 22 000 cm^{-1} are formally d-d transitions arising from the d-orbital manifold. It can be shown that nine transitions are possible within the total d-orbital manifold to the single hole of a $[Cu_2]^{3+}$ dimer. According to the selection rules of D_{3d} only five of these transitions are electric dipole allowed although out of state spin-orbit coupling relaxes these selection rules.

A Gaussian analysis of both the absorption spectrum and the MCD spectrum to determine the position and intensity of the individual transitions was carried out. The fit of the MCD spectrum obtained, together with the individual Gaussian curves is shown in **Figure 1.38c** The data are summarised in **Table 1.5**. Nine transitions have been identified in both the absorption and MCD spectrum. The observation of formally forbidden transitions under D_{3d} suggests that the centre of inversion is absent, that the effective symmetry around the copper ions is lowered from D_{3d} to D_3 and that inter-state spin-orbit coupling is operative.

The absorption spectrum is dominated by an intense transition at 13 800 cm^{-1} (band 5). The transition moment integral for transitions from the ground state (gs) to a given excited state (es) within the copper dimer is expected to be of the form shown in **Equation (1)** where α is the coefficient of mixing and R_A-R_B is the copper-copper internuclear distance.

Equation 1

$$(\psi_{es} | r | \psi_{gs}) \sim (1 - \alpha^2)(L_{es} | r | L_{gs}) + \alpha^2(R_A - R_B)$$

The first term represents the ligand contribution to a given transition and the second term the contribution of the two coppers A and B. Since Cu-N covalency is small,[130] ligand contributions to the molecular orbitals are limited and the term $(1-\alpha^2)$ in the transition moment is correspondingly small. Thus the transition moment will be dominated by the second term.

Band	MCD position cm^{-1}	Absorption position cm^{-1}	Splitting cm^{-1}	f_{osc}	C_o/D_o	Excited State	Transition
1	9349	9349	1623	0.0001	7.595	$^2\Delta^*_{1/2}$	$\delta^* \rightarrow \sigma^*$
2	10972	10972		0.0001	-12.822	$^2\Delta^*_{1/2}$	
3	10877	10877	2232	0.0019	0.588	$^2\Delta_{1/2}$	$\delta \rightarrow \sigma^*$
4	13109	13109		0.0042	-0.217	$^2\Delta_{1/2}$	
5	14230	13778		0.060	-0.026	$^2\Sigma$	$\sigma \rightarrow \sigma^*$
6	15718	15978	625	0.020	-0.03	$^2\Pi^*_{1/2}$	$\pi^* \rightarrow \sigma^*$
7	16347	16597		0.022	0.03	$^2\Pi^*_{1/2}$	
8	18290	18290	924	0.016	0.006	$^2\Pi_{1/2}$	$\pi \rightarrow \sigma^*$
9	19214	19614		0.008	0.016	$^2\Pi_{1/2}$	

Table 1.5 Summary of Gaussian analysis, identifying nine transitions.

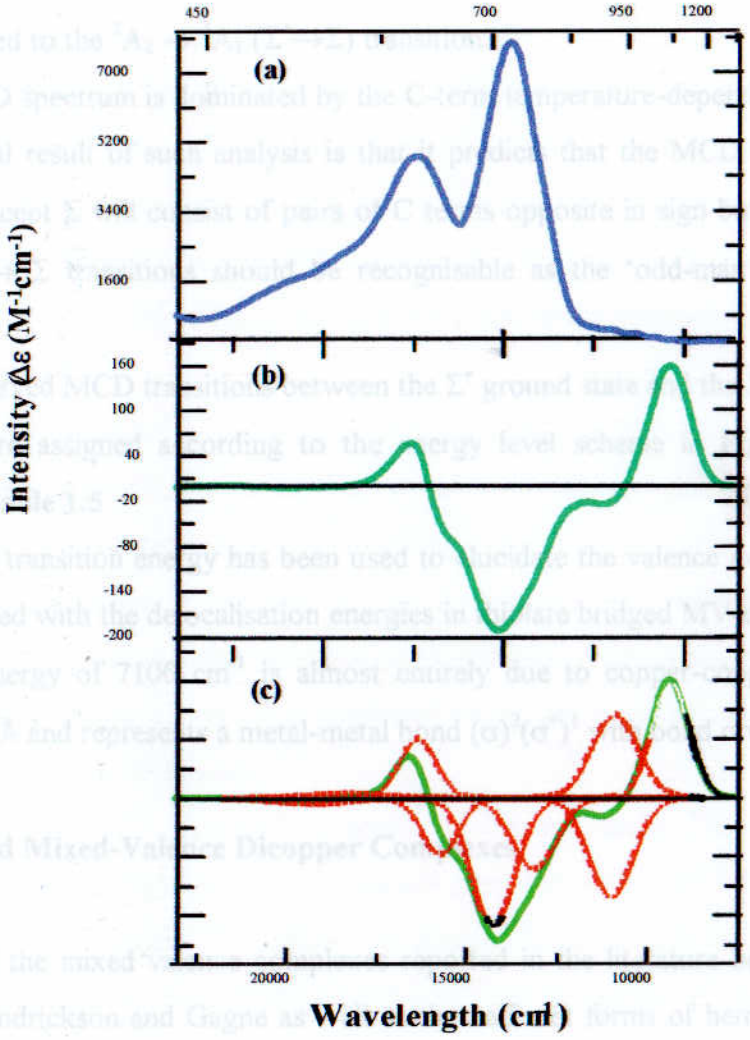

Figure 1.39 (a) The 4.2 K absorption spectrum of $[Cu_2GT]^{3+}$ obtained in a 1:1 (v/v) D_2O-ethane-1,2-diol solvent. (b) The 4.2 K MCD spectrum of $[Cu_2GT]^{3+}$ obtained in a a 1:1 (v/v) D_2O-ethane-1,2-diol solvent. (c) Simulation of the experimental MCD data obtained as the sum of nine Gaussian curves (shown as dotted lines).

Since this will be zero for transitions which do not involve bonding and anti-bonding molecular orbital combinations of the same orbital the most intense band in the absorption spectrum should be assigned to the $^2A_2 \rightarrow {}^2A_1$ ($\Sigma^* \rightarrow \Sigma$) transition.

The MCD spectrum is dominated by the C-term temperature-dependent behaviour. An important general result of such analysis is that it predicts that the MCD associated with all excited states except Σ will consist of pairs of C terms opposite in sign but equal in intensity. Therefore, $\Sigma^* \rightarrow \Sigma$ transitions should be recognisable as the 'odd-man out' in the MCD spectrum.

The observed MCD transitions between the Σ^* ground state and the Σ, Π, ,Π^*, Δ and Δ^* excited states are assigned according to the energy level scheme in **Figure 1.38** and are summarised in **Table 1.5**.

The MV transition energy has been used to elucidate the valence delocalisation energy which is compared with the delocalisation energies in thiolate bridged MV copper dimers. The delocalisation energy of 7100 cm^{-1} is almost entirely due to copper-copper σ overlap at a distance of 2.36 Å and represents a metal-metal bond $(\sigma)^2(\sigma^*)^1$ with bond order of 0.5.

1.22 *Localised Mixed-Valence Dicopper Complexes*

Many of the mixed valence complexes reported in the literature belong to Class I or Class II e.g. Hendrickson and Gagne as well as the half met forms of hemocyanin studied by Westmoreland. In general, localised ground states are favoured by the following factors:

1. Different environments for the interacting sites.
2. Large intersite distances.
3. Strong antiferromagnetic coupling between several unpaired spins on each site.
4. Dissimilar ions.

Gagne first reported an electrochemically generated mixed valence species for an O-bridged dicopper macrocycle.[131] Hendrickson[132], Owaka[133], Mandal[134] and Zacharias[135] followed up on this biologically mechanistically interesting research by making small changes to the ligand but still retaining the oxygen as a bridge between the pair of copper ions. These macrocycles were used to study intramolecular electron transfer and as models of the mixed

valence state detected for binuclear copper sites in the cuproproteins described previously. A brief description of the contribution to mixed valence copper chemistry by the aforementioned authors follows.

The mixed valence $Cu^{I}Cu^{II}$ macrocycle[132], (**Figure 1.40a**), was generated by the one electron electrochemical reduction of the binuclear Cu(II) macrocyclic complex. Solution EPR spectra were found to be temperature dependent. At room temperature a seven-line isotropic pattern is evident in the g = 2 region with a separation of 40-45 G. It was observed that on going from room temperature to liquid nitrogen temperature the seven-line spectrum became a four-line spectrum.

In contrast, Addison[136] *had earlier reported that the EPR spectrum for a related* binuclear mixed-valence $Cu^{II}Cu^{I}$ complex (**Figure 1.40b**) invariably exhibited a four-line copper hyperfine pattern at room temperature in solution. This is an example of a mixed valence complex where the electron is localised and the copper sites are not identical. The X-ray crystal structure presented may represent one conformational form of the mixed valent species in solution. The existence of two conformational forms may be instrumental in the solution intramolecular electron exchange rate.[137]

Henrickson *et al*[132] prepared a series of mixed valence binuclear Cu(II)/Cu(I) complexes of macrocyclic ligands similar to the one prepared by Gagne[131], replacing the methyl group by tert-butyl substituents. In addition the diamine linkages were varied (**Figure 1.40c**). As characterised by EPR, four of the complexes are delocalised at room temperature in solution and three are localised. Hendrickson and his coworkers systematically studied the factors affecting intramolecular electron transfer, first devising a means to prepare the mixed-valence dicopper complexes chemically and not electrochemically as Gagne had done. This was achieved by the chemical reduction of the dinuclear Cu(II) complexes with sodium dithionite.

Mandal *et al*[134] investigated how the stereochemistry, reactivity and redox behaviour of binuclear copper complexes of the type prepared by Gagne were affected by gradual reduction of the imine linkages. The complex $[Cu_2L^1(ClO_4)_2]$, (**Figure 1.41**), was reported to undergo four sequential one-electron transfers to generate dicopper species with oxidation states varying from +1 to +3 which was unprecedented in coupled systems of this sort. The solution

EPR spectra, at room temperature, for the mixed valent form, exhibit four hyperfine lines consistent with the interaction of the odd electron with just one copper centre. This is in contrast to the room temperature EPR behaviour of the imine macrocycle which exhibits a seven-line spectrum.[135]

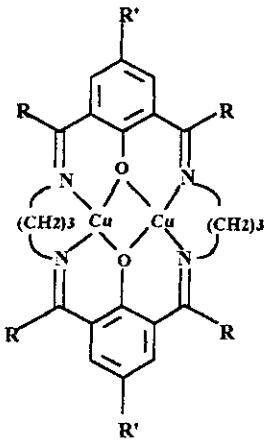

(a) R = H, R' = CH3

(b) R = CH3, R' = CH3

(c) R = H, R' = C(CH3)3

Figure 1.40

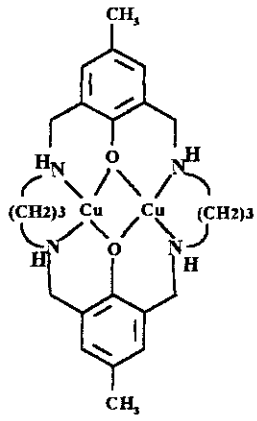

Figure 1.41

Electrochemical reduction of dinuclear Cu(II) complexes envisages an intermediate Cu^{II}-Cu^{I} species. Reversibility of such a reduction depends on the stability of this intermediate species. To confirm the stability of the intermediate Cu(II)-Cu(I) complex species Zacharias *et al*[135] attempted to synthesise mixed valence complexes by chemical methods. The mixed-valence Cu^{II}-Cu^{I} complexes could be synthesised by chemical methods, first by reacting the mononuclear copper complexes (ML') with *para* substituted anilines to give the metal-ligand system and the subsequent addition of a Cu(I) salt, (**Figure 1.42**).

All the complexes exhibited an intense absorption in the UV region with a band maxima at around 380 nm, which is due to intraligand charge transfer. The intervalence transfer (IT) band generally present in the near-IR region of the electronic spectrum is a characteristic feature of mixed valence complexes. The intensity and sharpness are also a function of the

extent of delocalisation. All the complexes exhibit a weak IT band at *ca.* 1000 nm. These features are characteristic of asymmetric mixed-valence complexes.

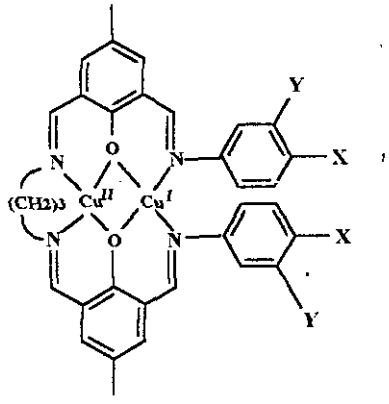

	X	Y
L1	H	H
L3	OMe	H

Figure 1.42

The complexes, even though different in the ligand environment, exhibited a four-line pattern on the EPR time scale. This indicates that slight asymmetry in the ligand environment does not affect considerably the localisation of the unpaired electron on one of the coppers. There were no signs of either mixed-valence species converting from ESR localised to ESR delocalised over the temperature range (298-150 K).

These models involve the d_{x2-y2} ground state where interaction can never be as efficient as in d_{z2}. Thus, the advantage of the azacryptates is strongly enforced.

1.23 Conclusion

This chapter has introduced the chemistry of copper in its most common Cu(I) and Cu(II) redox states, as well as reviewing mixed valence copper complexes.

The modelling of copper proteins has been discussed. How research groups have aimed to mimic the ligation geometry and possible environment of the active site in question. If this is achieved the spectroscopic and other properties of metalloproteins should be reproduced.

The remainder of this thesis describes the synthesis and properties of copper complexes, both mononuclear and dinuclear, involving macrobicyclic and/or acyclic hosts. The structure and physical properties of mixed-valence dicopper complexes which can function as models of the Cu_A site is the main subject of this present work.

CHAPTER 2

TRIPODAL LIGANDS

2.0. TRIPODAL LIGANDS

2.1. Introduction

The binding and activation of dioxygen by copper ions is important in numerous and diverse biological and catalytic processes.[1,2] Biomolecules having one or more copper ions in their active sites utilise the oxidising power of O_2 for respiration.[3] Copper-dioxygen interactions also play a role in synthetically useful stoichiometric and catalytic oxidative conversions of organic molecules. It is therefore apparent why much research has been centred on elucidating the nature and reactivity of copper-dioxygen adducts.[4,5]

Examples of such Cu_n-O_2 units in synthetic compounds that have been structurally characterised by X-ray crystallography are shown in **Figure 2.1**[6,7,8]. A representative demonstration of the success of synthetic model compounds is the development of the mechanism of reversible binding of O_2 to hemocyanin as mentioned in Chapter 1.

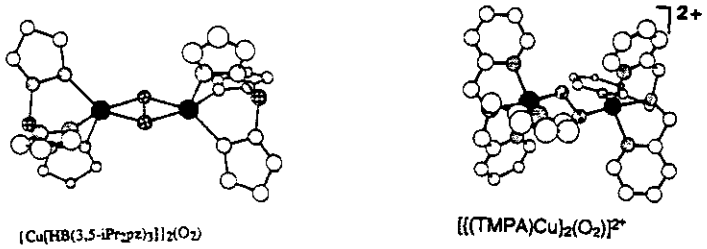

Figure 2.1

Studies on systems of this type are of importance in the elucidation of structure, spectroscopic and reactivity correlations in copper-dioxygen chemistry[9]. Copper ions serve as catalyst for oxidative conversion and because of this we are interested in examining basic Cu(I) and Cu(II)/O_2 reactivity e.g. dioxygen binding followed by activation allows for C-H oxidative processes in a variety of copper monoxygenases such as tyrosinase[4] and particulate methane monooxygenase[10]. Dioxygen binding and reduction to hydrogen peroxide or water (i.e. O-O cleavage reactions) occur in copper oxidases[4] and thus the chemistry of O_2 binding to Cu(I) centres is also relevant to enzymes such as ascorbate oxidase[10] and cytochrome c oxidase,[11] (reduction of O_2 at a dinuclear heme-iron copper centre).

2.1.1 Cu-O_2 (1:1) Adducts

Cu-O_2 (1:1) adducts are of interest since they can serve as precursors for 2:1 adducts via further reaction of Cu-O_2 with Cu(I).[12] Furthermore, recent studies have revealed the presence of such entities as important intermediates involved in the chemistry of several other copper protein active sites such as; dopamine β-hydoxylase,[13] and phenylalanine hydroxylase.[14] Cu(I)/O_2 reactions involve some degree of electron transfer as do most metal-dioxygen reactions. Therefore, the structures and physical properties of Cu(II) analogues of LCu(I) species are also of interest as the ligation and co-ordination geometry in such Cu(II) species may closely resemble that seen in Cu_nO_2 adducts. [15]

2.1.2 Peroxo-dinuclear Copper(II) Complexes

The μ-peroxo dicopper(II) (Cu_2-O_2 (2:1)) adduct complexes are of particular interest as models for *hemocyanin* and *tyrosinase*. Several types of co-ordination modes for the peroxo group for dicopper(II) are known[2]: -

2.1.2.1 Trans-μ-1,2-Peroxo Co-ordination

Karlin *et al* established the *trans*-μ-1,2-peroxo co-ordination mode for a complex with a tetradentate tripodal ligand (tris(2-pyridylmethyl)amine: TMPA),[6] **(Scheme 2.1).** Kinetic and thermodynamic properties have been determined for reactions between O_2 and the Cu(I) tripodal complexes, derived from TMPA, which show that ligand modifications dramatically affect the rate of formation and dissociation of the Cu-O_2 adducts. [16,17]

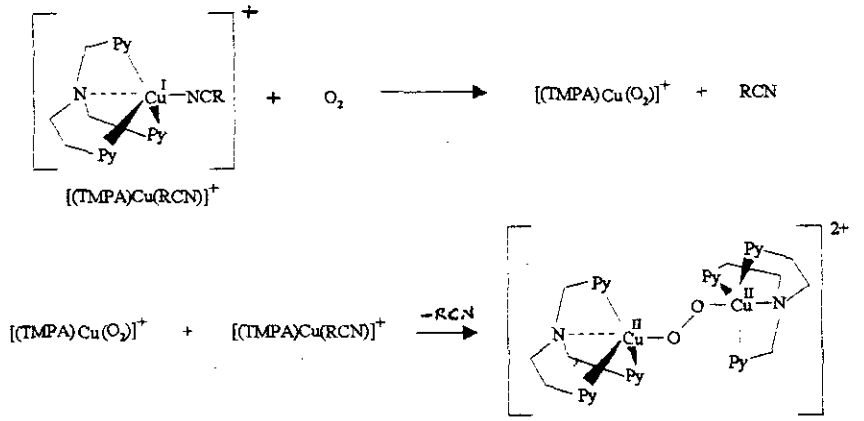

Scheme 2.1

2.1.2.2 μ-η²;η²-Peroxo Co-ordination

Kitajima *et al* followed up this work by establishment of the μ-η²;η²-peroxo co-ordination mode for dicopper(II) by using a series of tridentate hindered tripodal ligands (tris(3,5-dialkylpyrazolyl)borate).[7] They demonstrated that their μ-η²;η²-peroxo dicopper(II) complexes are excellent structural and functional models for the aforementioned copper proteins, **(Scheme 2.2).**

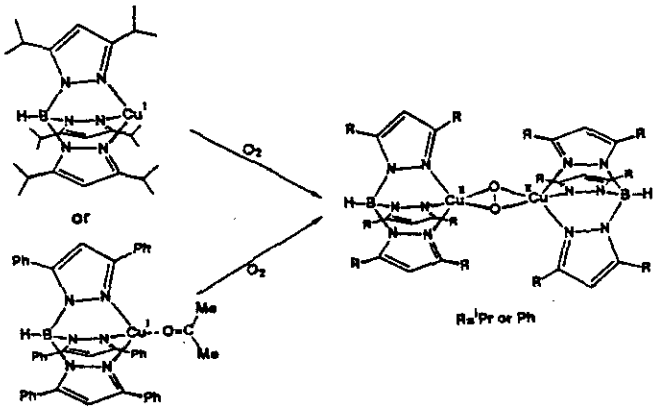

Scheme 2.2

Other types of peroxo co-ordination modes such as an unsymmetric terminal peroxo, μ-1,1-acylperoxo and -hydroperoxo co-ordination modes have also been proposed. The fact that dioxygen can bind in so many ways suggests that the stereochemistry of the peroxo

dicopper(II) complexes depends on the stereochemical and/or electronic effects of the ligands.[18]

2.1.3 Tripodal Tetradentate Ligands

A well documented approach to modelling and studying the redox and co-ordination chemistry of Cu(I) and Cu(II) of this type, is to study the complexes of tripodal tetradentate ligands. Tripodal ligands continue to find extensive use in the synthesis of metal complexes because of their ease of preparation, the wealth of spectroscopic and X-ray crystallographic data which has been generated for their metal complexes, and the predictable changes in the physical properties of the metal as the ligand sets are varied.[19]

The utilisation of imidazole (from histidine residues) as a donor to copper in many proteins[20] has prompted the use of unsaturated nitrogen donors in model studies. Tripodal ligands are expected to impose a non-planar geometry upon the copper ions, also favouring the reduced state.

There are a number of studies on complexes of tripodal ligands which have considered the impact of changing the steric features of the ligands on the reduced forms of the Cu(I)-Cu(II) couple.[12,21,22] Differences in the steric features of tripodal ligands can be manifested in a variety of ways. These include; differences in the hydrophobicity of the complexes, accessibility of the substrate (i.e. O_2) to the metal due to steric bulk of the ligand and the extent of steric match between the substrate and the complex.[12,19]

Suzuki *et al*[18] noted that the introduction of methyl groups to the TMPA ligands at the 6th position of the pyridyl groups significantly affected not only the reactivity of the Cu(I) complexes with dioxygen but also the stereochemistry and thermal stability of the peroxo dicopper(II) complexes.

Canary *et al* designed Cu(II) complexes of synthetic TMPA derivatives for molecular recognition studies, **Figure 2.2**. The use of copper ions to organise the organic ligand allows an opportunity to 'switch' the ligand between two different binding geometries if the $[Cu(L)]^{+}$ and $[Cu(L)]^{2+}$ complexes display different ligand geometries. One other objective was the design of electrochemical switches or chemical sensors based on co-ordination complexes.[23]

K.D. Karlin wrote ; "There is a great deal of evidence supporting the notion that Cu(I)-like environments dominate the co-ordination chemistry of copper in the redox active

metalloproteins. These include the type 1 'blue' copper centres in copper electron transfer proteins and multicopper oxidases as well as the binuclear centre in the oxygen carrier hemocyanin" [24]

Because of the interest in Cu(I) complexes with non-planar geometry and unsaturated sp^2 N ligands, we decided initially to examine the products of a [1+3] condensation reaction of tren and various substituted and non-substituted monoaldehydes as ligands for Cu(I).

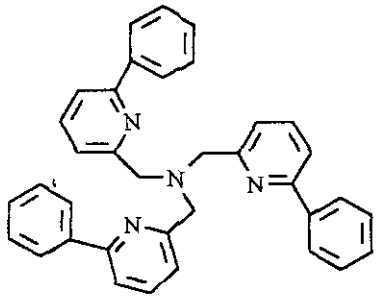

TPPA

Figure 2.2

2.2 Tripodal Ligands Derived From Tris(2-aminoethyl)amine and Tris(3-aminoisopropyl)amine

Podands are open chain ligands which usually do not have a preformed intramolecular cavity in which a cation can nest. They are, however, capable of assuming a cup shaped structure with an appropriate cation, during complexation, causing the whole ligand skeleton to be held in a podate conformation only by the cation/donor interactions. As the cavity is not preformed, entropic contribution to complexation is unfavourable and is reflected by a decrease in complex stability, relative to preorganised hosts such as cryptands.

The spectroscopic and structural characterisation (^{1}H NMR and X-ray crystallography) of a range of copper complexes of new Schiff-base ligands derived from tris(2-aminoethyl)amine (tren) and tris(3-aminoisopropyl)amine (trpn) is described in the following sections.

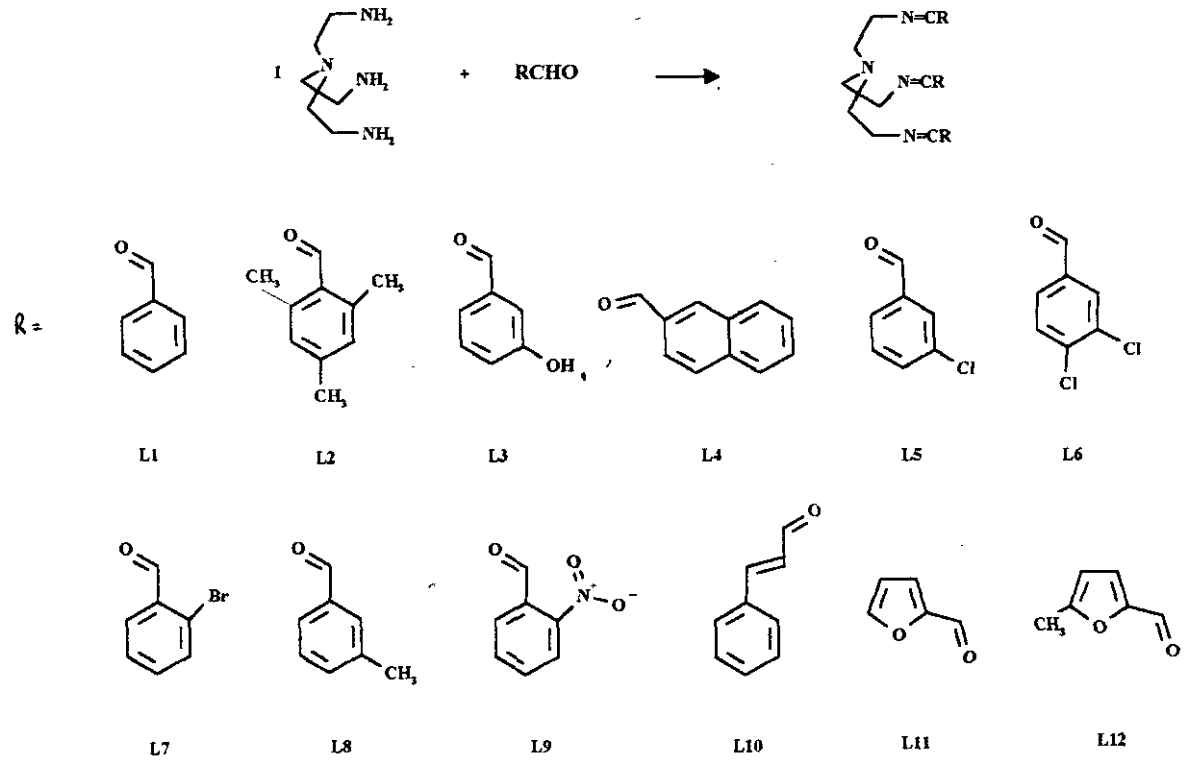

Scheme 2.3 Tren series podates

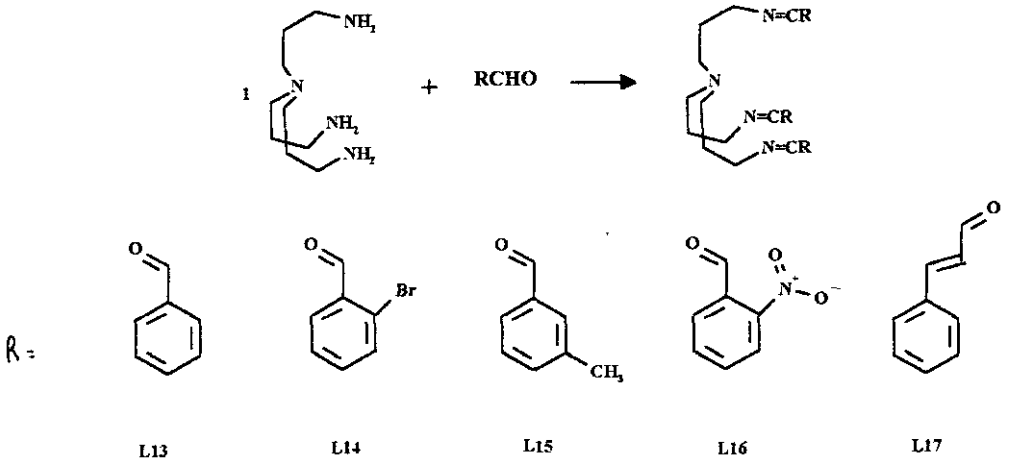

Scheme 2.4 Trpn series podates

The metal-free tren and trpn-based podands were formed by a [1+3] Schiff-base condensation reaction whereby a partially positive charge on the carbon of a carbonyl group is

attacked by an atom bearing a lone pair of electrons on e.g. a nitrogen atom of a tripodal amine, **(Scheme 2.5)**. The R group of the tripodal ligands was systematically varied with a view to testing how steric and/or electronic changes imposed upon the copper complex environment manifest itself in terms of structure, associated spectroscopy and reactivity patterns.

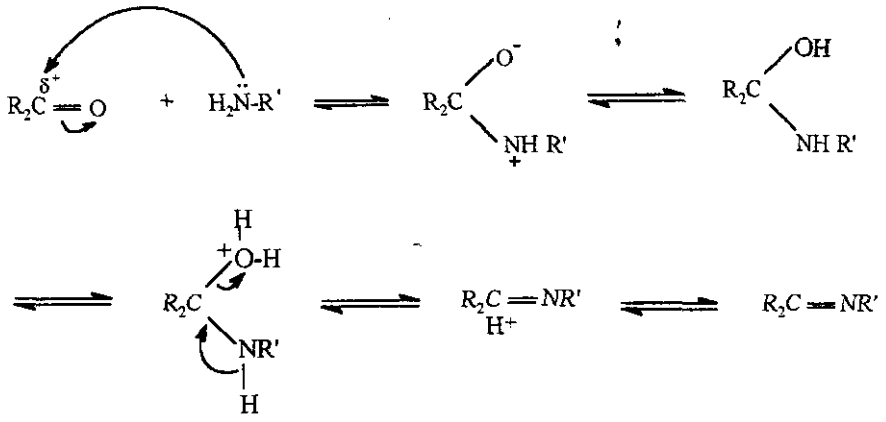

Scheme 2.5 Schiff base mechanism

Initial attempts at the synthesis of Cu(I) podates, using Cu(I) as template, involved the use of both aliphatic and aromatic aldehydes e.g. chlorobenzaldehyde. The synthesis was easiest with aromatic aldehydes. Synthesis using aliphatic aldehydes generally yields green or blue oils which analyse close to the $[Cutren]^{2+}$ complex.

The series of stable Cu(I) tripodal tetradentate ligands prepared has been shown to stabilise the Cu(I) ion, without oxidation or disproportionation to Cu(0) and Cu(II). It was hoped that the series might allow the correlation of the Cu(I) structure with O_2 reactivity. Any generalisations relating to the chemistry would be of interest in copper mediated oxidative reactions and the bioinorganic chemistry of copper

It soon became apparent that if Cu(I) was instead reacted with the preformed free ligand (where available in a pure state) the Cu(I) podates were easily obtained. This is due to the fact that the four potential N donor groups are in place and are able to co-ordinate to the incoming Cu(I) cation. In the template reaction there must be competition between the formation of the $[CuL]^{+}$ and a $[Cu(tren)]^{2+}$ species, even under a nitrogen atmosphere.

2.3 Metal-Free Tripodal Ligands

Clean, solid Schiff-base products were obtained during free ligand synthesis when tren was reacted with; benzaldehyde, mesitaldehyde, and naphtaldehyde, giving **L1**, **L2** and **L4,** respectively. Free podands were used in electrochemical experiments which are discussed in Chapter 2.23. Most other aldehydes produced oily products and these were immediately reacted to form the Cu(I) podates which will be discussed subsequently.

For all free ligands the presence of a strong imine peak at ~1640-1650 cm^{-1} and the absence of any carbonyl or amine resonances in the infrared spectrum was the first indication that a [1+3] Schiff base condensation had occurred.

2.3.1 No Cu(I) podates Isolable

Attempts were made to synthesise Cu(I) podates from branched and long chain monoaldehydes. Synthesis was attempted with acetaldehyde, isobutyraldehyde and butyraldehyde. It was hoped that incorporating a short, bulky, non-aromatic side chain might allow the interaction of oxygen leading to a 1:1 adduct $[CuL(O_2)]^+$ which could then react further with another Cu(I) podate. This is a similar reaction as that reported by K.D. Karlin.[25] The presence of such groups may also lower the electrochemical potential required for oxidation favouring dioxygen interaction.

Template and insertion synthetic methods were attempted but in all cases the products analysed close to $[Cutren]^{2+}$. Another tripodal ligand which failed to co-ordinate Cu(I) is the **L2** ligand.

2.3.2 L2

A white crystalline solid was obtained upon condensation of mesitaldehyde with tren. The mass spectrum showed only a small peak due to the parent ion (534, 20%) with the major peak being 376 (100%) corresponding to the loss of C-N=C-Ph$(CH_3)_3$, a fragmentation pattern similar to that of the podand made with benzaldehyde.

CHN analysis and ^1H NMR confirmed that [1+3] condensation occurred. The ^1H NMR shows clearly two signals for the methyl substituents, **(Figure 2.3)**. The *ortho* substituted

methyl groups are recognised by a sharp singlet integrating for 18H as opposed to 9H for the *para*-substituted methyl group. As a consequence of the anisotropic field produced by the circulating π electrons of both the imine bond and aromatic residues, the imino signal, which lies in the deshielded region of this field, is moved downfield to δ 8.55 ppm. The observation of just one singlet demonstrates the equivalence of the 3 strands of the podand. As in the cryptand series previously characterised,[26] the more shielded upfield methylene group (H_a) is assigned to the CH_2 group α to the bridgehead N while that of the CH_2 group (H_b) α to the imine N is assigned to the lower field signals. This is as a result of the local anisotropic field from the imine group deshielding the H_a protons relative to H_b - next to bridgehead, **(Table 2.1)**.

Reacting the free ligand with Cu(I) resulted only in the uncomplexed free ligand. Unlike the macrocycles and azacryptands the co-ordination site in podands is not preformed and the free ligand must adapt a convergent site to 'wrap' itself around the incoming Cu(I). In the case of mesistaldehyde, it is fair to conclude that bulky methyl groups present steric hindrance, preventing access to the co-ordination site, or alternatively that the necessary geometry for co-ordination of Cu(I) is not achievable. Attempts at template synthesis were also unsuccessful.

2.4 Tripodal Ligands Which Co-ordinate Cu^+

2.4.1 L1

This free ligand has been previously synthesised by Alyea *et al.*[27] He subsequently synthesised the $[Cu(I)L]^+$ by addition of an excess of $NaBPh_4$ to a stirred acetone solution of $Cu(OAc)_2.2H_2O$ and free ligand. We were able to synthesise the $[Cu(I)L]^+$ complex by both templating on Cu(I) and by insertion of Cu(I) into the free ligand. Our characterisation is reported in **Section 2.7.1**.

The EI mass spectrum of the free ligand showed only a small peak at 410 (10%) attributable to free ligand molecular ion. The majority of peaks were assigned to fragmentation of the free ligand which is common in EI mass spectroscopy. The proposed structure of the benzaldehyde-based podand was therefore confirmed by ^1H NMR.

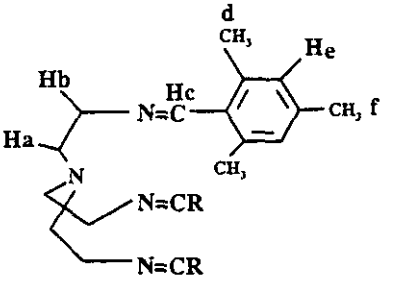

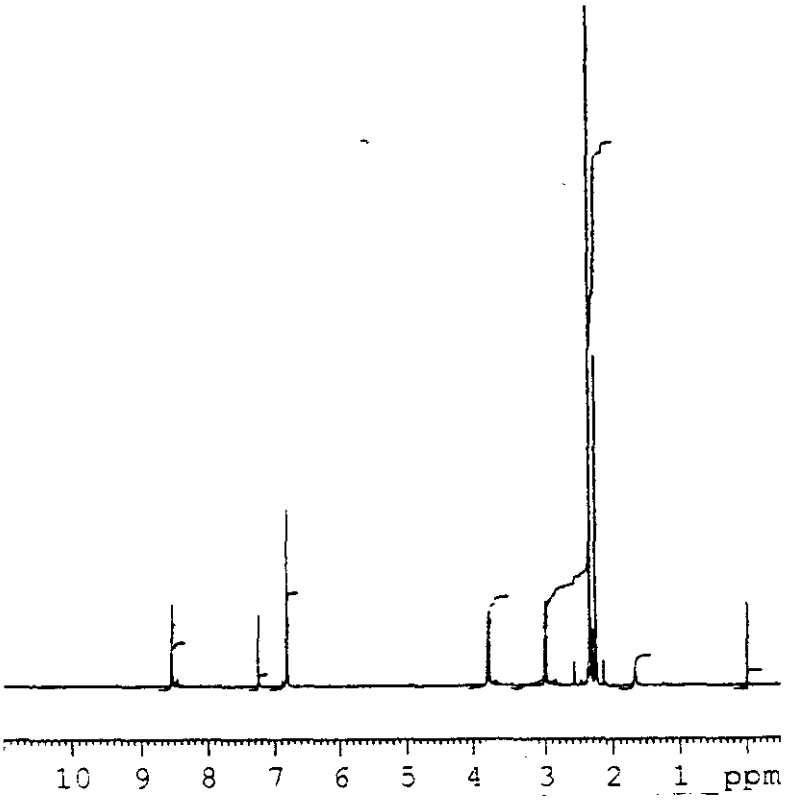

Figure 2.3 *^1H NMR of L2 in $CDCl_3$ at 300 K*

Table 2.1 *^1H NMR data for L2 in $CDCl_3$ at 300 K*

Compound	H_a	H_b	H_c	H_d	H_e	H_f
L2	3.00, t, 6H J = 7.05	3.78, t, 6H J = 6.8Hz	8.55, s, 3H	2.33, s, 18H	6.8, s, 6H	2.25, s, 9H

The ^{1}H NMR is simple, allowing assignment of the *ortho, meta* and *para* protons of the benzene ring as well as the methylene and imino protons. The *ortho* proton occurs as a doublet as it is coupled only to the *meta* proton. Both the *meta* and *para* protons occur as triplets, the *para* proton integrating for only three protons as opposed to 6 protons for the two *meta* positions on each aromatic ring, **(Table 2.2)**. The simplicity of the spectrum shows that the podand is fluxional in solution and that the three 'arms' of the podand host are equivalent.

2.4.2 L4

The high molecular weight of this compound caused immediate precipitation from solution resulting in a white crystalline solid. The mass spectrum indicated successful ligand formation with a molecular ion peak at 560 (10%). The fragmentation pattern recurring in all of these podands generates, as the major peak, the fragment attributed to the cleavage of C-N=C-R.

The infrared spectrum indicates the presence of the aromatic groups at 3058 cm^{-1}. The ^{1}H NMR spectrum is similar to that of L1 showing equivalence of axial and equatorial methylene signals and of the three strands of the podand ligand. As expected, the aromatic region is more complicated than in L1.

The remaining free podands were not isolated but the fact that Cu(I) podates were obtained indicates that their synthesis *in situ* was successful. As we are mainly interested in the Cu(I) podates and their interactions, the discussion will focus on this area. In designing the ligands we are aiming for a host where three imines and a bridgehead nitrogen are available for co-ordination to a Cu(I) ion. It is evident from the inability of **L2** to act as a ligand, that substituents on the benzene ring can affect the properties of the podand and, via steric effects at least, of the Cu(I) podates. A range of Cu(I) podates have been synthesised to examine the impact of such small changes to the free ligand.

2.5 Copper(I) Podates

For simplicity this discussion has been divided into 3 sections: The first describes characterisation of all Cu(I) podates by primary diagnostic tools - infra red, mass spectroscopy and NMR spectroscopy. The second describes the X-ray structures of 8 podates and any notable structural comparisons. The final section discusses electrochemistry of the complexes and the implications for oxygen interaction.

Section A

In synthesising Cu(I) podates by either a template or insertion method, a nitrogen atmosphere, as well as a high concentration of dry acetonitrile, was essential, at least until complexation was complete, to keep the copper ion in the lower redox state.

2.6 Characterisation of Cu(I) Podates

2.6.1 FAB Mass Spectroscopy

The appearance of the monopositive cations $[CuL]^+$ is expected in the FAB mass spectrum of [CuL]X podates, (X = counterion).

2.6.2 Infrared Spectra

In all cases infrared spectroscopy was of considerable value - the presence of an imine peak and absence of any carbonyl or amine peaks confirmed that a [1+3] Schiff base condensation had occurred. The presence of counterion e.g. ClO_4^- (peaks at 1098 and 621 cm^{-1}) also indicates that complexation had occurred. Upon complexation of the metal ion a shift in the imine resonance from ~1650 to ~1630 cm^{-1} is evident.

2.6.3 Electronic Spectra

The electronic spectra of the Cu(I) podates exhibit a high energy band in the region 280 nm ($\varepsilon \sim 10^4$ $M^{-1}cm^{-1}$) due to a $\pi \rightarrow \pi^*$ internal ligand transition. In most cases a Cu(I)-ligand

charge transfer transition is also visible. This MLCT is of medium intensity (~ 10^3 $M^{-1}cm^{-1}$) often tailing into the visible region.

2.7 Solution Stable Cu(I) Tren Podates

2.7.1 [CuL1](ClO_4)

The complex was successfully synthesised by both a template and insertion method. The major peak at 473 (100%) in the FAB mass spectrum is due to the $[CuL]^+$ ion.

The ^1H NMR spectrum of the complex is shown in **Figure 2.4** and the signals assigned in **Table 2.2**. The ^1H NMR reflects co-ordination of all four nitrogen donor atoms by the downfield shift of resonances due to adjacent protons. The shift is most marked for the imine protons [H_c, δ 0.40 (ppm)] but still significant [H_b δ 0.25 (ppm), H_a δ 0.3(ppm)] for the methylene protons. Resonances due to the phenyl ring protons are also affected, especially for the *ortho*-protons. These shifts are attributable to ring current effects as well as electronic effects due to conjugation with the co-ordinated C=N linkage rather than any consequence of any interaction of *ortho*-hydrogen atoms with the copper atom. It is noteworthy that the *ortho*-hydrogen atoms on each ring remain equivalent in the complex, i.e., each phenyl ring undergoes free rotation, at least in solution.

These results are comparable with those of the [Cu(Ph_3tren)][BPh_4] reported by Alyea.[27] The structure of [CuL1][ClO_4] has been determined crystallographically and is discussed in **Section B**.

Solid state NMR was obtained. In the ^{13}C spectra of $[CuL1]^+$ the methylene (δ 50-65 ppm), imine (δ ~160 ppm) and aromatic (δ 124-134 ppm) resonances are clearly recognisable, **(Figure 2.5a)**. The complexity in these regions suggests that the three strands of the podand may not be equivalent in the solid state. This contrasts with the solution ^1H NMR spectra which demonstrates equivalence by the appearance of only one imine peak. In the ^{15}N spectrum we would expect a simple four line multiplet for each imine signal; for one nitrogen coupling to one I = 3/2 copper nucleus we would expect a maximum of 4 lines. **Figure 2.5b** shows a more complex pattern than this between δ -125 and δ -100 ppm, which derives from coupling to $^{63,65}Cu$ together with inequivalence of ^{15}N nuclei. In the ^{35}Cl spectrum a narrow,

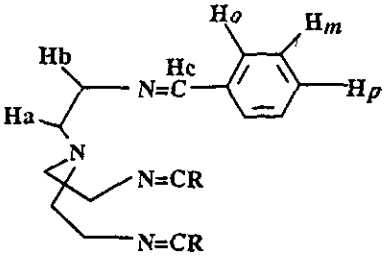

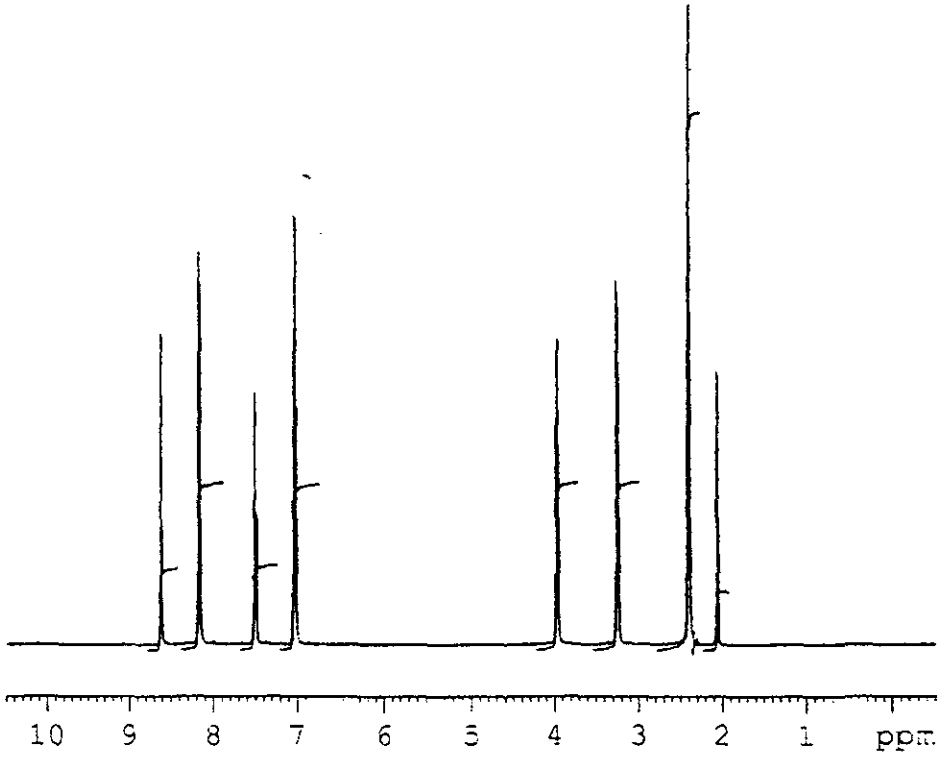

Figure 2.4 *^1H NMR of [CuL1](ClO$_4$) in CDCl$_3$ at 300 K*

Table 2.2 *^1H NMR data for L1 and [CuL1](ClO$_4$) at 298 K in CDCl$_3$*

Compound	H_a	H_b	H_c	H_o	H_p	H_m
L1	2.93, t, 6H J = 6.3	3.68, t, 6H J = 6.3	8.10, s, 3H	7.51, d, 6H J = 8.9	7.49, t, 3H J = 7.1	7.38, t, 6H J = 5.2
[CuL1](ClO$_4$)	3.24, s, 6H	3.93, s, 6H	8.5, s, 3H	8.01, d, 6H J = 7.6	7.35, t, 3H J = 7.4	6.75, t, 6H J = 7.6

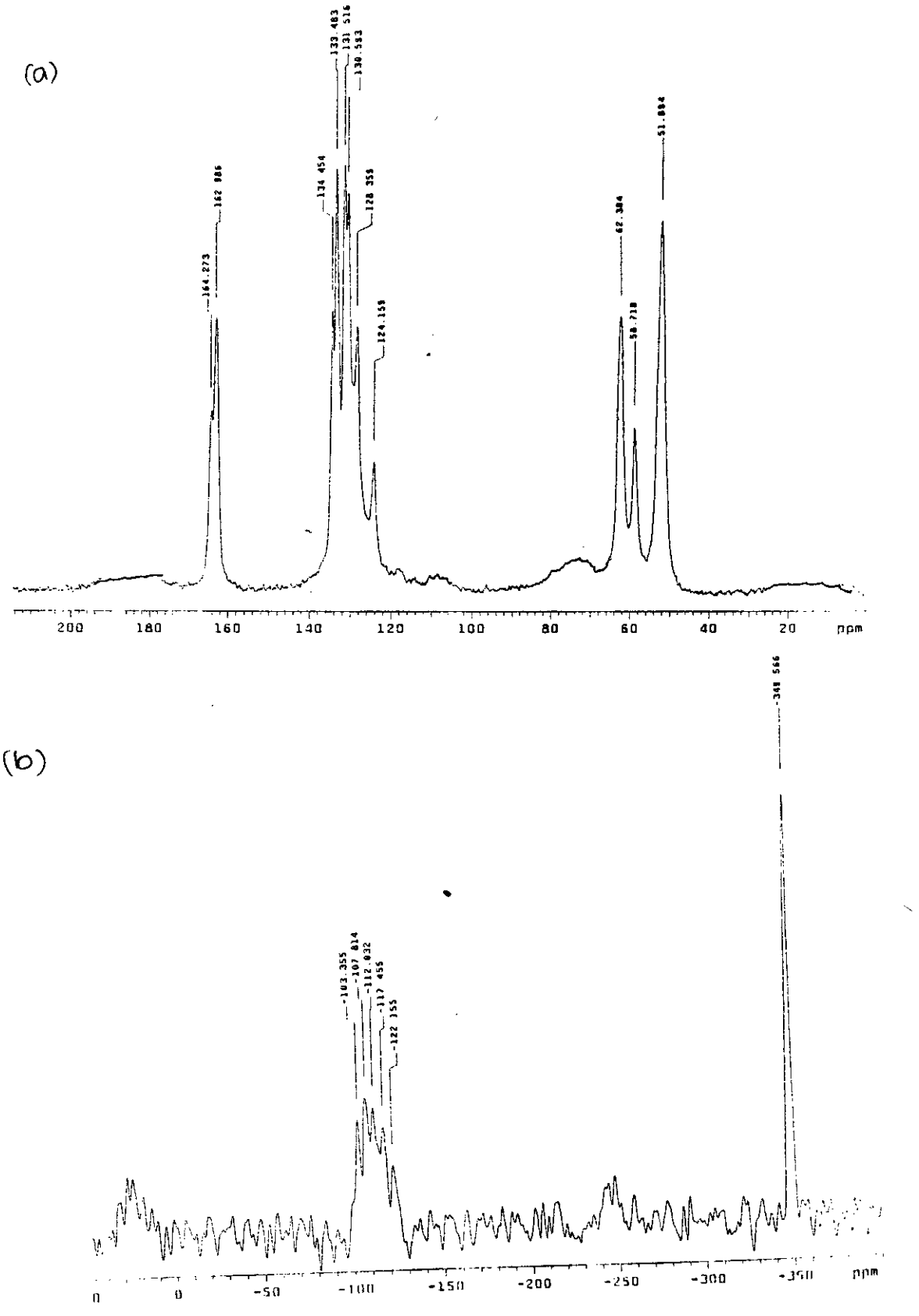

Figure 2.5 Solid State NMR of [CuL1](ClO$_4$); (a) ^{13}C spectrum, (b) ^{15}N spectrum

relatively symmetric line, indicates that the perchlorate anion is highly symmetric, so asymmetry in the solid state is restricted to the cation.

It is observed that the methylene and imine resonance of the solution ^1H NMR have the same pattern for all stable Cu (I) tren-based podates - a pair of triplets at (δ ~3-4 ppm) deriving from accidental equivalence of $^2J_{ax,eq}$ and $^3J_{ax,\ ax}$ and a singlet (δ ~ 8ppm) imino resonance, respectively. Therefore, only the aromatic resonances will be discussed with the full data recorded in tables. For the aromatic resonances, in most cases, only ortho coupling to the nearest neighbour is seen although meta coupling is sometimes evident.

2.7.2 [CuL^3] and [CuL^3] Intermediate

Free ligand synthesis was previously attempted by G. Morgan[26] but proved unsuccessful. However, when templating upon Cu(I), a yellow product insoluble in all common solvents, precipitated. Synthesis was attempted using both the perchlorate and triflate counterion. Although the infrared spectrum indicated absorption due to C=N and -OH, there was no evidence of any counterion. The FAB mass spectrum showed the presence of the complex with a peak at 522 (100%) which seems to discount any idea of polymerisation having occurred. Deprotonation of a hydroxy group must have occurred to generate the neutral complex. CHN analysis formulates the complex with one water molecule present but no counterion. ^1H NMR was not obtained due to insolubility of the complex.

2.7.3 [CuL4] (ClO_4)

This naphtalene-based podate was characterised by the FAB mass spectrum, $[CuL4]^+$ 623 (100%) and [CuL4](ClO_4) at 722 (5%). The ^1H NMR has an unusually simplified splitting pattern. The protons on the aromatic ring adjacent to the imine bond can easily be recognised - H_d appears as a singlet while H_e and H_f couple to one another, appearing as doublets. A decoupling experiment enabled assignment of H_e and H_f from the complicated aromatic region. H_f is assigned as the more downfield resonance owing to its short distance to the imine group. The second aromatic ring has a simple doublet, triplet, doublet, triplet pattern, **(Figure 2.6, Table 2.3)**.

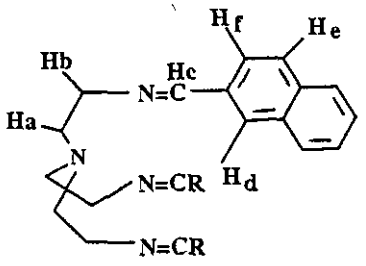

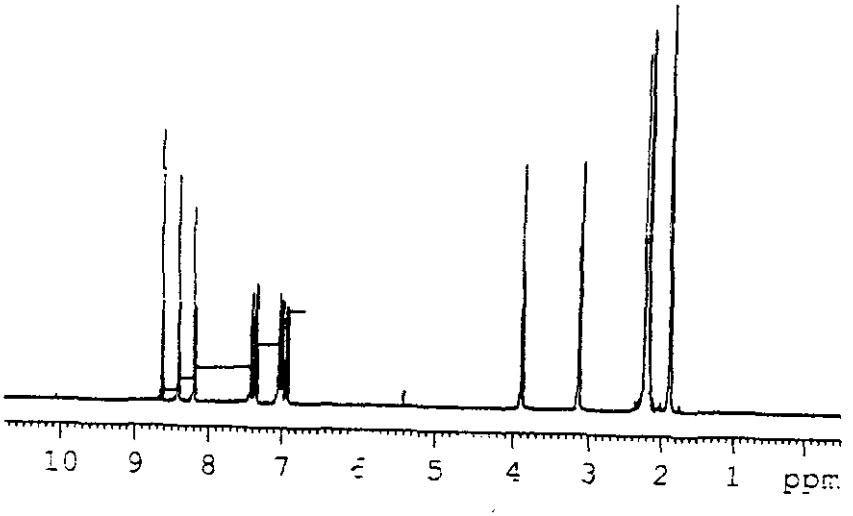

Figure 2.6 *^1H NMR of [CuL4](ClO$_4$) in d_3-MeCN at 300 K*

Table 2.3 *^1H NMR data for [CuL4](ClO$_4$) in d_3-MeCN at 300 K*

Compound	H_a	H_b	H_c	H_d	H_e	H_f	Aromatic H signals of 2nd ring.			
[CuL4] (ClO_4)	3.13, t, 6H, J = 9.9	3.88, t, 6H, J = 9.9	8.64, s, 3H,	8.42, s, 3H,	6.92, d, 3H, J = 8.4	8.19, d, 3H J = 8.4	7.43, d, 3H, J = 8.1	7.36, t, 3H, J = 7.9	6.99, t 3H J = 7.9	7.05 3H J =

2.7.4 [CuL6](ClO$_4$)

The effect of two electron-withdrawing groups substituted on the benzene ring was investigated for two reasons - steric and electronic factors. Would the presence of two chlorines prevent formation of the copper complex as was the case for mesitaldehyde, and if complex formation is successful will the two chlorines interact perhaps opening the pseudo cavity ? Would the electronic withdrawing effects of two chlorine atoms have any influence ? It is unclear whether the chlorines would reinforce or oppose one another. The X-ray crystal structure and electrochemical investigations of this complex are thus of considerable interest.

The complex was characterised by FAB mass spec., $[CuL6]^+$ 681 (100%) and [CuL6](ClO$_4$) (5%). Interestingly, there was a small peak corresponding to $[(CuL6)_2(ClO_4)]^+$ at 1462. On solution of the X-ray structure it can be seen that two Cu(I) podates interact with one another explaining the appearance of this mass unit, **(Section B)**.

The ^{1}H NMR spectrum shows very clearly that the Cl substituents are in the 3, 4 positions. H_f and H_e couple to one another appearing as doublets at δ 7.19 ppm (J = 8.2 Hz) and δ 7.76 ppm (J = 7.2 Hz), respectively. That the coupling constants appear different is due to the effect of a small *meta* coupling between H_d and H_f. H_e appears further downfield than H_f due to deshielding effects of its Cl neighbour. H_d, a singlet at δ 8.19 ppm, is not only next to an imine but also to a Cl hence the difference in shift in comparison to H_f.

The solid state ^{13}C NMR displays broader lines than those reported for [CuL1](ClO$_4$) and there is still some suggestion of inequivalence e.g. in the imino resonance. The ^{15}N spectra is similar to that of [CuL1](ClO$_4$) in line positions although the bridgehead N resonance is sharp. The ^{35}Cl spectrum has a broad but symmetric signal which suggests that the perchlorate ion is less well ordered than in [CuL1](ClO$_4$). The chlorines on the aromatic ring cannot be detected because their unsymmetric environment makes the line too broad to be detected, **(Figure 2.7)**.

2.7.5 [CuL10](ClO$_4$)

The complex was characterised by FAB mass spec, $[CuL10]^+$ 551 (100%) and [CuL10](ClO$_4$) (8%). The infrared spectrum displays a strong peak at 688 cm^{-1} indicating monosubstitution of the aromatic ring. Stretching vibrations of both the alkene and aromatic groups are evident at 2830-3100 cm^{-1}. This complex was synthesised to see if removing

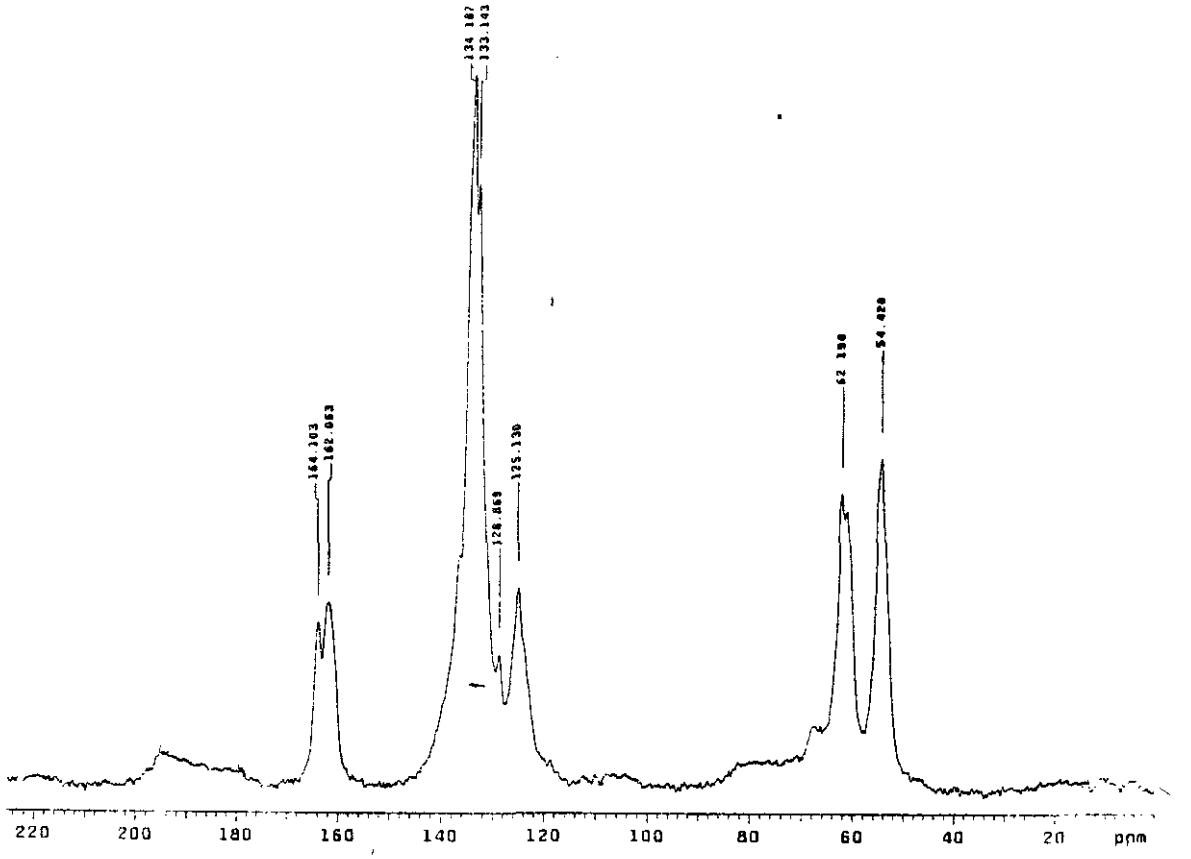

Figure 2.7(a) Solid State NMR of [CuL6](ClO$_4$); ^{13}C Spectrum

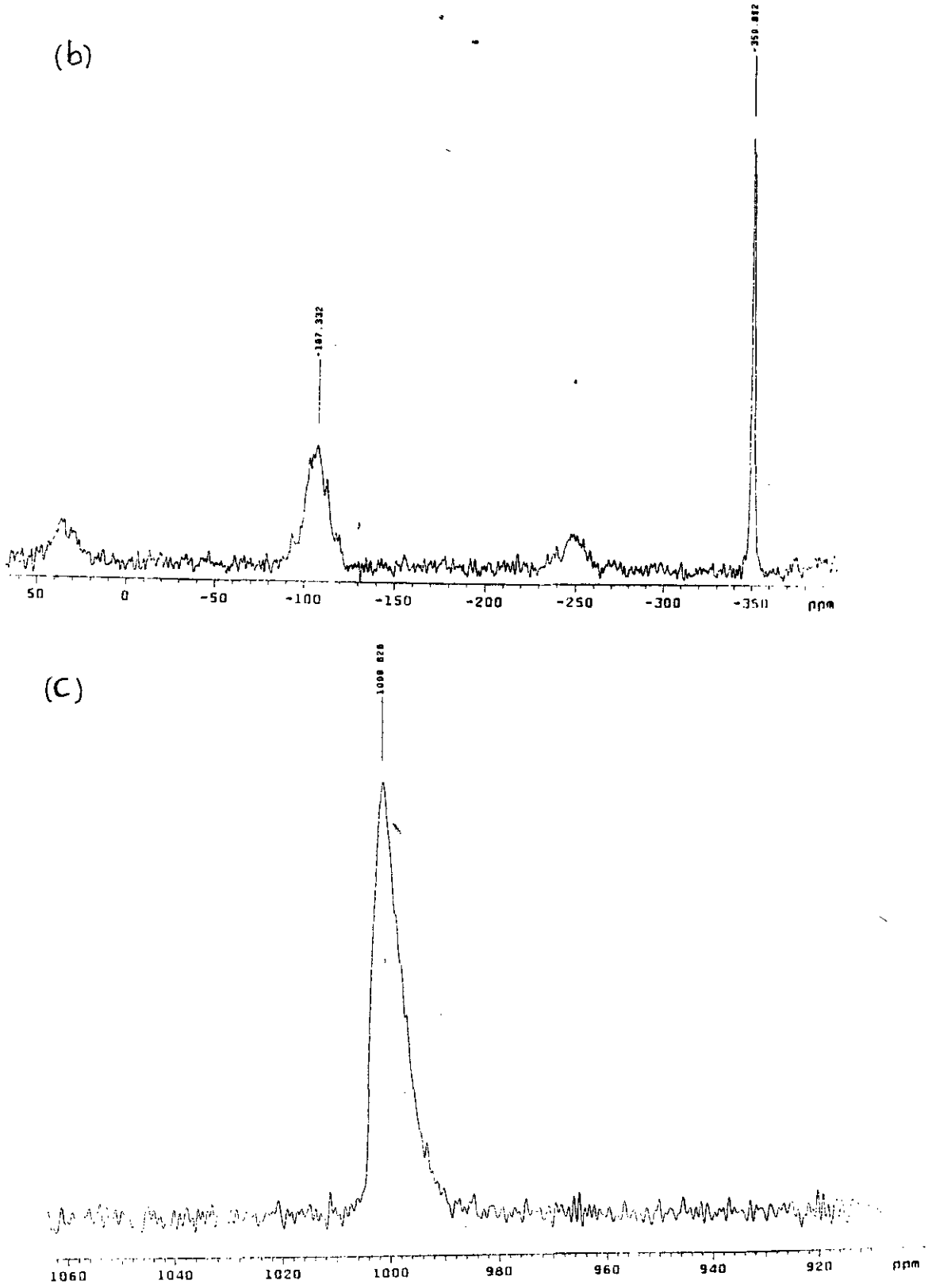

Figure 2.7 Solid State NMR of [CuL6](ClO$_4$); (b) ^{15}N spectrum, (c) ^{35}Cl spectrum.

hydrophobicity close to the Cu-imine plane would enable the complexes to react with dioxygen.

Figure 2.8 shows the aromatic region of the ^{1}H NMR spectrum. The imine resonance is clearly seen as a doublet due to coupling to H_d. H_d can couple to both H_e and H_c but as they are both adjacent to different groups a doublet of doublets is seen (J =8.6 Hz) in the region δ 7.14 - 7.20 ppm. A doublet at δ 7.32 ppm is due to H_e coupling to H_d. This is further downfield than H_d due to the deshielding effect of its aromatic neighbour. The *ortho, meta* and *para* protons show a similar pattern to that reported for [CuL1(ClO_4)]. The proton on the *para* position however occurs as a broad singlet as opposed to the expected triplets. The assignments were confirmed by 2D COSY and are shown in **Table 2.4**.

2.8 Unstable Cu(I) Tren Podates

2.8.1 [CuL5](BF_4)

It was hoped that inclusion of electron-withdrawing groups on the benzene ring could have an effect on the ability of the complex to react with dioxygen. The copper podand made from chlorobenzaldehye appeared to be aerobically less stable than its benzaldehyde analogue, generating a green solid along with the yellow crystalline product. A cleaner sample could be synthesised by precipitating the Cu(I) complex with the reducing tetraphenylborate counterion.

The infrared spectrum of [CuL5](BF_4) indicates the presence of the tetrafluroborate counterion (1072 and 680 cm^{-1}) and the presence of the molecular ion at 577 (100%) in the FAB mass spectrum shows that template synthesis of the complex was successful. The infrared spectrum also shows a strong peak at 680 cm^{-1} which is characteristic of a monosubstituted aromatic ring.

The ^{1}H NMR spectrum at 243 K in d_3-MeCN **(Figure 2.9)** shows very clearly that the Cl substituent is in the *meta* position. 2D COSY assigns the singlet at δ 8.03 ppm to H_d. The second *ortho* proton H_g (a doublet (J = 7.6 Hz) coupled to H_f) is more upfield at δ 7.81 ppm. Both protons are next to the imine H_d but the Cl substituent appears to have a small deshielding effect on H_d. H_e couples only to H_f and appearing as a doublet at δ 7.33 ppm (J = 8.0 Hz) whereas H_f is coupled to both H_e and H_g and due to the shielding effect appears more upfield as a triplet at 6.86 (J =7.9 Hz), **(Table 2.5)**.

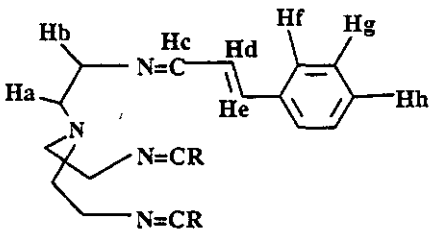

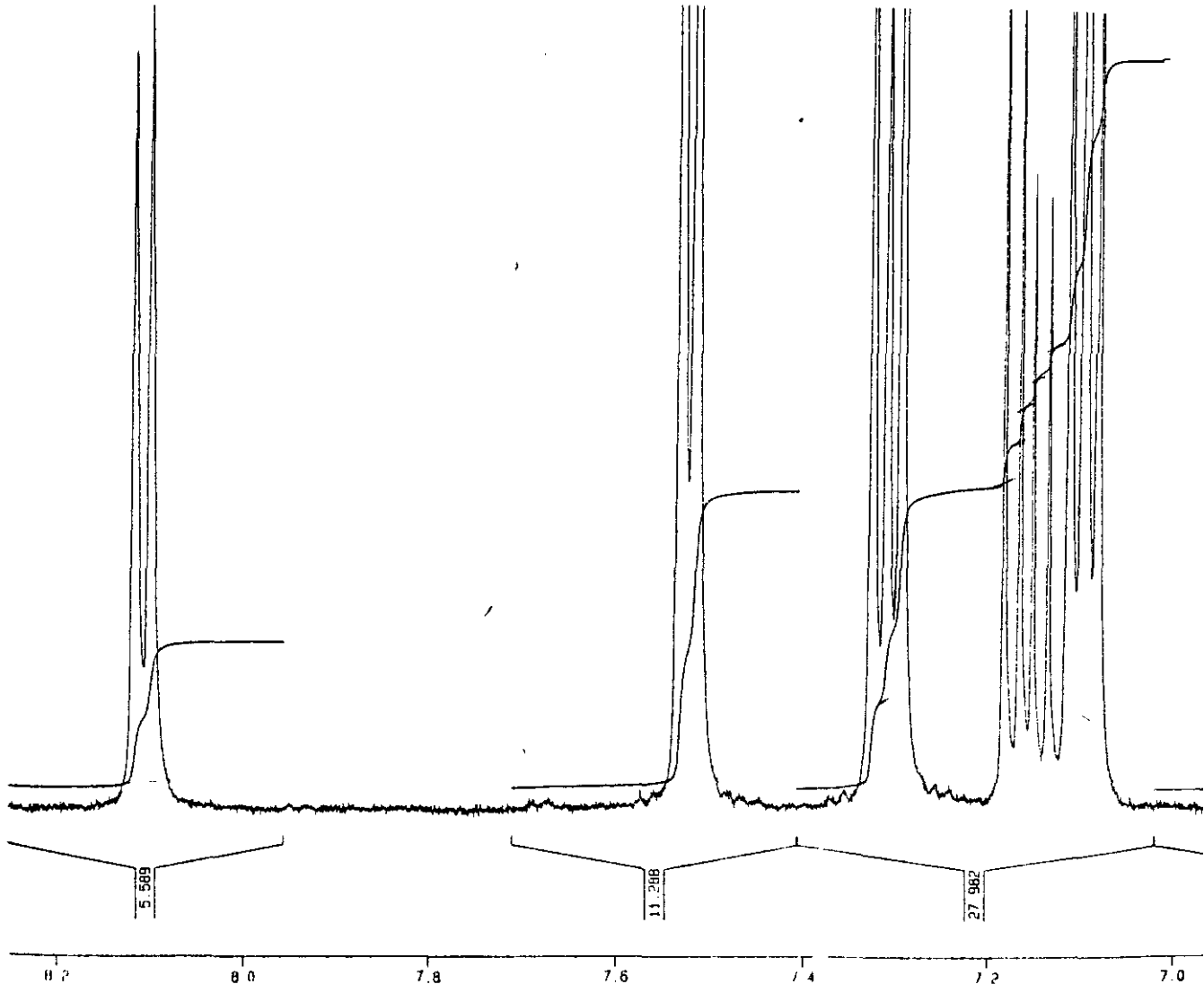

Figure 2.8 *^1H NMR of [CuL10](ClO$_4$) in d$_3$-MeCN at 300 K in aromatic region*

Table 2.4 *^1H NMR data for [CuL10](ClO$_4$) in d3-MeCN at 300 K*

Compound	H_a	H_b	H_c	H_d	H_e	H_f (*o*)	H_g (*m*)	H_h (*p*)
[CuL10] (ClO$_4$)	3.02, t, 6H, J = 5.8	3.69, t, 6H, J = 5.8	8.10, d, 3H, J = 8.6	7.14-7.17 dd, 3H, J = 8.6 J = 8.6	7.32, d. 3H, J = 7.8	7.52, d, 6H, J = 7.5	7.08, t, 6H, J = 7.8	7.29, s, 3H

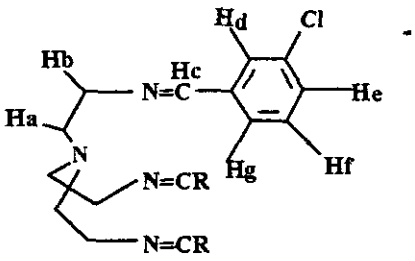

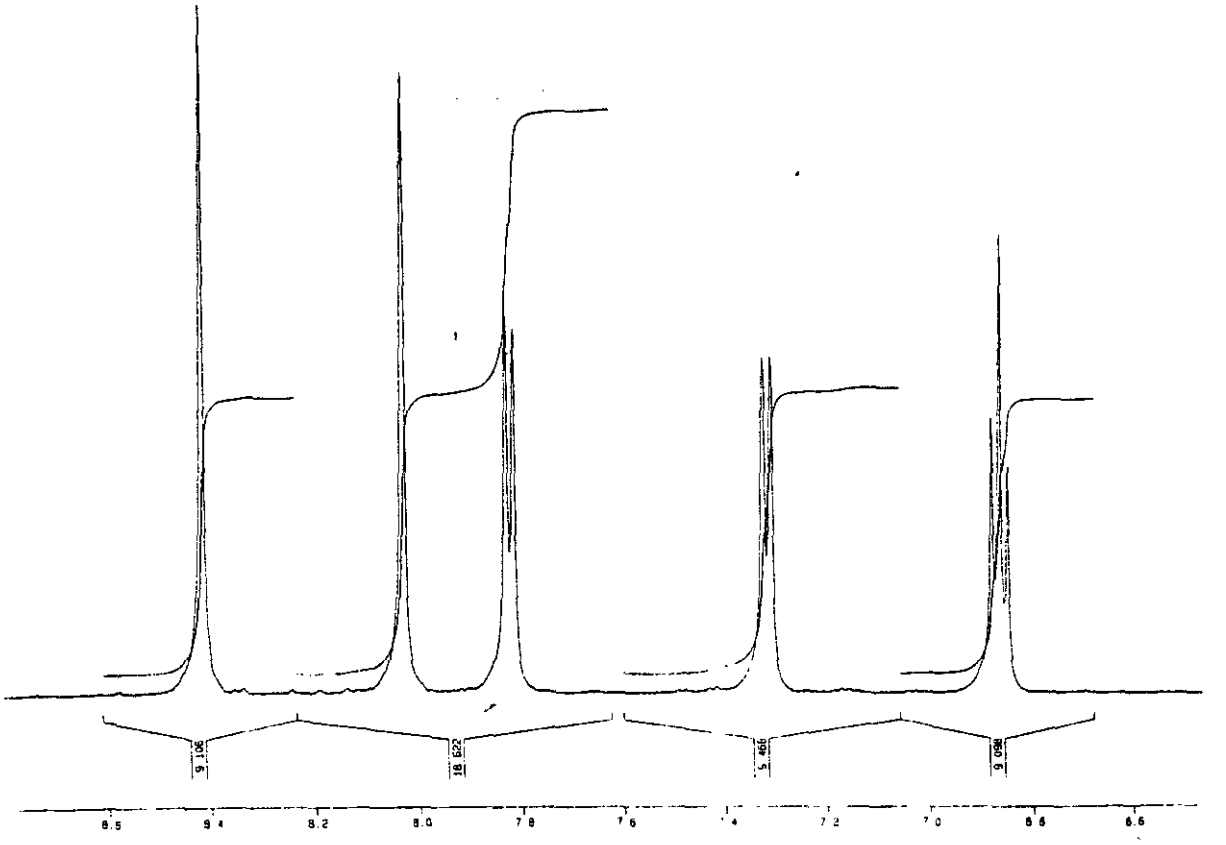

Figure 2.9 *^{1}H NMR of [CuL5](BF$_4$) in d3-MeCN at 243 K - aromatic region*

Table 2.5 *^{1}H NMR data for [CuL5](BF$_4$) in d3-MeCN at 243 K*

Compound	H_a	H_b	H_c	H_d	H_e	H_f	H_g
[CuL5] (BF$_4$)	3.0, s, 6H,	3.72, s, 6H,	8.38, s, 3H,	8.03, s, 3H,	7.33, d, 3H, J = 8.0	6.86, t, 3H, J = 7.9	7.81, d, 3H, J = 7.6

2.8.2 [CuL7](ClO$_4$)

The effect of substituting the larger and less electronegative bromine atom was investigated. The complex was characterised by FAB mass spec, [CuL7]$^+$ 711 (100%) and [CuL7](ClO$_4$) 810 (5%). A strong peak in the infrared spectrum at 759 cm^{-1} is characteristic of a *ortho*-disubstituted ring. The green tinge of the solid product and the observation of amine stretches in the infrared indicated that, even with argon protection and the use of dry solvents, a small degree of metal-assisted imine hydrolysis has occurred.

^{1}H NMR and 2D COSY spectra confirm that the Br substituent is in the *ortho* position. A doublet at δ 8.07 ppm (J = 7.25 Hz) assigned to H$_d$, arises from *ortho* coupling to H$_e$ only. The resonance is more downfield than both H$_e$ and H$_f$ due to its proximity to the electronegative bromine ion. H$_f$ is coupled to both H$_e$ and H$_g$ occurring as a triplet at δ 7.15 ppm (J = 7.2 Hz). H$_e$ couples to H$_f$ and H$_d$ appearing also as an unresolved triplet at δ 6.25 ppm. H$_g$ is coupled only to H$_f$ and appears as a doublet downfield due to its proximity to the imine at δ 7.6 ppm (J =7.45 Hz). The presence of Cu(II) impurity made acquisition of MAS spectra impracticable.

2.8.3 [CuL8](ClO$_4$)

The effect of a methyl substituent was investigated to see the effect of electron donation on the benzene ring. The complex was prepared for comparison with [CuL5](BF$_4$) to see if the redox properties were influenced by electron donation into the ring. It was also hoped that the methyl substituents might repel each other to an extent causing sufficient opening of the pseudo-cavity to permit an interaction of the podate with dioxygen.

The complex was characterised by FAB mass spec, [CuL8]$^+$ 516 (100%) and [CuL8](ClO$_4$) 615 (5%). As with [CuL6](ClO$_4$) there is also a peak that corresponds to the dimer, [(CuL8)$_2$(ClO$_4$)]$^+$ at 1132 (2%). The infrared spectrum indicates the presence of a *meta* disubstituted aromatic ring with characteristic peaks at 691, 791 and 876 cm^{-1}.

The ^{1}H NMR and 2D COSY spectra in d$_3$-MeCN confirms that the CH$_3$ substituent is in the *meta* position, **(Figure 2.10)**. A singlet at δ 7.92 ppm can be assigned to H$_d$. The second *ortho* proton H$_h$ (a doublet (J = 7.7 Hz) coupled to H*g* is seen upfield at δ 7.86 ppm. H$_f$ couples only to H$_g$ and appearing as a doublet at δ 7.22 ppm (J = 7.6 Hz) whereas H$_g$ is coupled to both H$_f$ and H$_h$ and due to the shielding effect appears more upfield as a triplet at δ

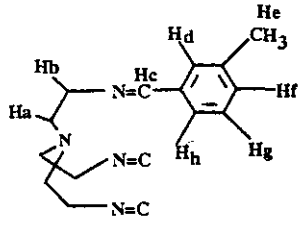

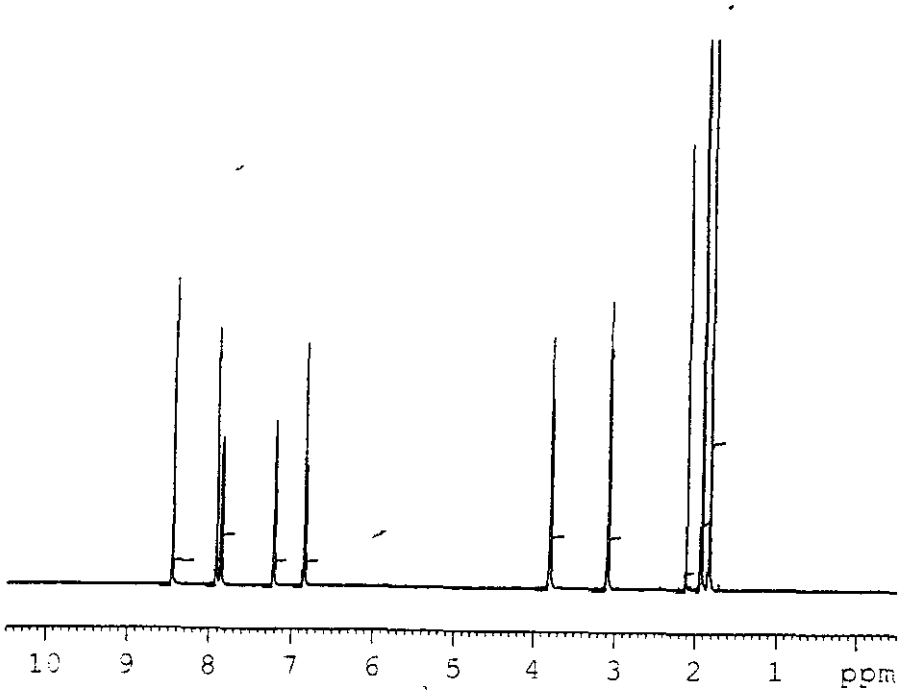

Figure 2.10 (a) ^1H NMR of [CuL8](ClO4),

Table 2.6 *^1H NMR data for [CuL8](ClO4) in d_3-MeCN at 300 K*

Compound	H_a	H_b	H_c	H_d	H_e	H_f	H_g	H_h
[CuL8](ClO4)	3.10, t, 6H, J = 5.5	3.80, t, 6H, J = 5.1	8.46, s, 3H,	7.92, s, 3H,	1.83, s, 9H,	7.22, d, 3H, J = 7.6	6.84, t, 3H, J = 7.7	7.86, d, 3H, J = 7.70

6.84 ppm (J =7.65 Hz). The methyl resonance, H_e, appears as a singlet at δ 1.83 ppm and integrates for 9 protons as opposed to 3 protons for each of the phenyl protons, **(Table 2.6)**. No solid state spectrum was obtained for the complex due to Cu(II) impurity.

2.8.4 [CuL9](ClO$_4$)

G. Morgan reported the crystal structure of the metal-free podand based on a [1+3] Schiff base condensation between tren and nitrobenzaldehyde.[26] In Cu(II) tripodal ligands studied by Palaniandavar *et al*,[28] NO_2 substitution has been shown to elevate the $E_{1/2}$ values of the Cu(II)/Cu(I) couple in the Cu(II) complexes. Thus, for our purposes, it is hoped that NO_2 substitution will make the Cu(II) redox state more easily accessed by enhancing π delocalisation.

The complex was characterised by FAB mass spectroscopy, [CuL9]$^+$ 608 (100%). The infrared spectrum shows strong peaks due to symmetric and asymmetric stretches of the nitro group at 1348 and 1522 cm^{-1}, respectively. Amine peaks are also evident indicating that, as for [CuL7]$^+$, a degree of metal-assisted imine hydrolysis has occurred.

The ^{1}H NMR spectrum in $CDCl_3$ has the same coupling pattern as its fellow *ortho*-substituted analogue, [CuL7](ClO$_4$). However, the situation changes in d_3-MeCN. The ^{1}H NMR spectrum in d_3-MeCN at 300 K has an extra set of peaks owing to either the presence of a different solution conformer of the podate or possibly cleavage of one strand in the more polar solvent, **(Figure 2.11)**.

2.9 Cu(I) Complexes of Potentially Heptadentate Tripodal Schiff Base Ligands

Although seven co-ordination is readily achieved by many transition metal ions it is quite rare that a single ligand can supply all seven donor atoms. L.J. Wilson and co-workers[29] designed the potentially heptadentate ligand Py$_3$tren. It was later reported during investigations into the bonding properties of Py$_3$tren that the seventh bond to the apical or bridgehead *nitrogen atom may only be considered as 'weakly bonding' in the cases involving Mn^{2+} and Co^{2+}*. Alyea *et al* reported the synthesis of two analogous ligands that contain thiophene and furan moieties in the pendant arms.[30] These potentially heptadentate tripodal Schiff base

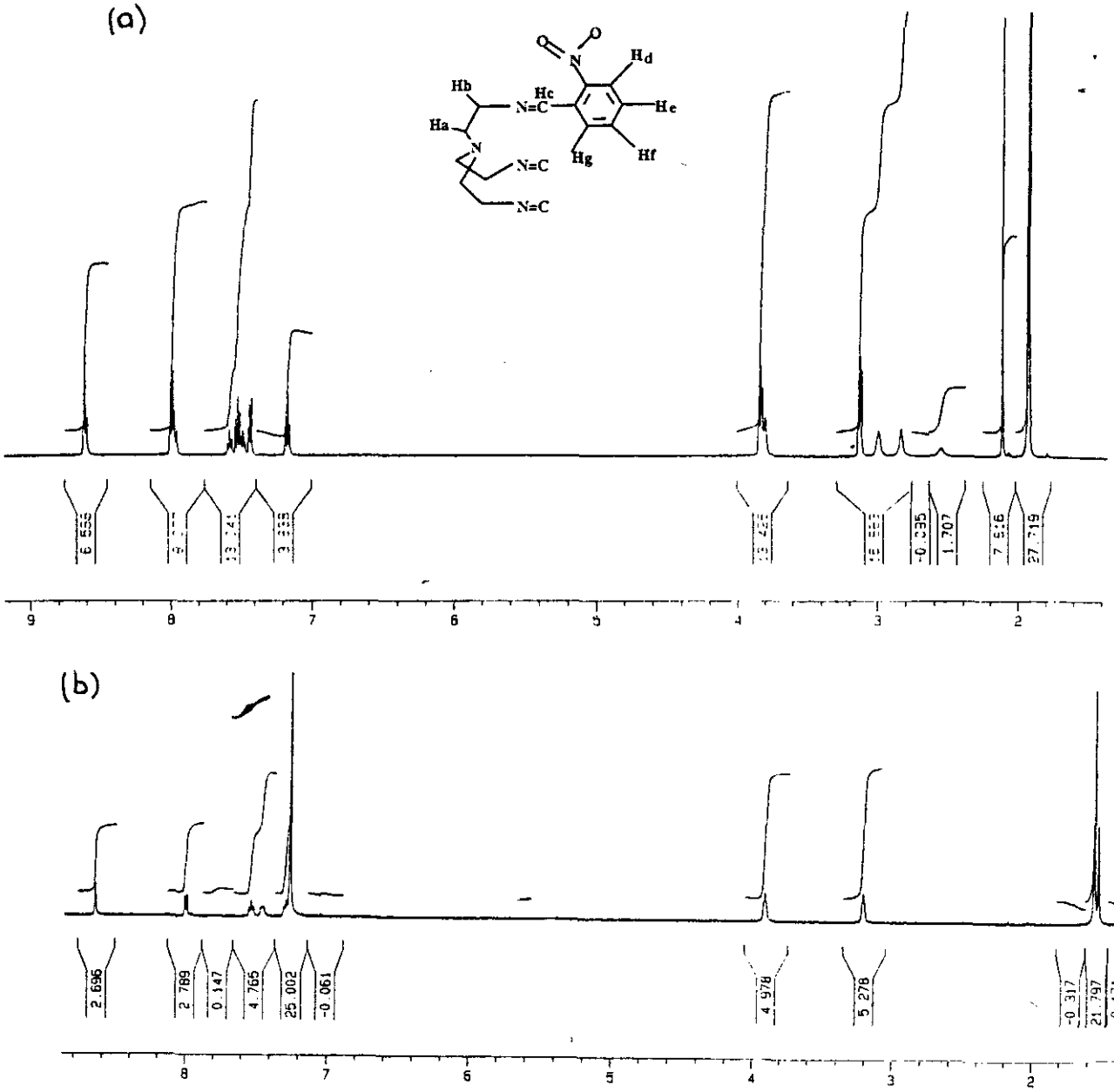

Figure 2.11 (a) ^1H NMR of [CuL9](ClO$_4$) in d_3-MeCN at 300 K, (b) ^1H NMR of [CuL9](ClO$_4$) in $CDCl_3$ at 300 K

Table 2.7 *^1H NMR data for [CuL9](ClO$_4$)*

Compound	H_a	H_b	H_c	H_d	H_e	H_f	H_g
[CuL9](ClO$_4$) in $CDCl_3$ at 300 K	3.20, t, 6H, J = 5.5	3.91 unresolved triplet	8.65, s, 3H,	8.05, d, 3H, J = 8.3	7.53, t, 3H, J = 7.4	7.29, masked by solvent	7.45, d, 3H, J = 7.3
[CuL9](ClO$_4$) in d_3-MeCN at 300 K	3.0, t, 6H, J = 5.5	3.75, t, 6H, J = 5.3	8.49, s, 3H,	7.91, d, 3H, J = 8.3	7.40, t, 3H, J = 7.9	6.99, t, 3H, J = 7.5	7.35, d, 3H, J = 7.6

ligands called S_3tren and O_3tren were expected to enhance metal interaction with the bridgehead nitrogen atom as compared to Py_3tren.

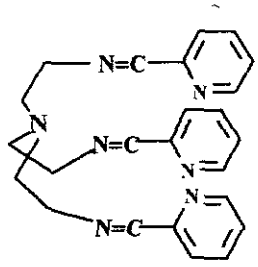

Figure 2.12 Structure of Py3tren

2.9.1 [CuL11](ClO$_4$)

The complex was characterised by FAB mass spec., peaks at 443 (100%) and 542 (20%) corresponding to [CuL11]$^+$ and [CuL11](ClO$_4$), respectively.

The ^{1}H NMR spectrum of the copper complex was compared to that of the free ligand reported by Alyea.[30] There are noticeable downfield shifts of proton resonances upon complexation of the Cu(I) cation. The most noticeable shift is for the imine C-H resonance ((L)7.91→(CuL) δ 8.44 ppm). The furan proton H_c (α to the imine substituent) occurs downfield, relative to free ligand, at δ 8.12 ppm as a doublet due to coupling to H_d. H_e is also a doublet and is more upfield at δ 7.57 ppm. The most shielded proton H_d appears as an unresolved triplet at δ 7.4 ppm. The methylenes occur in the usual position seen for other tren-based tripodal hosts.

2.9.2 [CuL12](ClO$_4$)

The methyl substituted furfural was reacted to see the effect of electron donation to a furan ring as opposed to electron donation to a benzene ring in [CuL1](ClO$_4$).

The complex was characterised by its FAB mass spectrum- peaks at 485 (100%) and 584 (25%) correspond to [CuL12]$^+$ and [CuL12](ClO$_4$), respectively. The ^{1}H NMR spectrum of the 5-methyl substituted podate is more simplified than its unsubstituted analogue. **(Figure 2.13)** The imine resonance is more upfield at δ 8.1 ppm. Doublets at δ 7.1 and δ 6.1 ppm are

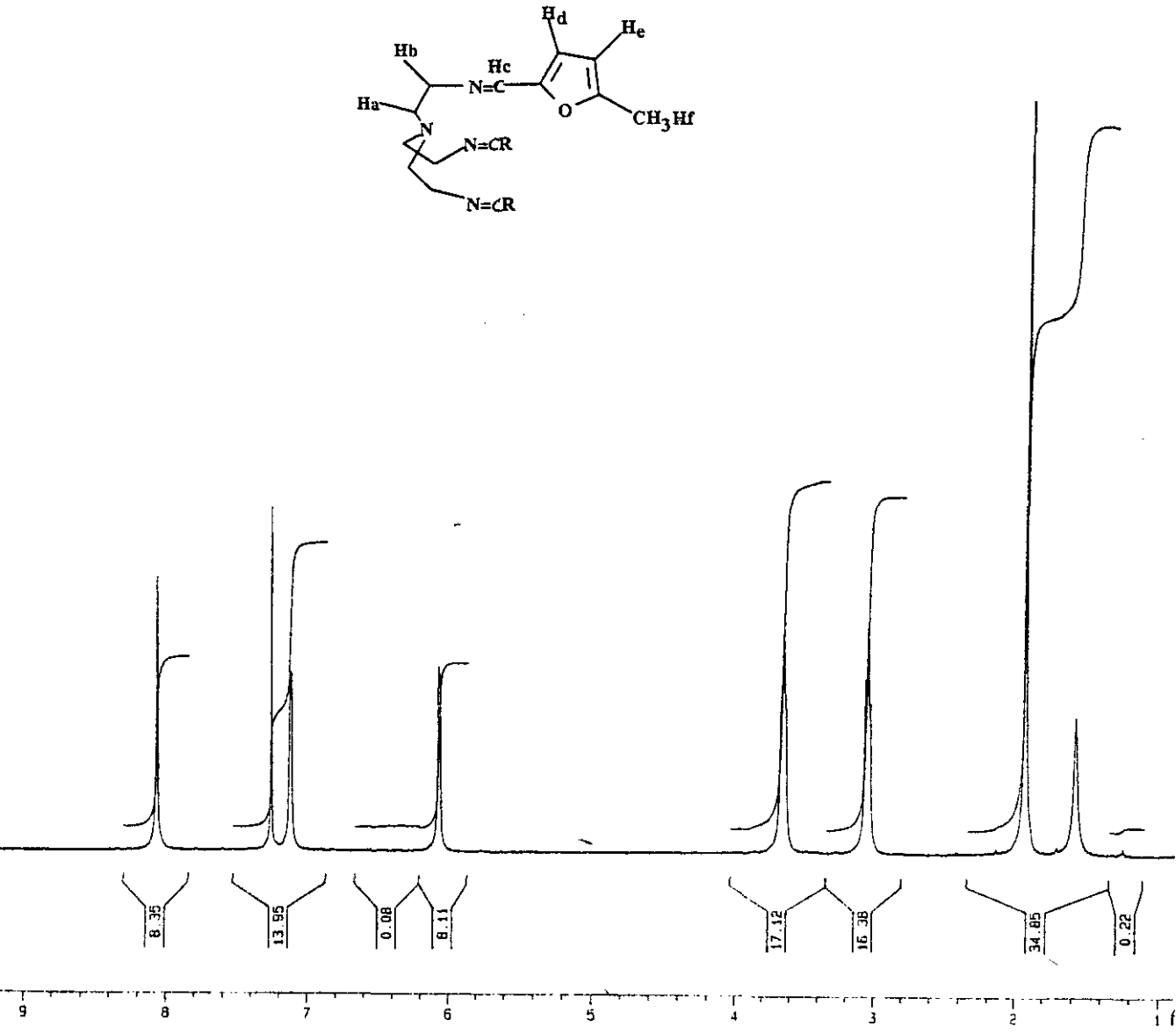

Figure 2.13 *^1H NMR of [CuL12](ClO$_4$) inCDCl$_3$ at 300 K*

Table 2.8 *^1H NMR data for [CuL12](ClO$_4$) inCDCl$_3$ at 300 K*

Compound	H_a	H_b	H_c	H_d	H_e	H_f
[CuL12] (ClO_4)	3.07, s, 6H,	3.88, s, 6H	8.07, s, 3H,	7.13 d, 3H J = 3.0	6.08, d, 3H, J = 2.8	1.93, s, 9H,

due to H_d and H_e, respectively. The methyl substituent is seen as a singlet at δ 2.0 ppm. The doublets and singlet integrate in the ratios 1:1:3 confirming the assignments, **(Table 2.8)**.

2.10 Trpn-Based Cu(I) Podates

The cap was extended by using trisisopropylamine in place of tris(ethylamine). Perhaps the increased flexibility of these podates would lead to a Cu(I) podate that could bind with dioxygen.

2.11 Solution Stable Cu(I) Trpn-Based Podates

2.11.1 [CuL14](ClO$_4$)]

The complex was characterised by FAB mass spec., $[CuL14]^+$ 753 (100%). ^{1}H NMR and 2D COSY spectra confirm that the Br substituent is in the *ortho* position. The coupling of the aromatic protons follows the same pattern as that reported for [CuL7](ClO$_4$)]. The chemical shifts and coupling constants are reported in **Table 2.9**.

The methylene region is well defined; H_a, couples to H_b only, appearing as a well resolved triplet at δ 2.8 ppm. H_c couples to H_b only and also occurs as a triplet at δ 3.55 ppm. H_c occurs more downfield than H_a because, as mentioned in section 2.3.2, the imine group causes a deshielding effect. H_b couples to both H_a and H_c appearing as a multiplet at δ 2.00 ppm. This is more upfield than the two sets of triplets due to their shielding effect, **(Figure 2.14)**.

In the ^{13}C solid state NMR spectrum, the broad signal between δ 115 and 130 ppm could be from the carbon attached to bromine. The remaining ^{13}C resonances are broad as is the ^{15}N spectrum, **(Figure 2.15).** The breadth presumably arises from the quadrupolar relaxation effects associated with $^{79, 81}$Br isotopes. In the ^{15}N spectrum there is a significant change in both bridgehead and imine ^{15}N co-ordination shifts compared to other ligands studied e.g. [CuL1(ClO$_4$)] and [CuL6](ClO$_4$). The splitting of imino and methylene resonance provides evidence for inequivalence of podand strands in the solid state (See X-ray crystallography in Section B).

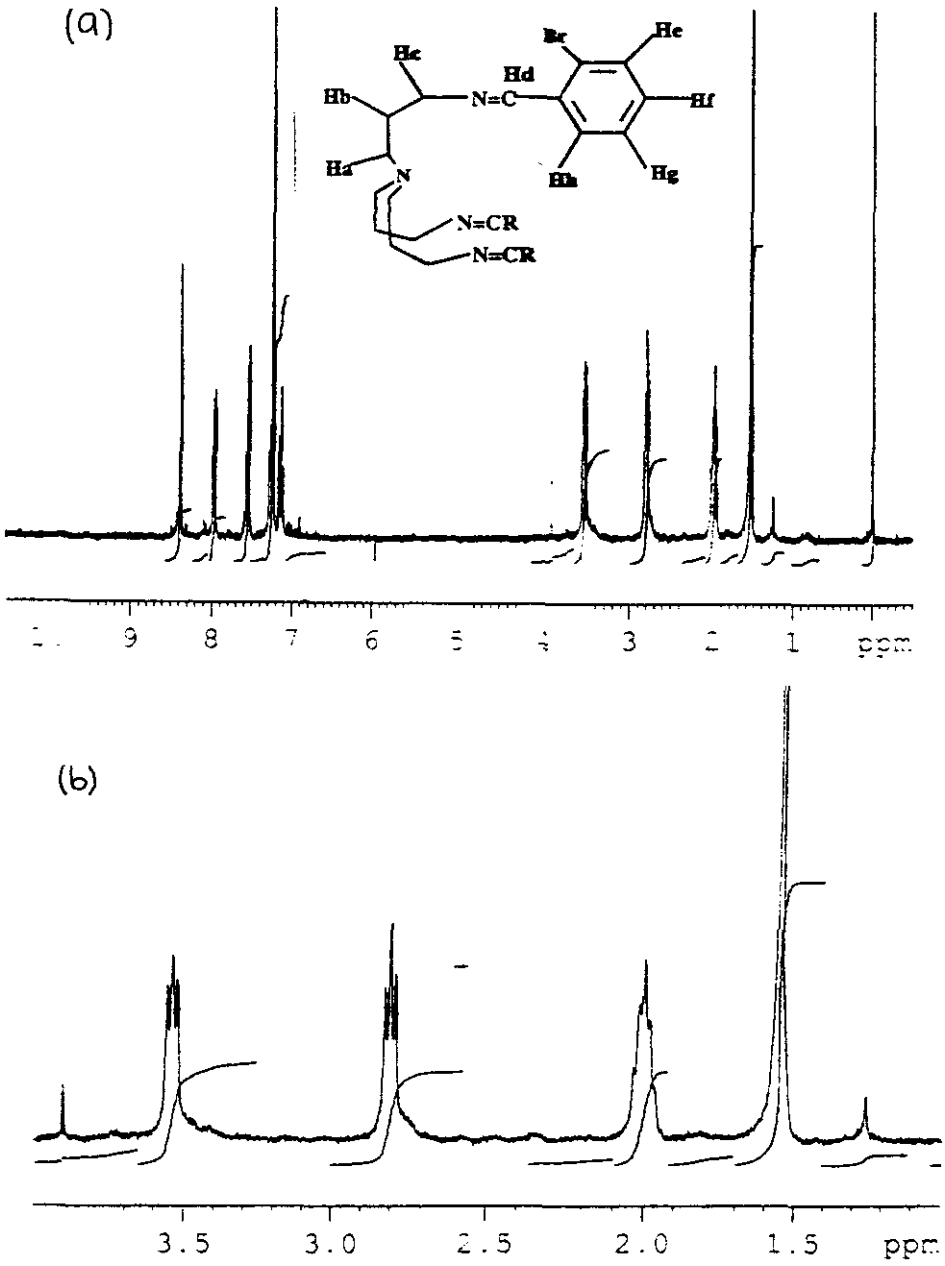

Figure 2.14 (a)^{1}H NMR of [CuL14](ClO$_4$) in CDCl$_3$ at 300 K, (b) ^{1}H NMR of [CuL14](ClO$_4$) in methylene region

Table 2.9 *^{1}H NMR data for [CuL14](ClO$_4$) in CDCl$_3$ at 300K*

Compound	H_a	H_b	H_c	H_d	H_e	H_f	H_g	H_h
[CuL14] $(ClO_4)_2$	2.8, t. 6H, J = 5.5	2, m 6H.	3.55, t. 6H. J = 5.3	8.4, s. 3H.	8.0, d. 3H. J = 6.0	7.15, t. 3H. J = 5.9	7.29. masked by solvent	7.55, d. 3H. J = 7.0

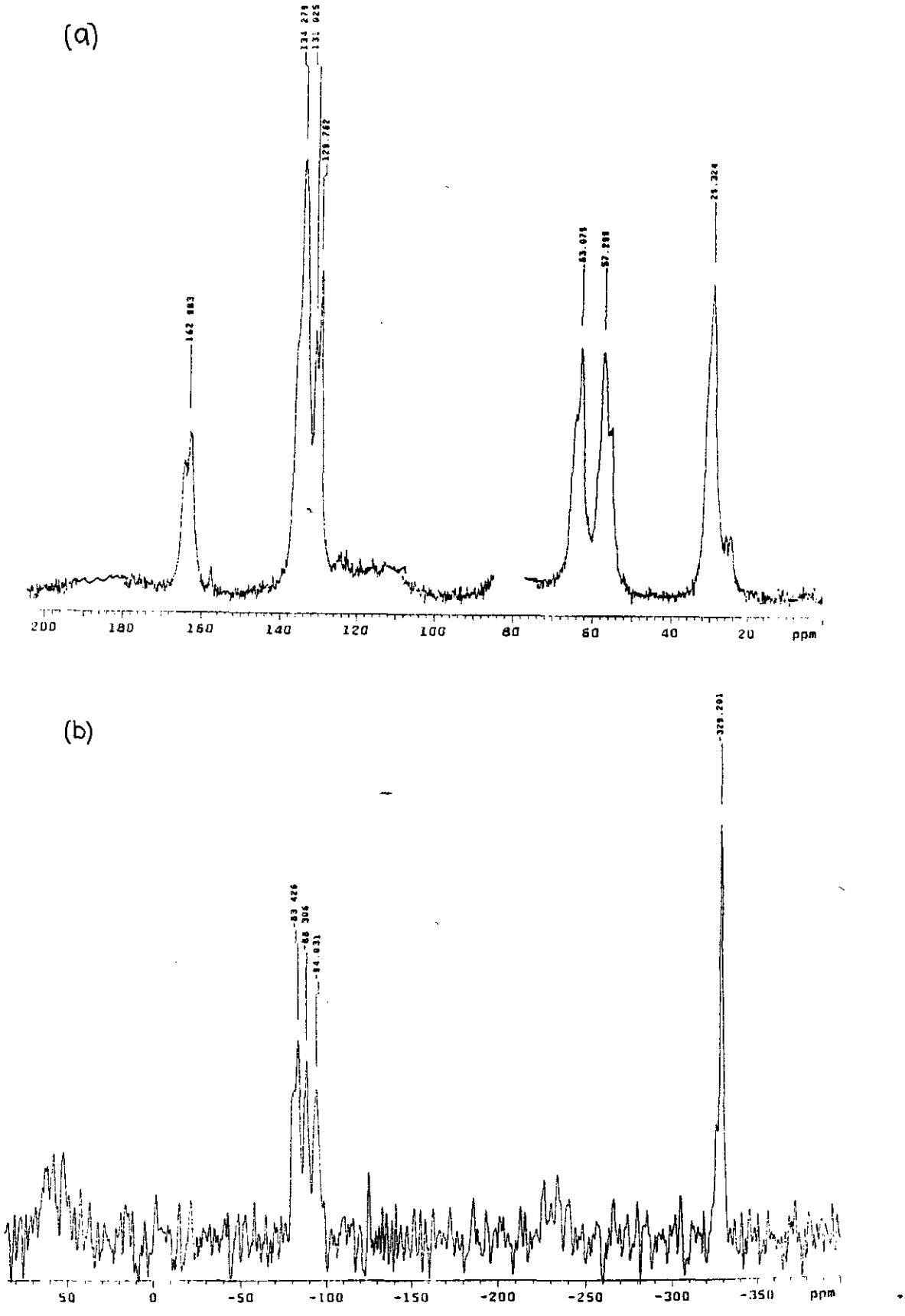

Figure 2.15 Solid State NMR of [CuL14](ClO$_4$); (a) ^{13}C Spectrum, (b) ^{15}N spectrum

2.11.2 [CuL15](ClO$_4$)

The complex was characterised by FAB mass spec., [CuL15]$^+$ 558 (100%). This podate was more stable than its tren-based analogue. There was no trace of any green oxidised Cu(II) species. The ^{1}H NMR and 2D COSY spectra indicate that the CH_3 substituent is in the *meta* position. The coupling pattern of the aromatic protons is the same as that reported for [CuL8](ClO$_4$)], with actual shifts reported in the experimental section. The imine and methylene proton pattern is as described for [CuL14](ClO$_4$)].

The ^{13}C solid MAS spectrum displays narrow lines in a complex pattern of resonances. There are three clear signals for the methyl groups at δ 19-20 ppm; each methylene carbon and the imine resonance is also split in 2:1 intensity ratio, suggesting one strand is different to the other two. The situation for the ^{15}N spectrum is also a complicated story. The high-frequency imino-N multiplet must be a combination of ^{63,65}Cu coupling and an inequivalent ^{15}N environment. Even the bridgehead N is split into a δ -328/-331 ppm doublet with intensity ratio 1:3:6. The ^{35}Cl spectrum displays a well-defined quadrupolar bandshape. This suggests that the sample is well ordered but with some distortion of the ClO_4^- ion, **(Figure 2.16)**.

2.11.3 [CuL16](ClO$_4$)

The infrared spectrum shows strong peaks due to symmetric and asymmetric stretches of the nitro group at 1343 and 1524 cm^{-1}, respectively. The complex was characterised by its FAB mass spectrum, [CuL16]$^+$ 651 (100%), [CuL16](ClO$_4$) 751 (7%). There are peaks in the FAB mass spectrum that correspond to [Cu$_2$L16]$^+$ (5%) and [Cu$_2$L16](ClO$_4$) (5%), **(Figure 2.17)**. From the data collected, it is impossible to tell if there is a second copper incorporated or whether these peaks arise because of dimerisation, possibly restricted to the FAB matrix.

The aromatic region of the ^{1}H NMR ($CDCl_3$) is unlike that reported for the analogous tren-capped complex, [CuL9](ClO$_4$). There is the familiar triplet, doublet, doublet, triplet pattern but what is different is the presence of a triplet at δ 8.4 ppm - more downfield than the imine resonance. This may be an effect of deshielding by the nitro current or perhaps a different solution conformer, **(Figure 2.18)**.

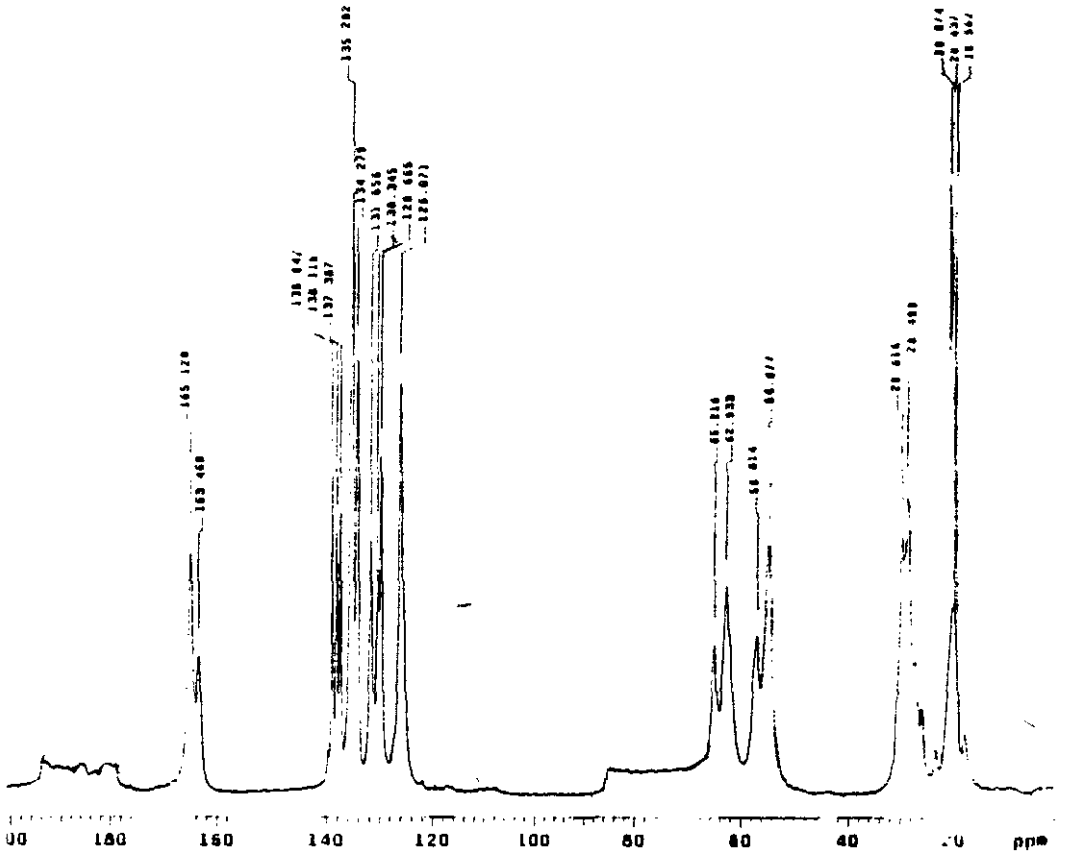

Figure 2.16(a) Solid State NMR of [CuL15](ClO4); ^{13}C Spectrum

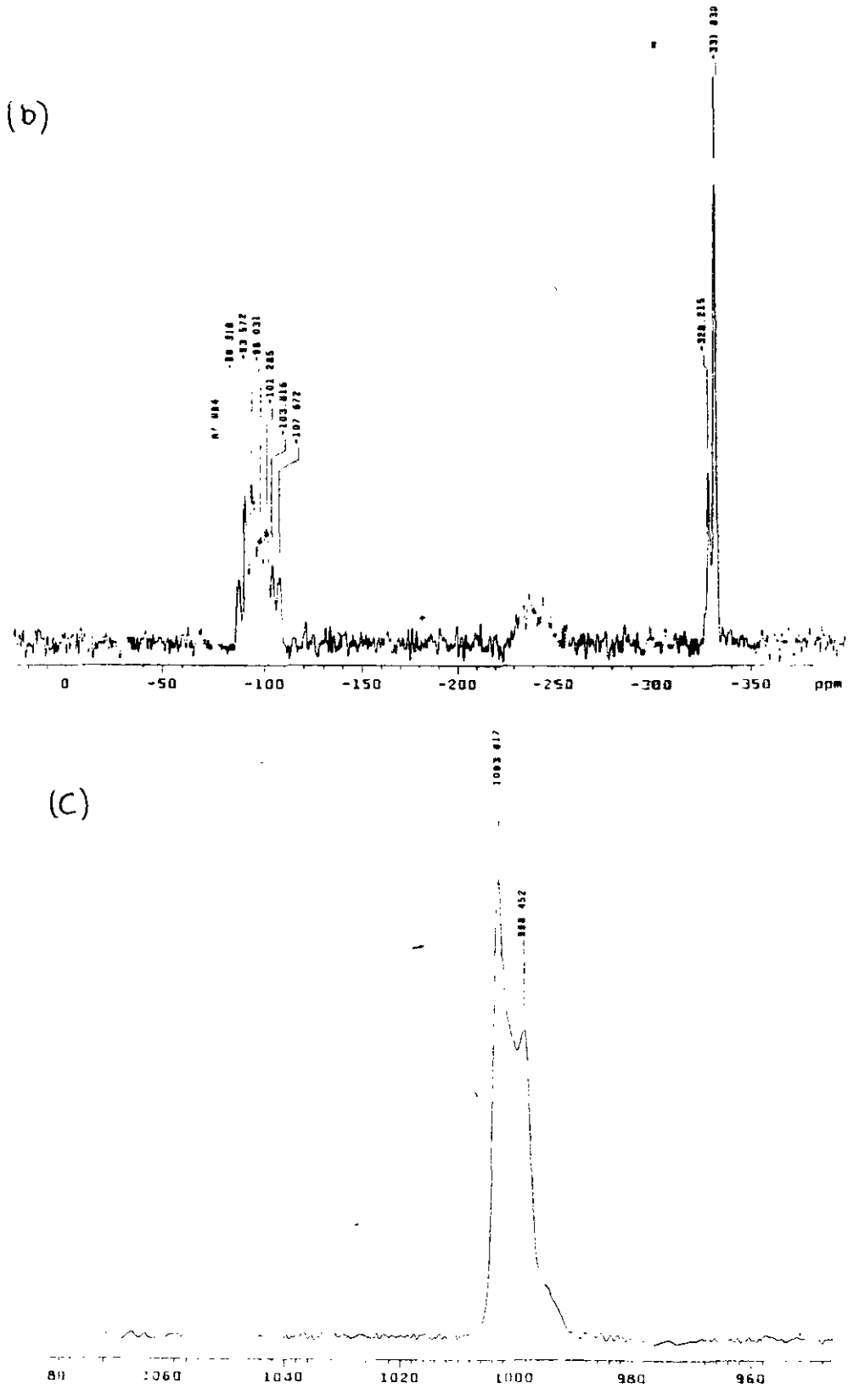

Figure 2.16 Solid State NMR of [CuL15](ClO$_4$); (b) ^{15}N spectrum, (c) ^{35}Cl spectrum.

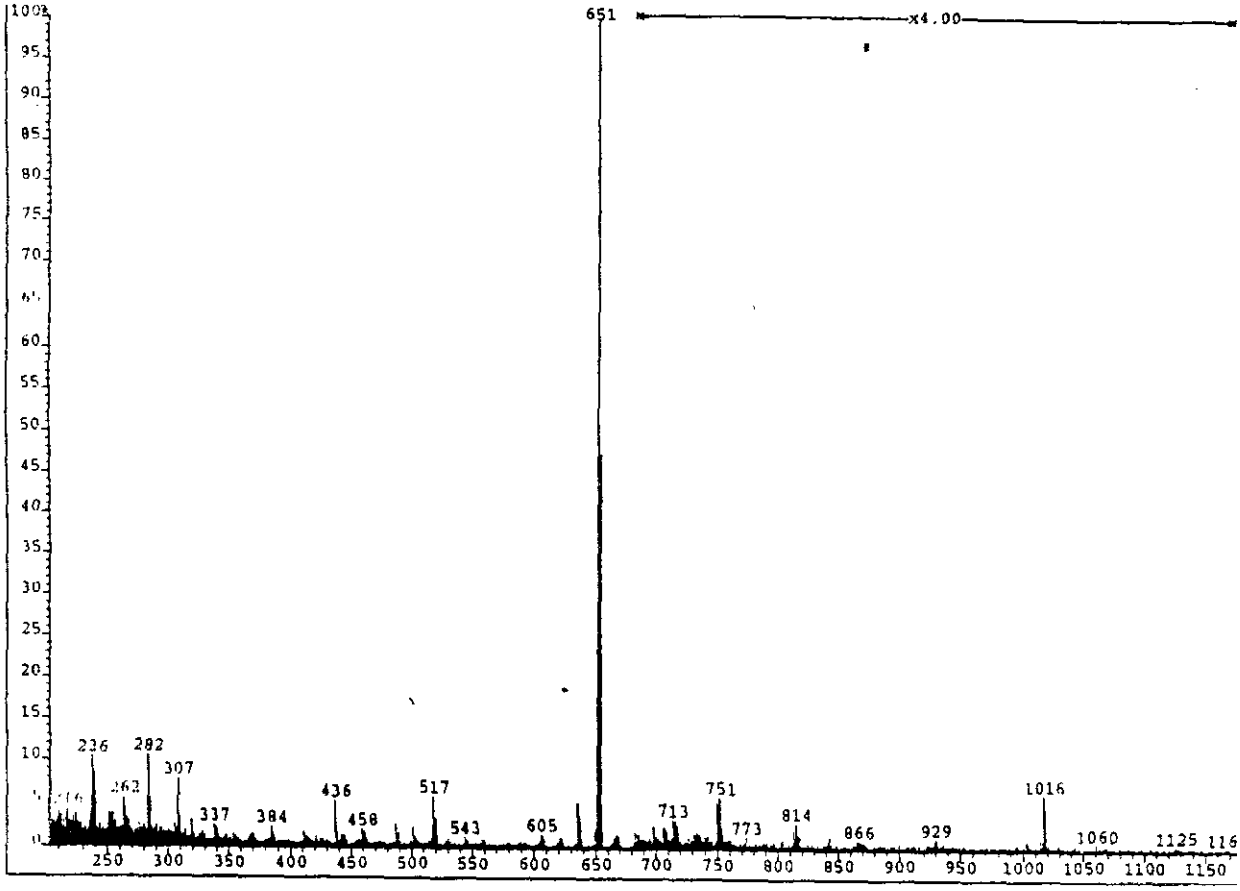

Figure 2.17 FAB Mass Spec. of [CuL16](ClO$_4$)

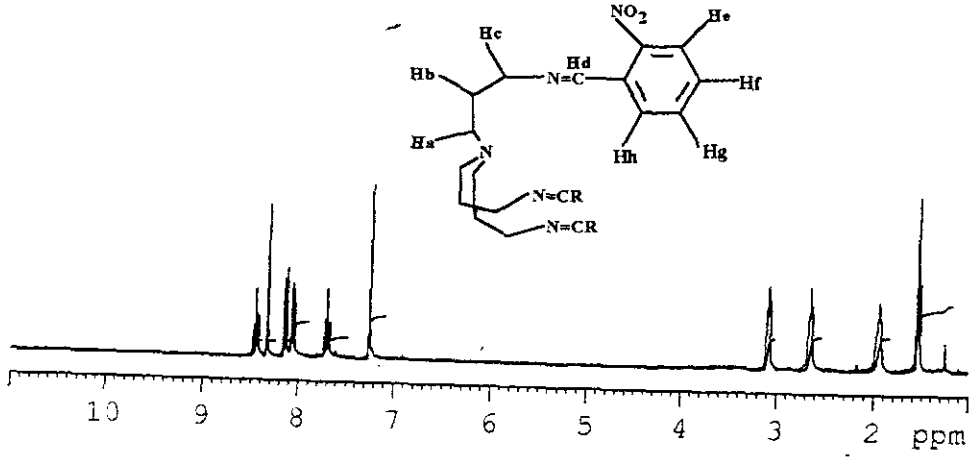

Figure 2.18 ^{1}H NMR of [CuL16](ClO$_4$) in CDCl$_3$ at 300K

Table 2.10 ^{1}H NMR data for [CuL16](ClO$_4$) in CDCl$_3$ at 300K

Compound	H_a	H_b	H_c	H_d	H_e	H_f	H_g	H_h
[CuL16] (ClO$_4$)	2.7, t. 6H, J = 5.1	1.95, m 6H,	3.10, t, 6H, J = 5.2	8.3, s, 3H,	8.05, d, 3H, J = 8.04	8.4, t, 3H, J = 7.6	7.6, t, 3H, J = 8.0	8.1, d, 3H, J = 7.6.

2.11.4 [CuL17](ClO$_4$)

The complex was characterised by FAB mass spec, $[CuL17]^+$ 593 (100%) and $[CuL17](ClO_4)]^+$ 692 (2%). The infrared spectrum displays a strong peak at 691 cm^{-1} indicating monosubstitution of the aromatic ring.

The ^{1}H NMR was not as simple as that recorded for the analogous complex [CuL10](ClO$_4$). There appears to be overlapping in the aromatic region which is not resolved sufficiently by decoupling experiments. The ^{13}C solid state NMR is well resolved and clean - there are single lines for the methylene and imine carbons but the aromatic resonances, although well resolved, are complex suggesting that some degree of coupling is being observed. The C=C group accounts for the appearance of peaks at δ 147-145 ppm. The imine ^{15}N spectrum is a fairly clean four-line pattern appearing in the normal imine range arising from coupling to one Cu nucleus. The ClO_4^- resonance consists of a single line.

2.12. Unstable Trpn-Based Cu(I) Podates

2.12.1 [CuL13] (ClO$_4$)

It is not clear why this podate is more prone to oxidation/hydrolysis than its tren-capped analogue. The solid Cu(I) complex formed upon insertion of Cu(I) into the preformed ligand was air sensitive. This was evident from the green colour of a Cu(II) species present and the ready oxidation on exposure to air, even in acetonitrile. The synthesis was repeated several times and only under an argon atmosphere was an acceptable product obtained. However, elemental analysis was unsatisfactory.

The major peak at 515 (100%) in the FAB mass spectrum arises from the monpositive $[CuL13]^+$ cation. The infrared spectrum provided further evidence of complex formation from the presence of perchlorate peaks at 1096 and 621 cm^{-1}. Amine stretches at ~3300 cm^{-1} indicated the presence of a copper amine complex.

It was anticipated that the aromatic region of the ^{1}H NMR would have a similar pattern to that reported for [CuL1](ClO$_4$)]. However, this was not the case possibly owing to the presence of a paramagnetic Cu(II) species which may be similar to that of the Cu(I) podate or simply a $[Cu(tren)]^{2+}$ complex. This would explain the broadness and extra signals in the

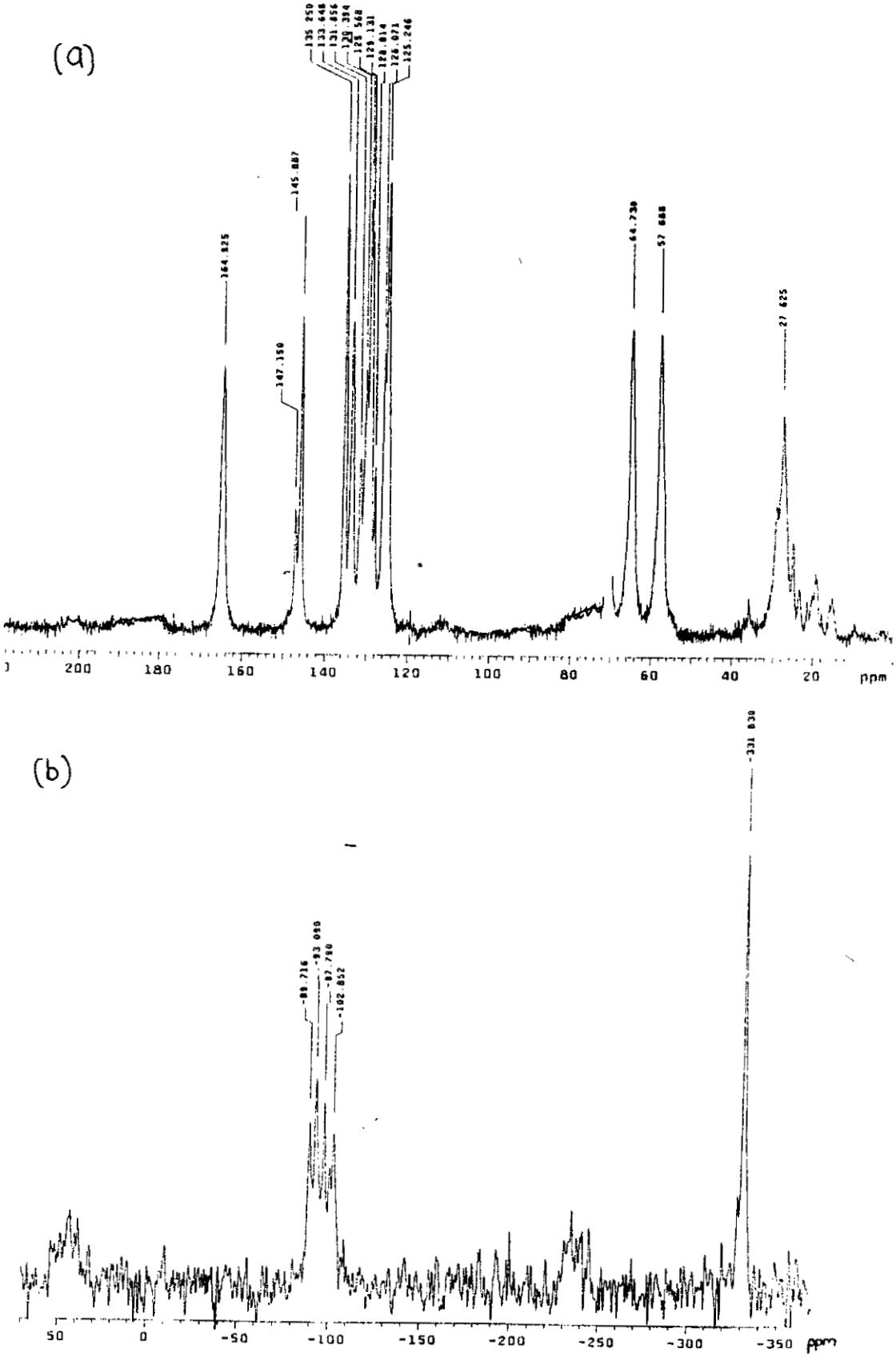

Figure 2.19 Solid State NMR of [CuL17](ClO$_4$) ; (a) ^{13}C spectrum, (b) ^{15}N spectrum

methylene region of the ^{1}H NMR. The FAB mass spec. shows a peak at 427 (55 %) which may be due to $\{[Cu(tren).MeCN(H_2O)_2]ClO_4\}^+$.

The ^{1}H NMR in **Figure 2.20** clearly show the difficulties in assigning the spectrum - the resonances are broad and proton integration does not equate. In analogous Cu(II) cryptates, the resonances of the methylenes are not shifted but are broadened, (Chapter 3E). Similarly, for this complex mixture, the unshifted and broad methylene signals make it seem likely that the second species is a $[Cu(II)tren]^{2+}$ complex. This paramagnetic complex is probably causing broadening of the $[Cu(I)L13](ClO_4)$ complex spectrum. There is only one imine resonance evident which would confirm this assignment of the impurity as a $[Cu(II)tren]^{2+}$. If hydrolysis of one podate arm had occurred to generate a second species, a second imine resonance would be present.

Conclusion

The characterisation of the Cu(I) podates by solution and solid state NMR has indicated that the stability of the Cu(I) podates is dependent on both the capping amine and the choice of substituted aromatic aldehyde. In general, the stable Cu(I) podates produce simple solution ^{1}H NMR spectra suggesting high symmetry. However, the solid state NMR spectra suggest some inequivalence in the bulk solid.

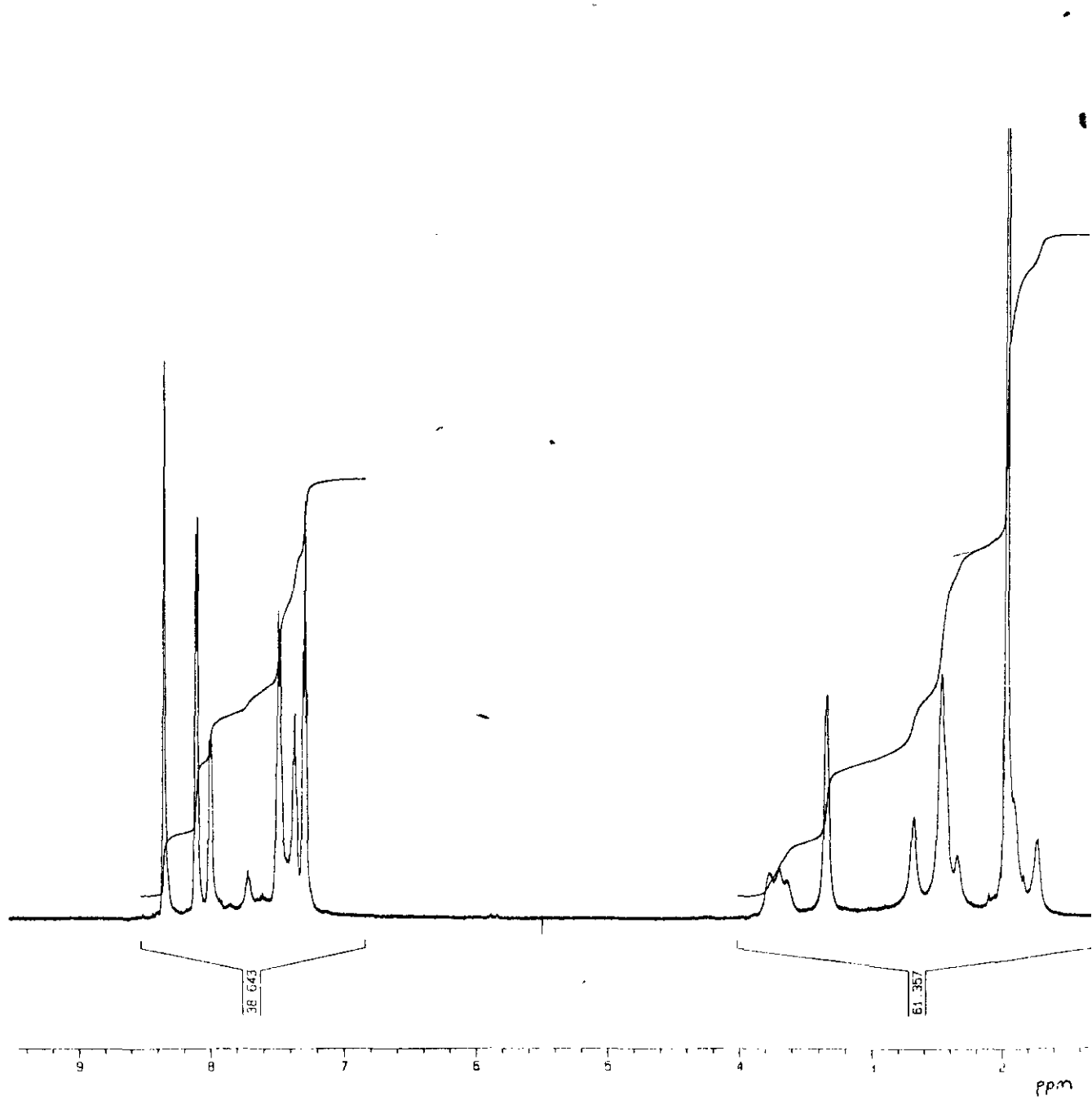

Figure 2.20 ^{1}H *NMR of [CuL13](ClO₄) in* d_3*-MeCN*

Section B

2.13 X-Ray Structural Analysis of Cu(I) Tripodal Complexes

The following Cu(I) tripodal complexes were studied by X-ray Crystallography: $[CuL1][ClO_4]$, $[CuL5][BF_4]$, $[CuL6][ClO_4]$, $[CuL9][ClO_4]$, $[CuL14][ClO_4]$, $[CuL15][ClO_4]$, $[CuL16][ClO_4]]$ and $[CuL17][ClO_4]$.

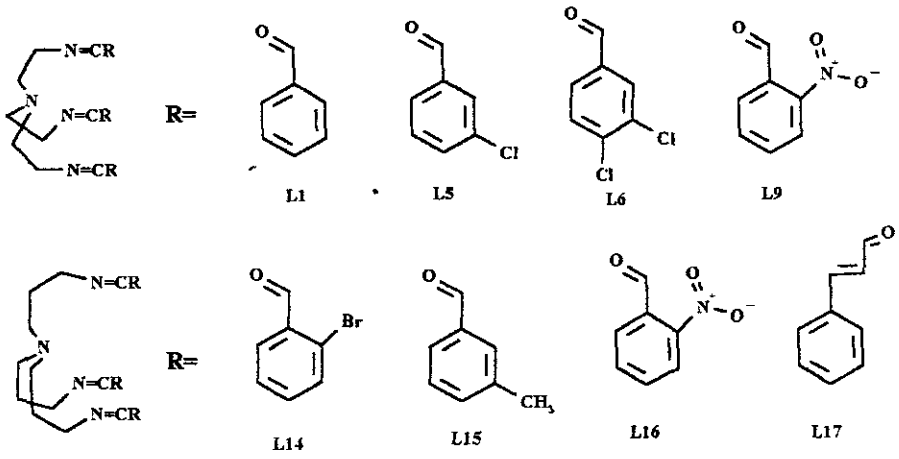

Scheme 2.5 Cu(I) podates studied by X-ray Crystallography

2.13.1 Generalisation of Cu(I) Geometry Attributable to both Cu(I) Tren and Trpn Capped Podates

The geometry around the Cu(I) centre is best described as a distorted trigonal pyramid. The Cu-N distances to the equatorial imine nitrogens [N(11), N(21), N(31)] are in the range of 1.99 - 2.02 Å, while the Cu-N(bridgehead) distances are longer and in the range 2.19 - 2.22 Å. In all cases, there is no obvious interaction with the either solvent or counterion molecules.

Unless stated, there are generally no intermolecular contacts and presumably the conformation adopted in the crystal structure serves to minimise intramolecular and crystal packing forces.

The C=N bond is always in the *trans* conformation. Whether it is *cis* or *trans* is

important to the overall shape of the podate. However, the cap size seems to play a significant part in determining the conformation adopted by the Cu(I) complexes.

2.14 Comparison of Tren Vs Trpn capping

The availability of the X-Ray crystal structures of [CuL9](ClO_4) and [CuL16](ClO_4) provides an opportunity to compare the effect of cap size when the substituted aromatic rings have identical substituents in the same position. Any generalisations derived from the different caps will be made. This will be followed with a look at other Cu(I) podates structurally characterised by X-Ray crystallography to see any further effects that result due to substitution at different positions of the ring by different heteroatoms.

2.14.1 Comparison of [CuL9][ClO_4] and [CuL16][ClO_4]

Single crystals of both a Cu(I) tren and a trpn-capped tripodal ligand derived from nitrobenzaldehyde were obtained by recrystallisation from acetonitrile. Inspection of these nitro-substituted podates is interesting as it has been proposed that *ortho* substituted nitro groups may induce steric hindrance as well as electronic effects.[31] In comparing CuL9 structure to the Cu(I) complexes of L5, L14 and L15 the nitro groups seem to be orientated *away from* and not *into* the pseudo cavity. This is due to steric and electronic effects causing the *ortho* substituted rings to get as far apart in space as possible. This is also the case for the *ortho* substituted trpn-capped podates.

2.14.1.1 [CuL9][ClO_4].2CH_3CN

The unit cell consists of one copper podate molecule, two uncoordinated acetonitrile molecules and a perchlorate counterion. The cation is shown in **Figure 2.21a.**

The Cu-N distances to the equatorial imine nitrogens [N(11), N(21), N(31)] are shown in **Table 2.11**. The copper ion sits 0.181 Å *above* the plane of the equatorial imine nitrogen atoms, while the apical tertiary amine (N1) lies 2.012 Å below that plane: the Cu-N(bridgehead) distance is 2.193 Å.

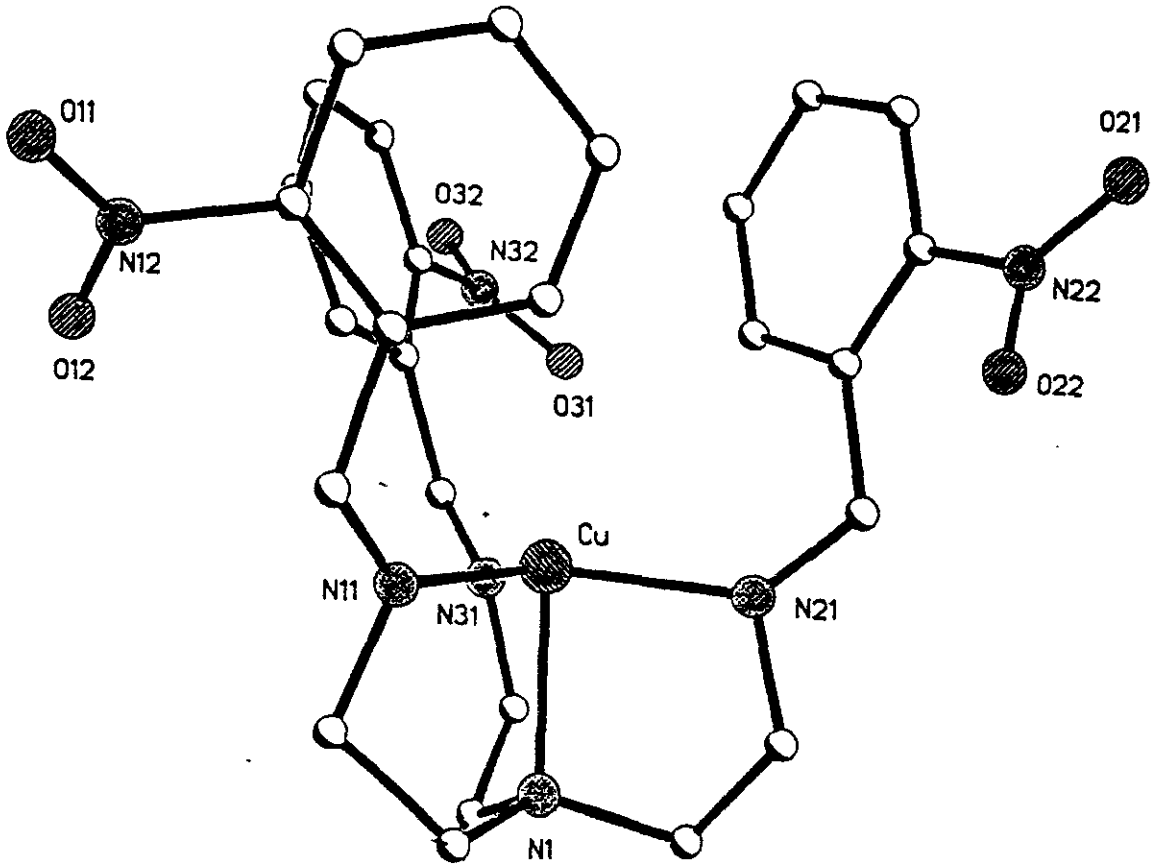

Figure 2.21a X-Ray structure of Cu(I) cation of nitro-substituted podate, [CuL9][ClO$_4$]

Table 2.11a Selected bond lengths [Å] and angles[^{o}] for [CuL9](ClO$_4$);

Cu-(N11)	1.989 (5)	Cu-(N21)	2.001 (4)
Cu-(N31)	2.014 (4)	Cu-(N1)	2.196 (4)
(N11)-Cu-(N1)	84.98 (19)	(N11)-Cu-(N21)	120.3 (16)
(N21)-Cu-(N1)	84.70 (17)	(N11)-Cu-(N31)	119.01 (18)
(N31)-Cu-(N1)	85.01 (15)	(N21)-Cu-(N31)	118.34 (19)

2.14.1.2 [CuL16][ClO_4]

The unit cell consists of a single copper podate cation and a perchlorate counterion. The cation is shown in **Figure 2.21b**. As for the tren-capped series, the geometry around the Cu(I) centre is a distorted trigonal pyramid comprised of four nitrogen donor atoms. The Cu-N distances to the equatorial imine nitrogens [N(11), N(21), N(31)] are shown in **Table 2.11b**.

The copper ion sits 0.167 Å *below* the plane of the equatorial imine nitrogen atoms, with the apical tertiary amine (N1) lying 2.36 Å below that plane. The Cu-N(bridgehead) distance is 2.189 Å.

As the tren cap is less flexible [CuL9][ClO_4] appears to stand more upright and as a consequence the plane of C-N(imine)-C to the CuN_3(imine) plane is approaching perpendicular. This is in contrast to the trpn-capped complex where the plane of C-N(imine)-C to the CuN_3(imine) plane is tending towards parallel. These angles have the effect that the tren-capped podates appear to have a deep cleft and can be described as goblet shaped, whilst the trpn-capped series have a shallower cleft appearing bowl-shaped. **Figure 2.21c** compares tren capped [CuL9][ClO_4] to trpn-capped [CuL16][ClO_4] clearly showing this analogy.

Although the Cu-N(bridgehead) distances are consistently in the region, 2.01 Å, regardless of cap size, it is the direction of the copper ion out of the imine plane that seems to influence the stability of the podate. For the tren cap series the copper ion is found to be always out of the plane of the imines *away* from the apical nitrogen. This has the consequence of reducing the N_{eq}-Cu-N_{ax} angle below 90°. The N_{eq}-Cu-N_{eq} angle reflects this out of plane as well as an asymmetry in positioning of the imine strands. For the more flexible trpn-capped podate the copper ion is also out of the plane of the imines but *towards* the bridgehead nitrogen. This flexibility allows a more regular geometry and the Cu-imine plane site appears concave. This concavity appears to offer the Cu(I) ion more protection from attack e.g. by oxygen.

Figure 2.22a shows a overlayed view of the analogous complexes projected down the N(bridgehead)-Cu vector while **Figure 2.22b** is a side-on view showing how it is the cap size that is responsible for any differences between the two complexes.

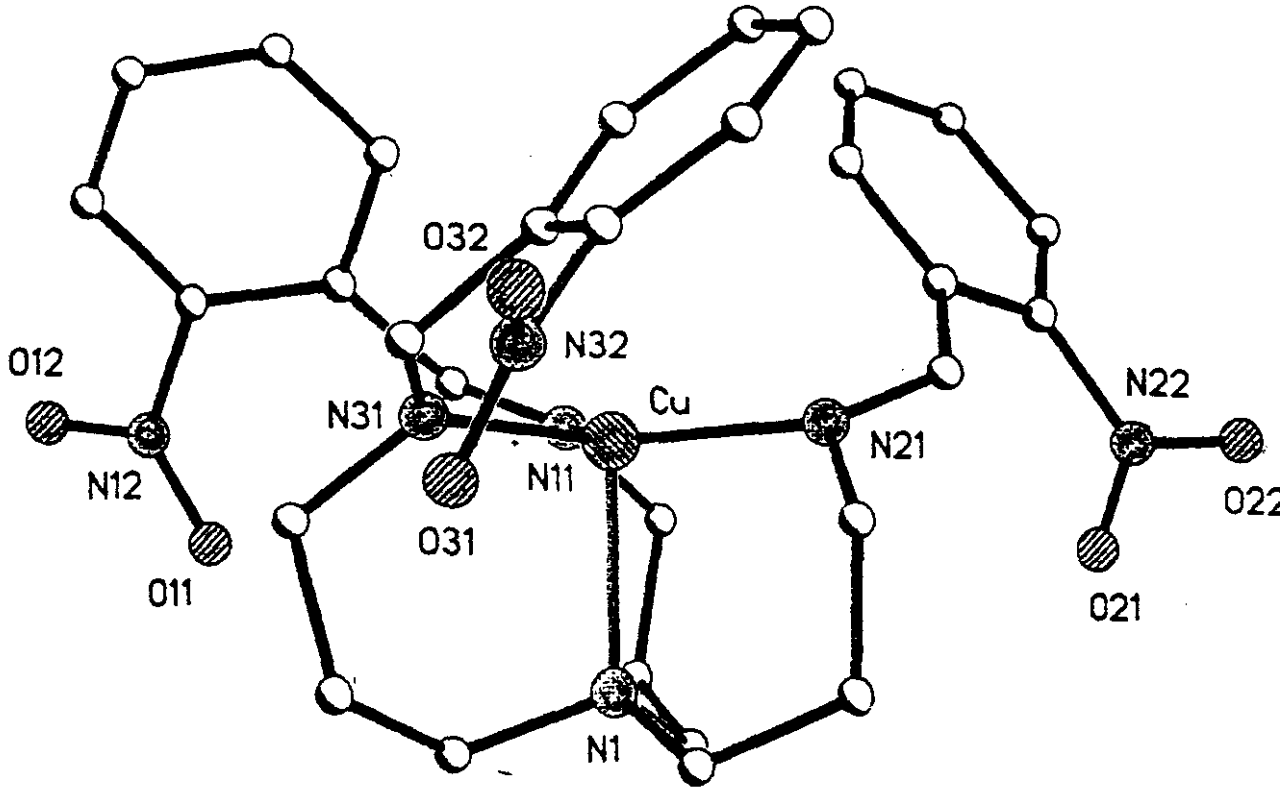

Figure 2.21b X-Ray structure of Cu(I) cation of nitro-substituted trpn-based podate, [CuL16][ClO$_4$]

Table 2.11b Selected bond lengths [Å] and angles[^{o}] for [CuL16](ClO$_4$);

Cu-(N11)	2.010 (3)	Cu-(N21)	2.006 (4)
Cu-(N31)	2.030 (3)	Cu-(N1)	2.189 (4)
(N11)-Cu-(N1)	94.79 (14)	(N11)-Cu-(N21)	121.39 (15)
(N21)-Cu-(N1)	94.48 (15)	(N11)-Cu-(N31)	117.44 (14)
(N31)-Cu-(N1)	94.99 (14)	(N21)-Cu-(N31)	119.13 (13)

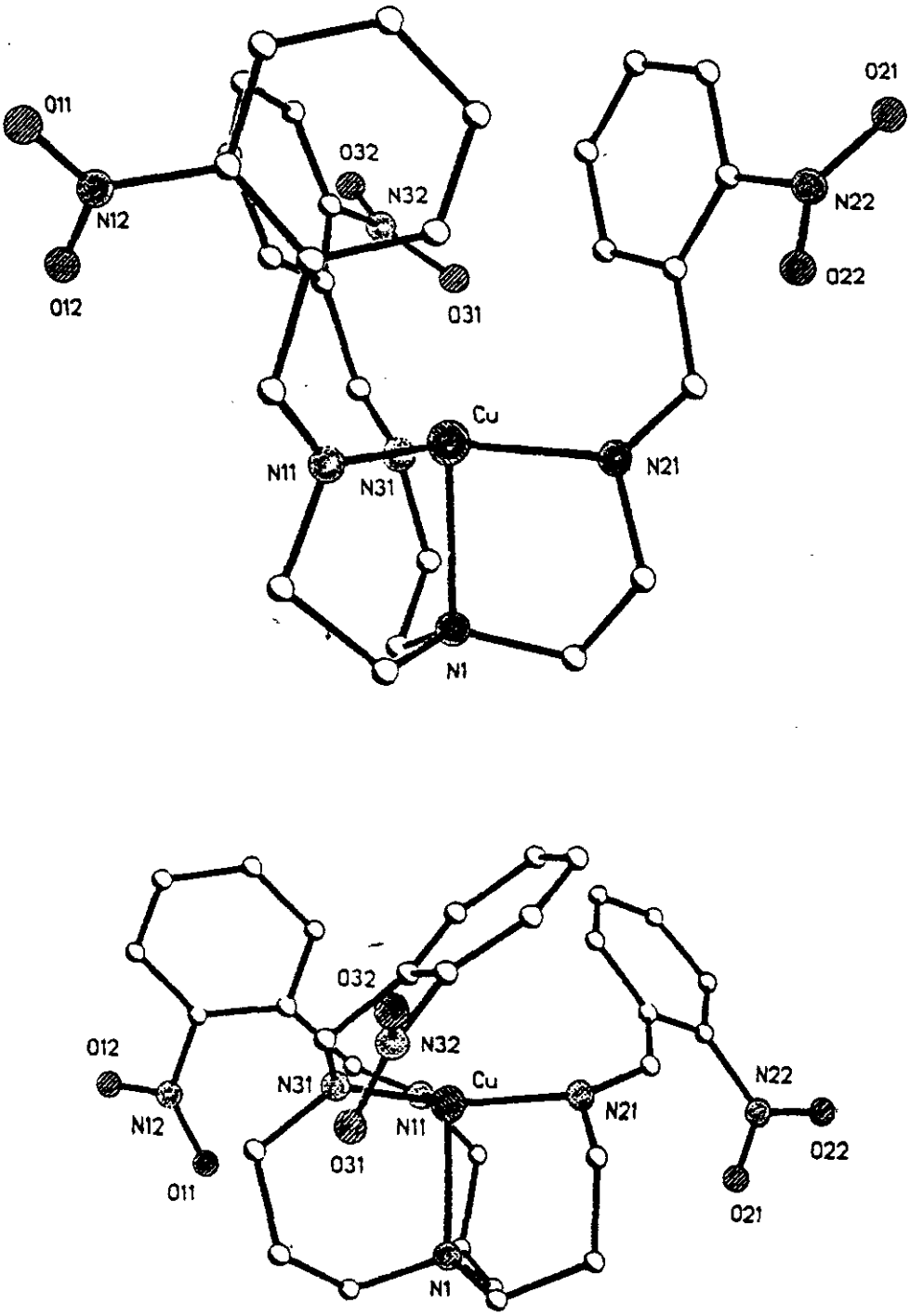

Figure 2.21c Comparison of The X-Ray Structures of [CuL9][ClO$_4$] and [CuL16][ClO$_4$]

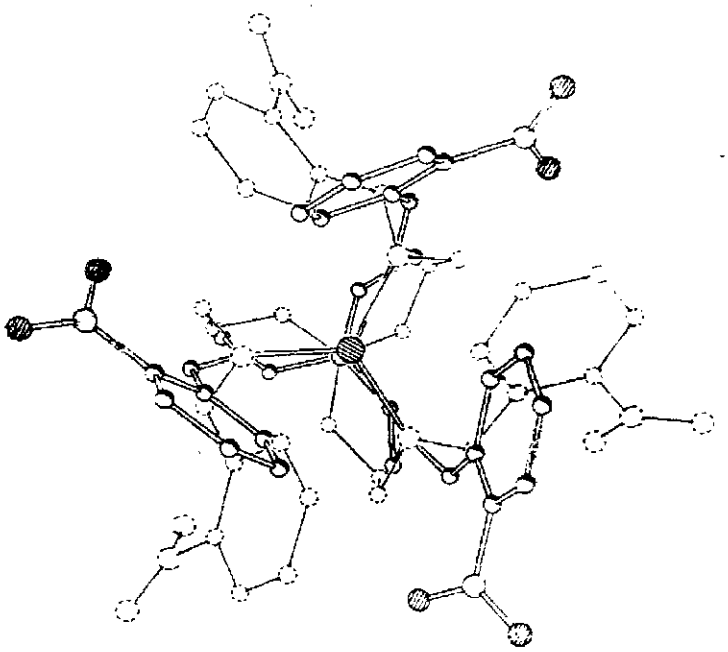

Figure 2.22a Overlayed view of [CuL9]$^+$ and [CuL16]$^+$ projected down N(bridgehead)-Cu vector

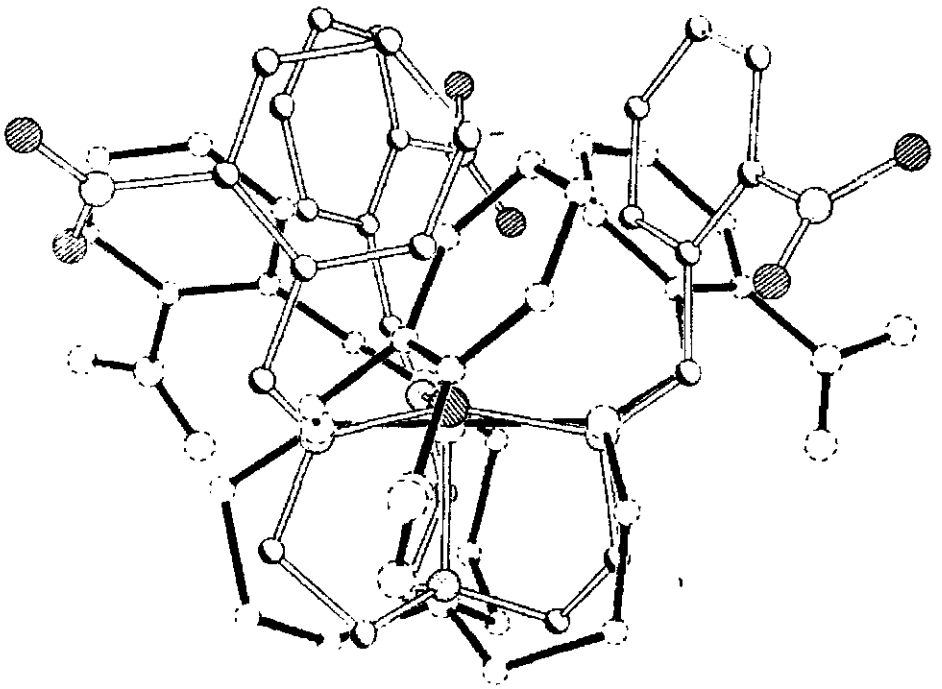

Figure 2.22b Overlayed side-on view of [CuL9]$^+$ and [CuL16]$^+$

It is now apparent how the rigidity of the imine and the geometry of the CuN_3 plane defines the cavity to a certain extent. It is also important to investigate the effect of; no-substitution, *meta*-substitution and disubstitution on the pseudo cavity.

2.15 Effect of No Substitution : X-Ray Structure of [CuL1][ClO_4]

The cation structure is shown in **Figure 2.23a**. The unit cell consists of a single copper podate cation and a perchlorate anion. The copper ion sits 0.18 Å above the plane of the equatorial imine nitrogen atoms, while the apical tertiary amine (N1) lies 2.041 Å below that plane: the Cu-N distance is 2.221 Å, **(Table 2.12)**.

This complex was the first of the Cu(I) podates to be characterised by X-ray crystallography. It gave the first indication that the phenyl rings are orientated inwards as if to form a pseudo cavity providing the Cu(I) with a 'protected' environment. The observed aerobic stability may be as a result of steric hindrance of dioxygen to access this pseudo cavity.

Intramolecular edge-to-face interactions are evident, **(Figure 2.23b)**. Recent theories of π-interaction stress the need to be aware of π-charge considerations when estimating crystal packing or other geometric relationships which involve interactions between aromatic rings. Electrostatic effects favour face-to-edge contacts between the negative π-charge and positive σ-bonding framework involving the H-C σ-bond. Face-to-edge π-σ interactions may contribute to the stability of this conformation.

2.16 A Meta-Substituted Cu(I) Podate : X-Ray Structure of [CuL5][BF_4]

The cation structure is shown in **Figure 2.24a**. The unit cell consists of a single copper podate cation and a tetrafluroborate counterion. The Cu ion lies 0.193 Å above the N2, N3 and N4 plane away from the N1 atom. The harder amine nitrogen binds more weakly to the Cu(I) ion with a distance of 2.209 Å, **(Table 2.13)**.

Intramolecular interactions are evident, **(Figure 2.24b)**. The chlorines seem to be orientated towards the centres of the neighbouring phenyl groups. Some attraction of the negative chlorine towards the positive centres of the phenyl rings is to be expected and is analogous to the CH-π ring interacting rationalised by Sanders and Hunter[32,33]. This may

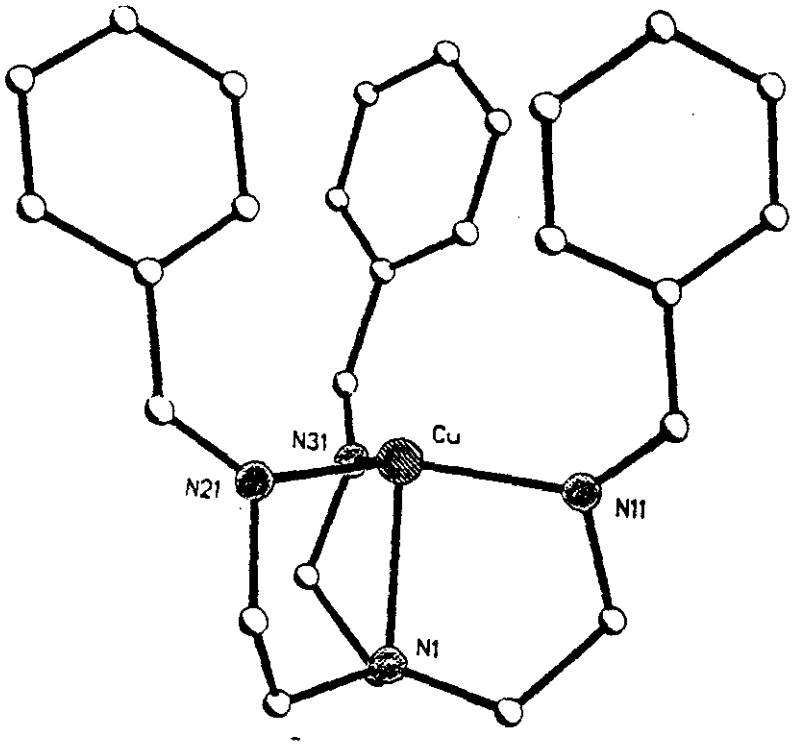

Figure 2.23a Structure of Non-substituted Podate, [CuL1]⁺

Table 2.12 Selected bond lengths [Å] and angles[°] for [CuL1](ClO₄);

Cu-(N21)	2.015(3)	Cu-(N11)	2.005 (3)
Cu-(N31)	2.020 (3)	Cu-(N1)	2.221 (3)
(N11)-Cu-(N1)	85.46 (10)	(N11)-Cu-(N21)	121.91(11)
(N21)-Cu-(N1)	84.3 (10)	(N21)-Cu-(N31)	114.45 (11)
(N31)-Cu-(N1)	84.84 (11)	(N11)-Cu-(N31)	121.27 (11)

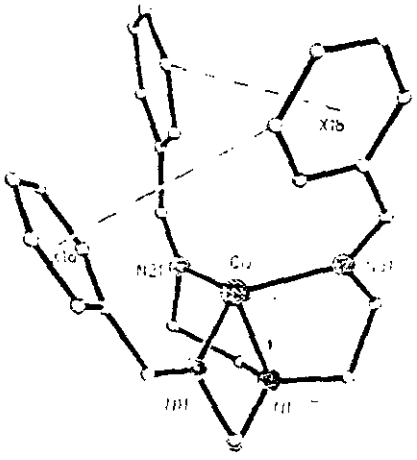

Figure 2.23b Intramolecular edge-to-face interactions in [CuL1]⁺

explain why the chlorines have turned into the ring as if to form a pseudo-cavity rather than turning out. The pseudo cavity may prevent access of oxygen and so offer protection against aerobic oxidation. It was noticed that on crystallisation, green and blue crystals were also present - one explanation for these oxidised products could be a different orientation of the chlorines which permits access of dioxygen or of another donor which stabilises the Cu(II) state. There are no obvious interactions with the fluoroborate anion.

There is evidence that halogen atoms in molecular solids do not function as inert spacers of a certain volume (close packing) but rather through specific anisotropic, electronic effects.[34] An indication, though not a confirmation, of the attractive nature of halogen-halogen interactions is provided by the failure of the so-called chloro-methyl exchange rule in many polychloroaromatics. Since these substituent groups have nearly the same volume as each other (Cl 20 Å^3; Me 24 Å^3), replacement of one by the other is not expected to change the crystal structure if the packing is governed strictly by the Kitaigorodskii close-packing model. This rule is valid for a large number of irregularly shaped aliphatic molecules but breaks down more or less routinely for chloroaromatics. An X-ray powder pattern recorded for the *meta*-substituted methyl analogue [CuL8][ClO_4] showed that the crystal structures would indeed differ although no X-ray structure was available to identify the nature of the difference, **Figure 2.24c**. In contrast, substitution of the chloro group by the electronically similar, though geometrically dissimilar bromo group (volumes Cl 20 Å^3, Br 26 Å^3) in many halogenated aromatics does not change the crystal structure.[34]

2.16.1 Structural Comparison of [CuL1][ClO_4], [CuL5][BF_4] and Jeyvak

The two structures were compared along with a previously characterised crystal, Jeyvak[27], which has the formula [$C_{27}H_{30}Cu(I)N_4$][BPh_4]. This complex cation is the same as [CuL1](ClO_4) but the counterion is tetraphenylborate.

The capping tren subunit is almost identical for all three cations. Bond angles and bond lengths are in close agreement. Differences occur in the spatial arrangement of the side arms. It was originally thought that Jeyvak and [CuL1][ClO_4] would have the same orientation of rings as the only difference between them was the counterion. However, it was noticed that this was not the case - the phenyl rings in [CuL1](ClO_4) deviate more from each other making

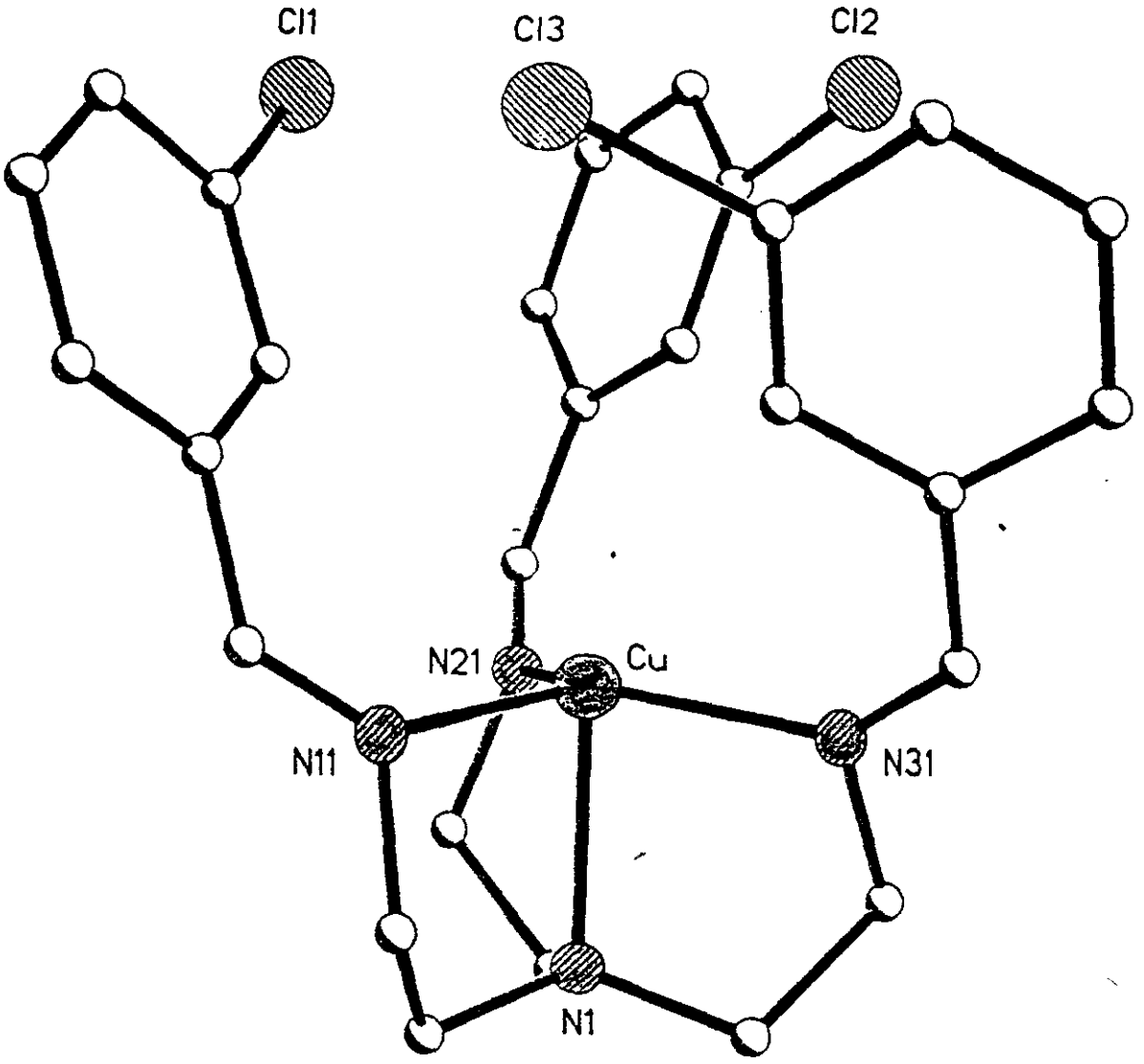

Figure 2.24a Cation structure of chlorine-substituted podate, [CuL5]$^{+}$

Table 2.13 Selected bond lengths [Å] and angles[^{0}] for [CuL5][BF_4];

Cu-(N21)	2.016 (5)	Cu-(N11)	2.029 (5)
Cu-(N31)	2.037 (5)	Cu-(N1)	2.209 (5)
(N11)-Cu-(N1)	84.6(2)	(N11)-Cu-(N21)	115.8 (2)
(N21)-Cu-(N1)	85.0 (2)	(N21)-Cu-(N31)	122.7 (2)
(N31)-Cu-(N1)	83.9 (2)	(N11)-Cu-(N31)	118.7 (2)

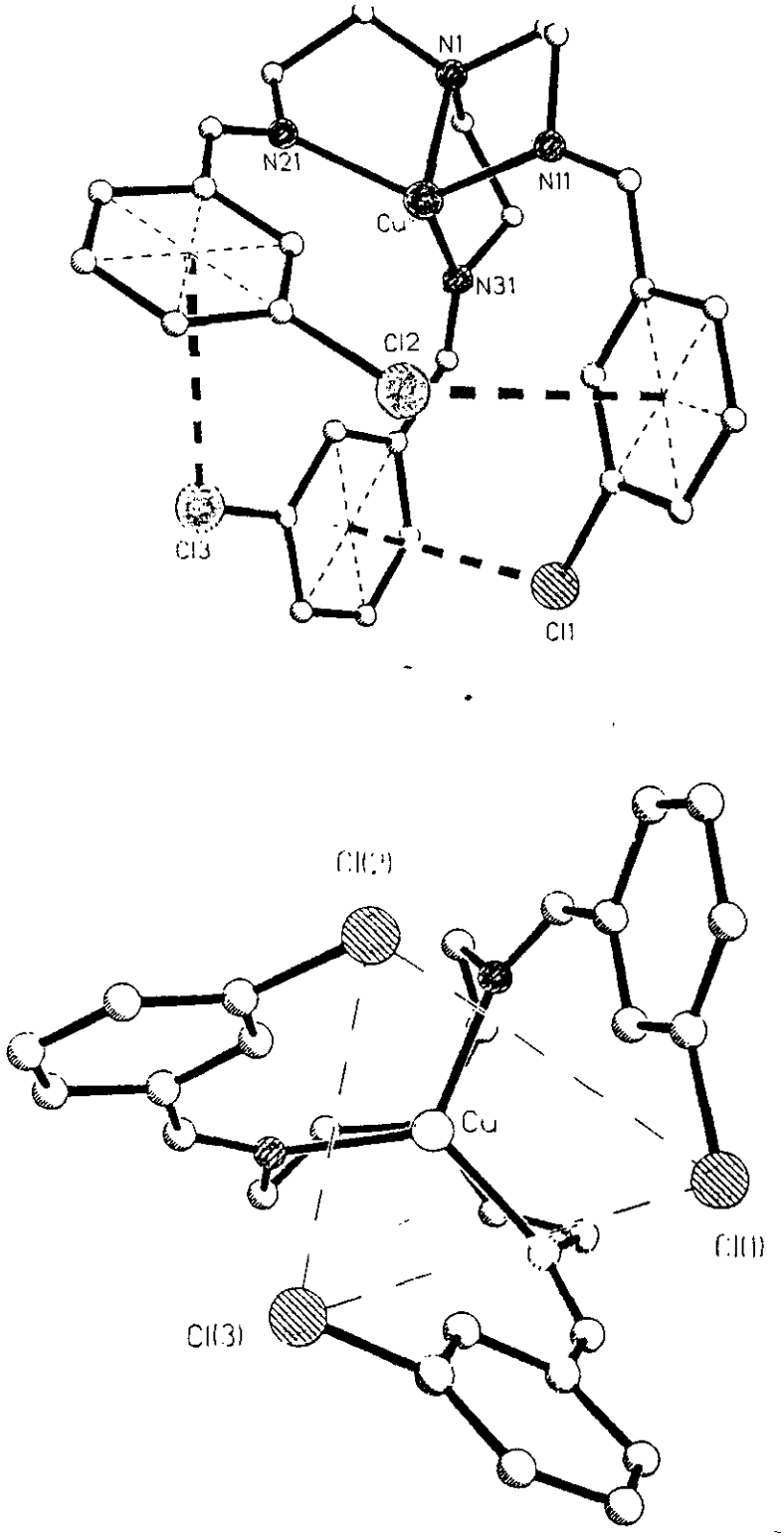

Figure 2.24b Intramolecular interactions in [CuL5][BF_4]

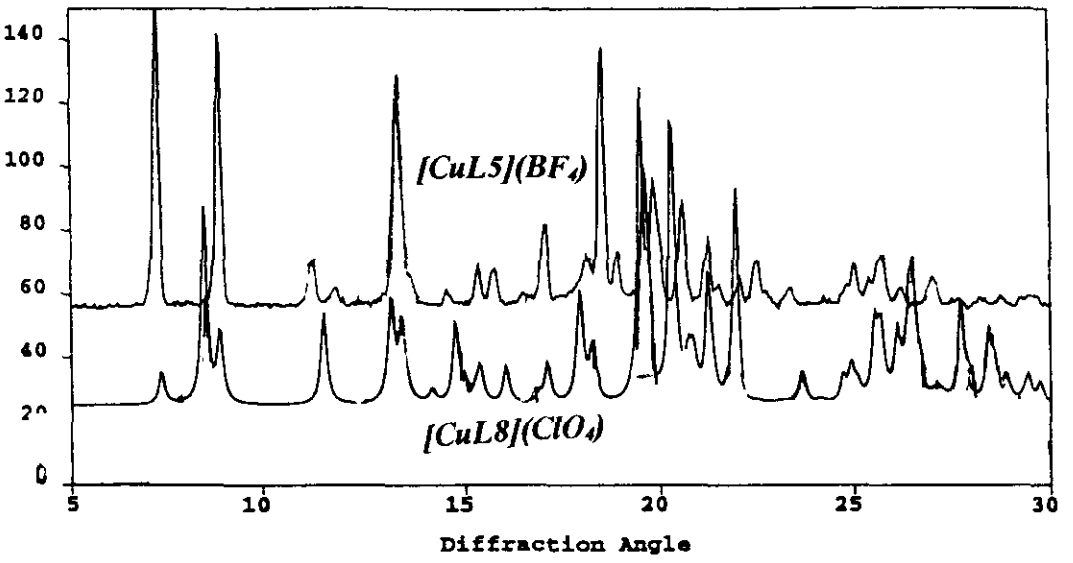

Figure 2.24c X-ray powder pattern comparing [CuL5](BF$_4$) and [CuL8](ClO$_4$)

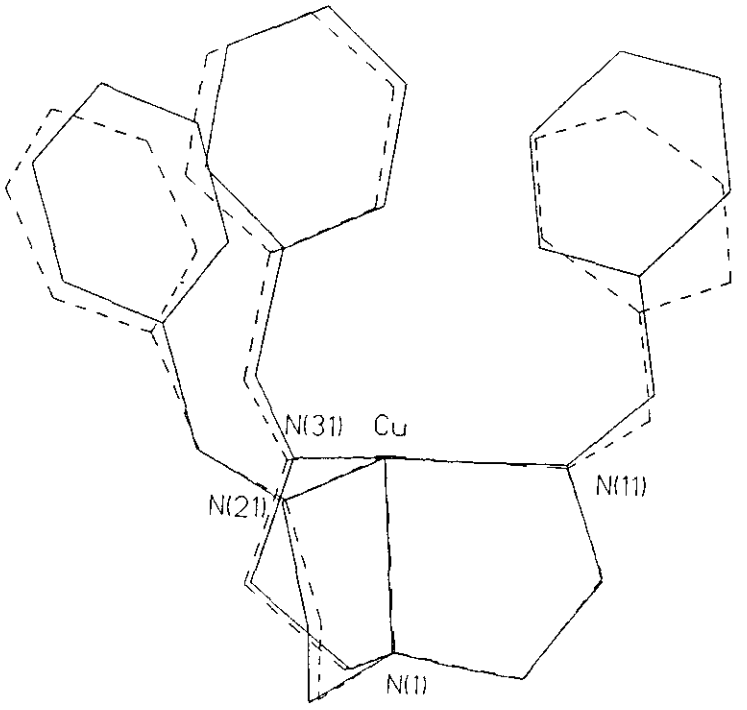

Figure 2.25a Comparison by overlapping of [CuL1]$^+$ and Jeyvak (- - -)

a smaller 'cavity' size, **(Figure 2.25a)**. Jeyvak may be experiencing π-π interactions from the tetraphenylborate counterions and therefore the phenyl rings are not tending towards each other. There is evidence pointing towards intermolecular face-to-edge interactions between BPh_4^- and podate aromatic rings in Jeyvak and this may lead to less intramolecular interaction and a larger cavity, **(Figure 2.25b)**. This highlights the opportunity available for the aromatic rings to 'twist' about the C-C(phenyl) axis. This means that any twisting will be affected by the substituent and/or it's position on the ring. We have already seen that even the choice of counterion can have some effect on the ring. A more pronounced 'twist' of the aromatic ring was noted in $[CuL5][BF_4]$, **(Figure 2.25c)**. This is probably due to the attraction of the chlorines for the adjacent positive phenyl centre.

2.17 A Disubstituted Cu(I) Podate : X-ray Structure of $[CuL6][ClO_4]$ (Figure 2.26)

There are two podate molecules and two perchlorate anions in the unit cell. The Cu-N distances to the equatorial imine nitrogens [N(11), N(21), N(31)] for each individual molecule of the unit cell are shown in **Table 2.14**. It can be seen that for Cu1 and Cu2 the copper ion sits 2.197 and 2.200 Å, respectively, below the plane of the equatorial imine nitrogen atoms.

On preliminary inspection of the X-ray crystal structure there are two factors to consider: effect of disubstitution and any Cl - Cl interactions.

There is an obvious attraction between the two independent copper podates in the unit cell, **(Figure 2.26b)**. This pseudo dimer seems to be held together by a Cl - Cl interaction (Cl-Cl distance = ~ 3.5 Å) between the molecules. This halogen interaction plays a significant part in determining the packing of the molecules. (Ramasubbu *et al* noted that halogen atoms in a molecule are particularly 'exposed' because of their monovalent nature. These features result in the great ubiquity of halogen- halogen contacts in organic structures. Since they are directional in nature, they are able to control crystal packing to a degree).[35]

Intramolecular interaction are also in operation, **(Figure 2.26c)**. The Cl substituted on the *meta* position of the ring is orientated towards the positive centre of the phenyl ring as was seen in the monosubstituted chlorine analogue, ($[CuL5][BF_4]$). In the first molecule, there are two short (3.3 Å) and one long (4 Å) Cl-X distances while for the second molecule there are two long (3.6 Å) and one short (3.3 Å) Cl-X distance. Presumably the conformation adopted in

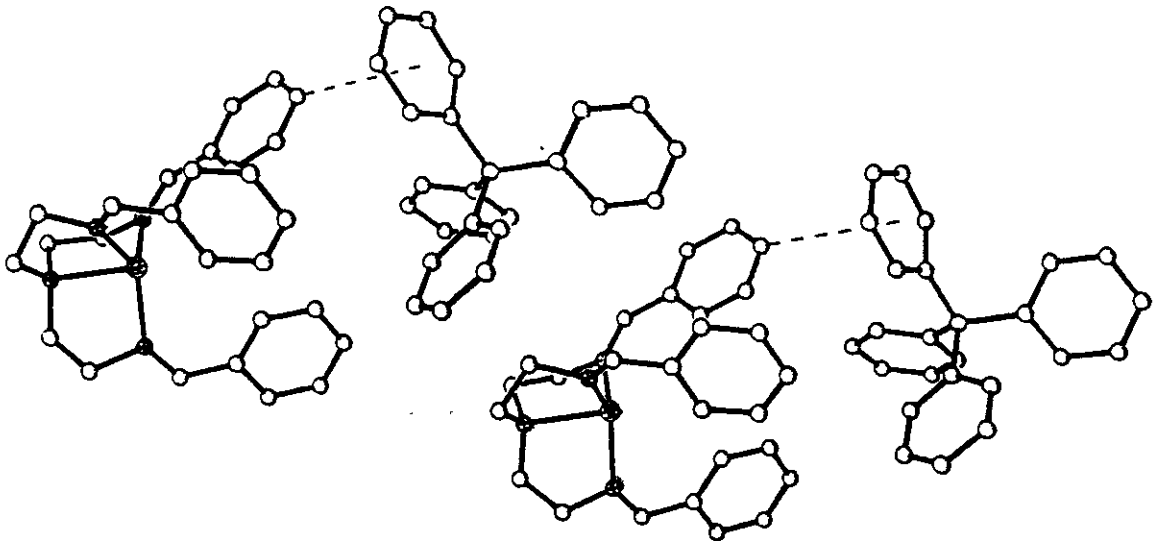

Figure 2.25b Intermolecular Edge-to-Face Interactions in Jeyvak

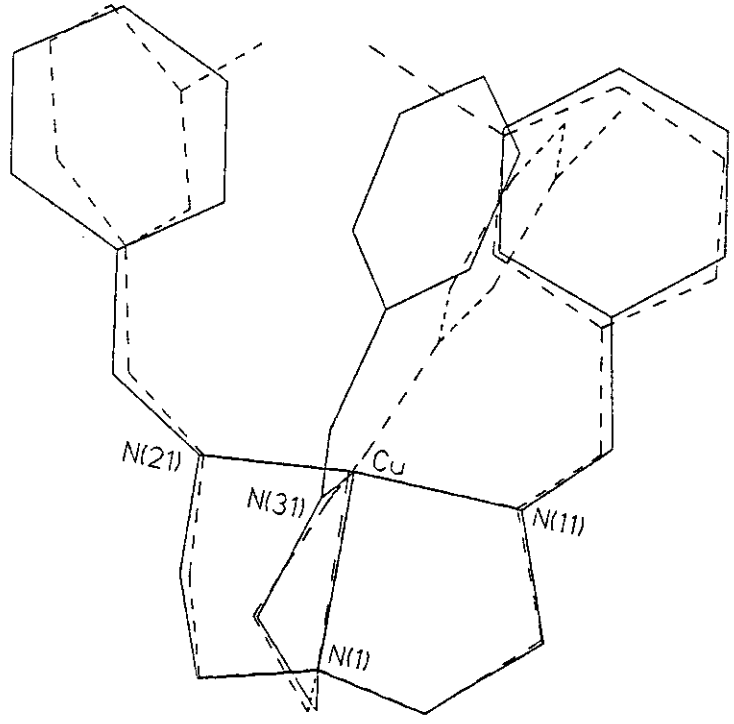

Figure 2.25c Comparison, by overlapping, of [CuL1]$^+$ and [CuL5]$^+$(- - -)

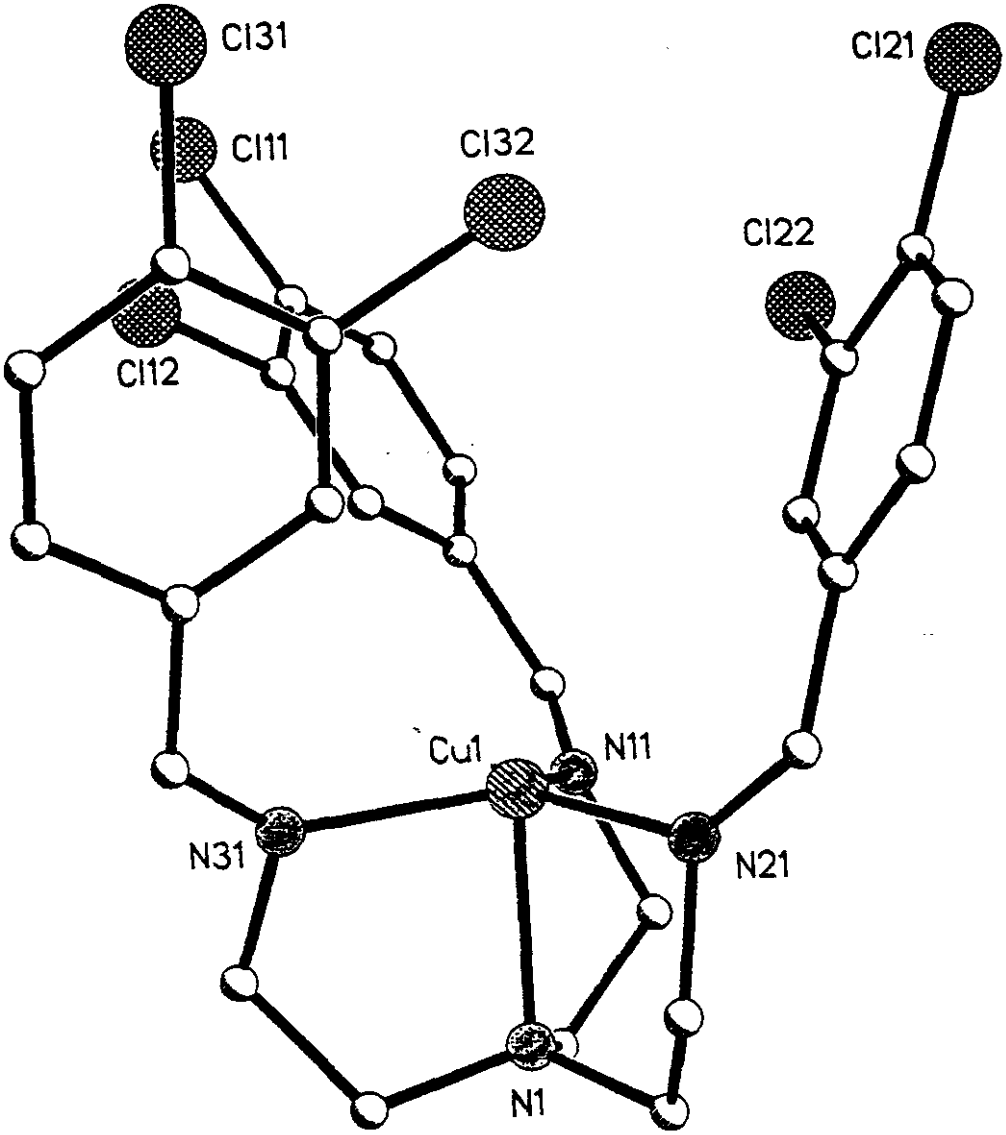

Figure 2.26a Cation structure of a di-substituted podate, [CuL6][ClO$_4$]

Table 2.14 Selected bond lengths [Å] and angles[^{0}] for [CuL6][ClO$_4$]

Molecule 1			
Cu-(N11)	2.006 (9)	Cu-(N21)	2.020 (7)
Cu-(N31)	2.012 (7)	Cu-(N1)	2.197 (8)
(N11)-Cu-(N1)	85.2 (4)	(N11)-Cu-(N21)	121.8 (3)
(N21)-Cu-(N1)	83.6 (15)	(N11)-Cu-(N31)	119.8 (3)
(N31)-Cu-(N1)	84.9 (14)	(N21)-Cu-(N31)	115.8 (3)
Molecule 2			
Cu2-(N41)	1.989 (3)	Cu2-(N51)	1.998 (4)
Cu2-(N61)	2.008 (3)	Cu2-(N2)	2.200 (9)
(N41)-Cu-(N2)	86.4 (5)	(N41)-Cu2-(N51)	119.2 (4)
(N51)-Cu-(N2)	84.3 (4)	(N41)-Cu2-(N61)	121.3 (4)
(N61)-Cu-(N2)	85.0 (3)	(N51)-Cu2-(N61)	117.5 (3)

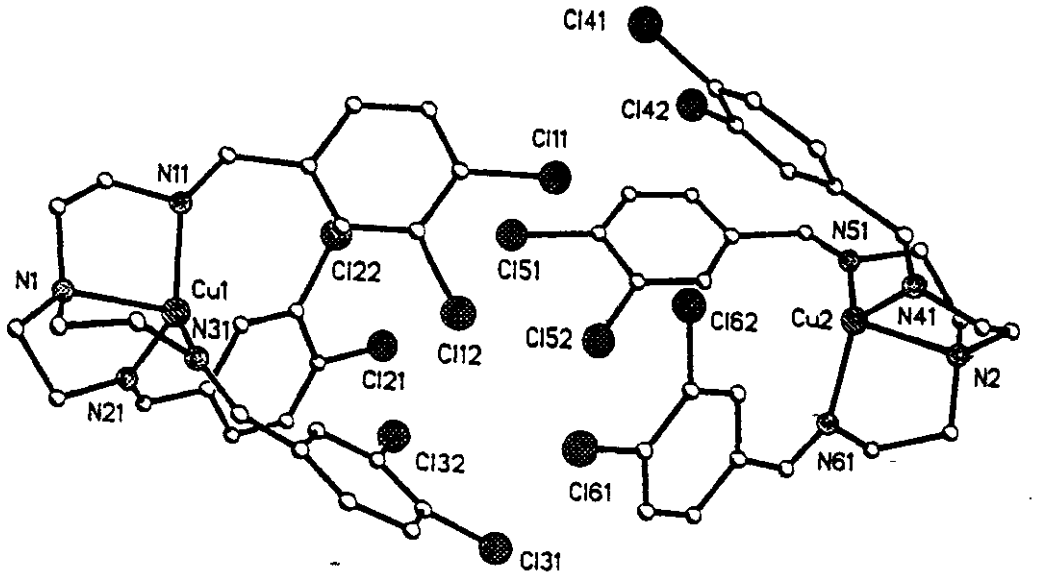

Figure 2.26b Intermolecular contacts in, [CuL6][ClO$_4$]

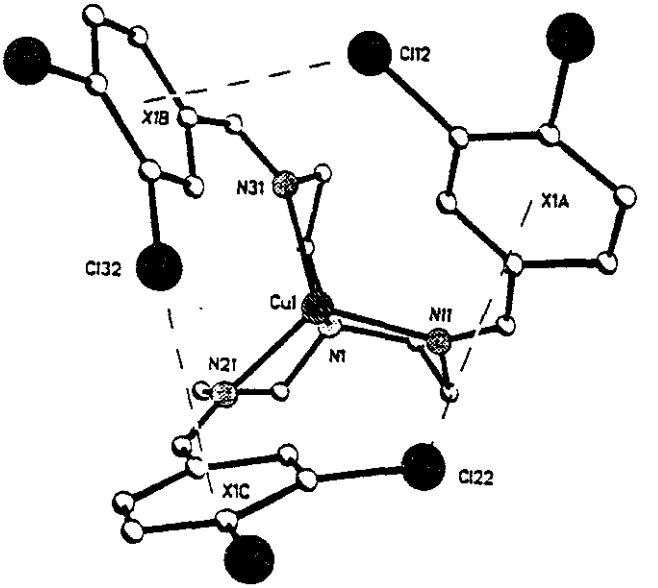

Figure 2.26c Intramolecular contacts in [CuL6][ClO$_4$]

the crystal structure serves to minimise intramolecular and crystal packing forces.

The *para*-substituted chlorines are not shown to cause any steric hindrance and therefore do not affect the intramolecular conformation. Therefore, comparing the structure of the disubstituted [CuL6][ClO_4], to the monosubstituted [CuL5][BF_4], there are similar intramolecular forces superimposed on additional intermolecular interactions.

The aggregation of two molecules (albeit in a single crystal) may contribute to the higher stability of this complex to oxidation. The Cu(I)→Cu(II) electrochemical potential for this complex was found to be higher than for the rest of the tren-cap series, (chapter 2.24.1). It is reasonable therefore to assume that the disubstituion has provided further protection against oxidation of the Cu(I) ion.

As in the tren-capped series X-ray structural characterisation allows comparison to be made on a range of trpn-capped podates. The effect of *ortho* and *meta* substitution can be compared as well as a lengthening of the carbon chain from the imine bond and the aromatic ring.

2.18 An Ortho Substituted Cu(I) Trpn-Capped Podate : [CuL14][ClO_4]

The unit cell consists of one trpn-capped copper podate molecule and a perchlorate counterion. As for the tren-capped series, the geometry around the Cu(I) centre is a distorted trigonal pyramid comprised of four nitrogen donor atoms. The Cu-N distances to the equatorial imine nitrogens [N(11), N(21), N(31)] are shown in **Table 2.15**.

The pseudo cavity appears more open than for the tren-capped halogen analogues. **Figure 2.27** shows two unique cations. Unlike the *mono-* and *dichloro*-substituted tren-capped analogues the bromines show no tendency to orient towards the centres of the neighbouring phenyl groups. Any intramolecular effects arise from their mutual repulsion. *Para*-H - π ring edge-to-face interactions seem important in the configuration of two of the strands, the third is involved in intermolecular Br-Br interactions. The two podates orient back to back, arising from weak attraction of a pair of bromine atoms from adjacent podate molecules. The Br-Br distance shown is 3.61 Å. The observation of such an intermolecular interaction is a further example of the types of halogen-halogen contacts discussed by Ramasubbu *et al.*[35]

The stereodrawing of the crystal structure of triphenylbromomethane shows a similar interaction, **(Figure 2.27b)**. Triphenylbromomethane was found to have the shortest reported value for a Br-Br contact of 3.203 Å.[36]

2.19 A Meta Substituted Cu(I) Trpn-Capped Podate : [CuL15][ClO_4].MeCN (Figure 2.28)

The unit cell consists of a copper podate molecule, a perchlorate counterion and an uncoordinated acetonitrile. The Cu-N distances to the equatorial imine nitrogens [N(11), N(21), N(31)] are shown in **Table 2.16**. The copper ion lies 0.165 Å below the plane of the equatorial imine nitrogen atoms, with the apical tertiary amine (N1) lying 2.35 Å below that plane: the Cu-N distance is large at 2.84 Å. It is interesting that the acetonitrile fails to co-ordinate given the effective 3-coordination of the Cu(I) ion.

There is no obvious interaction between the methyl groups and the neighbouring phenyl rings. It is interesting to comparing the imine N=C-C(aromatic) angle of the *ortho* bromo-substituted [CuL14][ClO_4] to the *meta* methyl-substituted [CuL15][ClO_4], **(Table 2.16)**. The angle for the three side arms of each molecule is in the range 123-128 °. This is interesting because, although it is obvious that the cap size (i.e. tren Vs trpn) is responsible for the geometry around the copper, it is fair to assume that the orientation of the aromatic rings to form the pseudo cavity may be controlled by substitution on the ring. Such effects may be steric or electronic. What is noticeable is that, although this N=C-C(aromatic) angle does not significantly vary, the orientation of the substituent *into* or *out of* the pseudo cavity does vary. It would be interesting to see if an *ortho* substituted methyl group would cause the pseudo cavity to open more due to steric hindrance of the methyl groups projecting into the cavity.

2.20 X-Ray Structure of [CuL17][ClO_4]

The unit cell contains four near identical Cu(I) podates and four perchlorate counterions. The Cu-N distances to the equatorial imine nitrogens [N(11), N(21), N(31)] for each individual molecule of the unit cell are shown in **Table 2.17**. There is a three-fold axis, **(Figure 2.29)**. It can be seen that for two molecules (Cu_1 and Cu_4) the copper ion sits ~0.357 Å below the plane of the equatorial imine nitrogen atoms while for Cu_2 and Cu_3 this distance is

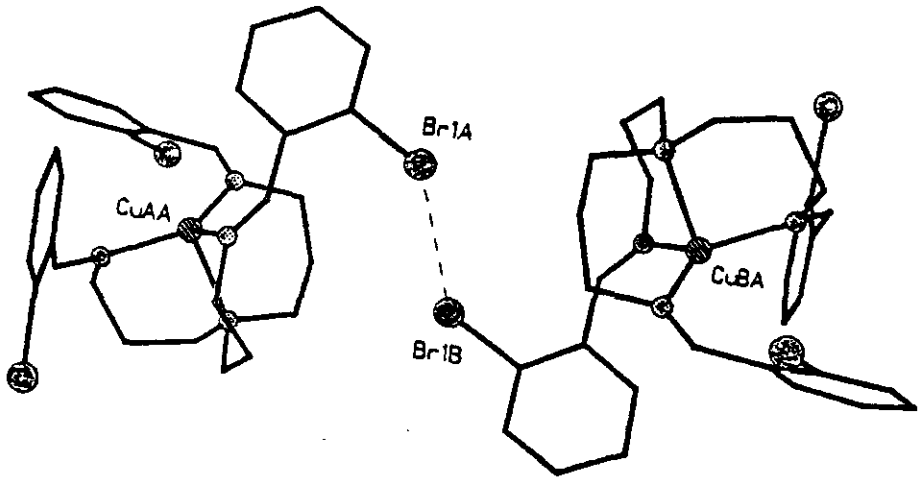

Figure 2.27a Structure of two unique cations of the di-substituted podate, [CuL14][ClO4]

Table 2.15 Selected bond lengths [Å] and angles[°] for [CuL14][ClO4]

Cu-(N21)	2.012 (5)	Cu-(N11)	2.005 (5)
Cu-(N31)	2.004 (5)	Cu-(N1)	2.211 (5)
(N11)-Cu-(N1)	94.83 (19)	(N11)-Cu-(N21)	119.02 (19)
(N21)-Cu-(N1)	94.50 (2)	(N21)-Cu-(N31)	121.10 (2)
(N31)-Cu-(N1)	93.22 (19)	(N11)-Cu-(N31)	118.33 (19)

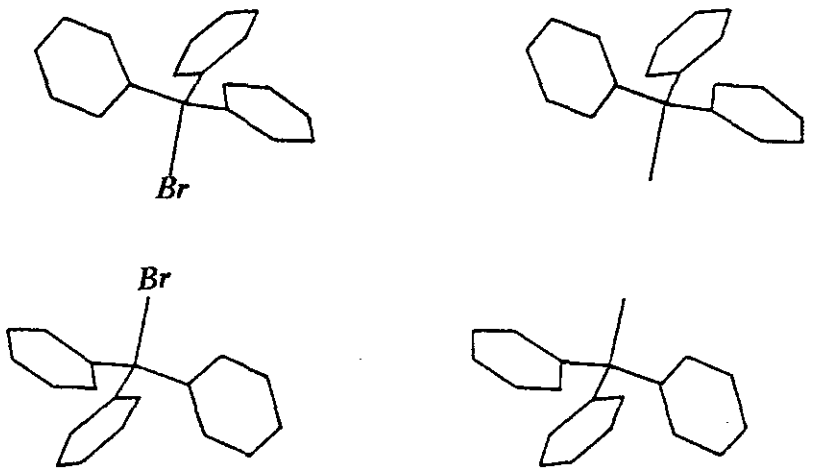

Figure 2.27b Stereodrawing of the crystal structure of triphenylbromomethane to show the short Br...Br contacts of 3.203 Å

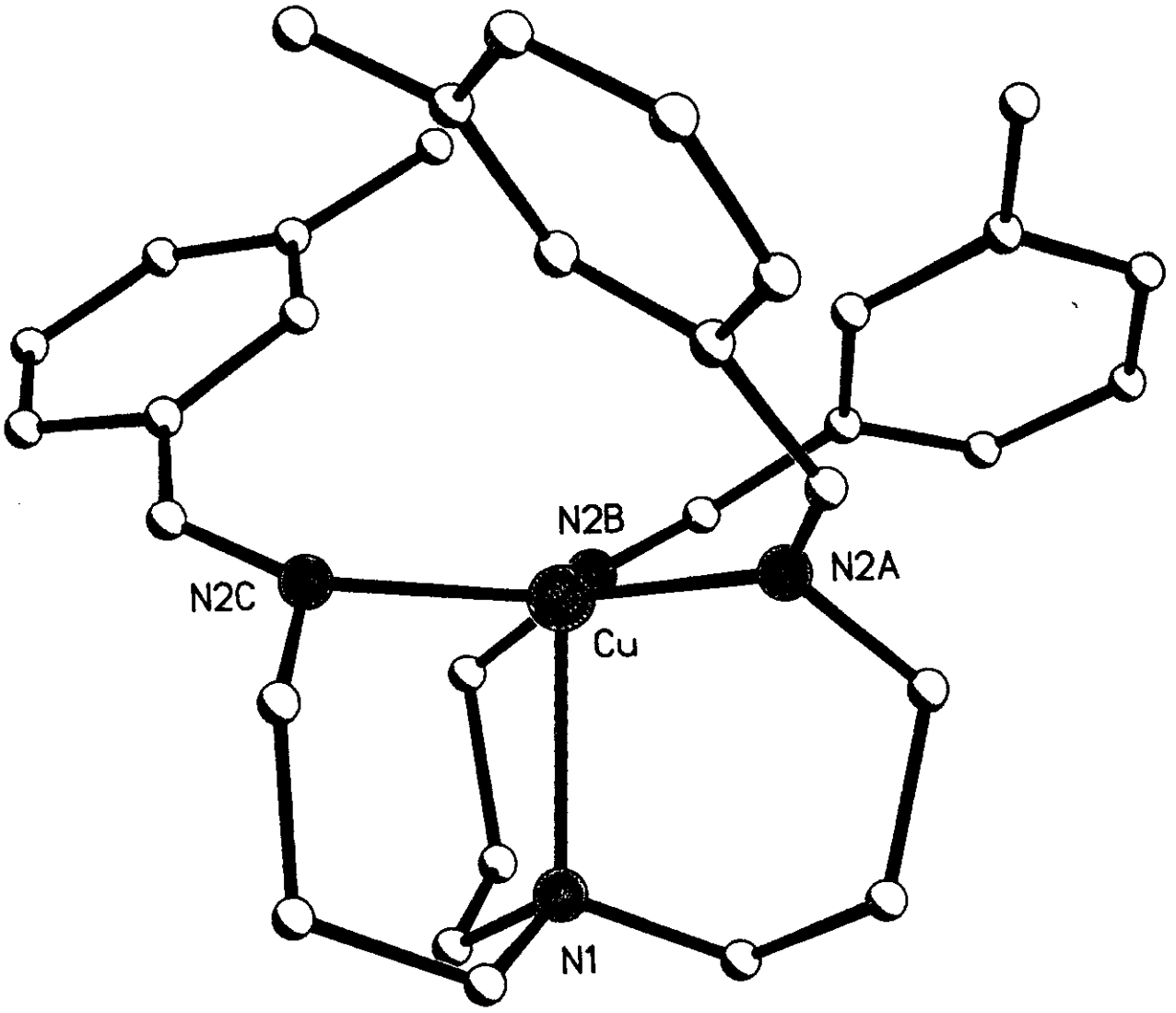

Figure 2.28 Cation X-ray structure of meta substituted trpn-podate, [CuL15][ClO$_4$]

Table 2.16 Selected bond lengths [Å] and angles[^{o}] for [CuL15][ClO$_4$]

Cu-(N2B)	2.037 (6)	Cu-(N2A)	2.016 (7)
Cu-(N2C)	2.031 (7)	Cu-(N1)	2.184 (6)
(N2A)-Cu-(N1)	96.3 (2)	(N2A)-Cu-(N2C)	121.7 (2)
(N2C)-Cu-(N1)	93.6 (2)	(N2A)-Cu-(N2B)	118.4 (2)
(N2B)-Cu-(N1)	94.1 (2)	(N2C)-Cu-(N2B)	118.0 (2)

shorter ~ 0.32 Å, **(Table 2.17)**.

Unlike the substituted aromatic ring analogues, there is an extra degree of flexibility owing to the longer carbon chain connecting the imine group to the aromatic ring. However, the *trans*-orientation at the double bond is responsible for creating the pseudo cavity. It can be envisaged that a *cis* orientation at the double bond might open the cavity up permitting the entry of dioxygen. **Figure 2.29b** shows that intramolecular π-σ interactions may contribute to the conformation of this complex.

2.21 Summary of the Generalisations of Tren Vs Trpn Capped Cu(I) podates

	Tren Capped	**Trpn Capped**
Plane of C-N(imine)-C to the CuN3 plane	Approaching perpendicular	Tending towards parallel
N(1)-Cu-(N) imine	~ 85°	~ 95°
Sitting of Cu in relation to plane defined by imines	Above the plane, away from the N bridgehead. Site is convex	Below the plane, towards the N-bridgehead. Site is concave
Nature of Molecular interactions	Intramolecular	Intermolecular

The X-ray structural comparison of tren versus trpn-capped Cu(I) podates concludes that: cap size does not significantly affect co-ordination geometry but may affect access of substrates such as O_2. The substituent position is not responsible for the co-ordination geometry, but the substituent itself and its interactions do affect the openness of the pseudo cavity.

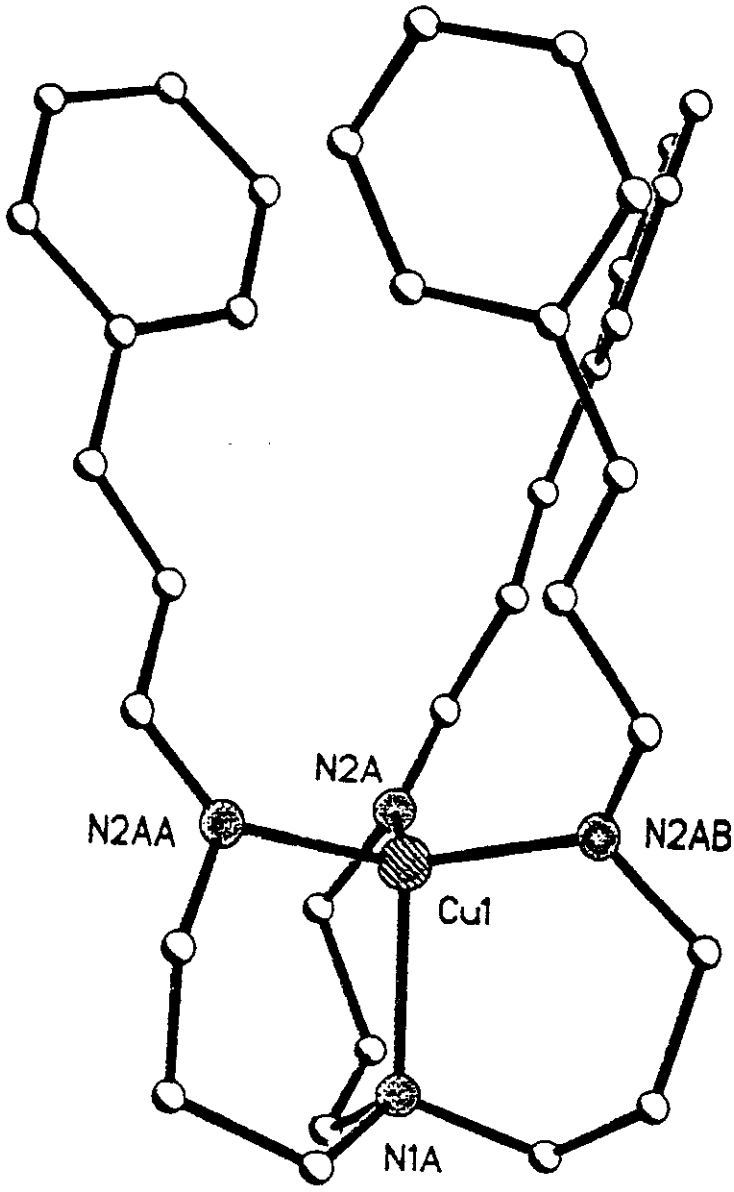

Figure 2.29 Cation structure of [CuL17]$^{+}$

Table 2.17 Selected bond lengths [Å] and angles[°] for [CuL17][ClO$_4$]

Cu (1)-(N2A)	2.011 (4)	Cu (2)-(N2B)	2.007 (4)
Cu (1)-(N1A)	2.203 (9)	Cu (2)-(N1B)	2.163 (8)
Cu (3)-(N2C)	2.004 (4)	Cu (4)-(N2D)	2.021 (4)
Cu (3)-(N1C)	2.220 (9)	Cu (4)-(N1D)	2.192 (9)
(N2A)-Cu-(1)-N(2A)	116.84 (7)	(N2B)-Cu-(2)-N(2B)	117.54 (6)
(N2A)-Cu-(1)-N(1A)	100.37 (12)	(N2B)-Cu-(2)-N(2B)	99.12 (12)
(N2C)-Cu-(3)-N(2C)	117.44 (7)	(N2D)-Cu-(4)-N(2D)	117.07 (7)
(N2C)-Cu-(3)-N(1C)	99.30 (13)	(N2D)-Cu-(4)-N(2D)	99.97 (12)

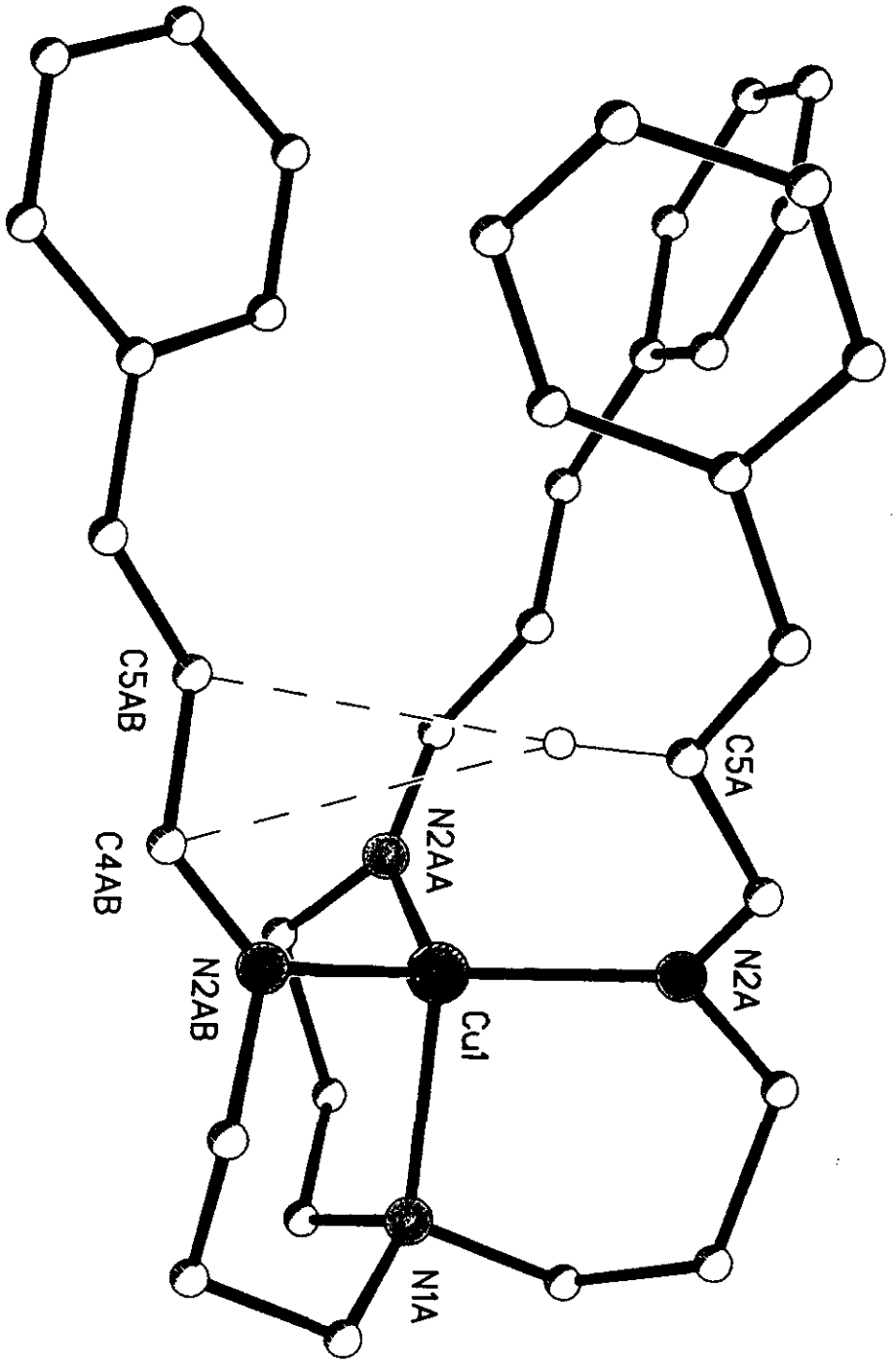

Figure 2.29b Structure of [CuL17]$^{+}$ showing intramolecular π-σ interactions

Section C

2.22 Cyclic Voltammetry.[37,38,39]

2.22.1 Introduction

Cyclic voltammetry has become a popular technique in the study of electrochemical reactions and is particularly useful in evaluating the effects of ligands on the oxidation/reduction potentials of cations in metal complexes and multinuclear clusters.[40] Knowledge of the electrochemistry of a metal complex can be useful in the selection of an appropriate oxidising agent to obtain a complex in the required oxidation state.

In voltammetry, a three electrode system is used where a potential is applied between the reference and the working electrodes, and the current flow between the working and the counter electrodes is measured. The current flowing at an electrode is measured as a function of the potential applied to the electrode. The data are typically presented graphically, as current-potential curves.

2.22.2 Fundamentals of Cyclic Voltammetry.

Cyclic voltammetry involves cycling the potential of the working electrode between the initial E_i, and final E_f potential, at a constant scan rate, while measuring the current. The current response is plotted as a function of the applied potential to give a current-voltage curve or cyclic voltammogram, which indicates the potentials at which the electrochemical processes (oxidation-reduction) occur. Diffusion is the principal mode of moving the electroactive species to the electrode surface as the experiment is performed at stationary electrodes, in an unstirred solution, over a short time period. Initially there is a rise in the current as electrolysis of the reactant occurs at the electrode surface. This causes a decrease in the concentration of the reactant on the electrode surface. When the scan is reversed the electrolysis process regenerates the starting material, in reversible cases, from the electrolysis product which has accumulated around the electrode.

The important parameters in cyclic voltammetry are the magnitude of the anodic and cathodic peak current, I_{pa} and I_{pc}, respectively, and the anodic and cathodic potentials E_{pa} and E_{pc}, respectively. The redox process is reversible when the ratio of the peak current, I_{pa}/I_{pc} is 1.

(literature report a range of 0.80-1.0 as acceptable for reversibility). When both the oxidised and reduced species are stable and rapidly exchange electrons with the working electrode in the same time scale of the experiment, the process is said to be reversible and cyclic voltammetry can then be used to calculate the reduction potential of the half reaction using the equation:-

Equation 1.1

$$E^{\circ} = \tfrac{1}{2}(E_{pa} + E_{pc})$$

The number of electrons transferred in a fully reversible electrode reaction, n, for a reversible couple can theoretically be determined from the separation between the peak potentials, ΔEp, shown in equation

Equation 1.2

$$\Delta Ep = E_{pa} - E_{pc} = 0.059/n\ V$$

The electrochemical oxidation of ferrocene provides the basis for judging electrochemical reversibility and permits a quantitative comparison of electrode potentials obtained using different reference electrodes or different solvents. The redox potential of ferrocene is accepted as a reference for reporting electrochemical oxidation-reduction systems.

Three main types of electrochemical processes have been identified, namely, reversible, quasireversible and irreversible processes.

1. ***Reversible processes*** are those in which the rate of electron transfer is greater than the rate of mass transport and both the oxidisable and the reducible species rapidly exchange electrons with the working electrode. The reaction is therefore fast enough to maintain the concentration of the oxidised [O] and [R] forms in equilibrium with each other.

$$O + ne^{-} \rightleftharpoons R$$

E_p is independent of υ (υ is the scan rate)

E_{pa}-E_{pc} = 0.059/nV at 25°C and is independent of υ

$I_{pa} = I_{pc}$

I_p is linearly dependent on concentration

The peak currents (i_{pa} and i_{pc}) obtained from cyclic voltammograms are described by the Randles-Sevcik equation: $I_p = (2.69 \times 10^5)\, n^{3/2}\, D^{1/2}\, C\upsilon^{1/2}$

Where : n = number of electrons involved

D = diffusion coefficient

C = concentration of electroactive species

υ = scan rate

2. For a ***quasireversible process***, the anodic and cathodic peak potentials shift further apart with increasing scan rate. The reverse peak may be shorter than the forward peak, probably as a result of an accompanying chemical reaction.

$$\mathbf{O + ne^- \rightleftharpoons R}$$

E_p is independent of υ.

E_{pa}-E_{pc} = 0.059/nV at low υ, increases with υ depending on electron transfer

I_{pa}/I_{pc} is not equal to 1.

3. When the reaction is totally ***irreversible***, the rate of electron transfer is much less than the rate of mass transport, resulting in a slow exchange of electrons at the working electrode. The result is a complete disappearance of the reverse peak probably due to a chemical reaction accompanying the electron transfer process.

$$\mathbf{O + ne^- \rightarrow R}$$

No I_{pa} evident or I_{pc} evident depending whether the process is oxidative or reductive respectively.

I_{pc} is linearly dependent on concentration.

2.22.3 Instrumentation

A typical CV apparatus is composed of a waveform generator which produces the required potential applied to the cell via a potentiostat, and a current to voltage convertor to measure the resulting current. The potentiostat ensures that the working electrode potential is not influenced by the reactions taking place and maintains a desired potential difference between the working electrode and the reference electrode. The current required to sustain the electrolysis at the working electrode is provided by the auxiliary or counter electrode.

There are many electrodes used in CV, ranging from the inert to reactive electrodes. Depending on the potential region of interest the electrode may function as inert or reactive. Inert electrodes, which do not chemically react in the given region under investigation, are most often used. For most non-aqueous solvents, platinum electrodes provide a very wide potential region, both anodic and cathodic. Acetonitrile is the most common solvent used as its voltage window is 3 V (Vs SCE), i.e. it does not undergo oxidation or reduction in this potential region.

A supporting electrolyte is employed to decrease the electrical resistance of the medium and to impede the migration of the charged reactants and products.[41] The supporting electrolyte often used is tetrabutylammonium perfluoroborate, as it has good solubility properties and is electrochemically inert within the voltage window of acetonitrile. Electrolytes are present in a large excess to the concentration of the reactant. The supporting electrolyte thus shields the reactant from the electric field near the electrode and the redox processes are therefore diffusion controlled.

The reference electrode is required to have a constant potential when an external potential is applied to the cell. The most commonly used reference electrode is the Saturated Calomel Electrode (S.C.E), in which Hg is in contact with Hg_2Cl_2/KCl paste which is then in contact with saturated KCl solution. Metal / metal ion electrodes are also employed in non-aqueous media, e.g. Ag/AgCl electrode.

2.23 Electrochemistry of Copper(I) Podates

2.23.1 Introduction

Electrochemistry can be used to establish whether there is a correlation between the redox potential and catalytic capabilities of copper complexes and to assess the ease of reduction of the complexes.[42] Many researchers have found that deviations in ligand steric effects cause redox potential alterations which lead to varied reactivity of reduced $[LCu]^+$ complexes with dioxygen.[43]

Factors known to influence the redox potential of copper complexes include :-

1. The flexibility or constraints imposed by chelating ligands, which might favour a geometry preferred by one metal ion oxidation state but not the other.
2. Types of donor atoms (i.e. O Vs N Vs S).[44]
3. Geometry of the co-ordination complex.[45]
4. Ligand substituent effects.

2.23.2 Previous Work on Cu(I) Podates

Canary *et al* were able to obtain structural characterisation of both Cu(I) and Cu(II) complexes of the ligand TPPA, (**Figure 2.30a**). In the structures all the nitrogen atoms of TPPA ligate the metal ion despite the presence of the bulky phenyl substituents. In the Cu(II) complex an additional acetonitrile ligand was observed, encased in a pseudo 'cavity' defined by the phenyl substituents.[46]

The copper atom geometry in $[(CuTPPA)(MeCN)]^{2+}$ resembles that in $[CuTPPA]^+$ with an additional apical acetonitrile ligand present. The Cu-N(1) bond is longer in $[CuTPPA]^+$ than in $[(CuTPPA)(MeCN)]^{2+}$ (2.15 Vs 2.00 Å) but all the other bonds and angles are very similar, and the distance of the copper atom away from the plane containing the 3 x pyridine nitrogen atoms is very similar (0.32 Vs 0.35 Å). The co-ordination geometry about the Cu atom also closely resembles that in the structure of $[Cu(TPA)(MeCN)](ClO_4)_2$[47] and other TMPA complexes.[48]

Figure 2.30b shows that in the Cu(I) complex of TPPA, two phenyl rings stack in a 'T' configuration as observed in solid benzene and in many protein aromatic side chains. The space-filling models indicate that the Cu(I) is completely encapsulated by the TPPA ligand. In

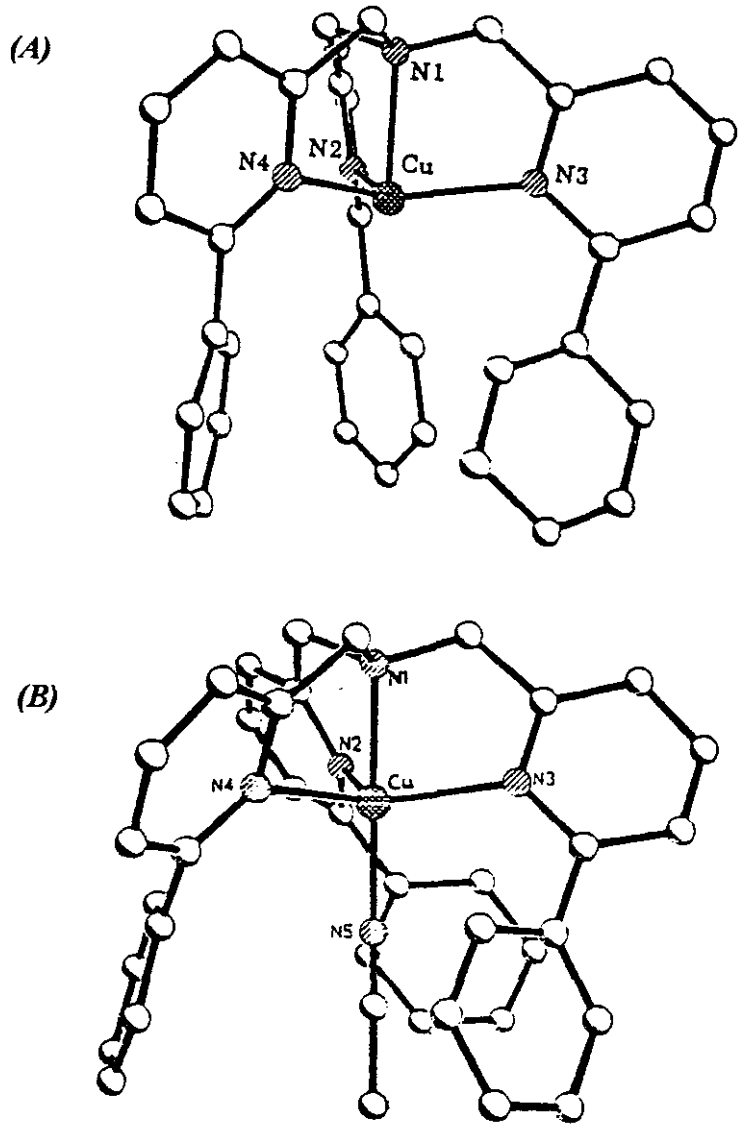

Figure 2.30a (A) Cationic portion of [Cu(TPPA)][BPh_4] (B) Cationic portion of [Cu(TPPA)(AN)](ClO_4)$_2$

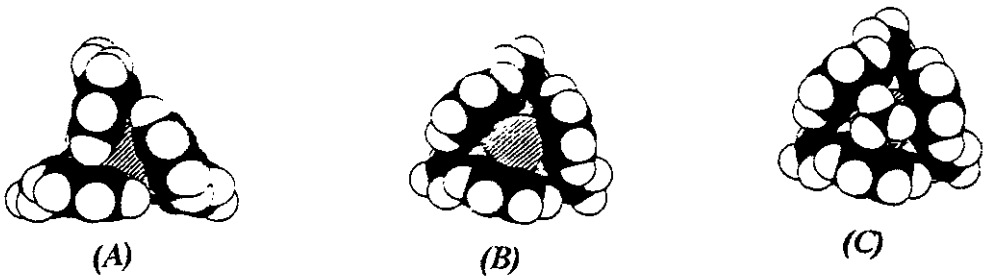

Figure 2.30b Space-filling models generated from X-ray co-ordinates, (A) [Cu(TPPA)]$^+$ (B) [Cu(TPPA)]$^{2+}$ with MeCN omitted to emphasise positional change of phenyl substituents compared to [Cu(TPPA)]$^+$ and (C) [Cu(TPPA)(AN)](ClO_4)$_2$

the Cu(II) complex the ligand creates a pseudocavity, in which an acetonitrile molecule is bound, by undergoing a helical 'twist'. Canary elegantly compares this conformational change in the ligand to that of a flower going from bud to bloom.[46]

Our systems have similarities to those reported by Canary *et al* and although at this stage an acetonitrile co-ordinated complex has not been isolated it has been envisaged that the systems could undergo such behaviour. Although O_2 binding is not evident in our podate systems, it is of interest to see if the Cu(II) redox state can be electrochemically accessed. Like all metal-dioxygen reactions, Cu(I)-O_2 reactions involve some degree of electron transfer. Thus, the structures and physical properties of Cu(II) analogues of $[LCu]^+$ are of interest since the ligation and coordinate geometry observed in such Cu(II) species may closely resemble that seen in Cu_nO_2 (n=1 or 2) adducts.[49,50]

2.23.3 Experimental

Measurements were performed with an Autolab PGSTAT 10 potentiostat. The apparatus was checked prior to use with ferrocene which has a well-defined redox potential between 0.4 -0.6V (Vs S.C.E).

Cyclic voltammetry was carried out at room temperature in a 20ml electrochemical cell fitted with a glassy carbon/gold working electrode, a platinum counter electrode, and an Ag/AgCl reference electrode. Dry acetonitrile containing 0.1M tetraethyl ammonium perchlorate, as a background electrolyte, was used as the solvent.

To 10 ml of acetonitrile, containing 0.1 M tetraethylammonium perchlorate, in an electrochemical cell was added approximately 5-10 mg of the podate being studied, making the solution concentration 10^{-3} mol dm^{-3}. The solution was purged with oxygen free nitrogen until all the solid had dissolved. The CV was recorded within the potential range of -0.5 to + 1.5 V. Three cycles were recorded at a scan rate of 100 mV/sec unless otherwise stated.

2.24 Results

2.24.1 Tren-Capped Cyclic Voltammetry : Gold Electrode

Monoaldehyde	Complex stability	CV nature	$E_{1/2}$ (V)	ΔE_p, (mV)	i_{pa}/i_{pc}
Trans-cinnamaldehyde	v. stable, pure Cu(I)	reversible [a]	+ 0.30	80	1.00
Methylfurfural	Cu(I) pure but Cu(II) accessible [c]	reversible [a]	+ 0.45	100	0.90
Furfural	Cu(I) pure but Cu(II) accessible [c]	reversible [a]	+0.48	90	0.85
2-Bromobenzaldehyde	small % Cu(II)	reversible [a]	+ 0.50	80	1.00
Benzaldehyde	v. stable, pure Cu(I)	reversible [a]	+ 0.55	90	0.80
3-Tolualdehyde	small % Cu(II)	quasi-reversible	+ 0.61	140	
3,4 Dichlorobenzaldehyde	v. stable, pure Cu(I)	reversible [b]	+ 0.65	70	0.80
Napthaldehyde	v. stable, pure Cu(I)	quasi-reversible [a]	+ 0.63	200	
2-Nitrobenzaldehyde	stable although 2 conformations or an impurity may be present	2 waves, (1) reversible (2) quasi-reversible [a]	1. + 0.44 2. + 0.18	1. 100 2. 100	1.00 -

[a] scan rate 100mV/s, [b] scan rate 20mV/s, [c] Alyea reported the Cu(II) product, [d] All potentials are w.r.t. ferrocene/ferrocenium couple.

2.24.2 Trpn-Capped Cyclic Voltammetry : Gold Electrode

Monoaldehyde	Complex stability	CV nature	$E_{1/2}$	ΔE_p, (mV)	i_{pa}/i_{pc}
Trans-cinnamaldehyde	v. stable, pure Cu (I)	reversible [a]	+ 0.57	130	1.0
2-Bromobenzaldehyde	v. stable, pure Cu (I)	quasi-reversible [a]	+ 0.72	100	
3-Tolualdehyde	v. stable, pure Cu (I)	quasi-reversible [a]	+ 0.76	150	
2-Nitrobenzaldehyde	v. stable, pure Cu (I)	reversible [a]	+ 0.76	80	1.0

The CV's are well-behaved and in most cases have a single, reversible electron wave with I_{pa}/I_{pc} approaching unity. Unless otherwise stated peak separations were less than 150mV at a scan rate of 100mV/s.

A typical reversible CV, seen in most of the Cu(I) tren and trpn based podates, is shown in **Figure 2.31**. The nitrobenzaldehyde-based tren podate $[CuL9]^+$ displays two waves and this further strengthens the idea that there are more than one stable Cu(I) form of this complex. The CV for this complex is shown in **Figure 2.32**.

2.25 Discussion

2.25.1 Possible Redox Processes for the Copper (I) Podates

1. Cu(I) oxidation/ Cu(II) reduction

$$[CuL]^+ \leftrightarrow [CuL]^{2+} + e^-$$

2. Cu(I) reduction

$$[CuL]^+ + e^- \rightarrow Cu(O)$$

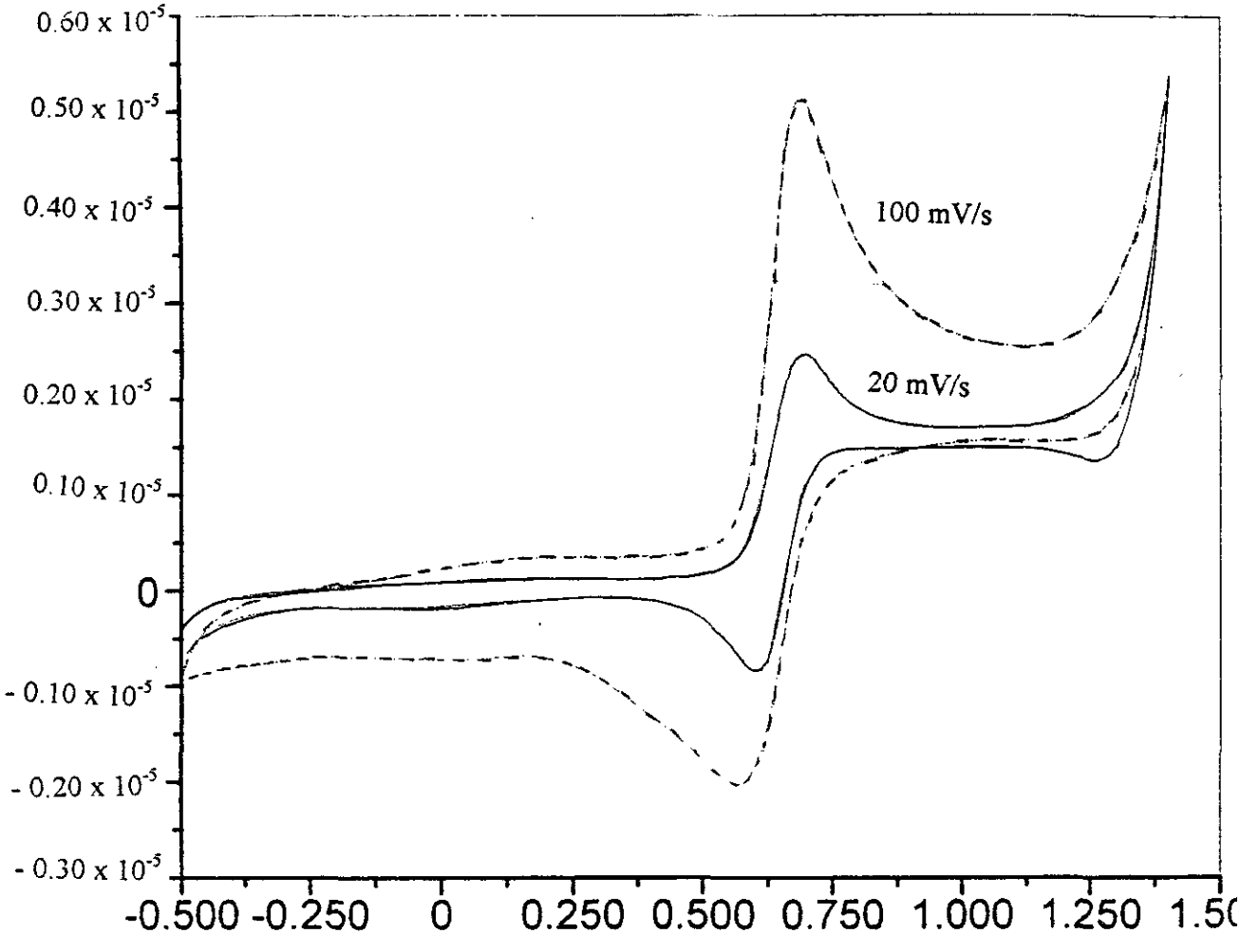

Figure 2.31 A reversible Cyclic voltammogram for [CuL6](ClO$_4$) at 100 mV/s and 20 mV/s

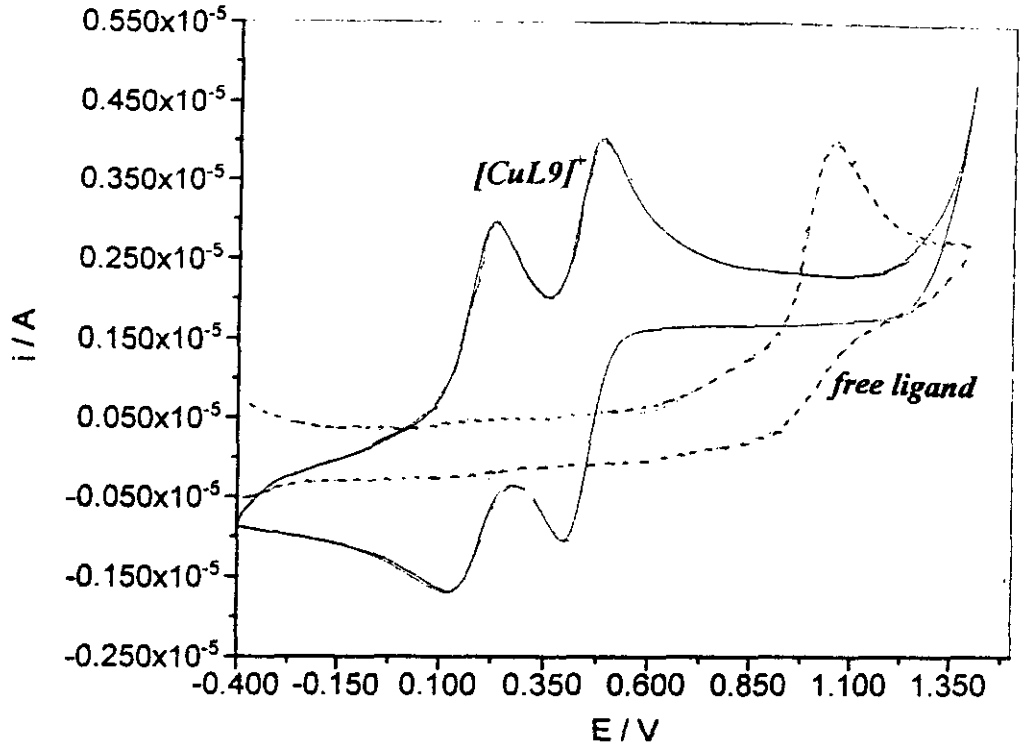

Figure 2.32a Cyclic voltammogram of [CuL9]+ and free ligand showing that redox is copper and not ligand based

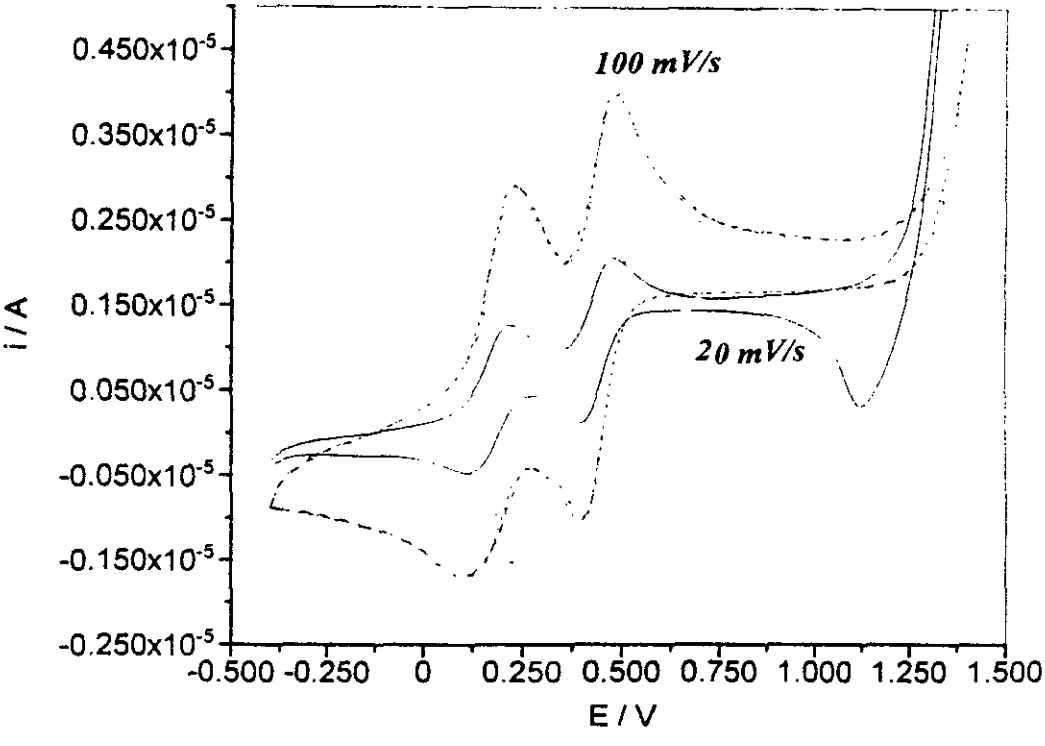

Figure 2.32b Cyclic voltammogram of [CuL9]+ showing copper redox only at 20 and 100 mV/s

3. Copper stripping

$$Cu\,(O) \rightarrow [CuL]^{+} + e^{-}$$

In initial experiments the CV's were recorded within the potential range -2 to +2 V, however, it became obvious that within these limits the Cu(I) was reduced to Cu(O) and this was seen as a broad peak in the region -0.2 to -1.0 V. This resulted in deposition of Cu(O) on the electrode. The Cu(O) is stripped off giving the sharp oxidative peak at $E_p^a = 0.5$ V. Often this process of deposition of Cu(O) and consequent stripping lead to irreversibility therefore subsequent experiments were recorded in the range - 0.5 - + 1.5 V, thus avoiding steps 2 and 3 above.

As discussed in section B, the complexes all have a common core - Cu(I) bonded to three imine nitrogens and a bridgehead nitrogen. All complexes showed a high positive potential for oxidation, however their electrochemical behaviour varied between reversible, quasi reversible and irreversible depending on: ring substitution, bridgehead type and electrode used.

The choice of working electrode influences the reversible nature of the Cu(I)/Cu(II) couple. In most cases the couple observed using the gold working electrode is more pronounced and reversible than when using a glassy carbon working electrode. In order that the structural differences of the podates can be compared results are discussed for experiments carried out using the gold electrode only.

Unsurprisingly our Cu(I) complexes are mostly stable with respect to oxidation in acetonitrile. Cu(I)/Cu(II) redox potentials range from + 0.3 to + 0.65 for tren-capped and for + 0.57 to + 0.76 for trpn-capped podates. It is relatively uncertain whether this is kinetic or thermodynamic stability owing to the lack of comparable data. It is obvious though that once synthesised, by an insertion method, the Cu(I) podates are difficult to oxidise. The X-ray structural data show that there is interaction between the aromatic strands and this may be sufficient to maintain a pseudo-cavity. Therefore, conformational change may be minimised upon redox.

These potentials in acetonitrile are more negative than the standard potentials for aqueous O_2 reduction, which tempts us to think that kinetic rather than thermodynamic factors

may be operating. However, potentials obtained in acetonitrile may not validly be compared with aqueous E°'s. Water is an inappropriate solvent for our podates because of the tendency to imine hydrolysis which makes it impossible to decide on the thermodynamic favourability of aerobic oxidations. However, it is clear that this will be less likely for the podates with more positive redox potentials. This is in agreement with results presented by Karlin *et al* who have shown that increased hydrophobicity next to the cuprous centre leads to a higher oxidation potential for the one-electron oxidation of Cu(I) to Cu(II).[12]

2.26 Correlation of Oxidation Potentials to Structure

2.26.1 Tren-Capped Cu (I) Podates

The half-wave potentials of the tren-capped podates as a function of aldehyde-derived side arm follow the trend:

Dichlorobenzaldehyde > Naphtaldehyde > Tolualdehyde > Benzaldehyde > *o*-Bromobenzaldehyde > Furfural > Methyl furfural > Trans cinnamaldehyde.

For the tren-capped series the Cu(I) is out of the plane of the imine groups and away from the bridgehead. The copper ion is more exposed and perhaps more likely to co-ordinate acetonitrile in a similar manner to that reported by Canary *et al.*[23]

The benzene ring and its substituted analogues require a higher voltage for oxidation than the trans-cinnamaldehyde or furan ring systems. The anomalous results for the dichlorobenzene analogue may be explained to be due to steric hindrance caused by the two chlorine atoms. The X-ray crystallographic structure shows that there is an attraction between two tripodal molecules - this may lead to an extra degree of stability of the cuprous state. If a twisting of the tripodal arms is expected to stabilise the Cu(II) ion in its preferred geometry, this may not be favourable due to steric effects caused by disubstitution of the ring. At fast scan rates the wave is irreversible and only quasi reversible if the scan rate is slowed to 20mV/s. The large peak separation, ΔE, at a scan rate of 100 mV/s which decreases with decreasing scan rate, indicates a kinetic barrier to electron transfer at the electrode surface.

It is possible that benzaldehyde, trans-cinnamaldehyde and furan rings have lower potentials because:

1. Benzaldehyde can 'twist' easier as there is no substitution effects. This may result either in the binding of acetonitrile and adopting a trigonal bipyramidal geometry or perhaps simply no additional binding and the formation of a square planar complex both of which are preferable to Cu(II).
2. Cinnamaldehyde has an extra degree of flexibility as well as being less hydrophobic at the Cu(I) site making the Cu(II) state more easily accessed.
3. The furan ring podates are not only smaller and less hydrophobic, they also have potential O donors which, being polar, may stabilise the copper(II) state.

2.26.2 Trpn-Capped Cu(I) Podates

A difference between tren-capped and trpn-capped podates derives from the different siting and degree of protection of the Cu(I) centre. There is less hydrophobic protection in this series and the complexes are more capable of acetonitrile coordination in the higher redox state.

The half-wave potentials of the trpn-capped podates as a function of aldehyde-derived side arm follow the trend:

Nitrobenzaldehyde > Tolualdehyde > Bromobenzaldehyde >Trans cinnamaldehyde

This trend is consistent with that in the tren series.

Apart from the nitrobenzaldehyde podates, this order follows the same order as the analogous tren capped Cu (I) podates. The potentials required for oxidation are, however, much higher than for the tren-capped podates as is indicated by the greater solution stability of the cuprous state observed during the synthesis of these podates. The products were easily synthesised and isolated in a nitrogen atmosphere and they showed no signs of oxidation. It was initially thought that expanding the cap would give an extra degree of flexibility which

would enable dioxygen to be bound. However, for most of the series the opposite was true - the products were more difficult to electrochemically oxidise.

X-ray crystallography indicates that the copper cation is only very slightly out of the plane of the imines and towards the N-bridgehead. The copper cation seems to be buried deeper into the 'pseudo' cavity. This would mean that the copper is less exposed to co-ordination by an acetonitrile molecule and electron transfer becomes more difficult. Another explanation is that the copper is now more tightly held and twisting to accommodate the necessary geometry change for accommodation of the Cu(II) redox state is more difficult.

2.27 Conclusion

Non-polar groups located proximal to the metal ion resulted in substantially more stable Cu(I) states. In bulkier solvents steric hindrance of solvent co-ordination to Cu(II) is probably still a major factor in determination of the Cu(I)/Cu(II) redox potential.[12]

Hydrophobicity in the Cu(I) complex environment may also play a role in affecting variations in the redox potentials of complexes. Increased hydrophobicity helps increase $E_{1/2}$ values, since a lower dielectric environment provided by e.g. non-polar quinolyl species favour lower charges and thus stabilises the Cu(I) relative to Cu(II) oxidation state.[52] Sorrell and Jameson showed that in tripodal Cu(II) complexes possessing geometries similar to those of the Cu(I) tripodal complexes discussed herein, the redox potential was more positive due to an environment of decreased polarity.[21]

Karlin noted 'When pyridyl donors of the parent TMPA ligand are replaced by quinoyl donors or when the modified TMPA ligand containing an electron-withdrawing ester substituent is used, the $E_{1/2}$ values of their Cu(I) complexes become more positive resulting in more thermodynamically stable Cu(I) complexes'.[12]

In summary, if Cu(I) podates capable of redox interaction with dioxygen are to be prepared we would need to aim for the following possibly unattainable characteristics :

1. Aliphatic instead of aromatic R-group.
2. A rigid head group which exposes Cu(I) to substitute dioxygen.
3. Steric protection.

The tren-capped cinnamaldehyde podate was our best attempt at producing a redox active Cu(I) podate. This podate had decreased hydrophobicity combined with good steric protection. In the future a longer polyene substituent might generate appropriate thermodynamic and kinetic behaviour.

2.28 Experimental for Podands and Copper(I) Podate Complexes

(general syntheses)

General procedure 1: Preparation of free ligands

The appropriate aldehyde (0.015mol) in methanol (50ml) was warmed on a hot plate to 50°C. A methanol solution of tren/trpn (0.010mol) was slowly dripped in. The resulting solution was stirred at 50°C for one hour. The solution was filtered and reduced in volume yielding the free ligand.

Podands - Free Ligands

Tren-based podands

L1

Benzaldehyde ($5.1x10^{-3}$mol, 0.55g) and tren ($1.7x10^{-3}$mol, 0.25g) were reacted according to the general procedure 1. The resulting orange oil was pumped to dryness yielding a pale yellow solid. This was recrystallised from MeCN/$CHCl_3$. (Yield = 70%)

C H N analysis:- $[C_{27}H_{30}N_4]$

	C %	H %	N %
Calc:	79.00	7.31	13.65
Found:	78.44	7.21	13.50

Infrared spectrum:- *Inter alia* (cm^{-1}) Aromatic; 3062, C-H aliphatic; 2952, 2848, C=N; 1647(s),

Mass spectrum:-	Formula	Peak	% of base peak
m/e^+	$[L1]^+$	410	10
	$-(PhC{=}N{-}CH_2CH_2)$	292	90

^{1}H NMR ($CDCl_3$, 300MHz, 300K)

2.93 (6H, t, J = 6.3, CH_2), 3.68 (6H, t, J = 6.3, CH_2), 8.10 (3H, s, HC=N), 7.51 (6H, d, J = 8.9, Ph), 7.49 (3H, t, J = 7.1, Ph), 7.38 (6H, t, J = 5.2, Ph)

L2

Tren ($1.7x10^{-3}$mol, 0.25g) and mesitaldehyde ($5.1x10^{-3}$mol, 0.76g) were reacted according to the general procedure 1. A white crystalline product precipitated from solution and was recovered by gravity filtration, whilst washing with ice-cold methanol. (Yield = 55%)

C H N analysis:- $[C_{36}H_{48}N_4]$

	C %	H %	N %
Calc.	80.50	8.96	10.45
Found.	79.83	8.80	10.87

Infrared spectrum:- *Inter alia* (cm^{-1}) Aromatic 3011, C-H aliphatic 2956, 2916,2853; C=N 1646(s);

Mass spectrum:-	Formula	Peak	% of base peak
m/e^+	$[L2]^{2+}$	534	20
	$-(CH_3)_3$-Ph-CN-CH	376	100

^{1}H NMR ($CDCl_3$, 300MHz, 300K)

3.00 (6H, t, J = 6.3, CH_2), 3.78 (6H, t, J = 6.3, CH_2), 8.55 (3H, s, HC=N), 2.33 (18H, s, CH_3), 2.25 (9H, s, CH_3), 6.8 (6H, s, Ph)

L4

Naphtaldehyde ($5.1x10^{-3}$mol, 0.80g) and tren ($1.7x10^{-3}$mol, 0.25g) were reacted according to the general procedure 1. A white crystalline product precipitated from solution and was recovered by gravity filtration, whilst washing with ice-cold methanol. (Yield = 78%)

C H N analysis:- $[C_{39}H_{36}N_4]$

	C %	H %	N %
Calc.	83.57	6.40	10.00
Found.	81.00	6.64	9.64

Infrared spectrum: *Inter alia* (cm^{-1}) C-H aliphatic 2952, 2874; C=N 1641;

Mass spectrum:-	Formula	Peak	% of base peak
m/e^+	$[L4]^+$	560	10

^{1}H NMR ($CDCl_3$, 500MHz, 300K)

2.93 (6H, t, J = 6.3, CH_2), 3.64 (6H, t, J = 6.3, CH_2), 7.95 (3H, s, HC=N), 7.93 (3H, s, Ph1), 7.83 (3H, d, J = 8.2, Ph1), 6.40 (overlap with Ph2, Ph1), 7.73 (3H, d, J = 8.6, Ph2), 7.52 (3H, t, J = 7.1, Ph2), 6.41 (overlap with Ph1, Ph2), 7.20 (masked by solvent, Ph2)

General procedure 2 : Preparation of Copper(I) podates by Insertion Method.

A solution of the appropriate amine (1.7×10^{-3} mol) was dissolved in methanol (20ml) and added dropwise to a stirring solution of the appropriate aldehyde (5.1×10^{-3} mol) in methanol. The solution was stirred at 40°C for 30 minutes and reduced in volume to yield an oil, or where stated, a solid product. *It is now necessary to maintain a nitrogen atmosphere.*

The product was dissolved in dry acetonitrile and stirred at 40°C. A deoxygenated solution of $Cu(MeCN)_4ClO_4$ in acetonitrile was added slowly with stirring. The solution was stirred for 30 minutes during which time a solid precipitated. This was filtered with a frit, washed with ice-cold acetonitrile and dried under a stream of nitrogen.

Cu(I) Tren-Based Podates

[CuL3]

Tren ($1.7x10^{-3}$mol, 0.25g) and m-hydroxybenzaldehyde ($5.1x10^{-3}$mol, 0.63g) were reacted according to the general procedure 2. The resulting oil was dissolved in acetonitrile and reacted with $Cu(MeCN)_4(CF_3SO_3)$ ($1.7x10^{-3}$mol, 0.64g). A yellow/green solid precipitated. This was washed with ice-cold acetonitrile and recovered by frit filtration under a stream of nitrogen. (Yield = 57%)

C H N analysis:- $[C_{27}H_{29}N_4O_3Cu]^{-}.H_2O$

	C %	H %	N %
Calc.	60.22	5.76	10.41
Found.	60.71	5.59	10.76

Infrared spectrum:- *Inter alia* (cm^{-1}) C-H aliphatic ; C=N ; No counterion peaks present

FAB mass spectrum:-	Formula	Peak	% of base peak
m/z	$[CuL3]^{+}$	522	100

The same product was obtained when $Cu(MeCN)_4(ClO_4)$ was reacted in place of $Cu(MeCN)_4(CF_3SO_3)$. (Yield = 45%)

[CuL4][ClO$_4$]

Naphtaldehyde ($5.1x10^{-3}$mol, 0.80g) and tren ($1.7x10^{-3}$mol, 0.25g) were reacted according to the general procedure 2. The resulting white crystalline product was dissolved in acetonitrile by heating and reacted with $Cu(MeCN)_4ClO_4$ ($1.7x10^{-3}$mol, 0.55g). An orange solid precipitated. This was washed with ice-cold acetonitrile and recovered by frit filtration under a stream of nitrogen. (Yield = 35%)

C H N analysis:- $[C_{39}H_{36}N_4Cu](ClO_4)$

	C %	H %	N %
Calc.	64.78	4.98	7.75
Found.	64.10	4.67	7.73

Infrared spectrum:- *Inter alia* (cm^{-1}) C-H aliphatic 2958, 2868; C=N 1630; ClO_4^- 1096, 622

FAB mass spectrum:-	Formula	Peak	% of base peak
m/z	$[CuL4]^+$	623	100

^{1}H NMR ($CDCl_3$, 500MHz, 300K)

3.13 (6H, t, J = 6.3, CH_2), 3.88 (6H, t, J = 6.3, CH_2), 8.64 (3H, s, HC=N), 8.42 (3H, s, Ph1), 8.19 (3H, d, J = 8.4, Ph1), 6.92 (3H, d, J = 8.4, Ph1), 7.43 (3H, d, J = 8.1, Ph2), 7.36 (3H, t, J = 7.9, Ph2), 6.99 (3H, t, J = 7.9, Ph2), 7.05 (3H, d, J = 8.0, Ph2)

[CuL5][BF_4]

Tren ($1.7x10^{-3}$mol, 0.25g) and 3-chlorobenzaldehyde ($5.1x10^{-3}$mol, 0.72g) were reacted according to general procedure 2. The resulting oil was dissolved in acetonitrile and reacted with $Cu(MeCN)_4BF_4$ ($1.71x10^{-3}$mol, 0.53g). A yellow/green solid precipitated. This was washed with ice-cold acetonitrile and recovered by frit filtration under a stream of nitrogen. (Yield = 68%)

C H N analysis:- $[C_{27}H_{27}N_4Cl_3Cu](BF_4)$

Satisfactory elemental analysis was not achieved most likely due to the presence of oxidised species.

Infrared spectrum:- *Inter alia* (cm^{-1}) C-H aliphatic 2958, 2868; C=N 1630; BF_4^- 1030, 1072,680

FAB mass spectrum:-	Formula	Peak	% of base peak
m/z	$[CuL5]^+$	577	100

^{1}H NMR (d_3-MeCN, 300MHz, 300K)

3.00 (6H, s, CH_2), 3.72 (6H, s, CH_2), 8.38 (3H, s, HC=N), 8.03 (6H, s, Ph), 7.33 (3H, d, J = 8.0, Ph), 6.86 (3H, t, J = 7.9, Ph), 7.81 (3H, d, J = 7.6, Ph)

[CuL6][ClO_4]

Dichlorobenzaldehyde ($5.1x10^{-3}$mol, 0.89g) and tren ($1.7x10^{-3}$mol, 0.25g) were reacted according to the general procedure 2. The resulting oil was dissolved in acetonitrile and reacted with $Cu(MeCN)_4ClO_4$ ($1.7x10^{-3}$mol, 0.55g). A yellow solid precipitated. This was washed with ice-cold acetonitrile and recovered by frit filtration under a stream of nitrogen. (Yield = 61%)

C H N analysis:-	$[C_{27}H_{24}N_4Cl_6Cu](ClO_4)$		
	C %	H %	N %
Calc.	41.56	3.10	7.18
Found.	41.44	3.07	7.17

Infrared spectrum:- *Inter alia* (cm^{-1}) C-H aliphatic 2916, 2858; C=N 1631; ClO_4^- 1092, 622

FAB mass spectrum:-	Formula	Peak	% of base peak
m/z	$[CuL6]^+$	681	100
	$[CuL6]ClO_4$	780	5
	$([Cu_2(L6)_2]ClO_4)^+$	1462	2

^{1}H NMR ($CDCl_3$, 300MHz, 300K)

3.20 (6H, s, CH_2), 3.90 (6H, s, CH_2), 8.50 (3H, s, HC=N), 8.20 (3H, s, Ph), 7.77 (3H, d, J = 7.2, Ph), 7.19 (3H, d, J = 8.2, Ph).

[CuL7][ClO_4]

Bromobenzaldehyde ($5.1x10^{-3}$mol, 0.95g) and tren ($1.7x10^{-3}$mol, 0.25g) were reacted according to the general procedure 2. The resulting oil was dissolved in acetonitrile and reacted with $Cu(MeCN)_4ClO_4$ ($1.7x10^{-3}$mol, 0.55g). A yellow/green solid precipitated. This was washed with ice-cold acetonitrile and recovered by frit filtration under a stream of nitrogen. (Yield = 79%)

C H N analysis:- $[C_{27}H_{27}N_4Br_3Cu](ClO_4)$

	C %	H %	N %
Calc.	40.02	3.36	6.91
Found.	38.30	3.39	7.49

Infrared spectrum: *Inter alia* (cm^{-1}) C-H aliphatic 2950, 2860; C=N 1637; ClO_4^- 1098, 1085, 621

FAB mass spectrum:-

m/z	Formula	Peak	% of base peak
	$[CuL7]^+$	711	100
	$[CuL7(ClO_4)]^+$	810	5

^{1}H NMR (d_3-MeCN, 500MHz, 300K)

3.31 (6H, s, CH_2), 4.01 (6H, s, CH_2), 8.77 (3H, s, HC=N), 8.07 (3H, d, J = 7.3, Ph), 6.25 (3H, s, Ph), 7.16 (3H, t, J = 7.2, Ph), 7.61 (3H, d, J = 7.4, Ph)

[CuL8][ClO_4]

Tolualdehyde ($5.1x10^{-3}$mol, 0.62g) and tren ($1.7x10^{-3}$mol, 0.25g) were reacted according to the general procedure 2. The resulting oil was dissolved in acetonitrile and reacted with $Cu(MeCN)_4ClO_4$ ($1.7x10^{-3}$mol, 0.55g). A yellow/green solid precipitated. This was washed with ice-cold acetonitrile and recovered by frit filtration under a stream of nitrogen. (Yield = 57%)

C H N analysis:- $[C_{30}H_{36}N_4Cu](ClO_4)$

	C %	H %	N %
Calc.	58.54	5.85	9.11
Found.	58.10	5.45	9.13

Infrared spectrum:- *Inter alia* (cm^{-1}) C-H aliphatic 2915, 2848; C=N 1629; ClO_4^- 1083, 622

FAB mass spectrum:-	Formula	Peak	% of base peak
m/z	$[CuL8]^+$	516	100
	$[CuL8(ClO_4)]^+$	615	15
	$[Cu_2L8_2(ClO_4)]^+$	1132	2

^{1}H NMR (d_3-MeCN, 500MHz, 300K)

3.10 (6H, t, J = 5.5, CH_2), 3.80 (6H, t, J = 5.1, CH_2), 8.46 (3H, s, HC=N), 7.92 (3H, s, Ph), 1.83 (9H, s, CH_3), 7.22 (3H, d, J = 7.6, Ph), 6.84 (3H, t, J = 7.7, Ph), 7.86 (3H, d, J = 7.7, Ph)

[CuL9][ClO_4]

Nitrobenzaldehyde ($5.1x10^{-3}$mol, 0.77g) and tren ($1.7x10^{-3}$mol, 0.25g) were reacted according to the general procedure 2. The resulting orange oil was dissolved in acetonitrile and reacted with $Cu(MeCN)_4ClO_4$ ($1.7x10^{-3}$mol, 0.55g). A dark red/brown crystalline solid precipitated. This was washed with ice-cold acetonitrile and recovered by frit filtration under a stream of nitrogen. (Yield = 52%)

C H N analysis:- $[C_{27}H_{27}N_7O_6Cu](ClO_4).\ 2H_2O$

	C %	H %	N %
Calc.	43.60	4.20	13.20
Found.	42.95	3.89	13.94

Infrared spectrum:- *Inter alia* (cm-1) C-H aliphatic 2852; C=N 1636; ClO_4^- 1089, 622

FAB mass spectrum:-	Formula	Peak	% of base peak
m/z	$[CuL9]^+$	608	100

^{1}H NMR (d_3-MeCN, 500MHz, 243K)

3.00 (6H, t, J = 5.5, CH_2), 3.75 (6H, t, J = 5.3, CH_2), 8.49 (3H, s, HC=N), 7.91 (3H, d, J = 8.3, Ph), 7.40 (3H, t, J = 7.9, Ph), 6.99 (3H, d, J = 7.50, Ph), 7.35 (3H, d, J = 7.6, Ph)

($CDCl_3$, 500MHz, 300K)

3.20 (6H, t, J = 5.5, CH_2), 3.91 (6H, unresolved, CH_2), 8.65 (3H, s, HC=N), 8.05 (3H, d, J = 8.3, Ph), 7.53 (3H, t, J = 7.4, Ph), 7.29 (3H, masked by solvent, Ph), 7.45 (3H, d, J = 7.3, Ph)

[CuL10][ClO_4]

Trans-cinnamaldehyde ($5.1x10^{-3}$mol, 0.67g) and tren ($1.7x10^{-3}$mol, 0.25g) were reacted according to the general procedure 2. The resulting oil was dissolved in acetonitrile and reacted with $Cu(MeCN)_4ClO_4$ ($1.7x10^{-3}$mol, 0.55g). A bright orange crystalline solid precipitated. This was washed with ice-cold acetonitrile and recovered by frit filtration under a stream of nitrogen (Yield 82%)

C H N analysis:- $[C_{33}H_{36}N_4Cu](ClO_4)$

	C %	H %	N %
Calc.	60.80	5.50	8.60
Found.	60.24	5.53	8.48

Infrared spectrum:- *Inter alia* (cm^{-1}) C-H aliphatic 2912, 2833; C=N 1627; ClO_4^- 1098, 623

FAB mass spectrum:-	Formula	Peak	% of base peak
m/z	$[CuL10]^+$	551	100
	$[CuL10(ClO_4)]^+$	650	8

^{1}H NMR (d_3-MeCN, 500MHz, 300K)

3.02 (6H, t, J = 5.8, CH_2), 3.69 (6H, t, J = 5.8, CH_2), 8.10 (3H, d, HC=N), 7.14-7.17 (3H, dd, J = 8.6, CH), 7.32 (3H, d, J = 7.8, Ph), 7.52 (6H, d, J = 7.5, Ph), 7.08 (6H, t, J = 7.8, Ph), 7.29 (3H, s, Ph)

[CuL11][ClO_4]

Tren ($1.7x10^{-3}$mol, 0.55g) and furfural ($5.1x10^{-3}$mol, 0.46g) were reacted according to the general procedure 2. The resulting oil was dissolved in acetonitrile and reacted with $Cu(MeCN)_4ClO_4$ ($1.7x10^{-3}$mol, 0.55g). The resulting tan coloured product precipitated from solution. This was washed with ice-cold acetonitrile and recovered by frit filtration under a stream of nitrogen. (Yield = 76%)

C H N analysis:- $[C_{21}H_{27}N_4O_3Cu](ClO_4)$

	C %	H %	N %
Calc.	46.20	4.95	10.30
Found	45.90	4.99	10.40

Infrared spectrum:- *Inter alia* (cm^{-1}) C-H aliphatic 2842; C=N 1636; ClO_4^- 1095, 622

FAB mass spectrum:-	Formula	Peak	% of base peak
m/z	$[CuL11]^+$	443	100
	$[CuL11(ClO_4)]^+$	542	20

^{1}H NMR ($CDCl_3$), 300MHz, 300K)

2.8 (6H, t, J = 5.8, CH_2), 3.6 (6H, t, J = 5.8, CH_2), 8.44 (3H, d, HC=N), 8.12 (3H, d, J = 2.4), 7.57 (3H, d, J = 2.6), 7.4 (3H, unresolved).

[CuL12][ClO_4]

5-methylfurfural ($3.1x10^{-3}$mol, 0.34g) and tren ($1.03x10^{-3}$mol, 0.15g) were reacted according to the general procedure 2. The resulting oil was dissolved in acetonitrile and

reacted with $Cu(MeCN)_4ClO_4$ ($1.03x10^{-3}$mol, 0.33g). An orange solid precipitated and was recovered by frit filtration under a stream of nitrogen (Yield = 60%)

C H N analysis:- $[C_{24}H_{33}N_4O_3Cu](ClO_4).H_2O$

	C	H	N
Calc.	47.76	5.80	9.29
Found.	48.28	5.03	9.61

Infrared spectrum:- *Inter alia* (cm^{-1}) C-H aliphatic 2912, 2850; C=N 1637; ClO_4^- 1096, 622

FAB mass spectrum:-	Formula	Peak	% of base peak
m/z	$[CuL12]^+$	486	100
	$[CuL12(ClO_4)]^+$	585	15

^{1}H NMR ($CDCl_3$, 300MHz, 300K)

3.07 (6H, s, CH_2), 3.88 (6H, s, J = 5.8, CH_2), 8.07 (3H, s, HC=N), 7.13 (3H, d, J = 3.0, Ar), 6.08 (3H, d, J = 2.8, Ar), 1.93 (9H, s, CH_3)

Cu(I) Trpn Podates

[CuL13][ClO_4]

Trpn ($1.7x10^{-3}$mol, 0.32g) and benzaldehyde ($5.1x10^{-3}$mol, 0.55g) were reacted according to the general procedure 2. The resulting oil was dissolved in acetonitrile and reacted with $Cu(MeCN)_4ClO_4$ ($1.7x10^{-3}$mol, 0.55g). The product was prone to oxidation and an argon atmosphere was necessary for successful synthesis. The resulting yellow/green coloured product precipitated from solution. This was washed with ice-cold acetonitrile and recovered by frit filtration under a stream of nitrogen. (Yield = 59%)

C H N analysis:- $C_{30}H_{36}N_4Cu(ClO_4)$

	C %	H %	N %
Calc.	58.63	5.86	9.12
Found.	52.70	6.26	10.08

Satisfactory elemental analysis was not obtained and this is most likely due to the presence of oxidised species.

Infrared spectrum: *Inter alia* (cm^{-1}) C-H aliphatic 2958, 2868; C=N 1627; ClO_4^- 1096, 623

FAB mass spectrum:-	Formula	Peak	% of base peak
m/z	$[CuL13]^+$	515	100
	$[(Cu(tren).MeCN.2H_2O)ClO_4]^+$	427	55

A satisfactory ^1H NMR was not obtained owing to solution instability.

[CuL14][ClO_4]

Bromobenzaldehyde ($5.1x10^{-3}$mol, 0.95g) and trpn ($1.7x10^{-3}$mol, 0.32g) were reacted according to the general procedure 2. The resulting oil was dissolved in acetonitrile and reacted with $Cu(MeCN)_4ClO_4$ ($1.7x10^{-3}$mol, 0.55g). A yellow solid precipitated. This was washed with ice-cold acetonitrile and recovered by frit filtration under a stream of nitrogen. (Yield =77%)

C H N analysis:- $[C_{30}H_{33}N_4BrCu](ClO_4)$

	C %	H %	N %
Calc.	42.28	3.90	6.57
Found.	42.52	3.88	6.61

Infrared spectrum:- *Inter alia* (cm^{-1}) C-H aliphatic 2963; C=N 1629; ClO_4^- 1089, 622

FAB mass spectrum:-	Formula	Peak	% of base peak
m/z	$[CuL14]^+$	753	100

^{1}H NMR ($CDCl_3$, 500MHz, 300K)

2.80 (6H, t, J = 5.5, CH_2), 2.00 (6H, m, CH_2), 3.55 (6H, t, J = 5.25, CH_2), 8.40 (3H, s, HC=N), 8.00 (3H, d, J = 6.0, Ph), 7.15 (3H, t, J = 5.9, Ph), 7.29 (3H, masked by solvent, Ph), 7.55 (3H, d, J = 7.0, Ph)

[CuL15][ClO_4]

Tolualdehyde ($5.1x10^{-3}$mol, 0.62g) and trpn ($1.7x10^{-3}$mol, 0.32g) were reacted according to the general procedure 2. The resulting oil was dissolved in acetonitrile and reacted with $Cu(MeCN)_4ClO_4$ ($1.7x10^{-3}$mol, 0.55g). A yellow solid precipitated This was washed with ice-cold acetonitrile and recovered by frit filtration under a stream of nitrogen. (Yield = 72%)

C H N analysis:- $[C_{33}H_{42}N_4Cu](ClO_4)$

	C %	H %	N %
Calc.	60.27	6.40	8.52
Found.	59.81	6.44	8.48

Infrared spectrum:- *Inter alia* (cm^{-1}) C-H aliphatic 2971, 2866; C=N 1623; ClO_4^- 1085, 622

FAB mass spectrum:-	Formula	Peak	% of base peak
m/z	$[CuL15]^+$	558	100
	$[Cu_2L15(ClO_4)]^+$	721	10

^{1}H NMR ($CDCl_3$, 500MHz, 300K)

2.66 (6H, s, CH_2), 2.0 (6H, m, CH_2) 3.39 (6H, t, J = 5.1, CH_2), 8.26 (3H, s, HC=N), 8.00 (3H, s, Ph), 2.16 (9H, s, CH_3), 7.20 (3H, d, J = 6.0, Ph), 7.07 (3H, t, J = 7.6, Ph), 7.83 (3H, d, J = 7.6, Ph)

[CuL16][ClO_4]

Nitrobenzaldehyde ($5.1x10^{-3}$mol, 0.77g) and trpn ($1.7x10^{-3}$mol, 0.32g) were reacted according to the general procedure 2. The resulting oil was dissolved in acetonitrile and

reacted with $Cu(MeCN)_4ClO_4$ ($1.7x10^{-3}$mol, 0.55g). A dark red/brown crystalline solid precipitated. This was washed with ice-cold acetonitrile and recovered by frit filtration under a stream of nitrogen. (Yield = 54%)

C H N analysis:- $[C_{30}H_{33}N_7O_6Cu](ClO_4)$

	C %	H %	N %
Calc.	48.00	4.43	13.06
Found.	47.21	4.30	12.78

Infrared spectrum:- *Inter alia* (cm^{-1}) C-H aliphatic 2965, C=N 1636; ClO_4^- 1090, 622

FAB mass spectrum:-

Formula	Peak	% of base peak
$[CuL16]^+$	651	100
$[CuL16(ClO_4)]^+$	751	10
$[Cu_2L16]^+$	713	5
$[Cu_2L16(ClO_4)]^+$	814	5

^{1}H NMR ($CDCl_3$, 500MHz, 300K)

2.70 (6H, t, J = 5.1, CH_2), 1.95 (6H, m, CH_2), 3.10 (6H, t, J = 5.2, CH_2), 8.30 (3H, s, HC=N), 8.05 (3H, d, J = 8.04, Ph), 8.4 (3H, t, J = 7.6, Ph), 7.6 (3H, t, J = 8.0, Ph), 8.1 (3H, d, J = 7.6, Ph)

[CuL17][ClO_4]

Trans-cinnamaldehyde ($5.1x10^{-3}$mol, 0.67g) and trpn ($1.7x10^{-3}$mol, 0.32g) were reacted according to the general procedure 2. The resulting oil was dissolved in acetonitrile and reacted with $Cu(MeCN)_4ClO_4$ ($1.7x10^{-3}$mol, 0.55g). An orange crystalline solid precipitated. This was washed with ice-cold acetonitrile and recovered by frit filtration under a stream of nitrogen. (Yield = 81%)

C H N analysis:- $[C_{36}H_{42}N_4Cu](ClO_4)$

	C %	H %	N %
Calc.	62.30	6.06	8.08
Found.	61.78	6.09	7.94

Infrared spectrum:- *Inter alia* (cm^{-1}) C-H aliphatic 2971, 2854; C=N 1623; ClO_4^- 1094, 622

FAB mass spectrum:-	Formula	Peak	% of base peak
m/z	$[CuL17]^+$	593	100
	$[CuL17(ClO_4)]^+$	692	2

General Procedure 3 ; Template Synthesis of Cu(I) Podates

The reactions were carried out under an inert atmosphere and deoxygenated solvents were used throughout.

The aldehyde ($2.8x10^{-3}$ mol) and appropriate copper template ($9.4x10^{-4}$ mol) were stirred in a mixture of acetonitrile/industrial alcohol (2:3), with heating, for a short period of time. An ethanolic solution of tren ($9.4x10^{-4}$ mol) was slowly dripped in and any colour change was noted. The solution was heated at 50°C for 1 hour and then reduced in volume until a yellow solid product precipitated. The product was washed with ice-cold acetonitrile, filtered through a frit and dried under nitrogen.

[CuL1][ClO_4]

Benzaldehyde (0.3g, $2.8x10^{-3}$mol), $Cu(MeCN)_4ClO_4$ (0.3g, $9.4x10^{-4}$ mol) and tren (0.14g, $9.4x10^{-4}$ mol) were reacted according to general procedure 3. A yellow solid precipitated and was recovered by frit filtration under a stream of nitrogen. (Yield = 92%)

C H N analysis:- $[C_{27}H_{30}N_4Cu\ (ClO_4)]$

	C %	H %	N %
Calc.	56.60	5.24	9.78
Found.	56.34	5.20	9.64

Infrared spectrum:- *Inter alia* (cm^{-1}) C-H aliphatic 2971, 2854; C=N 1633; ClO_4^- 1098, 622

FAB mass spectrum:-	Formula	Peak	% of base peak
m/z	$[CuL1]^+$	473	100

^{1}H NMR ($CDCl_3$, 300MHz, 300K)

3.24 (6H, s, CH_2), 3.93(6H, s, CH_2), 8.5 (3H, s, HC=N), 8.01 (6H, d, J = 7.6, Ph), 7.35 (3H, t, J = 7.4, Ph), 6.75 (6H, t, J = 7.6 Ph)

[CuL5][BF_4]

Chlorobenzaldehyde (0.4g, $2.8x10^{-3}$mol), $Cu(MeCN)_4ClO_4$ (0.3g, $9.4x10^{-4}$mol) and tren (0.14g, $9.4x10^{-4}$mol) were reacted according to general procedure 3. A yellow/green solid precipitated and was recovered by frit filtration under a stream of nitrogen. (Yield = 85%)

C H N analysis:- $[C_{27}H_{27}N_4CuCl_3](BF_4)$

	C %	H %	N %
Calc.	48.78	4.06	8.43
Found.	43.10	4.18	9.85

Infrared spectrum:-

Inter alia (cm^{-1}) C-H aliphatic 2971, 2854; C=N 1632; BF_4^- 1072, 680

FAB mass spectrum:-

Formula	Peak	% of base peak
$[CuL5]^+$	577	100

Analysis was not satisfactory, the green colour indicating the presence of an oxidised product. Recrystallisation gave yellow crystals of the Cu(I) podand but also blue and green crystals of an oxidised product.

CHAPTER 3

COPPER AZACRYPTANDS

Ligand Structures and Names used within Chapter

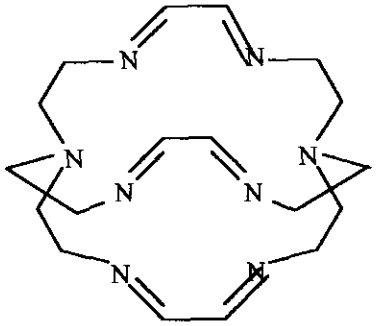

GT

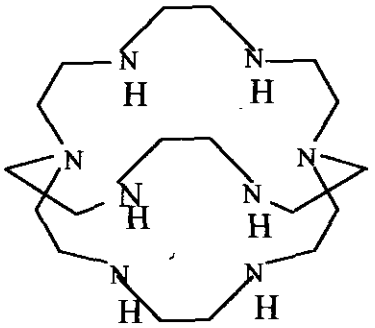

RGT

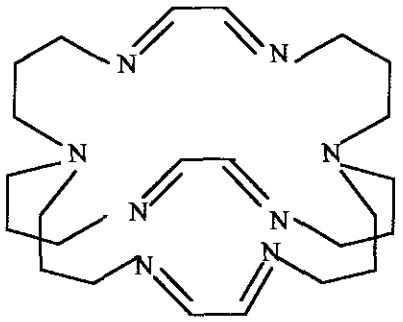

NGT

3.0 Introduction to Cryptands

Addition of one, two or three strands across a macrocycle creates the corresponding macrobi-, tri- or tetra-cycles. This brings complexation into the third dimension by creating an ellipsoidal or spherical cavity which is capable of completely encapsulating a co-ordinating metal ion. The earliest series of the cage ligands were developed by Lehn *et al* in the late 60's. These were entitled cryptands and the inclusion complexes they form were called cryptates.[1,2]

On formation of the metal cryptate an enhancement of many of the physical properties associated with complex formation has been observed. This is known as the cryptate effect and incorporates both kinetic and thermodynamic factors involved in complexation. Slow rates of formation and/or dissociation of the complex, high ligand field strengths and large stability constants are among the recognised properties which are enhanced relative to the analogous macrocyclic or acyclic chelates.[3]

The escalation of research in the area of macrocyclic and polymacrocyclic ligands has stimulated the development of imaginative and often complex synthetic strategies. Synthetic approaches to the formation of cryptand hosts may involve: -

3.1.1 Direct synthesis; strapping, capping and coupling.

The different approaches to cryptand assembly by direct syntheis are outlined schematically in **Scheme 3.1 (a)-(e)**. The synthetic strategy adopted in the first successful cryptand syntheses[4] and developed by subsequent groups[5] involved strapping an already-made macrocycle using a diacid chloride. This is performed under high dilution conditions so as to reduce competition with intermolecular reaction processes that could lead to undesired polymerisation by-products.[6]

3.1.2 Template Reactions

Template methods usually involve cryptand formation by stepwise or tripode coupling or tripode capping, in the presence of an external alkali, or transition metal ion template. Sargeson and coworkers[7] have used the template effect to generate azacryptands in high yield

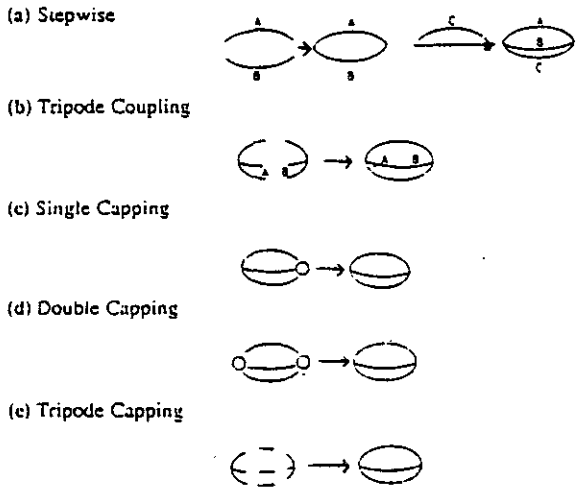

Scheme 3.1 Cryptand assembly by direct synthesis

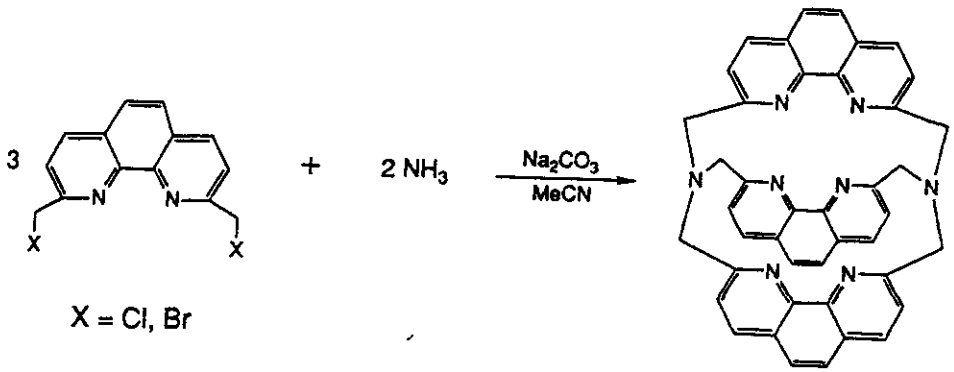

Scheme 3.2 Template synthesis of cryptands

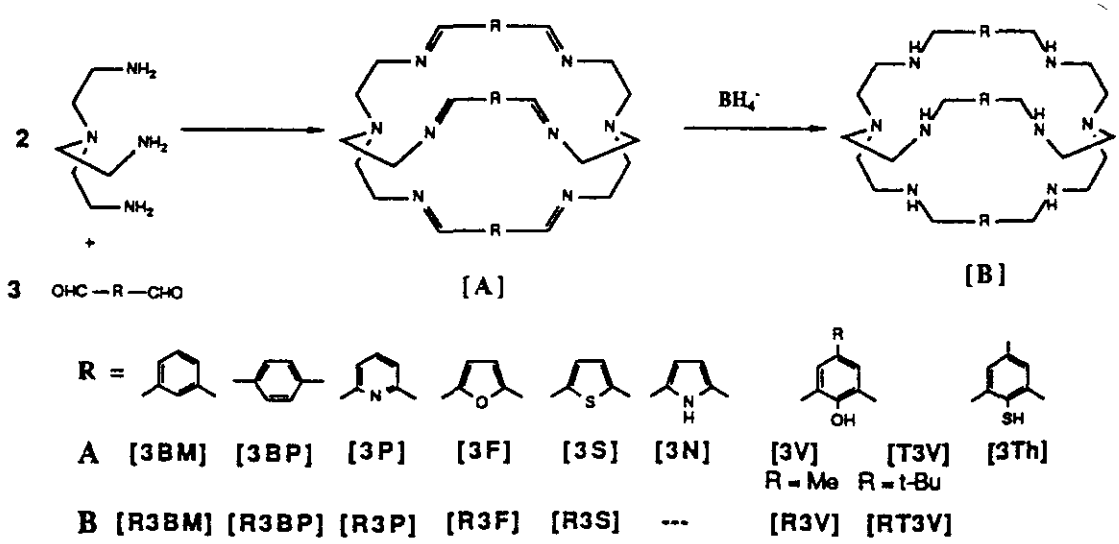

Scheme 3.3 The Azacryptand series developed by Nelson and coworkers

from simple precursors. **Scheme 3.2** illustrates a multistage mechanism, involving attack by NH_3 on the initially formed transient imino C=N. The main drawback is that a kinetically inert template cation is required for successful synthesis.

3.1.3 [2+3] Schiff base Condensation.

The [2+3] Schiff base condensation is a recent synthetic development[8] which creates easier routes to metal-free cryptands by a condensation reaction between two triamines and three dicarbonyls. Nelson *et al*[6] have demonstrated that this effective high yield tripod-coupling-capping route to azacryptands proceeds in high yield under mild conditions, without the need for high dilution techniques. By using a one-pot procedure, high yields have been obtained of several symmetric hexa-Schiff base crytands, despite the apparent need for six simultaneous condensations. Yields can, in most cases, be improved by the use of a template, although this may be due to cryptate insolubility assisting isolation of the product.

Once the three dimensional skeleton is assembled, the imine C=N bond of the cryptands can be readily reduced with $NaBH_4$ or $LiAlH_4$ to generate the analogous octaaminocryptands.[9,10] These are more chemically robust than their hexa-Schiff base precursors, leading to many advantages such as; ability to act as ligands for both cations and anions, an increase in flexibility, stability against hydrolysis and water solubility all of which are essential for application in vivo e.g. as imaging, carriers or sequestering agents.

A diverse range of bridgehead units have been employed in the synthesis of cryptands.[11] The largest single group involves a pair of N bridgeheads as there are a number of advantageous features associated with the synthesis. These include: -

1. Ability of the lone pair of electrons to participate in co-ordination.
2. The considerable flexibility associated with the ability of the lone pair of electrons on the nitrogen to undergo inversion.

3.1.4 Azacryptands

Azacryptands can be classified as molecules in which the majority of potential donors are nitrogen atoms. A comprehensive review of co-ordination chemistry of azacryptands has been carried out by Nelson *et al.*[6] For the purposes of this report the main points of relevance will be briefly discussed.

The azacryptand series in **Scheme 3.3** has been extensively studied over the last decade. Investigation into the end properties of these cages has led to inclusion complexes of the mononuclear and dinuclear type being formed with the toxic heavy metals, transition metals, alkali, alkaline earth cations and lanthanoid cations.[12,13]

3.1.5 Cryptand Conformation

It is common to describe cryptand ligands as imposing geometry on the encapsulated metals, although the co-ordination geometry is not absolutely fixed. The geometry of the cryptate is restrained within certain limits rather than constrained to one particular set of values. For the cryptands studied there are three main sources of flexibility.

1. The length of the strands in the cap, hence it would be expected that NGT would be more flexible than GT.
2. The length and rigidity of the linking strands, the reduced RGT being more flexible than the doubly bonded GT.
3. The helicity or twist of the crypt (rotation of one cap with respect to another).

The simplest measure of the helicity of the ligand is the twist angle φ, the rotation between the two sets of cap N atoms, **(Figure 3.1)**. In mononuclear cryptates a twist angle of 60° is required for octahedral geometry at the metal ion while a twist of 0° corresponds to D_{3h} (trigonal prismatic) symmetry. As the twist also affects the distance between the N_3 planes, and is influenced by the length and rigidity of the linker, most real examples represent compromise between the preferences of cryptand and metal ion.

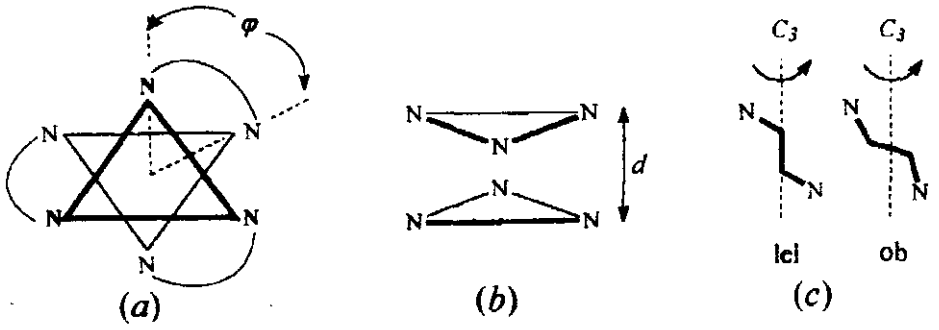

Figure 3.1 Parameters describing conformation in small azacryptands: (a) twist angle φ, (b) distance between N_3 plane and (c) ob and lel disposition of methylene spacers

Where the bridgehead atom X is a tertiary amine nitrogen, there are two conformational possibilities; the lone pair can be directed outward, away from the cavity, (*exo*) or it can be directed inward, possibly co-ordinating to encapsulated metals (*endo*).

Much of the pioneering work carried out in the period of 1960-1965 by Curtis[14] involved the *exo*-template effect in macrocyclic synthesis. This is where a metal ion is employed to act as a template for the cyclisation reactions due to the ability of the metal ion to organise the open chain reactions in a conformation favourable to ring closure. Inert metal ions such as the alkali, alkaline earth and lanthanide metals which form labile complexes are often employed due to their ease of subsequent removal and replacement of the metal ion i.e. transmetallation. It has been proposed that transmetallation involves a concerted process in which the incoming metal ion is partly bound to the ligand before the outgoing template ion is fully removed.

Endo template assembly causes ring enlargement or adds a further strand to an already existing smaller ring and involves all the pre-existing parts of the molecule.

In the case of the short caps, like those derived from tame (trisaminomethylmethine), the N_3 bite only permits the cap to bind to a single metal ion and thus the bridgehead is *exo*. In the cases of tren and trpn, the reverse usually applies; the bridgeheads are *endo* and the lone pairs may interact with encapsulated metal ions. Tren and trpn also differ from one another in

the preferred size of the N_3N_{br} pyramid and therefore in the preferred M-N distances and geometry as well as the orientation of the lone pairs on the nitrogen donors.

The spacers control the distance between the two sets of donors derived from the caps. In some cryptands the linkers may also carry donor atoms, providing the central metal ion with the desired geometry thus enabling us to vary the geometry around the central metal ion as desired. This distance is affected by the total length of the spacer but the pitch of helicity in the strands of the cage can play a major part and also influences the flexibility of the spacer.

It seems probable that dicopper cryptates of GT, RGT and NGT can act as possible modes for the biological electron transfer site Cu_A. This is mainly due to the small cavity size and associated short copper-copper bonding distance (~ 2.5 Å) similar to that seen in Cu_A. This chapter explores the synthesis of copper complexes of the named ligands and evidence towards the existence of a copper-copper bond in such systems.

3A Average-Valence Dicopper Complexes, Precursors and Related Compounds

A large amount of work was involved in development of reliable, high yielding routes to the average-valence cryptates. Although synthesised in the past, there has been many 'red herrings' such as the monocopper(II) GT and RGT cryptates and the Cu(II) carbinolamine complex. After initial confusion these complexes have in fact now aided our understanding of the synthesis and characterisation of the average valence complexes. It has been important to obtain the maximum information about the dicopper(I) and monocopper(II) systems for comparison with the average valence systems, in order that reliable physical measurements can be made and interpreted.

3A.1. GT

Nelson *et al* first reported the formation of this cryptand to occur via a template reaction of the triamine, tren, and glyoxal on Group II metals.[13] This was soon followed by the isolation of the free-ligand cryptand.[15] It is the near spherical nature of the small cavity within GT (N_{br}-N_{br} = 6.8 Å) and its relatively soft donor set which makes it an ideal site for the complexation of cations from all groups of the periodic table but particularly the transition metals.

[2+3] Schiff-base condensation was confirmed by the presence of a high intensity υ(C=N) absorption at 1633 cm^{-1} and the absence of any carbonyl or amine peaks in the infra-red spectrum. In addition, the EI mass spectrum showed a peak at 358 (85%). The yield of the ligand was found to be both temperature and solvent dependent. Polymerisation was evident if the condensation reaction was carried out above room temperature; an orange insoluble solid precipitated in such cases giving a poor C H N analysis and broad peaks in the ^1H NMR. When the synthesis was carried out at 0°C in isopropanol, a pale yellow solution developed and a crude yellow solid was obtained on removing the solvent. Soxhlet extraction of the crude product using a hexane/heptane (4:1) mixture generated a white crystalline solid in reasonable yield. This very pure cryptand is quite stable at room temperature and its solubility in a wide variety of polar solvents has aided synthesis of the copper GT complexes. The ^1H NMR spectrum is reported in **Chapter 3E**.

3A.2 $[SrGT][BPh_4]_2$

[2+3] Schiff-base condensation of the tripod amine, tren, with glyoxal on a group II metal, was the original method of synthesising the metal ion cryptates of the hexaimino cryptand GT. The presence of a medium intensity υ(C=N) absorption at 1616 cm^{-1} and the absence of any carbonyl or amine peaks in the infra-red spectrum confirmed that cryptate formation was complete. The infrared spectrum also displays strong absorptions due to the tetraphenylborate counterion indicating successful metal complexation. A sharp peak evident at 3510 cm^{-1} may be due to the presence of non-hydrogen bonded water co-ordinated to the metal ion. It was necessary to use tetraphenylborate as the counterion for successful isolation of the complex. However, as the main use of this route was for preparation of mixed valence copper complexes this caused no problems as it was easily removed by silver perchlorate.

3A.3 $[Cu_2^{I}GT](ClO_4)_2$ (This complex has previously been characterised by J. Nelson.[16])

Although we now realise that syntheses of $[Cu_2(1.5)GT]^{3+}$ proceeds via the dicopper (I) route, isolation of this complex is not necessary to form the average valence dicopper complex. However, synthesis and isolation of the complex was required for the purposes of comparison so that physical differences between the cryptates could be identified and explained to be arising from copper-copper bond formation. A good stock of this cryptate, in a very pure form, was also needed for both electron self-exchange and electrochemical investigations.

Original attempts at the preparation of $[Cu_2(I)GT](ClO_4)_2$ involved transmetallation of $[SrGT](BPh_4)_2$ using a 1:1 mixture of $Cu(ClO_4)_2$ and $Cu(O_2CCH_3)$. This method failed resulting instead in the formation of $[Cu_2(I)GT](BPh_4)_2$. Synthesis was successful by insertion of two Cu(I) cations from $[Cu(I)(MeCN)_4]ClO_4$ into the free ligand. A dark green/brown solid precipitated from a concentrated solution. This could be recrystallised from acetonitrile to yield large brown hexagonal crystals. If an aqueous solution was used, over a period of one week the complex became blue in colour. The UV/Vis spectrum of this solution is not that of the mixed valence complex and suggests that metal-assisted imine hydrolysis and possible rearrangement has occurred.

A typical infrared spectrum for complexes of GT was observed for $[Cu_2(I)GT](ClO_4)_2$. As is often observed in Cu(I)/imine systems, the imine band, appearing as a weak absorption band at 1599 cm^{-1} has been shifted and weakened on co-ordination. This is a significant shift of ν(C=N) from that reported for the free cryptand. This shift is also seen in other transition metal complexes of α-diimines and is as a result of the ligands ability to act as electron acceptors.[13] The strong perchlorate bands at 1096 and 623 cm^{-1} infer Cu(I) encapsulation into the GT cryptand. **Figure 3A.1** compares the infrared spectra of free GT and $[Cu_2GT]^{2+}$.

Peaks at 585 (100 %), $[Cu_2GT(ClO_4)]^+$ and 486 (85 %) $[Cu_2GT]^+$ in the FAB mass spectrum of the sample shows that a dinuclear copper(I) complex has been formed. There is a peak at 421 (27 %) which could be attributable to a monocopper species, however there is no corresponding peak at 520 which would be due to $[Cu(II)GT(ClO_4)]^+$- this makes its existence as a solid impurity unlikely. It is more probable that this peak arises in the course of the FAB mass spectrum process as the formulation of $[Cu_2(I)GT](ClO_4)_2$ fits the elemental analysis.

The structure was determined by single crystal X-ray crystallography by McKee and is discussed for comparison with the $[Cu_2(1.5)GT]$ structure in relation to copper-copper bond formation in **Chapter 3A.12**.[16]

3A.4 $[Cu(II)GT][ClO_4)_2.2MeCN$

The existence of a monocopper GT cryptate, as a significant impurity in some attempts at the synthesis of the average valence cryptate, had been suspected for the last eight years but never confirmed. Plausible evidence came from the appearance of four lines in the ESR spectrum which is characteristic of a Cu(II) species.[13]

The original (1990) attempted synthesis of $[Cu(II)GT](ClO_4)_2$ involved transmetallation of $[SrGT](BPh_4)_2$ with $[Cu_2(O_2CCH_3)_4(H_2O)_2]$ in 200ml acetonitrile/50ml ethanol using a GT:Cu stoichiometry of 1:1. The resulting dark green crystalline product was believed to be the monocopper cryptate. The fact that a large amount of acetonitrile was used in the synthesis, favouring the Cu(I) redox state, leads to the conclusion that this product is a mixture, in fact mainly dicopper(I) GT with the presence of a small amount of ESR detectable monocopper(II). A brown solution from which dark green/brown hexagonal crystals are isolated is also very characteristic in the synthesis of dicopper(I) GT.

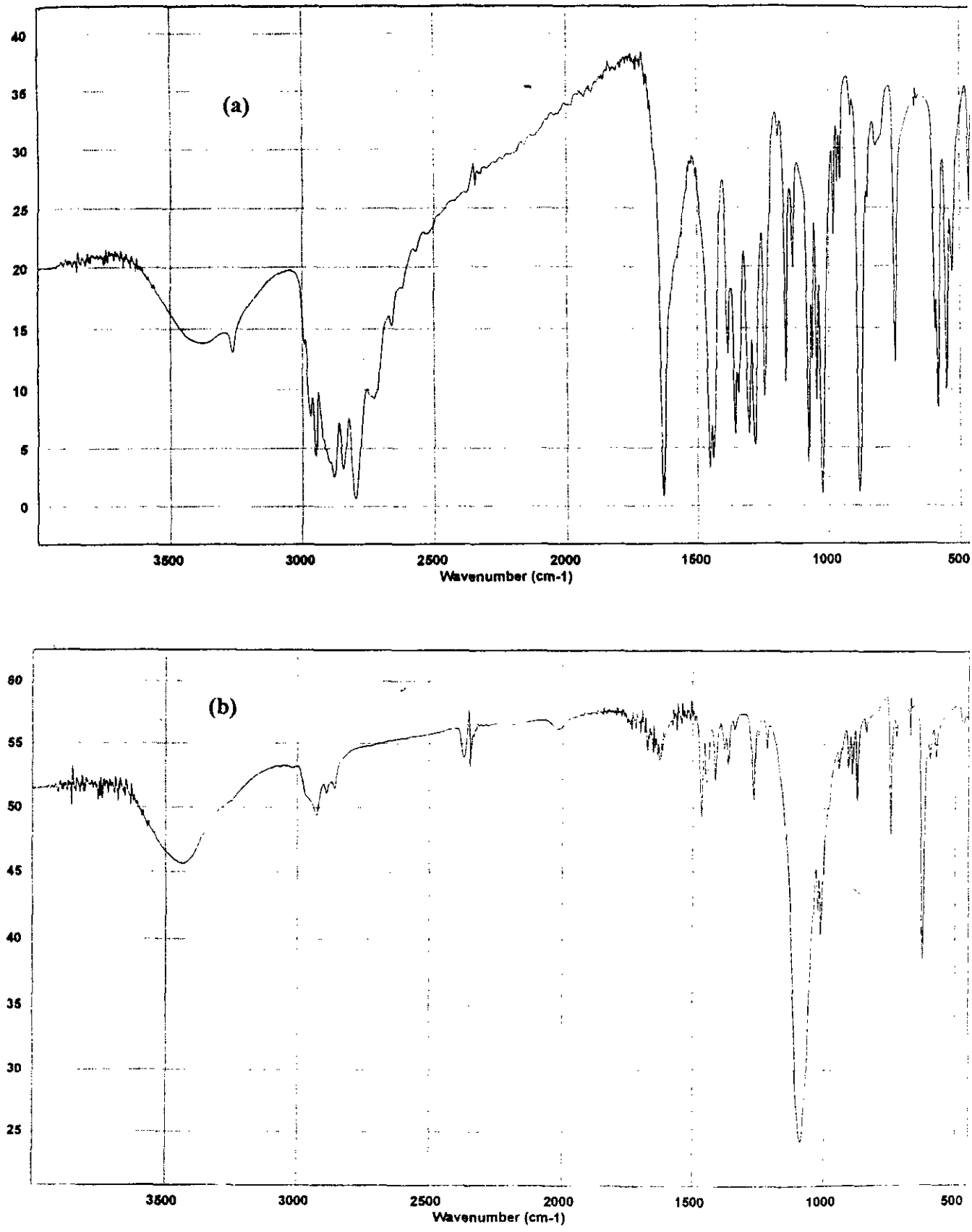

Figure 3A.1 Infrared spectra of (a) GT and (b) $[Cu_2GT](ClO_4)_2$

On hindsight, the CHN analysis obtained in earlier attempts and assigned to the formulation $[C_{18}H_{30}N_8Cu](ClO_4)_2.4H_2O$, is better matched to the formulation $[C_{18}H_{30}N_8Cu_2](ClO_4)_2$. In the original attempted synthesis the FAB mass spectrum showed a cluster at m/z 421 due to $[CuL]^+$ (100%), however, clusters were also evident at m/z 585 (10%) which could be attributed to $[Cu_2GT(ClO_4)]^+$. Although it was not unreasonable, at that stage, to assume that the major product was in fact the monocopper cryptate, the same pattern in the FAB mass spectrum can be seen for the dicopper (I) GT and the average valence GT so it seemed that mass spectroscopy alone is unable to distinguish the systems. When pure monocopper GT was eventually synthesised, (**Section G**) and confirmed by X-ray crystallography, there was no evidence of a dinuclear species in the FAB mass spectrum. **Figure 3A.2** compares the FAB mass spec of the dicopper and monocopper GT cryptate.

After repeated attempts at synthesising the monocopper crypt using a 1:1 ratio of free cryptand to $[Cu(MeCN)_4]ClO_4$ we realised that it was only when copper acetate and an alcohol solvent were used that the $[CuGT]^{2+}$ was obtained. A clean FAB mass spectrum of the product is seen with no peaks corresponding to a dicopper species. Peaks are evident at 421 (100%) and 520 (20%) corresponding to $[CuGT]^{2+}$ and $[CuGT(ClO_4)]^+$, respectively. What was unexpected in a Cu(II) complex, and therefore initially misleading, was the yellow/brown colour of the solid product. The electronic spectrum of the monocopper GT cryptate shows a charge transfer band at 365 nm (ε = 1750 $M^{-1}cm^{-1}$) and stronger transitions below 300 nm. Once this was recognised as being characteristic of $[CuGT]^{2+}$, it proved useful in synthesis as this colour was not seen in the course of the synthesis of either the dicopper (I) or average valence cryptates.

ESR, magnetic measurements and X-ray crystallography further confirm that this product is a monocopper(II) cryptate and not a Cu(I) species. The mononuclear Cu(II) cryptate exhibits a normal axial-type four line ESR spectrum with $g_{//}$ (2.281) > $g_{\perp}$ (2.084) and $A_{//}$ =145 G which is consistent with interaction of the odd electron with just one copper centre (I = 3/2). Magnetic susceptibility measurements also confirm its monocopper(II) nature via a virtually temperature-independent moment falling only slightly from 1.94 at 293 K to 1.82 at 80 K.

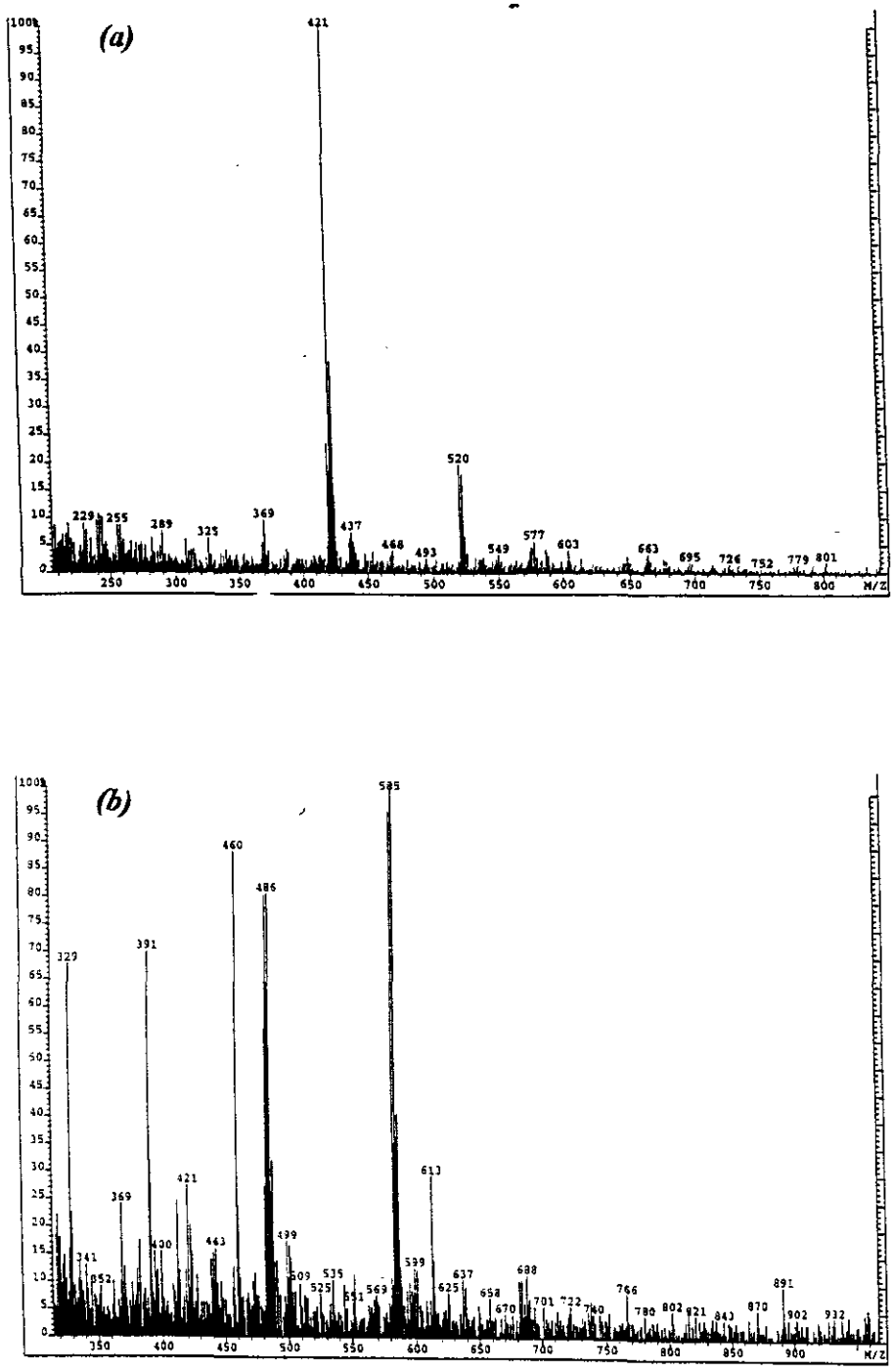

Figure 3A.2 FAB Mass Spectra of (a) Mononuclear $[Cu(II)GT](ClO_4)_2$ and (b) Dinuclear $[Cu_2GT](ClO_4)_2$

3A.4.1 X-Ray structure of $[Cu(II)GT][ClO_4)_2.2MeCN$[17]

X-ray quality crystals precipitated from the mother solution as yellow plates. The unit cell is composed of the $[CuGT]^{2+}$ cation, two independent perchlorate molecules and an acetonitrile molecule. The structure of the cation is shown in **Figure 3A.3**. The Cu(II) ion is co-ordinated to the six imino donors, but not to the bridgehead amines, and has effective D_3 symmetry. The amino N bridgehead atoms lie 3.24 Å from the metal ion within the near planar arrangement of adjacent methylene carbons, suggesting near sp^2 hybridisation of tertiary amine nitrogens.

The dihedral angle between adjacent imine groups in each chain is small [N11-C3-C4-N12 = 3.3°], suggesting that no significant distortion is imposed on the ligand. This generates a small ligand bite angle [N11-Cu-N12 = 76.0°(2)]. The distances from the Cu^{2+} to the six imino-N donor atoms fall into two sets: two long bonds and four short bonds. (**Table 3A.1**) This is expected as d^9, Cu^{2+} complexes are expected to show Jahn Teller distortions. In this system the distortion is the more common tetragonal extension, involving four strongly bound donors in a square plane and two more weakly bound axial donors (in e.g. $[Cu(NH_3)_4(H_2O)_2]$.

3A.5 RGT

The imine function of the macrobicycle GT may readily be hydrogenated using $NaBH_4$ in methanol solution to yield the octaamine derivative RGT. Complexes of RGT are expected to show enhanced flexibility relative to other small cryptates which have been studied, because (*cf.* Sargesons sar ligand) of the presence of the bridgehead nitrogen which is capable of inversion; or (*cf.* Sargesons sep ligand) of the longer methylene chain in the ligand cap; (or *cf.* GT) due to the absence of sterically restricting imine bonds.[6]

The relatively high basicity of the aminocryptands may be expected to favour protonation of any uncoordinated secondary or primary amino-N donor, as frequently seen in diamsar cryptates, even in the absence of deliberately added acid.

The white solid product was easily recognised from its infrared spectrum being obviously different from that of the parent hexaimine macrobicycle, (**Figure 3A.4**). The strong imine signal at ~1630 cm^{-1}, is removed and an NH peak is seen at 3259 cm^{-1}. X-ray crystallography[15] revealed that the broad absorption band, in the region 3528 cm^{-1}, was due to the presence of six adventitious lattice waters in the unit cell. The EI mass spectrum of RGT

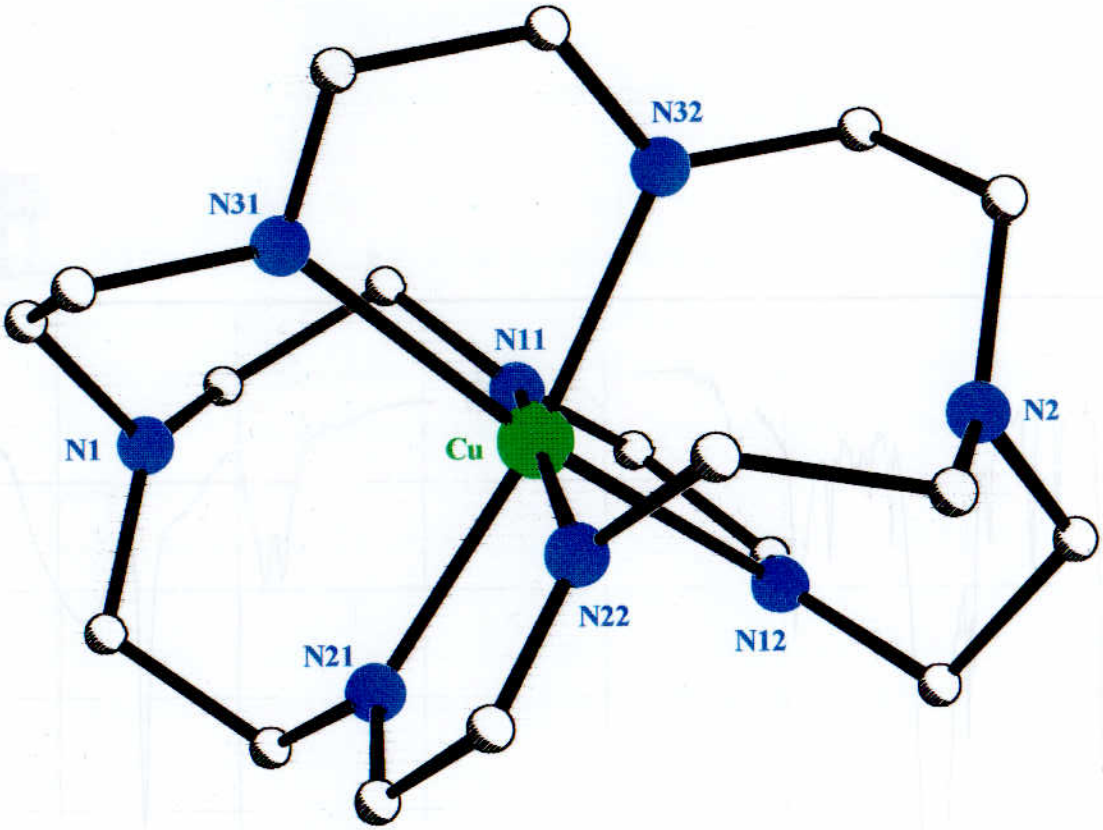

Figure 3A.3 X-ray structure of $[CuGT]^{2+}$ showing geometry around the metal cation

Table 3A.1. Selected bond lengths [Å] and Angles [°] for $[CuGT]^{2+}$.

Cu-N(11)	2.041(5)	Cu-N(22)	2.046(5)
Cu-N(21)	2.096(5)	Cu-N(32)	2.126(6)
Cu-N(12)	2.268(7)	Cu-N(31)	2.294(8)
N(11)-Cu-N(12)	76.0(2)	N(11)-Cu-N(22)	169.6(3)
N(11)-Cu-N(21)	95.9(2)	N(11)-Cu-N(32)	89.7(2)
N(11)-Cu-N(31)	97.3(2)	N(12)-Cu-N(31)	170.8(2)
N(21)-Cu-N(12)	91.5(3)	N(21)-Cu-N(32)	169.8(3)
N(21)-Cu-N(31)	95.4(3)	N(22)-Cu-N(31)	91.9(3)
N(22)-Cu-N(12)	95.3(3)	N(22)-Cu-N(32)	97.3(2)
N(22)-Cu-N(21)	78.4(2)	N(32)-Cu-N(12)	98.1(2)
N(32)-Cu-N(31)	75.4(3)		

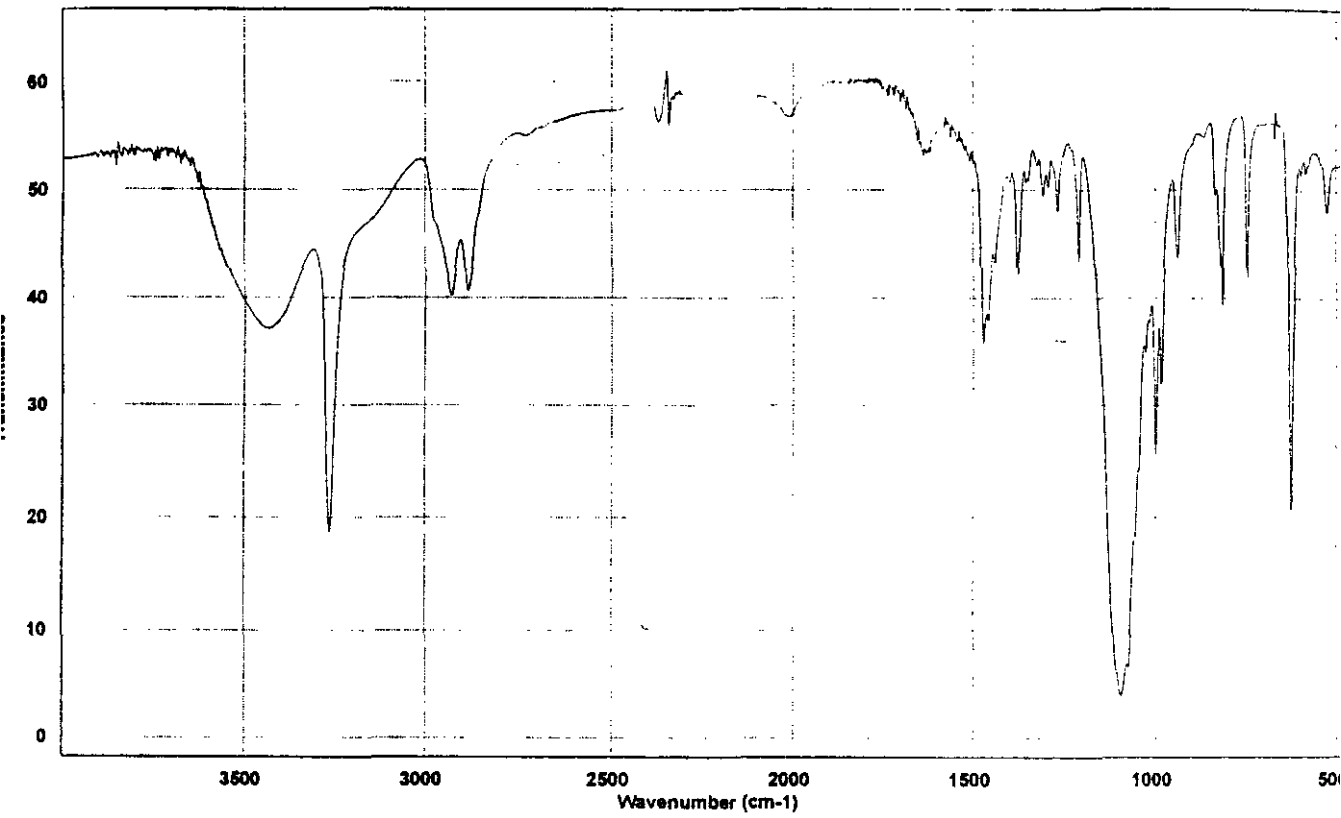

Figure 3A.4 Infrared spectrum of RGT

gave a peak at m/e 370 (15%) which could be assigned to the parent ion although the majority of peaks were due to fragmentation.

The ^{1}H NMR spectrum of RGT in d_4-MeOH is shown in **Figure 3A.5**. On removal of the C=N bond the H_a methylene proton signal moves upfield and is observed as a singlet at δ 2.8 ppm. Signals attributed to H_b and H_c are observed as triplets arising from vicinal coupling, at δ 2.5 and δ 2.7 ppm, respectively. No differentiation of equatorial and axial methylene signals was evident. On lowering the temperature, the signal is observed to broaden until at 253 K three signals are observed which show no fine structure and appears to be close to coalescence. This suggests that the rate of interconversion of axial and equatorial protons is approaching the time-scale of the ^{1}H NMR experiment. Although the NH resonance is typically broad in other ^{1}H NMR spectra of octaamine cryptands of this series, we were unable to locate it even following a D_2O shake carried out on the ^{1}H NMR spectrum of RGT in $CDCl_3$.

3A.6 [Cu(II)RGT][BPh_4]$_2$

Due to the presence of amine donors within this host, clean synthesis of a Cu(I) complex was not anticipated or indeed successful. The mononuclear Cu(II) complex was synthesised so that physical measurements recorded for the average-valence complex could be distinguished as originating from copper-copper bond formation or from metal-to-ligand interactions, as appropriate.

Unlike the copper-GT system, where use of 1:1 stoichiometry under appropriate solvent conditions generates the clean monocopper cryptate, the product of reaction of RGT with $Cu(ClO_4)_2.6H_2O$ in a 1:1 ratio is a mixture, principally containing the well characterised average-valence cryptate, $[Cu_2RGT](ClO_4)_3$, (See **Chapter 3A.11**). This is shown by examination of the ESR spectrum of the solid product from the 1:1 Cu:RGT reaction, where the characteristic seven-line pattern is dominant. Electronic spectral monitoring of the intense far-red absorption confirms that in methanol solution, under pH-neutral conditions, the dinuclear average-valence species dominates at 1:1 (and lower) Cu:RGT stoichiometry. Given the evidence for copper-copper bonding in these average-valence cryptates such predominance of the 2:1 form is unsurprising.

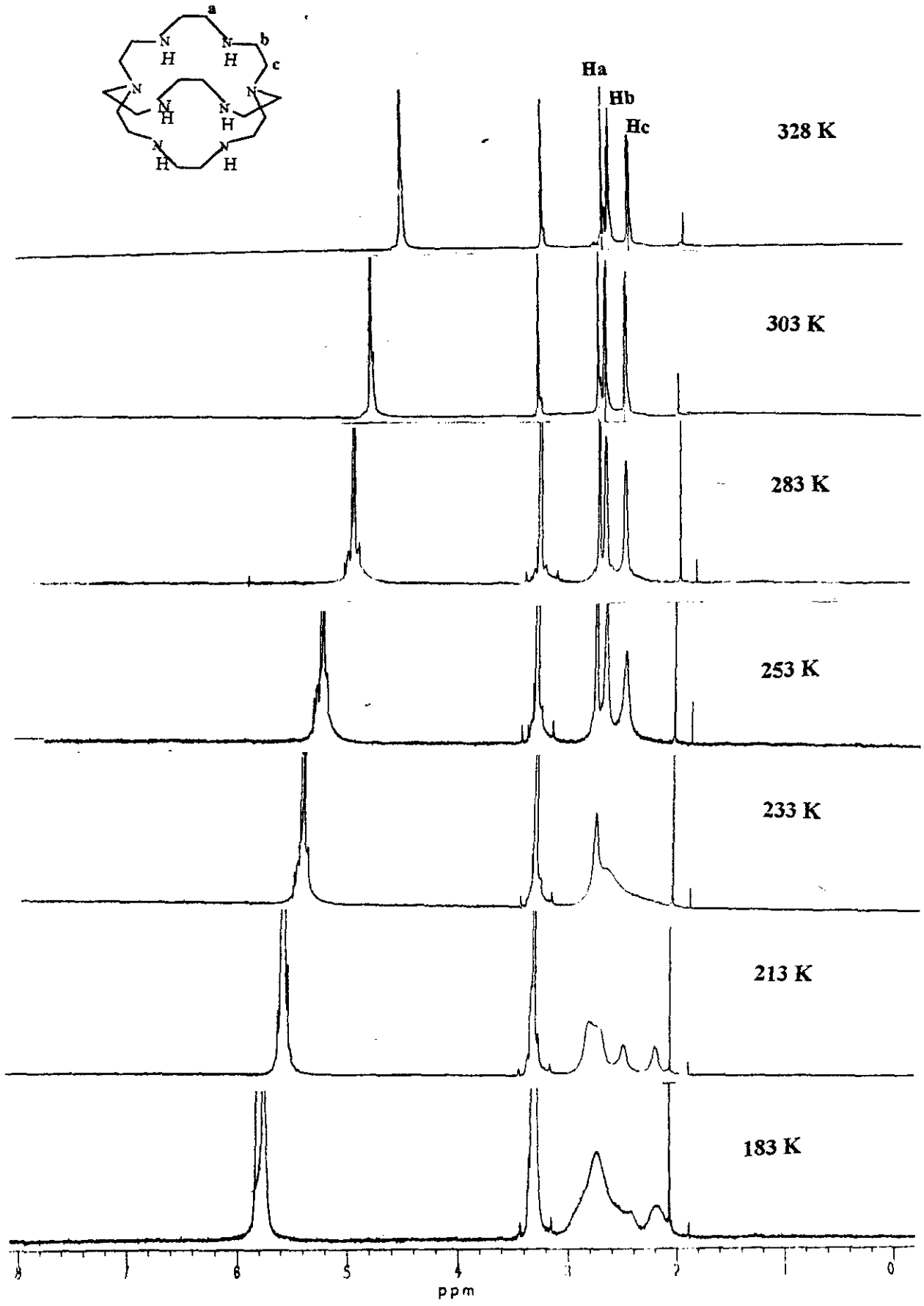

Figure 3A.5 ^{1}H *NMR of RGT in* d_4*-MeOH at 328, 303, 283, 253, 233, 213 and 183 K*

The attempt to isolate the monocopper(II) RGT cryptate succeeded only with BPh_4^- counterion where the insolubility of the product resulted in its' trapping! The infrared spectrum of the complex shows strong absorption bands at 3311 cm^{-1} (NH) and 1578, 1478, 1426, 735 and 708 cm^{-1} (BPh_4). The product was too insoluble for FAB mass spectrum, however, electrospray mass spectroscopy reveals that only one copper has been co-ordinated. There is no evidence of a dinuclear complex. The molecular ion peak is that of the monocopper species with one counterion i.e. $[Cu(II)RGT(BPh_4)]^+$, the usual pattern for these systems. A strong peak at m/e = 433 (60 %), attributed to $[Cu^{II}RGT]^{2+}$, also appears.

The ESR spectrum displays a normal axial-type four line spectrum with $g_{//}$ (2.214) > $g_{\perp}$(2.028) > 2.00 and $A_{//}$ = 170 G (in solid state) typical of a square pyramid Cu(II) geometry. This is also seen from the electronic spectrum - the green solution has a high-energy absorption band at 632 nm (ε cannot be obtained with certainty owing to the impurity of bulk powder) although there is no sign of a low-energy shoulder.[18]

Magnetic susceptibility measurements suggest impurity of the bulk solid. The moment is lower than expected for a monocopper(II) species. At 293 K the moment is 1.25 B.M. falling to 0.95 B.M. at 80 K. The impurities could be either an unidentified Cu(I) complex or perhaps some percentage of free ligand or $NaBPh_4$. Such impurities would also account for the poor elemental analysis.

3A.6.1 X-Ray Crystallographic Structure of $[Cu(II)RGT][BPh_4]_2$

It was of interest to obtain and compare the X-ray structure of $[Cu(II)RGT](BPh_4)_2$ against its $[Cu(II)GT](ClO_4)_2$ analogue. The pale green complex, $[Cu(II)RGT](BPh_4)_2$, was crystallised from acetonitrile resulting in dark green cubes. The crystal structure is shown in **Figure 3A.6**. This is one of the least symmetric cryptate structures solved for the series. For the larger cations a more symmetric central portion is adopted.

The copper is distorted square pyramidal, co-ordinated to five of the eight potential donors from one end of the cavity. **Table 3A.2** shows relevant bond lengths and angles. The poor match of the cation dimension with cavity size in this conformation presumably explains the tendency of cryptates of this, and similar small transition series cations, to adopt an alternative co-ordination mode which leaves some secondary amine donors uncoordinated and available for protonation. The conformational mobility allows a single Cu(II) cation to select

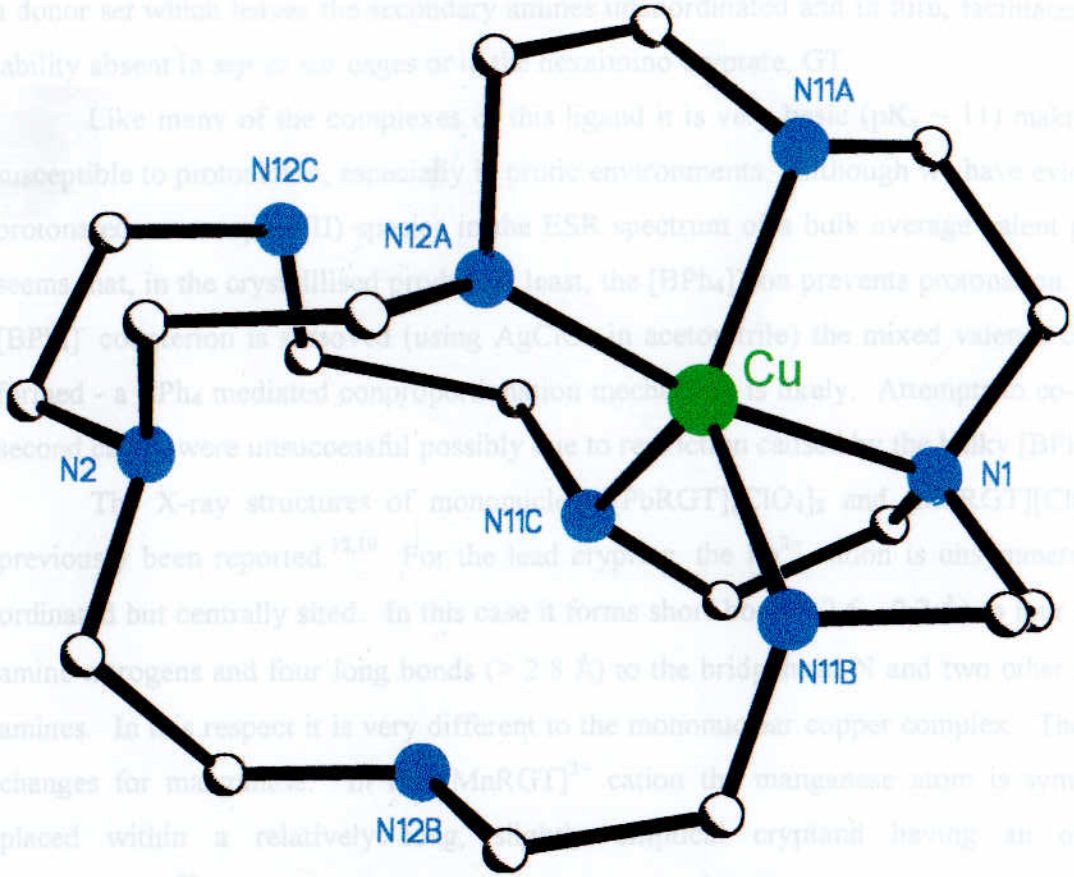

Figure 3A.6 X-Ray Structure of the cation of $[Cu(II)RGT]^{2+}$

Table 3A.2 Selected Bond Lengths [Å] and Angles [°] for $[CuRGT]^{2+}$

Cu(1)-N(1)	2.043(19)	Cu(1)-N(11B)	2.19(3)
Cu(1)-N(12A)	1.90(3)	Cu(1)-N(11C)	2.16(2)
Cu(1)-N(11A)	1.99(2)		
N(1)Cu(1)-N(11C)	84.0(9)	N(12A)-Cu(1)-N(1)	168.4(10)
N(1)-Cu(1)-N(11B)	83.1(9)	N(12A)-Cu(1)-N(11A)	84.0(10)
N(11A)-Cu(1)-N(1)	85.0(8)	N(12A)-Cu(1)-N(11C)	97.9(11)
N(11A)-Cu(1)-N(11C)	118.7(9)	N(12A)-Cu(1)-N(11B)	106.5(11)
N(11A)-Cu(1)-N(11B)	126.0(10)	N(12D)-Cu(2)-N(11F)	98.8(10)
N(11C)-Cu(1)-N(11B)	112.1(10)		

a donor set which leaves the secondary amines uncoordinated and in turn, facilitates a kinetic lability absent in *sep* or *sar* cages or in the hexaimino cryptate, GT.

Like many of the complexes of this ligand it is very basic ($pK_a \sim 11$) making it very susceptible to protonation, especially in protic environments. Although we have evidence of a protonated monocopper(II) species in the ESR spectrum of a bulk average valent powder, it seems that, in the crystalllised product at least, the $[BPh_4]^-$ ion prevents protonation. Once the $[BPh_4]^-$ counterion is removed (using $AgClO_4$ in acetonitrile) the mixed valence complex is formed - a BPh_4 mediated conproportionation mechanism is likely. Attempts to co-ordinate a second cation were unsuccessful possibly due to restriction caused by the bulky $[BPh_4]^-$ ion.

The X-ray structures of mononuclear $[PbRGT][ClO_4]_2$ and $[MnRGT][ClO_4]_2$ have previously been reported.[12,19] For the lead cryptate, the Pb^{2+} cation is unsymmetrically co-ordinated but centrally sited. In this case it forms short bonds (2.6 - 2.7 Å) to four secondary amine nitrogens and four long bonds (> 2.8 Å) to the bridgehead N and two other secondary amines. In this respect it is very different to the mononuclear copper complex. The situation changes for manganese. In the $[MnRGT]^{2+}$ cation the manganese atom is symmetrically placed within a relatively long, slightly elliptical cryptand having an overall *lel* conformation.[20] There is a wide range (2.36 - 2.53 Å) of Mn-N distances probably due to misfit between host and guest preferred dimensions, (**Figure 3A.7**).

3A.7 $[Cu_2NGT][ClO_4]_2$

Due to the versatility and ease of formation of the tren-capped series of cryptands it was hoped that similar dicopper complexes could be formed with the larger trispropylamino-derived cap. This could allow for a small increase in the distance between the coppers and it would be interesting to see the effect of any internuclear distance increase upon oxidation - would copper-copper bond formation occur?

A facile literature preparation of the tripodal amine tris(3-aminopropyl)amine (trpn) existed and the amine was synthesised in good yield according to **Scheme 3A.1**. Attempts to produce free cryptands by Schiff base reactions of dialdehydes shown in Scheme 3.3 with trpn has so far proved unsuccessful. This is not unexpected due to the increased chain length of the amine giving an extra degree of freedom, allowing polymerisation to compete with [2+3] ring closure, resulting in insoluble gelatinous polymeric solids. However, in the presence of a

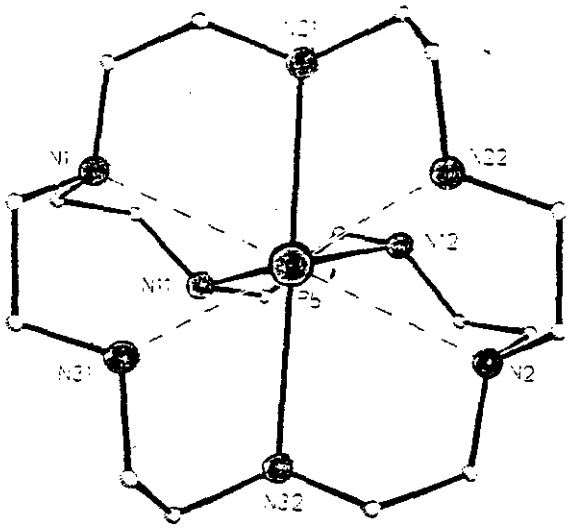

Figure 3A.7a X-ray structure of $[PbRGT]^{2+}$, Selected distances (Å): Pb-N 2.675 (11) - 2.737(13), Pb-N(bridgehead) 2.831 (1)

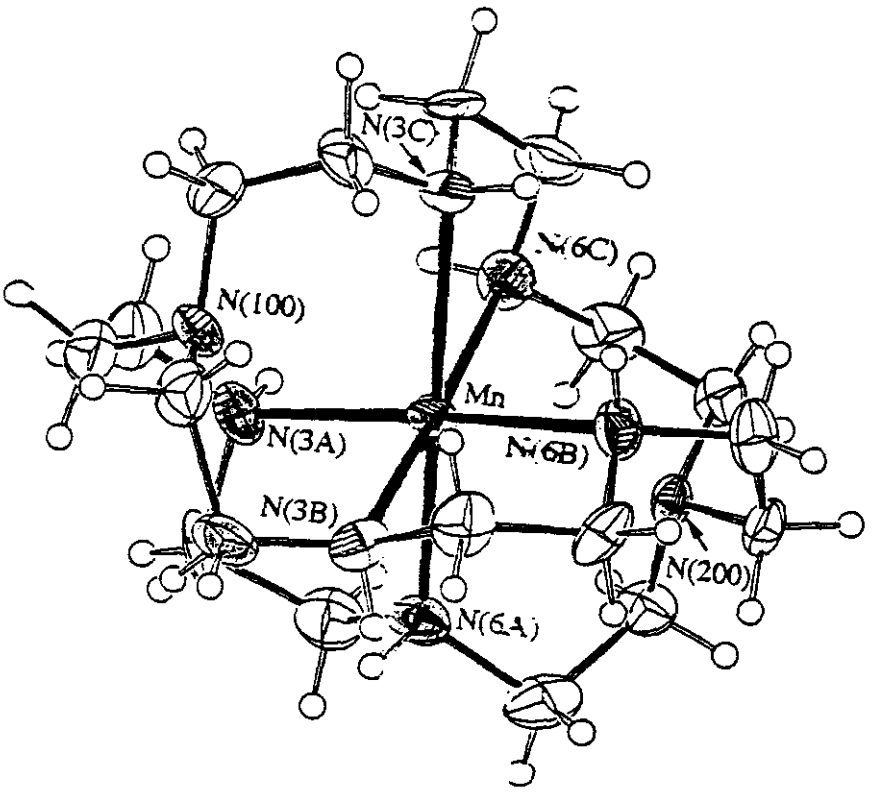

Figure 3A.7B X-ray structure of $[MnRGT]^{2+}$, Selected distances (Å): Mn-N 2.36(2) - 2.53(2), Mn-N(bridgehead) 2.80 (2)

suitable template ion, or pairs of ions, the amine and dialdehyde can be preorganised into conformations suitable for one-step assembly of the cryptand. G.Morgan has successfully synthesised trpn-capped cryptates by templating, using mainly Ag^{+} or occasionally Ba^{2+} or Pb^{2+}.[11] For the extended series shown in **Scheme 3A.2** template synthesis using silver etc. has been successful.

Unsuccessful attempts were again made to synthesise the cryptand NGT, for our purposes, by free ligand synthesis and also by templating on group II and the lanthanide earth metals. It was hoped that the low yield experienced in Cu(I) template synthesis[16] could be enhanced, leading to a better route to the dicopper systems and incidentally a fuller analysis of the co-ordination and geometries possible for this cryptate.

Although the $[Cu_2(I)NGT](ClO_4)_2$ complex could be obtained by a template synthesis, the synthesis was not always reliable and yields were low. We were able, at least partly, to explain this by the isolation of a stable carbinolaime by-product, *q.v.* **Chapter 3A.8**.

The infrared spectrum of the crude product displays strong characteristic absorbances for the perchlorate counterion. The absence of C=O stretches is an indication that ring closure has occurred to generate the macrobicyclic structure. However, intriguing features of the infrared spectrum, are the absorptions in the amine region at 3250 cm^{-1} and peaks at 1597, 1643 and 1664 cm^{-1}. These absorptions make it difficult to identify the characteristic imine absoption seen in the azacryptand series. As discussed earlier these are presumably due to the presence of a carbinolamine product similar to that identified in the reaction mixture or to a polymeric material derived from it (in many crops of the product there was insoluble material).

FAB mass spectrum was the most informative tool prior to X-ray studies in characterising the dicopper(I) complex. There are two dominant peaks: $[Cu_2NGT(ClO_4)\ H_2O]^{+}$ (687, 65%) and $[Cu_2NGT.H_2O]^{2+}$ (586, 50%) with less intense features corresponding to $[Cu_2NGT(ClO_4)]^{+}$ (667, 5%) and $[Cu_2NGT]^{2+}$ (568, 12%). The elemental analysis fits the formulation of $[Cu_2NGT](ClO_4)_2.2H_2O$. There are also peaks at 523 (10 %) and 623 (10 %) corresponding to $[CuNGT.H_2O]^{+}$ and $[CuNGT]ClO_4.H_2O$, respectively. The FAB mass spectrum does not show any peaks at 465 which could be assigned to the crystallised carbinolamine by-product and this may be due to instability in the FAB process. It is however possible that other carbinolamines exist in the bulk product and the peaks at 523 and 623 cm^{-1} are as a result of such complexes.

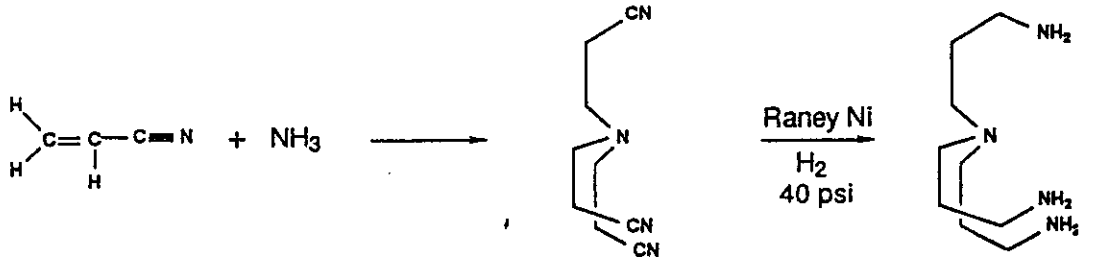

Scheme 3A.1 Synthesis of tris(3-aminopropyl)amine

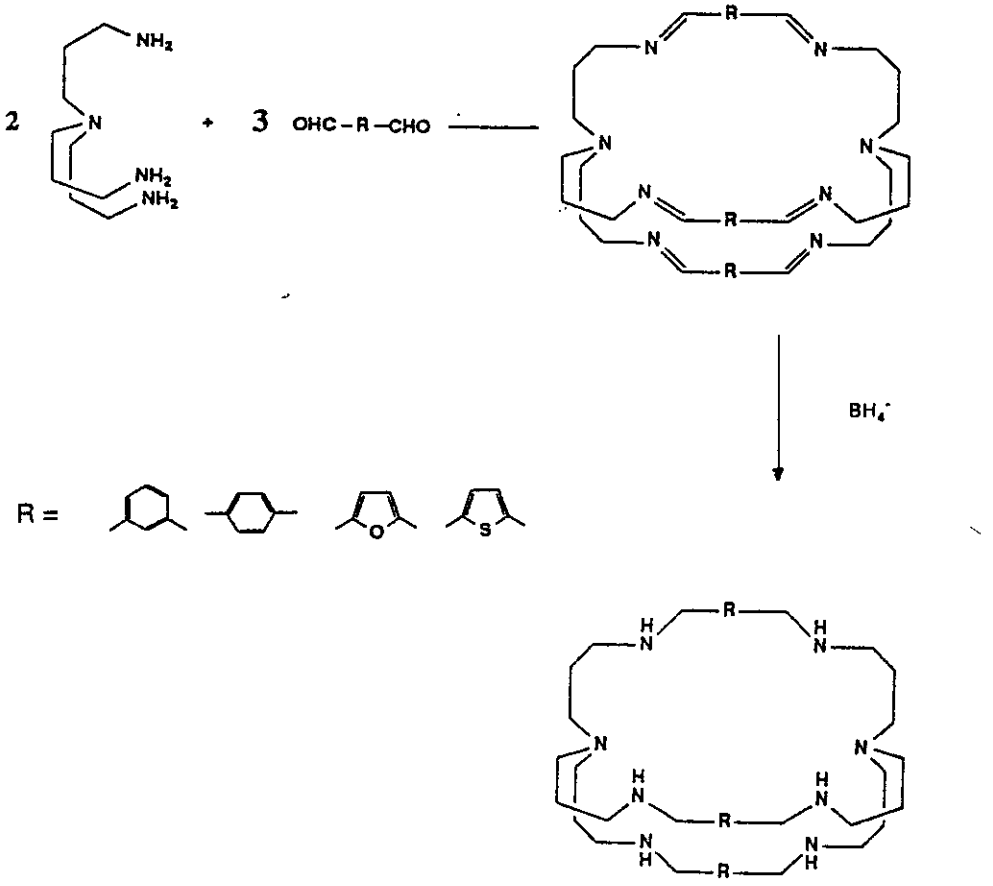

Scheme 3A.2 Schiff base formation of imino cryptands and reduction to octaamino cryptands

3A.7.1 X-Ray Structure of $[Cu_2NGT](ClO_4)_2$

The formula unit consists of discrete $[Cu_2NGT]^{2+}$ cations and two ClO_4^- counterions. A view of the cation is given in **Figure 3A.8** with a list of selected bond lengths and angles in **Table 3A.3** The trigonal pyramidal metal ions form a short bond to the imine nitrogens, Cu-N imine (2.003 Å) and a longer bond to the bridgehead nitrogen, Cu-N bridgehead (2.215 Å). The structure differs from the tren-capped crypts, as we have also observed in the tren and trpn-capped podate series, because the trpn cap gives the Cu(I) room to sit on the bridgehead side of the N3(imine) plane. The propylene strands in each of the capping subunits allow for enlargement of the cavity in comparison to the tren-capped analogue. This explains the copper-copper distance of 2.928 Å, which is significantly longer than that reported for dicopper(I) GT, (2.5 Å).

Previous X-ray structure determination of the mixed-valent $[Cu_2NGT]^{3+}$ ion had shown a Cu-Cu distance of ~ 2.4 Å - a dramatic shortening of internuclear distances has accompanied the oxidation process.[16] This is clear evidence for Cu-Cu bond formation and is discussed in **Chapter 3A.12.1**. We are currently investigating the process involved in the electrochemical oxidation, **Chapter 3D**.

3A.8 [Cu(Carbanolamine)]ClO_4

Carbinolamines have rarely been isolated and are generally regarded as a transient in Schiff base processes.[21] Its persistence in this reaction indicates it is competing successfully with $[Cu_2NGT](ClO_4)_2$ formation and is therefore a significant complex to investigate.

Template formation of the dicopper(I) NGT cryptate was often unsuccessful and yields were low. However, rather than assuming that a hydrolysis reaction has followed cryptate formation, it was often observed that when attempting to synthesise the dicopper (I) cryptate a blue/grey solid was retrieved. It was only when a bright blue crystal (a Cu(II) carbinolamine) crystallised from a solution of the average valence cryptate that we could envisage a reason for the poor yields. The FAB mass spectrum, ESR and magnetic data indicate that this is the powder form of the single blue crystals. The fact that the pure $[Cu_2NGT]^{2+}$ is very stable in aqueous solution, as judged by the long-term stability of it's D_2O ^1H NMR solution, also leads us to believe that a hydrolysis mechanism of the intact cryptate is not occurring and rather a competing template reaction is responsible.

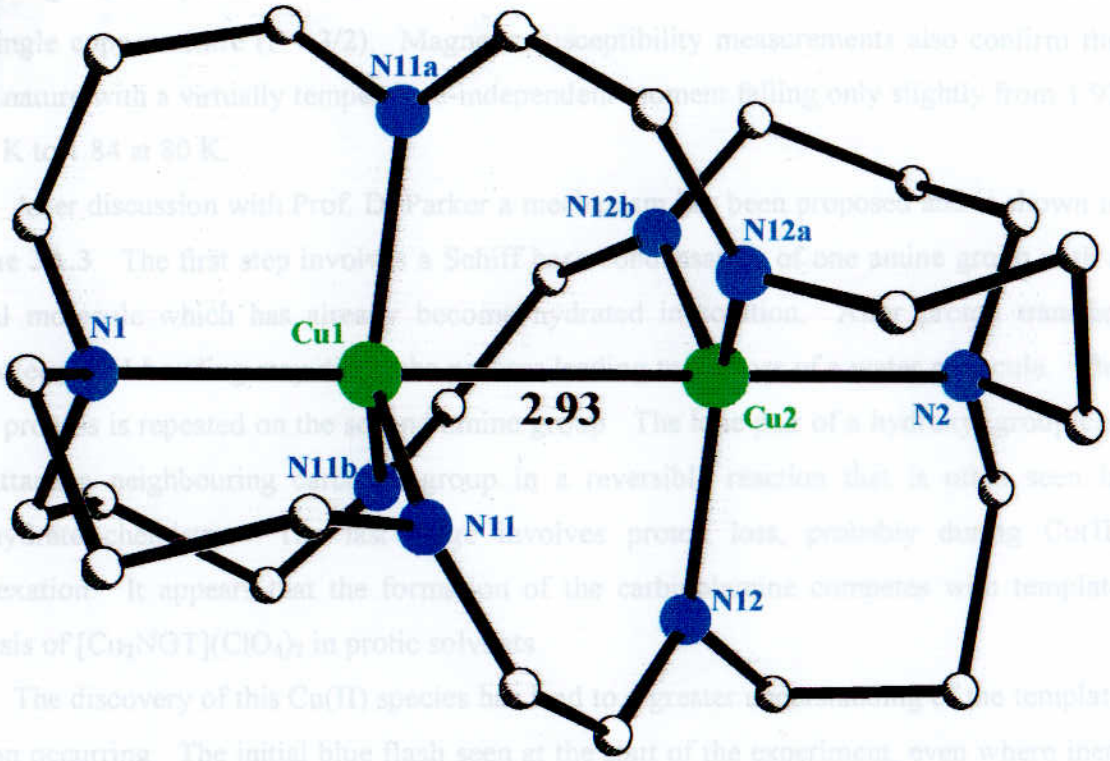

Figure 3A.8 X-ray structure of the cation of $[Cu_2NGT](ClO_4)_2$ showing Cu-Cu distance.

Table 3A.3 Selected bond lengths [Å] and angles [°] for $[Cu_2NGT](ClO_4)_2$.

Cu-Cu	2.928 (4)	Cu-N(3)	2.010(11)
Cu-N(1)	2.217 (15)		
N(3)-Cu-N(3)	119.18 (11)	N(1)-Cu-Cu	180.0 (3)
N(3)-Cu-N(1)	95.20 (4)	N(3)-Cu-Cu	84.80 (4)

The Cu(II) carbinolamine exhibits a normal axial-type four line ESR spectrum with $g_{//}$ (2.219) > g ⊥ (2.043) and $A_{//}$ =170 G which is consistent with interaction of the odd electron on a single copper centre (I = 3/2). Magnetic susceptibility measurements also confirm the Cu(II) nature with a virtually temperature-independent moment falling only slightly from 1.93 at 293 K to 1.84 at 80 K.

After discussion with Prof. D. Parker a mechanism has been proposed and is shown in **Scheme 3A.3**. The first step involves a Schiff base condensation of one amine group with a glyoxal molecule which has already become hydrated in solution. After proton transfer, intramolecular H-bonding may direct the process leading to the loss of a water molecule. The whole process is repeated on the second amine group. The lone pair of a hydroxyl group can then attack a neighbouring carbonyl group in a reversible reaction that is often seen in carbohydrate chemistry. The last stage involves proton loss, probably during Cu(II) complexation. It appears that the formation of the carbinolamine competes with template synthesis of $[Cu_2NGT](ClO_4)_2$ in protic solvents.

The discovery of this Cu(II) species has lead to a greater understanding of the template reaction occurring. The initial blue flash seen at the start of the experiment, even where inert atmospheric protection was used, was cause for concern and many attempts have been made to avoid it. However, it seems that the formation of the carbinolamine is inevitable but the yield can be reduced by altering reaction conditions. A large excess of acetonitrile favours the Cu(I) redox state and the use of argon over nitrogen seems to improve the quality of product. Unfortunately, it appears that the dicopper(I) cryptate and the carbinolamine are not the only products. A polymeric species appears to be the major product, in the form of a dark green insoluble solid. It is difficult to avoid this product even by working at high dilution.

3A.8.1 X-Ray Structure of [Cu(Carbanolamine)]ClO_4

The X-ray structure is interesting and clearly demonstrates a stabilised carbinolamine. The structure reveals that the carbinolamine is in fact deprotonated at O_{23}. There is only one perchlorate molecule in the unit cell. A 2:1 dialdehyde:amine stoichiometry is evident in this complex, although a 3:2 dialdehyde:amine ratio was used. The formulation is $[C_{13}H_{27}N_4O_4Cu][ClO_4]$. This was later confirmed by FAB mass spectrum which showed peaks at 365 (23%) and 465 (30%) attributable to $[Cu(Carbinolamine)]^+$ and $[Cu(Carbinolamine)]ClO_4$, respectively. The cation is shown in **Figure 3A.9**.

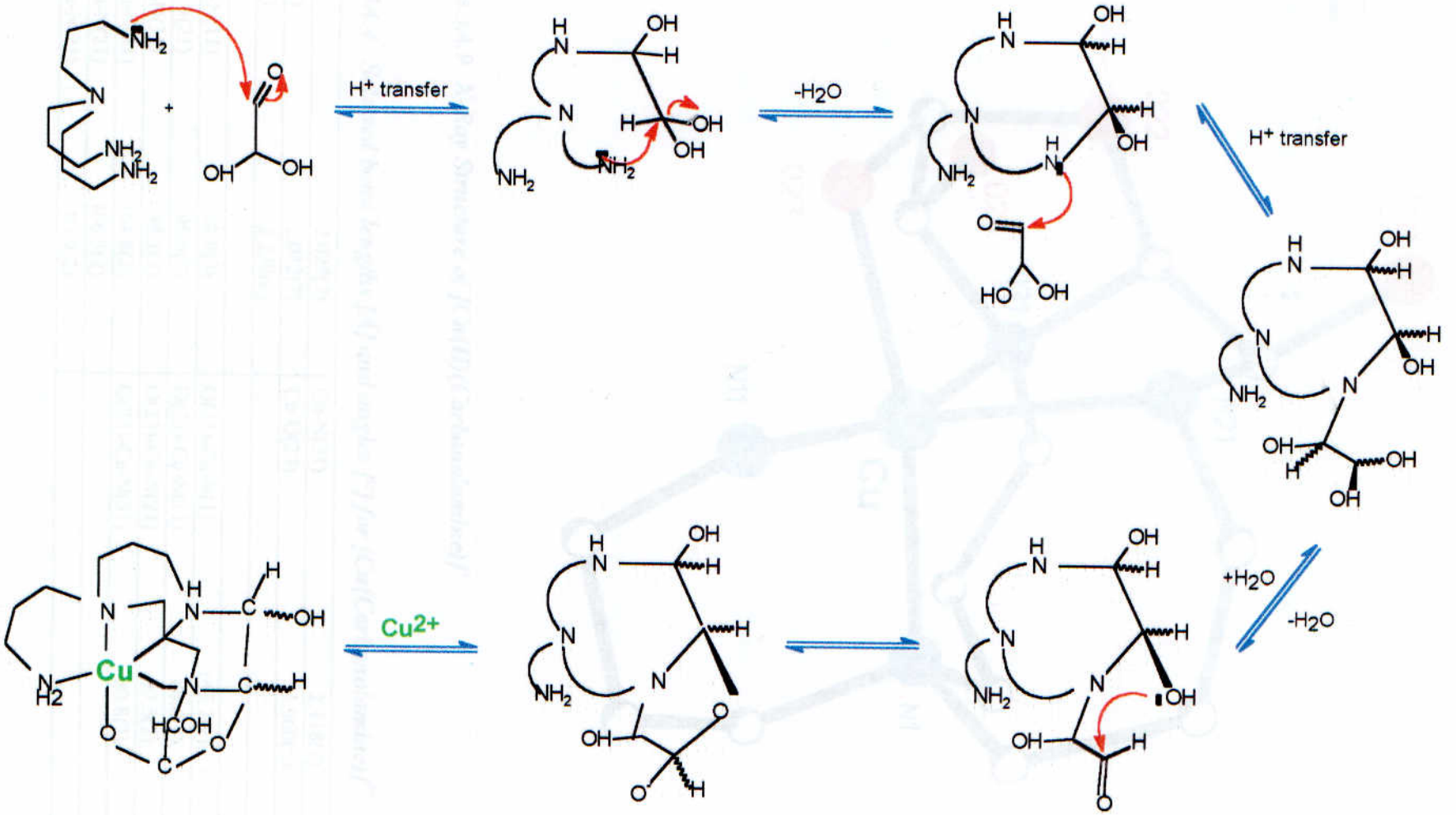

Scheme 3A.3 Proposed mechanism for the formation of [Cu(II)Carbinolamine]$^{+}$

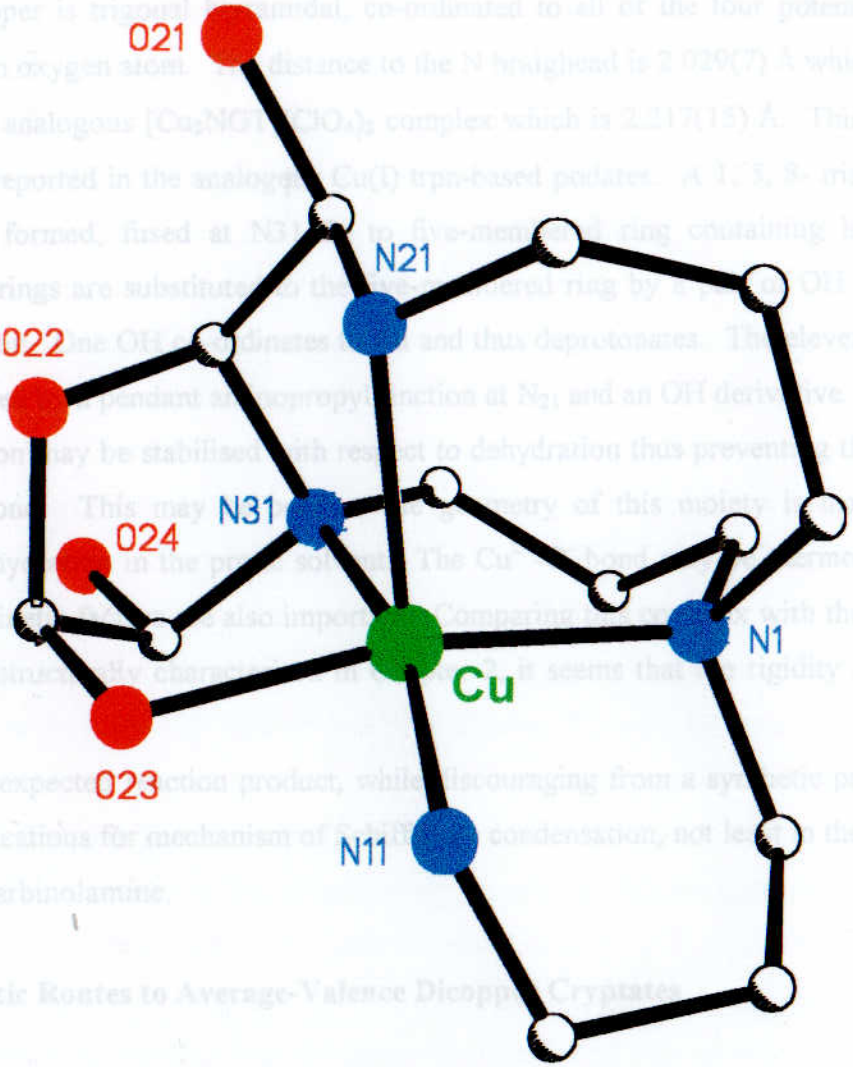

Figures 3A.9 X-Ray Structure of [Cu(II)(Carbanolamine)]$^{+}$

Table 3A.4 Selected bond lengths [Å] and angles [°] for [Cu(Carbanolamine)]$^{2+}$

Cu-N(1)	2.029(7)	Cu-N(31)	2.118(7)
Cu-N(11)	2.032(7)	Cu-O(23)	1.960(5)
Cu-N(21)	2.220(6)		
N(1)-Cu-N(11)	92.0(3)	O(23)-Cu-N(1)	165.7(2)
N(1)-Cu-N(21)	96.6(3)	O(23)-Cu-N(11)	86.6(3)
N(1)-Cu-N(31)	98.1(3)	O(23)-Cu-N(21)	97.5(2)
N(11)-Cu-N(31)	164.8(2)	O(23)-Cu-N(31)	80.8(2)
N(11)-Cu-N(21)	106.3(2)		
N(31)-Cu-N(21)	83.9(2)		

The copper is trigonal biyramidal, co-ordinated to all of the four potential nitrogen donors and to an oxygen atom. The distance to the N bridghead is 2.029(7) Å which is shorter than seen in its analogous $[Cu_2NGT](ClO_4)_2$ complex which is 2.217(15) Å. This distance is similar to that reported in the analogous Cu(I) trpn-based podates. A 1, 5, 8- triazaundecane ring has been formed, fused at N31-Cu to five-membered ring containing heteroacyclic oxygen. Both rings are substituted to the five-membered ring by a pair of OH functions in *trans*-diol fashion. One OH co-ordinates to Cu and thus deprotonates. The eleven-membered ring is substituted by a pendant aminopropylfunction at N_{21} and an OH derivative. The $H\text{-}N_{21}\text{-}C\text{-}O_{21}\text{-}H$ function may be stabilised with respect to dehydration thus preventing the formation of an imine bond. This may be because the geometry of this moiety is inappropriately disposed to dehydration in the protic solvent. The $Cu^{2+}\text{-}O^-$ bond may be thermodynamically stabilised but kinetic factors are also important. Comparing this complex with the Cu(I) trpn-based podates structurally characterised in Chapter 2, it seems that the rigidity may prevent dehydration.

This unexpected reaction product, while discouraging from a synthetic point of view, has many implications for mechanism of Schiff Base condensation, not least in the isolation of the stabilised carbinolamine.

3A.9 Synthetic Routes to Average-Valence Dicopper Cryptates

The $Cu^{1.5}\text{-}Cu^{1.5}$ site is not spontaneously formed without steric enforcement, but is achievable within a host which constrains the copper bonding orbitals to approach bonding distance (~ 2.4 Å) in a symmetric co-ordination environment which is acceptable to both the +1 and +2 oxidation state. The azacryptands discussed are ideal hosts for such purposes.

The octammine host, RGT, acts as a hard base[22] and therefore stabilises the +2 copper redox state producing the most stable and easily synthesised of the three delocalised mixed valence complexes. For this reason other research groups have reported several important aspects of this system with relevance to its use as a Cu_A model.[23]

3A.10 $[Cu_2GT]^{3+}$

Within GT the (+I, +I) state of dicopper is the most stable redox state, but this can readily undergo one-electron oxidation with mild oxidising agents such as Ag(I) and Ce(IV) to

generate $[Cu_2L]^{3+}$ salts. We have also been able to synthesise the average valence complex by addition of a Cu(I) salt to $[Cu(II)GT]^{2+}$. However, the synthesis and characterisation of this average valence dicopper complex has often proved difficult owing to solution instability. Although stable in the solid state, the product may be contaminated with the oxidant and attempts at recrystallisation often prove futile. The average-valence GT complex also rapidly decomposes in organic solvents.

The average-valence complex was characterised by satisfactory elemental analysis and the FAB mass spectrum could be assigned to $[Cu_2GT(ClO_4)]^+$ (684, 10%), $[Cu_2GT(ClO_4)]^{2+}$ (585, 100%) and $[Cu_2GT]^{3+}$ (484, 80%).

While carrying out spectroscopic experiments it became apparent that the average-valent form of this cryptate could be stabilised by using an excess of silver ion in aqueous solution. This procedure led to the isolation of small X-ray-quality crystals. The X-ray structure has recently been solved by V. McKee and is shown in **Figure 3A.10.** Previous structural data on the $[Cu_2GT]^{3+}$ system was only inferred, from the fact that the mixed-valent form could be successfully doped into dicopper(I) crystals in 30% proportion, proving isomorphism of dicopper(I) and dicopper(1.5) cryptates.

Figure 3A.10 confirms the isomorphism, as well as allowing determination of the bond lengths with greater accuracy. As steric constraint in this rigid small imine host does not allow much opportunity for alteration of the copper-copper internuclear distance in the non-bonded dicopper(I) and average valence forms, there is limited opportunity to reflect copper-copper bond formation through alteration of internuclear distances. However, a small but significant shortening from 2.488 (1) to 2.380 (5) Å is discernible which supports the idea of bond formation in the average-valent form.

3A.11 $[Cu^{1.5}RGT](ClO_4)_3$

The combination of the longer methylene chain and nitrogen bridgehead in the RGT cryptand is responsible for the existence of dicopper complexes, which are not conformationally possible within the tighter *sep* or *sar* cages.

The mixed valence copper complexes of RGT were found to be the most air stable of the three complexes. The complex can be formed from the reaction of a Cu(II) salt with the reduced ligand in methanol. Cu(II) acetate was the salt most often used because its' basicity

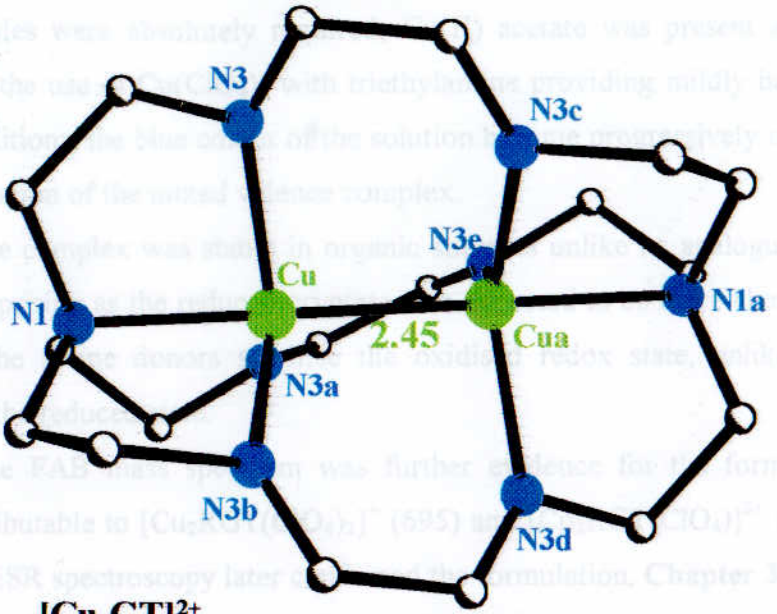

$[Cu_2GT]^{2+}$

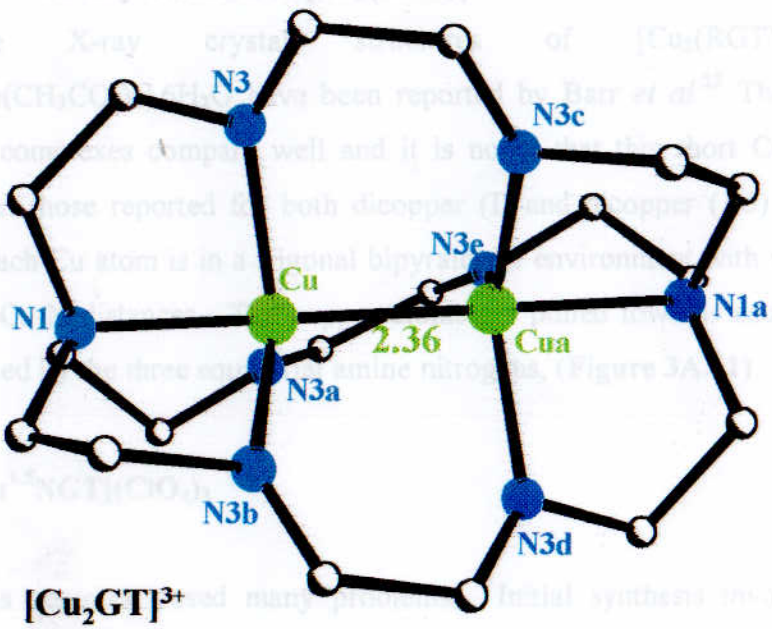

$[Cu_2GT]^{3+}$

Figure 3A.10. X-ray cation structures of $[Cu_2GT]^{2+}$ versus $[Cu_2GT]^{3+}$

minimised any possible chance of protonation. However, it soon became obvious that when pure samples were absolutely required, Cu(II) acetate was present as a contaminant. This prompted the use of $Cu(ClO_4)_2$ with triethylamine providing mildly basic conditions. Under these conditions, the blue colour of the solution became progressively more intense, indicating slow formation of the mixed valence complex.

The complex was stable in organic solvents unlike its analogue $[Cu(1.5)GT]^{3+}$. This was unsurprising as the reduced cryptates are expected to be more chemically robust and also because the amine donors stabilise the oxidised redox state, unlike imine donors which stabilises the reduced state.

The FAB mass spectrum was further evidence for the formulation $[Cu_2(RGT)]^{3+}$- peaks attributable to $[Cu_2RGT(ClO_4)_2]^+$ (695) and $[Cu_2RGT(ClO_4)]^{2+}$ (596) respectively were present. ESR spectroscopy later confirmed the formulation, **Chapter 3C**.

3A.11.1 X-Ray Struture of $[Cu_2(RGT)]^{3+}$

The X-ray crystal structures of $[Cu_2(RGT)(NO_3)_3].2H_2O$ and $[Cu_2(RGT)(CH_3CO_2)_3].6H_2O$ have been reported by Barr *et al.*[23] The Cu-Cu distances for these two complexes compare well and it is noted that this short Cu-Cu bond distance is shorter than those reported for both dicopper (I) and dicopper (1.5) complexes of the GT system. Each Cu atom is in a trigonal bipyramidal environment with very similar apical and equatorial Cu-N distances. The copper atoms are pulled towards each other and out of the plane defined by the three equatorial amine nitrogens, (**Figure 3A.11**).

3A.12 $[Cu^{1.5}NGT](ClO_4)_3$

This complex posed many problems! Initial synthesis involved oxidation of the dicopper(I) cryptate with Ag^+ in acetonitrile. Although acetonitrile favours the Cu(I) state it appeared to be the only solvent that was suitable to dissolve the dicopper(I) cryptate. In fact X-ray quality crystals were obtained albeit in very low yield.

It was anticipated that using water as a solvent would cause disproportionation of the $[Cu_2(I)NGT](ClO_4)_2$. However, the product was found to be moderately water soluble producing a clean solution, as judged by ^1H NMR. Upon Ag(I) oxidation a blue solution was formed and this was found (UV/Vis and ESR[24]) to be the average valence complex. After

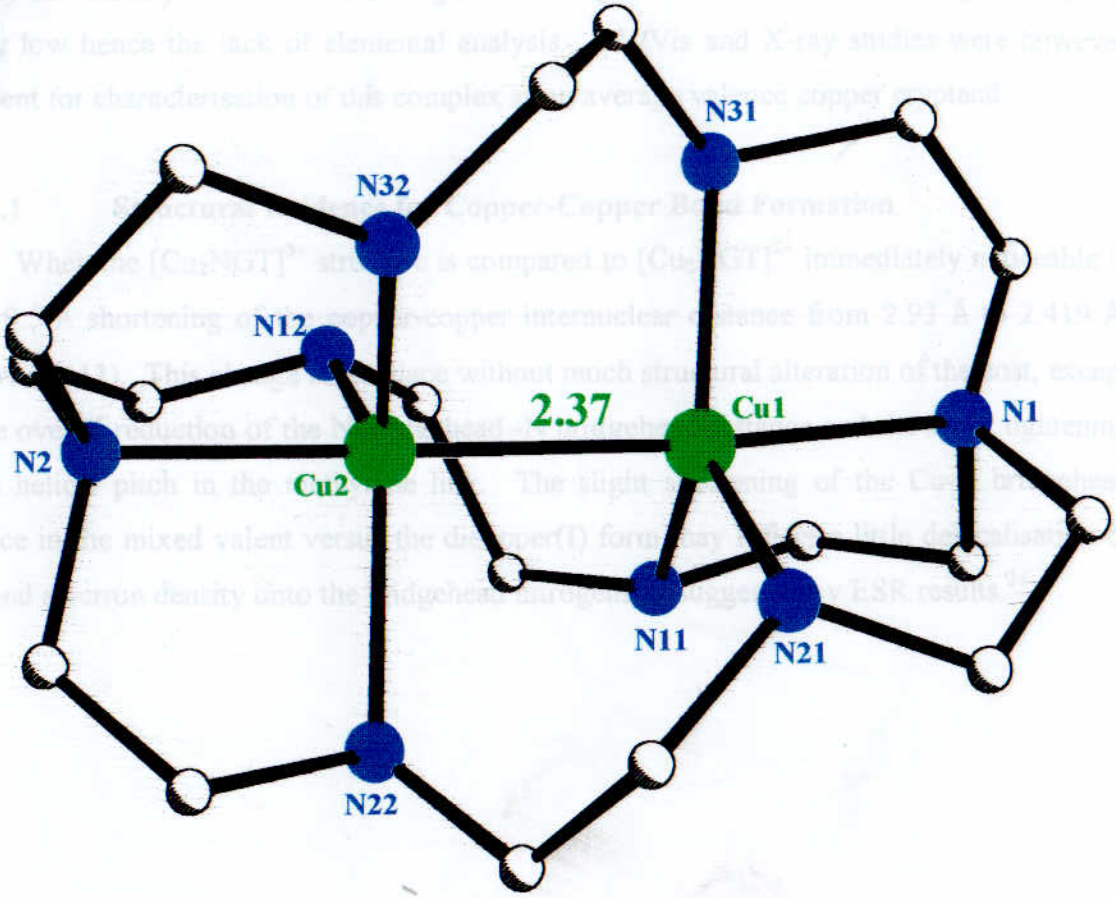

Figure 3A.11 X-Ray structure of $[Cu_2RGT]^{3+}$: Selected distances (Å) Cu-N 2.06, Cu- N_3 plane 0.12, Cu-N_{br} 2.05

slow evaporation of the aqueous solvent, dark green cubic crystals were produced and this was the only satisfactory method of achieving solid average valence NGT. The solid product yield is very low hence the lack of elemental analysis. UV/Vis and X-ray studies were however sufficient for characterisation of this complex as an average valence copper cryptand.

3A.12.1 Structural Evidence for Copper-Copper Bond Formation

When the $[Cu_2NGT]^{3+}$ structure is compared to $[Cu_2NGT]^{2+}$ immediately noticeable is the > 0.5 Å shortening of the copper-copper internuclear distance from 2.93 Å to 2.419 Å, (**Figure 3A.12**). This change takes place without much structural alteration of the host, except for the overall reduction of the N-bridgehead -N bridgehead distance and the slight tightening of the helical pitch in the methylene link. The slight shortening of the Cu-N bridgehead distance in the mixed valent versus the dicopper(I) form may reflect a little delocalisation of the bond electron density onto the bridgehead nitrogens as suggested by ESR results.[24]

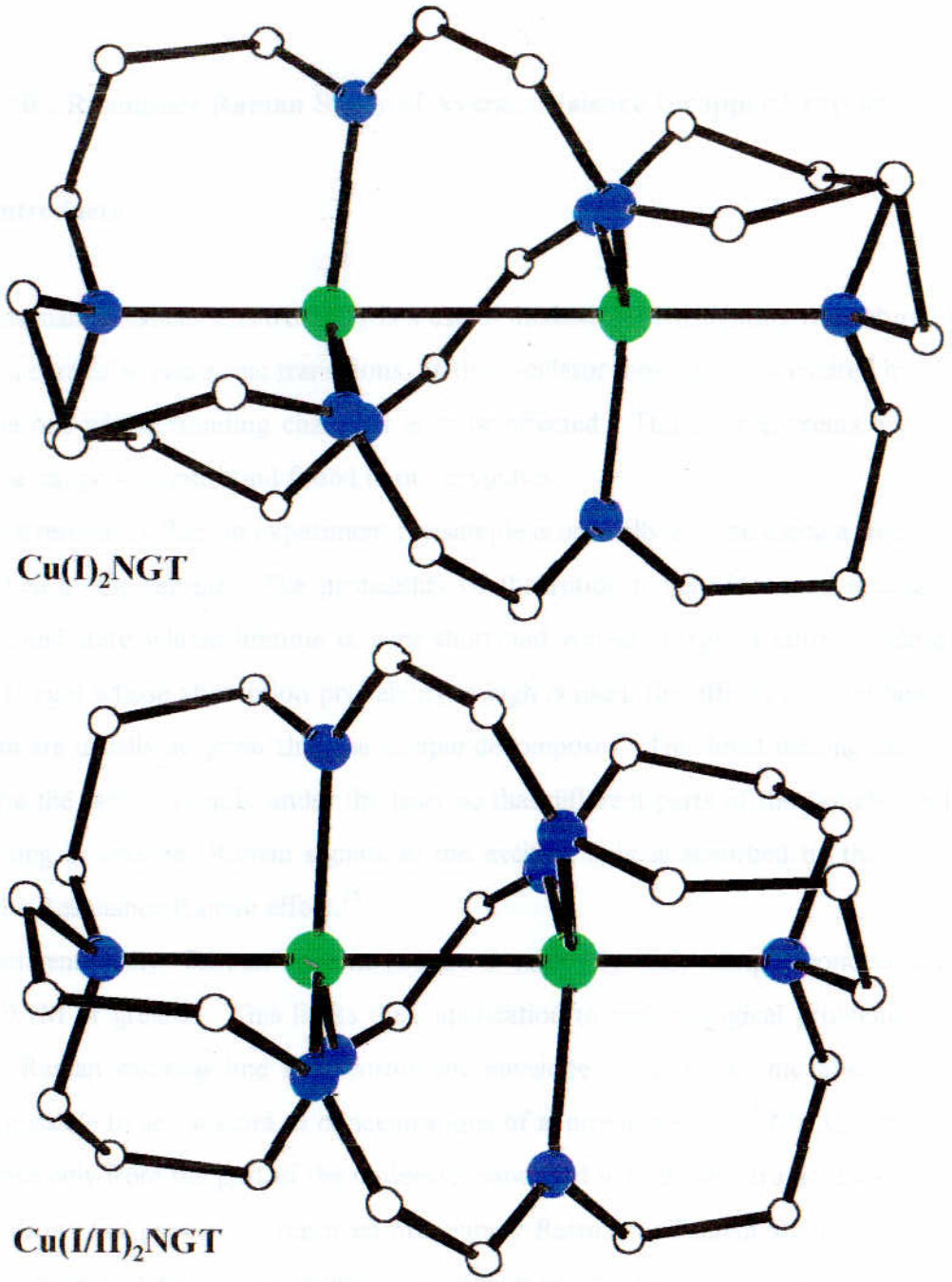

Figure 3A.12. X-ray cation structures of $[Cu_2NGT]^{2+}$ versus $[Cu_2NGT]^{3+}$

Table 3A.5. Comparison of $[Cu_2NGT]^{2+}$ versus $[Cu_2NGT]^{3+}$ dimensions

	$[Cu_2NGT]^{2+}$	$[Cu_2NGT]^{3+}$
Cu-Cu	2.93	2.42
N_{br}-N_{br}	7.32	6.53
Cu-N(im)	2.04	2.02
Cu-N_3 plane	0.24	0.13
'en' torsion	28.1	32.5
twist	65.6	56.2

Chapter 3B : Resonance Raman Study of Average Valence Dicopper Cryptates

3B. 1 Introduction

Resonance Raman spectroscopy is a useful method of investigating the nature of orbitals involved in particular electronic transitions, as the oscillator most strongly excited by a transition will be the one whose bonding character is most affected. Thus, it represents a good way of probing the copper-copper bond found in our cryptates.

In a resonance Raman experiment the sample is normally excited using a frequency that is not absorbed by the sample. The probability of absorption is very low, and excitation is to a virtual excited state whose lifetime is very short and whose energy is correspondingly poorly defined. If light whose absorption probability is high is used, the effects of local heating by the laser beam are usually so great that the sample decomposes. This local heating can be avoided by spinning the sample rapidly under the laser so that different parts of the sample are heated in turn resulting in stronger Raman signals as the exciting light is absorbed by the sample. This effect is the Resonance Raman effect.[25]

Conventionally, Raman spectra require a relatively high sample concentration in the order of 0.1M or greater. This limits their application to real biological problems. However, when the Raman exciting line falls within the envelope of an electronic absorption band, it becomes possible to see spectra at concentrations of approximately 10^{-5} M. Qualitatively, these spectra arise only from the part of the molecule associated with the electronic transition.[25]

Nelson *et al* previously reported preliminary Resonance Raman studies on the average-valence dicopper systems concentrating on excitation into far-red absorptions.[26] They found that enhancement of a pair of modes below 300 cm^{-1} depended markedly on the exciting wavelength. This account extends the wavelength range of the study and describes the results of ^{65}Cu isotopic substitution experiments. In addition, results from a normal co-ordinate analysis are discussed which elucidate the nature of the low frequency modes.

3B.2 Experimental

Resonance Raman spectra were recorded in the UV region at 363.8 nm where possible and over a range of wavelengths spanning the visible-NIR absorption for all three complexes. Experiments were carried out by Drs C. Coates and Ala Al-Obaidi at The Queen's University of Belfast in collaboration with Professor J.J. Mc Garvey. The synthesis of the isotopically labelled complexes is reported in **Chapter 3G**.

Resonance Raman were recorded over the range 700-950 nm using a Ti-sapphire laser (Spectral Physics Model 3900) pumped by an Ar^+ laser (Spectral Physics Model 2025). Spectra were recorded in a back-scattering geometry on a cooled CCD detector (Princeton Instruments model LN/UV 1152) coupled to a single spectrograph (Jobin-Yvon HR640), with a 300 grooves/mm grating for the near-ir studies or a 1200 grooves/mm element for the UV region. Notch or super-notch holographic filters were used to attenuate laser (Rayleigh) scattering. To enhance detector sensitivity in the red, the CCD was operated at a temperature of -80 °C instead of the usual -120 °C for the UV-visible region. Saturated aqueous (~10 mM) solutions of the complexes were used with $NaNO_3$ as internal standard for the construction of excitation profiles.

3B.3 Results

The resonance Raman (RR) spectrum was recorded at an excitation wavelength of 363.8 nm for $[Cu_2RGT]^{3+}$ in aqueous solution. The principle features appear at frequencies > 300 cm^{-1} with no visible bands occurring at lower frequencies. RR spectra at this excitation wavelength for $[Cu_2GT]^{3+}$ and $[Cu_2NGT]^{3+}$ were too weak to use. It is proposed that this low intensity is partly due to the poor match of the exciting frequency with significant absorption in the hexaimine cryptates, but may also derive from the differences in the nature of transition excited at this wavelength in the octaamine versus hexaimine systems.

RR spectra over a range of excitation wavelengths (700-910 nm) enabled a more detailed study of the vibrational mode patterns as a function of excitation wavelength (λ_{exc}). Representative spectra for all three average-valence complexes are shown in **Figure 3B.1**

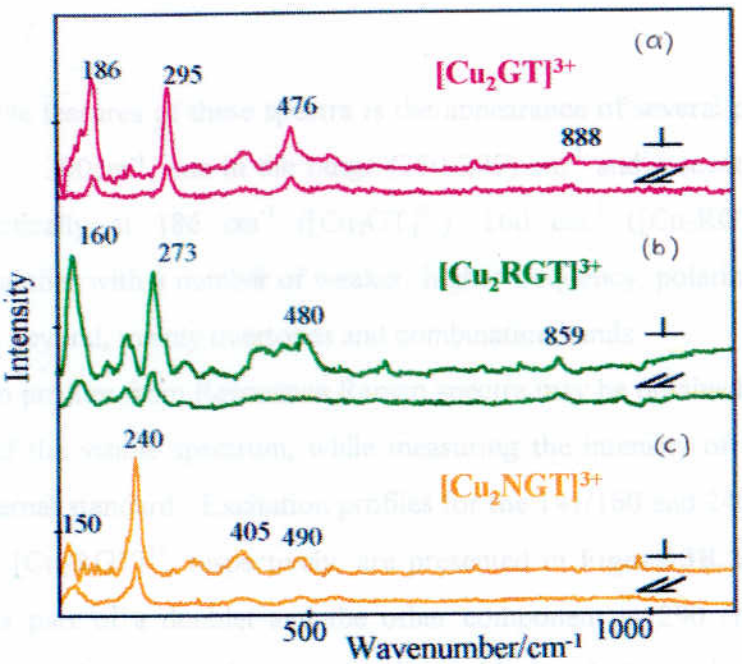

Figure 3B.1 Resonance Raman for 3 average valence complexes at; (a) 840 nm and (b, c) 810 nm

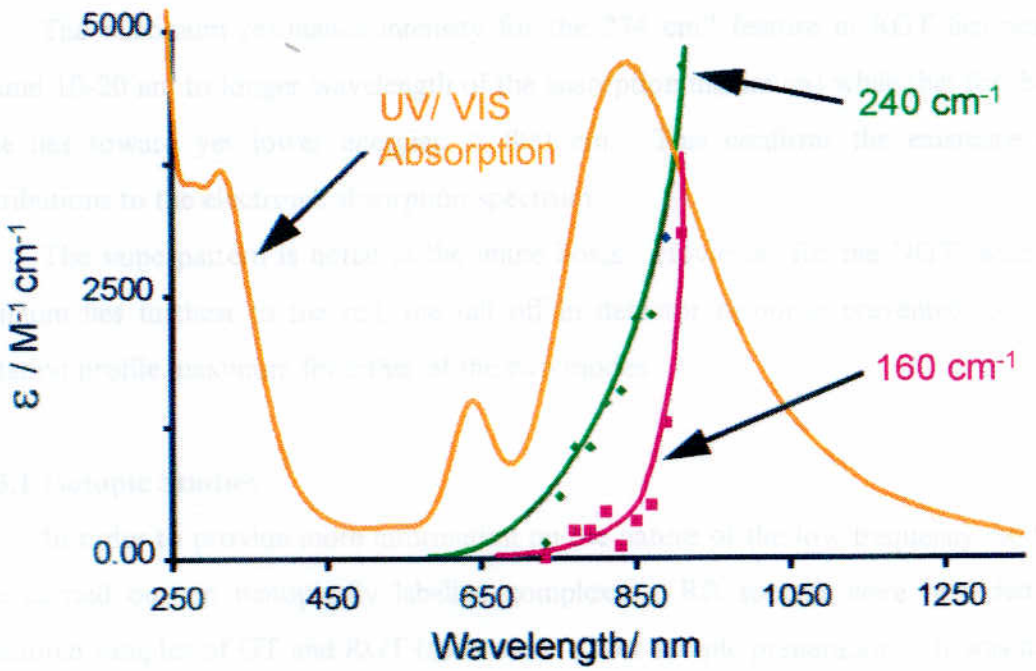

Figure 3B.2 Resonance Raman excitation profile for the 160- and 240- cm^{-1} bands of NGT

The notable features of these spectra is the appearance of several polarized bands in the frequency range < 300cm^{-1}, one in the range (250-295) cm^{-1} and a second in the range (140-185) cm^{-1}, specifically at 186 cm^{-1} ($[Cu_2GT]^{3+}$), 160 cm^{-1} ($[Cu_2RGT]^{3+}$) and 150 cm^{-1} ($[Cu_2NGT]^{3+}$) together with a number of weaker, higher frequency, polarized features extending to 1000 cm^{-1} and beyond, mainly overtones and combination bands.

Excitation profiles from Resonance Raman spectra may be obtained by tuning a dye laser over the range of the visible spectrum, while measuring the intensity of several Raman bands relative to an internal standard. Excitation profiles for the 141/160 and 240/274 cm^{-1} features of $[Cu_2NGT]^{3+}$ and $[Cu_2RGT]^{3+}$, respectively, are presented in **Figure 3B.2.** In $[Cu_2RGT]^{3+}$ the 274 cm^{-1} band is part of a doublet and the other component at 290 cm^{-1} shows a different excitation profile which is more closely coincident with the electronic band maximum, **Figure 3B.2c.** The short term stability of GT in aqueous solution increased the difficulty of constructing an extensive excitation profile. In all of these cases both modes are enhanced through excitation within the near-IR absorption envelope although the maximum enhancement of the intensity does not exactly coincide with the NIR absorption maximum for either mode.

The maximum resonance intensity for the 274 cm^{-1} feature in RGT lies near 770 nm (around 10-20 nm to longer wavelength of the absorption maximum) while that for the 160 cm^{-1} mode lies toward yet lower energies, > 800 nm. This confirms the existence of several contributions to the electronic absorption spectrum.

The same pattern is noted in the imine hosts. However, for the NGT, where the NIR maximum lies furthest to the red, the fall off in detector response prevented location of the excitation profile maximum for either of the two modes.

3B.3.1 Isotopic Studies

In order to provide more information on the nature of the low frequency modes, studies were carried out on isotopically labelled complexes. RR spectra were recorded for ^{65}Cu-substituted samples of GT and RGT (see section G for sample preparation). It was not possible to generate a ^{65}Cu substituted sample of NGT due to synthetic restrictions imposed by the necessary template synthesis on Cu(I). The results at λ_{exc} = 810 nm are shown in **Figure 3B.3**.

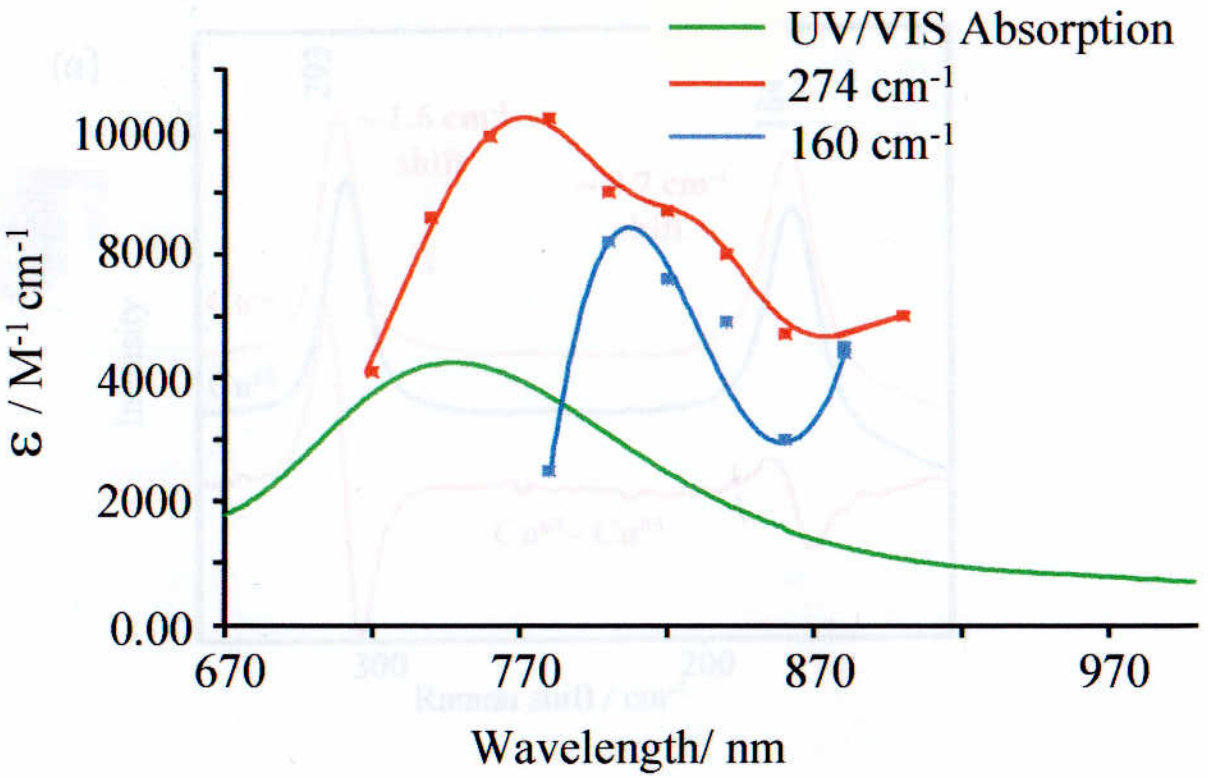

Figure 3B.2b R.R. excitation profile for the 160 and 274 cm^{-1} features of $[Cu_2RGT]^{3+}$.

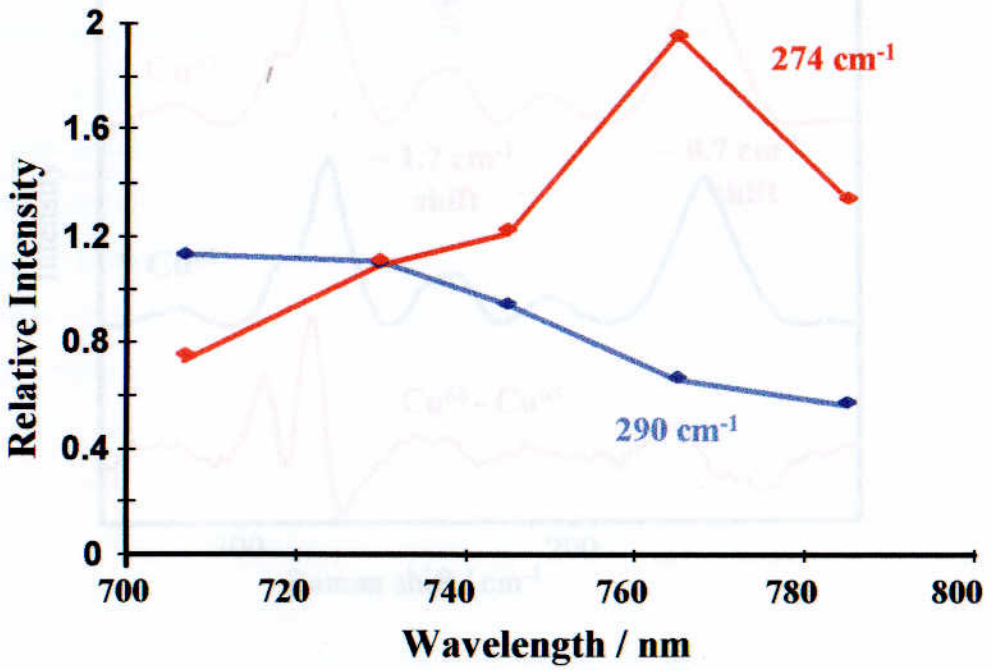

Figure 3B.2c Comparison of the R.R. excitation profile of the 274 cm^{-1} feature with that of the 290 cm^{-1} component for $[Cu_2RGT]^{3+}$.

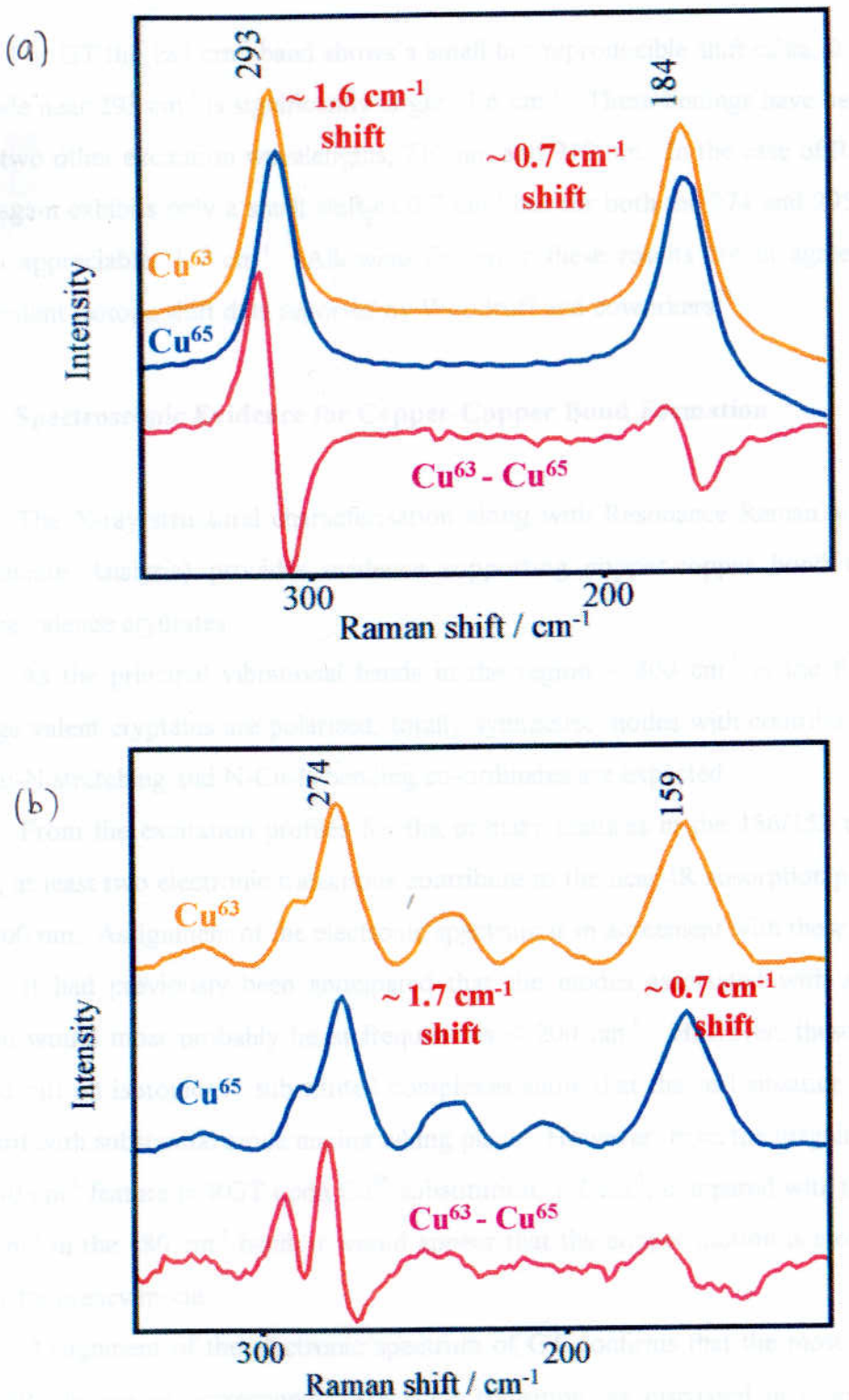

Figure 3B.3 *Influence of isotopic substitution ($^{63}Cu \rightarrow {}^{65}Cu$) on the low frequency region of the Resonance Raman spectra of; (a) $[Cu_2GT]^{3+}$ and (b) $[Cu_2RGT]^{3+}$. Spectra were recorded at 810 nm excitation in saturated aqueous solution*

For GT the 184 cm^{-1} band shows a small but reproducible shift of ca. 0.7 cm^{-1}. That for the mode near 293 cm^{-1} is significantly larger, 1.6 cm^{-1}. These findings have been confirmed for GT at two other excitation wavelengths, 710 nm and 910 nm. In the case of RGT the 159 cm^{-1} mode again exhibits only a small shift of 0.7 cm^{-1} but for both the 274 and 295 cm^{-1} modes the shift is appreciable, 1.7 cm^{-1}. Allowing for error these results are in agreement with other independent isotope shift data reported by Woodruff and coworkers[27].

3B.4 Spectroscopic Evidence for Copper-Copper Bond Formation

The X-ray structural characterisation along with Resonance Raman and NCA (Normal Co-ordinate Analysis) provides evidence supporting copper-copper bond formation in the average valence cryptates.

As the principal vibrational bands in the region < 800 cm^{-1} in the RR spectra of the average valent cryptates are polarised, totally symmetric modes with contributions from Cu-Cu and Cu-N stretching and N-Cu-N bending co-ordinates are expected.

From the excitation profiles for the primary features in the 186/150 and 240/295 cm^{-1} range, at least two electronic transitions contribute to the near-IR absorption profile in the range 700-900 nm. Assignment of the electronic spectrum is in agreement with these findings.

It had previously been anticipated that the modes associated with substantial Cu-Cu motion would most probably lie at frequencies < 200 cm^{-1}. However, these RR experiments carried out on isotopically substituted complexes show that the real situation is not so straight forward with substantial mode mixing taking place. However, from the magnitude of the shift in the 290 cm^{-1} feature in RGT upon Cu^{65} substitution, 1.7 cm^{-1}, compared with the smaller shift of -0.7 cm^{-1} in the 180 cm^{-1} band, it would appear that the copper motion is more involved in the higher frequency mode.

Assignment of the electronic spectrum of GT confirms that the most intense feature of the NIR absorption corresponds to a σ-σ^* transition, as discussed in Chapter 1. Thus, its excitation is expected to give rise to enhancement of the Cu-Cu stretching mode in the RR spectrum. The isotope data show that the largest contribution from a Cu-Cu stretch is to the 250/290 cm^{-1} feature and this is in line with the excitation profile. An approximate Normal Co-

ordinate Analysis (NCA) (carried out by G Baranovich at the Institut R Boskovic, Croatia) does not however indicate the existence of a pure Cu-Cu stretching mode, although the 240/295 cm^{-1} mode shows a greater contribution from a Cu-Cu stretching co-ordinate than does any other.

Both RR and MCD data indicate a second component in the electronic spectra and this excites a second, lower frequency, mode which the isotope shifts suggest, has a smaller contribution from Cu-Cu motion. The assignment of the electronic spectrum suggests that this component is being enhanced upon excitation of a δ - σ^* transition, which may be expected to affect Cu-N_e as well as Cu-Cu orbital overlap. The NCA suggests substantial contribution in this case from the N_e-Cu-N_a bending motion. It is interesting in this connection to note that IR-active modes at around 180-190 cm^{-1} are seen in both mono-Cu(II) and di-Cu(I) as well as in the average valence cryptates. There may be bending modes with similar frequency but different symmetry.

Although interaction of Cu-Cu and Cu-N vibrational modes with cryptand skeletal modes is not included in the NCA, it is to be expected that such an interaction would influence the observed frequencies to some extent. The trends in the low frequency modes e.g.: 186 (GT), 160 (RGT), 150 (NGT), are qualitatively in accord with expectation in this respect. Interaction with skeletal modes of the cryptand will be most marked in the tightest and most rigid cryptand (GT) and least marked in the most flexible (NGT).

3B.5 Summary of Normal Co-ordinate Analysis

In view of the large number of vibrational degrees of freedom for the three complexes, coupled with a lack of sufficiently comprehensive vibrational data, an approximate normal co-ordinate analysis (NCA) only has been attempted. This was performed on the 10-atom skeletal structure, N-CuN_3-CuN_3-N (common to all three cryptates and hereafter referred to as CuN), taken to belong to the point group D_3, inferred from X-ray structures. It is assumed that D_3 symmetry applies in solution, even though lower symmetry may exist in the solid state or other matrixes.

The relevant structural parameters for CuN are given in **Table 3B.1.** The reducible representation for the 10-atom system in the assumed D_3 point group is composed of the

vibrational modes, $5A_1 + 3A_2 + 8E$. For convenience, the internal co-ordinates used in this work are labelled and described in **Table 3B.2**. Since the charge distributions along the principal C_3 axis are expected to differ substantially from those orthogonal to this axis, distinct force constants are defined to describe the Cu-axial-N and Cu-equatorial-N stretching co-ordinates.

The following approach was adopted: taking m_N as 14.0067, isotope data for $[^{63}Cu_2RGT]^{3+}$ and $[^{65}Cu_2RGT]^{3+}$, from resonance Raman spectra reported by Woodruff *et al.*, were used to generate an initial force field for this system. Six of the force constants in **Table 3B.2** were adjusted to fit eight frequencies, the remainder being assigned "reasonable" values on the grounds that they exert no influence on the A_1 modes. The force constants that emerge from the initial input data for the $[^{63}Cu_2RGT]^{3+}$ and $[^{65}Cu_2RGT]^{3+}$ are shown in **Table 3B.2**. In view of the highly approximate nature of the NCA used, detailed comment on the magnitudes of the force constants is largely unwarranted. While the magnitudes are smaller than might be expected, we have no baseline values with which to make comparison in the present instance.

Table 3B.1 Structural Parameters (Bonds, Å and Angles, deg) for Dicopper(I) and Dicopper (1.5) Complexes

Parameter	$Cu_2GT(ClO_4)_2$	$Cu_2GT(ClO_4)_3$	$Cu_2NGT(ClO_4)_2$	$Cu_2NGT(ClO_4)_3$	$Cu_2RGT(NO_3)_3$[c]
Cu-Cu	2.448 (1)	2.380 (5)	2.928 (4)	2.419 (1)	2.364 (1)
Cu-N_{ax}	2.218 (3)	2.040 (2)	2.220 (2)	2.055 (1)[a]	2.066 (5)[a]
Cu-N_{eq}	1.999 (3)	1.960 (2)	2.010 (1)	2.022 (4)[a]	2.067 (3)[a]
N_{ax}-Cu-N_{eq}	84.9 (1)	85.5 (4)	95.2 (4)	93.7 (1)[a]	86.1 (1)[a]
Cu distance from equatorial plane[b]	0.18	0.15	-0.18	-0.13	0.13a

[a] Mean of independent values. [b] Positive values describe displacement of the copper ion toward the centre of the cage. [c] Data for the nitrate salt rather than the perchlorate

We were unable to chose optimum masses for the N atoms in the ligands. The relative magnitudes of the force constants in **Table 3B.2** for the Cu-N_{ax} and Cu-N_{eq} bonds are

qualitatively in line with the crystallographic data in **Table 3B.1**. However, this should only be regarded as coincidental since the NCA is based on RGT, for which the Cu-N_{ax} and Cu-N_{eq} distances differ by only 0.01 Å. The force field derived from RGT was then used to calculate vibrational frequencies for GT and NGT, with m_N = 14.0067 and m_{Cu} = 63.546. The results for the lowest frequency modes, < 300 cm^{-1}, together with the potential energy distributions (PEDs), are not much different from those for RGT, shown in **Table 3B.3**, because the geometry differences between the CuN models are not large enough. Although the spectral region up to *ca.*1100 cm^{-1} has been probed, we concentrate on the region < 400 cm^{-1} for the purposes of comparison with the results of the NC analysis.

Table 3B.2 Force Constants for CuN obtained from Isotopic Frequency Shifts[28] for $[^{63}Cu_2RGT]^{3+}$ and $[^{65}Cu_2RGT]^{3+}$

Internal co-ordinate description	Co-ordinate label	Force constant[c]	Error[d]
Cu-N_{ax} stretch	R	0.628	0.023
Cu-Cu stretch	Q	1.558	0.337
Cu-N_{eq} stretch	S	0.873	0.001
Symmetry-adapted combination of N_{ax}-CuP-N_{eq} bends	A	1.134	0.098
Symmetry-adapted combination of N_{eq}-Cu-N_{eq} bends	B	2.700	0.0
Symmetry-adapted combination of N_{ax}-Cu-Cu linear bends	A	0.110	0.0
Torsional mode	T	2.900	0.0
(Cu-N_{ax} stretch)(Cu-Cu stretch) interaction	RQ	0.178	0.045
(Cu-N_{ax} stretch)(Nax-Cu-Neq bend) interaction	RA = -QA	-.184	0.109

[c] Force constants in mdyn/Å (stretch), [d] Zero error means that the corresponding force constant was kept fixed.

Using the spectroscopic data for GT for which isotopic shifts have been measured for two features (**Figure 3B.3**), a different force field was obtained which may arise largely from the simplistic assumption that effective nitrogen masses are 14.0067 in all cases. Despite the approximate nature of the NCA, a number of interesting conclusions emerge. Most strikingly, the PEDs show that the Cu-Cu stretching vibration is strongly coupled not only to Cu-N_{axial} stretching motion but also to N_{ax}-Cu-N_{eq} bending co-ordinates.

Table 3B.3 Observed and Calculated Isotopic Frequency Shifts (cm^{-1}) and Potential Energy Distributions[a] (PED)

	$[^{63}Cu_2RGT]^{3+}$			$[^{65}Cu_2RGT]^{3+}$		
ν_i[b]	obsd	calcd	PED	obsd	calcd	PED
$1(A_1)$	327.0[c]	327.2	96S	327		97S
$2(A_1)$	289.0[d]	289.0	90R 55Q 15A	286.6[d]	286.8	101R 41Q 10A
$3(A_1)$	275.0[d]	275.0	39Q 28A 20R	273.0[d]	273.2	52Q 34A
$4(A_1)$	164.0[d]	163.8	68A 17Q	163.3[d]	163.6	67A 17Q

[a] See Table 3B.2, [b] Symmetry species in D_3, [c] See figure 3B.1, [d] Reference 27

3B.6 Conclusions

Despite the unavoidable mixing of modes in these strongly coupled oscillators which prevents the observation of a pure Cu-Cu stretching motion, we can conclude that the mode with the greatest share of this motion is a relatively high frequency one aroun 270-290 cm^{-1} in all three cases. The force constant emerging from the NCA is unexpectedly high for a one-electron bond, almost double that attributed to Cu-Cu stretching in Cu_A site of CCO and indeed compares favourably to that of Cu_2 which involves a two-electron bond. To some extent, this must be reflect the neglected coupling of Cu-Cu and Cu-N modes with skeletal modes of the cryptand, but it also emphasises the efficiency of interaction between appropriately disposed orbitals in mixed valence dicopper systems. The striking reduction in Cu-Cu distance in NGT upon one-electron oxidation from the dicopper(I) state likewise illustrates the facility with which the one-electron bond may be formed.

Although comparison of the X-ray structures of two pairs of dicopper(I) and dicopper (1.5) complexes provided valuable evidence for copper-copper bond formation, Resonance Raman spectroscopy fails to identify a clean copper-copper stretching mode. This is due to extensive mixing of several stretching and bending modes. However, isotopic substitution experiments indicate significant Cu-Cu character in the ~250 cm^{-1} mode.

3C.1.1 Introduction to ENDOR

ENDOR (*e*lectron ***n***uclear ***do***uble ***r***esonance) was introduced in 1956 by George Feher in order to resolve hyperfine and nuclear quadrupole couplings which are not accessible in the EPR spectra. In this technique the spin system is simultaneously irradiated by a microwave and a radio frequency field.[28,29]

The development of ENDOR has resulted in an enhanced understanding of the metal co-ordination environment in metalloproteins and has frequently clarified unambiguously the nature of ligands which have remained obscure in EPR i.e. it gives enhanced spectral resolution of ENDOR in comparison to EPR. It is particularly useful in biology because only the ligands adjacent to the paramagnetic site are observable, thus, in favourable cases, enabling identification of co-ordinated amino acids.

3C.1.2 EPR versus ENDOR

Metalloproteins are usually studied as solids (frozen aqueous solutions, glasses, single crystals) at low temperature. However, for an EPR experiment, these conditions yield inhomogenously broadened lines due to unresolved hyperfine interaction and orientation distribution of paramagnetic centres.

For complicated spin systems, the number of EPR lines become much greater than the number of ENDOR lines. This is due to the different selection rules for EPR and ENDOR transitions. In an EPR spectrum ($\Delta ms = \pm 1$, $\Delta mI = 0$) the number of lines increases multiplicatively with the number of non-equivalent nuclei whereas in ENDOR ($\Delta ms = 0$, $\Delta mI = \pm 1$) the corresponding increase is only additive. As the total spectral widths in EPR and ENDOR are of the same order of magnitude, the average spectral density is much smaller in the ENDOR than in the EPR display, i.e. if there are n equivalent nuclei there will be $2nI + 1$ lines in ESR but only 2 lines in the corresponding ENDOR spectrum. Thus, hyperfine couplings which cannot be observed in a single crystal EPR spectrum because of inhomogeneous line broadening, may frequently be resolved with ENDOR.

For compounds containing nuclei with $I \geq 1$, the ENDOR spectrum is characterised by first order splittings due to nuclear quadrupole interactions. In EPR this coupling gives rise to small and usually non-detectable second order shifts. ENDOR therefore represents a very

sensitive method to study quadrupole couplings of ligands and central ions in paramagnetic transition metal complexes.

ENDOR has a greater superiority compared to EPR in providing detailed information about the distribution of spin densities (via measurement of hyperfine couplings) and about local charge densities (quadrupole couplings) in extended ligand systems. Moreover, ENDOR yields additional information, such as identification of nuclei (from the nuclear Zeeman frequency) and evaluation of relative signs of hyperfine and quadrupole splittings.

3C.1.3 Basic Principles

ENDOR uses high-power microwave radiation to saturate the electron resonance transition under investigation.[30] The applied magnetic field and the microwave frequency are held constant throughout the experiment, at the resonance condition, but at the same time a nuclear resonance frequency is now applied. The actual frequency of the additional radiation is continuously varied, and the effect that it has on the saturated electron resonance line is observed. The principle of the method can be illustrated by the example in **Figure 3C.1**.

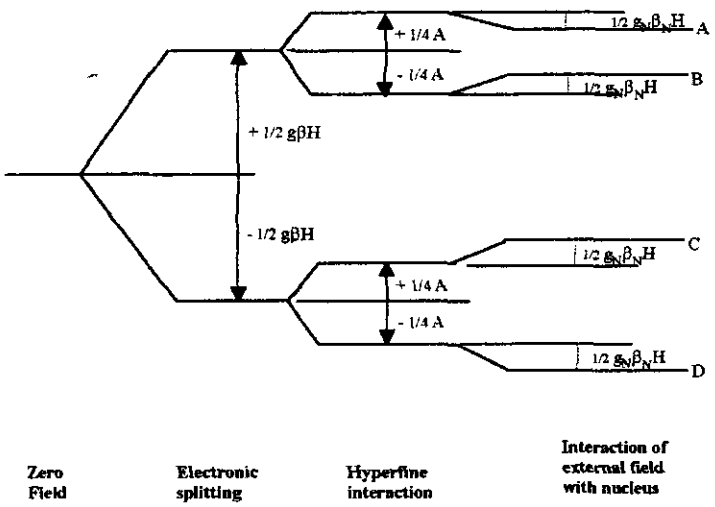

Figure 3C.1 Detailed energy-level splitting associated with proton interaction

Thus, each of the original single electron resonance levels are split into two by the interaction with the nuclear spin of the proton, as shown in **Figure 3C.1**, and this energy of hyperfine interaction can be denoted by ¼ A. As well as this normal hyperfine interaction

between the magnetic moments of the unpaired electron and the protons, there is a direct effect of the externally applied magnetic field, H, on the nuclear magnetic moment itself. This is usually much smaller than the hyperfine interaction in normal electron resonance spectra, but it will produce a small shift in the four component levels as indicated in **Figure 3C.1**. The actual energy of these four levels is shown below:

Level	**Energy**
A	$\frac{1}{2}$ gBH + $\frac{1}{4}$ A - $\frac{1}{2}$ $g_N B_N H$
B	$\frac{1}{2}$ gBH - $\frac{1}{4}$ A + $\frac{1}{2}$ $g_N B_N H$
C	-$\frac{1}{2}$ gBH + $\frac{1}{4}$ A + $\frac{1}{2}$ $g_N B_N H$
D	-$\frac{1}{2}$ gBH - $\frac{1}{4}$ A - $\frac{1}{2}$ $g_N B_N H$

Thus, it can be seen from these detailed expressions, and also from the final energy spacing in **Figure 3C.1**, that the energy difference between levels A and B is not quite the same as that between C and D.

In the ENDOR technique, the high power electron resonance frequency is applied to saturate one of the electron resonance transition, such as that between A and D in **Figure 3C.2a**. The result of this saturation will be to increase the population of the energy level A, and hence to give level A a higher population than level B. Whilst this saturation is taking place, a radio frequency is also applied to the sample with a frequency such that $h\nu_{r.f}$ is equal to the splitting between A and B. This then stimulates transitions from A to B and the populations of the two levels will return to the normal equilibrium values. As a result, the saturation of the electron transition will be removed and a strong electron resonance line will then be obtained in place of the weakened saturation condition. The net result is that, if the detecting system is kept set on the electron resonance signal, a sudden increase in intensity will be obtained when the nuclear resonance signal sweeps through the condition:

$$\mathbf{h\nu_{r.f} = \frac{1}{2} A - g_N B_N H}$$

A similar situation arises when the radio frequency sweeps through the resonance value corresponding to the nuclear transition between levels C and D. The saturation of the electron

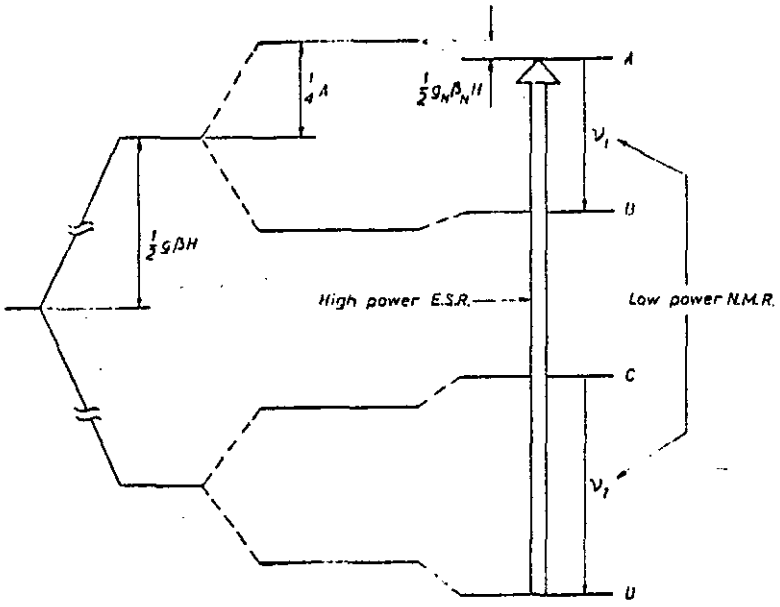

(a)

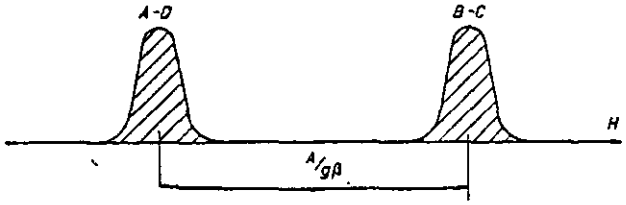

ESR with constant microwave frequency

(b)

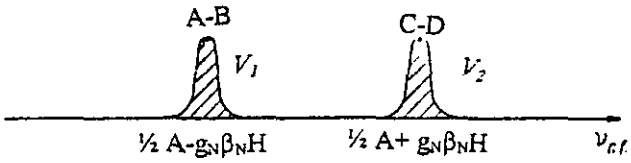

ENDOR with constant microwave frequency and magnetic field

(c)

Figure 3C.2 ENDOR for single proton interaction, (a) Saturation of E.S.R. absorption and desaturation by radio-frequency resonance, (b)E.S.R. spectrum that is expected. (c) ENDOR spectrum that will be observed.

resonance will have reduced the number of atoms in the level D, but when the nuclear resonance transition is induced by the radio-frequency field the populations of levels C and D will be more or less equalised, and as a result the electron resonance signal being observed will suddenly become desaturated resulting in a large signal. It follows from this that, if the radiofrequency signal is swept slowly through a range of values centred on $\nu = A/2h$, a large increase in the electron resonance signal will be obtained when the frequency satisfies either the conditions given by:

$$h\nu_{r.f} = \tfrac{1}{2} A \pm g_N B_N H$$

From these two values of the radio-frequency resonance signal the values of both A and g_N can be deduced very accurately.

The normal electron resonance signal that would be expected from such a system is shown in **Figure 3C.2b** and compared with the ENDOR spectrum that would be obtained as shown in **Figure 3C.2c**.

The vertical axis represents actual absorption produced by the electron resonance transition; the horizontal axis corresponds to the changing frequency of the applied radio-frequency field. Absorption lines will therefore be obtained whenever this frequency corresponds to an actual hyperfine splitting present in the overall energy level pattern. Thus, the positions of the lines corresponds to splittings and not to different nuclear orientations.

In fact if exactly the same analysis had been applied to a system containing four equally coupled protons instead of one, only two ENDOR resonance lines would have been obtained, whereas five separate electron resonance lines are to be expected. In order to explain this, the two sets of five equally spaced component levels, which were predicted for the four interacting protons, are shown with the additional effect of the external field on the nucleus added. It is evident that although there are still five electron resonance lines, at different frequencies, between these two sets of levels, there are only two ENDOR transitions of different frequency i.e. at the frequency corresponding to the energy gap between components of the top set and at the different frequency corresponding to the different gap between the components of the bottom set. The resultant ESR and ENDOR spectra are shown in **Figure 3C.3**.

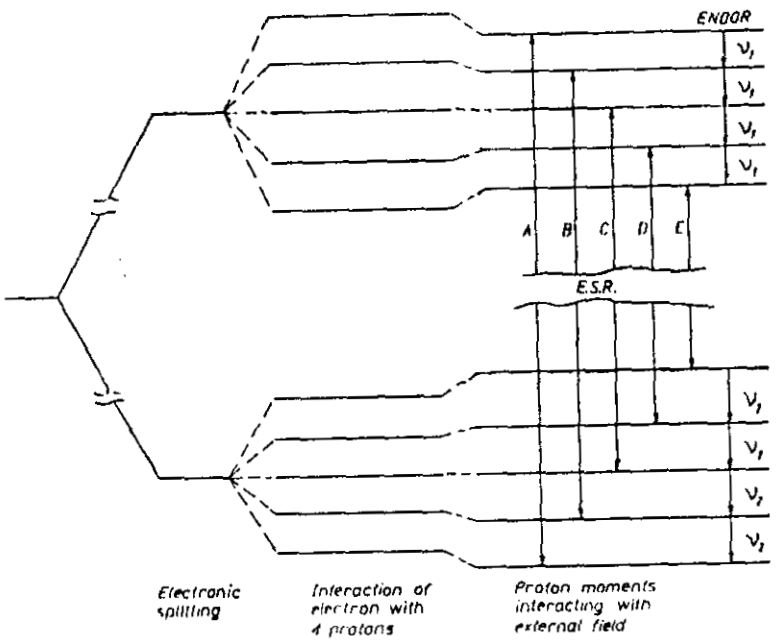

(a)

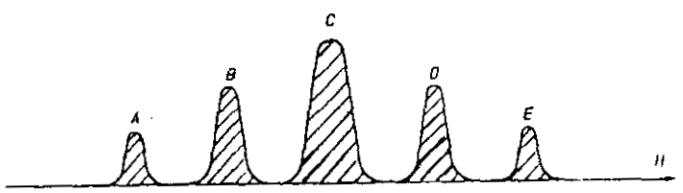

ESR with constant microwave frequency

(b)

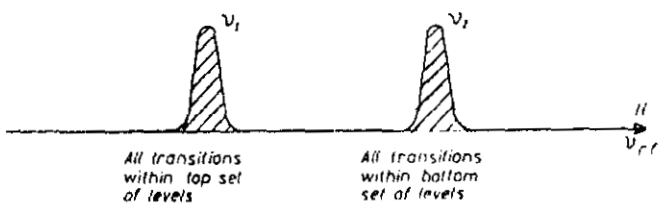

ENDOR with constant microwave frequency and magnetic field

(c)

Figure 3C.3 ENDOR for interaction with four protons, (a) Detailed energy levels for interaction with four equally coupled protons (b)E.S.R. spectrum that is expected. (c) ENDOR spectrum that will be observed.

It is clear that the ENDOR spectrum is much simpler and also gives a more direct measurement of the two coupling parameters involved. The difference between the two types of spectrum becomes even more marked if there is unequal coupling to some of the protons, thus one unequally coupled proton causes all the other hyperfine lines to be split by its own interaction. Unequal couplings therefore increase the complexity of the electron resonance spectra by multiplying factor, whereas each new class of inequivalent nuclei only gives rise to a total addition of two extra lines in the ENDOR spectrum. It therefore follows that any hyperfine pattern in which there are any large number of interacting nuclei, and especially if they are not all equally coupled, will normally produce a hyperfine pattern which is extremely difficult to resolve by ordinary electron resonance means. However, the ENDOR spectrum remains relatively simple and just possesses two lines for each type of inequivalent proton.

The ENDOR technique was initially used to study unresolved hyperfine structure in inorganic crystals and proved extremely powerful in resolving splittings which were completely lost in hyperfine patterns buried inside the normal line-width of the electron resonance spectrum.

3C.1.4 What To Look For

In metalloproteins, in principle, two different contributions of nuclear interaction with the unpaired spin need to be considered - that of the central metal ion and that of the ligands.

Ligand nuclei studied are usually:

1. Protons (^{1}H nuclear spin = I = ½)
2. Nitrogens (^{14}N, I= 1, ^{15}N, I = ½)

Only scattered information has been obtained about central metal interactions.

The majority of ENDOR data has been obtained from frozen solution and glasses of metalloproteins, resulting in powder type of EPR and ENDOR spectra. This arises not only because of a general difficulty in crystallising specimens, but also because in frozen solutions the physiologically relevant conformations of the protein can be more easily be achieved e.g. by adjustment of pH and addition of effectors to the solution prior to freezing.

The technique of orientation selection, introduced by *Rist* and *Hyde*,[31] can provide information on ligand interaction in such samples and may provide for a full tensor analysis. It involves selection of such portions of the EPR powder spectrum for ENDOR analysis in which the paramagnetic complex has a well defined, narrow range of orientations with respect to the external magnetic field. This is possible when either g or a hyperfine anisotropy dominate the other magnetic interactions. In this case, an extreme part of the EPR spectrum is built up by centres for which the magnetic field is directed along a principle interaction axis. The corresponding ENDOR is single-crystal like.

EPR powder spectra of rhombic g symmetry can be analysed at the highest and lowest field portions of the EPR spectrum. The intermediate g-turning point selects contribution of molecules from many different orientations for which $g_h = g_{int}$. As a consequence, a large number of ENDOR transitions should be found for the intermediate g-turning point providing for strong broadening. Resolvable intensity build up should then stem mostly from those complexes for which that g-factor is a principal element. Observation in the derivative mode suppresses the broad contributions.

When conventional X-band (~9 GHz) EPR-ENDOR is used, powder ENDOR spectra of metalloproteins often suffer from a lack of spectral separation between weakly coupled ^1H interactions centred around ν_n and ^{14}N couplings of ligands. This problem is sometimes handled by measuring at two or more frequencies about 0.8 GHz or so apart. A real advantage in separation due to the large difference in the field-dependent part ν_n for ^{14}N (~1 MHz at 9 GHz) and ^1H (~14 MHz at 9 GHz) can be obtained at Q-band frequencies (~35 GHz). This also would enhance the orientation selection preciseness on the EPR side which would be of particular importance for cases of comparable g and hyperfine anisotropy as is frequently encountered in low-spin metalloproteins.[32]

3C.2.1 Electron Nuclear Double Resonance of Copper(II) Tetraimidazole.[33]

In order to illustrate the application of the technique to copper model complexes I will describe analogous work on similar ligand copper complexes.

During the course of an ENDOR investigation of the Cu protein, superoxide dismutase, it was evident that the spectra obtained were not open to simple interpretation. Therefore,

Camp *et al* carried out an ENDOR study of the copper-tetraimidazole complex, whose major structural features closely approximate the Cu^{2+} binding site of superoxide dismutase. This model complex enabled a control of the isotopic composition of the ligand groups i.e. the ^{14}N replaced by ^{15}N and the protons for deuterium.

In principle, it is possible to measure the degree of interaction between the unpaired electron of the copper and several nearby atoms of the ligand group. In addition, it is possible to vary solvent environment and examine its effect on the ENDOR spectra.

Before recording the ENDOR spectra, the EPR spectrum was examined in order to select a set of orientation for the ENDOR (**Figure 3C.4**). The apparently axial spectrum clearly shows three of the four $^{65}Cu(II)$ hyperfine peaks centred about $g_{//} \sim 2.255$. The fourth is hidden under the nitrogen superhyperfine structure (SHF) in the vicinity of 3200 G; the splitting of the latter is about 15 G. The lowest field ^{65}Cu hyperfine peak (near 2600 G) is resolved into nine smaller peaks, which for I = 1 corresponds to four equivalent nitrogens. Their splitting is approximately 12.5 G.

ENDOR measurements are most often performed at the extreme field limits of the EPR spectrum (indicated by the arrows). These positions are most likely to give double resonance results corresponding to predominately one orientation for the complex i.e. single crystal-like spectra. For a square planar complex, this is especially true for the magnetic field in the orientation corresponding to $g_{//} \sim 2.255$. At this g value, the magnetic field lies along the normal to the plane of the complex, whereas, the field direction corresponding to $g_{\perp}$ will lie within the plane of the complex.

The authors make a distinction between the magnitudes of the fields corresponding to $g_{//}$ (2.255), $g_{\perp}$ (~ 2) and $g_{//}$-extreme (2.52), $g_{\perp}$-extreme (~1.98). As shown in **Figure 3C.4** the field corresponding to the $g_{//}$-extreme is set apart from the position of $g_{//}$ because of the presence of the copper hyperfine splitting (~ 196 G). If ENDOR were performed at the precise field value for $g_{//}$, complicating effects related to the anisotropy of the copper hyperfine structure would arise. For the same reason, ENDOR performed at the $g_{\perp}$ extreme does not refer to an experiment done at the precise field value for $g_{\perp}$, but rather to ENDOR done at the high field extreme (g = 1.98). At this extreme the assumption is that anisotropic effects associated with the EPR powder pattern will be lessened, and that the dominant contribution to

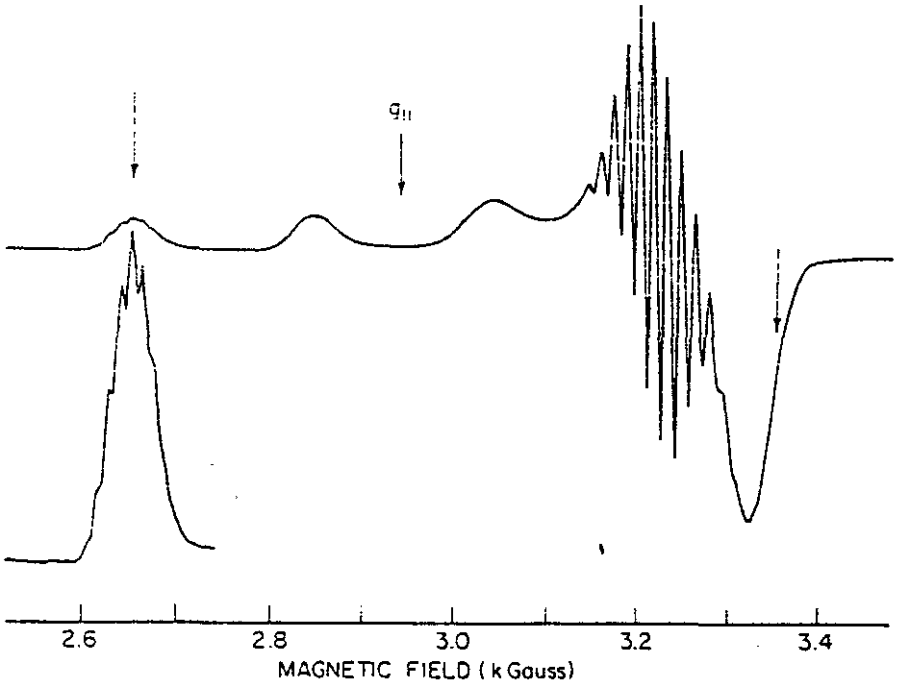

Figure 3C.4 EPR spectrum of $^{65}Cu(II)(Im)_4$

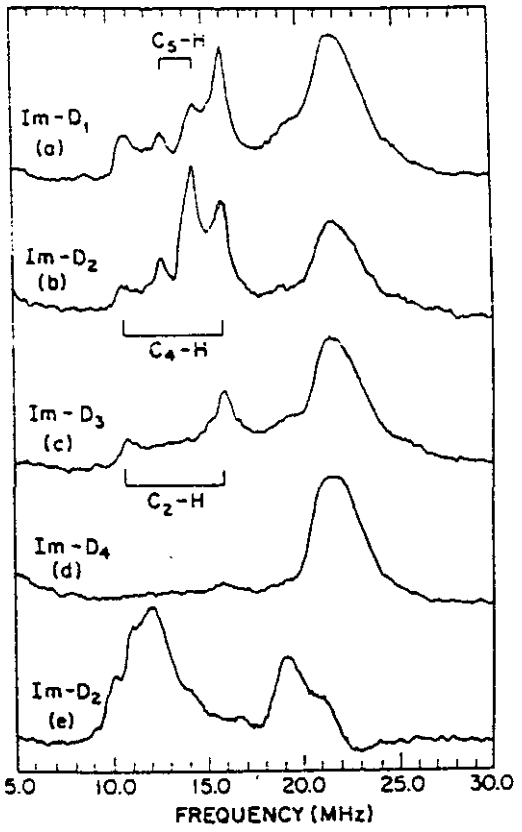

Figure 3C.5 shows ENDOR from selectively deuterated samples in completely deuterated solvent, (a) C_2, C_4, C_5, protonated, (b) C_4, C_5, protonated, (c) C_2 protonated, (d) completely deuterated, (e) trace taken at $g_{//}$ extreme

the ENDOR response will come from those molecules oriented so that the field is nearly within the plane of the complex.

3C.2.1 Proton ENDOR

From proton ENDOR one wants to be able to identify the effects of specific protons and, if possible, to derive some information relevant to the particular molecular structure at hand. The author was able to clearly present results which allow probable identification of the imidazole protons and suggest that the imidazole has been rotated in random fashion about the Cu-N axis.

Figure 3C.5 show ENDOR spectra from four selectively deuterated complexes. The large peak appearing near 22 MHz in all of the traces is due to the nearest-neighbour nitrogen. The ENDOR spectra shown in **Figure 3C.5** were taken at the $g_{\perp}$ extreme because this field position was the only one that brought out sharp structure in the proton range (9-17 MHz).

The C_2-proton can be clearly identified in **Figure 3C.5c** as it is the only proton observed. This was the starting point for assigning the other protons and their effect. The maximum effect of the hyperfine effect of the C_2-proton at $g_{\perp}$ is given by the frequency difference (~ 5.2 MHz) between the two peaks centred about the free proton frequency, 13.2 MHz.

Both the C_5 and C_4 protons are present in **Figure 3C.5b.** The steric symmetry between C_2-H and C_4-H enabled their assignment - the inner portion (with splitting = 1.7 MHz) is due to C_5-H and the outer portion (with splitting = 5.28 MHz) is due to C_4-H. These assignments are tentative because as well as dipolar interactions between the unpaired electron and the proton there is also a contact interaction which may have a different value for the protons attached to C_2 and C_4. The observed hyperfine effect will be the sum of the contact and dipolar terms.

The identification is tentative also because at $g_{\perp}$ the ENDOR response will be the result of the superposition of many orientations of the complex with respect to the static field H_0. At best, such a powder pattern will involve those orientations for which H_0 is in the Cu-N molecular plane. Thus, it was concluded that the inner region of **Figure 3C.5b** contains contributions from both C_5 and C_4 protons. Therefore, the contribution to the other region is assigned cautiously to C_4-H.

Figure 3C.5e shows the best resolution found for Im-D2 when H_0 is in the $g_{//}$ direction. What is interesting is that the sharpest features appear at the $g_{\perp}$ extreme and not at the $g_{//}$ extreme. There are examples in the literature where the reverse is true. This is because, for axial symmetry, one usually expects the highest number of equivalent nuclei when H_0 is along $g_{//}$; in ENDOR, increasing the number of equivalent nuclei reduces the number of resonances.

3C.2.2 Near-neighbour Nitrogen ENDOR.

A ^{14}N (I = 1) nucleus coupled to an unpaired electron should present up to four peaks owing to the electron-nuclear hyperfine, nuclear Zeeman and nuclear quadrupole effects. The first of these yields only one resonance centred at ½ the hyperfine constant (A/2). The nuclear Zeeman term splits this peak into two with separation given by $2g_NB_NH_0$, where g_N and B_N are the nuclear magnetogyric ration and nuclear magneton, respectively. The third term will split each of these peaks into two more with a separation of twice the quadrupole energy along the effective field direction.

Four peaks do not show up in **Figure 3C.5** but **Figure 3C.5e** does show two unresolved features which may be a nuclear splitting. Here again there is an unexpectedly broad resonance. This resonance was confirmed as arising from the near nitrogen by the fact that the approximate hyperfine constants $A(g_{\perp}) = 41.6 \pm 1.5$ MHz and $A(g_{//})$ 39.8 ± 1.5 MHz agree well with the measured SHF splittings in the EPR spectrum. The resonance shows little structure and seems consistent with a picture that requires some inequivalence among the various imidazoles.

3C.3. ENDOR Study of Copper Azacryptates

3C.3.1 Introduction

The extent of copper-copper bonding in the Cu_A assembly is currently a matter of debate. It is thus important to fully investigate the spectroscopy of both the natural site and small molecule models to reveal details of the electronic distribution within and around the dicopper (1.5) site.

As discussed in **Chapter 1.21** the electronic spectroscopy of our-average valence dicopper cryptates has been assigned on the basis of group theoretical arguments and simulation of both absorption and MCD profiles. This has established the "intervalence" σ-σ^* transition from within which copper-copper stretching modes may be excited and enhanced.[34] The Resonance Raman study in Chapter 3B has identified two low frequency modes with appreciable Cu-Cu stretching character, and normal co-ordinate analysis reveals that a force constant associated with this vibration is relatively high for a one-electron bond.

ESR spectroscopy is also a valuable method that allows investigation of the electron distribution in the copper-copper bond. An X- and Q-band study establishes the delocalisation of the unpaired electron over both nuclei down to 4 K.[24] This indicates, via analysis of the anisotropic component of the hyperfine constant, that not all the unpaired electron density resides on the copper ions. Although no hyperfine coupling to ligands was seen in the ESR spectra the predicted delocalisation of unpaired spin onto ligands suggests that it should be observable in ENDOR spectroscopy, with coupling constants reflecting the degree of delocalisation. ENDOR spectroscopy should thus be capable of probing the weakly coupled *environment of the average-valence site, both in* Cu_A *and in our model average-valence* compounds which may serve as calibrants.

3C.3.2 The Hexaimine GT system

3C.3.2.1 Mononuclear GT ; $[CuGT](ClO_4)_2.H_2O$ in CD_3OD/D_2O at 10 K

As discussed in Chapter 3A and demonstrated by X-ray crystallography, the co-ordination site in the monocopper complexes is obviously different from that in the average-valence dicopper cryptates. However, utilisation of the same imine donors makes them useful for the purposes of comparison with the average-valence systems. A notable problem which affects the comparison, however, derives from the geometrical disposition of the ligand in relation to the magnetic orbitals of the Cu(II) cation. The monocopper(II) complexes show the "normal" dx^2-y^2 ground state ESR spectrum with $g_z < g_{x,y}$ and $A_{//} > A_{\perp}$, while the average-valence systems show the reverse ordering. The $A_{//}$ values are also much larger than $A_{\perp}$. This derives from the regular trigonal geometry adopted in the latter compared with distorted octahedral in the mononuclear structure.

Progress has been made in interpreting the ENDOR spectra obtained from this monocopper GT complex. However, it must be understood that the ENDOR experiments are at this stage incomplete. In order to interpret the EPR and ENDOR spectra obtained, the following assumptions have been made:

1. The EPR spectrum has (at X-band) axial symmetry and therefore the g-tensor and the metal hyperfine tensors are coincident. The EPR axes are coincident with the molecular axes, i.e. $g_{//} = A_{//} \sim$ z-axis (see X-ray crystal structure).
2. The *local* ligand hyperfine tensor axes will almost certainly NOT be coincident with the other axis systems in this case as, from the X-ray structure, practically no protons are along the z-axis or in the x-y plane. Generally in these systems, the local proton hyperfine tensors will have their largest component pointing roughly in a straight line from the proton to the metal centre; similarly the nitrogen atoms. This may not be the case if there is a lot of spin delocalised onto the ligand. Hence, in the case of the nitrogen atoms in the x-y plane, the local nuclear hyperfine tensor will have its parallel axis perpendicular to the metal g (and hyperfine) tensor parallel axis.
3. It is assumed that the local ^1H hyperfine tensors are axial. Although this may be an over simplification it should hold for the nitrogen atoms.

Before discussing the ENDOR results, it is important to understand what the EPR spectrum actually represents for an axial system with no metal hyperfine coupling.

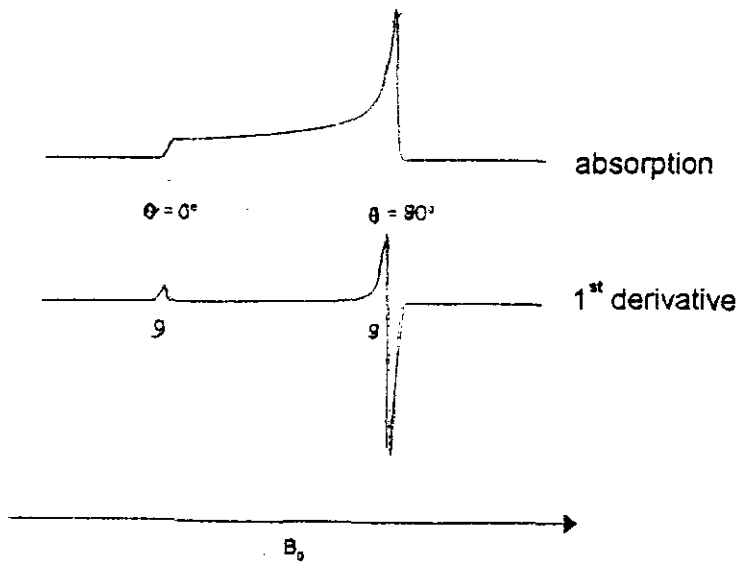

Figure 3C. 6

If we consider an octahedral metal complex, defined as follows:

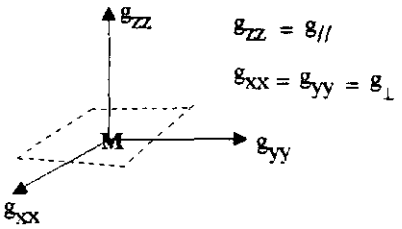

Figure 3C.7

The low field onset of resonances occurs at a field at which those molecules in the sample which have their maximum principal value of the g-tensor (in this case g_{zz}) parallel to the applied magnetic field (B_0) come into resonance, i.e.

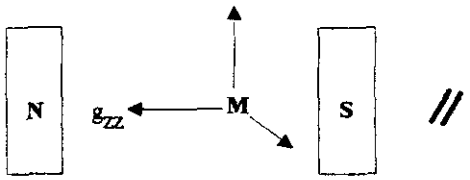

Figure 3C. 8

The high field feature occurs when those molecules that have (in this case) g_{zz} perpendicular to the applied field, come into resonance, i.e.

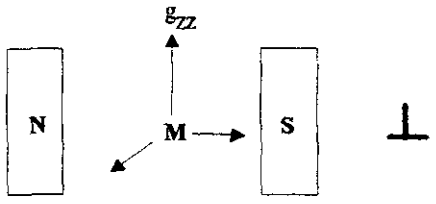

Figure 3C. 9

Between these extremes lie a huge range of other values. Alternatively, we can think of this on a molecular level as a magnetic field vector moving smoothly from $g_{//}$ to $g_{\perp}$ as we move from $g_{//}$ to $g_{\perp}$ in the EPR spectrum

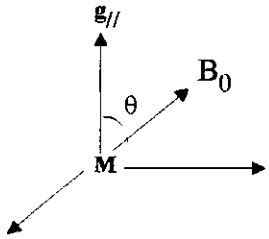

Figure 3C. 10

Hence, the ENDOR spectrum corresponds to the molecular orientation(s) selected by a field applied at an angle θ to the parallel axis. The value of θ may be calculated using the formula shown below, (more complicated expressions being required for systems with hyperfine couplings).

$$\theta = \cos^{-1} [g^2_\theta - g^2_\perp / g^2_{//} - g^2_\perp]^{1/2}$$

However, in our system, we have to consider metal hyperfine interactions and a simple interpretation becomes impossible.

An attempt was made to simulate the data using a program which was obtained from Erickson & Lund. At this stage we are able to obtain a reasonable simulation of the ENDOR spectrum recorded at θ = 0°, **Figure 3C.11.** The two broad features either side of the spectrum were originally thought to be nitrogen resonances. However, this is uncertain owing to a noisy spectrum but we do suspect that the nitrogen signals are somewhere beneath the proton signal. Unfortunately, only a high frequency (Q or W-band) spectrum, which is unavailable, could confirm this.

Simulations of ENDOR spectra recorded in the perpendicular region of the EPR spectrum have been attempted. Unfortunately, these weren't successful, and we were unable to get a correlation with the parameters used for the parallel feature. In principle it should be possible to simulate any field position in the spectrum using just the one set of parameters - this would be a requirement for a correct simulation.

The problem may be broken down thus:

(1). Can any of the protons be assigned to the signals in the ENDOR spectrum?

(2). Can any of the principal values of the local hyperfine tensor be assigned, thus giving structural information?

The obvious answer to (1) would be to do an isotopic labelling experiment to assign a particular proton(s). The answer to (2) would be to do a magnetic angle selection experiment to generate "road maps" of the assigned proton couplings and thus determine the hyperfine matrices. The plan was to use the X-ray data and point (2) above to see whether any of the large (and therefore obvious) proton resonances in the ENDOR spectra could be determined by effectively working backwards. **Figure 3C.12** shows the "working" X-ray figure.

In order to explain the reasoning in more detail, it is necessary to discuss the EPR spectrum and what the different points in it represent in terms of the ENDOR spectra obtained from them. As shown, the low field flank of the spectrum represents $\theta = 0°$ (i.e. the parallel feature). The perpendicular feature represents $\theta = 90°$. An ENDOR spectrum taken at the low field extreme of the EPR spectrum (in this case the lowest field of the four parallel features) represents a field vector looking straight up the z-axis and a so called single crystal type ENDOR spectrum is obtained. Any proton lying on the z axis will have the field pointing straight along the parallel axis of its local hyperfine tensor and so will give two peaks corresponding to $A_{//}$. Similarly, protons in the x-y plane will give their perpendicular couplings at this position. Protons in other positions will give lines corresponding to appropriate components of the couplings which will not correspond to true perpendicular and parallel values. As the field increases, so θ increases, and we select planes of orientations. This results in powder type ENDOR spectra with features corresponding to "parallel" and "perpendicular" components of the local hyperfine tensors. These values are not necessarily the true perpendicular and parallel values as they will depend on the relative orientation of the local hyperfine tensor and the field vector.

Four parallel features are present which are due to the metal hyperfine coupling. As the field moves away from the lowest parallel feature then θ increases to a value of x°. At this point, the second parallel feature is encountered and two values of θ are selected, $\theta = x°$ and $\theta = 0°$, corresponding to the first and second hyperfine features, respectively. As the field increases and more hyperfine features are encountered, more angles of θ are selected, so that by the time $g_{\perp}$ is reached the spectra have become extremely complicated.

There is, however, a second situation that can arise (normally in organic molecules) where the g anisotropy is very small and the hyperfine couplings are not resolved. This results in a single broad line in the EPR spectrum. Under these circumstances recording the ENDOR

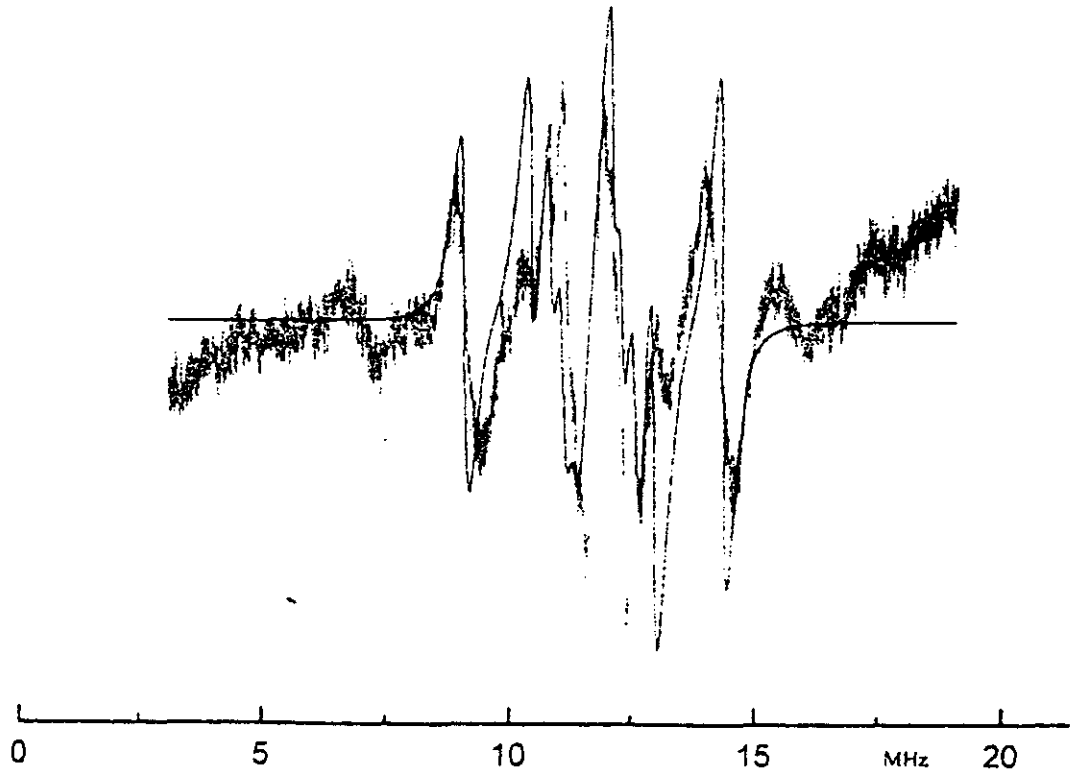

Figure 3C.11 ENDOR simulation of $[Cu(II)GT]^{2+}$

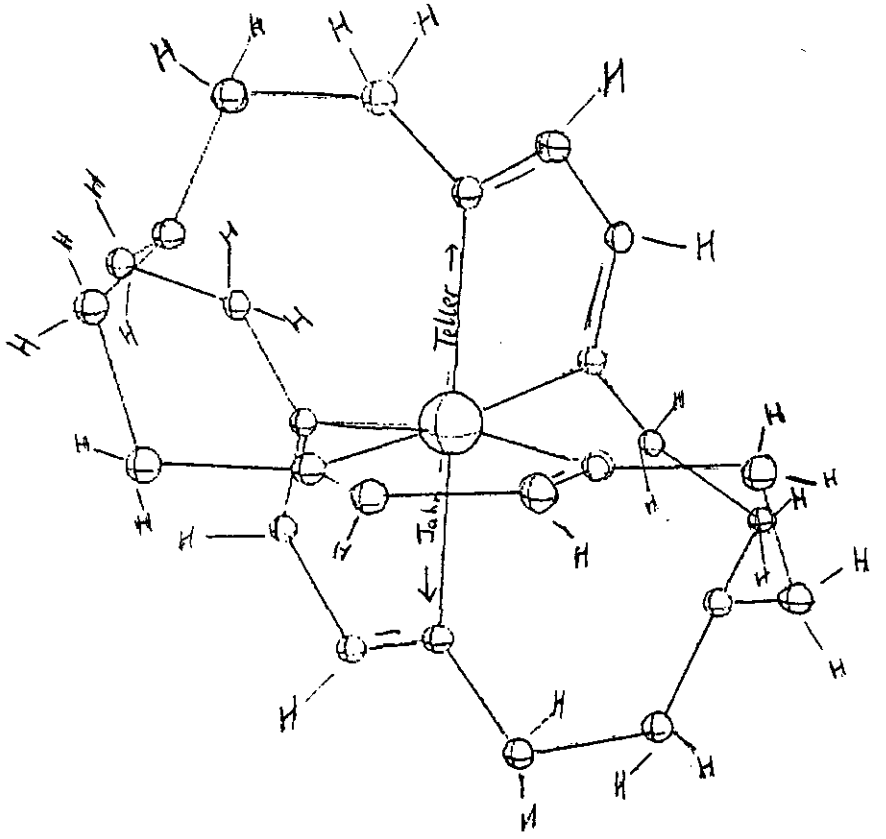

Figure 3C.12 The working X-ray of $[Cu(II)GT]^{2+}$

spectrum with the field set to the centre of this line results in the selection of the vast majority of magnetic orientations. This in turn produces a true powder ENDOR spectrum with features corresponding to parallel and perpendicular components of the local hyperfine tensors; in this case though, they are the principal values and correspond to the true parallel and perpendicular values.

In the case of mono Cu(II) GT the highest field parallel feature appears to fall on the perpendicular, which in turn is not particularly well resolved but the ENDOR is reproducible. Hence, in this region we are assuming that a true ENDOR spectrum is observed and that the features correspond to principal values of the local hyperfine tensors.

Therefore, the ENDOR spectra were recorded as labelled in the EPR spectrum, (**Figure 3C.13**). Nine ENDOR spectra were recorded in the low field region of the EPR spectrum above (from 2721 Gauss to 2881.27) corresponding to $\theta = 0° - \theta = 40°$. These angles were calculated from a rough simulation of the EPR spectrum to obtain the parameters: $A_{//} = 480$ MHz, $A_{\perp} = 100$ MHz, $g_{//} = 2.29$ and $g_{\perp} = 2.115$.

From these it is possible to calculate the resonant field for the four nuclear spin states and thus obtain the magnetic angle, **Figure 3C.13**. No allowance for the presence of two isotopes has been made. The spectra presented in **Figure 3C.14** are the ENDOR spectra recorded at the field positions and angles indicated.

These spectra show small changes as the field increases but at this stage we cannot confidently assign the large couplings or in fact determine a maximum coupling. However, it does seem that the peaks in the wings of the ENDOR spectra almost certainly arise from protons which are close to the copper nucleus.

Unfortunately, we are unable to see the nitrogen spectrum. Higher field ENDOR spectra would help as this would increase the intensity of the nitrogen signals, as well as providing better nuclear separation so that nitrogen peaks, if they were under the proton signals at X-band, would be visible. ^{15}N labelling would be a possible solution as the nitrogen atoms would be relatively easy to follow by ENDOR, but as it is not certain that the nitrogen couplings aren't under the proton signals, this would at this stage be almost impracticable. Simulations may be possible but we would have to identify a proton(s) by labelling.

The experiments so far explain what is happening in the ENDOR spectra and shows why a straightforward answer is not possible at the moment.

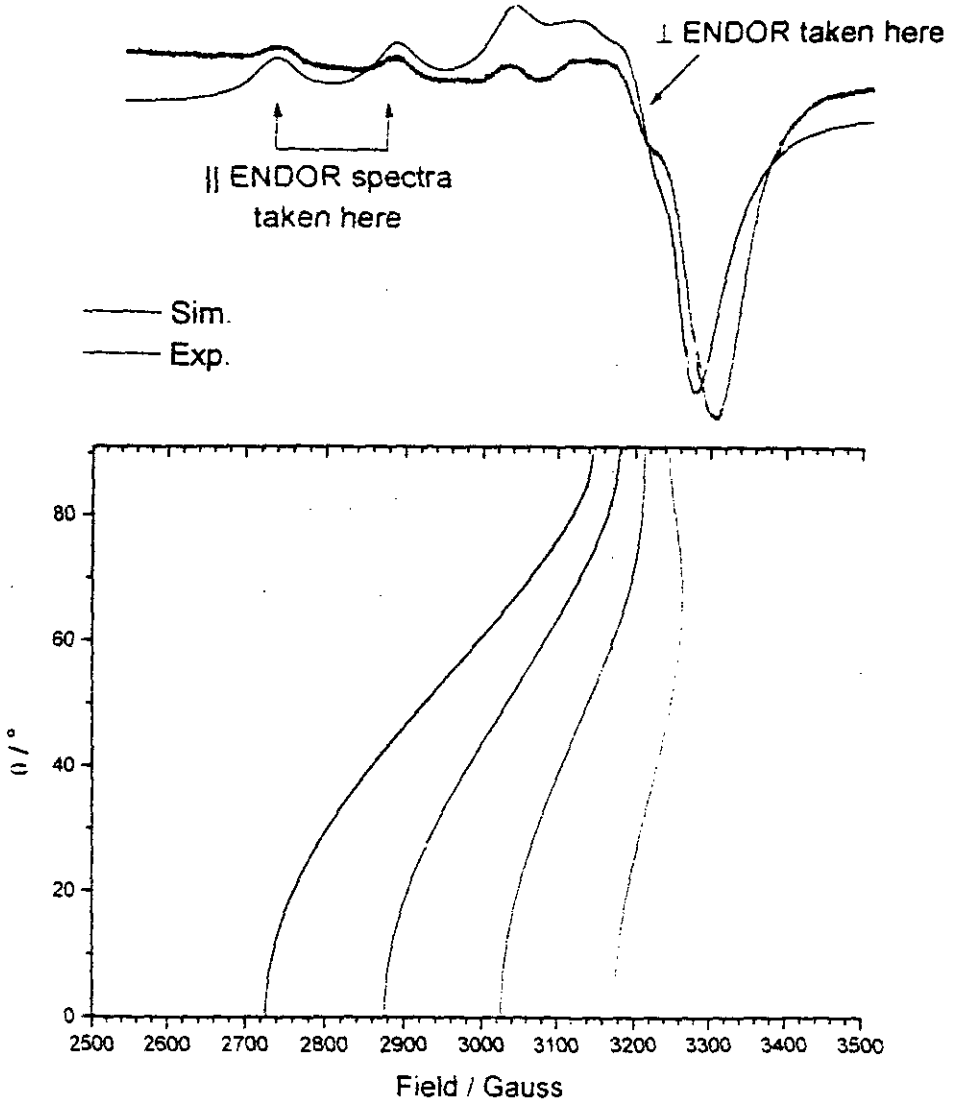

Figure 3C.13 $[Cu(II)GT]^{2+}$ ESR and subsequent magnetic angle

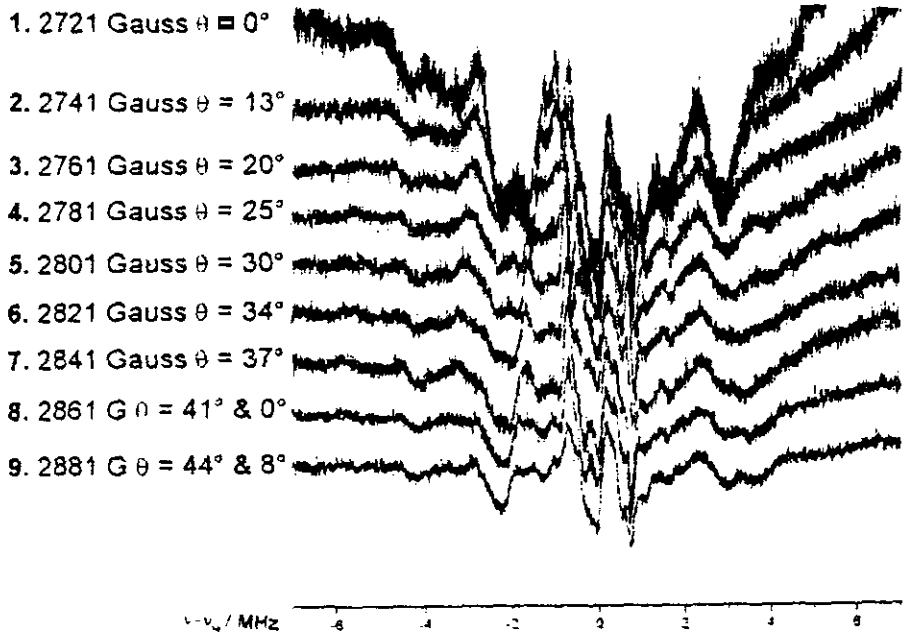

Figure 3C.14 ENDOR spectra recorded at field positons and angles indicated.

The remainder of this chapter reports the ENDOR spectra and couplings for mononuclear RGT and the dinuclear average-valence copper complexes. An attempt has been made to sort out any N, (N)H, and/or imino H couplings. Any smaller couplings may be assigned to methylenes differentiated either by axial or equatorial disposition, by position α or β to the N, or both. However, it should be noted that as these are preliminary experiments any assignments are tentative and discussion is thus limited.

3C.3.2.2 $[Cu_2GT][ClO_4]_3 . 2H_2O$

Comparison of the results for the monocopper(II) and dicopper(1.5) systems, even in a qualitative fashion, does not show an appreciable difference in delocalisation of the unpaired spin onto the ligand.

On first inspection of the ENDOR spectrum of the average valence dicopper GT cryptate we expected to observe resonances due to three sets of equivalent protons. However, the ENDOR spectrum displays more peaks than we would expect. This may be due to a Cu(II) impurity arising as a result of disproportionation. However, it is possible that the hyperfine tensor isn't quite axial and both the x and y components of the perpendicular splitting are observed. As is observed in other analogous systems, axial and equatorial methylene positions are differentiated and this would also account for the extra ENDOR couplings. The observation of five clear resonances shows that the axial and equatorial methylene positions are not equivalent.[35]

Figure 3C.15 shows the ENDOR spectra recorded at position 3 of the ESR spectrum. Couplings were converted using the formula:

$$A_{gauss} = [(g_{effective}/g_e)\, A_{MHz}] / 2.8 \rightarrow A_{gauss} = 0.406\, A_{MHz}$$

Nitrogen Couplings at 2963.94 Gauss

There are two peaks at *ca.* 4.6 and 6.4 MHz. The separation between these features is 1.8 MHz which corresponds with the value of 2νN. This results in a value for A_N of about 11 MHz. This comes from the mid-point of the doublet at 1.8 MHz - coupling of 5.5 is equal to ½ A.

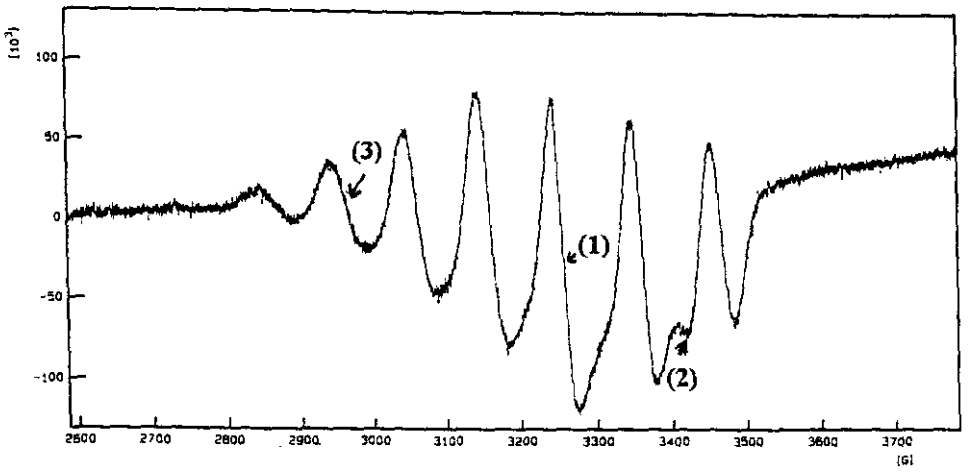

Figure 3C. 15a ESR spectrum of $[Cu_2GT](ClO_4)_3.2H_2O$, showing positions where ENDOR spectra recorded

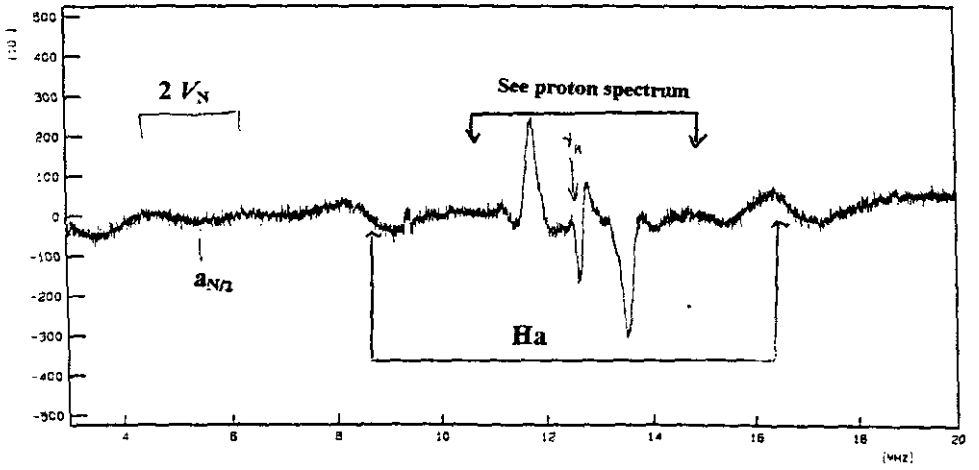

Figure 3C.15b Nitrogen Couplings of $[Cu_2GT](ClO_4)_3.2H_2O$ at 2963.94 Gauss

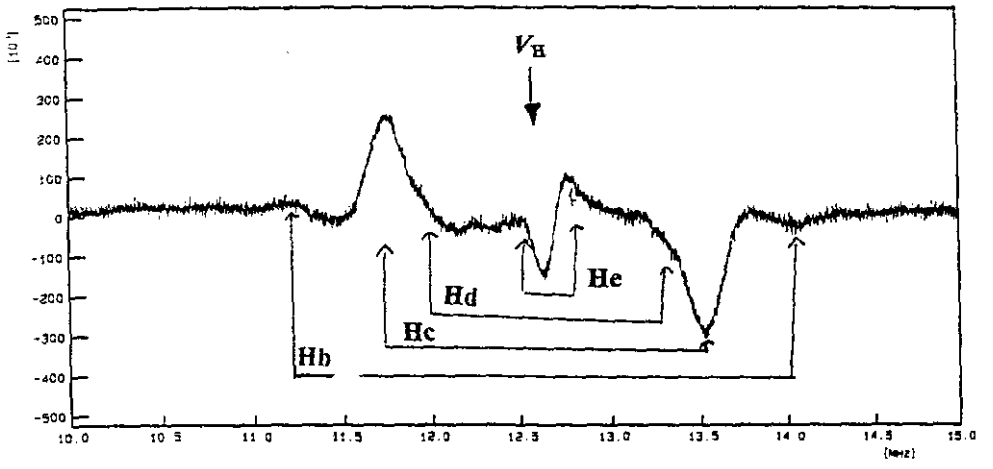

Figure 3C.15c Proton Couplings of $[Cu_2GT](ClO_4)_3.2H_2O$ at 2963.94 Gauss

Proton Couplings at 2963.94 Gauss

An artifact appearing at *ca* 10 MHz on weak systems such as this appears as a broad, out of phase signal and it is possible that this may interfere with some of the outer, low frequency lines. **Table 3C.1** shows observed couplings for the protons in $[Cu_2GT](ClO_4)_3.2H_2O$ and their tentative assignments.

Table 3C.1 Observed Couplings for $[Cu_2GT][ClO_4]_3.2H_2O$ at 2963.94 Gauss,

νH = 12.62 MHz, $2\nu N$ = 1.82MHz, g effective = 2.28 and $A_{gauss} = 0.406\ A_{MHz}$

MHz	Gauss	Proton
8.1	3.3	Imine $C{=}N_\perp$
2.6	1.1	$\alpha\ CH_\perp$
1.8	0.7	$\alpha\ CH_\perp$
1.3	0.5	$\beta\ CH_\perp$
0.3	0.1	$\beta\ CH_\perp$

Figures 3C.16a and 3C.16b show ENDOR spectra recorded at position 2 of the ESR spectrum. There should be significant contribution from the parallel as well as the perpendicular orientations.

Couplings at 3413.20 Gauss

There are features present at this field position which are not present in spectra recorded for almost pure $\perp$ spectra. Therefore, these may be assigned to components arising from the parallel g-factor. Some of the perpendicular features are hidden under the parallel signals but the agreement is quite good for a noisy spectrum.

Table 3C.2 Observed Proton Couplings for $[Cu_2GT][ClO_4]_3.2H_2O$ at 3413.20 Gauss

νH = 14.53 MHz, $2\nu N$ = 2.10 MHz, g effective = 2.07 and $A_{gauss} = 0.368\ A_{MHz}$

MHz	Gauss	Proton
9.62	3.54	Imine $CH_{//}$
3.96	1.46	$\alpha\ CH_{//}$
2.69	0.99	$\alpha\ CH_\perp$
~ 1.85	0.67	$\alpha\ CH_\perp$
1.50	0.55	$\beta\ CH_{//}$
~ 0.99	0.36	$\beta\ CH_{//}$

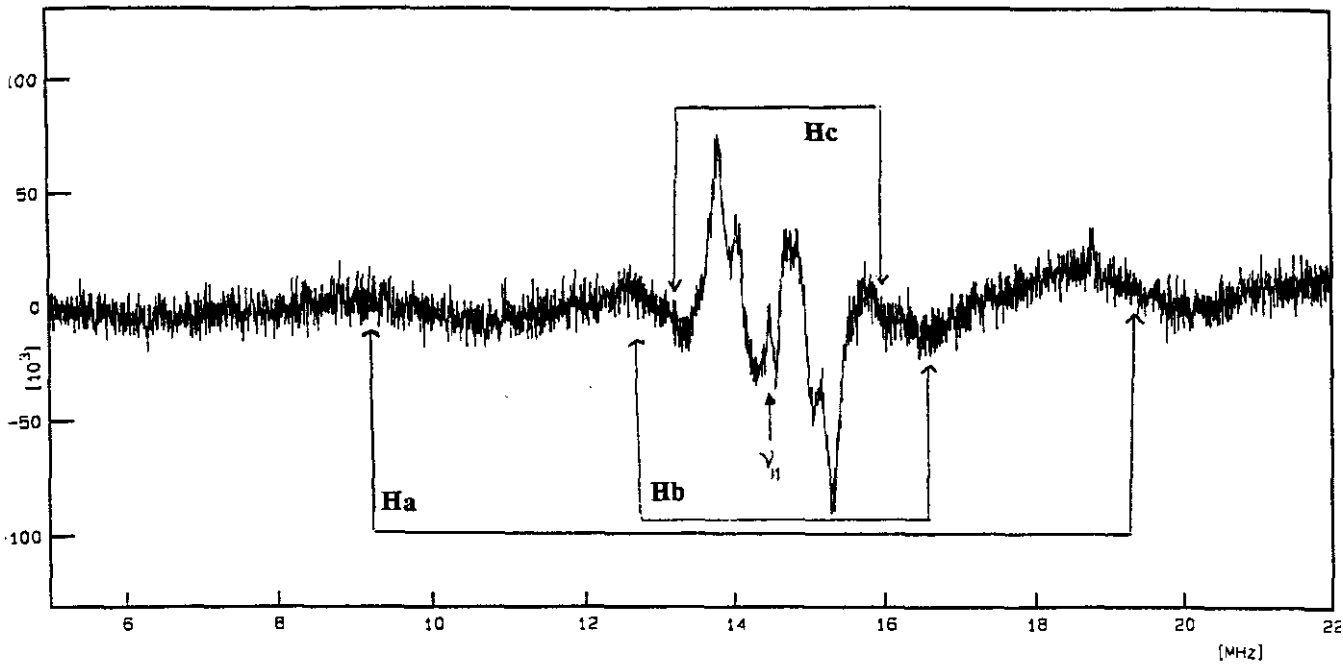

Figure 3C.16a *Proton Couplings of $[Cu_2GT](ClO_4)_3.2H_2O$ at 3413.20 Gauss*

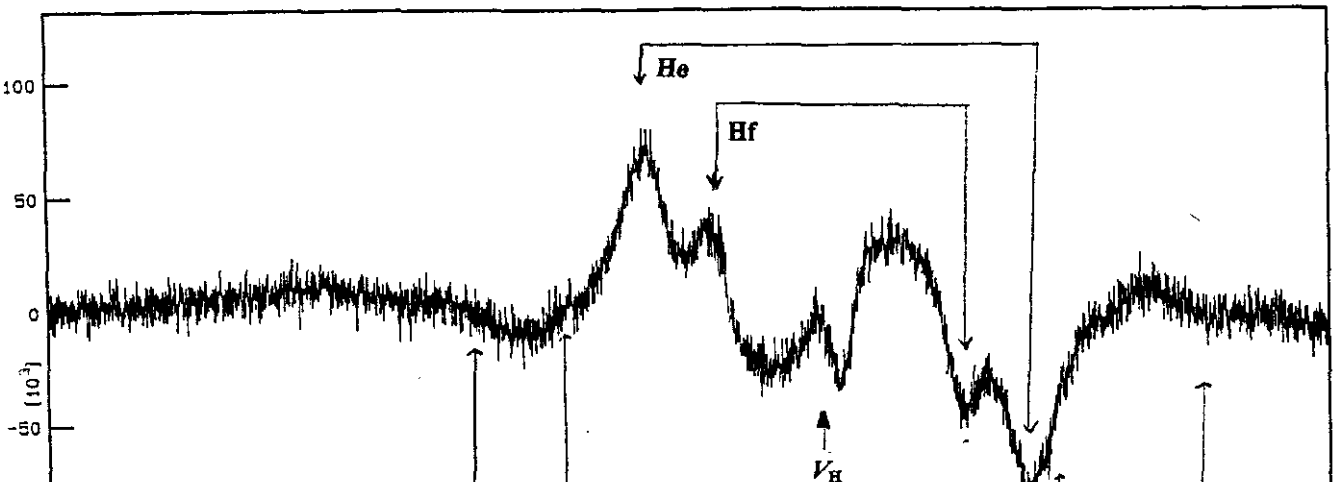

Figure 3C.16b *Proton Couplings of $[Cu_2GT](ClO_4)_3.2H_2O$ in range 12-16 MHz at 3413.20 Gauss*

Complications may arise from the fact that the electron of the Cu-Cu bond lies in the dz^2 orbital and hence there is an uneven contribution of spin via the imine bond and the bridgehead nitrogen. Many of the complexes studied in the literature are mononuclear complexes therefore it is difficult to be sure of the contribution of a dinuclear species.

3C.3.3 The Octaamine RGT System

3C.3.3.1 [CuRGT] $[BPh_4]_2$

As discussed the monocopper(II) RGT complex could be obtained in a pure state only as the tetraphenylborate salt. Unfortunately this complex had low solubility in normal ENDOR solvent systems. No ENDOR spectrum was observable in the solid state and a 1:1 dimethoxyethane/DMF mixture was required to achieve sufficient solubility for good ENDOR.

The ESR spectrum of the frozen solution was not typical of axial Cu^{2+}, but shows an irregular eight-line pattern, arising from the overlap of two four-line patterns. This may arise as a result of overlap of $g_{//}$ and $g_{\perp}$ components with comparable hyperfine splitting. This situation applies in environments which are strongly distorted away from the preferred square-based axial geometry of Cu^{2+}. Another possible explanation is the occurrence of two separate species, differing solvation and/or co-ordination geometry. This seems most probable because when the tetraphenylborate counterion is removed the electronic spectrum indicates that the mixed valence system is formed. A $[BPh_4]^-$ mediated conproportionation is likely.

The complexity of the spectrum prevented selection of suitable irradiation positions for single-crystal like spectra, and indeed none of the spectra obtained appear single crystal like. The difficulty of separating parallel and perpendicular spectra in this case prevents further attempts at assignment of these spectra.

3C.3.3.2 $[Cu_2RGT][ClO_4]_3 . 3H_2O$

Spectra for this complex were obtained as an MeOH glass over a range of temperature from 8 to 25 K. As noted in the average-valence GT system, it was not possible to obtain pure parallel type ENDOR spectra by irradiating at the position of the shoulder representing the parallel component in the ESR spectrum. However, well-resolved perpendicular spectra were obtained by saturation at the most intense feature of the seven line ESR pattern. The largest

coupling at ~6.4 MHz may correspond to coupling to the NH proton, while the smaller couplings may represent the six methylene protons, **Figure 3C.17**.

Two ^{14}N couplings are resolved: one clear doublet corresponding to 4.6 gauss and a second, less well defined 6.4 gauss coupling, partly underlying the 10 MHz ^{1}H feature. The tertiary N-bridgehead is indeed expected to generate stronger coupling to $[Cu_2(1.5)]^{3+}$, on the basis of orbital overlap considerations, than the secondary N(H) donors. Therefore, these couplings may be tentatively assigned on the basis of this ordering.

Nitrogen Couplings at 3135.4 Gauss

There are two peaks at ca. 5.4 and 7.5 MHz. The separation between these features is 2.1 MHz which is slightly larger than the value of 2νN which is 1.92 MHz. This results in a value for A_N of about 12.9 MHz (5.48 Gauss) for the first and 17.4 for a possible second suggested N-coupling. These larger values indicate more localisation onto the N in comparison to GT.

Proton Couplings at 3135.4 Gauss

Table 3C.3 Observed Proton Couplings for $[Cu_2RGT][ClO_4]_3.3H_2O$ at 3135.4 Gauss

νH = 13.346 MHz, 2νN = 1.92 MHz, g effective = 2.15 and $A_{gauss} = 0.383\ A_{MHz}$

MHz	Gauss	Proton
6.4	2.46	NH
3.8	1.45	$CH_{//}$
2.7	1.05	$CH_{//}$
1.6	0.64	$CH_{//}$
0.5	0.55	$CH_{//}$

Without further experiments it is impossible to confidently assign the protons. Are the two larger couplings at 3.8 and 2.7 MHz due to the central protons α to the NH, or α and β to the N bridgehead? Can the axial and equatorial protons be distinguished or are they hidden under other features ? It is also possible that further unresolved features exist.

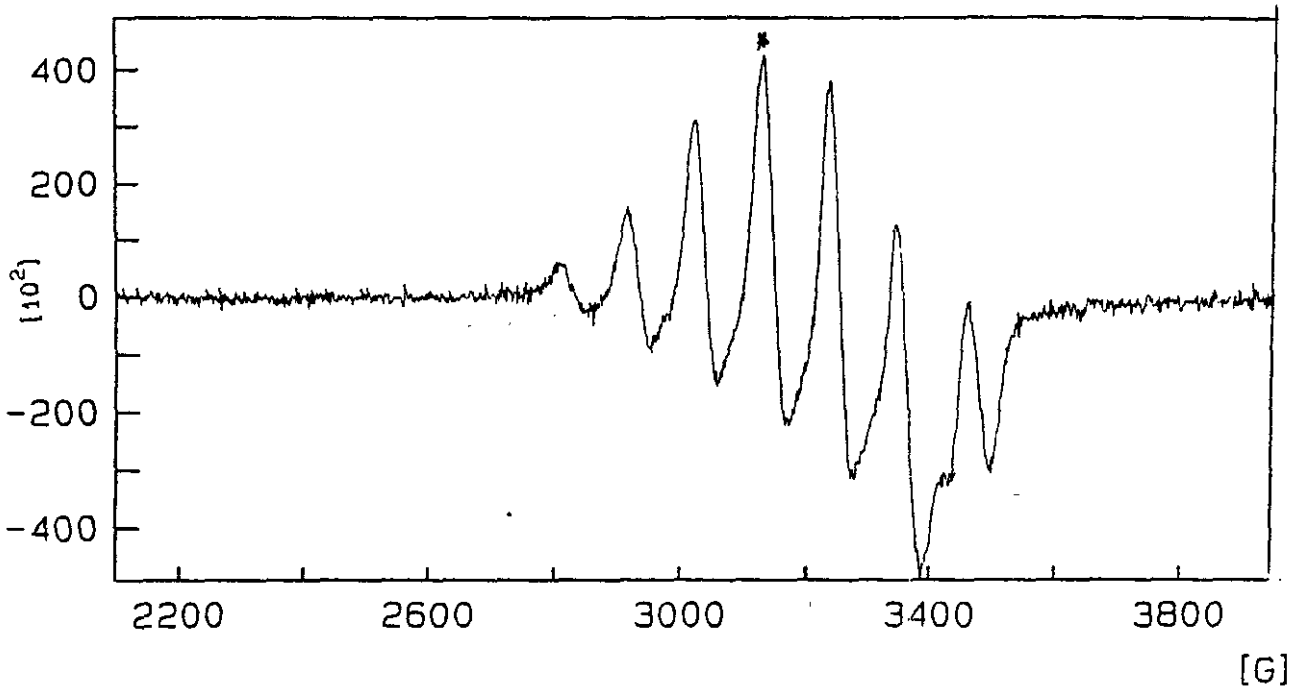

Figure 3C.17a *ESR spectrum of $[Cu_2RGT](ClO_4)_3.3H_2O$ showing position where ENDOR spectrum recorded (*)*

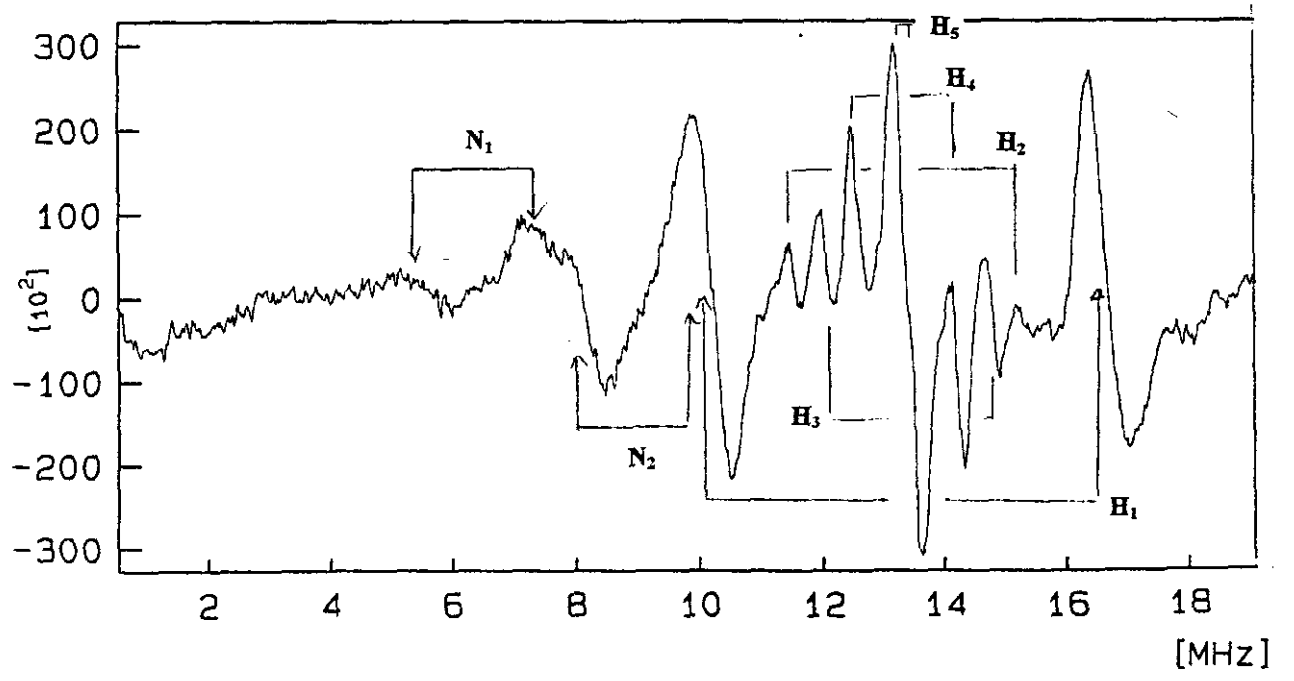

Figure 3C.17b *ENDOR spectrum of $Cu_2RGT](ClO_4)_3.3H_2O$ at 3135.4 Gauss*

3C.3.4.1 The NGT system; $[Cu_2NGT][ClO_4]_3$.

Saturation at the most intense fourth line position of the ESR spectrum generated a broad single-crystal like perpendicular ENDOR spectrum, free from any parallel contamination, **Figure 3C.18**. Three clear proton resonances are seen (~ 1.8, 1.26 and 0.97 MHz) with the possibility of a fourth at low a $a_\perp$.value (0.48 MHz). All of the observed proton couplings are small, the two largest being no more than half the equivalent value for the other iminocryptate studied. Taken in conjunction with a smaller ESR A_{iso} observed for this system, this implies either less mixing of 4s character in the Cu(1.5) magnetic orbital or a larger delocalisation of unpaired spin onto the N atom. However, couplings to N were not visible in the 2-30 MHz region where they might be expected. For NGT a carbinolamine product (as discussed in **Chapter 3A.8**) is a by-product which may cause spurious results. Low quality broad spectra prevent identification of the nitrogen resonances.

3C.4 Conclusion

The coupling constants observed in the average-valence versus mononuclear cryptates are very similar. For the average-valence system this must reflect the degree of electron delocalisation of the unpaired spin between the Cu(1.5) cations with the one-electron bond. Although no such bond is possible for a mononuclear centre the coupling constants reported indicate that there is significant electron delocalisation onto the copper ion.

Apart from the obviously different imino CH and NH protons, the remaining coupling constants in average valence RGT and GT are similar and small, reflecting their similar geometry and the low level of unpaired spin on the ligands.

The larger average-valence iminocryptate remains something of a puzzle. Electronic spectroscopy indicates a lower energy σ-σ^* transition suggesting a weaker Cu-Cu bond, while the smaller $A_\perp$ coupling in the ESR spectrum would suggest more delocalisation of unpaired spin onto the ligands, a greater covalency in the copper-ligand bond. Accordingly, we expect larger hyperfine couplings rather than smaller values in this case. It seems likely that this puzzle will not be resolved until more sophisticated studies using pulsed and higher field ENDOR spectra are undertaken. Further experiments involving Q and W-band ENDOR spectroscopy and isotopic labelling are planned.

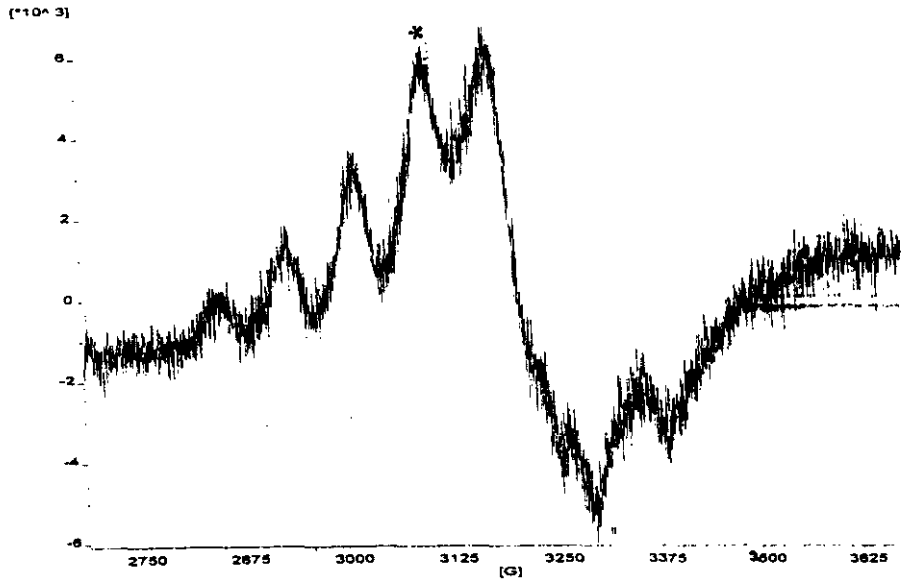

Figure 3C.18a *ESR spectrum of $[Cu_2NGT](ClO_4)_3$ showing position where ENDOR spectrum recorded (*)*

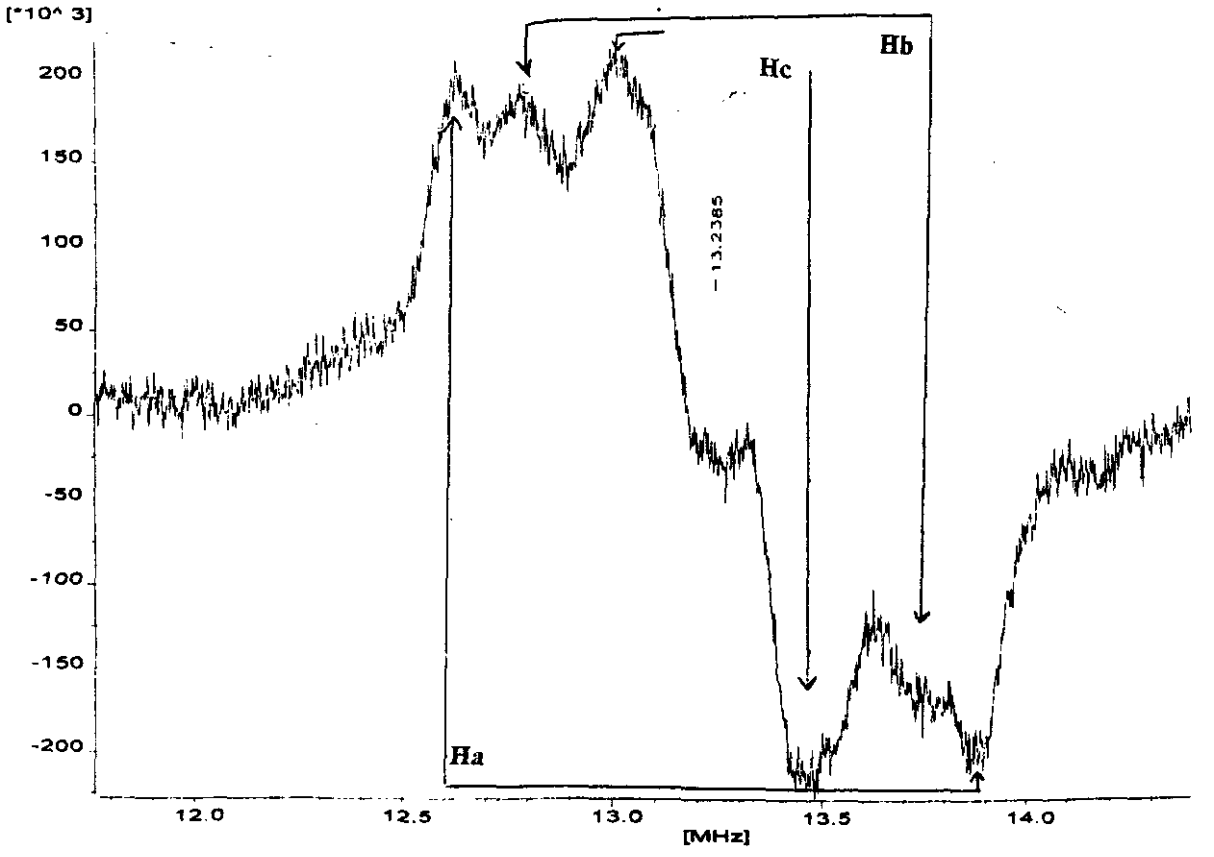

Figure 3C.18b *ENDOR spectrum of $Cu_2NGT](ClO_4)_3$ at 3110.14 Gauss*

3D Electrochemistry of Copper Cryptates

The catalytic activity of many metalloproteins is associated with a redox change of the metal ion, either in electron transfer processes or in oxidation or reduction of a substrate.[36] The redox potential of the metal ion is obviously of fundamental importance and is highly dependent on the nature of its binding site within the protein.

3D.1 Structural Preferences and Reactivity of the Copper Oxidation States

The large energy of hydration as well as the comparatively small radius of the Cu(II) ion contributes to the stability of Cu(II) over Cu(I) in aqueous solution. Among the reasons for the unique co-ordination chemistry of copper are the almost 'noble' character of the metal, the intermediate stability and reactivity of the d^{10} configuration in Cu(I).[37]

The character of the metal-ligand interaction in Cu(II) complexes is frequently, but not always, ionic and it has been found that pronounced Jahn-Teller distortion often leads to stabilisation of the Cu(II) state. Different extents of axial elongation of the octahedron can thus produce square-bipyramidal, square-pyramidal or square-planar co-ordination geometries. These are not favoured geometries for Cu(I) and thus deviations from these energy minimum structures are necessary for rapid Cu(II)/Cu(I) oxidation state changes and consequently for efficient electron transfer. These deviations may require specific, strained conformations (entactic state concept) achieved through ligand design as observed in electron-transfer in proteins or in low molecular weight model compounds.[38]

3D.2 Cryptands in Redox Studies

Complexes of synthetic macrocycles and cryptands have provided convenient systems for the evaluation of the dependence of oxidation/reduction properties on the detailed structure of the ligand, while imposing an approximately constant donor set and co-ordination geometry on a given metal ion. Such geometric constraints will influence the electron transfer kinetics of a particular redox couple as well as the thermodynamics of the system. The inertness of many

macrocyclic and macrobicyclic systems also makes them attractive for electrochemical studies since the redox changes are less likely to be influenced by competing equilibria involving ligand dissociation than those in non-cyclic systems.

Unfortunately, Cu(I) disproportionation in aqueous systems, as well as the geometric changes associated with Cu(I)/Cu(II) redox activity, often prevent full and meaningful studies on a series of ligands. However, Sargeson and co-workers[39] have successfully investigated the effect of cage ligand structure on redox potential of the (II)/(III) couple for the encapsulated cobalt ion. The use of cryptands in such studies prevents the metal ion binding different axial ligands or moving out of the plane of the ring as is possible in macrocyclic studies. Various types of change in cryptand structure have been investigated as have different bridgehead atoms (N or C), substituents on the bridgehead carbon atom, charged cages, cavity sizes, various degrees of unsaturation or ring strain in the cage.

Thus, the factors influencing redox potentials are summarised below:

1. Negative charges in the ligand favour the higher oxidation state of the metal ion.
2. Electron-withdrawing substituents stabilise the lower oxidation state.
3. Increase of cavity size favours the lower oxidation state.
4. Strong σ-donor ligands favour high oxidation states.
5. Strong π-acceptor donor ligands favour low oxidation states.

3D.3 Electrochemical Investigation of Dicopper Azacryptands

The siting of copper in a co-ordination environment composed of soft donors such as sp^2 N is a recurrent theme in bioinorganic chemistry. Such an environment frequently generates a borderline Cu(I)/Cu(II) stability for utilisation in enzyme-mediated redox transformations. We are interested in investigating the electrochemistry of the dicopper azacryptates owing to their possibility as models for the Cu_A site.

The electrochemical studies of the dicopper(I) and dicopper(1.5) cryptates were performed in collaboration with Drs. K. Lo and D. Keeley at the New Chemistry Laboratory, Oxford University.

3D.3.1 $[Cu_2(I)GT](ClO_4)_2$

In 50 mM aqueous phosphate buffer at pH 7.0, a reversible couple at + 190 mV Vs S.C.E. was recorded using a glassy carbon electrode. Similar observation was found when platinum or gold electrodes were used, (**Table 3D.1**).

Table 3D.1 ***$[Cu^{I}_2(GT)]^{2+}$: 0.2 mM solution in 0.1 M $NaNO_3$, Gold electrode, scan rate = 10 mV/s.***

Electrode	E_a^1	E_c^1	ΔE	I_{pa}/I_{pc}
$[Cu_2GT]^{2+}$	150	205	55	1.1

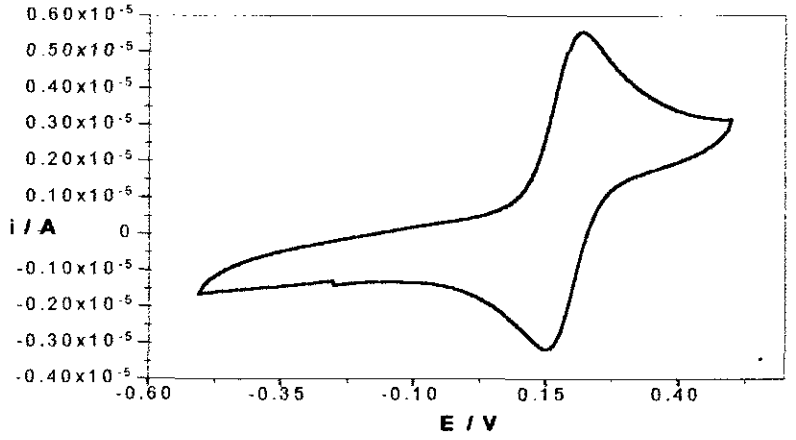

Figure 3D.1 ***$[Cu^{I}_2(GT)]^{2+}$: 0.2 mM solution in 0.1 M $NaNO_3$, gold electrode, scan rate = 10 mV/s.***

At this stage it was assumed that this was a reversible one electron oxidation of the dicopper complex to the mixed valent state. X-ray crystallography has also revealed the $[Cu_2^{I}GT]^{2+}$ and $[Cu_2^{1.5}GT]^{3+}$ dimers are isomorphous with one another providing further evidence for this idea. However, we cannot dismiss the possibility that there is in fact a two-electron oxidation forming $[Cu_2^{II}GT]^{4+}$. This idea is further discussed in **3D.3.3**.

The pH dependence was investigated and it was found that:

1. Above pH 7 some reversibility is lost and a second reduction peak appears at -120 mV.

2. Below pH 7 the 190 mV couple is unchanged whilst a sharp oxidation peak grows at - 95 mV. This resembles a copper stripping peak. It was found that this peak was due to the oxidation of an adsorbed species, possibly a protonated Cu(I) species.

3D.3.2 $[Cu_2(1.5)GT](ClO_4)_3$

Initial experiments on this average-valence complex were difficult to perform as it was found to have limited stability in an aqueous buffer solution. However in a 0.1 M $NaNO_{3(aq)}$ solution, the complex had sufficient stability (up to 3 to 4 hours under room-temperature conditions) before the blue-mixed valence colour changed to green. The UV-Vis spectrum of this green solution revealed the presence of a new absorption band at 390 nm as the absorption peaks at 608 and 764 nm became progressively weaker. The appearance of this familiar band at 390 nm indicates that the complex undergoes disproportionation with the formation of the complex $[Cu_2^{I}GT]^{2+}$ (and one or more Cu(II) species). There is also ESR spectral evidence for the formation of the mono $[Cu(II)GT]^{2+}$ complex.

The CV of $[Cu_2(1.5)GT](ClO_4)_3$ in 0.1 M $NaNO_3$ was carried out using a gold working electrode. Due to the decomposition problems the electrochemical measurements were carried out immediately after the addition of the solid sample of $[Cu_2(I,II)(GT)]^{3+}$ into the electrochemical cell. A reversible couple was seen at + 180 mV but the solution decomposed within 2 hours. This couple at + 180 mV is probably due to redox of the mixed-valence complex, although there is a possibility that it might arise from a two-electron oxidation of $[Cu_2^{I}GT]^{2+}$, formed as a product of disproportionation. Some copper deposition was also observed visually on the electrode and on the CV.

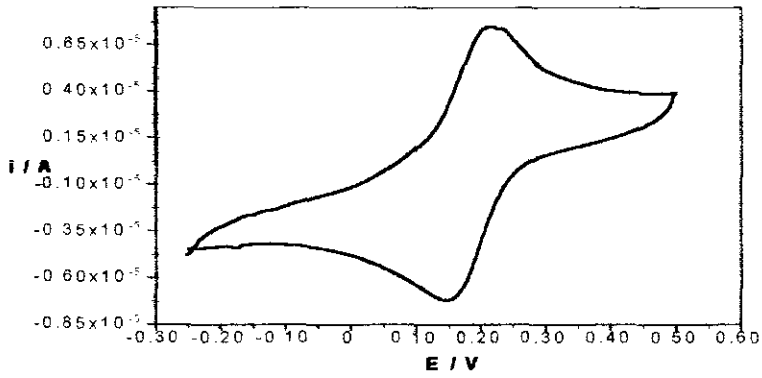

Figure 3D.2 $[Cu^{1.5}{}_2(GT)]^{3+}$: 0.2 mM solution in 0.1 M $NaNO_3$, gold electrode, scan rate = 20 mV/s.

In order to stabilise the average valence complex and confirm the nature of the redox process, CV measurements were repeated in the presence of silver ions. A solution of $AgNO_3$ (2 mM) in 0.1 M $NaNO_3$ reveals a strong oxidation signal at + 440 mV and a weaker reverse signal at + 310 mV due to Ag(I/O) redox, **(Figure 3D.3)**. This average valence complex was stable in solution for 24 hours. Afterwards, the complex appears to be oxidised to some Cu(II) species (perhaps Cu(II)Ag(I) or Cu(II)GT- the solution becomes pale blue in colour with some precipitation). Unfortunately, the important copper couple is embedded into the strong silver signals. Therefore, a less concentrated $AgNO_3$ solution was used.

The CV of a solution containing $[Cu_2(I,II)(GT)]^{3+}$ (893 uM, micromolar), $AgNO_3$ (223 uM) in 0.1 M $NaNO_3$ solution (Cu_2:Ag = 4:1) reveals a reversible couple at + 190 mV (E_{pc} = 220 mV, E_{pa} = 160 mV) and again strong silver signals centred at + 330 mV (E_{pc} = 380 mV, E_{pa} = 290 mV). The amplitudes of these two couples are comparable to each other. In other words, the copper couple can be resolved. The + 190 mV couple observed results from the oxidation of the reduced form of the mixed-valence complex $[Cu_2(I,II)GT]^{3+}$. At this stage we can't say if this is to $[Cu_2(I,II)GT]^{3+}$ or $[Cu_2(II,II)GT]^{4+}$.

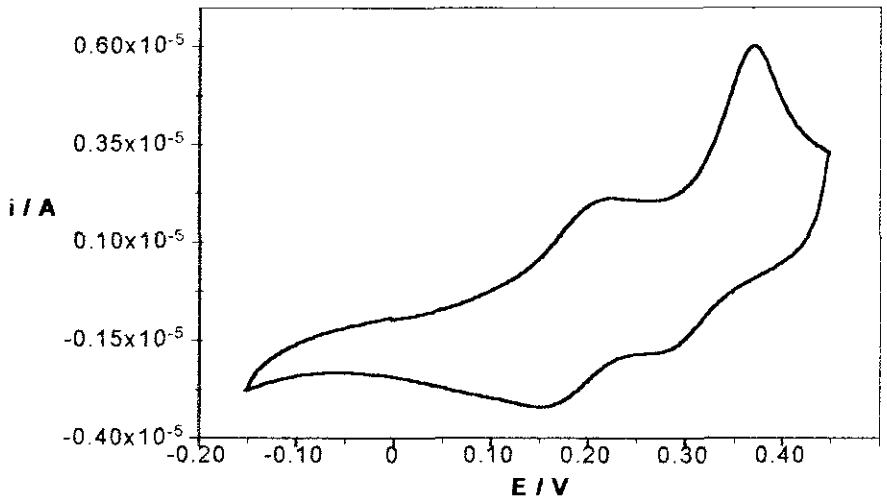

Figure 3D.3 ***$[Cu^{1.5}{}_2(GT)]^{3+}$: 893 μM solution in 0.1 M $NaNO_3$ in the presence of 223 μM $AgNO_3$. Gold electrode, scan rate = 20 mV/s.***

Table 3D.2 Electrochemical data for $[Cu_2GT]^{3+}$

Electrode	E_a^1	E_c^1	ΔE	I_{pa}/I_{pc}	E_a^1	E_c^1	ΔE	I_{pa}/I_{pc}
$[Cu_2GT]^{3+}$	150	220	70	1.2	No second couple observed			
$[Cu_2GT]^{3+}$ + Ag	160	220	80	-	Ag^+/Ag^o 280	380	90	-

3D.3.3 $[Cu_2(I)NGT](ClO_4)_2$

The electrochemical behaviour of $[Cu_2(I)NGT]^{2+}$ on a glassy carbon electrode is comparable to that of the analogous $[Cu_2(I)GT]^{2+}$. Using a 0.2 mM solution in 0.1 M $NaNO_3$ at a scan rate of 10 mV/s, the complex has a reversible couple centred at + 150 mV.

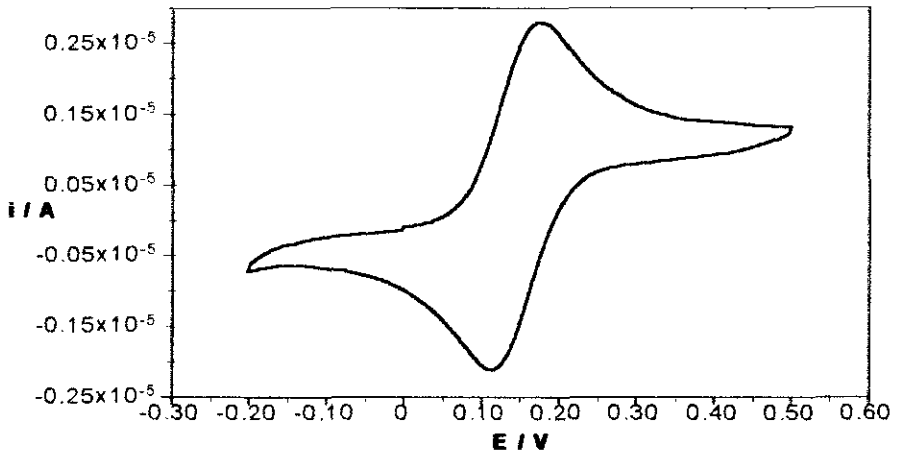

Figure 3D.4 ***$[Cu^{I}_{2}(NGT)]^{2+}$: ca. 0.2 mM solution in 0.1 M $NaNO_3$, EPG electrode, scan rate = 10 mV/s.***

However, the situation shows interesting differences when using a gold electrode. For a CV starting at 0 V (all Vs S.C.E) and scanning to the positive direction, there is a peak at + 200 mV and another one at + 320 mV. For the reverse scan there is a peak at + 110 mV. The peak heights for the forward ones were found to vary with scan rates. At high scan rates the more positive oxidation peak is of larger amplitude. At higher scan rate (such as 500 mV/s), a new hump at + 240 mV is discernible in the reverse scan. The hump may be the reduction signal corresponding to the oxidation peak at + 320 mV. However, at low scan rates i.e. 10, 5 and 2 mV/s, the reduction component of the second couple is gone and the second oxidation component becomes less visible. There is only one couple centred at *ca.* 150 mV which presumably corresponds to a reversible one-electron process, (**Figure 3D.5**).

Table 3D.3 Electrochemical data for $[Cu_2NGT]^{2+}$

[a] Scan rates 10, 5 and 2 mV/s

Electrode	E_a^1	E_c^1	ΔE	I_{pa}/I_{pc}
Glassy carbon	120	180	60	1
Gold [a]	100	200	100	-

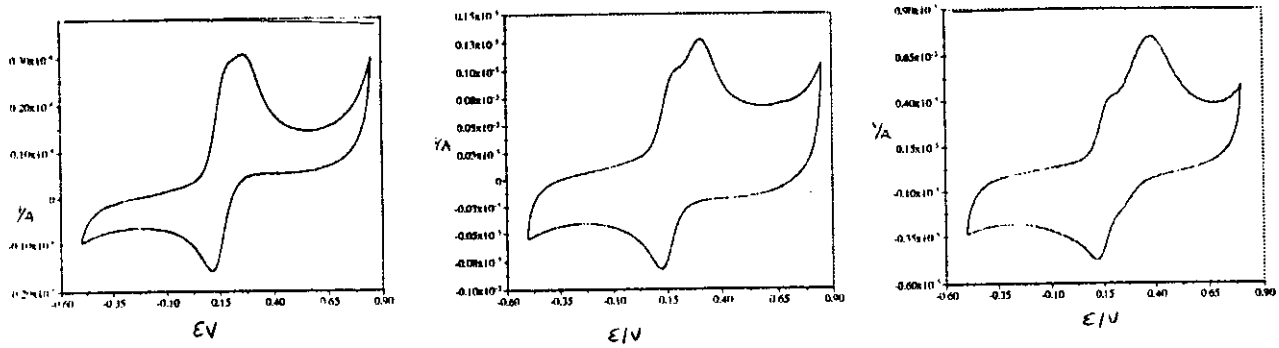

Scan rate = 5 mVs^{-1} Scan rate = 50 mVs^{-1} Scan rate = 500 mVs^{-1}

Figure 3D.5 $[Cu^{I}_{2}NGT]^{2+}$: ca. 0.2 mM solution in 0.1 M $NaNO_3$, gold electrode, scan rate = (a) 5 mVs^{-1}, .(b) 50 mVs^{-1}, (c) 500 mVs^{-1}.

Proposals for the Observed Electrochemical behaviour of $[Cu_2^{I}GT]^{2+}$ and $[Cu_2^{I}NGT]^{2+}$

(1) As we saw in Chapter 3A, the X-ray structural data shows that there is a contraction of 0.5 Å on going from the reduced dicopper(I) NGT to the oxidised average valence form. On the basis of these structural findings, one suggestion is that the least positive couple (+ 180 mV) is due to the oxidation of $[Cu_2(I)NGT]$ to $[Cu^{I}Cu^{II}NGT]^{3+}$. This localised mixed-valence complex is electroactive and its oxidation gives rise to the + 320 mV wave. There are two possibilities for the second transient couple :

(a) For fast scan rates, before the oxidised species 'shrink' to form the average valence complex, further oxidation of the mixed valence species to $[Cu_2(II,II)(NGT)]^{4+}$ can be observed. This is not stable hence the reverse signal (+ 240 mV) only shows up at higher scan rate. That the further oxidation of the (I, II) mixed valence species to the electrochemically unfavourable (II, II) state is not very endergonic may suggest some degree of bond formation (perhaps bond order) in the (II, II) state, insufficient however to compete with overall stability in the (I, II) state, **(Figure 3D.5c)**.

(b) At slow speeds the effective concerted process $Cu_2(I, I) \rightarrow Cu_2(1.5)$ is directly observed i.e. after the first electron transfer, the localised mixed valence transient species has enough time to rearrange its geometry and thus undergoes Cu-Cu bond contraction, leading to the formation of the average species $[Cu_2^{1.5}NGT]^{3+}$. This delocalised product cannot be

oxidised at an accessible potential (i.e. it is not electroactive) and hence no second couple is observed, **(Figure 3D.5a)**.

Table 3D.4 X-ray crystal data of Cu-Cu bond distances (Å) in GT and NGT.

$[Cu_2^{I}GT]^{2+}$	2.45	$[Cu_2^{I}NGT]^{2+}$.	2.93
$[Cu_2^{L5}GT]^{3+}$	2.36	$[Cu_2^{L5}NGT]^{3+}$.	2.42
Δd_{Cu-Cu}	-0.11	Δd_{Cu-Cu}	-0.49

It must be emphasised that this proposal cannot explain why the second wave shows up at low complex concentrations **(Figure 3D.6a)** and it cannot account for the fact that the GT system also exhibits similar electrochemistry, **(Figure 3D.6b)**. However, in the case of GT, it is also important to note that the complex is not stable during electrochemical measurement. It has been found that $[Cu_2^{I}GT]^{2+}$ and the mononuclear complex $[Cu(II)GT]^{2+}$ are formed from a disproportionation reaction.

(2) Another suggestion is that a two-electron oxidation is occurring producing $[Cu_2^{II}NGT]^{4+}$. This species subsequently undergoes conproportionation with $[Cu_2^{I}NGT]^{2+}$ in the bulk solution resulting in the more stable average-valence complex. This couple is the typical shape for a catalytic wave providing further evidence towards a conproportionation reaction.

$$[Cu_2^{II}NGT]^{4+} + [Cu_2^{I}NGT]^{2+} \rightarrow 2[Cu_2^{L5}NGT]^{3+}$$

The second wave is less significant for $[Cu_2^{I}GT]^{2+}$ than $[Cu_2^{I}NGT]^{2+}$. It appears that the conproportionation process between the highly reactive species $[Cu_2^{II}L]^{4+}$ and $[Cu_2^{I}L)]^{2+}$ in the bulk solution is much efficient for the GT complex than the NGT counterpart.

Unlike the first suggestion this proposal accounts for the fact that the second wave only shows up at low concentrations of the complex and at high scan rates. These results have stimulated much interest in understanding the mechanism occurring and further studies are in progress.

After considering the behaviour of the analogous NGT complex, it is also proposed that

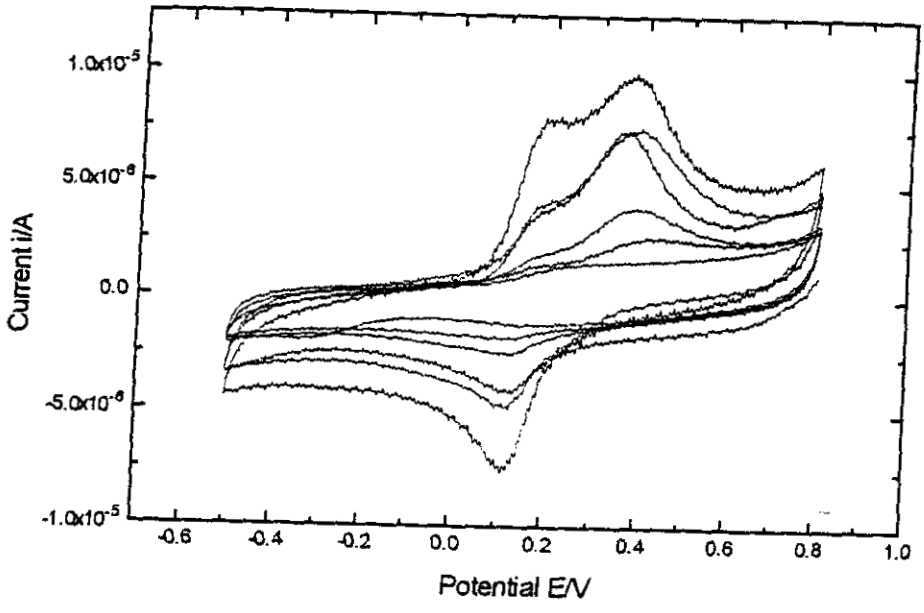

Figure 3D.6a Concentration dependence on electrochemistry of $[Cu_2NGT](ClO_4)_2$ at 500 mV/s. Conc. = 2, 1, 0.5, 0.2, 0.1 and 0.05 mM

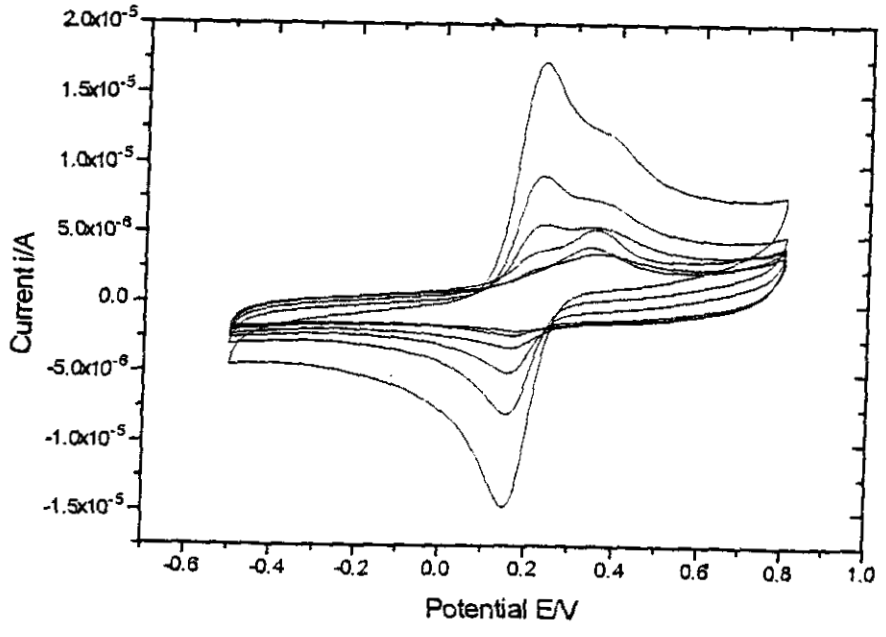

Figure 3D.6b Concentration dependence on electrochemistry of $[Cu_2GT](ClO_4)_2$ at 500 mV/s, Conc. = 2, 1, 0.5, 0.2, 0.1 and 0.05 mM

the couple at + 190 mV Vs. S.C.E. can be assigned to the oxidation of $[Cu^{I}_{2}(GT)]^{2+}$ to $[Cu^{II}_{2}(GT)]^{4+}$. This redox reaction is diffusion-controlled. The two-electron oxidation product, $[Cu^{II}_{2}(GT)]^{4+}$, is unstable and decomposes readily forming a mixture of products.

3D.3.4 $[Cu_2(1.5)RGT](ClO_4)_3$

Investigations with this system revealed that behaviour of this compound is dependent on both the electrode surface used and also the pH (as befits the more basic ligand). **(Figures 3D.7 and 3D.8).**

Above pH 7 the cyclic voltammograms show little dependence on pH, whilst below pH 7, a sharp oxidation peak at ~ - 50 mV is seen. The peak grows as the pH is lowered and has been found to be due to a strongly adsorbed species. When a glassy carbon electrode is used the couple is present without prior reduction of $[Cu_2(1.5)RGT]^{3+}$.

Using a glassy carbon electrode a prominent couple with a mid-point potential of - 380 mV and a smaller couple at - 110 mV are observed. The couple at the more positive potential is still obscured when the potential is maintained above that necessary for the second reduction. This implies that the couple is not due to a product of the redox process at - 380 mV but is most likely due to the oxidation of a second component - perhaps a protonated mononuclear copper cryptate. Neither of the couples are a result of the adsorption of species on the electrode surface.

3D.5 Electrochemical data for $[Cu_2RGT]^{3+}$

Electrode	E_a^1	E_c^1	ΔE	I_{pa}/I_{pc}	E_a^2	E_c^2	ΔE
Glassy carbon	-410	-350	60	1.1	-140	-100	40
Gold	-410	-350	60	-	+180	+ 60	60

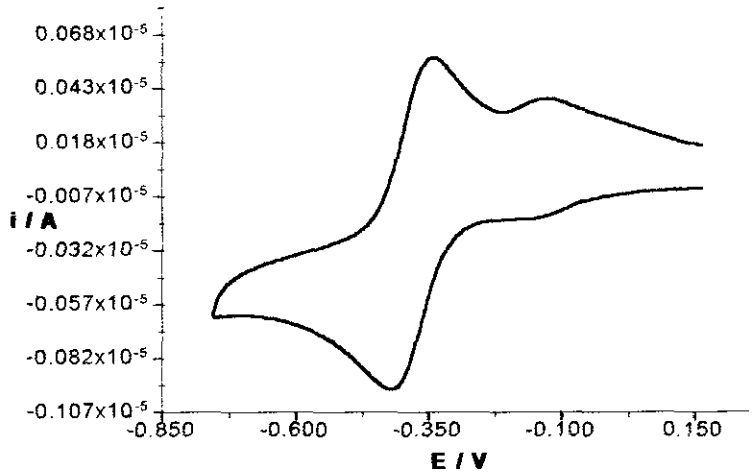

Figure 3D.7 $[Cu^{1.5}{}_2RGT]^{3+}$: 0.2 mM solution in 50 mM phosphate buffer at pH 7.0. EPG electrode, scan rate = 20 mV/s.

Using a gold electrode the couple at - 380 mV is again observed but a second component is observed at higher potential, 120 mV, which is now comparable in intensity to the - 380 mV one, **(Figure 3D.8)**.

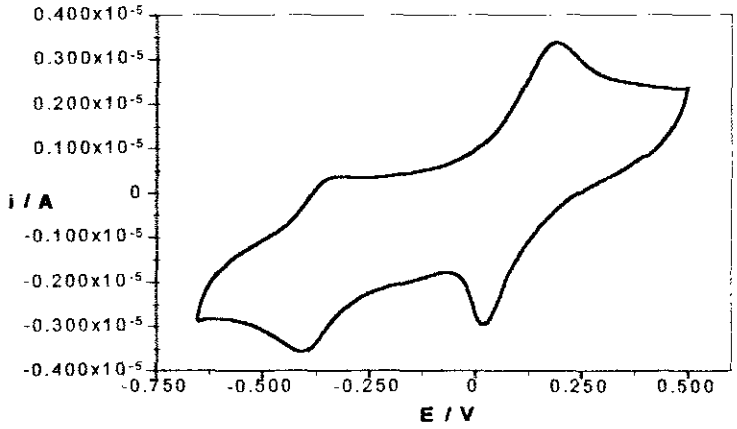

Figure 3D.8 $[Cu^{1.5}{}_2RGT]^{3+}$: 0.2 mM solution in 50 mM phosphate buffer at pH 7.0. Gold electrode, scan rate = 20 mV/s.

This second couple seems to be a product of the reduction of $[Cu_2(1.5)RGT]^{3+}$ as it can only be seen if the potential is swept below - 380 mV. The species appears to be weakly adsorbed onto the electrode although it has completely desorbed after two successive scans. It seems that the second couple (120 mV) is due to the two-electron oxidation of adsorbed $[Cu_2(I)RGT]^{2+}$ to $[Cu_2(II)RGT]^{4+}$. The -380 mV near-reversible couple is attributed to the +2/+3 redox process.

The sharp reduction peak at *ca* 0.4 mV only appears when the potential is scanned below - 380 mV. This may be due to a decomposition product of $[Cu'_2RGT]^{2+}$ which has only a transient existence on the electrode.

3D.4 Comparison of Imine versus Amine Azacryptates

The imine hosts, GT and NGT, favour enhanced thermodynamic stability of the +1 oxidation state in the encapsulated copper ion, while the amine host, RGT, shows an enhanced stability of the +2 redox state.

Where thermodynamic considerations permit access to both the +2 or mixed valence state of copper encapsulated within the imine cryptates, kinetic factors must be responsible for stabilising the dicopper(I) state in aqueous media under aerobic conditions. (E° values $[Cu_2^{I}GT]^{2+}$ = 195 mV , $[Cu_2^{I}NGT]^{2+}$ = ~ 150 mV (Vs Ag/AgCl), Vs O_2/H_2O pH 7 = 1230 (Vs H_2/H^+) mV in aqueous media).

The implication is that $[Cu_2^{I}GT]^{2+}$ and $[Cu_2^{I}NGT]^{2+}$ in aqueous media are thermodynamically capable of being oxidised by atmospheric oxygen. These cryptates are stable in air, as judged by the absence of colour change or development of ESR spectra on exposure to air or dioxygen. As the redox potential of the O_2/H_2O couple under neutral conditions is close to that of Ag/Ag^+, examination of the response to Ag^+ oxidation can give information on the existence of kinetic barriers to air oxidation.

As previously discussed treatment of $[Cu_2^{I}GT]^{2+}$ and $[Cu_2^{I}NGT]^{2+}$ with Ag^+, instantly generates the average valence intensely blue $[Cu_2^{I}GT]^{3+}$ and $[Cu_2^{I}NGT]^{3+}$ species, respectively. Although a blue colour can be observed in aqueous solutions of $[Cu_2^{I}GT]^{2+}$ exposed to an oxygen atmosphere after a period of weeks - UV/Vis spectra show that this is not the average

valence product. In an aqueous solution of $[Cu_2NGT]^{2+}$ no blue colour develops within a period of weeks.

3D.5 Conclusion

In summary, none of the dicopper(I) cryptates of the azacryptand series studied by Nelson (**Figure 3A.1**) react with atmospheric oxygen in aqueous solution, despite the favourable thermodynamics evident in many cases.

The ease of reduction of the average-valence GT to a Cu(I) complex results from a co-ordination environment that favours tetrahedral geometry. The α-diimine groups of the GT and NGT cryptands are likely to contribute to the elevation of the Cu (I,I)/ Cu(I,II) redox potential since they can exert effective withdrawal of electron density from the metal through the π system. This stabilisation of low oxidation studies also extends even to a (O,O) redox state. Reversible reduction of $[Cu_2'GT]^{2+}$ in CH_3CN to a Cu(O) species has been observed in Belfast some time ago. Further investigation of the reduction in imine systems will be carried out using acetonitrile as the solvent.

The transient peaks corresponding to the Cu(II,II) state on a gold electrode are very interesting in a bioinorganic context and suggest the possibility of a bonding interaction in sterically constrained Cu(II,II) which warrants further investigation. Further, the electrochemistry of $[Cu_2'GT]^{2+}$ and $[Cu_2^{I}NGT)\ ]^{2+}$ are being undertaken using a rotating disk and ring disk electrode. If these experiments support the hypothesis of Cu^{II}-Cu^{II} bonding, rapid spectroscopic monitoring of the redox process would be of considerable interest.

3E NMR of Azacryptates

3E.1.0 Nuclear Magnetic Resonance (NMR)[40]

A proton has the spin quantum number I = ½ which generates, in a magnetic field, (2I + 1) two energy states. These are characterised by the nuclear spin quantum number M_I = + ½ and M_I = - ½ and are separated by the amount ΔE which is field dependent.

Equation 3E.1

$$\Delta E = h\gamma B_o/2\pi$$

In the absence of a magnetic field these states are degenerate and therefore equally populated. However, on application of a magnetic field, B_o, they become non degenerate with the lower energy level parallel to the applied field and corresponding to M_I = + ½ and labelled α. The upper state with M_I = - ½ in which the magnetic moment is anti-parallel to B_o is labelled β.

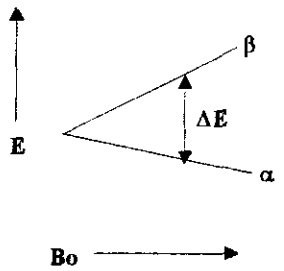

Figure 3E.1

These states are unequally populated, the ratio of the population being given by the Boltzmann equation:-

Equation 3E.2

$$N\beta/N\alpha = \exp(-\Delta E/kT)$$

Nβ = the population of the lower state, Nα = the population of the upper state.

The bulk magnetisation, M, which is the sum of the individual spins, is aligned with the applied field and can be conveniently described using vector diagrams as the Z direction, (**Figure 3E.2**).

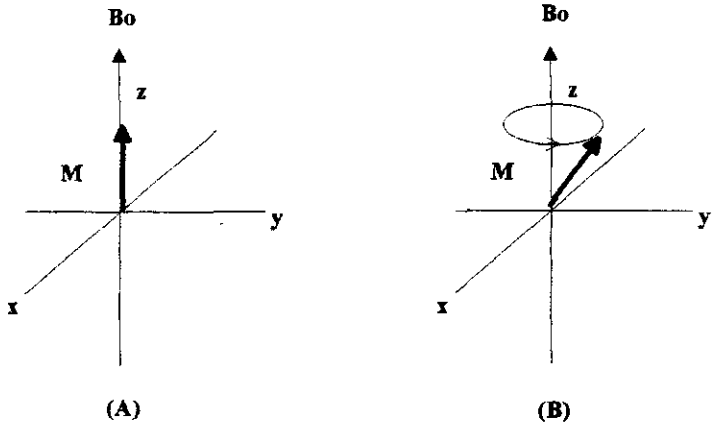

Figure 3E.2 The behaviour of the bulk magnetisation, M (A) at equilibrium and (B) after perturbation by the pulse.

The NMR phenomenon occurs when nuclei aligned with the applied field are induced to absorb energy and change their spin orientation with respect to their applied field. Irradiation at an appropriate radiofrequency B_1 (which is applied along the x axis perpendicular to B_o) causes displacement or preturbation of the induced magnetisation from the applied field which in turn causes a torque force to be generated by B_o on M which results in precission of M about B_o at a frequency γB_o radians/second. This motion is known as the *Larmour precession*. As can be seen from the vector diagram **Figure 3E.2B**, a component of the precessing magnitisation has now been introduced in the xy plane.

After perturbation the system will behave like any other physical system and return to equilibrium i.e. the population of the states will return to a Boltzmann distribution and magnetisation will again be aligned along the field axis and have an equilibrium value M_o. The return to equilibrium i.e. the population of the states will return to a Boltzmann distribution and magnetisation will again be aligned along the field axis and have an equilibrium value M_o. The return to equilibrium is not instantaneous but usually occurs with a first order rate constant, R, via *spin-lattice* and *spin-spin relaxation.*

3E.1.1 Spin - lattice Relaxation (T_1)

The M_z component of the magnetisation can return to equilibrium when an interaction between the spin nuclei and the random magnetic fields of the surroundings or lattice occurs which originate in the rotations and the translations (but not vibrations which are too high in frequency) of the neighbouring molecules. A number of mechanisms contribute to the exchange of energy between the spin system and its surroundings (e.g. dipole-dipole interactions with other nuclei) and additively result in what is known as spin - lattice relaxation. This is responsible for maintaining the unequal distribution of spin states and is given a first order rate constant R_1. Since relaxation phenomena are usually studied by time dependence measurements, it is common to see the relaxation time constant T_1 (which in effect is equal to half life time required for a perturbed system of a nucleus to reach equilibrium conditions) used rather than the relaxation constant.

Equation 3E.3

$$R_1 = 1/T_1$$

For the ^1H or ^{13}C nuclei in diamagnetic molecules in solution R_1 is of the order of a few s^{-1} or less and will therefore require a time of the order of a few seconds for spin system to return to equilibrium. (T_1 can be measured using the inversion recovery technique in NMR).

3E.1.2 Spin - spin relaxation (T_2)

The xy component of magnetisation will also relax to equilibrium, however the xy magnetisation can also be lost by an additional contribution to relaxation which involves the upper state transferring its energy to neighbouring identical nuclei by mutual exchange of spin (scalar interactions) causing the components of the xy magnetisation to fan out or dephase producing a net xy magnetisation of zero. The relaxation rate constant in the xy plane is described by R_2, while the relaxation time constant is denoted by T_2 and are related as follows:-

Equation 3E.4

$$R_2 = 1/T_2$$

If the signal decays rapidly (i.e. large R_2 or short T_2) the line in the spectrum is broad; conversely if the line is sharp, R_2 is small and T_2 is long resulting in the spin - spin relaxation to be slow. (T_2 can also be measured by the *Hahn's spin echo* technique). The resonance line width can be determined by **Equation 3E.5**.

Equation 3E.5

$$\Delta V_{1/2} = R_2/\pi$$

$\Delta V_{1/2}$ = the full width at half the height of the peak.

These additional processes do not necessarily require any change in energy and result in a $T_1 \geq T_2$ relationship being adhered to.

The rate of absorption (resonance) is consequently governed by the rate of relaxation of the H^+ to the ground state which in turn relates to the intensity of signal. Water protons have a naturally fast relaxation rate and this can be enhanced or catalysed by the close proximity of a paramagnetic ion such as Mn^{2+}, Fe^{3+}, Cr^{3+}, Cu^{2+} or Gd^{3+}.

3E.2.0 Solid state NMR

The major difficulties of solid state NMR are all associated with the immobility of the nuclei in solids. The first major difficulty with solids is that dipolar couplings are not averaged to zero by molecular tumbling and that long range couplings are also important because the material is not fluid. The combined effect of these couplings is to give very broad resonances. Secondly, the chemical shift of a nucleus depends on the orientation of the molecule with respect to the magnetic field, and in solids the effect of this chemical shift anisotropy is not averaged out by molecular tumbling, and so leads to line broadening. Finally, because of the immobility of the nuclei, the relaxation time T_1 is very long leading to spectra with poor signal-to-noise ratios.

However, these very large linewidths can be reduced. The effects of chemical anisotropy can be averaged out by a technique known as Magic Angle sample Spinning (MAS). If a sample is rotated rapidly about an axis inclined at an angle θ to the magnetic field, the

expression describing the line broadening due to chemical shift anisotropy includes a term $(3\cos^2\theta - 1)$. When θ is 54.7 (i.e. the magic angle) this term vanishes, and so the anisotropy effects can be eliminated providing the rotation is rapid enough. This will reveal fine structure which was previously obscured.

In practice the rotation rate is limited by the mechanical strength of sample containers. Modern materials enable rotation rates sufficient for the removal of line broadening due to chemical shift anisotropy for nuclei such as ^{13}C to be achieved but for some other nuclei, particularly those of heavy elements, the rotation is not fast enough. Consequently each single resonance in a spectrum is replaced by a central line and a series of uniformly spaced spinning sidebands.

Provided the rotation rate is greater than the linewidths, dipolar couplings are also averaged by magic angle spinning, just as they are for molecules tumbling in solution. The problem of long relaxation times remains. This is particularly important for dilute spin, insensitive nuclei, but it may be overcome for dilute nuclei with spin ½ in the presence of abundant spins, by a technique known as cross-polarisation (CP). The effect of this is to transfer magnetisation from the abundant spin (usually ^1H) to the dilute spin such as ^{13}C or ^{15}N.

Using one or more of these methods (the combination of magic angle spinning with cross polarisation is often referred to as the CP-MAS technique), high resolution spectra of solids may be obtained.

Many examples in the literature show how solid phase NMR studies can be used to investigate interactions between molecules.[41] In addition, this technique can be used in conjunction with solution NMR studies and will also show up any major changes in structure within a molecule on going from solution to solid phase.

3E.3. NMR Study of Azacryptates

NMR spectroscopy can provide valuable data on the rates of dynamic processes, and as the dicopper(I) cryptates are diamagnetic, we can look at how the NMR solution spectra may vary with temperature. A study of the free ligand GT was also undertaken. For comparison, the MAS solid state spectra of these complexes and the parent ligand have also been studied.

3E.4. Solution NMR

3E.4.1. ^{1}H and ^{13}C Solution NMR of Free ligand GT

The good solubility of GT in non-polar solvents allowed observation of both ^{1}H NMR and ^{13}C NMR spectra in $CDCl_3$ solution. A sharp singlet at δ 7.75 ppm is observed at all temperatures in the ^{1}H NMR spectra. The fluxionality of the methylene bond at ambient temperature is evident from the observation of only three signals in the high field region of the spectra; these are broad and thus near coalescence. By lowering the temperature the signals broaden further, then gradually sharpen until at 218 K each of the methylene groups are frozen out into a well resolved triplets and doublets set i.e. AA'BB' spectrum. In these systems, as previously reported by N. Martin[12], the more shielded upfield methylene group ($H_{d,e}$) is assigned to the CH_2 group α to the bridge N while that of the CH_2 group ($H_{b,c}$) α to the imine N is assigned to the lower field signals. This is a result of the local anisotropic field from the imine group deshielding the $H_{b,c}$ protons relative to the $H_{d,e}$ protons. Again the geminal coupling splits the signal from the equatorial proton into a doublet and further splitting resulting from the small vicinal coupling is not resolved. The triplet feature arises from the accidental equality of unrelated couplings i.e. axial protons which are split firstly by geminal coupling to the equatorial proton and then further split by vicinal coupling to the axial proton on the adjacent carbon both have coupling constants in the order of J = 10-12 Hz. Vicinal axial/axial coupling is efficient compared to that between axial/equatorial components which is therefore usually not resolved.

In the ^{13}C NMR spectrum a simple three line spectrum corresponding to equivalence of the three strands and both ends is observed at 300 K, **(Figure 3E.3c)**.

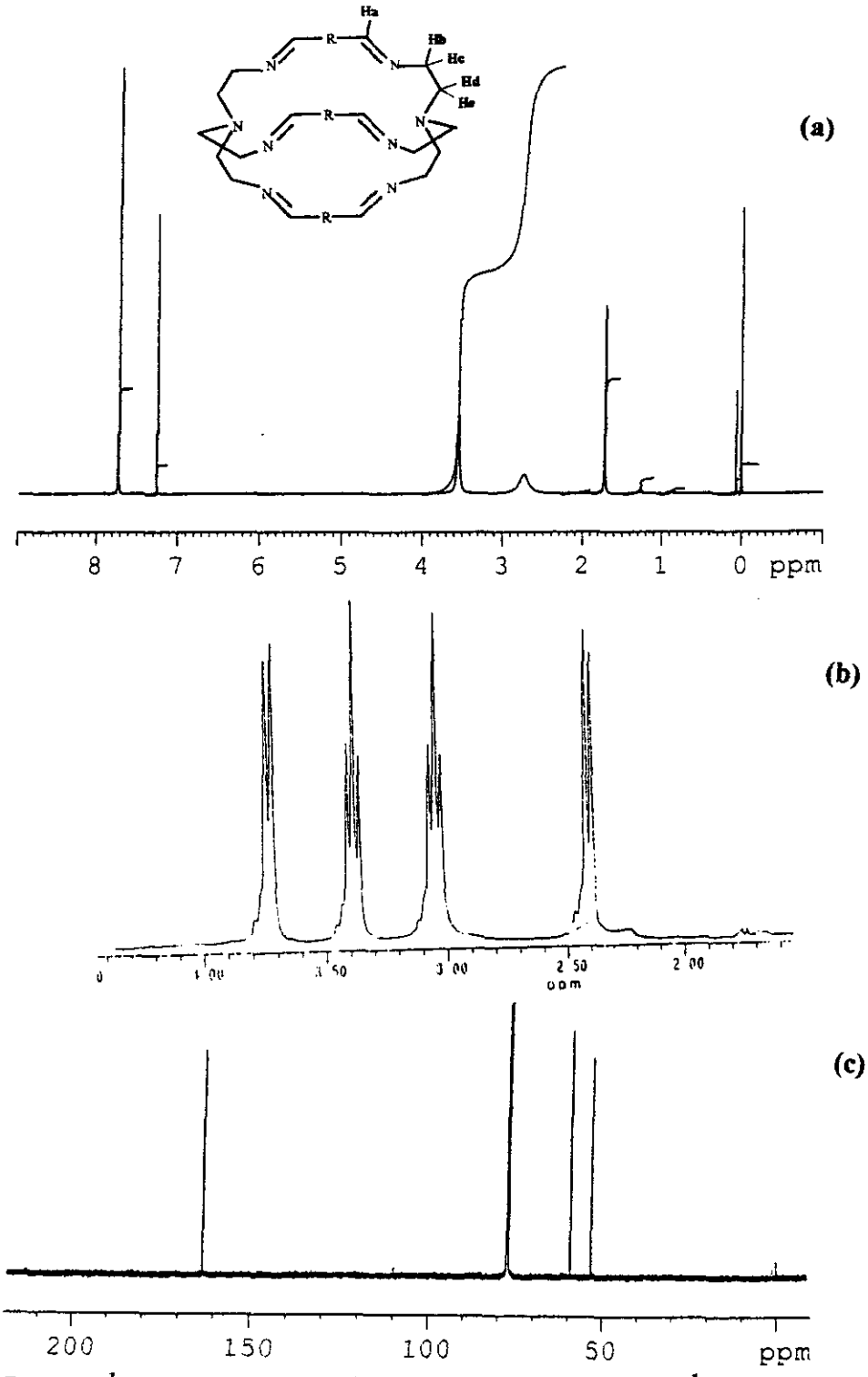

Figure 3E.3 (a) ^{1}H NMR free ligand GT in $CDCl_3$ at 298 K, (b) ^{1}H NMR GT in $CDCl_3$ at 218 K (c) ^{13}C NMR

Table 3E.1 ^{1}H NMR data for free ligand GT

T/K	Lattice solvent	H_a	H_b	H_c	H_d	H_e
298	1.31, 2.78	7.70	3.60		2.75	
218		7.80	3.74 (d)	3.42 (t)	3.08 (t)	2.42 (d)

3E.4.2 ^{1}H NMR of $[Cu_2^{I}GT]^{2+}$

The presence of only one imine and two methylene sets of protons shows symmetric placement of two copper ions in the cavity. The ^{1}H NMR spectrum of $[Cu_2^{I}GT[(ClO_4)_2$ in d_3-MeCN at ambient temperature is shown in **Figure 3E.4b** The spectrum is simpler than its parent ligand but is well resolved (similar to those reported by J Hunter[13] and N. Martin[12]). Two sets of unresolved triplets arise due to vicinal coupling of the methylene protons α to the imine with the pair adjacent to the N bridgehead and vice versa. The appearance of just two sets of triplets in the methylene region shows that axial and equatorial protons are not differentiated i.e. these protons are rapidly exchanging. This is due to some dynamic process taking place faster than the NMR timescale which allows their interchange, so a time-averaged chemical shift and coupling are seen.

There is no evidence of lability in this case - on addition of free GT the broad spectrum of both the Cu(I) cryptate and the free cryptand can be seen independent of one another, **Figure 3E.4c**. The unresolved triplet pattern for the methylene protons may arise because the donor disposition necessary for dinuclearity in this small cryptate necessitates a more open conformation of the methylene cap, thus generating greater mobility of conformation.

3E.4.3 ^{1}H NMR spectrum of $[Cu_2^{I.5}GT]^{3+}$, $[Cu^{II}GT]^{2+}$,$[Cu^{II}RGT]^{2+}$ and $[Cu_2^{1.5}RGT]^{3+}$

^{1}H NMR spectroscopy is not viewed as a viable solution characterisation technique for paramagnetic Cu(II) complexes because slow electronic relaxation leads to broad and often unobservable resonances. However, ^{1}H NMR spectroscopy has been shown to be applicable to characterisation of the structure of binuclear Cu(II) complexes with magnetic coupling that ranges from weakly ferromagnetic to strongly antiferromagnetic.[42]

Because there is limited information on average valence species in the literature ^{1}H NMR of all complexes was attempted. Average-valence dicopper complexes show broadness underneath the ^{1}H NMR peak positions of the free ligand. The position of this resonance is in the same region but is broadened beyond recognition. Both ^{1}H NMR and 2D COSY spectra in D_2O were recorded and the downfield region to 100 ppm examined, **(Figure 3E.5)**.

It seems that the dicopper(I) species is always present, to some extent, in a solution of $[Cu_2^{1.5}GT]^{3+}$, therefore the observation of broad peaks at dicopper(I) resonance positions could have been due to the diamagnetic complex being broadened by the paramagnetic average

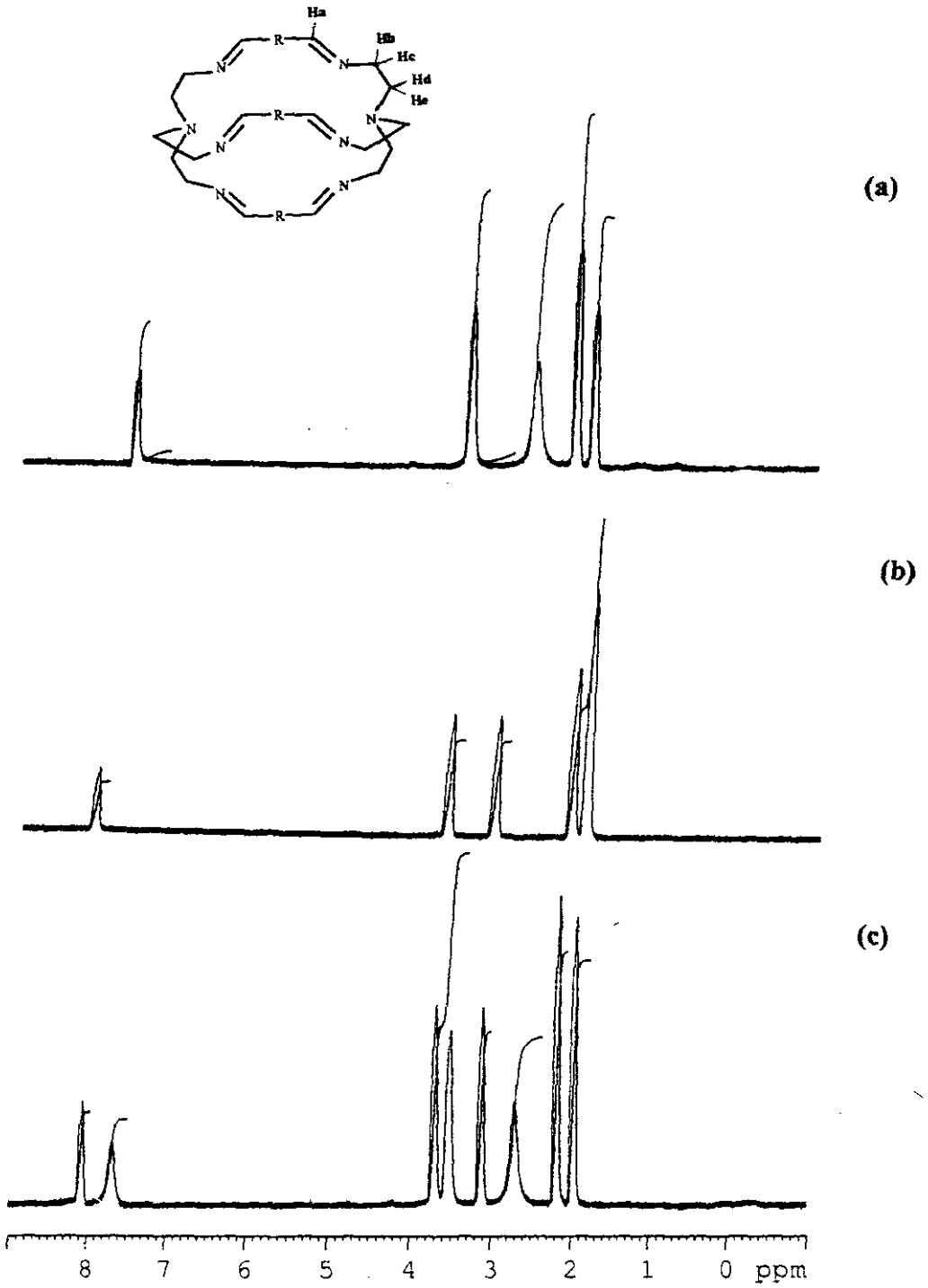

Compound d_3-MeCN	Lattice solvent	H_a	H_b	H_c	H_d	H_e
GT	1.90	7.60	3.40		2.60	
$[Cu_2GT](ClO_4)_2$	1.90	8.10	3.75		3.10	

Figure 3E.4 (a) ^{1}H NMR free ligand GT in d_3MeCN at 298 K, (b) ^{1}H NMR $[Cu_2GT](ClO_4)_2$ in d_3MeCN at 298 K (c) ^{1}H NMR of GT and $[Cu_2GT](ClO_4)_2$ in d_3MeCN at 298 K

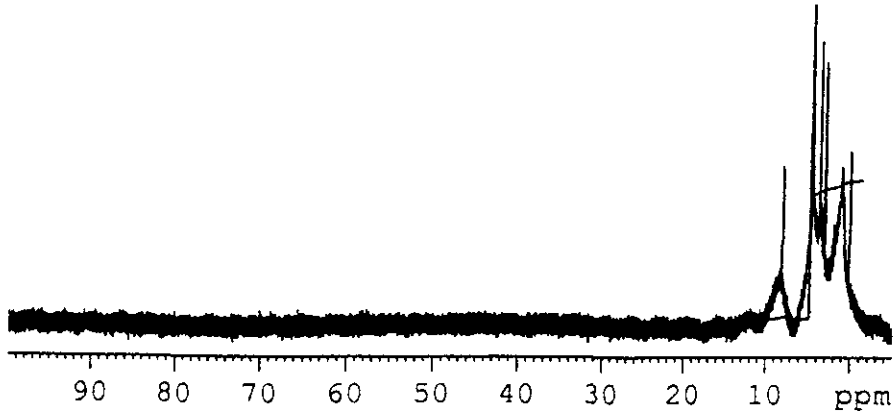

Figure 3E.5 *^1H NMR of $[Cu_2GT](ClO_4)_3$ in D_2O- no evidence of paramagnetic shifting*

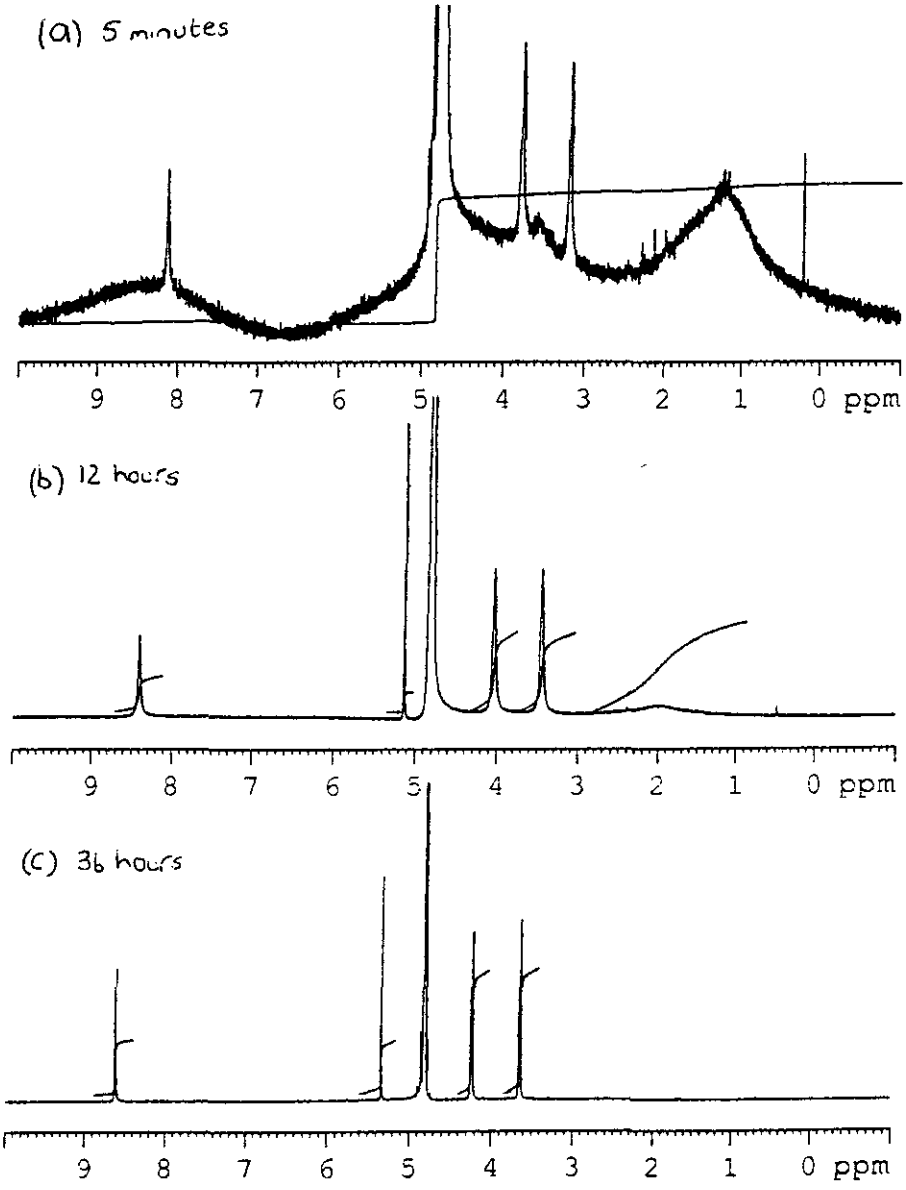

Figure 3E.6 *^1H NMR of $[Cu_2GT](ClO_4)_3$ in D_2O - decay to $[Cu_2GT](ClO_4)_2$ and an undetectable Cu(II) species.*

valence complex. The observation of similar broadening in the average valence dicopper cryptate of the amine host, RGT, where a dicopper(I) species is unlikely, leads us to assume that average valence species cause only broadening of the proton resonance but does not appreciably shift them. **Figure 3E.6** shows how the average valence product decays over a period of days leaving a dicopper(I) cryptate and an unknown Cu(II) complex which is undetectable by ^{1}H NMR.

3E.4.4.1 ^{1}H NMR spectrum of $[Cu_2^INGT]^{2+}$

Proton ^{1}H NMR spectra for $[Cu_2^INGT]^{2+}$ recorded at room temperature in d_3-MeCN exhibit more complex ^{1}H NMR spectra than the analogous tren-capped dicopper azacryptates. This suggests solvolysis and/or the existence of more than one solution conformation of this complex. The ability to recover the original $[Cu_2NGT](ClO_4)_2$ from the solvent suggests that if solvolysis exists it is reversible.

Despite the barriers to full assignment caused by substantial overlapping of signals in d_3-MeCN, especially in the methylene region, valuable conformational information could be obtained from D_2O solution spectra. Because $[Cu_2NGT]^{2+}$ is more flexible than the tren-capped analogue, $[Cu_2GT]^{2+}$, the NGT ligand can be more tightly co-ordinated, and thus shows differentiation of axial and equatorial methylene protons at ambient temperatures.

In D_2O the copper cryptate exists in just one dinuclear conformation in solution. There is only one imine signal and a set of resonances in the methylene region that can be attributed to the CH_2 groups. The presence of more than one imine resonance would indicate asymmetry in the siting of the copper ions. The pair of copper ions are held securely in the cavity and do not exchange very fast, nor is any other rapid dynamic process in operation. The D_2O experiment seems to show, on first sighting, a simple coupling pattern suggesting, as in the case of free GT, the existence of accidental equivalent geminal, axial/equatorial and axial/axial vicinal coupling which can be confirmed by decoupling experiments, **(Figure 3E.7)**.

3E.4.4.2 Decoupling Experiment of $[Cu^I_2NGT]^{2+}$ in D_2O

On first glance at the methylene region a doublet, triplet, triplet, multiplet, doublet pattern is seen. The simplicity of the pattern is similar to that reported for the free cryptands with the expected additional signals due to the extra methylene group. The axial proton which

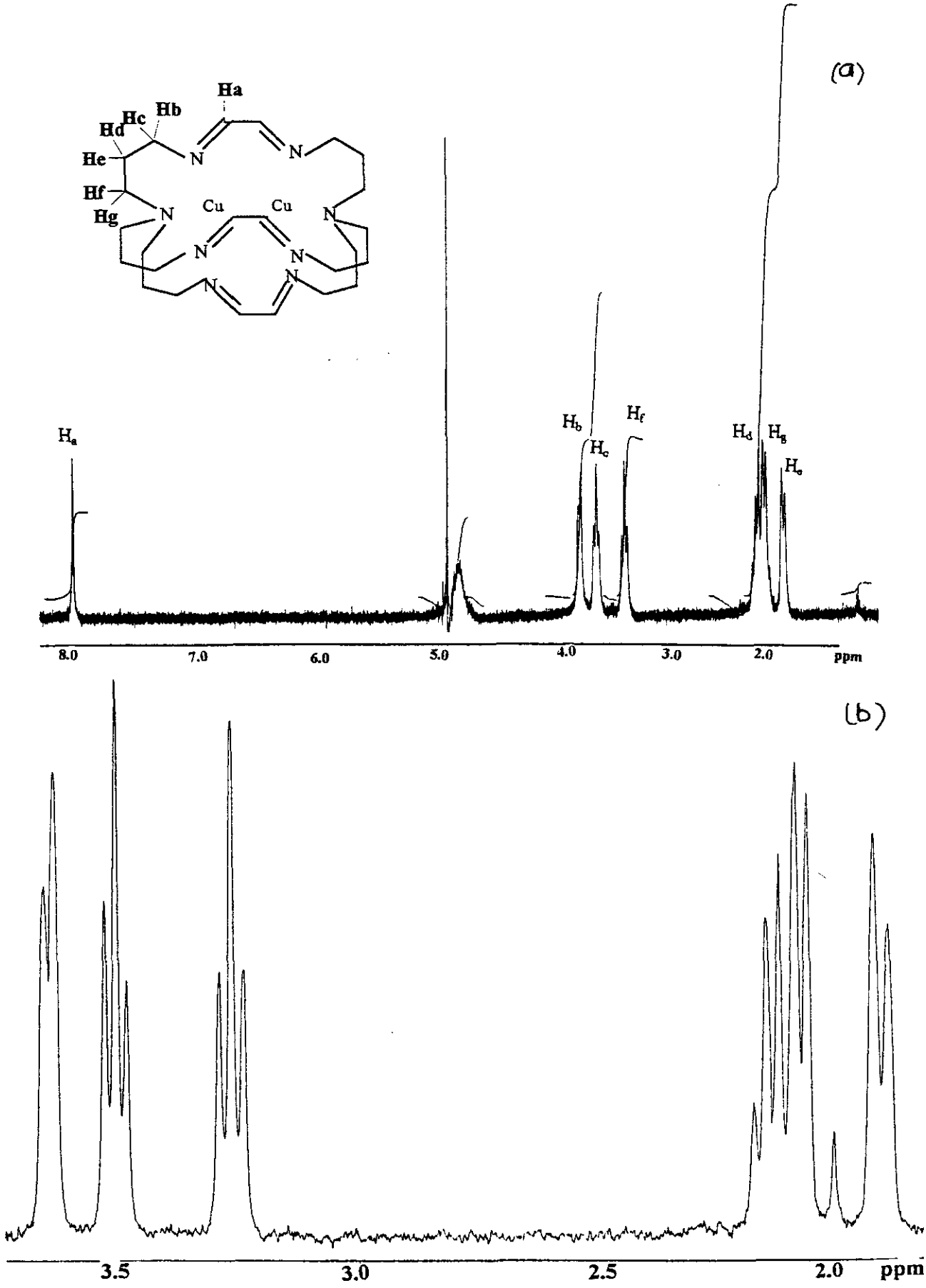

Figure 3E.7 ^1H *NMR of* $[Cu_2NGT](ClO_4)_2$ *in* D_2O *(a) full spectrum, (b) methylene region*

is between two methylene neighbours, appears as the multiplet while the equatorial signal for this central methylene remains a doublet. However, further investigation is needed in order to determine which doublet couples to which triplet. A decoupling experiment as well as 2D COSY was carried out in order to assign the accidental equality of peaks. As discussed for GT a doublet/triplet/triplet/doublet pattern arises for each extreme methylene due to geminal coupling occurring within each methylene, with vicinal coupling to axial protons on adjacent carbon atoms, **(Figure 3E.8)**.

Assignment of H_b/H_c and H_f/H_g

The protons H_b and H_c are next to an imine group and as a result of deshielding will occur downfield relative to the protons on the remaining methylenes (H_d, H_e, H_f and H_g). Irradiation of the doublet at δ 3.67 ppm causes the triplet at δ 3.54 ppm to become a doublet (J = 10.70 Hz), **(Figure 3E.8a)**. This is because geminal coupling of the axial and equatorial protons is lost and only axial/axial coupling with the neighbouring methylene proton (H_d) is occurring. The same pattern is seen when the doublet of H_f at δ 2.07 ppm is irradiated - the triplet at δ 3.30 ppm becomes a doublet (J = 10.70 Hz), **(Figure 3E.8b)**.

Irradiation of the triplet at δ 3.54 ppm, **(Figure 3E.8c)**, causes the doublet at δ 3.64 ppm to become a singlet as axial/equatorial geminal coupling is lost. This is expected and the same pattern arises when irradiating the triplet at δ 3.30 ppm - this doublet hidden within the multiplet at δ 2 - 2.2 ppm becomes a singlet, **(Figure 3E.8d)**.

Assignment of Hd/He

When the triplets at δ 3.54 and δ 3.30 ppm are irradiated, **(Figures 3E.8c and 3E.8d)**, the multiplet at δ 2.1 ppm resembles a doublet of doublets indicating that the triplets arise from coupling by accidentally equivalent axial/axial vicinal and axial/equatorial geminal coupling. The doublet at δ 1.90 ppm is unaffected as it arises only from geminal coupling of H_d/H_e. **Figure 3E.8e** shows that decoupling of the multiplet at δ 2.1 ppm causes the triplets to become doublets. They have lost axial/axial coupling of vicinal protons. The doublet at δ 1.90 ppm, arising from geminal axial/equatorial coupling, becomes a singlet confirming the assignnment of this doublet and the multiplet as due to proton H_d/H_e.

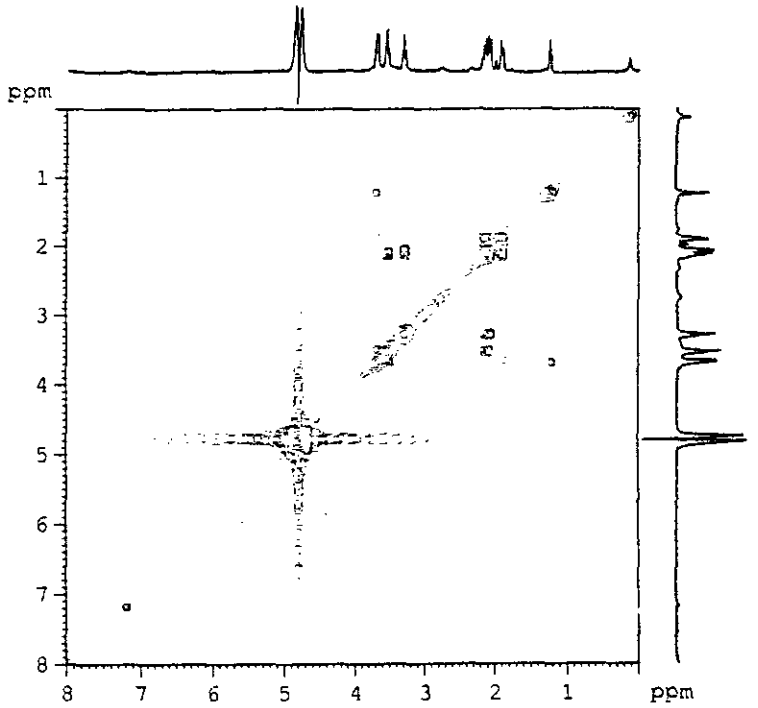

Figure 3E.7c 2D COSY spectrum of $[Cu_2NGT](ClO_4)_2$]

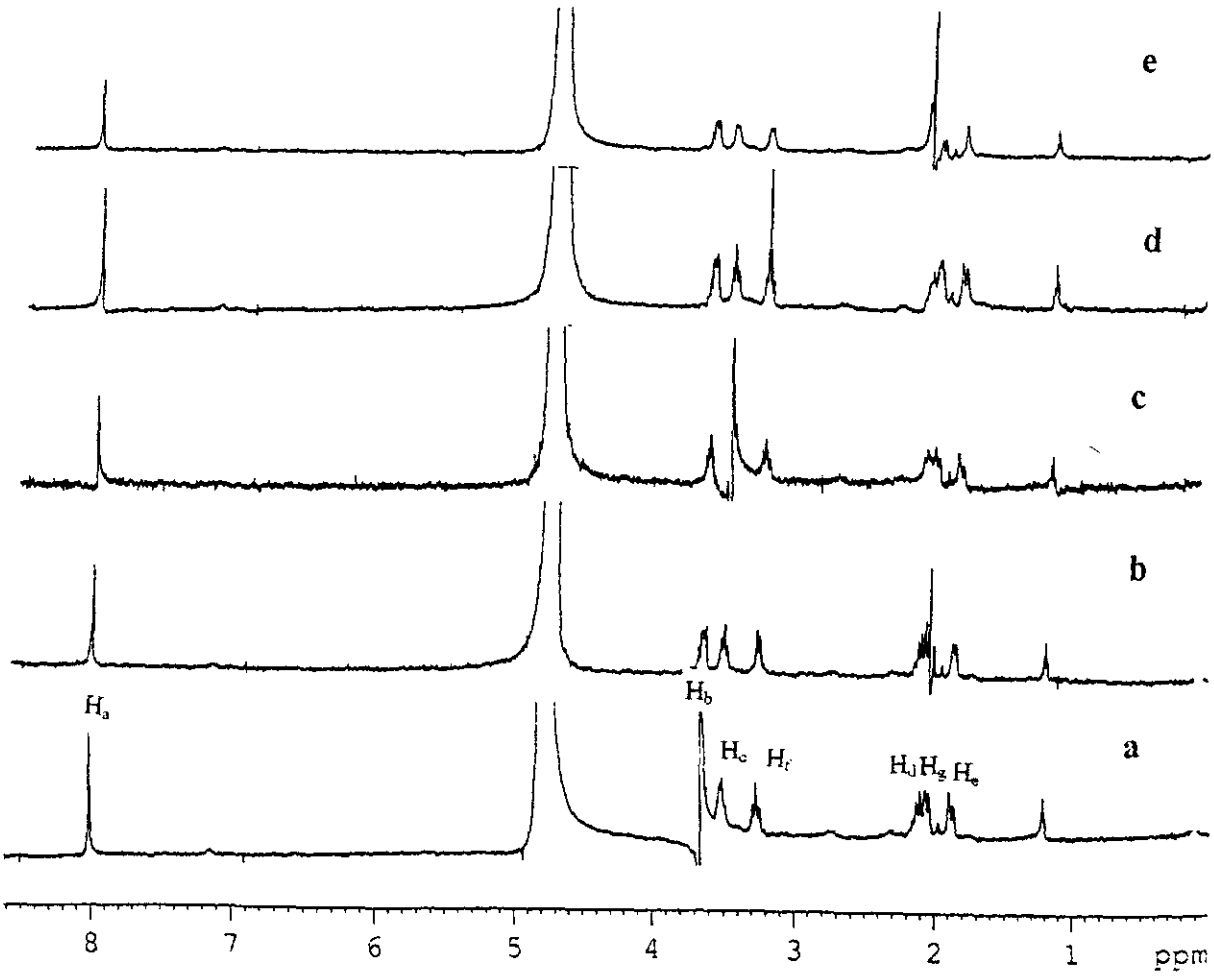

Figure 3E.8 Decoupling experiments for $[Cu_2NGT](ClO_4)_2$]

The 2D COSY spectrum resolves the relationship between the doublet and triplets and confirms the assignments of protons. **Table 3E.3** summarises the assignments of protons H_a-H_e.

Table 3E.3 1H NMR shift data for $[Cu^{I}_{2}NGT]^{2+}$ in D_2O

Proton	H_a	H_b/H_c	H_d/H_e	H_f/H_g
Chemical shift (ppm)	8.05 (s)	3.67(d) 3.54 (t)	1.90(d) 2.1 (m)	2.07(d) 3.30 (t)

3E.5 Solid state NMR

Comparison with spectra obtained in the solid state should establish the presence or absence of decomplexation equilibria in solution. However, this comparison poses difficulty in some cases, as proton spectra are unmanageably broad and complex in the solid state, while the solubility required for ^{13}C spectra is often lacking in the cryptate systems.

3E.5.1 Free ligand, GT

The ^{13}C spectrum of the free ligand, $[GT.H_2O]$, is broad and appears less well resolved than for other free cryptates, (**Figure 3E.9a**). There are two imino-carbon signals separated by around 100 Hz. The methylene resonances, partly because of increased breadth of signal but also in consequence of " co-ordination" shifts which move the C_D and C_E resonances in opposite directions, are spread over nearly 500 Hz in place of the ~ 200-250 Hz seen for the cadmium and mercury cryptates.[35] Compared to the $CDCl_3$ solution spectrum of GT, the higher frequency resonance of each pair appears close to the chemical shift seen in the solution spectrum (which is simpler and has just three ^{13}C resonances at δ 163.058, 59.061 and 52.953 ppm).

The CP-MAS ^{15}N spectrum of GT is weak but shows the usual N-bridgehead signal centred around δ -347 ppm, together with an imino-N resonance which takes the form of three lines in the δ 18-21 ppm region, (**Figure 3E.9b**). This demonstrates, firstly, that the bridgehead-N resonance is relatively unaffected by change from divergent to convergent conformation, and secondly that the imino-N shift is, in contrast, sensitive to conformational and co-ordination effects in the co-ordinated ligand. As the X-ray structure of GT shows no

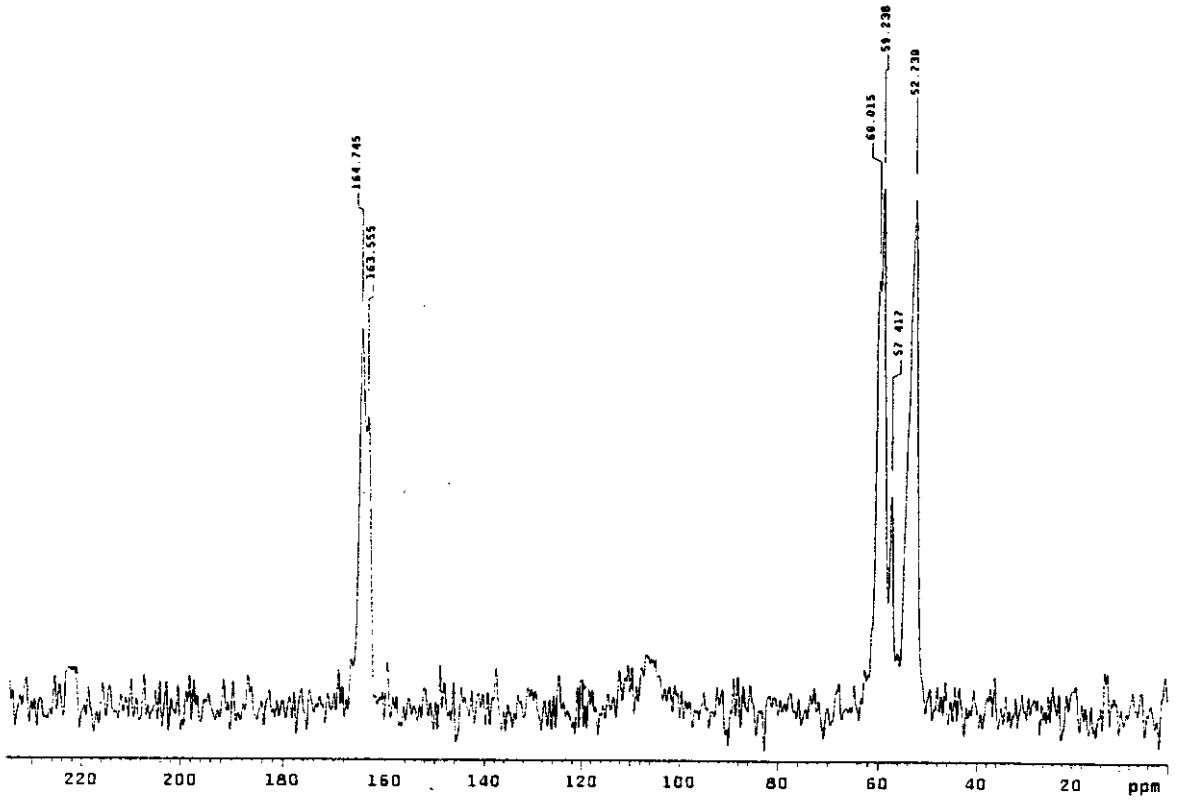

Figure 3E.9a ^{13}C solid state NMR of GT.H_2O

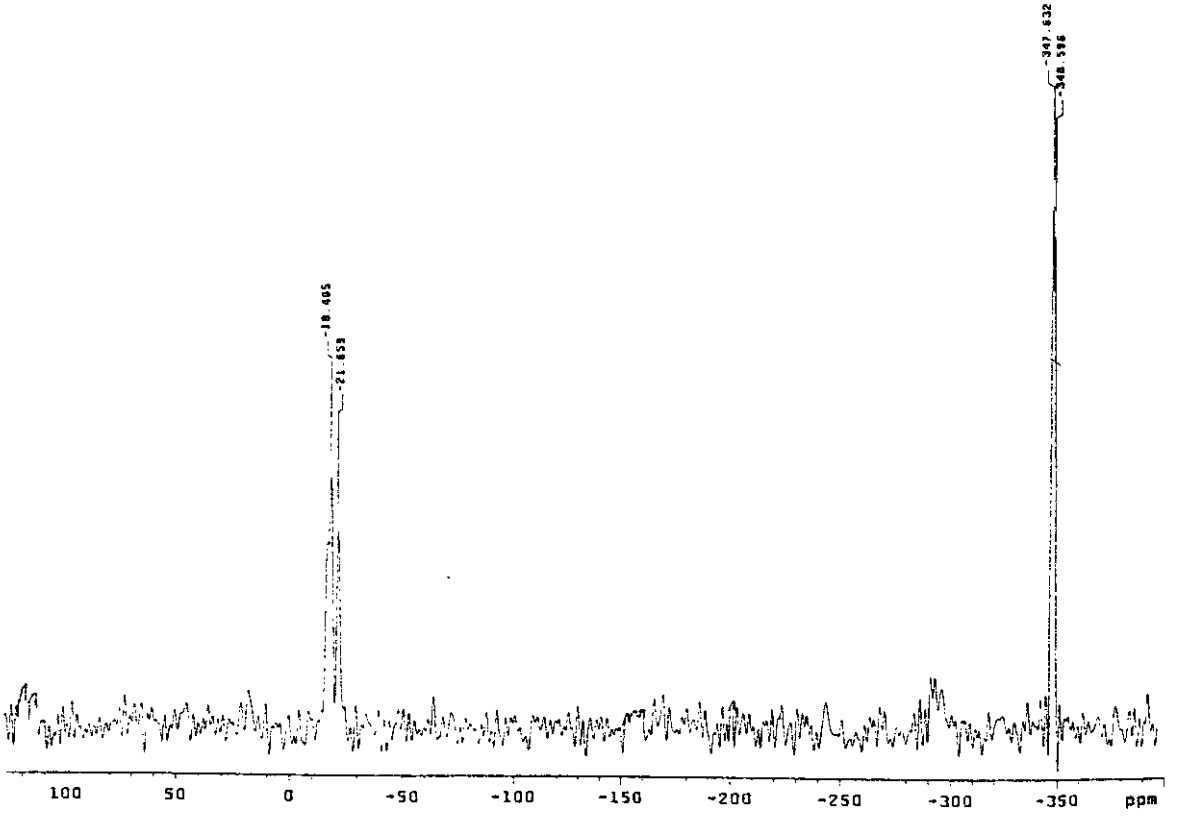

Figure 3E.9b ^{15}N solid state NMR of GT.H_2O

difference between the strands or ends of the cryptand, the splitting of the imino -N resonance in GT may derive from H-bonding effects in this hydrated form of the free ligand.

Table 3E.4 Solid State NMR data for free ligand GT

Spectrum	ν/MHz	Reference	Imino carbon	Methylene carbon
^{13}C	75.4	TMS	164.7(s), 163.6 (sh)	60.0, 59.2, 57.4, 52.7
Spectrum	**ν/MHz**	**Reference**	**Imino nitrogen**	**Bridgehead nitrogen**
^{15}N	30.4	NH_4NO_3	—17.5 (sh), -18.4, -21.7	-347.6, -348.6

3E.5.2 $Cu^{I}_2GT(ClO_4)_2$

This spectra is of interest because the simplicity of its ^1H solution spectra initially suggests the possibility of dissociation in solution, which could have generated ligand spectra time-averaged between the co-ordinated and uncoordinated situations. In the case of the dicopper(I) complex, the ^{13}C CP-MAS spectrum is simple and similar to the CD_3CN solution spectrum, showing in this case that the solution conformation is no different from that revealed in the X-ray crystallographic structure. In both solid state and CD_3CN solution spectra, just one sharp imino-C signal at $\delta \sim 155$ ppm and a pair of methylene resonances at $\delta \sim 51$ - 52 and ~ 61.5 ppm are observed, confirming the X-ray finding that the two ends and three strands of the cryptand are equivalent, **(Figure 3E.10a)**.

The ^{15}N spectrum is more complex however, and the origin of this complexity can be unambiguously attributed by running the spectrum at two different frequencies. The ^{15}N spectrum of the imino-N, **(Figure 3E.10b),** at both 30.4 and 20.3 MHz takes the form of a well defined four-line resonance centred near 100 ppm. The different chemical shifts of the four resonances at these two frequencies, together with insensititivity to spectrometer frequency of the spacing in Hz of the four-line pattern, means that they must be attributed to coupling of ^{15}N to the I = 3/2 copper nuclei.[35] There is no previously reported observation of ^{15}N, $^{63,65}Cu$ coupling with which our observed coupling may be compared, but the solid state NMR spectra recorded on selected Cu(I) podates (Chapter 2) indicates that ^{15}N, $^{63,65}Cu$ couplings of the order of 120-180 Hz are general in Cu(I) imino complexes. The N_{br} signal appears as a singlet

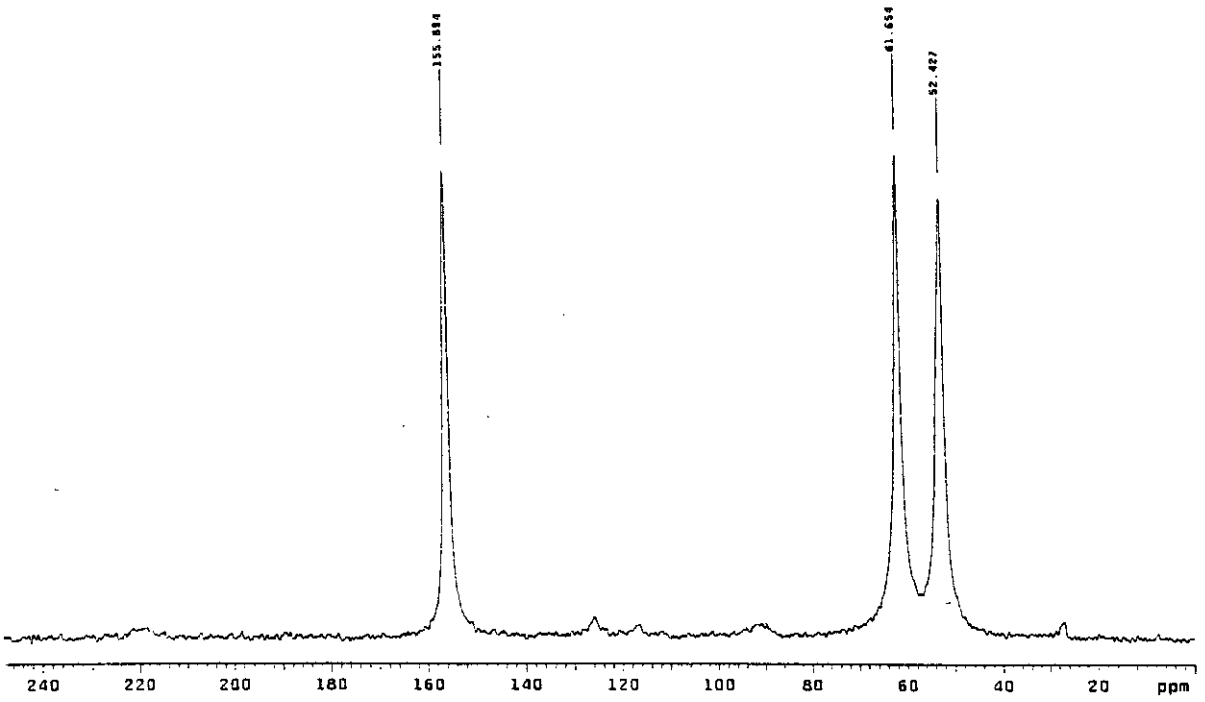

Figure 3E.10a ^{13}C *solid state NMR of* $[Cu_2GT](ClO_4)_2$

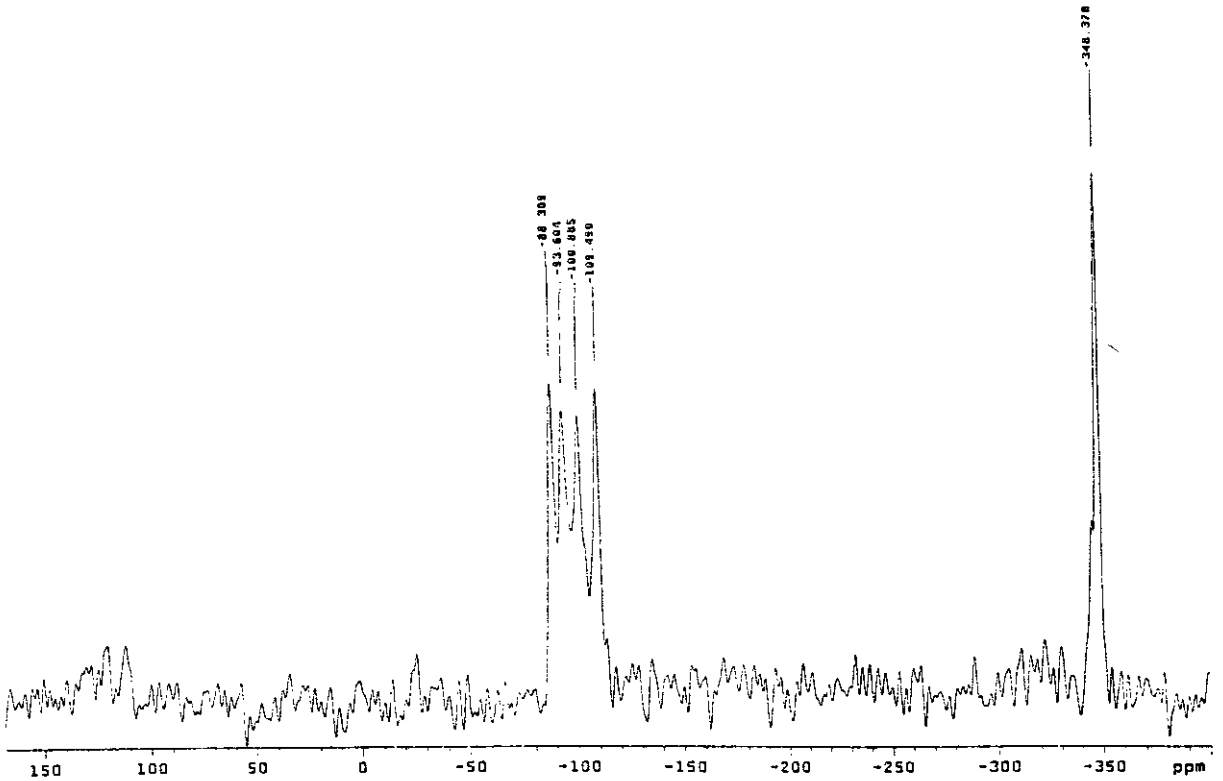

Figure 3E.10b ^{15}N *solid state NMR of* $[Cu_2GT](ClO_4)_2$

at δ -348 ppm in both the 20 and 30 MHz spectra providing a good check on consistency of instrumental parameters. This value is very close to those (δ -347 ppm) seen in the free cryptand, confirming that co-ordination of the N_{br} in Cu_2GT has had little effect on its chemical shift. In contrast, the ^{15}N chemical shift of the imino-N is significantly more negative in this cryptate than in any other GT derivatives so far examined, suggesting that back bonding from Cu(I) cations to the imino-π system has increased electron density on the N-donor.

This well resolved coupling between ^{15}N and encapsulated Cu(I) points to high symmetry and strong interaction which also show the largest ^{15}N co-ordination shifts.

Table 3E.5 Solid State NMR data for $[Cu_2GT](ClO_4)_2$

Spectrum	**ν/MHz**	**Reference**	**Imino carbon**	**Methylene carbon**
^{13}C	75.4	TMS	155.9	61.7, 52.4
Spectrum	**ν/MHz**	**Reference**	**Imino nitrogen**	**Bridgehead nitrogen**
^{15}N	30.4	NH_4NO_3	-91.9, -95.1, -99.5, -104.9	-347.9
^{15}N	30.4	NH_4NO_3	-88.3, -93.6, -100.9, -109.5	-348.4

In conclusion, the ^{15}N MAS study illustrates the potential value of this technique in furnishing information on structure and bonding in co-ordination compounds. The experiments confirm the X-ray findings that the two ends and three strands of the GT cryptand are equivalent.

3F.1.0 Introduction to Electron Self-Exchange

There are two types of reaction pathway for electron transfer (or redox) reactions as first put forth by Taube: [43]

1. **Outer sphere mechanism**: There is no covalently linked intermediate and the electron just 'hops' from one centre to the next, **Figure 3F.1A**.

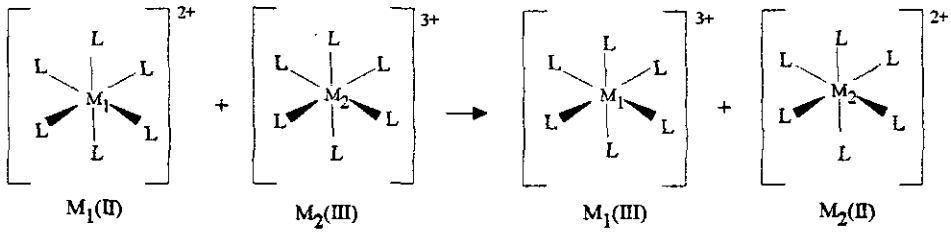

Figure 3F.1A The outer-sphere mechanism for an electron transfer reaction between two complexes.

2. **Inner sphere mechanism**: This mechanism involves the formation of a covalent bridge through which the electron is passed in the electron transfer process. It is restricted to those complexes containing at least one ligand which can bridge between two metal centres. Examples of such ligands are the halides, hydoxy or oxo groups, thiocyanate as well as a variety of conjugated organic ligands, **Figure 3F.1B**.

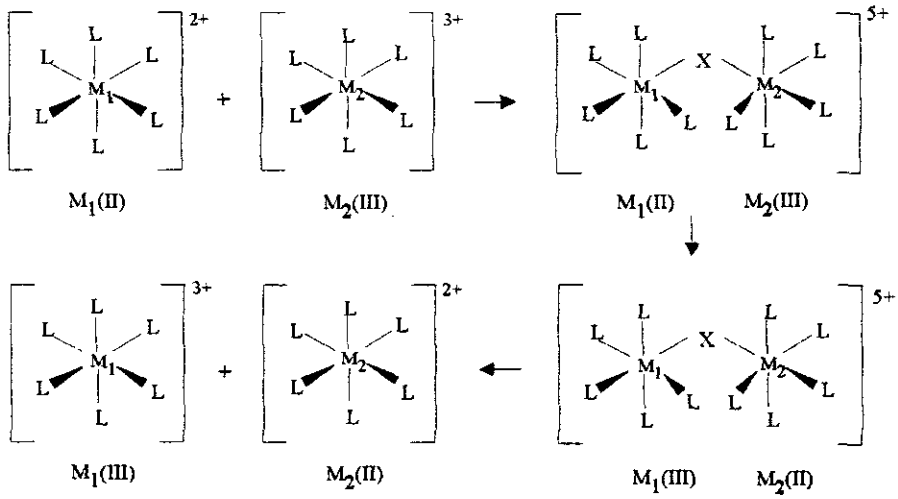

Figure 3F.1B The inner-sphere mechanism for an electron transfer reaction between two complexes.

Rate constants for outer-sphere reactions range from 10^{-9} to 10^{10} sec^{-1}. Although no information about mechanism is directly obtained from the rate constant or the rate equation, some quantitative interpretations of the rates of outer-sphere reactions can be made. It is possible to determine the rate constant, k_{12}, for the reaction of two complex ions. Marcus and Hush have developed a theory which bears their names that relates the value of k_{12} to the rates (k_{11} and k_{22}) of the 'Self-Exchange' reactions of the two components.[44,45]

3F.1.1 Copper Proteins in Electron Transfer

Cuproproteins involved in biological redox chemistry have recently stimulated interest in deciphering relationships between the structural and electron-transfer properties of Cu(II)/Cu(I) couples at active sites. For blue copper proteins only the outer sphere mechanism is possible. In particular, plastocyanin and azurin have been extensively studied.[46] While these blue copper sites are expected to have relatively small co-ordination sphere reorganisation energies during the outer-sphere Cu(II)-Cu(I) electron transfer process, their rates of electron self-exchange vary significantly from $\leq 2 \times 10^4$ $M^{-1}s^{-1}$ for French bean plastocyanin to 1.3×10^6 $M^{-1}s^{-1}$ for *Pseudomonas aeruginosa azurin*.[47] Owing to the complicated nature of electron self-exchange for metalloproteins, and the lack of information on precise geometric change, it is impossible to determine how the rates of electron transfer may be influenced by the near invariance of the active site geometries to changes in valence state.[48,49]

In general, electron transfer reactions in copper complexes are associated with a drastic change in co-ordination geometry which imposes a large reorganisational Franck Condon barrier on the redox process and can hinder facile electron transfer.

One approach toward further understanding of biological electron-transfer processes is to study small molecule copper compounds of related structure and/or function. Small-molecule model compounds for copper protein electron-transfer dynamics should ideally demonstrate co-ordination number invariance and an outer sphere mechanism of electron transfer.[4] There are very few cases in the literature of copper complexes which meet both criteria. The high kinetic lability of copper and its tendency to adopt different co-ordination

numbers and geometries in the +1 and +2 oxidation state pose formidable obstacles in the design and synthesis of appropriate small molecule systems.[48,50]

Table 3F.1 Electron Self-Exchange Rate Constants of Selected [CuII,I(L)]$^{2+,+}$ couples

Complex	K_{ex}, $M^{-1}s^{-1}$	Solvent	Ref	T, K
$Cu^{I,II}(imidH)_2DAP](BF_4)_{1,2}$	1.31 (0.16) x 10^4	CD_3CN	51	298
$Cu^{I,II}(py)_2DAP](BF_4)_{1,2}$	1.76 (0.16) x 10^3	CD_3CN	49	298
$[Cu^{I,II}(Az)]$	2.4 (1.0) x 10^6	D_2O	52	298
$[Cu^{I,II}(Pc)]$	< 2 x 10^4	D_2O	53	323

Examples of Cu^I/Cu^{II} redox couples with equivalent ligation are rare. Recently, Garner and coworkers showed that in the complexes, $[Cu^I(bimdpk)_2][PF_6]$ and $[Cu^{II}(bimdpk)_2][BF_4]$,[54] the geometry is intermediate between tetrahedral and square planar. As a consequence the redox process Cu(I/)Cu(II) was found to be reversible (0.59 V, vs SCE) and the electron self-exchange rate constant in acetonitrile was reported to be 1.9 x 10^4 $M^{-1}s^{-1}$.

Figure 3F.2 displays the ligands for which self-exchange rate constant data are available and X-ray structural data have been determined for both the +1 and +2 oxidation states.[50, 51]

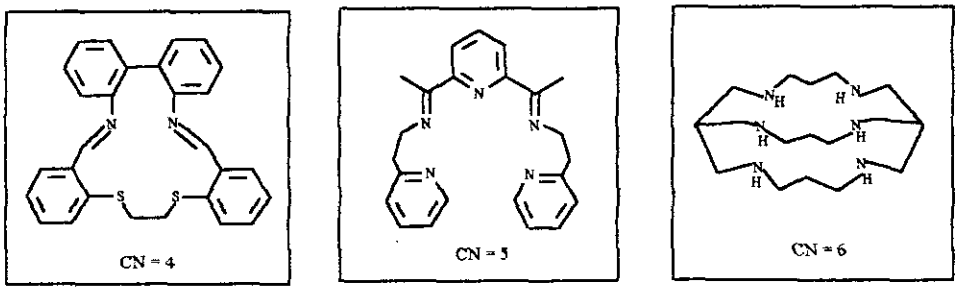

Figure 3F.2

This section reports the technique of ^1H NMR line-broadening for the determination of the electron self-exchange rate constant of the couple $[Cu_2^I(GT)]^{2+}$ + $[Cu_2^{1.5}(GT)]^{3+}$ ⇔ $[Cu_2^{1.5}(GT)]^{3+}$ + $[Cu_2^I(GT)]^{2+}$. As these compounds are potential models for the Cu_A site it enhances the importance of investigating such electron transfer reactions.

3F.2.0 NMR Line Broadening

One of the earliest observations in NMR spectroscopy was, that on addition of a paramagnetic species, significant broadening of the ^1H NMR resonance of the diamagnetic species was observed. The degree of broadening reflects the extent of the interaction between the unpaired electron and the nucleus in question. Fast relaxing unpaired electrons provide efficient pathways for nuclear relaxation. The nuclear relaxation rate enhancement involves the two mechanisms referred to as **T1** and **T2** (spin - lattice and spin-spin, respectively) as described previously in Chapter 3E.

3F.2.1 Bloch Equation[45]

In determining the relaxation times for interconversion between diamagnetic and paramagnetic species McConnell and Berger derived the following expression from the Bloch equations, **Equation 3F.1**.

Equation 3F.1

$$K_{11} = 1/P\,[\,(1/T_2)_{DP} - (1/T_2)_D]$$

where $(T_2)_D$ is the transverse relaxation time of ^1H for a solution containing only the diamagnetic species and $(T_2)_{DP}$ is the corresponding quantity for a solution containing both the diamagnetic and paramagnetic species, [P] being the concentration of added paramagnetic species.

In the derivation of this equation the following conditions are assumed: $\tau_D > \tau_p$, $((\delta\omega)\tau_p/2)2 > 1$, $(T_2)_D \geq \tau_D$, where τ_D and τ_p are the mean lifetimes of the diamagnetic and paramagnetic species, respectively. Following electron transfer, τ_p is the paramagnetic spin-lattice relaxation time, $\delta\omega$ is the hyperfine splitting of the electron resonance of the paramagnetic species, due to the proton and $(T_2)_D$ is the spin-spin relaxation time for the diamagnetic species.

In the present investigation, it was determined that all the foregoing conditions were met, thus a modified equation (**Equation 3F.2**) is valid for the system reported here.

Equation 3F.2

$$1/T_2 = \pi\Delta\nu_{1/2}$$

$1/T_2$ can be determined from the line width ($\Delta\nu_{1/2}$) by using the relationship in **Equation 3F.2**. $\nu_{1/2}$ is equal to the width at half height of the broadened resonance in the ^1H NMR spectrum. The self-exchange rate constant, k_{ex}, may then be obtained as the slope of a plot of $1/T_2$ vs. concentration of added [Cu(II)L].

Equation 3F.3

$$1/T_2 = k_{ex}[Cu(II)L] + 1/T_{2n}$$
$$y = mx + c$$

Our experiment is adapted from literature reports[49,51,52], with the paramagnetic average valence dicopper ligand $[Cu_2^{1.5}GT]^{3+}$ being used to investigate line broadening on the diamagnetic $[Cu_2^{I}GT]^{2+}$. The GT ligand was used as its oxidised and reduced forms are isomorphous, therefore displaying co-ordination number invariance and low reorganisation energy. The encapsulated complex also possess an imine peak for which the ^1H NMR resonance is both intense and well separated from the remainder of the spectrum.[55] As shown in **Figure 3F.3**, the signal of the imine proton, at δ 8.15 ppm, broadens upon addition of the paramagnetic average valence complex. The complete ^1H NMR spectrum of $[Cu_2^{I}GT]^{2+}$ and $[Cu_2^{I}GT]^{3+}$has previously been discussed in **Section 3E**.

3F.3 Determination of Self-Exchange Rate Constant at 25° C, without Constant Ionic strength.

Experimental

The self-exchange electron transfer constant, k_{ex} ($M^{-1}s^{-1}$) for the $[Cu_2^{1/1.5}GT]^{2/3+}$ couple has been determined in D_2O at 300 K. $[Cu_2GT](ClO_4)_2$ and $[Cu_2GT](ClO_4)_3$ were prepared as described in Chapter 3G. The various samples for ^1H NMR were prepared by gradually

increasing the concentration of the paramagnetic component $[Cu_2GT](ClO_4)_3$ from 1.63 x 10^{-4} M to 15.1 x 10^{-4} M in a 0.5 ml solution of $[Cu_2GT](ClO_4)_2$.

1. A stock solution of $[Cu^{I}_2GT](ClO_4)_2$was prepared in a 10 ml volumetric flask by dissolving 10.3 mg $[Cu^{I}_2GT](ClO_4)_2$ (1.5 mM) in 10 ml D_2O.
2. 0.1 (0.06mg, 7.64 x 10^{-7} mol), 0.3 (0.17mg, 2.16 x 10^{-7} mol), 0.5 (0.29mg, 3.70 x 10^{-7} mol), 0.7 (0.41mg, 0.522 x 10^{-7} mol) and 0.9 (0.52mg, 6.6 x 10^{-7} mol) equivalents of $[Cu_2^{1.5}GT](ClO_4)_3$ were carefully weighed into the labelled NMR tubes.
3. 0.5 ml of $[Cu^{I}_2GT](ClO_4)_2$ in D_2O was syringed into each NMR tube and shaken to ensure complete solvation. The ^1H NMR spectrum was immediately recorded at 300 K.
4. A ^1H NMR spectrum was recorded of $[Cu^{I}_2GT](ClO_4)_2$ only.
5. A typical plot for this experiment shows increasing broadness of the imine peak upon addition of paramagnetic species $[Cu_2^{1.5}GT]^{3+}$, **(Figure 3F.3)**.

The paramagnetic contribution to the spin-spin relaxation was evaluated by calculating peak width at half height (WHHM) of each imine peak and subtracting the WHHM of the diamagnetic $[Cu^{I}_2GT]^{2+}$. Line widths of D_2O were checked to be constant at 3 ± 1 Hz throughout the course of the experiment.

Values of $1/T_2$ are listed in **Table 3F.2** and a typical plot of $1/T_2$ versus added $[Cu_2^{1.5}GT]^{3+}$ is illustrated in **Figure 3F.4** It can be seen that the extent of broadening is linearly dependent on the concentration of $[Cu_2^{I.5}L]^{3+}$. This linear relationship affords k_{ex} as the slope and $1/T_{2n}$ as the intercept.

Table 3F.2 NMR experiment at 300 K in D_2O

$[Cu_2(1.5)GT]^{3+}$ (x 10^{-4}) M	3.0	6.3	9.3	12.3	15.1
k_{obs}/s^{-1}	10.1	15.2	25.3	27.8	32.9

A plot of this data gives; $\mathbf{k_{ex} = 2.1 \times 10^{4}\ M^{-1}s^{-1}}$ at T = 300 K.

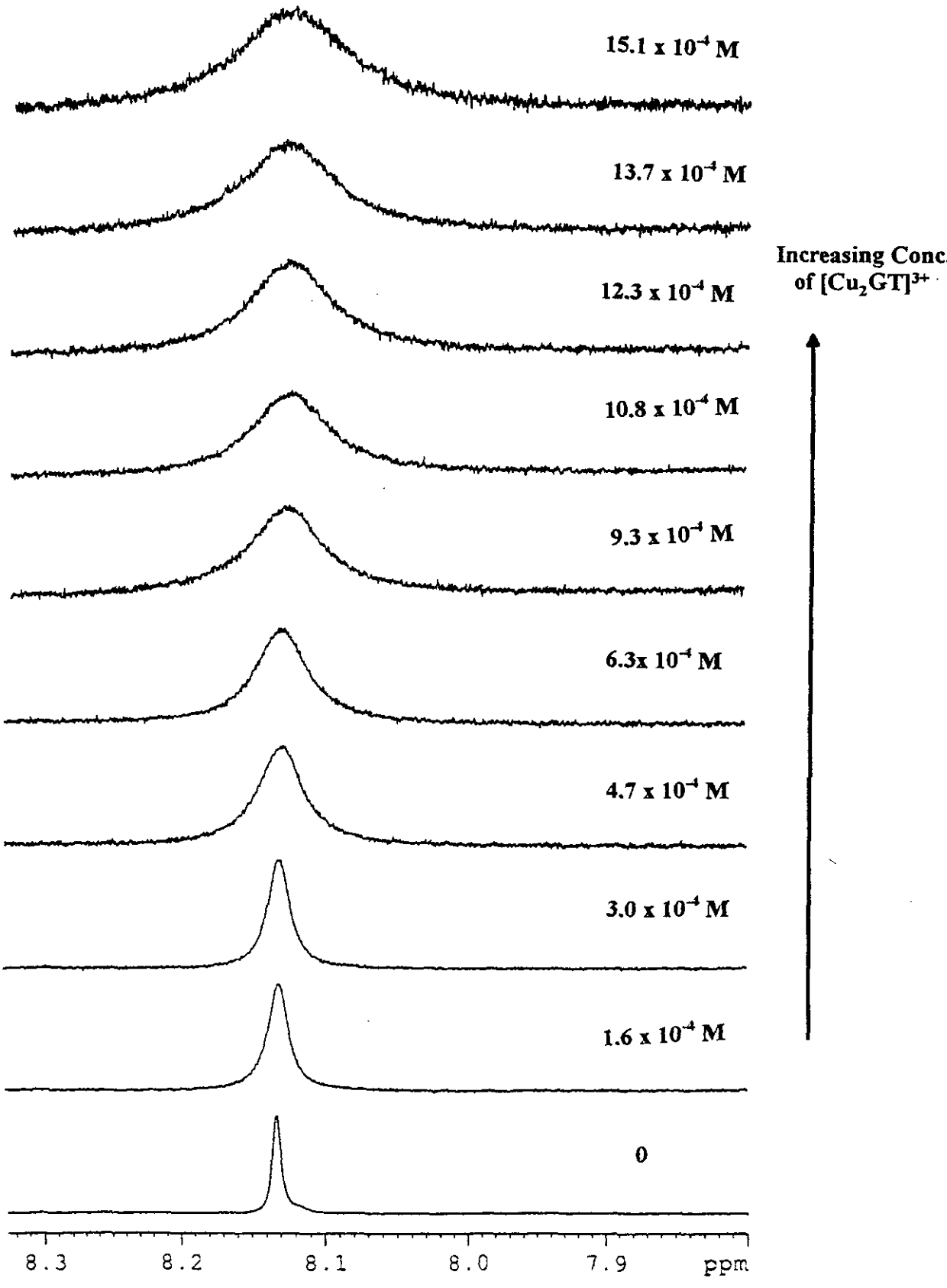

Figure 3F.3 Broadening of the imine proton upon addition of paramagnetic $[Cu_2GT]^{3+}$

3F.4.1 Determination of Self-Exchange Rate Constant at 25° C corrected to 0.1 M Ionic Strength.

The effect of constant ionic strength was investigated. This experiment was essentially the same as that described in 3F.3 except $NaNO_3$ (0.1 M) was added to the stock solution of $[Cu^{I}_{2}GT]^{2+}$. **Figure 3F.3** shows the broadening of the imine signal for this experiment. The calculated values of k_{obs}/s^{-1} are shown in **Table 3F.3**.

Table 3F.3 NMR experiment at 300K in D_2O. (I = 0.1 M $NaNO_3$), conc. of $[Cu_{2}(I)GT]^{2+}$ = 1.5 mM

$[Cu_2(1.5)GT]^{3+}$ ($x\ 10^{-4}$) M	1.6	3.0	4.7	6.3	9.3	10.8	12.3	13.7	15.1
k_{obs}/s^{-1}	13.2	17.6	39.6	52.8	70.4	88.0	96.8	118.8	127.6

A plot of this data gives; k_{ex} = **$8.4 \times 10^{4}\ M^{-1}s^{-1}$** at μ = 0.1 M $NaNO_3$ and T = 300 K.

3F.5.1 Variable Temperature Studies

These experiments were repeated at 278 K and 288 K in order that the enthalpic and entropic contribution to electron transfer could be determined from an Eyring Plot. The results of the variable temperature studies are given in **Tables 3F.4** and **3F.5**. All values are corrected to 0.10 M ionic strength.

Table 3F.4 NMR experiment at 278 K in D_2O. (I = 0.1 M $NaNO_3$), conc of $[Cu_{2}(I)GT]^{2+}$ = 1.5 mM

$[Cu_2(1.5)GT]^{3+}$ ($x\ 10^{-4}$) M	6.4	7.9	9.7	11.0	12.3
k_{obs}/s^{-1}	22.6	26.4	35.8	47.1	49.0

A plot of this data gives; k_{ex} = **$3.6 \times 10^{4}\ M^{-1}s^{-1}$** at μ = 0.1 M $NaNO_3$ and T = 278 K.

Table 3F.5 NMR experiment at 288 K in D_2O, (I = 0.1 M $NaNO_3$), conc. of $[Cu_2(I)GT]^{2+}$ = 1.5mM

$[Cu_2(1.5)GT]^{3+}$ ($x\ 10^{-4}$) M	4.6	6.4	7.9	9.7	11.0	12.3
k_{obs}/s^{-1}	18.5	27.8	33.3	46.25	51.8	61.05

A plot of this data gives; k_{ex} = **4.8 x 10^4 $M^{-1}s^{-1}$** at μ = 0.1 M $NaNO_3$ and T = 288 K.

3F.5.2 Activation Parameters

For the experiments recorded at 278, 288 and 300 K, variable-temperature data were plotted according to **Equation 3F.4.** The Eyring plot is shown in **Figure 3F.5**.

Equation 3F.4

$$K = (kT/h)e^{-\Delta G/RT}$$

Where K is the Boltzmann constant, h is Plancks constant and R is the Universal gas constant.

The values of ΔH and ΔS were then calculated using the data in **Table 3F.6.**

Table 3F.6 Electron Self-Exchange data at 300, 288 and 278 K for Eyring Plot

T^{-1} (K^{-1})	k ex ($M^{-1}s^{-1}$)	ln k/T
0.0033	8.4 x 10^4	5.64
0.0035	4.8 x 10^4	5.12
0.0036	3.6 x 10^4	4.86

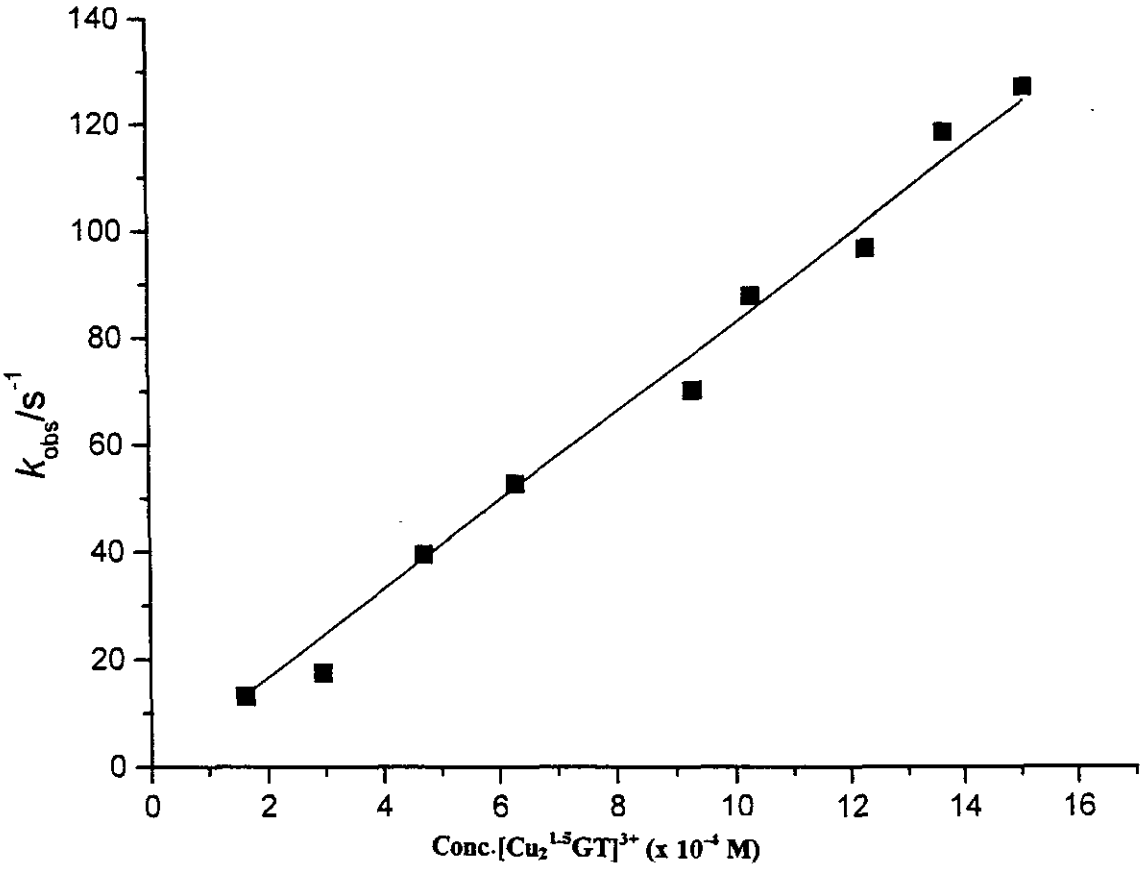

Figure 3F.4 Typical plot of $1/T_2$ versus conc. of added $[Cu_2^{1.5}GT]^{3+}$

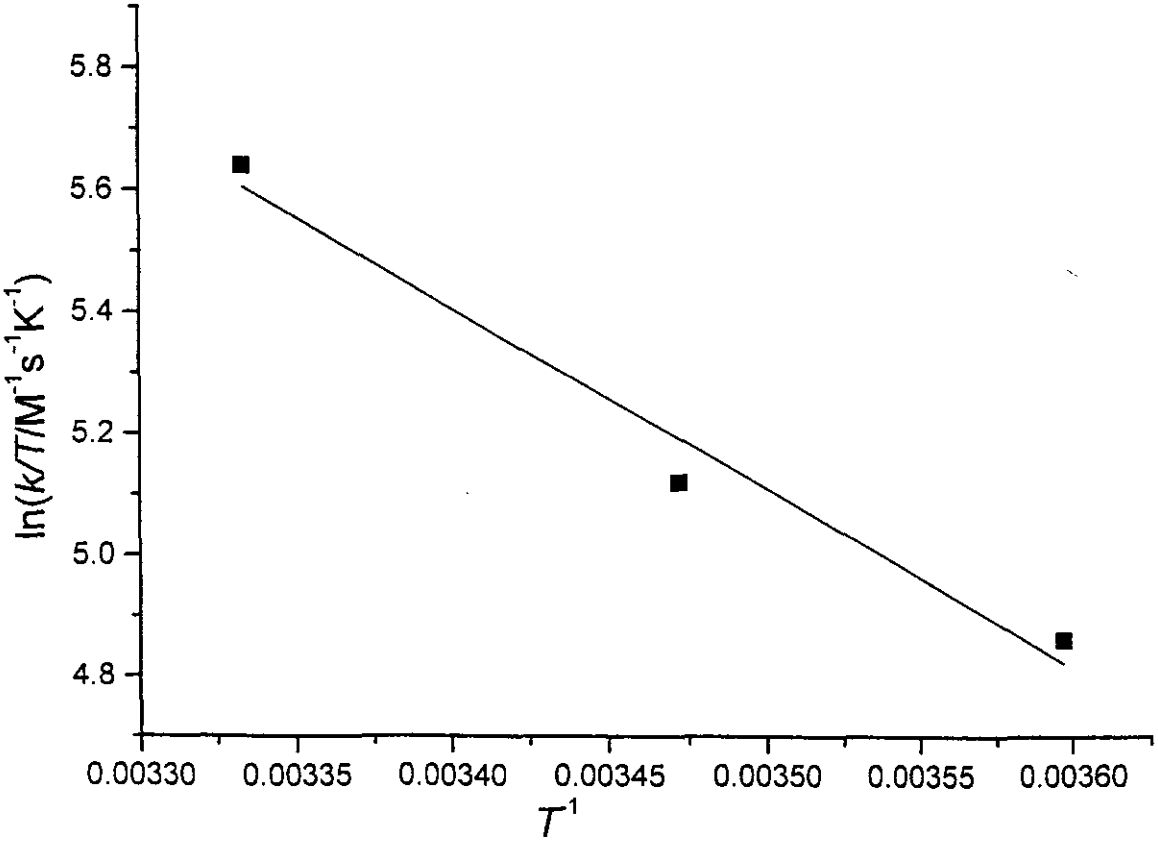

Figure 3F.5 An Eyring plot to determine activation parameters.

3F.5.2.1 Calculation of Activation Enthalpy, ΔH

$$\ln k/T = \ln k/h + \Delta S/R - \Delta H/RT$$

$$\Delta H = R \times \text{Slope}$$

$$\Delta H = 8.314\ JK^{-1}mol^{-1} \times -2968\ K^{1}$$

$$= 24.7\ kJmol^{-1}$$

$$\Delta H \text{ Error} = 8.314\ JK^{-1}mol^{-1} \times 478\ K^{1}$$

$$= 3.9\ kJ\ mol^{-1}$$

$$\mathbf{\Delta H = 25 \pm 4\ kJ\ mol^{-1}}$$

3F.5.2.2 Calculation of Activation Entropy, ΔS

$$\Delta S = R(\text{int} - \text{Ink} / h) \qquad b = 15.497 \pm 1.659$$

$$= 8.314\ (15.497 - \ln (1.38 \times 10^{-23} / 6.63 \times 10^{-34})$$

$$= 8.314\ (15.497 - 23.76)$$

$$= 8.314 \times - 8.263$$

$$= - 68.698$$

$$\text{Error} = 8.314 \times 1.659 = 13.8$$

$$\mathbf{\Delta S = - 69 \pm 14\ JK^{-1}mol^{-1}}$$

3F.6 Discussion

Large rate constants are favoured by several factors including; short internuclear distance, approximate orbital overlap (to provide an electronic pathway for the exchange) and similar co-ordination geometries for the reduced and oxidised species (to minimise ligand and solvent reorganisation). Ligand loss or exchange adds an additional complication that can affect observed rates.

Most reports on copper complexes pertain to outer-sphere reactions, which often appear to proceed with rates on the order of 10^3 - 10^4 $M^{-1}s^{-1}$, (**Table 3F.1**). A complicating factor in the analysis is that the copper co-ordination geometry may change with the oxidation state and that the solvent is often involved in the co-ordination of the metal.

Of various copper complexes of these azacryptates discussed, this specific system was chosen for the current study on the basis of its several advantageous properties including:

1. A simple $[Cu_2^{I}L]^{2+}$ ^1H NMR spectrum with a sharp singlet peak for the imine resonance.
2. Good stability of the Cu(I) complex with respect to air oxidation.
3. Reasonable thermodynamic stability of the $[Cu_2^{1.5}GT]^{3+}$.
4. Simple electrochemical behaviour (as discussed in **Chapter 3E**).

3F.7 Conclusion

In conclusion the results indicate a fast rate of electron transfer for our model system, although not as fast as reported for azurin. Marcus cross relationship experiments were attempted using the amine complex $[Cu_2RGT](ClO_4)_3$ as the paramagnetic line broadening reagent. However, these experiments were not successful, no broadening was observed as relaxation for this system is not fast enough on the NMR time scale. Future experiments will concentrate on the NGT system where we expect both a Marcus cross relationship with GT and a standard experiment as described in this section to be successful.

Chapter 3G Experimental Procedures for the Synthesis of Complexes Described in Chapter 3

3G.1 General Procedures.

Unless otherwise stated, the organic starting materials (Aldrich, Lancaster and Acros) and the metal salts (Aldrich) were obtained from the afore named chemical suppliers and used without further purification. Unless dried solvents were specified solvents of general purpose reagent standard were used directly in synthesis.

Solvents were dried as follows:-

1. Methanol and industrial methanol were dried using the Grignard method.

(5mg magnesium turnings, 60 ml alcohol and one crystal of iodine were refluxed until all the magnesium was converted to the (m)ethoxide. Then (900 ml) alcohol was added and refluxed for a further hour before being distilled and stored in an air tight flask over 4 Å molecular sieves.

2. Acetonitrile : Acetonitrile was stirred over CaH until gas evolution ceased and then distilled from P_2O_5 (5 g/L) in all glass apparatus. The distillate was refluxed over CaH (5 g/L) for at least one hour, distilled and stored over 4 Å molecular sieves.

3. DMF was brought from Aldrich Chemical Company as analytical grade.

N.B. Extreme care must be exercised when working with perchlorate salts as they may be violently explosive when scratched or warmed in the solid state.

3G.2 Instruments

NMR spectra were recorded on General Electric QE30 or GN-Ω500 instruments at QUB. The chemical shifts in the proton spectra are recorded in parts per million (ppm δ) using tetramethylsilane (TMS) as an internal standard.

Data for single crystal X-ray diffraction studies were collected on a Siemens P3/V2000 diffractometer. Structures were solved using direct methods with the SHELXL 86 program and refined by full matrix least squares method using SHELXL 93.5.

ESR were recorded at the Open University, Milton Keynes on a Varian E109 spectrometer and ESR plus ENDOR spectra were recorded at the National ESR and ENDOR centre at Cardiff University.

Magnetic measurements (sample size between 20 and 30 mg) were determined using an Oxford Instruments Faraday Magnetic Susceptibility Balance with a resistive electromagnet and an Oxford Instruments cryostat was employed as a temperature control down to 80 K.

FAB mass spectroscopy was carried out by EPSRC MS service at the University of Swansea. Mass spectra were recorded on an AEI-MSS 902 instrument updated by VG instruments

operating at 70 eV using a heated inlet system at QUB.

Microanalyses were carried out on a Perkin-Elmer PE240 automatic CHN analyser. Infrared (KBr discs) and Uv/Vis spectra were recorded on a BioRad FTS 185 FTIR spectrometer and a Perkin Elmer Lamda 9 Uv/vis/near IR spectrometer, respectively.

3G.3 GT; Free ligand synthesis.[15]

A 40% (by weight) aqueous solution of glyoxal (10g) was added slowly to isopropanol (200ml). This alcoholic solution was added dropwise over a period of 6 hours to an ice cold solution of tren (6.8g, 0.047mol) in isopropanol (100ml). After addition was complete the solution was stirred at room temperature for a further 2 hours. The solvent was removed under vacuum yielding an orange jelly-like solid. This polymeric solid was stirred in dichloromethane for two hours and was reduced in volume. Celite was added to the filtrate and the solid was pumped to dryness. The solid material was transferred to a soxhlet thimble and extracted with a 4:1 mixture hexane/heptane over a period of 60 hours. The resulting cloudy solution was clarified by vacuum filtration and a crystalline white cryptand precipitated. (Yield = 40 %). A crystalline sample was obtained by recrystallisation from $MeCN/CHCl_3$.

C H N analysis:- $[C_{18}H_{30}N_8]$

	C %	H %	N %
Calc.	60.33	8.38	31.28
Found	60.40	8.52	30.78

Infrared spectrum:-

Inter alia (cm^{-1}) C-H 2843, 2879, C=N 1633

Mass spectrum:-

m/e^+	Formula	Peak	% of base peak
	$[GT]^+$	358	85

3G.4 Template Synthesis of GT

$[SrGT](BPh_4)_2.2H_2O$[13]

Glyoxal (1.74g, 0.03mol) and $Sr(ClO_4)_2$ (2.87g, 0.01mol) were refluxed gently in methanol (200ml) for 15 minutes. Tren (2.92g, 0.02mol) in methanol (400ml) was added dropwise and the reaction mixture was refluxed gently for 30 minutes. The mixture was filtered into a solution of $NaBPh_4$ (4.8g, 0.014mol) in 80ml of methanol with swirling as precipitation took place This was filtered by suction yielding a cream coloured solid, (Yield = 58%).

C H N analysis:- $[C_{18}H_{30}N_8Sr](BPh_4)_2.2H_2O$

	C %	H %	N %
Calc.	70.74	6.66	10.00
Found	69.99	6.76	10.23

Infrared spectrum:-

Inter alia (cm^{-1}) C-H 2843, C=N 1616; BPh_4^- 1580, 1480, 1428, 735, 707, OH 3510.

FAB mass spectrum:-

m/z	Formula	Peak	% of base peak
	$[SrGT]^{2+}$	446	100

3G.5 Preparation of Dinuclear Copper(I) Cryptates using Free GT.

$[Cu_2(I)GT](ClO_4)_2$[16]

The reaction was carried out under nitrogen and dry deoxygenated solvents were used throughout.

GT (130mg, 3.6 x 10^{-4} mol) was dissolved in chloroform (10ml) and filtered onto a stirring solution of $[Cu(MeCN)_4]ClO_4$ (200mg, 6.1 x 10^{-4}) in an acetonitrile/ethanol (5ml/5ml) mixture. The resultant brown solution was reduced in volume and an intensely coloured dark green/brown solid precipitated. This was recrystallised from acetonitrile in air and left to evaporate yielding large brown hexagonal crystals.

C H N analysis:- $[C_{18}H_{30}N_8Cu_2](ClO_4)_2$.

	C %	H %	N %
Calc.	31.59	4.39	16.37
Found	31.83	4.33	16.16

Infrared spectrum:-

Inter alia (cm^{-1}) C-H 2860, C=N 1599; ClO_4^- 1096, 623, OH 3431.

FAB mass spectrum:-

m/z	Formula	Peak	% of base peak
	$[Cu_2GT]^{2+}$	486	85
	$[Cu_2GT(ClO_4)]^{+}$	585	100

3G.6 Preparation of Mononuclear Copper (II) Cryptates using Free GT.

$[Cu^{II}GT](ClO_4)_2.H_2O$

$[Cu_2(O_2CCH_3)_4(H_2O)_2]$ (55mg, $2.7x10^{-4}$mol) was dissolved in ethanol (15ml) and added to a stirring solution of GT (100mg, $2.7x10^{-4}$mol) in methanol (20ml) at room temperature. The resulting brown solution was stirred at room temperature for twenty minutes. A methanol solution of $LiClO_4$ was added and a yellow solid product precipitated. This could be recrystallised from a 50:50 acetonitrile/ethanol solvent mixture yielding a light yellow-brown crystalline product. (Yield = 85 %)

C H N analysis:- $[C_{18}H_{30}N_8Cu](ClO_4)_2.H_2O$

	C %	H %	N %
Calc.	33.80	5.01	17.50
Found	33.87	4.81	17.26

Infrared spectrum:-

Inter alia (cm^{-1}) C-H 2860,2916, C=N 1617; ClO_4^- 1085, 622

FAB mass spectrum:-

m/z	Formula	Peak	% of base peak
	$[CuGT]^{2+}$	421	100
	$[CuGT(ClO_4)]^{+}$	520	15
	$[(CuGT)_2(ClO_4)_3]^{+}$	1141	3

3G.7 Mixed Valence Copper Complexes of GT

3G.7.1 Mixed Valence Copper Complexes of GT by Insertion

$[Cu_2GT](ClO_4)_3$

GT (128mg, $3.6x10^{-4}$mol) in chloroform (10ml) was stirred with $Cu^I(MeCN)_4ClO_4$ (153mg, $4.7x10^{-4}$mol) in an acetonitrile/ethanol (1:2) mixture. The yellow solution was reduced to half volume and $Ag(ClO_4)$ (55mg, $2.7x10^{-4}$mol) was added. A blue/green solid was immediately retrieved by filtration.

The procedure was also attempted for $Cu_2GT(CF_3SO_3)_3$ and $Cu_2GT(BF_4)_3$ using the appropriate template.

All products were blue/green solids. Owing to the higher solubility of these counterions and the solution instability of this cryptate, satisfactory analysis was obtained only for the perchlorate salts synthesised by this method.

C H N analysis:- $[C_{18}H_{30}N_8Cu_2](ClO_4)_3.2H_2O$

	C %	H %	N %
Calc.	26.34	4.14	13.65
Found	26.60	4.00	13.30

Infrared spectrum:-

Inter alia (cm^{-1}) C-H 2885, C=N 1629; ClO_4^- 1091, 624, OH 3433.

FAB mass spectrum:-

m/z	Formula	Peak	% of base peak
	$[Cu_2GT]^{3+}$	484	80
	$[Cu_2GT(ClO_4)]^{2+}$	585	100
	$[Cu_2GT(ClO_4)]^{+}$	684	10

3G.7.2 Mixed Valence Copper Complexes of GT by Transmetallation.

$[Cu_2GT](ClO_4)_3$[13,16]

$SrGT(BPh_4)_2$ (510mg, $4.7x10^{-4}$mol) in acetonitrile (50ml) and $AgClO_4$ (187mg, $9x\ 10^{-4}$mol) in EtOH (30ml) were stirred together at room temperature for 10 minutes. The solution was then filtered to remove $Ag(BPh_4)$. $[Cu_2(O_2CCH_3)_4(H_2O)_2]$(199mg $1x10^{-3}$mol) in methanol (30ml) was added and the dark green solution was refluxed for 10 minutes. The heat was removed and excess $LiClO_4$ (0.3g) was added. The solution was reduced in volume and then cooled to give a blue/green solid product which was isolated by filtration.

The preparations of $[Cu_2GT(CF_3SO_3)_3$ and $[Cu_2GT](BF_4)_3$ were the same as above but using $Ag(CF_3SO_3)$, $Li(CF_3SO_3)$ and $Ag(BF_4)$, $Na(BF_4)$, respectively.

C H N analysis:- $[C_{18}H_{30}N_8Cu_2](ClO_4)_3$

Satisfactory elemental analysis was not obtained by this method.

Infrared spectrum:-

Inter alia (cm^{-1}) C-H 2848, C=N v.weak ; ClO_4^- 1090, 623

FAB mass spectrum:-

m/z	Formula	Peak	% of base peak
	$[Cu_2GT]^{3+}$	484	75
	$[Cu_2GT(ClO_4)]^{2+}$	585	100
	$[Cu_2GT(ClO_4)]^{+}$	684	10
	$[Cu_2GT]$	421	27

$[C_{18}H_{30}N_8Cu_2](BF_4)_3$

Satisfactory elemental analysis was not obtained for this counterion by this method.

Infrared spectrum:-

Inter alia (cm^{-1}) C-H 2870, C=N v. weak; BF_4^- 1054, 670

FAB mass spectrum:-

m/z	Formula	Peak	% of base peak
	$[Cu_2GT]^{3+}$	484	40
	$[Cu_2GT(BF_4)]^{2+}$	571	52
	$[Cu_2GT(ClO_4)]^{+}$	658	9
	[CuGT]	421	27

3G.8 Experimental Procedures for the Synthesis of RGT and its Copper Complexes.

The preparation followed that of GT until the jelly like solid was formed on reducing in volume. This solid was dissolved in methanol, then filtered to leave an orange solution.

The remaining synthesis was performed under nitrogen atmosphere.

The orange solution was heated to reflux and then $NaBH_4$ was added in small amounts with stirring until the solution was white and cloudy. The solution was stirred for a further hour and then reduced in volume to give a white waxy product. Boric acid residues were removed by dissolving the waxy solid with an aqueous solution of NaOH. This cloudy solution was extracted with chloroform. After reducing in volume the oily product was crystallised from a minimum amount of water yielding a white powder. This could be crystallised from H_2O. (Yield = 75 %)

C H N analysis:- $[C_{18}H_{42}N_8].4H_2O$ - crystalline sample

	C %	H %	N %
Calc.	48.87	11.32	24.82
Found	48.75	11.39	24.94

Infrared spectrum:-

Inter alia (cm^{-1}) C-H 2805, 2891, 2960, NH 3259

Mass spectrum:-

m/e$^+$	Formula	Peak	% of base peak
	$[RGT]^+$	370	15
	$[RGT/2]^+$	185	82

3G.9 Mixed Valence Copper Complexes of RGT.

$[Cu_2RGT](ClO_4)_3.2H_2O$

RGT (149mg, $4.05x10^{-4}$mol) was dissolved in chloroform (5ml)/ethanol (15ml). $[Cu_2(O_2CCH_3)_4(H_2O)_2]$ (240mg, $1.2x10^{-3}$mol) was added and the deep blue mixture was stirred for 10 minutes at room temperature. $Li(ClO_4)$ (excess) was added and the solution turned bright blue as the product precipitated. This was filtered and reduced in volume to give a royal blue solid product.

Synthesis of $[Cu_2RGT](CF_3SO_3)_3$ and $[Cu_2RGT](BF_4)_3$ was the same as above but using the appropriate $Li(CF_3SO_3)$ and $Na(BF_4)$, respectively, as counterions.

C H N analysis:- $[C_{18}H_{42}N_8Cu_2](ClO_4)_3.2H_2O$

	C %	H %	N %
Calc.	26.04	5.63	13.51
Found	26.11	5.28	13.57

Infrared spectrum:-

Inter alia (cm^{-1}) C-H 2882, 2927; ClO_4^- 1097, 624, NH 3256, OH 3468

FAB mass spectrum:-

m/z	Formula	Peak	% of base peak
	$[Cu_2RGT(ClO_4)]^{2+}$	595	45
	$[Cu_2RGT(ClO_4)_2]^+$	696	45
	$[Cu_2RGT(ClO_4)_2]^+$	796	100

[Cu_2RGT](CF_3SO_3)$_3$.2H_2O

C H N analysis:- [$C_{18}H_{42}N_8Cu_2$](CF_3SO_3)$_3$.2H_2O

	C %	H %	N %
Calc.	25.70	4.69	11.42
Found	25.30	4.63	10.90

Infrared spectrum:-

Inter alia (cm^{-1}) C-H 2882, 2927; $CF_3SO_3^-$ 1267, 1226, 1167, 1031, 638, NH 3236, 1587, OH 3447

FAB mass spectrum:-

m/z	Formula	Peak	% of base peak
	[Cu_2RGT]$^{3+}$	495	20
	[Cu_2RGT(CF_3SO_3)]$^{2+}$	645	100

3G.10 [Cu(II)RGT](BPh_4)$_2$.2H_2O

RGT (100mg, 2.7x10^{-4}mol) was dissolved in MeCN(10ml) and filtered into a stirring solution of [$Cu_2(O_2CCH_3)_4(H_2O)_2$](54mg, 2.7x10^{-4}mol) in EtOH. The blue solution was stirred for 10 minutes before adding a solution of Na(BPh_4) (185mg, 5.4 x 10^{-4}mol) in MeCN. A green solution resulted and upon slow evaporation in air green cuboidal crystals were produced. These analysed as the monocopper cryptate.

When the solvent was water, a green powder immediately precipitated and was also found to be the monocopper RGT species.

C H N analysis:- [$C_{18}H_{42}N_8Cu$](BPh_4)$_2$.2H_2O

Satisfactory elemental analysis was not achieved owing to the possible presence of a protonated cryptate in the bulk.

Infrared spectrum:-

Inter alia (cm^{-1}) C-H 2882, 2927; BPh_4^- 1582, 1481, 1425, 737, 708, NH 3256, OH 3468

FAB mass spectrum:-

m/z	Formula	Peak	% of base peak
	$[CuRGT]^{2+}$	433	60
	$[Cu_2RGT(BPh_4)]^+$	752	5

3G.11 Experimental Procedures for the Synthesis of NGT and its Complexes.

TRPN[11,56]

Acrylonitrile (40.25g, 0.76mol) was slowly dripped in over a period of 8 hours to a 35% aqueous ammonia solution (17g, 0.30mol) while stirring at 30°C on an oil bath. This mixture was stirred at 30°C for a further 2 hours before water (32ml) was added and a further quantity of acrylonitrile (40.25g, 0.76mol) was dripped in overnight. After addition was completed the mixture was heated to 80°C and refluxed for a further 60 hours. The excess acrylonitrile and water were distilled off under reduced pressure and the remaining white liquid was placed in a freezer until a hard waxy solid formed. This was recrystallised from ethanol to yield white needle-like crystals, (Yield = 85%).

Hydrogenation

Tris 2(cyanoethyl)amine (12.26g, 0.07mol) and Rainey nickel slurry (10g) in EtOH were added to a 1 L hydrogenation vessel containing a solution of NaOH (4.66g, 0.12mol) in EtOH (142ml) and water (8ml). The mixture was placed under hydrogen (40psi) in a hydrogenation apparatus and shaken until hydrogen uptake was complete. The catalyst was vacuum filtered over high flow super cell with EtOH, before being washed with water to deactivate. EtOH was removed under reduced pressure and the oily residue was taken up in dichloromethane causing precipitation of excess NaOH which was removed by filtration. The filtrate was dried with sodium sulfate, filtered and distilled to yield tris-3-aminopropylamine. (Yield = 61%)

C H N analysis:- $[C_9H_{24}H_4]$

	C %	H %	N %
Calc.	57.45	12.76	29.79
Found	57.33	12.54	29.43

Infrared spectrum:-

Inter alia (cm^{-1}) C-H 3110, nitrile CN 2550, OH 3330.

Mass spectrum:-

m/e^+	Formula	Peak	% of base peak
	$[Trpn]^+$	188	100

Cu_2(I)NGT$(ClO_4)_2.2H_2O$

Dry distilled solvents were used and an argon atmosphere was maintained throughout.

Glyoxal (0.52g, 0.009mol) was dissolved in a minimum amount of EtOH (10ml). Acetonitrile (300ml) was added and the solution was stirred to ensure complete dissolution of glyoxal. $[Cu(MeCN)_4]ClO_4$ (1.92g, 0.006mol) was added as solid and the solution was warmed to 60-70°C. Trpn (1.14g, 0.006mol) was dissolved in the minimum amount of degassed EtOH/MeCN and added dropwise to the stirring solution. The solution instantly became blue but then quickly turned dark brown. The reacting solution was kept at 60-70°C and stirred for 30 minutes. $Li(ClO_4)$ was added and the solution reduced in volume by bubbling with argon. A brown solid precipitated and this was collected by frit filtration under a nitrogen atmosphere. (Yield = 16%)

C H N analysis:- $[C_{24}H_{42}N_8Cu_2](ClO_4)_2.2H_2O$

	C %	H %	N %
Calc.	35.8	5.7	13.9
Found	35.6	5.3	13.8

Infrared spectrum:-

Inter alia (cm^{-1}), C=N 1644; ClO_4^- 1103, 623, NH 3268

FAB mass spectrum:-

m/z	Formula	Peak	% of base peak
	$[Cu_2NGT]^{2+}.H_2O$	586	50
	$[Cu_2NGT(ClO_4)]^{+}.H_2O$	685	62
	$[Cu_2NGT]^{2+}$	568	12

$[Cu_2(1.5)NGT](ClO_4)_3$ by Ag^+ Oxidation

1. For X-ray Quality Crystals

$[Cu_2NGT](ClO_4)_2.2H_2O$ (110mg, 1.4 x 10^{-4} mol) was dissolved in acetonitrile. The solution was filtered onto a solution of $Ag(ClO_4)$ in EtOH, warmed gently, and any excess silver was removed by filtration. Silver precipitated over a period of a week and at this stage it was possible to pick out green crystals of the mixed valence complex although the mixture was predominately the dicopper(I) cryptate.

2. For Physical Measurements.

$[Cu_2NGT](ClO_4)_2.2H_2O$ (110mg, 1.4 x 10^{-4} mol) was dissolved in distilled water. There was no evidence of disproportionation occurring. $Ag(ClO_4)$ was added and a pale blue colour was immediately seen. Dark green/black cubed shaped crystals appeared after a period of weeks. The average valence complex was characterised by its electronic spectrum. Suitable analysis was not achieved due to lack of sufficient sample.

C H N analysis:- $[C_{24}H_{42}N_8Cu_2](ClO_4)_3.2H_2O$: Insufficient solid sample for analysis.

Infrared spectrum:-

Inter alia (cm^{-1}), C=N 1636; ClO_4^- 1090, 622,

FAB mass spectrum:-

m/z	Formula	Peak	% of base peak
	$([Cu_2NGT](ClO_4)_2)^{+}.H_2O$	788	15

3G.12 Isotopically labelled Mixed Valence Complexes for Resonance Raman.

$[^{65}Cu_2(1.5)GT](ClO_4)_3$

As the only available source of ^{65}Cu was as the $^{65}Cu(II)(NO_3)_2$ salt a new method of synthesising $[Cu_2(1.5)GT](ClO_4)_3$ was required.

GT (0.2 g 5.6×10^{-4} mol) was dissolved in water and two equivalents of ascorbic acid were added to the stirring solution. $^{65}Cu(NO_3)_2$ (0.2 g, 1.1×10^{-3} mol) was added to this solution and the colour changed from blue to yellow, $[Cu_2GT]^{2+}$. $Ag(ClO_4)$ was added to the yellow solution, causing the immediate appearance of the blue colour associated with the mixed valence complex. The mixed valence nature was confirmed by Uv/Vis spectroscopy prior to resonance Raman spectroscopic studies.

$[^{65}Cu_2(1.5)RGT](ClO_4)_3$

RGT (0.149g, 4.05×10^{-4}mol) was dissolved in chloroform (5ml)/ethanol (15ml), and a few drops of triethylamine were added to provide basic conditions. Upon addition of $^{65}Cu(NO_3)_2$ (0.227g, 1.2×10^{-3}mol) a light blue solution was formed. This was stirred overnight, at room temperature, until the solution became bright blue. $Li(ClO_4)$ (excess) was added, the solution was then filtered and reduced in volume to give a royal blue solid product. (Yield = 68 %). The mixed valence nature was confirmed by Uv/Vis spectroscopy prior to resonance Raman.

CHAPTER 4

THIOLATE SYSTEMS

Chapter 4 The Development of Thiolate Azacryptates.

4.1 3Th;The Thiolate Cryptate

Research into the synthesis, structure and properties of copper complexes of thiolate-containing ligands might shed light on the structure and mechanism of action of thiolate-containing metalloproteins such as those discussed for the Cu_A site of cytochrome c oxidase.[1]

The development of a thiolate-based cryptand, **3Th**, has been our long term goal. It is envisaged that such a cryptate would have a similar capacity for metal induced deprotonation as the phenolate-based ligands developed by Nelson *et al.*[2] The resulting cryptate would therefore have two sites available for the formation of a dinuclear complex, in which the 'soft' S-donor group could act as a bridging unit between pairs of soft metal cations. In addition, the properties of these complexes are expected to provide an interesting contrast to those of complexes of the widely used phenol and pyridine 'head units' which provide much harder donors.[3]

4.2 Synthesis of S-(2,6-diformyl-4-methylphenyl)dimethylthiocarbomate

My predecessor N. Martin spent much time developing a reproducible synthesis of the thiolate-containing ligand precursor S-(2,6-diformyl-4-methylphenyl) dimethylthiocarbomate.[4] The route followed a slightly modified synthesis to that employed by Newman and Karnes, who reported a synthetic route to S-aryl dialkylthiocarbomates in high yield via pyrolytic rearrangement of o-aryl dialkylthiocarbomates.[5] Although the synthesis of S-(2,6-diformyl-4-methylphenyl) dimethylthiocarbomate by N. Martin was successful in achieving a very pure product, the yield was very small and unforeseen problems in removing the protecting group have since been encountered.

N. Martin's report gives a good spectroscopic characterisation of both the intermediate and final products. The spectra clearly indicate how the protected thiolate-containing dialdehyde can be distinguished from its phenolate precursor, **(Figure 4.1 and 4.2)**.

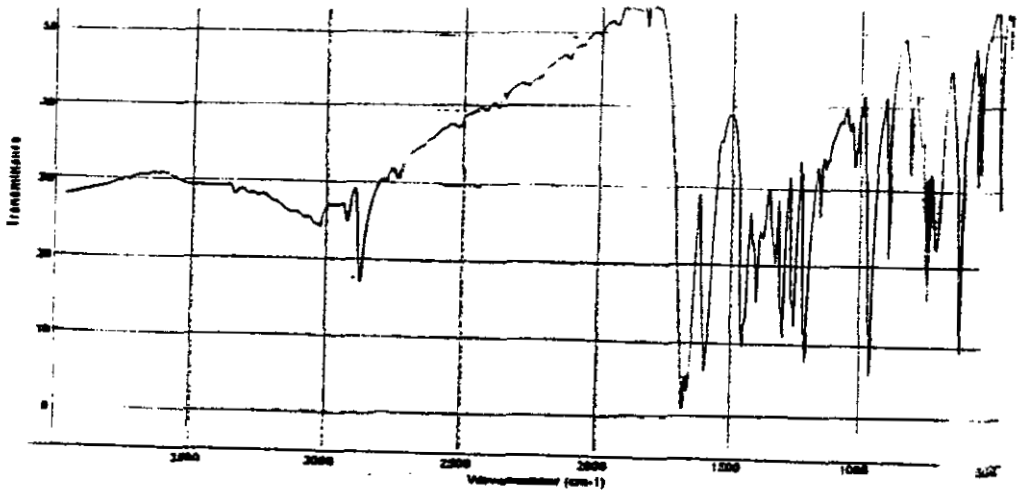

Figure 4.1a Infrared spectrum of 2,6 diformyl-4-methyl phenol

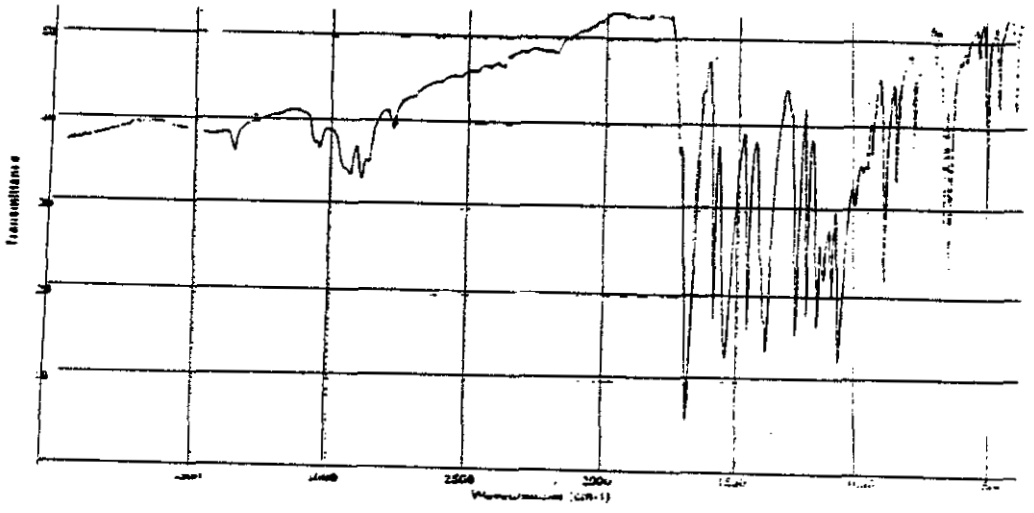

Figure 4.1b Infrared spectrum of O-(2,6 diformyl-4-methyl phenyl) dimethylthiocarbamate

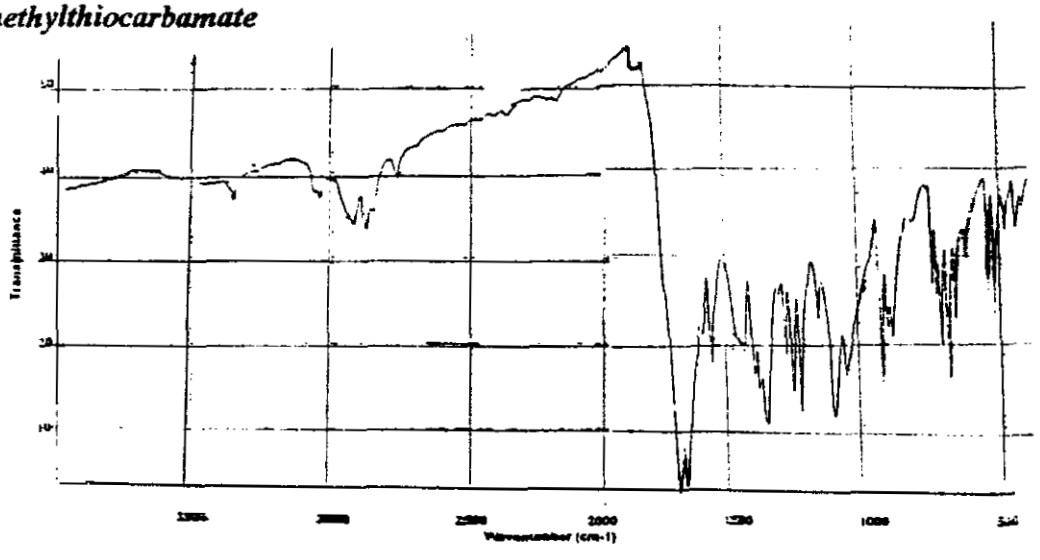

Figure 4.1c Infrared spectrum of S-(2,6 diformyl-4-methyl phenyl) dimethylthiocarbamate

4.2.1 DFMP ; 2,6-diformyl-4-methylphenol

Recent research has found that the starting material, DHMP (2,6-dimethanol-4-methyl phenol) should be freshly synthesised for the whole reaction to be successful. DHMP bought from Aldrich was found to give poor yields and an inferior product. Oxidation of DHMP with MnO_2 gives the dialdehyde, DFMP (2,6-diformyl-4-methylphenol). Synthesis of; 2,6-diformyl-4-methylphenol from 4-methylphenol (p-cresol) is shown in **Scheme 4.1**.

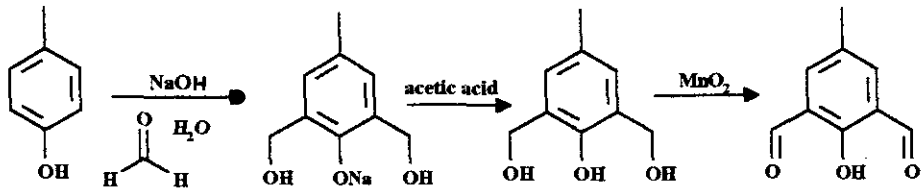

Scheme 4.1

4.2.2 O-(2,6-diformyl-4-methylphenyl)dimethylthiocarbamate (Scheme 4.2)

The synthesis of S-(2,6 diformyl-4-methylphenyl)dimethylthiocarbamate by N. Martin involved the reaction of NaOH with 2,6 diformyl-4-methylphenol and isolation of the sodium complex prior to reaction of dimethylthiocarbomoyl. However, it was found that if NaH was substituted for NaOH the dimethylthiocarbomyl could be added to the reaction mixture without the need to isolate the sodium complex, (**Scheme 4.2**). It was important that the product O-(2,6-diformyl-4-methylphenyl)dimethylthiocarbamate was pure and that all traces of 2,6-diformyl-4-methylphenol were removed. Dissolving the product in dichloromethane, while washing with water, ensured removal of the sodium complex. Very pure product was obtained after several washings with a weak acid, water, and a weak basic solution followed by drying over $MgSO_4$. The product must be dried overnight in a dessicator prior to use.

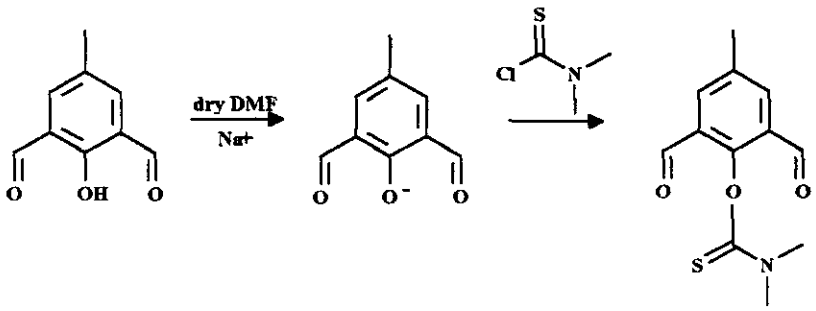

Scheme 4.2

The infrared spectrum of the pale yellow solid shows strong absorption bands at 1548 and 1193 cm^{-1} which are characteristic of O-aryldialkythiocarbamates, **(Figure 4.1b)**. In the ^1H NMR spectrum the N-methyl protons appear as two signals superimposed on one another at approximately δ 3.5 ppm, **(Figure 4.2b)**.

4.2.3 Thermal Rearrangement

Thermal rearrangement **(Scheme 4.3)** was best performed in 2g portions. A study by S. Brooker found that the optimum temperature was 180°C.[6] If the temperature was lower than this rearrangement did not fully occur and temperatures above 180°C caused degradation of the dialdehyde. S-(2,6-diformyl-4-methylphenyl)dimethylthiocarbamate was obtained in very pure form by washing the melt with ether and ethanol.

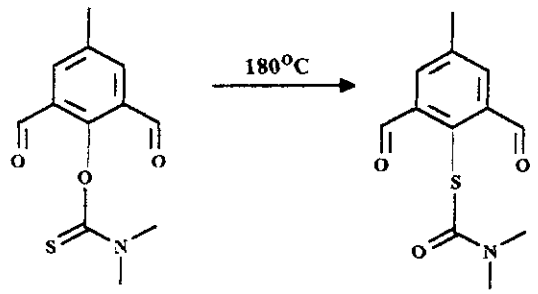

Scheme 4.3

Successful thermolysis was confirmed by inspection of the infrared and ^1H NMR spectra, **(Figure 4.1c and 4.2c)**. The infrared spectra shows that the bands at 1548 and 1193 cm^{-1}, characteristic of O-aryldialkythiocarbamates, had disappeared. The methylene region of

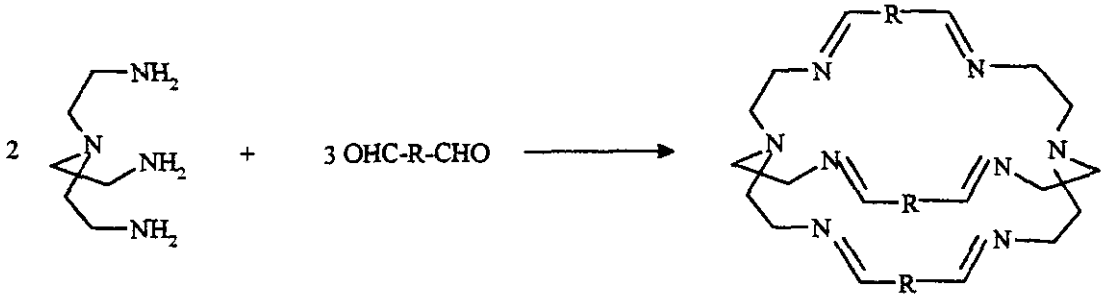

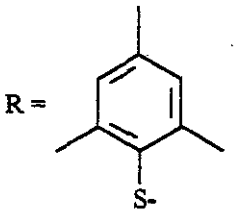

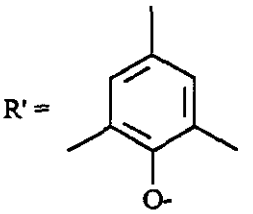

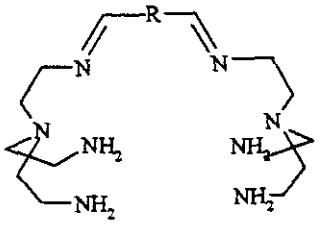

L2

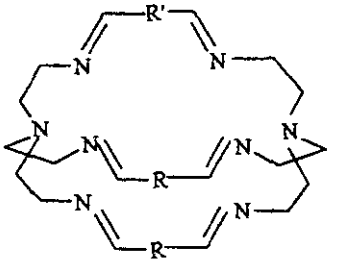

L3

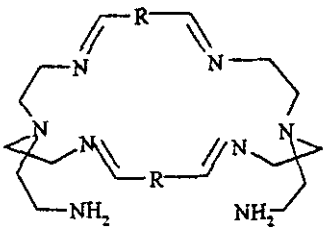

L4

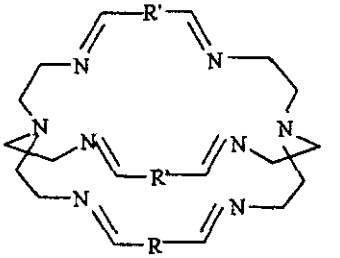

L5

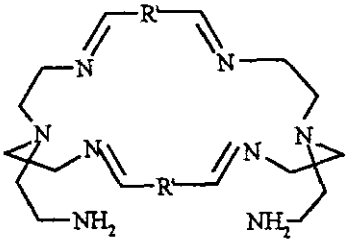

L6

Scheme 4.4

the ^{1}H NMR *spectrum significantly different - the two superimposed signals observed for the* N-methyl groups in the O-(2,6-diformyl-4-methylphenyl)dimethylthiocarbamate compound are observed to separate into two individual signals. The downfield shift is due to deshielding of the protons on one methyl group as a result of interaction with the circulating π electrons of the carbonyl group.

4.3 Cryptate Synthesis

Although the thiolate-containing dialdehyde has successfully been incorporated into macrocycles, to date, the successful synthesis of a thiolate-based cryptate has not been reported. The problems in obtaining the starting dialdehyde make the synthesis even more difficult as only small scale approach is feasible. Sulphur can also be difficult to handle due to the tendency to form disulphides.[7]

Failure to produce the free ligand, L1, under a variety of temperature and high dilution conditions in alcoholic solvents, prompted a template synthesis approach. The products obtained from attempted template synthesis on silver, copper, zinc, cadmium and lead seem to indicate that a variety of products with similar solubilities can be produced. The most success seems to come when using silver as a template ion although the presence of other impurities such as pendant arm macrocycles make complete characterisation impossible. Characterisation of the products was very dependent on FAB and ES mass spectrometries, as polymeric products often exhibited similar solubilities, infra red spectral features and elemental analysis.

4.3.1 Template Synthesis with Copper (I)

Copper(I) is often successful as a metal template for cryptates.[8] Therefore it was hoped, that owing to its 'soft' nature, this cation would be an ideal template for the thiolate-containing cryptate.

The infrared spectrum of the product gives peaks that can be assigned to imine and amine stretches. This aided our assignment of the FAB mass spectrum which also indicates that a variety of products are formed. The olive green colour of the solid product obtained suggests a degree of oxidation of Cu(I). Acetonitrile was used and a nitrogen atmosphere maintained but the products were often green. This was unsurprising since possible products are pendant arms with amine donors which favour the +2 oxidation state.

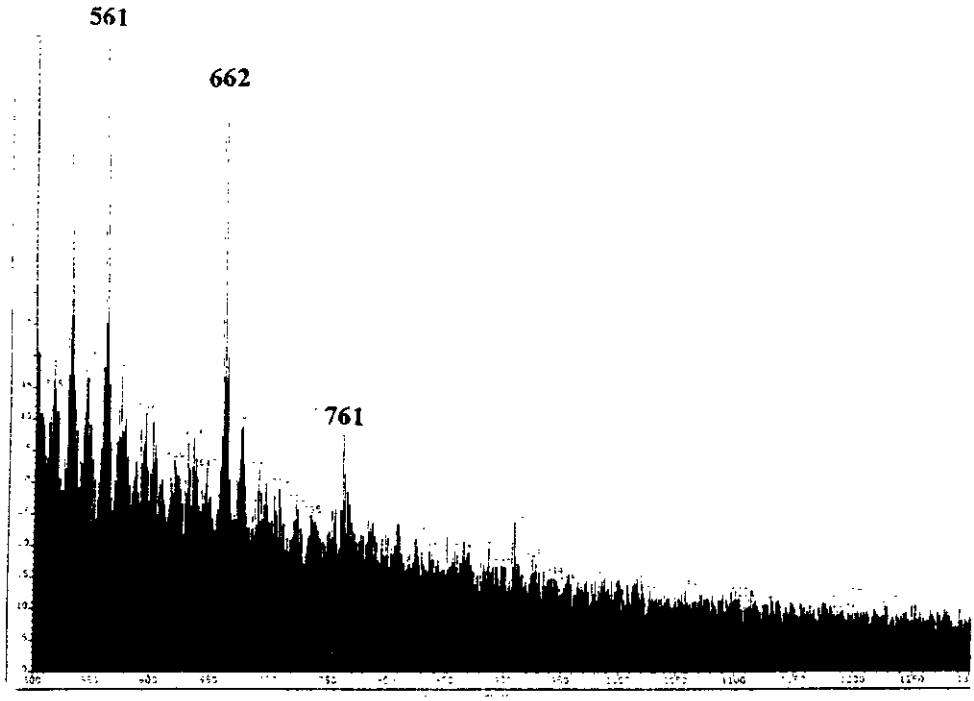

Figure 4.3 FAB mass spec. of Copper Thiolate System indicating dipendant ligand complex is formed, [CuL2]

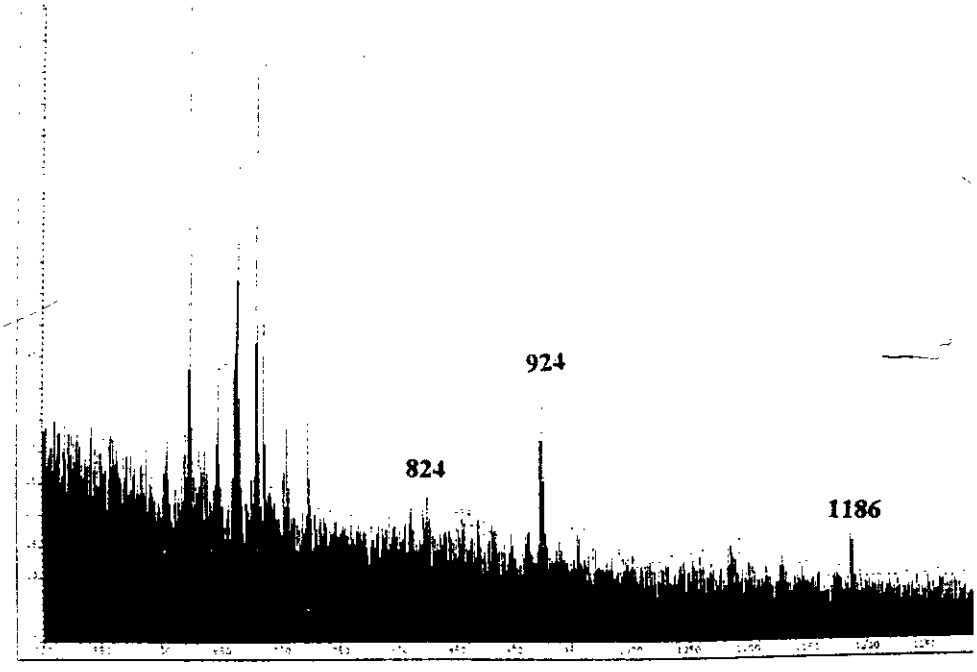

Figure 4.4 FAB mass spec. of Copper Thiolate System indicating intact cryptate is formed

The FAB mass spectrum shows peaks that can be assigned to $[Cu(Tren)]^{2+}$. This by-product would account for the amine stretches in the infrared. A peak is observable at 722 (6%) which could be assigned to protonated ligand. However, due to the supposed combination of complexes present in the mixture, it is impossible to say if this is protonation of the sulphur or imine groups. The most prominent peaks observed are those of copper complexes of the dipendant ligand, L2, (**Scheme 4.4**). Peaks at 561 (100%), 662 (90%) and 761(40%) are attributable to $[Cu_2L2]^{2+}$, $[(Cu_2L2)ClO_4]^+$ and $[(Cu_2L2)(ClO_4)_2]$, respectively, **(Figure 4.3)**. However, peaks were present that could be assigned to $[(CuL1)(ClO_4).MeCN]$ at 924 (40%), $[(CuL1).MeCN]^+$ at 824 (25%) and $[(Cu_2L1)(ClO_4)_3.MeCN]^+$ at 1186 (15 %), **(Figure 4.4)**.

If the FAB mass spectrum analysis is correct it would seem that by optimising the conditions, by changing either solvent, temperature and/or reaction time, a pure product may be attainable. Recrystallisation was not successful probably due to similar solubilities of the products.

4.3.2 Template Synthesis with Silver

Silver has successfully been used as a template ion in the formation of the trpn-capped cryptate series prepared by G. Morgan.[9] The ability of silver to readily co-ordinate to the four available nitrogen donors makes it promising as a template ion.

Silver(I) nitrate was chosen as the template ion but in most cases $Li(ClO_4)$ was added to precipitate the metal complex. As a result of this the infrared spectrum showed peaks that could be attributed to both counterions being present. This observation and the lack of any amine stretches aided assignment of the FAB mass spectrum.

The dominant peak in the electrospray mass spectrum at 1100 (100%) could be attributed to $[(Ag_2L1)(NO_3)(ClO_4)]$ or $[(Ag_2L1)(NO_3)_2].2H_2O$, **(Figure 4.5a)**. The existence of a peak at 997 in the FAB mass spectrum which may be assigned to $[(Ag_2L1)(NO_3)]^+$ makes the former product most likely responsible for the peak at 1100, **(Figure 4.5b)**. There is also a strong signal at 1062 (100%) which could be assigned to $[(Ag_2L1)(NO_3)_2]$, however **Figure 4.5c** also shows a peak at 830 (35%) which can be assigned to the mononuclear complex, [AgL1]. This is plausible as the FAB mass spectrum of X-ray structurally characterised dinuclear silver trpn-capped cryptates often shows the mononuclear complex as the dominant

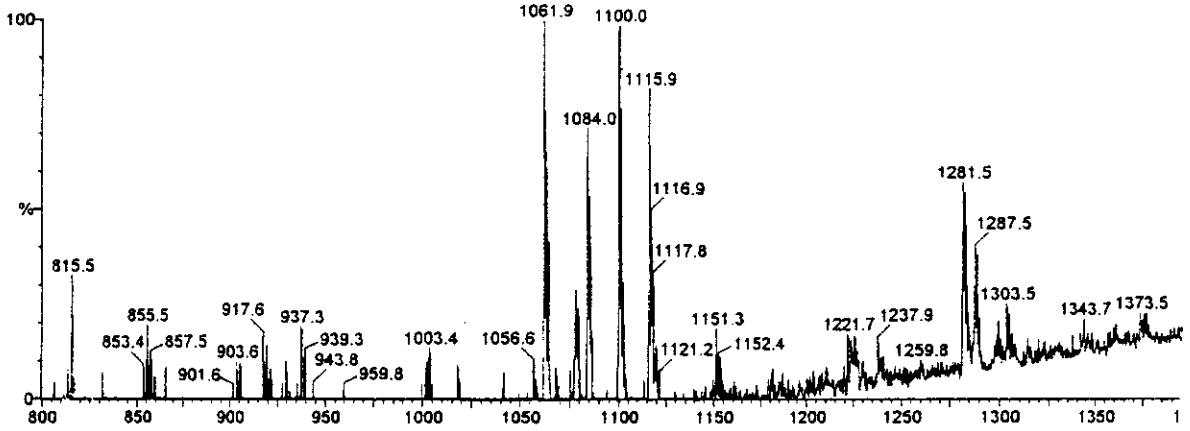

Figure 4.5a Electrospray mass spec. of Silver Thiolate System indicating intact ligand is formed, [Ag_2L1].

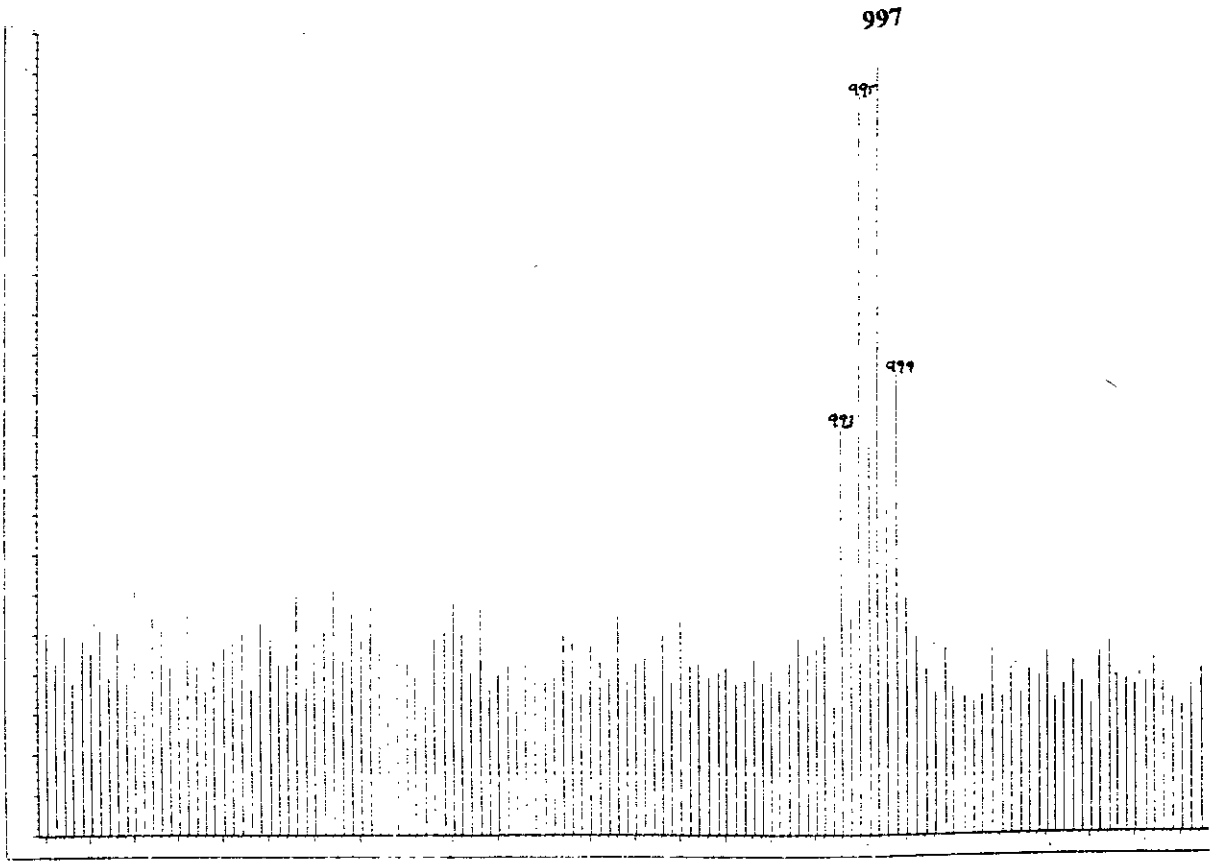

Figure 4.5b FAB mass spec. of Silver Thiolate System confirming intact ligand is formed, [Ag_2L1].

peak. There are several peaks which can be assigned to mononuclear and dinuclear complexes, where the protecting group has either associated with the complex or has not been fully removed, e.g. peaks a 1281 (60%) and 1109 (100%) could possibly be assigned to $[(Ag_2L1)(ClO_4)_2].2CONMe_2$, and to $[(Ag_2L1)(ClO_4)].CONMe_2$ respectively, while peaks at 903 (65%) and 1103 (40%) to $[(AgL1]^+.CONMe_2$ and $[(AgL1)(ClO_4)].CONMe_2$, respectively.

The complex formed was soluble in acetonitrile. The ^1H NMR spectrum in d_3-MeCN is difficult to interpret owing to overlapping in the methylene region, **(Figure 4.6)**. This is unsurprising if the protecting group is still in place. There is also no evidence of aldehyde protons further downfield leading us to believe that a Schiff base condensation has occurred. A promising result is that the aromatic region and imine region integrate for the correct amount of protons and also that they are related by NOE (irradiation of the imine proton, gives enhancement of the aromatic and of a methylene doublet, presumably $H_{c(eq)}$).

4.3.3 Template Synthesis with Cadmium and Lead.

Both cadmium(II) and lead(II) have an affinity for soft donors such as sulfur and have been used on a number of occasions in the template formation of cryptates and therefore may be ideal as a template ion.

N. Martin[4] found that when templating with cadmium and lead, the products were of the phenolate cryptate even though the starting thiolate-containing dialdehyde was found to be pure and most definitely the rearranged ligand. The synthesis, at this stage, had been attempted without any attempt at cleavage of the protecting subunit of the thiol group. Recent reports by Brooker[5] suggested that for macrocyclic (and therefore probably macrobicyclic) formation, removal, e.g. by nucleophilic base hydrolysis, of the dimethylcarbamoyl protecting group prior to attempts at ligand formation was essential.

The possibility also arises that when templating with Cd^{2+}, the cryptate is not composed of three thiolate groups but a combination of phenolate and thiolate head groups. This would account for the low percentage of sulphur in the elemental analysis and the presence of NH_2 stretches in the infrared spectrum.

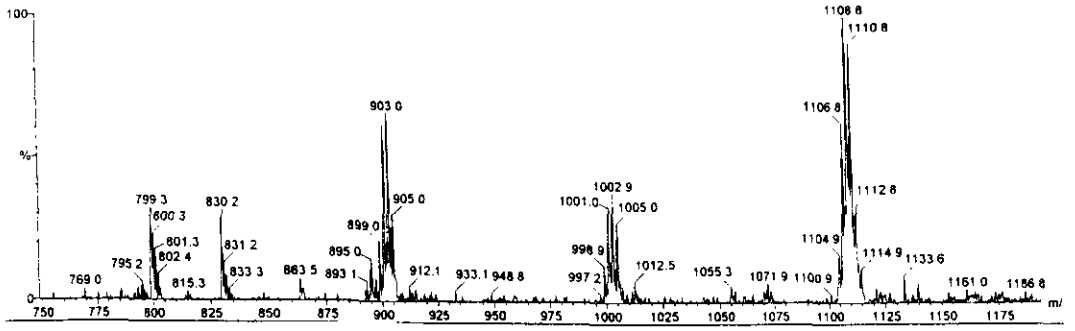

Figure 4.5c Electrospray mass spec. of Silver Thiolate System suggesting mononuclear complex is formed, [AgL1].

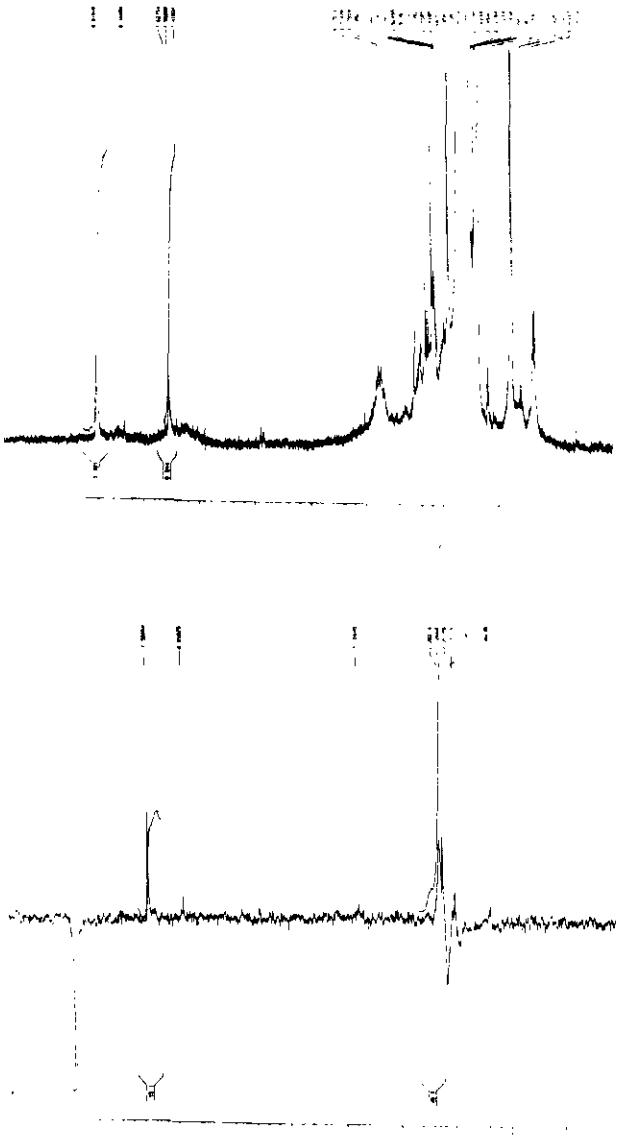

Figure 4.6 ^{1}H NMR and NOE of $[Ag_2L1]$

4.3.3.1 Lead

For the lead complex it is most probable that the majority of the product is polymeric as the complex was almost insoluble. Peaks in the FAB mass spectrum at 1138 (30%)and 1442 (8%) can be assigned to $[Pb_2L1]^{4+}$ and $[Pb_3L1]^{6+}$ respectively. However it is unlikely that the cryptate could host more than one lead ion and this makes the possibility of polymerisation more likely.

4.3.3.2 Cadmium

The infrared spectrum of the product gives peaks that can be assigned to imine (1637 cm^{-1}) and amine (3423 cm^{-1}) stretches. Characteristic absorbances for the perchlorate counterion were visible at 1099 and 623 cm^{-1}. This infrared spectrum has aided our assignment of the FAB mass spectrum which also suggests that a variety of products are formed.

Peaks in the FAB mass spectrum at 930 (100%), 946 (68%), and 1260 (42%) may be assigned to $[CdL1(ClO_4)]^+$, $[Cd_2L1]^{4+}$ and $[Cd_2L1(ClO_4)_3]^+.H_2O$, respectively, **(Figure 4.7a)**. However, the peak at 930 (100%) can also be assigned to $[Cd_2L3]^{4+}$ **(Scheme 4.4)**. This is a strong possibility as a peak at 913 (100%), in the electrospray mass spectrum, may be assigned to $[Cd_2L5]^{4+}$ indicating that one or two phenolate head groups can be incorporated, **(Figure 4.7b)**. This would also account for the low percentage of sulphur (3.22%) found in the elemental analysis. Peaks at 695 (55%) and 795 (35%) suggest the existence of the phenolate-containing pendent arms ligand $[CdL6]^{2+}.2H_2O$ and $[CdL6(ClO_4)]^+.2H_2O$, **(Scheme 4.4)**.

4.3.4 Template Synthesis with Zinc

The infrared spectrum of the product gives peaks that can be assigned to imine (1636 cm^{-1}) and amine (3281 and 3333 cm^{-1}) stretches, **(Figure 4.8).** Characteristic absorbances for the perchlorate counterion were visible at 1098 and 623 cm^{-1}.

Evidence for the intact cryptate, L1, comes from the presence of peaks in the electrospray mass spectrum at 1053 (100%), 1149 (70%) and 1187 (35%) which correspond to $[Zn_23HL1(ClO_4)_2]^{2+}$, $[Zn_2L1(ClO_4)_3]^+$ and $[Zn_2L1(ClO_4)_3]^+.2H_2O$, respectively, **(Figure 4.9a)**.

However, the dominant product appears to be the mononuclear pendant arm complexes of the ligand L4, **(Scheme 4.4)**. Proposed mononuclear complexes include $[Zn.2HL4].H_2O$

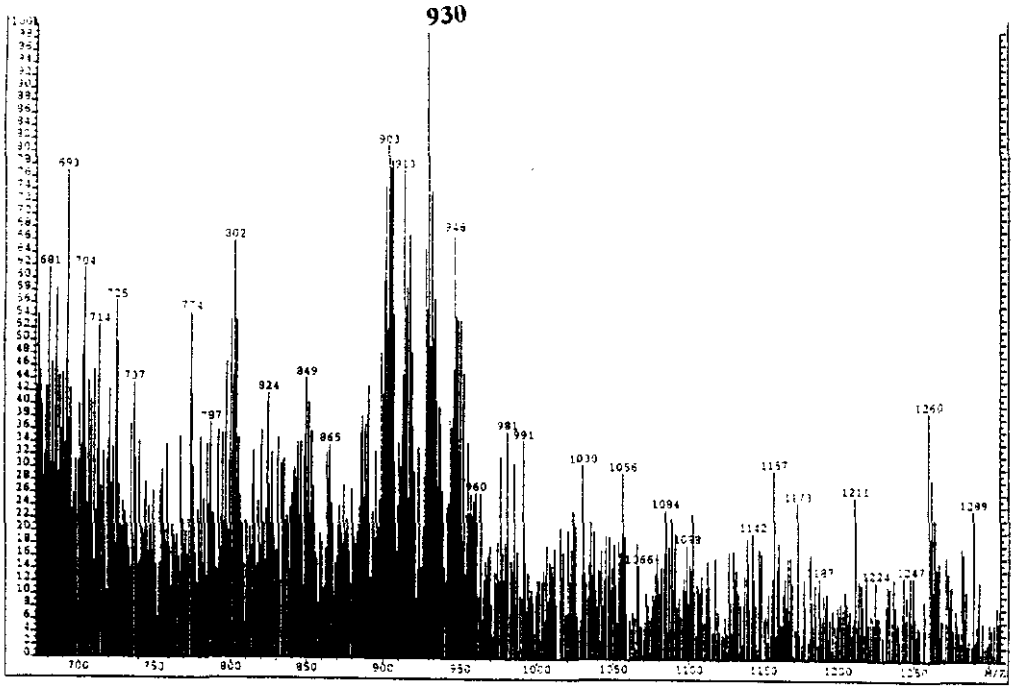

Figure 4.7a ***FAB mass spec. of Cadmium Thiolate system indicating intact thiolate ligand is formed, [Cd$_x$L1].***

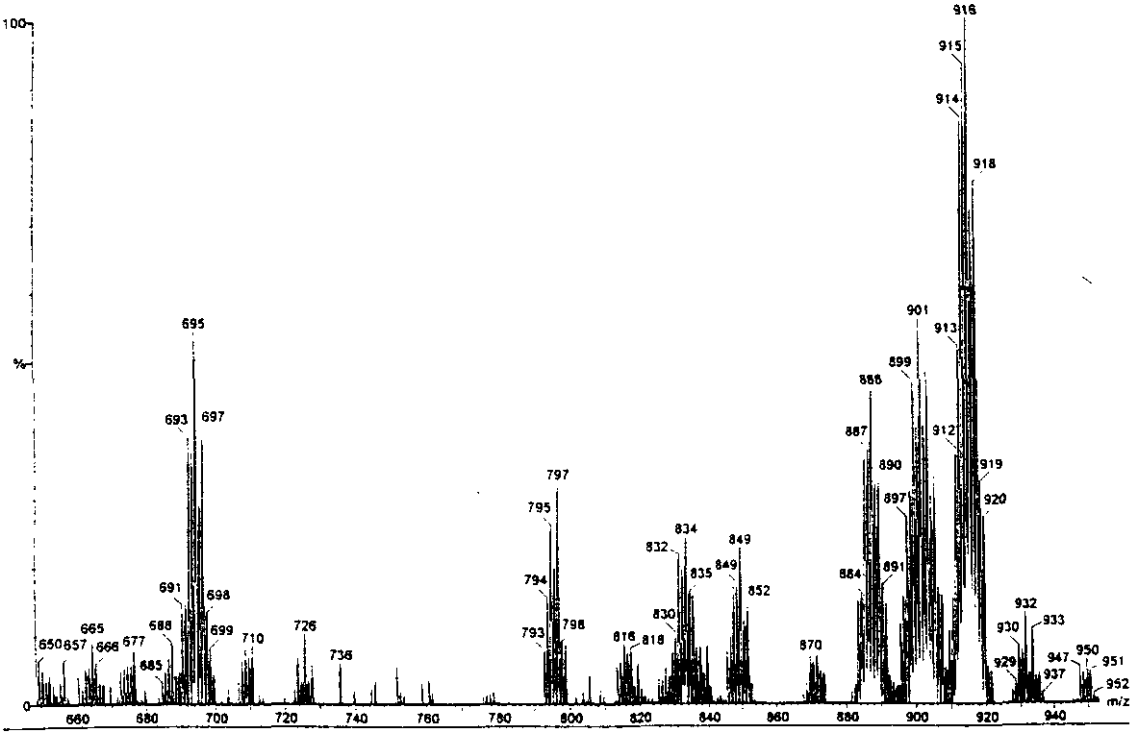

Figure 4.7b ***Electrospray mass spec. of Cadmium Thiolate system indicating that phenolate head groups may be incorporated.***

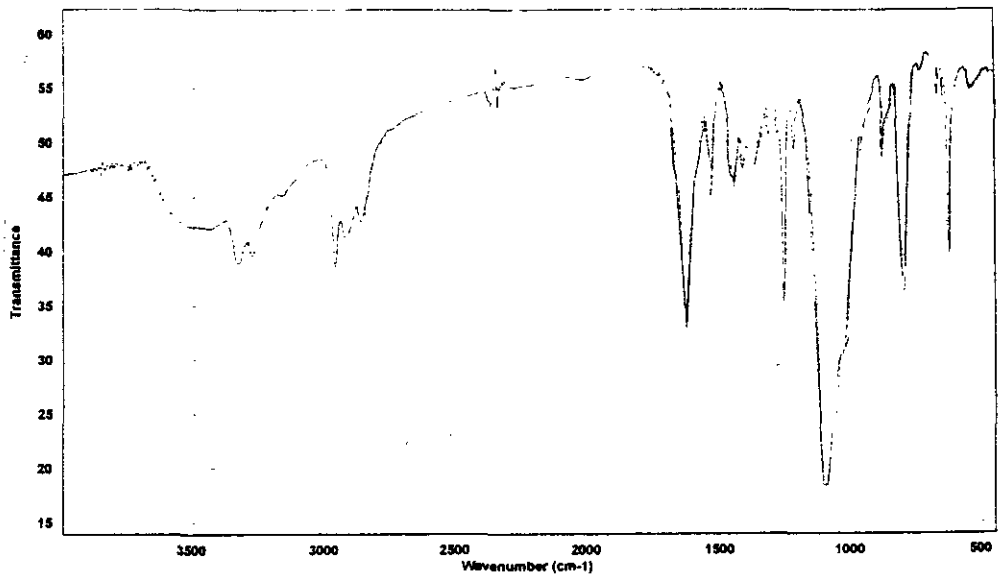

Figure 4.8 Infrared Spectrum of Zinc Thiolate System

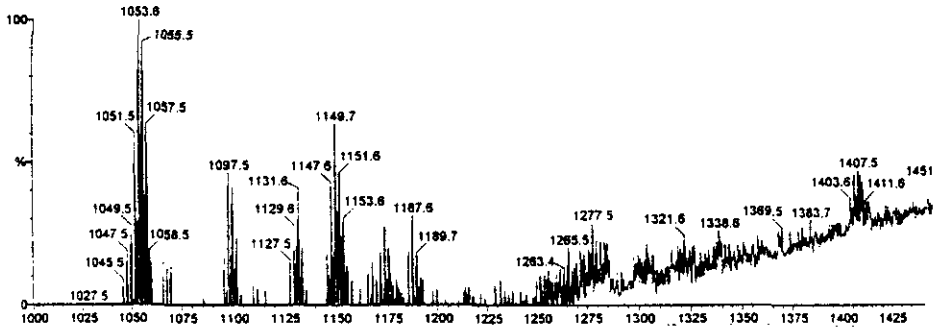

Figure 4.9a Electrospray mass spec. of Zinc Thiolate System indicating intact cryptate is formed.

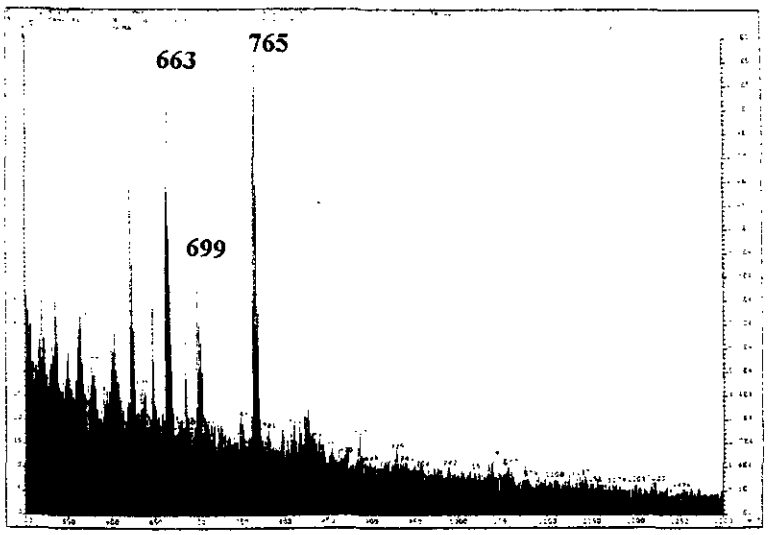

Figure 4.9b FAB mass spec. of Zinc Thiolate System indicating pendant arm complexes, [ZnL4] are formed.

(m/z^+ 663, 95%), $[Zn.2HL4].ClO_4.H_2O$ (m/z^+ 765, 100%), $[ZnL4]^{2+}.2H_2O$ (m/z^+ 679, 100%), and $[Zn.2HL4].3H_2O$ (m/z^+ 699, 100%), **(Figure 4.9b)**.

Whether protonation of the thiolate sulphur has occurred as opposed to protonation of the imine group cannot be deduced. The existence of characteristic absorptions due to perchlorate are evident in the infrared spectrum so it would seem that protonation of the sulphur group is most likely. However, the complex nature of the solid product makes this only a possibility and not a certainty.

4.4 Conclusion

At least in the case of the disilver product and in several other metal (e.g. dizinc) products there is evidence for the formation of the intact thiolate cryptate. In the future these promising experiments can be followed up with investigations into the effect of e.g. different counterions/solvent and reaction conditions. Altering these parameters may hopefully result in isolation of a pure intact thiolate cryptate.

4.5 Experimental

4.5.1. Synthesis of 2,6-diformyl-4-methylthiophenol

4-methylphenol (p-cresol) (108g, 1mol) was added to a solution of NaOH (40g, 1mol) in H_2O (160ml). The mixture was stirred for up to 20 minutes until a golden brown solution had formed. Formaldehyde (35% solution in water, 2mol) was added to the stirring solution and then the mixture was left to stand for up to 2 days until an off white solid had precipitated. This solid was collected by filtration and the filtrate was left to stand to obtain a second crop of off-white solid. After washing the solid with saturated NaCl solution (100ml), it was fully dissolved in water (1000ml) and then acidified to pH ~5 with acetic acid causing a fine white powder (2,6-dihydroxy-methyl-4-methylphenol, DHMP) to precipitate. After stirring for 10 minutes the white powder was collected by filtration and dried in a vacuum dessicator overnight. (Yield = 60%).

MnO_2 (100g) (supplied by ACROS) was activated in a furnace at 150°C overnight. It was then cooled to room temperature and added to a slurry of 50g of 2,6-dihydroxy-methyl-4-methylphenol (DHMP) in toluene (70ml). This mixture was refluxed overnight during which time a bright yellow colour developed. The solution was then filtered and dried over $MgSO_4$. After removing the $MgSO_4$, the solution was reduced in volume and pumped to dryness. (Yield = 73%).

C H N analysis:- $[C_8H_8O_3]$

	C %	H %
Calc.	65.85	4.88
Found.	65.92	4.59

Infrared spectrum:-

Inter alia (cm^{-1}) C-H 2932, 2677; C=O 1680, phenol 1648

Mass spectrum:-

m/e^+	Formula	Peak	% of base peak
	$[C_8H_8O_3]^+$	165	100

4.5.2 O-(2,6-diformyl-4-methylphenyl)dimethylthiocarbomate

60 % NaH (1.6g , 0.67 mol) in mineral oil was added to a stirring suspension of DFMP (9g, 0.61 mol) in dry DMF on an ice bath. This was stirred for 15 minutes during which time hydrogen gas evolved and at hick yellow/orange slurry developed. A solution of dimethylthiocarbomyl (10g, 0.81mol) in dry DMF (20ml) was slowly added to the slurry. The ice bath was removed and the resulting mixture was stirred at 40°C for one and a half hours during which time a brown/red solid precipitated. The mixture was washed with ice cold water (200ml) and the solid was collected by filtration. The solid was dissolved in dichloromethane, washed with water, dilute HCl, water, weak Na_2CO_3 solution and finally water to remove unreacted DFMP. The deep red dichloromethane layer was dried over $MgSO_4$, then evaporated to dryness producing a pale brown solid. (Yield = 75%).

C H N analysis:- $[C_{12}H_{13}NO_3S]$

	C %	H %	N %
Calc.	57.37	5.18	5.57
Found	57.55	5.30	5.66

Infrared spectrum:-

Inter alia (cm^{-1}) C-H 2927, 2887, O-aryl dialkylthiocarbomate 1549, 1193.

Mass spectrum:-

m/e^+	Formula	Peak	% of base peak
	$[C_{12}H_{13}SNO_3]^+$	251	10
	$[C_{12}H_{13}NO_3]^+$	218	90

4.5.3 S-(2,6-diformyl-4-methylphenyl)dimethylthiocarbomate; thermal rearrangement

The pale brown precipitate of 2,6-diformyl-4-N,N-dimethylthiocarbamoylphenol was thermally rearranged in 2g portions.

2,6-diformyl-4-N,N-dimethylthiocarbamoylphenol was placed in a quickfit finger with an attached condenser and N_2 filled balloon. The finger was placed in a flask of refluxing ethanolamine (or benzaldeyde) and heated at ~180°C for 20 minutes. The melt was cooled to room temperature and then dissolved with a small amount of dichloromethane. The process

was repeated for all 2 g portions. All the dichloromethane portions were added together and evaporated to dryness. The thick red liquid was allowed to solidify and a few drops of ethanol were added. Washing the viscous red liquid with ether produced a cream powder which could be isolated by filtration. (Yield = 40 %).

C H N analysis:- $[C_{12}H_{13}NO_3S]$

	C %	H %	N %
Calc.	57.37	5.18	5.57
Found	57.85	5.22	5.68

Infrared spectrum:-

Inter alia (cm^{-1}) C-H 2925, 2840, 1549 peak is absent

Mass spectrum:-

m/e$^+$	Formula	Peak	% of base peak
	$[C_{12}H_{13}SNO_3]^+$	251	10

Attempts at Synthesis of Thiolate-Containing Cryptates using S-(2,6-diformyl-4-methylphenyl)dimethylthiocarbomate as Dialdehyde Spacer

4.5.4 General procedure 1

A nitrogen atmosphere was maintained throughout the following experiments

S-(2,6-diformyl-4-methylphenyl) dimethylthiocarbomate (0.125g, 0.5mmol) was dissolved in isopropanol (40ml) and brought to reflux. Ground NaOH (0.20g, 0.5mmol) was added to the yellow solution and there was an immediate colour change to bright orange. The solution was refluxed for 4 hours until deprotonation was complete (the reaction was monitored by TLC at regular intervals to determine when deprotonation was complete). A solution of the appropriate metal salt (0.5mmol) was added and a colour change to yellow was noted. Tren (0.48g, 0.33mmol) in deoxygenated ethanol was added dropwise over a period of one hour to the solution. After stirring for a further one hour $LiClO_4$ in ethanol (10ml) was added slowly causing a precipitate to form. The flask was placed in an ice bath and the solution was stirred for 15 minutes before filtering. The solid product was washed with ice cold methanol before recrystallisation was attempted.

For all metal complexes attempted CHN analysis was unacceptable owing to the difficulty in obtaining a single pure product. FAB mass spec. indicated the presence of a mixture of products in varying yields including: intact thiolate cryptate, pendant arm macrocycles and phenolate-containing complexes.

4.5.5 Attempted Synthesis of Copper Cryptate

$[Cu(I)(MeCN)_4]ClO_4$ (0.163g, 0.5mmol) was reacted with tren (0.049g, 0.33mmol) and S-(2,6-diformyl-4-methylphenyl)dimethylthiocarbomate (0.125g, 0.5mmol) according to general procedure 1. The solid products from this reaction varied between olive green and yellow in colour, even under an inert atmosphere. (Yield = 66 %).

Infrared spectrum:-

Inter alia (cm^{-1}) C=N 1638, CH 2963, ClO_4^- 1100, 623, NH 3431, 3348

The infrared spectrum was inconclusive in determining cryptate formation as peaks exist for both imine and ν NH_2. This indicates that the reaction produces a mixture of products.

Evidence for intact cryptate L1

FAB mass spectrum:-

m/z	Formula	Peak	% of base peak
	$[CuL1]ClO_4.MeCN$	924	45
	$[CuL1]ClO_4$	824	25
	[HL1]	722	6
	$[Cu_2L1]ClO_4.MeCN$	986	trace

Evidence for thiolate-containing dipendent arm, L2

FAB mass spectrum:-

m/z	Formula	Peak	% of base peak
	$[Cu_2L2]$	561	100

$[Cu_2L2]ClO_4$	662	90
$[Cu_2L2](ClO_4)_2$	761	40

4.5.6 Attempted Synthesis of Silver Cryptate.

$Ag(NO_3)$ (0.05g, 0.33mmol) was reacted with tren (0.049g, 0.33mmol) and S-(2,6-diformyl-4-methylphenyl)dimethylthiocarbomate (0.125g, 0.5mmol) according to general procedure 1. A crystalline brown product precipitated over a period of hours. Recrystallisation was attempted in MeCN. (Yield = 56 %).

Infrared spectrum:-

Inter alia (cm^{-1}) C=N 1635, CH 2963, ClO_4^- 1091, 626, NO_3^-, 1384, 1146

Evidence for intact cryptate L1

Electrospray mass spectrum:-

m/z	Formula	Peak	% of base peak
	[AgL1]	830	35
	$[AgL1].CONMe_2$	903	65
	$[AgL1].(ClO_4).CONMe_2$	1003	40
	$[Ag_2L1].(NO_3)_2.2H_2O$	1100	100
	$[Ag_2L1].(NO_3)_2.$	1062	100
	$[Ag_2L1].(ClO_4)_2.2CONMe_2$	1281	60
	$[Ag_2L1].(ClO_4).CONMe_2$	1109	100

FAB mass spectrum:-

m/z			
	$[Ag_2L1(NO_3)]^+$	997	100
	$[AgL1].CONMe_2.H_2O$	922	50

4.5.7 Attempted Synthesis of Cadmium Cryptate.

$Cd(ClO_4)_2.3H_2O$ (0.12g, 0.33mmol) was reacted with tren (0.049g, 0.33mmol) and S-(2,6-diformyl-4-methylphenyl)dimethylthiocarbomate (0.125g, 0.5mmol) according to general procedure 1. A yellow product precipitated. (Yield = 73 %).

Infrared spectrum:-

Inter alia (cm^{-1}) C=N 1637, CH 2963, ClO_4^- 1099, 623, NH 3423,

The infrared spectrum is inconclusive in determining cryptate formation as FAB mass spec. peaks exist for both imine and amine complexes. This indicates that the reaction produces a mixture of products.

Evidence for intact cryptate L1

Electrospray mass spectrum:-

m/z	Formula	Peak	% of base peak
	$[CdL1]^{2+}$	830	30
	$[CdL1]^+(ClO_4)$	930	15

FAB mass spectrum:-

m/z	Formula	Peak	% of base peak
	$[Cd_2L1](ClO_4)_3.H_2O$	1260	40
	$[Cd_2L1]$	946	65
	$[Cd_2L1].(ClO_4)_2$	1146	5
	[CdL1]	834	10
	$[CdL1].CONMe_2$	903	10

Evidence for phenolate-containg dipendent macrocycle L6

Electrospray mass spectrum:-

m/z	Formula	Peak	% of base peak
	$[CdL6].2H_2O$	695	55

$[CdL6](ClO_4).2H_2O$	795	35

Evidence for mixed thiolate/phenolate-containing cryptate L3

FAB mass spectrum:-

m/z⁺	Formula	Peak	% of base peak
	$[Cd_2L3]$	930	100

Evidence for mixed thiolate/phenolate-containing cryptate L5

FAB mass spectrum:-

m/z⁺	Formula	Peak	% of base peak
	$[Cd_2L5]$	913	100

4.5.8 Attempted Synthesis of Lead Cryptate.

$Pb(ClO_4)_2.3H_2O$ (0.152g, 0.33mmol) was reacted with tren (0.49g, 0.33mmol) and S-(2,6-diformyl-4-methylphenyl)dimethylthiocarbomate (0.125g, 0.5mmol) according to general procedure 1. An insoluble yellow product precipitated. (Yield = 76%).

Infrared spectrum:-

Inter alia (cm^{-1}) C=N 1627, CH 2963, ClO_4^- 1095, 622

Evidence for intact cryptate L1

Electrospray mass spectrum:-

m/z⁺	Formula	Peak	% of base peak
	$[PbL1](ClO_4).CONMe_2$	1095	5

FAB mass spectrum:-

m/z⁺	Formula	Peak	% of base peak
	$[Pb_2L]$	1138	30
	$[Pb_3L]$	1442	6

The presence of di and trinuclear lead complexes is not really considered to be possible unless alternative 'exclusive' sites are used.. The presence of the FAB mass spectrum peaks and the broad nature of the infrared spectrum, together with insolubility may indicate polymerisation.

4.5.9 Attempted Synthesis of Zinc Cryptate

$Zn(ClO_4)_2.6H_2O$ (0.123g, 0.33mmol) was reacted with tren (0.049g, 0.33mmol) and S-(2,6-diformyl-4-methylphenyl)dimethylthiocarbamate (0.125g, 0.5mmol) according to general procedure 1. A yellow product precipitated. Recrystallisation from MeCN resulted in colourless, needle-like crystals. (Yield = 45%).

Infrared spectrum:-

Inter alia (cm^{-1}) C=N 1636, CH 2967, ClO_4^- 1098, 623, NH 3281, 3333

FAB mass spec. indicates that the reaction produces a mixture of products.

Evidence for intact cryptate L1

FAB mass spectrum:-

m/z	Formula	Peak	% of base peak
	$[Zn_2L1](ClO_4)_2$	1053	100
	$[Zn_2L1](ClO_4)_3$	1149	70
	$[Zn_2L1](ClO_4)_3.2H_2O$	1187	35

Evidence for thiolate-containing dipendent arm, L4

FAB mass spectrum:-

m/z	Formula	Peak	% base peak
	$[ZnL4].H_2O$	663	95
	$[ZnL4].2H_2O$	679	100
	$[ZnL4].3H_2O$	699	52
	$[ZnL4].(ClO_4).H_2O$	765	100
	$[Zn_2L4].H_2O$	727	10

APPENDIX 1

MIXED VALENCE THEORY

5.0 The Mixed Valence Phenomenon in EPR Spectroscopy[1]

Mixed valence theory is applied to a d^9,d^{10} [Cu(I) Cu(II)] dimer. In 5.1 the basic theory is introduced, in 5.2 the system g and metal hyperfine tensors of mixed valence dimers are derived.

5.1 Mixed Valence Theory.

$|i,\sigma\rangle$ describes the basis state where the extra electron is localised on site i of M available sites with spin σ ($\sigma = \uparrow,\downarrow$). This set of basis functions is assumed to be complete and orthonormal. The Hamiltonian used is similar to those described in references 2 and 3.

Equation 5.1

$$H = \Sigma\ E_i c_i^{+} c_i\ +\ \Sigma\ \Sigma\ V_{ij} c_j^{+} c_i$$

E_i describes the energy of the zero order states in absence of any intersite interaction whereas V describes the interaction between pairs of subsystems. C_i^{+} and C_i are creation and annihilation operators for the extra electron at site i. The eigenstates for a twosite system are given by:

Equation 5.2

$$1,2: \quad |\sigma\rangle = \alpha|A,\sigma\rangle + \sqrt{(1-\alpha^2)}\,|B,\sigma\rangle$$

$$3,4: \quad \sqrt{(1-\alpha^2)}\,|A,\sigma\rangle - \alpha|B,\sigma\rangle$$

The energies $W_{1,2}$ and $W_{3,4}$ of the two Kramers doublets described by Equation 5.2 are given by

Equation 5.3:-

$$W_{1,2} = \tfrac{1}{2}(E_A + E_B) - \tfrac{1}{2}\sqrt{\Delta^2 + 4|V|^2}$$

$$W_{3,4} = \tfrac{1}{2}(E_A + E_B) + \tfrac{1}{2}\sqrt{\Delta^2 + 4|V|^2}$$

Where $\Delta = E_B - E_A$

The mixing parameter α is given by **Equation 5.4:-**

$$\alpha = \frac{\sqrt{2}}{2} \quad \frac{\Delta + \sqrt{\Delta^2 + 4|V|^2}}{\sqrt{(\Delta^2 + 4|V|^2 \, \Delta\sqrt{(\Delta^2 + 4|V|^2))}}}$$

The energies $W_{1,2}$ and $W_{3,4}$ and α depend on the nuclear configuration through vibronic coupling; a harmonic dependence of the energies E_i on the totally symmetric stretching mode of each site is assumed.[1-4]

Equation 5.5

$$E_A(q_A'q_B) = E_A^{red}(0) + E_B^{ox}(0) + \tfrac{1}{2} kq^2_A + \tfrac{1}{2} kq^2_B + lq_B$$

$$E_B(q_A'q_B) = E_A^{ox}(0) + E_B^{red}(0) + \tfrac{1}{2} kq^2_A + \tfrac{1}{2} kq^2_B + lq_A$$

k represents the harmonic force constants of the totally symmetric vibrations, l determines the change in bond length upon reduction. Assuming that V does not depend on the co-ordinate $q = (q_A - q_B)/\sqrt{2}$ the equations for $W_{1,2}$ and $W_{3,4}$ are rewritten :

Equation 5.6

$$W_{1,2} = \tfrac{1}{2} Q^2 - \tfrac{1}{2} \sqrt{(\Delta_0 + 2\lambda Q)^2 + 4|V|^2}$$

$$W_{3,4} = \tfrac{1}{2} Q^2 + \tfrac{1}{2} \sqrt{(\Delta_0 + 2\lambda Q)^2 + 4|V|^2}$$

Where $\Delta_0 = E_A^{ox}(0) - E_A^{red}(0) + E_B^{red}(0) - E_B^{ox}(0)$, $\lambda = l\sqrt{\hbar\omega/2k}$ and $Q = \sqrt{k/\hbar\omega}q$ is the energy of the vibration corresponding to the q co-ordinate. For a symmetrical dimer with $\Delta_0 = 0$ α is given by **Equation 5.7**:-

$$\alpha(Q) = \frac{\sqrt{2}}{2} \quad \frac{V}{\sqrt{(4|V|^2 + 4\lambda^2Q^2 + \lambda Q\sqrt{(4\lambda^2Q^2 + 4|V|^2))}}}$$

$|\alpha(Q)|^2$ is the probability of finding the system in one of the states $|A,\sigma\rangle$ when the nuclear configuration is at position Q. The energies correspond to the Born-Oppenheimer potential

energy surfaces for the four states possible. It is reasonable to assume that the mixed valence dimer will choose the nuclear configuration with the lowest total energy Q The minima of the *surfaces described by* $W_{1,2}$ *and* $W_{3,4}$ *occur at :*

Equation 5.8

$$Q = \pm \lambda^{-1} \sqrt{(\lambda^4 - V^2)}$$

For $\lambda^2 >> |V|$ there are two minima at $Q = \pm \lambda$; the probability of finding the system in one of the states $|A,\sigma\rangle$ is $|\alpha(-\lambda)|^2 \sim 0$ and $|\alpha(-\lambda)|^2 \sim 1$, i.e. at $Q = -\lambda$ the unpaired electron is on subsystem A and at $Q = +\lambda$ the electron is localised on subsystem B. For $|V| >> \lambda^2$ there is only one minimum ($Q = 0$) on the surface corresponding to $W_{1,2}$ (Q) and $|\alpha(0)|^2 = ½$; i.e. the electron is delocalised over the two subsystems. For $\lambda^2 >> |V|$ equations(5.1)-(5.7) imply a spontaneous breaking of the molecular symmetry into a point group of lower symmetry.

5.2 EPR Spectra of Mixed Valence Dimers

Application of a magnetic field H will split the degeneracy of the two doublets, the Zeeman frequencies for the two doublets are given by **Equation 5.9:-**

$$\omega_{ze}^{(i)} = g^{(i)}(Q)\beta H/h$$

The two Kramers doublets are given by i (=1,2). To calculate the time evolution of an ensemble of identical systems under the influence of a linearly polarized microwave field the equation of motion for the density operator must be solved:

Equation 5.10

$$ih \frac{d\rho}{dt} = [H, \rho]$$

Through random phase assumption the initial conditions for this system of differential equations are given by[4]:

Equation 5.11

$$\rho_{ij}(Q, t=0) = \delta_i Z^{-1} \exp(-1/kT\{(Q) + W_{ze}^{(i)}(Q)\})$$

where the density matrix is formulated in the basis of definite energy states, and Z is the partition function given by:

Equation 5.12

$$Z = f\Sigma \exp(-1/kT\{W_i(Q) + W_{ze}^{(i)}(Q)\})dQ$$

where $W_{Ze}^{(i)}$ are the Zeeman energies for the four states, and the nuclear motion is treated classically. The continuous wave absorption spectrum is calculated as described.[4]

Equation 5.13

$$S(\omega) = Im(Tr(S_+\rho))$$

Note that to a good approximation the microwave will introduce no coherences between states of different Kramers doublets. Thus the expected spectrum will be the sum of the individual subspectra from the two doublets. The main difference is that the populations of the two doublets are coupled via the initial conditions and that the subspectra are integrated over the co-ordinate Q.

The final expression for the EPR spectrum of the mixed valence dimer as a function of frequency is:

Equation 5.14

$$S(\omega)) = f\left\{\frac{D_1^0(Q)T_2\omega_{11}(Q)}{1+T_2^2(\omega-\omega_{Ze}^{(1)}(Q))^2 + \frac{1}{2}\omega_{11}^2(Q)T_1T_2} + \frac{D_2^0(Q)T_2\omega_{12}(Q)}{1+T_2^2(\omega-\omega_{Ze}^{(2)}(Q))^2 + \frac{1}{2}\omega_{12}^2(Q)T_1T_2}\right\}dQ$$

T_1 and T_2 are the electronic relaxation times, $\omega_{ii} = \frac{1}{2}g^{(i)}\beta H_1$ are the transition moments for transitions within the two doublets, and $D_i^0(Q)$ are the weighted population differences given

by:

Equation 5.15

$$D_1^0(Q) = Z^{-1}\{\exp(-\sim 1/kT\{W_2(Q) + \tfrac{1}{2}h\omega_{Ze}^{(1)}\}) - \exp(-\sim 1/kT\{W_1(Q) - \tfrac{1}{2}h\omega_{Ze}^{(1)}\}$$

$$D_2^0(Q) = Z^{-1}\{\exp(-\sim 1/kT\{W_4(Q) + \tfrac{1}{2}h\omega_{Ze}^{(2)}\}) - \exp(-\sim 1/kT\{W_3(Q) - \tfrac{1}{2}h\omega_{Ze}^{(2)}\}$$

These equations describe the extreme cases of fully localised or fully delocalised dimers. In the case of partial localisation they fail to predict the correct temperature dependence of the spectrum (delocalisation at higher temperatures). This is probably because an inhomogenous nuclear process ('hopping' over the barrier) has been neglected. Furthermore, the Bom-Oppenheimer assumption may be no longer valid in the 'class II' limit.

5.3 The System g and Metal Hyperfine Tensors

The [Cu(I) Cu(II)] dimer is divided into two hypothetical subsystems Cu_{A1} and Cu_{A2} the odd electron resides in turn on each of the subsystems. It is assumed that in the local frame of the two subsystems the corresponding g and A tensors are collinear; it will be shown, however, that this assumption is not true in general for the system g-tensor and the two individual hyperfine tensors.

The system g tensor is found by building the matrices of the magnetic moment operator of the two doublets. and by comparing those to the equivalent matrices formed by the application of a spin Hamilton operator. The basis states are assumed to be corrected for spin-orbit coupling, i.e. the states are no true eigenfunctions of the S^2 and S_z, operators but contain small admixtures of singly excited states with opposite spin quantum numbers. If overlap between functions on different subsystems is neglected which is consistent with the initial assumptions of orthogonal basis states - the result is essentially a delocalization weighted sum of the hypothetical monomer g-tensors of the two subsystems:

Equation 5.16

$$\mathbf{g}^{(1)}(Q) = \alpha^2(Q)\mathbf{g}^{(A)} + (1 - \alpha^2(Q))\mathbf{g}^{(B)}$$

$$\mathbf{g}^{(2)}(Q) = \alpha^2(Q)\mathbf{g}^{(B)} + (1 - \alpha^2(Q))\mathbf{g}^{(A)}$$

Note that the individual tensors $g^{(A,B)}$ must be expressed in the same co-ordinate frame. This is arbitrarily taken to be the frame where $g^{(A)}$ is diagonal; $g^{(B)}$ is rotated in the frame of $g^{(A)}$ using the three Euler angles α, β, γ through the rotation matrix $T(\alpha, \beta, \gamma)$.

Equation 5.17

$$\mathbf{g}^{(1)}(Q) = \alpha^2(Q)\mathbf{g}^{(A)} + (1 - \alpha^2(Q))\mathbf{T}\mathbf{g}^{(B)}\mathbf{T}^T$$

$$\mathbf{g}^{(2)}(Q) = \alpha^2(Q)\mathbf{T}\mathbf{g}^{(B)}\mathbf{T}^T + (1 - \alpha^2(Q))\mathbf{g}^{(A)}$$

Clearly, the system g-tensor is not diagonal in this frame unless the principal axes of $\mathbf{g}^{(A)}$and $\mathbf{g}^{(B)}$ coincide.

It is known that in square-planar Cu(II) complexes the largest component of g is normal to the plane defined by the ligands.[5] A symmetrical dimer is made from two square-planar Cu sites, with the two planes forming an angle β. A delocalised mixed valence complex is assumed, i.e. $\alpha^2 = ½$ for all values of Q. With $\alpha = \gamma = 0$ and $\beta = 180°$-O the non-diagonal system g-tensor is obtained. Upon diagonalisation of the non-diagonal system g-tensor the principal values are found to be those given by Equation 5.18.

Equation 5.18

$$g_1^{obs} = ½ (g_x + g_z) + ½ \cos(\beta)(g_x - g_z)$$

$$g_2^{obs} = g_y$$

$$g_3^{obs} = ½ (g_x + g_z) + ½ \cos(\beta)(g_z - g_x)$$

Evaluation of the local hyperfine tensors, with respect to the orientation of the system g-tensor, results in tilting of the A-tensors at angles $\pm ½ \beta$ with respect to the global reference frame:

Equation 5.19

$$\mathbf{A}^{(A)} = ½ R(0, -½\beta, 0)\mathbf{A}^{(A)}\mathbf{R}^T(0, -½\beta, 0)$$

$$\mathbf{A}^{(B)} = ½ R(0, -½\beta, 0)\mathbf{A}^{(B)}\mathbf{R}^T(0, +½\beta, 0)$$

R is the usual Euler angle rotation matrix $A^{(i)}$ are the hyperfine tensors and $A^{(i)}$ the hyperfine tensors in the frame of the diagonal system g-tensor. Furthermore, the hyperfine values are reduced to ~50 % of the value observed for the monomeric copper site. A seven line hyperfine structure in a mixed-valence copper dimer is only possible in the completely delocalised case, i.e. ($|V| >> \lambda^2$). Since λ^2 is in the order of magnitude of a vibration (hundreds of wavenumbers) V must be in the order of magnitude of thousands of wavenumbers to ensure a delocalised class III mixed-valence dimer as observed in the Cu_A center of COX and N_2OR.

APPENDIX 2

CRYSTALLOGRAPHY DATA

X-ray Data Collection and Refinement Parameters for X-ray Crystal Structures described in Chapters 2 and 3.

Below is a full description of the X-ray experiment for [CuL5](BF_4). The X-ray data collection and refinement parameters for remaining crystal structures can be written in the same manner, but for simplicity are summarised in tabular form.

Crystal data: **[CuL5](BF$_4$)**, **$C_{27}H_{27}BrCl_3CuF_4N_4$**, yellow thin plate, crystal dimensions 0.68 x 0.56 x 0.08 mm^3, monoclinic, a = 25.208(5), b = 11.531 (2), c = 20.820 (3) Å, U = 5760 (2) $Å^3$, u = 1.088 mm^{-1}, space group C2/c, Z = 8, F (000) 2704.

Data was collected at 293 (2) K on a Siemens P4 four circle diffractometer using graphite monochromated Mo-Kα radiation (λ = 0.71073). Unit cell parameters were determined by non-linear least squares refinement of 35 actually centered reflections ($9 < 2\sigma < 25°$). Using 1.4° ω-scans at $5min^{-1}$, 3857 reflections were collected in the range ($2.09 < 2\sigma < 45°$), 3385 unique reflections (R_{int} = 0.0189) were used in the refinement. Crystal stability was monitored by recording three check reflections every 97 reflections and no significant variation was observed. The data were corrected for Lorentz and polarisation effects and an empirical absorption correction was applied based on φ-scan data (T_{max} = 0.900. T_{min} = 0.612).

The structure was solved by direct methods[1], which revealed all the non-hydrogen atoms. Hydrogen atoms were inserted at calculated positions with isotropic temperature factors 1.2 times the equivalent isotropic U of their carrier atoms. All the data were used for refinement on F^2 which converged with R1 = 0.0823, wR2 = 0.1369, GOOF = 1.044[and conventional R = 0.0500 ($I > 2\sigma$ (I))] for 361 parameters. The final difference map showed no significant residual electron density. All programs used in the structure refinement are contained in the SHELXL-93[2] package.

Table 1 Data Collection and Refinement Parameters for X-ray structures of Cu(I) *Podates described in Chapter 2*

Crystal	**[CuL6](ClO$_4$)**	**[CuL17](ClO$_4$)**	**[CuL15](ClO$_4$)**	**[CuL13](ClO$_4$)**
Temperature	163 (2)	163 (2)	163 (2)	163 (2)
Wavelength (λ)	0.71073	0.71073	0.71073	0.71073
Crystal system	Triclinic	Rhombohedral	Orthorhombic	Monoclinic
Space group	P-1	R3	P c b a	P2(1)/n
Unit cell a (Å)	11.5825 (5)	12.1567 (4)	17.5515 (9)	9.4928 (5)
b (Å)	12.9374 (6)	12.1567 (4)	18.1039 (11)	18.4325 (10)
c (Å)	23.2581 (11)	80.970 (4)	21.4731 (13)	19.0640 (11)
α (°)	80.7930 (10)	90	90	90
β (°)	77.0170 (10)	90	90	103.863 (10)
γ (°)	71.450 (10)	120	90	90
Volume (Å)^3	3204.8 (3)	10363.0 (7)	6823.1 (7)	3238.6 (3)
Z	4	12	8	4
Absorption coeff. (mm^{-1})	1.307	0.753	0.764	4.500
Reflections collected	11308	23671	18388	24532
Independent reflections	8893	9024	4363	5702
R_{int}	0.0377	0.0512	0.1054	0.0706
Final R1 [I > 2σ (I)]	0.1076	0.0577	0.0914	0.0615
wR2 (all data)	0.2506	0.1637	0.1864	0.1547

Table 2 Data Collection and Refinement Parameters for X-ray structures of Cu(I) Podates described *in* Chapter 2

Crystal	[CuL9](ClO$_4$)	[CuL16](ClO$_4$)	[CuL5](BF$_4$)	[CuL1](ClO$_4$)
Temperature	163 (2)	163 (2)	293 (2)	123 (2)
Wavelength (λ)	0.71073	0.71073	0.71073	0.71073
Crystal system	Triclinic	Monoclinic	Monoclinic	Monoclinic
Space group	P-1	$P2_1/c$	C2/c	P2(1)/n
Unit cell a(Å)	11.2620 (15)	9.5403 (4)	25.208 (5)	12.548 (5)
b (Å)	13.5521 (18)	18.6471 (9)	11.531 (2)	17.133 (7)
c (Å)	13.984 (2)	19.2443 (10)	20.820 (3)	12.692 (5)
α (°)	111.755 (11)	90	90	90
β (°)	102.859 (13)	103.99 (10)	107.87	106.82 (2)
γ (°)	104.178 (11)	90	90	90
Volume (Å)^3	1801 (4)	3322.0 (3)	5760 (2)	2611.9 (18)
Z	2	4	8	4
Absorption coeff. (mm^{-1})	0.748	0.805	1.088	0.979
Reflections collected	4075	10612	3857	4814
Independent reflections	3759	5354	3385	4593
R_{int}	0.0152	0.0405	0.0189	0.0216
Final R1 [I > 2σ (I)]	0.0492	0.0623	0.0500	0.0370
wR2 (all data)	0.1361	0.1658	0.1369	0.1094

Table 3 Data Collection and Refinement Parameters for X-ray structures of Cu Azacryptates described in Chapter 3

Crystal	**[CuGT]$(ClO_4)_2$**	**[CuRGT] $(BPh_4)_2$**	**[Cu_2NGT] $(ClO_4)_2$**	**[Cu(II) Carbinolamine] (ClO_4)**
Temperature	293 (2)	293 (2)	153 (2)	153 (2)
Wavelength (λ)	0.71073	0.71073	0.71073	0.71073
Crystal system	Monoclinic	Tetragonal	Rhombohedral	Monoclinic
Space group	P2(1)	P4(3)	R32	P2(2)/c
Unit cell a(Å)	9.5500 (10)	17.800 (2)	9.2790 (10)	13.557 (6)
b (Å)	13.3070 (10)	17.800 (2)	9.2790 (10)	9.134 (5)
c (Å)	11.411 (2)	35.329(7)	32.846 (9)	15.133 (8)
α (°)	90	90	90	90
β (°)	95.89	90	90	101.74
γ (°)	90	90	120	90
Volume $(Å)^3$	1442.5(3)	11194 (3)	2449.1 (8)	1834.7 (16)
Z	2	8	3	4
Absorption coeff. (mm^{-1})	1.001	0.440	1.523	1.387
Reflections collected	4025	8216	1873	2869
Independent reflections	3086	7151	720	2374
R_{int}	0.0517	0.0775	0.0525	0.0526
Final R1 [I > 2σ (I)]	0.0432	0.1398	0.0755	0.0661
wR2 (all data)	0.1060	0.3273	0.2274	0.2048

APPENDIX 3

REFERENCES

References

Chapter 1

1. E. I. Solomon, M. J. Baldwin, and M. D. Lowery, *Chem. Rev.*, **1992**, 92, 521-542.

2. W. Kaim, J. Rall, *Chem., Int. Ed. Engl.*, **1996**, 35, 43.

3. S.J. Lippard, J.M. Berg, *Principles of Bioinorganic Chemistry*, University Science Books, Mill Valley, California, **1994**.

4. R. Malkin, B.G. Malmstrom, *Adv. Enzymol.*, **1970**, 33, 177.

5. M.D. Allendorf, D. J. Spira and E.I. Solomon, *Proc. Natl. Acad. Sci.* U.S.A., **1985**, 82, 3063.

6. H. Beinert, In *Biochemistry of Copper*, J. Peisach, P. Aisen and W. E. Blumberg, Eds., Academic Press, New York, London. **1966**, 213-234.

7. A.G. Sykes, *Adv. Inorg. Chem.*, **1991**, 36, 377.

8. V. McKee, *Adv. Inorg. Chem.*, **1993**, 40, 323.

9. E. I. Solomon, B.L. Hemming, D. E. Root, In *Bioinorganic Chemistry of Copper*, K. D. Karlin and Z. Tyeklar Eds., Chapman and Hall, New York, **1993**, 3-20.

10. E.T Adman, *Adv. Prot. Chem.*, **1991**, 42, 145.

11. P.M.H. Kroneck, W.E. Antholine, H. Koteich, D. H. W. Kastrau, F. Neese, and W.G. Zumft, In *Bioinorganic Chemistry of Copper*, K. D. Karlin and Z. Tyeklar Eds., Chapman and Hall, New York, **1993**; 419-426.

12. K. Mc Killop, *Ph.D. Thesis*, **1987**, The Queen's University of Belfast.

13. D. F. Shriver, P.W. Atkins, C.H. Langford, *Inorganic Chemistry*, Oxford University Press, **1990.**

14. B.J. Hathaway, *Chem. Rev.*, **1983**, 52, 87-169.

15. F. Neese, *Ph.D. Thesis*, **1996**, Konstanz University, Germany.

16. D. R. McMillin, *J. Chem. Ed.*, **1985**, 62, 997.

17. F. A. Cotton and G. Wilkinson, *Adv. Inorg. Chem.*, 2nd Ed. London. Interscience Publishers, **1966.**

18. F. A. Cotton, G. Wilkinson and P. L. Gaus, '*Basic Inorganic Chemistry*' 2nd Edition. John Wiley and Sons, Chichester, **1987**.

19. L. E. Orgel, *'An Introduction to Transition Metal Chemsitry'* Metheven & Co. ltd. London, **1967.**

20. D. F. Shriver, P. W. Atkins and C. H. Langford, *'Inorganic Chemistry'* Oxford University Press, **1990.**

21. T. D. Smith and J. R. Pilbrow, *Coord. Chem. Rev.*, **1974**, 13, 178.

22. C. N. Banwell in *'Fundamentals of Molecular Spectroscopy'*, McGraw-Hill, 3rd Edn. Berkshire, **1983**.

23. D. Marrs, *PhD Thesis*, The Open University, U. K. **1990.**

24. T. N. Sorrell and D. L. Jameson, *J. Am Chem. Soc.*, **1983**, 105, 6013.

25. P. G. Eller, D. C. Bradley, M. B. Hursthouse and D. W. Meek, *Coord. Chem. Rev.*, **1977**, 24, 1.

26. F. H. Jardine, *Adv. Inorg. Radiochem.*, **1975**, 17, 115.

27. U. Sakaguchi and A.W. Addison, *J. Chem. Soc., Dalton Trans.*, **1978**, 600.

28. H. Yokoi and A.W. Addison, *Inorg. Chem.*, **1977**, 16, 1341.

29. P. Hemmerich, In *Biochemistry of Copper*, J. Peisach, P. Aisen and W. E. Blumberg, Eds., Academic Press, New York, London. **1966**; 15-35.

30. F.A. Cotton, G. Wilkinson, P.L Gaus, *Basic Inorganic Chemistry*, **1976**, John Wiley, New York, London, Sydney.

31. E.N. Baker, *J. Mol. Biol.*, **1988**, 203, 1071.

32. M.C. Silvestrinin, M. Brunori, M. J. Wilson and V. M. Darley-Usmar, *J. Inorg. Biochem.*, **1981**, 14, 327.

33. P. M. Colman, H. C. Freeman, J M. Guss, M. Murata, V. A. Norris, J. A. M Ramshaw and M. P. Ventakappa, *Nature (London)*, **1978**, 272, 319.

34. G.E. Noris, B. F. Anderson and E. N. Baker, *J. Mol. Biol.*, **1983**, 165, 501.

35. C. M. Groenveld, S. Dahlin, B. Reinhammar, G. W. Canters, *J. Am Chem. Soc.*, **1987**, 109, 3247.

36. B.G. Malmstrom, *Eur. J. Biochem.*, **1994**, 233, 711.

37. R. A. Marcus, N. Sutin, *Biochem. Biophys. Acta.*, **1985**, 811, 49.

38. M.J. Ettinger and D. J. Kosman In *Copper Proteins*, Ed., T.G. Spiro, Wiley, New York, **1981**, 219.

39. J. W. Whittaker, In *Bioinorganic Chemistry of Copper*, K. D. Karlin and Z. Tyeklar Eds., Chapman and Hall, New York, **1993**, 447-458.

40. J. J. Villafranca, *Copper Proteins*, Ed., T.G. Spiro, Wiley, New York, **1981**, 264.

41. N. J. Blackburn, In *Bioinorganic Chemistry of Copper*, K. D. Karlin and Z. Tyeklar Eds., Chapman and Hall, New York, **1993**, 164-183.

42. J.A. Trainer, E.D. Getzoff, K. M. Been, J. S. Richardson and D.C. Richardson, *J. Mol. Biol.*, **1982**, 160, 181.

43. D. M. Dooley, D. E. Brown, A. W. Clague, J. N. Kemsley, C. D. McCahon, M. A. McGuirl, P. N. Turowski, W.S. McIntire, J. A. Farrar and A. J. Thomson, In *Bioinorganic Chemistry of Copper*, K. D. Karlin and Z. Tyeklar Eds., Chapman and Hall, New York, **1993**; 459-470.

44. A G. Sykes in *Advances in Inorganic and Bioinorganic mechanisms*, Ed. A. G. Sykes, Academic Press, London, **1982**, 1, 121.

45. A. Volbeda and W.G.J. Hol, *J. Mol. Biol.*, **1989**, 209, 249.

46. B. Hazes, K. A. Magnus, C. Bonaventura, J. Bonaventura, Z. Dauter, K. H. Kalk and W.G.J. Hol, *J Protein Sci.*, **1993**, 2, 576.

47. K. A. Magnus, H. Ton-That, J. E. Carpenter, *Chem. Rev.*, **1994**, 94, 727.

48. N. Kitajima and Y. Moro-oka, *Chem. Rev.*, **1994**, 94, 737.

49. E. I. Solomon, B. L. Hemming and D. E. Root, In *Bioinorganic Chemistry of Copper*, K. D. Karlin and Z. Tyeklar Eds., Chapman and Hall, New York, **1993**; 3-20.

50. N. Kitajima, T. Koda, S. Hashimoto, T. Kitigawa and Y. Moro-oka, *J. Chem.Soc., Chem. Commun.*, **1988**, 151.

51. N Kitajima, T. Koda, S. Hashimoto, T. Kitigawa and Y. Moro-oka, *J. Am. Chem. Soc.*, **1991**, 113, 5664.

52. K. A. Magnus, H. Ton-That, J. E. Carpenter, In *Bioinorganic Chemistry of Copper*, K. D. Karlin and Z. Tyeklar Eds., Chapman and Hall, New York, **1993**, 143-150.

53. K. Lerch, *Metal ions in Biological systems*, Ed., H. Sigel, Marcel Dekker Inc., New York, **1981**, 13, 144.

54. E. I. Solomon, K. W. Penfield and D. E. Wilcox, *Struct. Bonding*, **1983**, 53, 1.

55. A. Messerschmidt, A. Rossi, R. Ladenstein, R. Huber, M. Bolognesi, G. Gatti, A. Marchesinin, R. Petruzelli and A. Finazzo-Agro, *J. Mol. Biol.*, **1989**, 206, 513.

56. J.L. Cole, P.A. Clark and E. I. Solomon, *J. Am. Chem. Soc.*, **1990**, 112, 9534.

57. A. Messerschmidt, R. Ladenstein, R. Hubev, M. Bolognesi, L. Avigliano, R. Petruzelli, A. Rossi and A. Finazzo-Agro, *J. Mol. Biol.*, **1992**, 224, 179.

58. A. Messerschmidt, H. Luecke and R. Huber, *J. Mol. Biol.*, **1993**, 230, 997.

59. N. J. Blackburn, M. E. Barr, W. H. Woodruff, J. van der Oost and S. de Vries, *Biochemistry*, **1994**, 33, 10401.

60. R. H. Holm, P. Kennepohl and E. I. Solomon, *Chem. Rev.*, **1996**, 96, 2239-2314.

61. S. Iwata, C. Ostermeler, B. Ludwig and H. Michel, *Nature*, **1995**, 376, 660.

62. B.G. Malmstrom, R. Aasa, *FEBS Lett.*, **1993**, 325, 49.

63. H. Beinert, D. E. Griffith, D.C. Wharton and R. H. Sands, *J. Biol. Chem.*, **1962**, 237, 2337.

64. G. Henkel, A. Muller, S. Weissgraber, G. Buse, T. Soulimane, G. C. M. Steffens and H. F. Nolting, *Angew. Chem. Int. Ed. Engl.*, **1995**, 34, 1488.

65. J. A. Farrar, A. J. Thomson, M. R. Cheesman, D. M. Dooley and W. G. Zumft, *FEBS Lett.*, **1991**, 294, 11.

66. P. M. H. Kroneck, W.E. Antholine, D. H. W. Kastrau, G. Buse, G. C. M. Steffens, W. G. Zumft, *FEBS Lett.*, **1990**, 268, 274.

67. C. Harding, V. McKee and J. Nelson, *J. Am. Chem. Soc.*, **1991**, 113, 9684.

68. H. Beinert, *Eur. J. Biochem.*, **1997** 245, 521.

69. C.R. Andrew, J. Han, S. de Vries, J. van der Oost, B. A. Averill, T. M. Loehr and J. Sanders-Loehr, *J. Am. Chem. Soc.*, **1994**, 116, 10805.

70. S. Larsson, B. Kallebring, P. Wittung and B. G. Malmstrom, *Proc. Natl. Acad. Sci.*, U.S.A. **1995**, 92, 7167.

71. J. A. Farrar, P. Lappalainen, W. G. Zumft, M. Saraste and A. J. Thomson, *Eur. J. Biochem.*, **1995** 232, 294.

72. C. R. Andrew, P. Lappalainen, M. Saraste, M. T. Hay, Y. Lu, C. Dennison, G. W. Canters, J. A Fee, J. A. Slutter, N. Nakamura and J. Sanders-Loehr, *J. Am. Chem. Soc.*, **1995**, 117, 10759.

73. C. R. Andrew, R. Fraczkiewicz, R. S. Czernuszewicz, P. Lappalainen, M. Saraste and J. Sanders-Loehr, *J. Am. Chem. Soc.*, **1996**, 118, 10436.

74. S. E. Wallace-Williams, C. A. James, S. de Vries, M. Saraste, P. Lappalainen, J. van der Oost, M. Fabian, G. Palmer and W. H. Woodruff, *J. Am. Chem. Soc.*, **1996**, 118, 3986.

75. T. Tsukihara, H. Aoyama, E. Yamashita, T. Tomizaki, H. Yamaguchi, K. Shinzawa-Itoh, R. Nakashima, R. Yaono and S. Yoshikawa, *Science*, **1995**, 269, 1069.

76. M. Wilmanns, P. Lappalainen, M. Kelly, E. Sauer-Eriksson and M. Saraste, *Proc. Natl. Acad. Sci.* U.S.A., **1995**, 92, 11955.

77. E. I. Solomon, *Copper Coordination Chemistry: Biochemical and Inorganic Perspectives*, Eds. K. D. Karlin and J. Zubieta, Adenine Press, New York, **1983**, 1-22.

78. H. A. O. Hill., *Chem. Br.*, **1976**, 12, 119.

79. D. E. Fenton, *Pure Appl. Chem.*, **1989**, 61, 903.

80. E. Bouwman, W. L. Driessen and J. Reedijk, *Coord. Chem. Rev.*, **1990**, 104, 143.

81. N. Kitajima and W. B. Tolman, *Progress in Inorganic Chemistry*, Ed. K. D. Karlin, John Wiley, New York, **1995**, 43, 420.

82. E. John, P. K. Bharadwaj, J. A. Potenza, H. J. Schugar, *Inorg. Chem.*, **1986**, 25, 3065.

83. L. Casella, M. Gullotti, E. Suardi, M. Sisti, R. Pagliarin and P. Zanello, *J. Chem. Soc., Dalton Trans.*, **1990**, 2843.

84. N. Kitajima, K. Fujisawa and Y. Moro-oka, *J. Am. Chem. Soc.*, **1990**, 112, 3210.

85. P. K. Coughlin, A. E. Martin, J. C. Dewan, E. Watanabe, J. E. Bulkowski, J. M. Lehn and S. J. Lippard, *Inorg. Chem.*, **1984**, 23, 1004.

86. J. De Mendoza, E. Mesa, J. C. Rodriguez-Ubis, P. Vasquez, F. Vogtle, P. M. Windscheif, K. Rissanen, J. M. Lehn, D. Lilienbaum, R. Ziessel, *Angew. Chem., Int. Ed. Engl.*, **1991**, 30, 1331.

87. M. G. B. Drew, D. Marrs, J. Hunter and J. Nelson, *J. Chem. Soc., Dalton Trans.*, **1992**, 11.

88. M. Sato, S. Nagae, M. Uehara, J. Nakaya, *J. Chem. Soc., Chem. Commun.*, **1984**, 1661.

89. Q. Lu, Q. H. Luo, A. B. Dai, G. Z. Hu, *J. Chem. Soc., Chem. Commun.*, **1990**, 1429.

90. J-L. Pierre, P. Chautemps, S. Refaif, C. Beguin, A. El. Marzouki, G. Serratrice, E. Saint-Aman and P. Rey, *J. Am. Chem. Soc.*, **1995**, 117, 1965.

91. K. D. Karlin and J. Zubieta (Eds), *Copper Coordination Chemsitry: Biochemical and Inorganic Perspectives*, Adenine Press, New York, **1983**.

92. K. D. Karlin and Y Gultneh, *Journal of Chemical Education*, **1985**, 62, 11, 983.

93. S. M. Nelson, F. Esho, A. Lavery, and M. G. B. Drew, *J. Am. Chem. Soc.*, **1983**, 105, 5693.

94. A. D. Zuberbuhler, In *Copper Coordination Chemsitry: Biochemical and Inorganic Perspectives*, K. D. Karlin and J. Zubieta (Eds), Adenine Press, New York, **1983**.

95. R. R. Jacobson, Z. Tyeklar, A. Farooq, K. D. Karlin, S. Liu, J. Zubieta, *J. Am. Chem. Soc.*, **1988**, 110, 3690.

96. Z. Tyeklar, R. R. Jacobson, N. Wei, N. Murthy, J. Zubieta and K. D. Karlin, *J. Am. Chem. Soc.*, **1993**, 115, 2677.

97. I. Sanyal, R. W. Strange, N. J. Blackburn and K. D. Karlin, *J. Am. Chem. Soc.*, **1991**, 113, 4692.

98. T. N. Sorrell and A. S. Borovik, *J. Chem. Soc., Chem. Comm.*, **1984**, 1489.

99. L. Casella, M. Gullotti, G. Pallanza and L. Rigoni, *J. Am. Chem. Soc.*, **1988**, 110, 4221.

100. M. Reglier, C. Jorand and B. Waegell, *J. Chem. Soc., Chem. Comm.*, **1990**, 1752.

101. N. Kitajima, K. Fujisawa and Y. Moro-oka, *J. Am. Chem. Soc.*, **1989**, 111, 8975.

102. N. Kitajima, T. Koda, S. Hashimoto, T. Kitagawa and Y. Moro-oka, *J. Am. Chem. Soc.*, **1991**, 113, 5664.

103. N. Kitajima, K. Fujisawa, C. Fujimoto, Y. Moro-oka, S. Hashimoto, T. Kitigawa, K. Toriumi, K. Tatsumi and A. Nakamura, *J. Am. Chem.Soc.*, **1992**, 114, 1277.

104. S. Meenkumari, A. R. Chakravorty, *J. Chem. Soc., Dalton Trans.*, **1992**, 2749 : M. Angaroni, G. A. Ardizzola, T. Beringhell, G. La Monica, D. Gatteschi, N. Masciocchi and M. Moret, *J. Chem. Soc., Dalton Trans.*, **1990**, 3305 and references therein.

105. H. Adams, N. A. Bailey, M. J. S. Dwyer, D. E. Fenton, P. C. Hellier and P. D. Hempstead, *J. Chem. Soc., Chem. Comm.*, **1991**, 1297.

106. H. Adams, N. A. Bailey, M. J. S. Dwyer, D. E. Fenton, P. C. Hellier, P. D. Hempstead and J. M. Latour, *J. Chem. Soc., Dalton Trans.*, **1993**, 1207,

107. K. D. Karlin, Q. F. Gan, A. Farooq, S. Liu and J. Zubieta, *Inorg, Chem.*, **1990**, 29, 2549.

108. P. Hubberstey and C. E. Russell, *J. Chem. Soc., Chem. Comm.*, **1995**, 959.

109. N. S. Hush, *Prog. Inorg. Chem.*, **1967**, 8, 391.

110. M. B. Robin and P. Day, *Adv. Inorg. Radiochem.*, **1967**, 10, 247.

111. T.D. Westmoreland, D. E. Wilcox, M. J. Baldwin, W. B. Mims and E. I. Solomon, *J. Am. Chem. Soc.*, **1989**, 111, 6106.

112. D. N. Hendrickson, R. C. Long, Y. T. Hwang ,H. R. Chang, *Biological and Inorganic Copper Chemsitry*, K. D. Karlin and J. Zubieta (Eds), Adenine Press, New York, **1983**, 223-237.

113. D. Gatteschi, C. Mealli and L. Sacconi, *Inorg. Chem.*, **1976**, 15, 11.

114. R. R. Gagne, C. A. Koval, T. J. Smith and M. Cimolino, *J. Am. Chem. Soc.*, **1979**, 16, 4571.

115. T. D. Westmoreland, D. E. Wilcox, M. J. Baldwin, W. B. Mimms, E. I. Solomon, *J. Am. Chem. Soc.*, **1989**, 111, 6106.

116. M. Dunaj-Jurco, G. Ondrejovic and M. Melnik, *Coord. Chem Rev.*, **1988**, 83, 1-28

117. G. Blondin, J. J. Girerd, *Chem. Rev.*, **1990**, 90, 1359.

118. C. Creutz, H. Taube, *J. Am. Chem. Soc.*, **1969**, 91, 3988.

119. R. P. Houser, V. G. Young, Jr., and W. B. Tolman, *J. Am. Chem. Soc.*, **1996**, 118, 2101.

120. D. M. Dooley, M. A. McGuirl, A. C. Rosenzweig, J. A. Landin, R. A. Scott, W. G. Zumft, F. Devlin and P. J. Stephens, *Inorg. Chem.*, **1991**, 30, 3006.

121. J. A. Farrar, A. J. Thomson, M. R. Cheeseman, D. M. Dooley and W. G. Zumft, *FEBS Lett.*, **1991**, 294, 11.

122. T. H, Stevens, C. T. Martin, H. Wang, G. W. Brudvig, C. P. Scholes, S. I. Chan, *J. Biol. Chem.*, **1982**, 257, 12106.

123. W. E. Antholine, D. H W. Kastrau, G. C. M. Steffens, G. Buse, W. G. Zumft and P. M. H. Kroneck, *Eur. J. Biochem.*, **1992**, 209, 875.

124. J. A. Farrar, F. Neese, P Lappalainen, P. M. H. Kroneck, M. Saraste, W. G. Zumft and A. J. Thomson, *J. Am. Chem. Soc.*, **1996**, 118, 11501.

125. S. E. Wallace-Williams, C. A. James, S. de. Vries, M. Saraste, P. Lappalainen, J. van der Oost, M. Fabian, G. Palmer and W. H. Woodruff, *J. Am. Chem. Soc.*, **1996**, 118, 3986.

126. (a)C. R. Andrew, J. Han, S. de Vries, J. van der Oost, B. A. Averill, T. M. Loehr and J. Sanders-Loehr, *J. Am. Chem. Soc.*, **1995**, 116, 10805. (b) C. R. Andrew, P. Lappalainen, M. Saraste, M. T. Hay, Y. Lu, C. Dennison, G. W. Canters, J. A. Fee, C. E. Slutter, N. Nakamura, and J. Sanders-Loehr, *J. Am. Chem. Soc.*, **1995**, 117, 10759.

127. R. K. Chanda, R. Kumar and D. G. Tuck, *Can. J. Chem.*, **1987**, 665, 1336.

128. J. A. Farrrar, V. McKee, A. H. R. Al-Obaidi, J. J. McGarvey, J. Nelson and A. J. Thomson, *Inorg. Chem.*, **1995**, 34, 1302.

129. C. Harding, J. Nelson, M. C. R. Symons and J. Wyatt, *J. Chem. Soc., Chem. Commun.*, **1994**, 2499.

130. J. A. Farrrar, R. Grinter, F. Neese, J. Nelson and A. J. Thomson, *J. Chem. Soc., Dalton Trans.*, **1997**, 4083.

131. R. R. Gagne, C. A. Koval and T. J. Smith, *J. Am. Chem. Soc.*, **1977**, 99, 8367.

132. R. C. Long and D. Hendrickson, *J. Am. Chem. Soc.*, **1983**, 105, 1513.

133. H. Okawa, M. Tadokoro, Y. Aratake, M. Ohba, K. Shindo, M. Mitsumi, M. Koikawa, M. Tomono and D. E. Fenton, *J. Chem. Soc., Dalton Trans.*, **1993**, 253.

134. S. K. Mandal, L. K. Thompson, K. Nag, J. P. Charland and E. J. Gabe, *Inorg. Chem.*, **1987**, 26, 1391.

135. B. Srinivas and P. S. Zacharias, *Polyhedron*, **1992**, 11, 1949.

136. A. W. Addison, *Inorg. Nucl. Chem. Lett.*, **1976**, 12, 899.

137. R. R. Gagne, L. M. Henling and T. J. Kistenmacher, *Inorg. Chem.*, **1980**, 19, 1226.

Chapter 2

1. K. D Karlin, Y. Gultneh. *Prog. Inorg. Chem.*, **1987**, 35, 219-328.

2. N. Kitajima, Y. Moro-oka, *Chem. Rev.*, **1994**, 94, 737-757.

3. S. Mahapatra, J.A. Halfen, E. C. Wilkinson, G. Pan, X. Wang, V. G. Young Jr., C. J. Cramer, L. Que, Jr., and W. B. Tolman. *J. Am Chem. Soc.*, **1996**, 118, 11555.

4. E. I. Solomon, M. J. Baldwin, and M. D. Lowery, *Chem. Rev.*, **1992**, 92, 521

5. E. I. Solomon, F. Tuczek, D.E. Root, C. A. Brown, *Chem. Rev.*, **1994**, 94, 827.

6. Z. Tyeklar, R. R. Jacobson, N. Wei, N. N. Murthy, J. Zubieta and K. D. Karlin, *J. Am Chem. Soc.*, **1993**, 115, 2677.

7. N. Kitajima, K. Fujisawa, C. Fujimoto, Y. Moro-oka, S. Hashimoto, T. Kitigawa, K. Toriumi, K. Tatsumi and A. Nakamura, *J. Am. Chem. Soc.*, **1992**, 114, 1277-1291.

8. K. Fujisawa, M. Tanaka, Y. Moro-oka, N. Kitajima, *J. Am. Chem. Soc.*, **1994**, 116, 12079-12080.

9. (a) K. McKillop, PhD Thesis, QUB, **1987**. (b) K. D. Karlin and Z. Tyeklar, *Bioinorganic Chemistry of Copper*, Eds Chapman and Hall, New York, **1993**.

10. A. Messerschmidt. In *Bioinorganic Chemistry of Copper*, K. D. Karlin and Z. Tyeklar Eds., Chapman and Hall, New York, 1993; 471-484.

11. (a) G. T. Babcock, M. Wikstrom, *Nature*, **1992**, 356, 301. (b) J. A. Fee, W.E. Antholine, C. Fan, R. J. Gurbiel, K. Surerus, M. Werst, B. M. Hoffman, In *Bioinorganic Chemistry of Copper*, K. D. Karlin and Z. Tyeklar Eds., Chapman and Hall, New York, **1993**, 485-500.

12. N. Wei, N. N. Murthy, Q. Chen, J. Zubieta and K. D. Karlin, *Inorg. Chem.*, **1994**, 33, 1953.

13. M.C. Brenner, J. P. Klimman. *Biochemistry*, **1989**, 28, 4664.

14. S.O. Pember, K. A. Johnson, J. J. Villafranca, S. J. Benkovic, *Biochemistry*, **1989**, 28, 2124.

15. N. Wei, N. Murthy, and K. D. .Karlin, *Inorg. Chem.*, **1994**, 33, 6093.

16. K. D. Karlin, N. Wei, B. Jung, S. Kaderli, and A. D. Zuberbuhler, *J. Am. Chem.Soc.*, **1991**, 113, 5868.

17. K. D. Karlin, N. Wei, B. Jung, S. Kaderli, P. Niklaus, A. D. Zuberbuhler, *J. Am. Chem. Soc.*, **1993**, 115, 9506.

18. K. Uozumi, Y. Hayashi, M. Suzuki and A. Uehara, *Chem. Lett.*, **1993**, 963.

19. M.R. Malachowski, H. B. Huynh, L. J. Tomlinson, R. S. Kelly and J. W. Furbee Jr., *J. Chem. Soc., Dalton Trans.*, **1995**, 31.

20. E. T. Adman, *Adv. Prot. Chem.*, **1991**, 42, 145.

21. T. N. Sorrell and D. L. Jameson, *Inorg. Chem.*, **1982**, 21, 1014.

22. S. Chen, J. F. Richardson and R.M. Buchanan, *Inorg. Chem.*, **1994**, 33, 2376.

23. C. Chuang, K. Lim, Q. Chen, J. Zubieta and J.W. Canary, *Inorg. Chem.*, **1995**, 34, 2562.

24. K. D. Karlin, J. C. Hayes, S. Juen, J. P. Hutchinson and J. Zubieta, *Inorg. Chem.*, **1982**, 21, 4106.

25. I. Sanyal, R.W. Strange, N. J. Blackburn and K. D. Karlin, *J. Am. Chem. Soc.*, **1991**, 113, 4692.

26. G.G. Morgan, PhD. Thesis, The Open University 1995.

27. E. C. Alyea, G. Ferguson, M. Jennings, Z. Xu, *Polyhedron*, **1990**, 9, 739.

28. R. Uma, R. Viswanathan, M. Palaniandavar and M. Lakshminarayanan, *J. Chem. Soc., Dalton Trans.*, **1994**, 1219.

29. L. J. Wilson and N. J. Rose, *J. Am. Chem. Soc.*, **1968**, 90, 6041.

30. E. C. Alyea, G. Ferguson, M. Jennings, B Li, Z. Xu, X. You and S. Liu, *Polyhedron*, **1990**, 9, 2463.

31. R. Uma, R. Viswanathan, M. Palaniandavar and M. Lakshminarayanan, *J. Chem. Soc. Dalton Trans.*, **1994**, 1219.

32. C. A. Hunter and J. K. M. Sanders, *J. Am. Chem. Soc.*, **1990**, 112, 5525.

33. C. A. Hunter, P. T. Leighton and J. K. M. Sanders., *J. Chem.Soc. Perkin., Trans.* I, **1989**, 547.

34. G. R. Desiraju in Crystal Engineering - The design of organic solids, Elsevier Science **1989**.

35. N. Ramasubbu, P. Parthasarathy and P. Murray-Rust., *J. Am. Chem. Soc.*, **1986**, 108, 4308

36. A. Dunand and R. Gerdil, Acta Cryst., B40, 59, **1984**.

37. P. H. Rieger, Electrochemistry, Chapman and Hall, 2nd Edition, **1994**.

38. B. D. Hibbert, Introduction to Electrochemistry, Macmillan, physical Science Series, **1993**.

39. P. T. Kissinger and W. R. Heineman, *J. Chemical Ed.*, **1983**, 60, 702.

40. M. J. Powers and T. J. Meyer, *J. Am. Chem. Soc.*, **1980**, 102, 1289.

41. A. J. Bard and L. R. Faulkner, Electrochemical Methods. Fundamentals and Applications, John Wiley and Sons, New York, **1980**.

42. M. R. Malachowski, H. B. Huynh, L. J. Tomlinson, R. S. Kelly and J. W. Furbee Jr., *J. Chem. Soc., Dalton Trans.*, **1995**, 31.

43. N. Wei, N. N. Murthy and K. D. Karlin, *Inorg. Chem.*, **1994**, 33, 6093.

44. K. D. Karlin and J. K. Yandell, *Inorg. Chem.*, **1984**, 23, 1184.

45. K. D. Karlin, B. I. Cohen, J. C. Hayes, A. Farooq, J. Zubieta, *Inorg. Chem.*, **1987**, 26 147.

46. C. Chuang, K. Lim, Q. Chen, J. Zubieta and J.W. Canary, *Inorg. Chem.*, **1995**, 34, 2562.

47. P. P. Paul, A. Tyeklar, A. Farooq, K. D. Karlin, S. Liu, J. Zubieta, *J. Am. Chem. Soc.*, **1990**, 112, 2430.

48. K. D. Karlin, J. C. Hayes, S. Juen, J. P. Hutchinson, J. Zubieta, *Inorg. Chem.*, **1982**, 21, 4106.

49. N. Wei, N. N. Murthy and K. D. Karlin, *Inorg. Chem.*, **1994**, 33, 6093.

50. K. D. Karlin, N. Wei, B. Jung, S. Kaderli, P. Niklaus and A. D. Zuberbuhler, *J. Am. Chem. Soc.*, **1993**, 115, 9506.

Chapter 3

1. B. Dietrich, J. -M Lehn and J. -P. Sauvage, *Tetrahedron Lett.*, **1969**, 34, 2885.

2. L. F Lindloy, *The Chemistry of Macrocyclic Ligand Complexes*, Cambridge University Press, Cambridge, 1989.

3. J.-M. Lehn and J.-P. Sauvage, *J. Am. Chem. Soc.*, **1978**, 100, 4914.

4. H. E. Simmons and C. H. Park, *J. Am. Chem. Soc.*, **1968**, 90, 2431.

5. B. Dietrich. J. -M Lehn and J. -P. Sauvage, *Tetrahedron*, **1973**, 29, 1629.

6. J. Nelson, V. McKee and G. Morgan, *In Progress in Inorganic Chemistry*, **1998**, 47, 167-316.

7. I.I. Creaser, J MacB, Harrowfield, A. J. Herlt, A. M Sargeson, M. R. Snow and J Springborg, *J. Am. Chem. Soc.*, **1977**, 99, 3181.

8. J. Nelson and D. McDowell, *Tetrahedron Lett.*, **1988**. 385.

9. M. G. B. Drew, D. McDowell and J. Nelson, *Polyhedron*, **1988**, 7, 2229.

10. K. Ragunathan and P. K. Bharadwaj, *Polyhedron*, **1995**, 14, 693.

11. G. Morgan, *PhD Thesis*, The Open University, U.K, **1995**.

12. N. Martin, *PhD Thesis*, The Queen's University of Belfast, U. K. **1996.**

13. M. J. Hunter, PhD Thesis, The Open University, U. K, 1991.

14. N. F. Curtis, *Coord. Chem. Rev.*, **1968**, 13, 3-47.

15. P. H. Smith, M. E. Barr, J. R. Brainard, D. K. Ford, H. Freiser, S. Muralidharan, S. D. Reilly, R. R. Ryan, L. A. Silks III and W. Yu. *J. Org. Chem.*, **1993**, 58, 7939.

16. C. Harding, V. McKee and J. Nelson, *J. Am. Chem, Soc.*, **1991**, 113, 9684.

17. A. Al-Obaidi, G- Baranovic, J. Coyle, C. G. Coates, J. J..Mc Garvey, V. McKee and J Nelson, *Inorg, Chem.*, **1998**, 37, 3567.

18. N. Wei, N. Murthy, and K. D. Karlin, *Inorg. Chem.*, **1994**, 33, 6093.

19. J. Coyle, M. G. B. Drew, C. J Harding, J. Nelson and R. M. Town, *J. Chem. Soc., Dalton Trans.*, **1997**, 123.

20. A. M. Sargeson, *Pure Appl Chem.*, **1986**, 58, 1511.

21. R. T. Morrison and R. N. Boyd, *Organic Chemistry*, Allyn and Bacon, Inc., **1987**.

22. M. Gerloch. E. C Constable, *Transition metal Chemistry*, VCH Weinheim. New York, Basel, Cambridge and Tokyo, **1994**.

23. M. E. Barr, P. H. Smith, W. E. Antholine and B. J. Spencer, *J. Chem. Soc., Chem Commun.*, **1993**, 1649.

24. C. Harding, J. Nelson, J. Wyatt and M. C. R. Symons, *J. Chem. Soc., Chem Commun.*, **1991**, 2499.

25. K. Nakamoto, *Infra-red and Raman Spectra of Inorganic and Coordination Compounds*, 5th Ed., J. Wiley and Sons, Inc., **1998**.

26. J. A. Farrar, *Inorg. Chem.*, **1995**, 34, 1302.

27. A. P. Shreve, S. Franzen, S. E. Wallace-Williams, M. E. Barr and W. H. Woodruff, Poster presentation at XV ICORS University of Pittsburgh, Pittsburgh, PA, **1996**.

28. G. Feher, *Phys. Rev.*, **1956**, 103, 500 also G. Feher, *Phys. Rev.*, **1959**, 114, 1219.

29. A. Schweiger, *Electron Nuclear Double Resonance of Transition Metal Complexes with Organic ligands*, **1982**, Springer-Verlag Berlin Heidelberg New York.

30. D.J.E.Ingram, *Biological and Biochemical Applications of Electron Spin Resonance*, Adam Hilger Ltd, London.

31. G. H. Rist and J. S. Hyde, *J. Chem. Phys.*, **1968**, 49, 2449 and G. H. Rist and J. S. Hyde, *J. Chem. Phys.* **1969**, 50, 4532.

32. J. Huttermann and R. Kappl, *J. Metal Ions in Biological Systems*, **1987**, 22, 1-80.

33. H.L. Van Camp, R. H. Sands and J. A. Fee, *J. Chem. Phys.*, **1981**, 75, 2098.

34. J. A. Farrar, R. Grinter, F. Neese, J. Nelson and A. J. Thomson, *J. Chem. Soc., Dalton Trans.*, **1997**, 4083.

35. D. C. Apperley, W. Clegg, S. Coles, J. L. Coyle, N. Martin, B. Maubert, V. McKee and J. Nelson, *J. Chem. Soc., Dalton Trans.*, **1999**, 229.

36. S. J. Lippard and J. M. Berg, in *Principles of Bioinorganic Chemistry*, University Science Books, 1994.

37. W. Kaim and J. Rall, *Angew. Chem. Int. Ed. Engl.*, **1996**, 35, 43.

38. S. Knapp, T. P. Keenan, X. Zhang, R. Fikar, J. A. Potenza, H. J. Schugar, *J. Am. Chem. Soc.*, **1990**, 112, 3452.

39. A. M. Sargeson, *Pure Appl. Chem.*, **1986**, 58.1511 and references contained therein.

40. J. K. M. Saunders and B. K. Hunter in 'Modern N. M. R. Spectroscopy' Oxford University Press, **1988**.

41. M. Mehring, High Resolution NMR in solids, 2nd Edn., Springer-Verlag, Berlin, Heidelberg and New York.

42. N. Murthy, K. D. Karlin, I. Bertini and C. Luchinat, *J. Am. Chem. Soc.*, **1997**, 119, 2156.

43. C. Creutz and H Taube, *J. Am. Chem. Soc.*, **1969**, 91, 3988.

44. M. Gerloch, E. C. Constable, In *Transition Metal Chemistry*, Weinheim, **1994**.

45. M. Q. Vande Linde, K. Juntunen, Ole Mols, M. B. Ksebati, D. Ochrymowycz and D. B. Rorabacher, *Inorg. Chem.*, **1991**, 30, 5037.

46. D. K. Coggin, J. A. Gonzalez, A. M. Kook, C. Bergman, T. D. Brennan, W. R. Scheidt, D. M. Stanbury and L. J. Wilson, *Inorg. Chem.*, **1991**, 30, 1125.

47. C M. Groeneveld, J. van Rijn, J. Reedijk and G, Canters, *J. Am. Chem. Soc.*, **1988**, 110, 4893.

48. S. Knapp, T. P. Keenan, X. Zhang, R. Fikar, J. A. Potenza and H. J. Schugar, *J. Am. Chem. Soc.*, **1990**, 112, 3452.

49. J. A. Goodwin, D. M. Stanbury, L.J. Wilson, C. W. Eigenbrot and W. R. Scheidt, *Inorg. Chem.*, **1987**, 109, 2979.

50. S. Flanagan, J. A. Gonzalez, J. E. Bradshaw, L. J. Wilson, D. M. Stanbury, K. J. Haller and W. R. Scheidt, In *Bioinorganic Chemistry of Copper*, K. D. Karlin and Z. Tyeklar Eds, Chapman and Hall, New York, **1993**, 91-97.

51. J. A. Goodwin, G. A. Bodager, L.J. Wilson and D. M. Stanbury, W. R. Scheidt. *Inorg. Chem.*, **1989**, 28, 35.

52. C M. Groeneveld, S. Dahnil, B. Reinhammar and G.W. Canters. *J. Am Chem. Soc.*, **1987**, 109, 3247.

53. J. K. Beattie, D. J. Fensom, H. C. Freeman, E. Woodcock. H. A. O Hill, A. O. Stokes. *Biochim. Biophys. Acta*, **1975**, 405, 109-114.

54. J. McMaster, R. L. Beddoes, D. Collinson, D. R. Eardley, M. Helliwell and C. D. Garner, *Chem. Eur. J.*, **1996**, 2, 685.

55. T. M. Donlevy, L. R. Gahan and T. W. Hambley, *Inorg. Chem.*, **1994**, 33, 2668.

56. J. L. Van Winkle, J. D. McClure and P. H. Williams, *J. Org. Chem*, **1965**, 31 3300, also J. Chin, M. Banaszezyk, V. Jubian and X. Zou, J. Am. Chem. Soc., **1989**, 103, 4073.

Chapter 4

1. S. Iwata, C. Ostermeier, B. Ludwig and H. Michel, *Nature*, **1995**, 376, 660.
2. J. Nelson, V. McKee and G. G. Morgan, in *Progress in Inorganic Chemistry*, 1998, 47, 167-316.
3. L. F. Lindloy, *The Chemistry of Macrocyclic Ligand Complexes*, Cambridge University Press, Cambridge, **1989**.
4. N. Martin, Ph.D Thesis, The Queen's University of Belfast, **1996**.
5. M. S. Newman and H. A. Karnes, *J. Org. Chem.*, **1966**, 31, 3980.
6. S. Brooker, P. D. Croucher and F. M. Roxburgh, *J. Chem. Soc., Dalton Trans.*, **1996**, 3031.
7. J. M. Downes, J. Whelan and B. Bosnich., *Inorg. Chem.*, **1981**, 20, 1081-1086.
8. C. Harding, V. McKee and J. Nelson, *J. Am Chem. Soc.*,**1991**, 113, 9684.
9. G.G. Morgan, PhD Thesis, The Open University 1995.

Appendix 1

1. F. N. Neese, Ph.D. Thesis, **1996**, University of Konstanz, Germany.
2. J.J Girerd, *J. Chem. Phys.*, **1983**, 79, 1766.
3. A. K. Kok, M. J. Ondrechen, *J. Am. Chem. Soc.*, **1985**, 107, 6161.
4. S. B. Piepho, E. R. Krausz and P N. Schatz, *J. Am. Chem. Soc.*, **1978**, 100, 2966.
5. N. M. Atherton, *Principles of Electron Spin Resonance*, 2nd Ed. Ellis Horwood Prentice Hall, **1993**.
6. B. J. Hathaway, *Chem. Rev.*, **1983**, 52, 87.

Appendix 2

1. G. M. Sheldrick, SHELXL-86, Acta Cryst, A46, **1990**, 467.
2. G. M. Sheldrick, SHELXL-93, University of Gottingen.